METALS. SUPERCONDUCTORS

Galvanomagnetic properties of the $Al_{1-x}Si_x$ nonequilibrium substitutional solid solutions

N. E. Sluchanko, V. V. Glushkov, S. V. Demishev, M. V. Kondrin, N. A. Samarin, V. V. Brazhkin, I. Braunserade, and V. V. Moshchalkov

General Physics Institute, Russian Academy of Sciences, 117942 Moscow, Russia
(Submitted June 2, 1998)
Fiz. Tverd. Tela (St. Petersburg) **41**, 3–10 (January 1999)

Galvanomagnetic characteristics of the $Al_{1-x}Si_x$ solid solutions ($x<12$ at. %) have been studied within a broad range of temperatures (1.8–290 K) and magnetic fields (up to 15 T). An anomaly in the concentration dependence of the Hall coefficient $R_H(x,T=290\ \mathrm{K})$ has been revealed near the boundary of absolute instability ($x<8.5$ at. %) of compounds in the $Al_{1-x}Si_x$ series. The variation of the Hall coefficient and of the magnetoresistance in the $Al_{1-x}Si_x$ series at low ($T<77$ K) temperatures is analyzed within models taking into account the anisotropy in conduction-band electron scattering. © *1999 American Institute of Physics.* [S1063-7834(99)00101-X]

The $Al_{1-x}Si_x$ nonequilibrium solid solutions prepared by quenching under high pressure (up to 10 GPa) exhibit considerable variations in physical properties induced by substitutional effects.[1,2] It was shown[1] that an increase in the concentration of silicon dissolved in the fcc Al matrix up to 20 at. % raises the superconducting transition temperature up to 11 K [for polycrystalline Al, $T_c=1.18$ K (Ref. 3)]. The increase of T_c by an order of magnitude in the immediate vicinity of the lattice instability[4] is accompanied by a noticeable softening of the phonon spectrum in the $Al_{1-x}Si_x$ solid solutions.[5] Such features observed in compounds having a simple crystal structure permit one to consider the $Al_{1-x}Si_x$ fcc solid solutions as a convenient model for studying the nature of superconductivity enhancement near a lattice instability.

This matter is of practical importance in connection with the recent discovery of new classes of superconducting compounds, namely, HTSC oxides, organic metals, and superconducting fullerenes, for which the proximity to a crystal-structure instability is, in most cases, the deciding factor for the onset and enhancement of superconductivity.

The comparatively recent study[6,7] of a number of physical properties of the $Al_{1-x}Si_x$ model solid solutions permitted one to connect the observed variations in the characteristics of the superconducting state in these substances with a considerable enhancement of the electron-phonon interaction near a lattice instability. At the same time no comprehensive investigation has been made thus far of the effect of the nonequilibrium state of silicon in a disordered solid-solution matrix on carrier characteristics.

Studies of dilute ($x\leqslant 0.01$) Al-based solid solutions showed that the behavior of the Hall coefficient and magnetoresistance in weak magnetic fields at low temperatures is extremely sensitive to the nature of carrier scattering by the impurity potential, and that it is governed by the specific characteristics of the dissolved element and the actual type of substitution-induced lattice defects.[8–12] In the Al(Si) system, the host lattice disorder is associated not only with the random distribution of the substitutional impurity but with local strain-induced changes in the scattering potential as well. Therefore studies of the galvanomagnetic properties of the $Al_{1-x}Si_x$ solid solutions may improve our understanding of the role played by disorder in an fcc structure, which may be caused both by Si substitution for Al and by changes in the lattice parameters in the vicinity of a structural instability. Of additional interest is the possibility of analyzing the changes in the conduction-band parameters and of correlating them with the characteristics of the system in normal and superconducting states for large (up to 20 at. %) concentrations of the dissolved element.

The results of preliminary studies of the Hall effect in $Al_{1-x}Si_x$ solid solutions carried out at helium temperatures have already been published.[13] This work reports an integrated investigation of the galvanomagnetic properties of $Al_{1-x}Si_x$ solid solutions within a broad range of temperatures (1.6–290 K) and magnetic fields (up to 15 T).

1. EXPERIMENTAL TECHNIQUES

Samples of $Al_{1-x}Si_x$ solid solutions with silicon contents up to 11.5 at. % were prepared by quenching under high-pressure (up to 10 GPa) in a TOROID-type chamber.[14] The procedures of synthesis, characterization, and preparation for measurements of $Al_{1-x}Si_x$ samples were described elsewhere.[2,6,7] A 99.9 at. % pure Al sample subjected to thermal and pressure treatments similar to those used in the synthesis of the samples under study was employed as a reference.

The resistivity ρ and Hall voltage U_H of samples shaped as cylindrical plates were measured in the van der Pauw

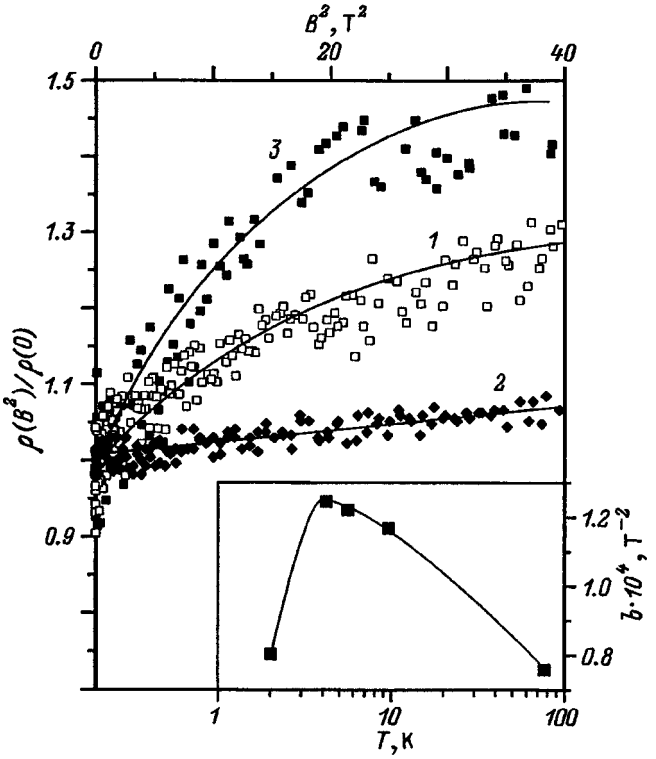

FIG. 1. Field dependences of the magnetoresistance of (*1*) pressure-treated Al and $Al_{0.965}Si_{0.035}$ solid solution in (*2*) the initial and (*3*) annealed state. The inset shows the temperature dependence of the magnetoresistance coefficient $b=\Delta\rho/\rho B^2$ of an $Al_{0.935}Si_{0.065}$ sample.

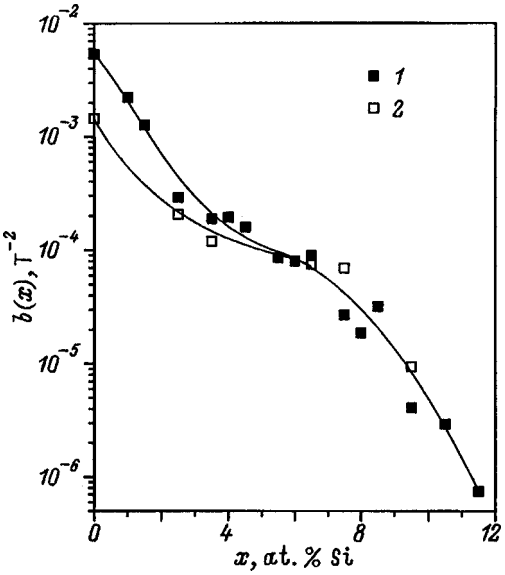

FIG. 2. Concentration dependence of the $b\,(x)$ coefficient in the $Al_{1-x}Si_x$ series for (*1*) 4.2 K and (*2*) 77 K.

geometry (see, e.g., Ref. 15). The computer-controlled experimental arrangement for galvanomagnetic measurements permitted measuring the ρ and U_H parameters with a relative error down to 0.1%. The random error was determined by the measurement arrangement chosen and varied within 5–10%, depending on the actual experimental conditions.

The field dependences were studied by means of a superconducting coil generating magnetic fields of up to 6 T (temperature range 1.6−20 K), a SOLENOID setup of the GPI, a water-cooled, Bitter-type magnet producing fields of up to 15 T (4.2−77 K), and a water-cooled electromagnet for magnetic fields of up to 1.3 T (290 K). A detailed description of the techniques used to measure the galvanomagnetic properties can be found in Ref. 16.

2. EXPERIMENTAL RESULTS

Figure 1 shows experimental magnetic-field dependences of the resistivity ρ obtained for $Al_{1-x}Si_x$ compositions at helium temperature. In the weak magnetic-field domain, magnetoresistance $\Delta\rho\,(B)/\rho$ is a quadratic function of external magnetic field. $Al_{1-x}Si_x$ samples with low silicon contents exhibit a tendency to saturation with further increase of B. For example, the $\rho\,(B)$ dependence of pressure-treated Al measured at helium temperature (curve *1* in Fig. 1) shows significant deviations from linearity in fields $B>3$ T when plotted against B^2. The observed behavior correlates with the saturation-type relation typical of pure Al (Ref. 17) and Al-based dilute alloys.[10–12]

$Al_{1-x}Si_x$ alloys with $x\geqslant 2$ at. % do not show any trend to saturation in $\rho\,(B^2)$ curves throughout the magnetic-field range covered, $B<15$ T (curve *2* in Fig. 1). Note that a growth in the concentration of dissolved silicon results in a considerable decrease in the amplitude of positive magnetoresistance. The coefficient of proportionality $b\,(x)=\Delta\rho/(\rho B^2)$ derived by fitting the experimental data to a linear relation in the (ρ, B^2) coordinates falls off monotonically at helium temperature from $1.26\times10^{-3}\,T^{-2}$ for $x=1.5$ at. % to $7.5\times10^{-7}\,T^{-2}$ for $x=11.5$ at. % (Fig. 2). The rate of variation of the magnetoresistance coefficient $b\,(x)$ is seen to decrease noticeably within the concentration interval of 3−7 at. % Si (see Fig. 2). It should be stressed that this concentration interval is characterized only by an insignificant decrease of the residual resistivity in the $Al_{1-x}Si_x$ series,[6] which permits one to assign the observed slowing down in the rate of variation of the magnetoresistance parameter $b\,(x)$ to the reduced efficiency of conduction-band electron scattering from lattice defects, which are induced by increasing concentration of the substitutional impurity.

Note also that an anneal (~10 min at $T=620$ K) initiating total decomposition of supersaturated solid solutions in the $Al_{1-x}Si_x$ series brings about an increase of magnetoresistance. After the anneal, the $\rho\,(B^2)$ relation turns out to resemble the behavior of the magnetoresistance of pure aluminum and exhibits a trend to saturation in strong magnetic fields (curve *3* in Fig. 1).

The positive magnetoresistance of samples heated above the helium temperature also decreases due to the appearance of an additional channel of scattering by phonons (see the inset to Fig. 1). The magnetoresistance of $Al_{1-x}Si_x$ behaves with temperature, on the whole, similarly to the way observed earlier in the dilute alloys $Al_{1-x}Ge_x$ ($x<0.005$) and $Al_{1-x}Zn_x$ ($x<0.002$).[18] At the same time, one should not overlook the unusual decrease of magnetoresistance in $Al_{1-x}Si_x$ samples with $x>3$ at. % as the temperature is lowered to 1.8 K.

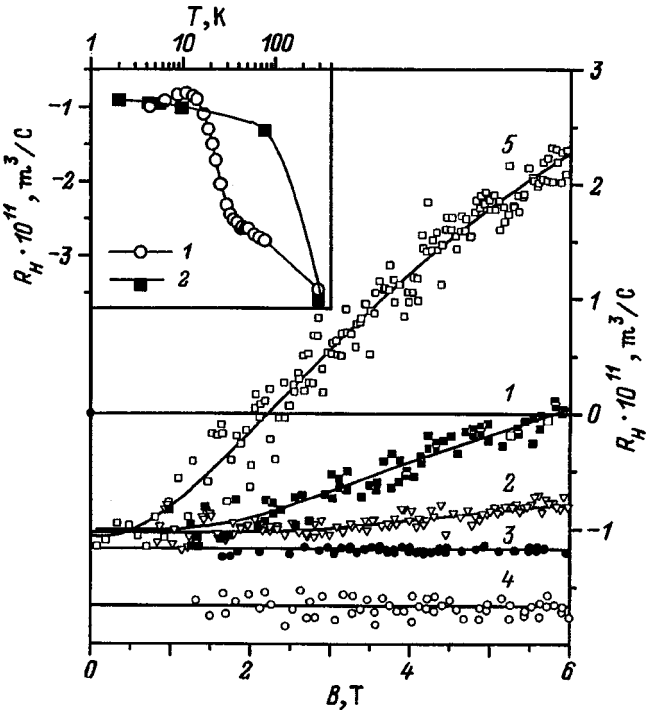

FIG. 3. $R_H(B)$ dependences for $Al_{1-x}Si_x$ solid-solution compositions (at. %): *1* — 0, *2* — 1.5, *3* — 4.5, and *4* — 9.5, as well as for (*5*) annealed $Al_{0.935}Si_{0.065}$ sample. The inset shows temperature dependences of the Hall coefficient for (*1*) pure polycrystalline Al (Ref. 20) and (*2*) $Al_{0.935}Si_{0.065}$ solid solution.

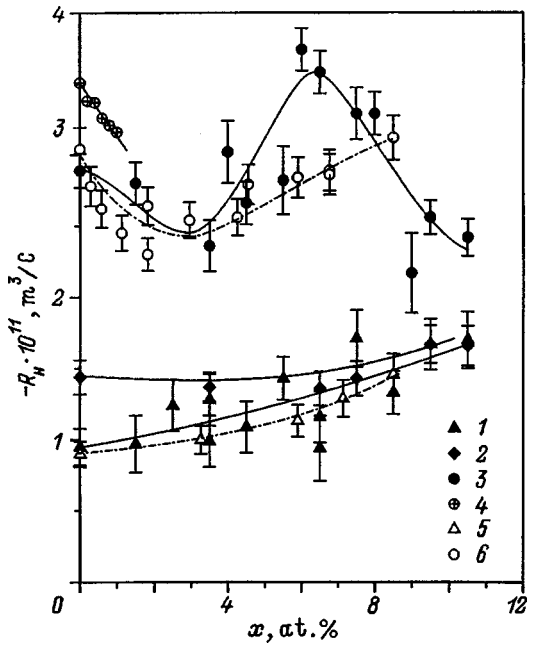

FIG. 4. Concentration dependence of the Hall coefficient R_H for $Al_{1-x}Si_x$ solid solutions obtained at T(K): (*1*) 4.2, (*2*) 77, and (*3*) 290; (*4*) $R_H(x)$ relation for Al-Si alloys (Ref. 19) and (*5*) variation of the Hall coefficient R_H(4.2 K) and (*6*) R_H(290 K) under successive annealing of the metastable composition $Al_{0.915}Si_{0.085}$

It should be stressed that unlike the relation specified by the Kohler rule (see, e.g., Refs. 8 and 10) the quantity $\Delta\rho(B,x)/\rho$ is not a universal function of the ratio $B/\rho(T,x,B=0)$, with deviations from this relation becoming particularly pronounced within the $0.02<x<0.08$ composition interval.

The results of an investigation of the Hall coefficient R_H of pressure-treated aluminum and of $Al_{1-x}Si_x$ solid solutions performed at helium temperature in magnetic fields of up to 6 T are presented graphically in Fig. 3. Note the nonlinear behavior of the R_H dependence on magnetic field for Al and $Al_{1-x}Si_x$ solid solutions containing up to 1.5 at. % Si (see, e.g., curves *1* and *2* in Fig. 3). The considerable increase of the sign-inversion field for the R_H parameter (up to 5.7 T) of the Al sample compared to that for pure polycrystalline Al [for aluminum, $B_{\text{inv}}=0.05$ T (Ref. 17)] should apparently be assigned to the effects of thermal and pressure treatments and to an increase in the number of structural defects in a sample synthesized under pressure.

Dissolution of silicon in aluminum causes a further increase of B_{inv}. For $x_{\text{Si}}>2.5$ at. %, the Hall coefficient R_H at helium temperature is practically constant in fields of up to 6 T, whereas the absolute value of R_H (4.2 K) increases with silicon content (curves *3* and *4* in Fig. 3; see also Fig. 4). Measurements of $R_H(B, 4.2\text{ K})$ performed on the SOLENOID setup for the compositions with $x=0.035$ and 0.065 showed the Hall coefficient to remain constant within experimental error in magnetic fields of up to 15 T.

Because the value of B_{inv} determines the transition from the weak to strong magnetic-field range,[17,19] the absence of changes in $R_H(B)$ within the field range covered should apparently be assigned to the small carrier mean free path as a result of strong impurity scattering in $Al_{1-x}Si_x$ compounds. Thus the values of R_H measured in this work for $Al_{1-x}Si_x$ compositions with $x>0.03$ in magnetic fields of up to 15 T correspond to the weak magnetic-field limit. Note that Hall coefficient measurements on $Al_{1-x}Si_x$ alloys obtained by annealing $Al_{1-x}Si_x$ compounds for ~ 10 min at $T=620$ K, a process initiating total decomposition of the supersaturated solid solutions, permitted determination of the inversion field $B_{\text{inv}}=2.1$ T (see, e.g., curve *5* in Fig. 3). Obviously enough, the observed decrease of B_{inv} compared to the inversion field for pressure-treated Al should be associated with a partial annealing of intrinsic defects in the Al-based fcc matrix.

The essentially nonmonotonic temperature dependence of the Hall coefficient in Al observed[20] in the weak-field domain (curve *1*, inset to Fig. 3) stimulated interest in investigation of the nature of $R_H(T)$ variation in the $Al_{1-x}Si_x$ substitutional solid-solution series. The typical $R_H(T)$ relation obtained in this work (curve *2*, inset to Fig. 3) demonstrates a noticeable decrease of the Hall coefficient with increasing temperature observed to occur in the immediate vicinity of the helium temperature [$dR_H/dT \approx -1.4-2\times10^{-7}$ m³/(C·K) for $T\leqslant 15$ K]. This behavior is typical of all compounds in the $Al_{1-x}Si_x$ series within the Si concentration interval studied. It should be stressed that in contrast to the results obtained[20] for pure Al, in $Al_{1-x}Si_x$ compositions with $x>0.01$ one did not observe nonmonotonic behavior of $R_H(T)$ throughout the temperature range studied, $2<T<290$ K (see inset to Fig. 3).

At the same time, near room temperature, the concentration dependence of the Hall coefficient derived from mea-

surements on $Al_{1-x}Si_x$ samples having different compositions was found to be essentially nonmonotonic (curve *3*, Fig. 4). For comparison, Fig. 4 presents also $R_H(x)$ relations for $Al_{1-x}Si_x$ compounds measured at helium (1) and nitrogen (2) temperatures. One readily sees that, despite the large scatter among the absolute values of the Hall coefficient observed at helium temperature, the $R_H(x)$ relations obtained at $T=4.2$ and 77 K are fitted, within experimental error, by monotonic curves, whereas the room-temperature Hall coefficient depends on Si concentration in $Al_{1-x}Si_x$ in an essentially nonlinear manner. The initial decrease of $R_H(x)$ in absolute magnitude for $x<3$ at. % correlates perfectly with the results of Ref. 21 (curve *4* in Fig. 4), to be replaced by a growth of $|R_H|$ within the $3\leqslant x\leqslant 7$ at. % interval, with a maximum of $R_H=3.5\times10^{-11}$ m^2/C at $x\approx6.5$ at. %. The small discrepancies in absolute value of the Hall coefficient $R_H(x,\ 290\ K)$ existing between the results of Ref. 21 ($x\leqslant0.01$) and the present data should be associated, in our opinion, with the specific features of our method of high-pressure synthesis[14], which offers a possibility of considerably reducing the vacancy concentration in the samples under study.[2,13]

To obtain additional information on the behavior of the concentration dependence $R_H(x,290\,K)$, Hall coefficient measurements in states corresponding to different stages in decomposition of the $Al_{0.92}Si_{0.08}$ solid solution were performed under step-by-step isothermal annealing. Decomposition of the metastable state in $Al_{1-x}Si_x$ compounds is accompanied by depletion of the solid-solution matrix associated with formation of submicron-size semiconducting silicon inclusions.[22] In this case the transport properties of an alloy undergoing a phase transformation, in particular, the electrical resistance, could be expected to be determined not by inclusions of the semiconducting Si, but rather by percolation over the depleted ''low-Ohmic'' $Al_{1-x}Si_x$ solid-solution matrix, following the variation of silicon content in the metallic phase. This assumption is experimentally supported by the observed correlation between the residual-resistivity relation $\rho_0(x_{Si})$ in the Al-Si series and the decrease of ρ_0 of the $Al_{1-x}Si_x$ solid solution under annealing.[16] In these conditions, the silicon content in metallic phase at an intermediate stage of $Al_{1-x}Si_x$ solid-solution decomposition is derived from the transition temperature to superconducting state, with due account of the well-known $T_c(x)$ relation for the $Al_{1-x}Si_x$ compounds.[1]

Hall-coefficient measurements made under step-by-step annealing of the solid solution reveal a change in the nature of the $R_H(x)$ relation observed as the temperature is increased from the helium (curve *5* in Fig. 4) to room temperature (curve *6* in Fig. 4). It should be pointed out that at helium temperature the behavior of the Hall coefficient in different annealing stages of an $Al_{0.915}Si_{0.085}$ sample follows closely the concentration dependence $|R_H|(x,\ 4.2\ K)$ (see curves *1* and *5* in Fig. 4). At the same time, in the course of decomposition of the $Al_{0.915}Si_{0.085}$ solid solution, one does not observe, near room temperature, any maximum in the $R_H(x)$ dependence for intermediate states of the $Al_{1-x}Si_x$ system (curve *6* in Fig. 4).

The observed differences in the behavior of the $R_H(x,\ 290\ K)$ dependences within the $4\leqslant x\leqslant8.5$ at. % concentration region (curves *3* and *6* in Fig. 4) should be assigned, in our opinion, to microscopic-scale differences existing among samples of the $Al_{1-x}Si_x$ solid-solution system; these differences appear in the course of the high-pressure synthesis and the subsequent step-by-step annealing of the starting $Al_{0.915}Si_{0.085}$ composition, in which the latter passes through a sequence of states corresponding to alloys whose $Al_{1-x}Si_x$ matrix contains submicron-size semiconducting Si inclusions. Within this concentration region, one may expect polyatomic silicon clusters to dominate over single atoms in the fcc lattice of the Al solid solution.[7] In these conditions, the early stages of solid-solution decomposition involve apparently local rearrangement of the cluster structure, which changes irreversibly the silicon valence-electron configuration and, hence, the scattering impurity potential.

In later stages of decomposition of supersaturated $Al_{1-x}Si_x$ solid solutions (with silicon concentration in the metallic phase of the Al-Si alloy less than 4 at. %), as also in $Al_{1-x}Si_x$ solid solutions within the corresponding concentration region, the metallic phase is dominated by single silicon atoms. In this concentration region, the increase of $|R_H|_{T=290\,K}$ observed to occur during annealing (curve *6* in Fig. 4) correlates with the concentration dependence $R_H(x,290\ K)$ in the $Al_{1-x}Si_x$ series (curve *3* in Fig. 4), and is apparently caused by the decrease of silicon concentration in the metallic phase accompanying the solid-solution decomposition. The small differences between the absolute values of the Hall coefficient can be associated with the disappearance of local strains and defects generated in the course of quenching under high pressure.

3. DISCUSSION OF RESULTS

The galvanomagnetic characteristics of metals in weak magnetic fields are determined by the anisotropy of electronic state scattering at the Fermi surface.[23,24] In the isotropic case (the electron mean free path $l=\text{const}$) and for a spherical Fermi surface, the relations $R_H=R_{FE}=(nec)^{-1}$, $\Delta\rho/\rho=0$ (Ref. 24) corresponding to the free-electron approximation are upheld. Thus the substantial deviation of the R_H of the $Al_{1-x}Si_x$ solid solutions from $R_{FE}=-3.47\times10^{-11}$ m^3/C observed in this work at low temperatures attests to the need of taking into account the anisotropy even in the conditions of strong impurity scattering.

Direct inclusion of galvanomagnetic characteristics[23] is made difficult by the lack of quantitative information on the $l(\mathbf{k})$ dependence. At the same time if one makes some simplifying assumptions, measurements of R_H and $\rho(B)$ can provide qualitative information on the anisotropy of the l parameter on the Fermi surface.[24] In particular, the Hall coefficient and magnetoresistance can be expressed within the three-carrier-group model[8–12] through the averaged mean free paths l_- and l_{++} of electrons and holes of the second Brillouin zone, and l_{--} of the third-zone electrons[24]:

$$\Delta\rho/\rho_0=(R_{FE}B/\rho_0)^2 g_m(l_{--}^3+l_{++}^3)/l_-^3\,, \tag{1}$$

$$R_H=R_{FE}(1+g_h(l_{--}^2-l_{++}^2)/l_-^2)\,, \tag{2}$$

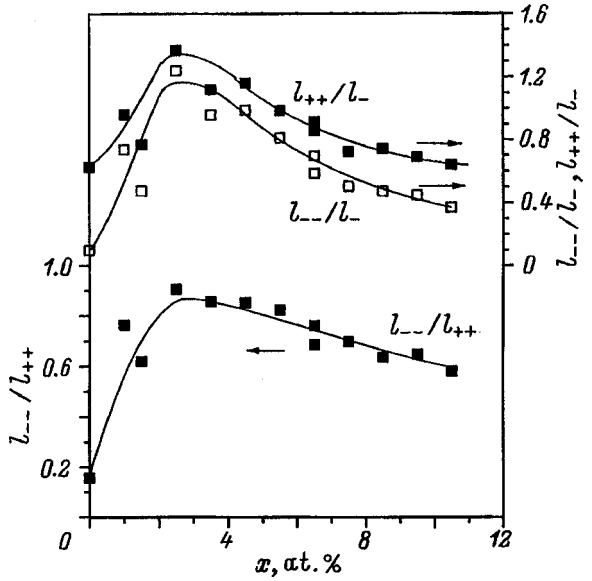

FIG. 5. Variation of carrier scattering characteristics with increasing silicon concentration in the $Al_{1-x}Si_x$ series obtained at 4.2 K.

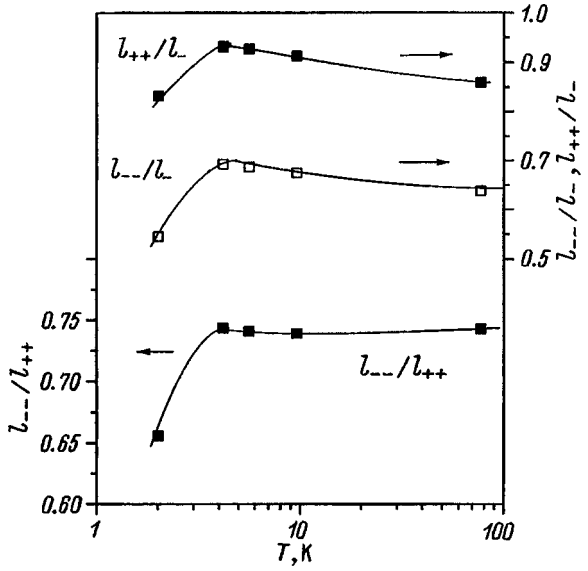

FIG. 6. Temperature dependence of the anisotropy parameters for the $Al_{0.935}Si_{0.065}$ solid solution.

where g_m and g_n are coefficients depending on the Fermi-surface geometry (numerical calculations made for Al-Si alloys give for them 50 and 1.875, respectively[11]).

The results of the calculations of l_-/l_{++} and l_-/l_{--}, as well as of the anisotropy parameter l_{--}/l_{++} (see Ref. 12), made using Eqs. (1) and (2) for $T=4.2$ K are presented graphically in Fig. 5. The $l_{--}<l_{++}$ relationship is seen to be satisfied at helium temperature throughout the $Al_{1-x}Si_x$ concentration range covered. The growth of silicon concentration in the solid solution up to 2.5 at. % is accompanied by an increase of the l_{--}/l_- and l_{++}/l_- parameters, which should be assigned to an increasing efficiency of electron scattering at the spherical part of the aluminum Fermi surface. This behavior characterizes apparently the anisotropy of carrier scattering by single scattering-impurity atoms, and it is in agreement with the cases of Al-based dilute solid solutions studied earlier[8–11]. Further increase of silicon content in the solid solution ($x>2.5$ at. %) entails a monotonic falloff of both l_{--}/l_- and l_{++}/l_-, as well as of the anisotropy parameter l_{--}/l_{++}. Because this concentration region is characterized by formation of polyatomic silicon clusters in the fcc lattice[7] and gives rise to considerable distortions in short-range structure comparable to the mean-free path, the observed behavior should be associated with the specific features of silicon atoms in metastable state originating from the essential role played by Si–Si-type bonds. It should be stressed that the metastable state of silicon in the metallic matrix is responsible also for the noticeable deviation of the residual resistivity of the $Al_{1-x}Si_x$ solid solutions from a linear behavior for $x>2.5$ at. %.[7]

An increase in temperature turns on the phonon scattering mechanism and results in effective mixing of electronic states and Fermi-surface isotropization.[20] A comparison of the Hall coefficient behavior for pure polycrystalline Al (Ref. 20) and $Al_{1-x}Si_x$ solid solutions (see inset in Fig. 3) stresses the need of taking into account the electron spectrum anisotropy when calculating conduction-band electron characteristics for $Al_{1-x}Si_x$ solid solutions down to nitrogen temperature.

An analysis of the temperature dependences of the Hall coefficient and magnetoresistance of an $Al_{0.935}Si_{0.065}$ sample (see insets to Figs. 1 and 3) made in terms of model (1) and (2) shows that, as the temperature is increased from helium to nitrogen temperature, the anisotropy parameter l_{--}/l_{++} remains practically constant (Fig. 6). This trend, characteristic of $Al_{1-x}Si_x$ compositions with $x>3$ at. %, indicates apparently that the mean free paths for electronic and hole states in the third and second Brillouin zones behave similarly with temperature. At the same time the decrease of l_{--}/l_- and l_{++}/l_- with increasing temperature (Fig. 6) implies, in our opinion, that the electronic states at zone edges interact stronger with the phonon subsystem than the states in the spherical part of the Fermi surface.

It should be stressed that the three-group model, Eqs. (1) and (2), used in the analysis of experimental data provides only qualitative information on the anisotropy of carrier scattering in the $Al_{1-x}Si_x$ solid solutions.[10,24] Note also that the applicability of Eqs. (1) and (2) within a broad range of substitutional impurity concentrations is based on the aluminum Fermi surface in the objects under study retaining its topology.[24] A change in the Fermi surface topology in $Al_{1-x}Si_x$ solid solutions may originate both from the nonisovalent character of silicon substitution for Al and from the associated change in the parameters of the aluminum fcc lattice. At the same time x-ray emission and NMR spectroscopy of the $Al_{1-x}Si_x$ solid solutions suggest that the conduction band and density of states at Fermi level remain practically unchanged in the $Al_{1-x}Si_x$ series,[7] which supports the validity of using the three-carrier group model, Eqs. (1) and (2), in making estimates based on experimental data (Figs. 2 and 4).

Close to room temperature ($T\sim 290$ K), inelastic scattering mechanisms become dominant, which reduces Fermi-surface anisotropy effects in $Al_{1-x}Si_x$ compounds. In these

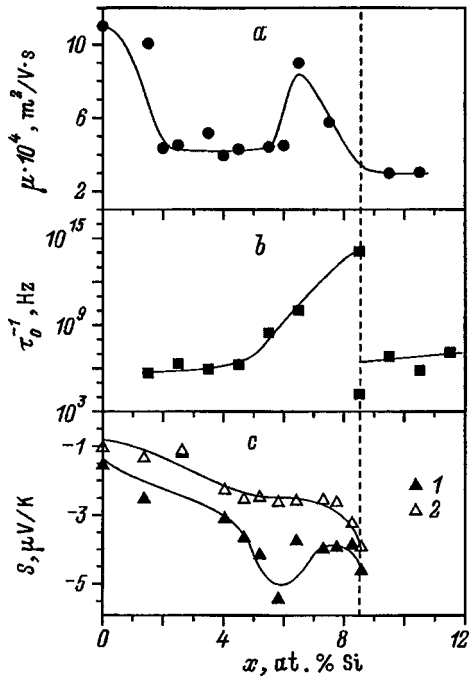

FIG. 7. (a) Concentration dependence of carrier mobility μ (x, 290 K) in the $Al_{1-x}Si_x$ solid-solution series; (b) Variation of the characteristic frequency of atomic displacements τ_0^{-1} with increasing silicon concentration in the $Al_{1-x}Si_x$ series (Ref. 22); (c) Variation of the Seebeck coefficient $S(x)$ under successive annealing of the $Al_{0.915}Si_{0.085}$ solid solution (*1*) in the vicinity of the maximum in $S(T)$ and (*2*) at $T=250$ K (Ref. 25).

conditions, experimental relations $R_H(x,\ 290\,\mathrm{K})$ and $\rho(x,\ 290\,\mathrm{K})$ in the $Al_{1-x}Si_x$ series can be used to estimate the behavior of the Hall mobility $\mu_H=R_H/\rho$ in the single-carrier-type approximation. Within this approximation, the nonmonotonic Hall-coefficient relation $R_H(x)$ near $x\approx 6.5$ at. % ($T=290$ K) (curve *3* in Fig. 4) will give rise to a maximum in the $\mu_H(x)$ curve (see Fig. 7a). Because the conduction-band parameters are unaffected by increasing Si content in $Al_{1-x}Si_x$ solid solutions, the substantial contribution to the observed features may be due to a change in the nature of carrier scattering in the vicinity of the spinodal.

A comparison with a study of the stability region and decomposition kinetics shows that supersaturated $Al_{1-x}Si_x$ solid solutions are absolutely unstable above room temperature for Si concentrations higher than ~ 8 at. %.[22] As one approaches the spinodal with increasing x in the $Al_{1-x}Si_x$ series, the characteristic atomic-displacement times become shorter to reach $\tau_0^{-1}\approx 10^{-13}$ s at $x\approx 8$ at. % (Fig. 7b). The observed increase in atomic mobility near the concentration $x\approx 6.5$ at. % turns out to correlate with the growth of the Hall mobility (Fig. 7a and 7b).

Thus based on the models used here approaching the region of instability for an fcc structure with increasing temperature is accompanied by a simultaneous increase of mobility in both the atomic and electronic subsystems. An additional argument for the existence of this correlation in the behavior of the mobilities comes from the considerable enhancement of electron-phonon interaction (EPI) and an increase in the superconducting transition temperature T_c with increasing silicon concentration in the $Al_{1-x}Si_x$ solid solutions. In view of the significant increase of the diffusion contribution $S(x,T)$ with increasing x (Ref. 25) and of the anomalous concentration dependence of the Seebeck coefficient (Fig. 7c), revealed in the study of the temperature dependence of thermopower in the $Al_{1-x}Si_x$ series, an adequate analysis of the variation of carrier characteristics in this system requires taking adequately into account EPI effects in the vicinity of the structural lattice instability.

It should be pointed out in this connection that a comprehensive inclusion of the totality of the factors governing the magneto-transport and thermoelectrical characteristics of nonequilibrium metals would presently be difficult for a number of reasons. Indeed, formation of polyatomic Si clusters generates considerable local strains in the fcc structure of the $Al_{1-x}Si_x$ solid solutions. The existence in a doped metal of such regions having a dynamically disordered lattice gives rise to additional inelastic scattering of conduction electrons by impurity atoms,[26] which requires taking into account interference effects in electron-phonon-impurity scattering.[26,27] On the other hand, inclusion of strong EPI in the atomic-chain model suggests[28] that the description of the properties of the electron and phonon subsystems is possibly made with violation of the adiabatic approximation. Thus the existing difficulties do not permit quantitative estimation of the characteristics of the $Al_{1-x}Si_x$ solid solutions studied in this work.

To conclude, we have presented the results of a study of the magnetoresistance $\Delta\rho(B)/\rho$ and Hall coefficient R_H in nonequilibrium $Al_{1-x}Si_x$ solid solutions ($x<0.12$) performed within a broad range of temperatures ($1.6<T<300$ K) and magnetic fields ($B<15$ T). Because of the strong impurity scattering in $Al_{1-x}Si_x$ compounds with $x>0.02$, the B variation range covered here satisfies the conditions typical of weak magnetic fields ($\omega\tau\ll 1$). The features observed in the concentration dependences $\Delta\rho(B)/\rho(x,T)$ and $R_H(x,T)$ for compositions in the $Al_{1-x}Si_x$ series, as well as the variation of galvanomagnetic coefficients under step-by-step isothermal annealing, which leads to decomposition of supersaturated $Al_{1-x}Si_x$ solid solutions, are associated with a change in the efficiency of conduction-band electron scattering by lattice defects originating from substitution of silicon for aluminum.

An anomalous behavior of the Hall coefficient $|R_H(x)|$ corresponding to a substantial increase of the Hall mobility of conduction-band electrons μ_H in $Al_{1-x}Si_x$ compositions with silicon contents $x\approx 6.5$ at. % has been revealed near room temperature. The possibility of a correlation between the variation of $R_H(x,\ 290\,\mathrm{K})$ and $\mu(x,\ 290\,\mathrm{K})$ with the increase of atomic mobility under strong electron-phonon coupling near the boundary of absolute instability in the $Al_{1-x}Si_x$ solid solutions is discussed.

The nature of variation in the conduction-band electron mean free path with silicon concentration in the $Al_{1-x}Si_x$ series has been analyzed within the three carrier-group model. The results obtained suggest the need of taking into account the carrier scattering anisotropy when considering the transport characteristics of $Al_{1-x}Si_x$ solid solutions at helium and intermediate temperatures.

Support of the Russian Fund for Fundamental Research

(Grants 96-02-16176 and 98-02-17163), INTAS (Grant 96-0451), and of the ''Fullerenes and Atomic Clusters'' and ''Fundamental Spectroscopy'' Programs of the Ministry of Science and Technology of the Russian Federation is gratefully acknowledged.

*)E-mail: glushkov@H.gpi.ru

[1] V. F. Degtyareva, G. V. Chipenko, I. T. Belash, O. I. Barkalov, and E. G. Ponyatovskii, Phys. Status Solidi A **89**, K127 (1985).
[2] V. V. Brazhkin, S. V. Popova, R. N. Voloshin, L. M. Stanev, and I. G. Spirov, High Press. Res. **6**, 333 (1992).
[3] *Physical Quantities* [In Russian], edited by I. S. Grigor'ev and E. Z. Meĭlikhov (Énergoatomizdat, Moscow, 1991), 1232 pp.
[4] N. E. Sluchanko, V. V. Glushkov, S. V. Demishev, N. A. Samarin, and V. V. Brazhkin, Ferroelectrics **177**, 17 (1996).
[5] J. Chevrier, J. B. Suck, J. J. Capponi, and M. Perroux, Phys. Rev. Lett. **61**, 554 (1988).
[6] V. V. Brazhkin, V. V. Glushkov, S. V. Demishev, Yu. I. Kosichkin, N. E. Sluchanko, and A. I. Shulgin, J. Phys. F **5**, 5933 (1993).
[7] N. E. Sluchanko, V. V. Glushkov, S. V. Demishev, N. A. Samarin, A. K. Savchenko, J. Singleton, W. Hayes, V. V. Brazhkin, A. A. Gippius, and A. I. Shulgin, Phys. Rev. B **51**, 1112 (1995).
[8] K. Böning, K. Pfändner, P. Rosner, and M. Schlüter, J. Phys. F **5**, 1176 (1975).
[9] C. Papastaikoudis, E. Rocofillou, W. Tselfes, and K. Chountas, Z. Phys. B **25**, 131 (1976).
[10] W. Kesternich, H. Ullmaier, and W. Schilling, J. Phys. F **6**, 1867 (1976).
[11] P. Papazisi, A. Travlos, and C. Papastaikoudis, J. Phys.: Condens. Matter **2**, 6189 (1990).
[12] N. Boukos and C. Papastaikoudis, Phys. Rev. B **46**, 4508 (1992).
[13] V. V. Brazhkin, V. V. Glushkov, S. V. Demishev, Yu. V. Kosichkin, N. E. Sluchanko, and A. I. Shul'gin, Fiz. Tverd. Tela (St. Petersburg) **35**, 481 (1993) [Phys. Solid State **35**, 248 (1993)].
[14] L. G. Khvostantsev, L. F. Vereshchagin, and A. P. Novikov, High Temp.-High Press. **9**, 637 (1977).
[15] K. Seeger, *Semiconductor Physics* (Springer, Wien, 1973; Mir, Moscow, 1977), 631 pp.
[16] V. V. Glushkov, Dissertation, Cand. Phys.-Math. Sci., MFTI, Moscow (1996), 138 pp.
[17] E. S. Borovik, Zh. Eksp. Teor. Fiz. **23**, 83 (1952).
[18] E. Rocofillou and C. Papathanassopoulos, Physica B **100**, 99 (1980).
[19] K. Førsvoll and I. Holwech, Philos. Mag. **10**, 921 (1964).
[20] R. D. Barnard and A. E. E. Abdel Rahiem, J. Phys. F **10**, 2739 (1980).
[21] J. M. Bradley and J. Stringer, J. Phys. F **4**, 839 (1974).
[22] N. E. Sluchanko, V. V. Glushkov, S. V. Demishev, A. K. Savchenko, and V. V. Brazhkin, J. Phys.: Condens. Matter **6**, 9079 (1994).
[23] M. J. Tsui, J. Phys. Soc. Jpn. **13**, 979 (1958).
[24] W. Kesternich, Phys. Rev. B **13**, 4227 (1976).
[25] N. E. Sluchanko, V. V. Glushkov, S. V. Demishev, M. V. Kondrin, N. A. Samarin, V. V. Brazhkin, and V. V. Moshchalkov, Zh. Éksp. Teor. Fiz. **113**, 339 (1998) [JETP **86** 190 (1998)].
[26] A. P. Zhernov, N. A. Chernoplekov, and É. Mrozan, *Metals with Nonmagnetic Impurities* [In Russian] (Énergoatomizdat, Moscow, 1992), 368 pp.
[27] M. Yu. Reĭzer and A. V. Sergeev, Zh. Éksp. Teor. Fiz. **92**, 2291 (1987) [Sov. Phys. JETP **65**, 1291 (1987)].
[28] C. C. Yu and P. W. Anderson, Phys. Rev. B **29**, 6165 (1984).

Translated by G. Skrebtsov

Quantum Monte Carlo investigation of the $2D$ Heisenberg model with $S=1/2$

S. S. Aplesnin

L. V. Kirenskiĭ Institute of Physics, Siberian Branch of the Russian Academy of Sciences, 660036 Krasnoyarsk, Russia

(Submitted July 9, 1998)
Fiz. Tverd. Tela (St. Petersburg) **41**, 116–121 (January 1999)

The two-dimensional ($2D$) Heisenberg model with anisotropic exchange ($\Delta=1-J_x/J_z$) and $S=1/2$ is investigated by the quantum Monte Carlo method. The energy, susceptibility, specific heat, spin-spin correlation functions, and correlation radius are calculated. The sublattice magnetization (σ) and the Néel temperature of the anisotropic antiferromagnet are logarithmic functions of the exchange anisotropy: $1/\sigma+1+0.13(1)\ln(1/\Delta)$. Crossover of the static magnetic structural factor as a function of temperature from power-law to exponential occurs for $T_c/J\approx 0.4$. The correlation radius can be approximated by $1/\xi=2.05T^{1.0(6)}/\exp(1.0(4)/T)$. For La_2CuO_4 the sublattice magnetization is calculated as $\sigma=0.45$, the exchange is $J=(1125-1305)$ K; for Er_2CuO_4 $J\sim 625$ K and the exchange anisotropy $\Delta\sim 0.003$. The temperature dependence of the static structural magnetic factor and the correlation radius above the Néel temperature in these compounds can be explained by the formation of topological excitations (spinons). © *1999 American Institute of Physics.* [S1063-7834(99)02401-6]

Many theoretical works on the two-dimensional ($2D$) Heisenberg antiferromagnet (AF) with a square lattice with spin $S=1/2$ have appeared in the last few years. Substantial theoretical efforts have been made to confirm or reject Anderson's idea of a quantum disordered ground state[1] in the $2D$ Heisenberg model with antiferromagnetic interactions. In a number of works, the critical spin below which there is no long-range AF order at $T=0$ was found to be $S_c=1-3/2$.[2,3] Chakravarty, Halperin, and Nelson,[4] using the renormalization-group method and the nonlinear σ model in $2+1$ space, obtained long-range AF order (LRO) in the ground state. They neglected the Hopf term $h\theta H_{hopf}(\theta=2\pi S)$,[5] which can change the magnetic state substantially. The theories with topological invariants[6] do not assume long-range order in the ground state. A similar result is obtained in the monograph Ref. 7 where, on the basis of the Lieb, Schultz, and Mattis theorem,[8] it is asserted that the two-dimensional spin-1/2 Heisenberg antiferromagnet possesses a ground state which may turn out to be non-Néel and can have either broken translational symmetry or gapless excitations.

Most exact calculations for small lattices 4×4 and 4×6 give AF ordering[9–11] with energy $E/NJ=0.67-0.7$. Advances in computational technology make it possible to use large lattices with $N=26$ and 32,[12,13] which give asymptotic vanishing of the long-range antiferromagnetic order as $\sim 1/N$. Monte Carlo (MC) modeling makes it possible to use lattices ranging in size from 20×20 to 128×128.[14–18] These calculations, which use a variational algorithm[17] and the renormalization group,[19,20] likewise give the existence of $2D$ AF and $T=0$. The type of magnetic state calculated on the basis of variational methods depends on the choice of the initial (trial) wave function and, in some cases, it gives no long-range order in magnets. Trajectory MC methods[15,16,21] employ finite temperatures, and it is difficult to draw any conclusions about the ground state based on an investigation of an isotropic model only.

A number of problems also arise in investigations of the quasi-two-dimensional compounds La_2CuO_4,[22,23] Er_2CuO_4,[24–26] and $Sr_2CuO_2Cl_2$.[27] Experimental investigations of these crystals indicate ionic bonds,[28] while the ordered moment falls in the range $\sigma=0.4-0.44$, which is much less than the theoretical estimates for $2D$ Heisenberg AF $\sigma=0.6-0.64$.[4,29] Above the Néel temperature, up to $(1.5-2)T_N$, there exist strong two-dimensional spin correlations so that the correlation radius varies exponentially, for example, in La_2CuO_4 from 40 Å at 450 K up to 400 Å at 200 K,[23] while the static magnetic structure factor $S(Q)$ varies with temperature very slowly, which also does not agree with theoretical calculations predicting exponential behavior $S(Q)\sim T^2\exp(-A/T)$.[4] In the isostructural compounds La_2NiO_4[30] and La_2CoO_4[31] with spin $S=1/2$ and 3/2, a two-dimensional Ising phase transition is observed in the neutron scattering intensity near $1.02T_N$, in complete analogy with K_2NiF_4 which possesses magnetic anisotropy of the same order of magnitude as La_2CuO_4. The magnetic susceptibility $\chi(T)$ in these compounds[26] at temperatures $T>T_N$ demonstrates anomalous temperature behavior — a very smooth temperature dependence in the region $T_N<T<(1.5-2)T_N$, and an inflection in the temperature dependence $\chi(T)$ at the limit of this interval. Therefore the magnetic moment of the copper ion and the temperature behavior of the spin correlations above T_N are unique and cannot be explained on the basis of existing theoretical calculations in a $2D$ Heisenberg model with $S=1/2$.

Thus, two important problems can be identified from the review presented above. The first problem is the unknown nature of the ground state of a $2D$ AF. Quantum fluctuations that can completely destroy long-range order are very substantial because of the low dimension of the space and the

low spin. The second problem is to explain using the Heisenberg model with nearest-neighbor interaction and to estimate the magnetic moment, temperature dependence of the susceptibility, and static magnetic structure factor $S(Q)$ for $T > T_N$ in quasi-two-dimensional compounds based on copper ions with spin $S=1/2$ without using additional interactions.

In the present paper we use the quantum Monte Carlo method employing a trajectory algorithm.[32] The basic idea of the algorithm is to convert the quantum D-dimensional problem to a classical $(D+1)$-dimensional problem by introducing ''time'' cuts in imaginary time space $0<\tau<1/T$ and to implement an MC procedure in the ''imaginary time — coordinate'' space.

1. MODEL AND METHOD

Let us consider a Heisenberg anisotropic AF with antiferromagnetic nearest-neighbor interaction $(J<0)$ on a square lattice whose sites are occupied by spins $S=1/2$ directed along the OZ axis in the direction of the external field. The Hamiltonian has the form

$$H=-\frac{1}{2}\sum_{h=1}^{4}\sum_{i=1}^{N}\{J^{zz}(h)S_i^zS_{i+h}^z+J^{x,y}(h)\times(S_i^xS_{i+h}^x+S_i^yS_{i+h}^y)\}-\sum_{i=1}^{N}H_i^zS_i^z, \quad (1)$$

where $\Delta=1-J^{x,y}/J^z$ is the easy-axis type exchange anisotropy, H^z is the external magnetic field, and N is the total number of spins.

The MC algorithm and computational method have been described in detail in a previous work.[33] The Hamiltonian is divided into four-spin clusters on a placquette and the commutation between the clusters is taken into account by Trotter's relation. In the present paper, periodic boundary conditions in the Trotter direction and along the lattice are used in the MC procedure. The linear size of the lattice is $L=40,48,64$, and 80 and $m=16$, 32, and 48. The number of MC steps per spin ranges from 3000 to 10000. One MC step is determined by rotating all spins on a $L\times L\times 4m$ lattice. The following were calculated: the energy E, the specific $C=dE/dT$, the magnetization M, the susceptibility in an external field $\chi=M/H$, the pair and four-spin correlations in the longitudinal and transverse spin components, their Fourier spectrum, the sublattice magnetization $\sigma=\lim_{r\to\infty}\sqrt{\mathrm{abs}(\langle S_0^zS_r^z\rangle)}$, and the correlation radius ξ from the approximation of the spin correlation function as

$$R(r)=A/r^{\eta}\exp(-r/\xi), \quad (2)$$

where $R(r)$ is the normalized correlation function $R(r)=|\langle S^z(0)S^z(r)\rangle|-\langle S^z\rangle^2$.

2. DISCUSSION

We shall determine the energy and spin correlation functions of an isotropic AF in the ground state by two methods: asymptotic continuation of these quantities determined for an anisotropic AF with $\Delta=1-J^{x,y}/J^z\to 0$ and for an isotropic AF with $T\to 0$. The finite lattice dimensions employed in the MC calculations cut off the region of long-wavelength excitations at the wave number $k\sim\pi/L$ and limit the minimum exchange anisotropy, which satisfies $\sqrt{\Delta}>\pi/L$. Under this condition the contribution of long-wavelength excitations to the thermodynamics will be exponentially small.

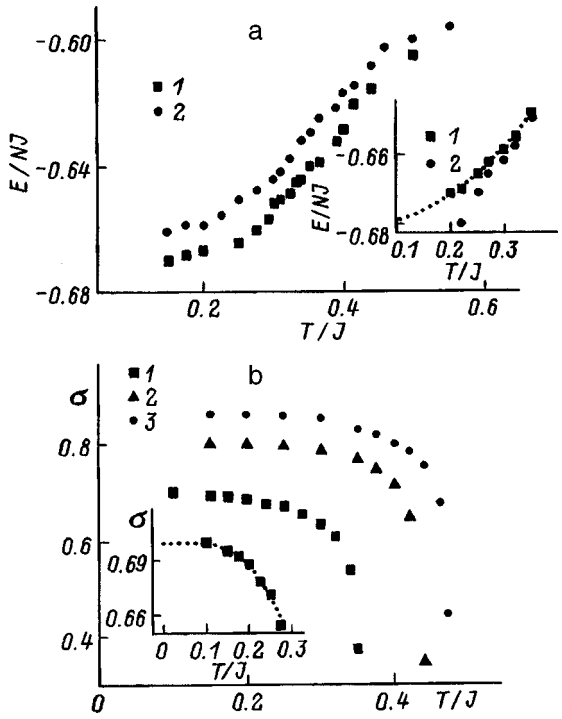

FIG. 1. Temperature dependences of the energy E/NJ of an anisotropic AF with $\Delta=0.02(1)$, $0.075(2)$ and an isotropic AF (inset: $\Delta=0.0, m=32(1)$, $16(2)$) (a) and the sublattice magnetization σ of an AF with $\Delta=0.05(1)$, $0.15(2)$, $0.25(3)$ (b). Inset: The dotted lines show the power-law functions $E=-0.682(4)+0.35T^{2.0(2)}$ (a) and $\sigma=0.70(3)-3.(4)T^{3.(2)}$ (b).

We shall calculate the temperature dependences of the energy, sublattice magnetization, and spin correlation functions for a number of exchange anisotropy constants $\Delta\geqslant 0.005$. The typical dependences are shown in Fig. 1. At low temperatures, less than the gap between the ground and excited state $T<4SJ\sqrt{\Delta(1+\Delta)}$, we extrapolate the computed quantity A using a power law $A=A(T=0)-\alpha T^{\beta}$ (shown by the dotted line in the inset in Fig. 1) and an exponential law $A=A(T=0)-\alpha\exp(-\beta/T)$ with three adjustable parameters α,β, and A at $T=0$. The extrapolated values of E and $\langle S^z(0)S^z(r=1)\rangle$ for an anisotropic AF in the ground state are shown in Fig. 2. The dependence of these quantities on the exchange anisotropy can be approximated by the function $A=A(\Delta=0)\pm 1/\exp(\alpha/\Delta^{\beta})$ with the adjustable parameters α,β, and $A(0)$. The corresponding parameters are: for the energy $\alpha=1.61(7)$, $\beta=0.26(5)$; for the correlation functions $\langle S^z(0)S^z(r=1)\rangle\alpha=2.(1)$, $\beta=0.165(7)$. The energy of the $2D$ isotropic Heisenberg model in the ground state $E=-0.684(6)$ agrees well with the energy obtained by exact diagonalization $E=-0.68445$.[12] The spin-spin correlation function $\langle S^z(0)S^z(r=1)\rangle=-0.120(4)$ agrees quite well with the result $\langle S^z(0)S^z(r=1)\rangle=-0.114(4)$.[11]

The sublattice magnetization can be interpolated by the logarithmic law $1/\sigma=1+0.13(1)\ln(1/\Delta)$ (Fig. 3). In the in-

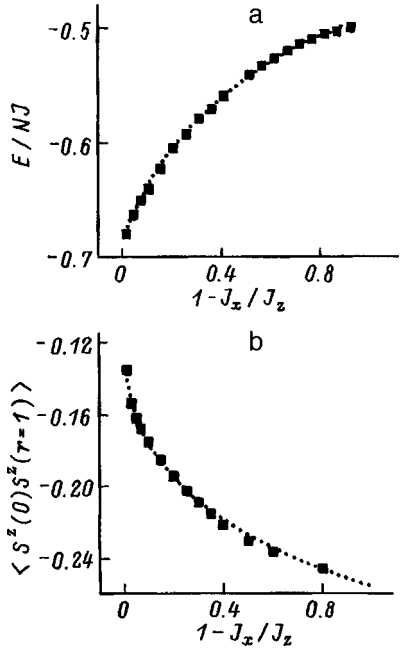

FIG. 2. The energy E/NJ (a) and nearest-neighbors correlation functions $\langle S_0^z S_1^z \rangle$ (b) of an AF in the ground state as a function of the exchange anisotropy $\Delta = 1 - J_x/J_z$. The lines show the interpolation functions $E = -0.684(6) + 1/\exp(1.61(7)/\Delta^{0.26(5)})$, $\langle S^z(0)S^z(r=1)\rangle = -0.120(4) + 1/\exp(2(1)/\Delta^{0.165(7)})$.

set in Fig. 3 the reciprocal of the magnetization is a function of $\ln(\Delta)$ is described well by a linear function. This means that there is no long-range antiferromagnetic order in the ground state in an isotropic ($\Delta = 0$, $\ln\Delta \to \infty$) $2D$ Heisenberg model. For the minimum anisotropy $\Delta = 0.005$ the sublattice magnetization is $\sigma = 0.29$, or (in Bohr magnetons with $g = 2$) $\sigma = 0.58\mu_B$. We shall determine the Néel temperature

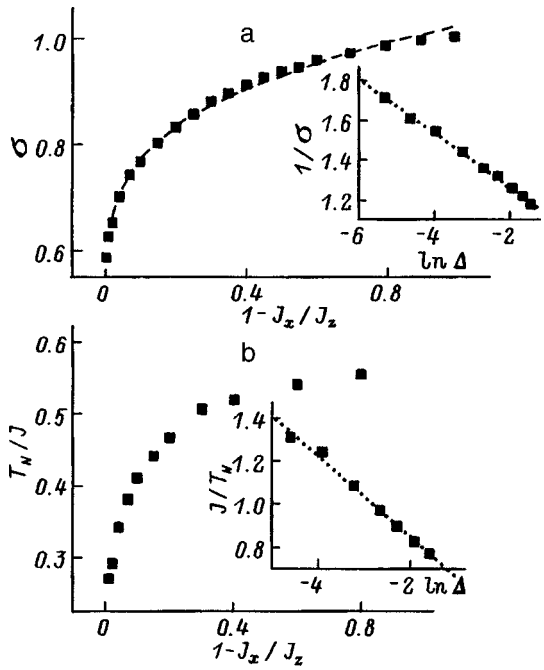

FIG. 3. Sublattice magnetization σ (a) and Néel temperature T_N/J (b) of an AF as a function of the exchange anisotropy. Inset: $1/\sigma$ (a) and J/T_N (b) versus $\ln\Delta$.

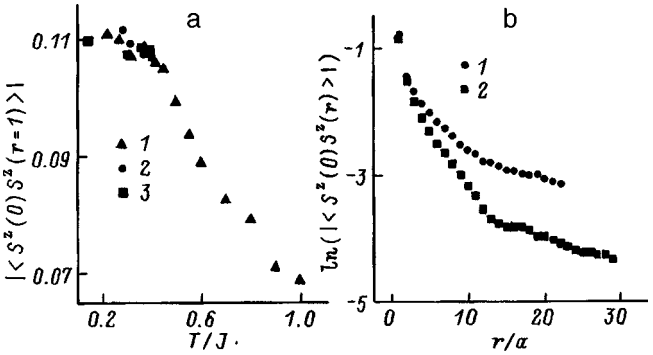

FIG. 4. Correlation functions with respect to the longitudinal components for AFs on 40×40 (*1*), 64×64 (*2*), 80×80 (*3*) lattices at distance $r/a = 1$ (a) and distance dependence of the logarithm of the spin-spin correlation function for $T/J = 0.28$ (*1*) 0.37 (*2*) (b).

of anisotropic AF from the maximum of the heat capacity, the point of inflection of the susceptibility, and $\sigma \to 0$ (Fig. 1). The dependence of $T_N(\Delta)$ on the exchange anisotropy (Fig. 3) likewise can be interpolated well by a logarithmic law for $\Delta \ll 1$ $T_N = 2/\ln(11/\Delta)$.

The temperature dependence of the energy of an isotropic AF in the interval $0.15 \leqslant T/J \leqslant 0.35$ can be approximated by a cubic polynomial with zero coefficients for the odd-numbered powers $E(T) = -0.682(4) + 0.35(3)T^{2.0(2)}$ (Fig. 1). The asymptotic continuation of the spin correlation functions in this interval for the longitudinal and transverse components (Fig. 4) gives $\langle S^z(0)S^z(r=1)\rangle = -0.113(3)$ and $\langle S^+(0)S^-(r=1)\rangle = -0.228(5)$, which agrees well with the results $\langle S^+(0)S^-(r=1)\rangle = -0.22823(2)$.[12] This confirms Anderson's idea of the existence of a singlet ground state, where $2\langle S^z(0)S^z(r=1)\rangle \approx \langle S^+(0)S^-(r=1)\rangle$ and the magnetic state can be represented by a superposition over all realizations of the singlet pairs. In other words, each pair of neighboring spins in the lattice plane is in a singlet state, but the combination of neighboring spins in a pair is always changing. If the singlets are ordered, then the four-spin correlation function at odd distances is greater than at even distances. The MC calculation of $\langle S_0^z S_1^z S_r^z S_{r+1}^z \rangle$ does not lead to this conclusion.

The correlation radius calculated from the distance dependence of the spin-spin correlation function (Fig. 4b) can be approximated well at temperatures $T/J \geqslant 0.26$ by the function $1/\xi = 2.05T^{1.0(6)}/\exp(1.0(4)/T)$, shown in Fig. 5a. In the singlet state the spin correlation function is a power-law function of distance. The excitations in this model are interacting spinons or solitons. The probability of excitation of a spinon (soliton) is $W \sim \exp(-E_s/T)$, where $E_s = J$ in the $1D$ Heisenberg model, and in the $2D$ model the excitation energy of a spinon (soliton) is two times higher since two singlet pairs must be broken in order to preserve cubic symmetry. The average distance between the temperature-excited spinons is $l(T) \sim 1\sqrt{W} \sim \exp(J/T)$. This can be represented in the form of a quasilattice embedded in a gas of singlet pairs (Fig. 6), where the spinons are represented by arrows. The spinons are correlated with one another. The correlation could vary as power law $\xi_s/l \sim A/T^{\alpha}$, where l is the quasilattice constant of the spins and decreases with increasing

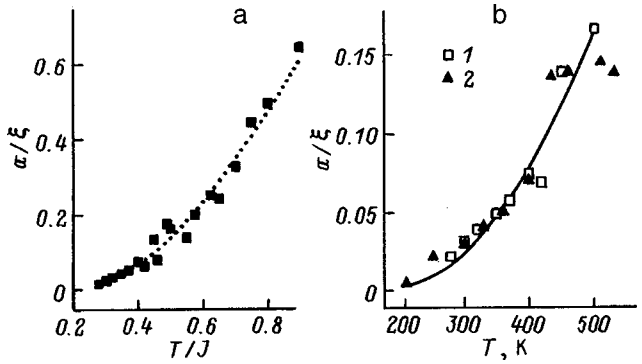

FIG. 5. Reciprocal of the correlation radius a/ξ, calculated by the MC method (a), (b, 1) and measured in a neutron scattering experiment in La_2CuO_4[23] (b, 2).[23]

temperature. The correlation radius at low temperatures should vary exponentially $\xi_s \sim A/T^{\alpha}\exp(J/T)$. There exists a minimum soliton size, determined by the ratio of the surface and volume magnetic energy for which the quasilattice becomes unstable at $T/J=0.37-0.4$.

The static magnetic factor, the Fourier component $S^z(Q)$ at $Q=\pi/a$, varies very little at temperatures $T/J<0.4$ as a function of temperature and the dimensions of the lattice (Fig. 7a). For $T/J>0.4$ the temperature dependence of $S^z(Q)$ is the same as in a paramagnet. At low temperatures the Fourier spectrum of the spin correlation function can be represented as a superposition of the Fourier correlation function of the singlets $S_{SN}(q)\sim A/q^{-(2-\eta)}$ and spinons $S_{SP}(k)\sim B/((k-\pi)^2+1/\xi^2)$. Singlet pairs make the main contribution to the neutron scattering intensity in the limit $q\to\pi$, since the spin density is low and the contribution of the spins is $\sim W_{SP}(q)$. The temperature derivatives of the specific heat and susceptibility in this temperature range (Fig. 8) have a maximum, and $d\chi/dT$ and dC/dT to the right and left of T_c differ substantially. For comparison, the values of $\chi(T)$ and $C(T)$ calculated with a super computer,[16] on a $L=128\times128$ lattice with two orders of magnitude more MC steps than the present work, are shown in Fig. 8. The authors of Ref. 16 also noted violation of the relation $\ln(S(Q)\xi^{-2})\sim\ln(T/J)$ for $T/J=0.35$. Just as in Ref. 16, for $T/J<0.4$ the exponent η in Eq. (2) tends to decrease with temperature from $\eta=0.55$ to 0.35 at $T/J=0.26$.

Weakly anisotropic AFs have two transition temperatures: the Néel temperature, associated with a breakdown of long-range order, and T_c associated with breakdown of topological magnetic formations (solitons). The size of a soliton is inversely proportional to the magnitude of the anisotropy. For this reason, a quasilattice of solitons (spinons) is formed when the exchange anisotropy reaches the critical value $\Delta\approx0.05$ at temperatures $T/J<0.4$. The magnetic structure of the factor $S(Q)$ (Fig. 7b), the spin correlation functions

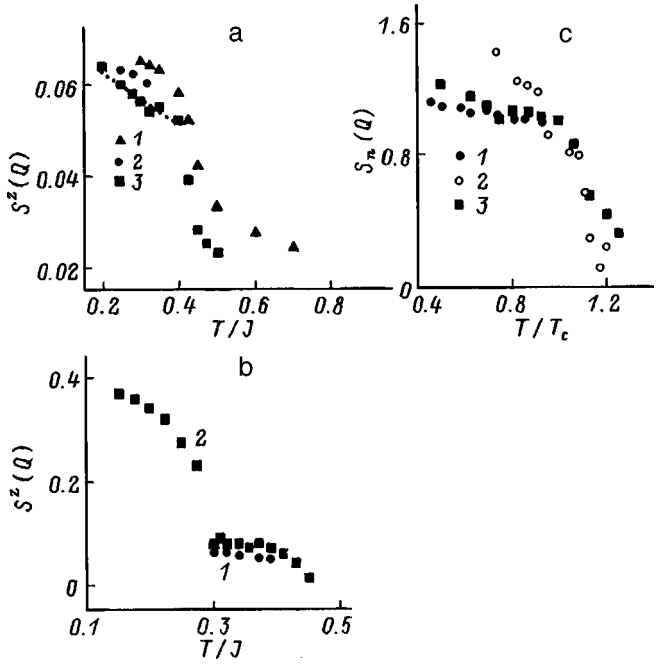

FIG. 7. Static magnetic structure factor $S^z(Q)$ for $Q=\pi/a$ and $L=40$ (*1*), 64 (*2*), 80 (*3*) in the isotropic (a) and anisotropic ($\Delta=0.02$,$L=40$ (*1*), 80 (*2*)) (b) cases as a function of temperature. c — Normalized static magnetic factor $S(Q,T)/S(Q,T=T_c)$, determined by the MC method for $T_c/J=0.4$ (*1*) and from neutron scattering in Er_2CuO_4[24] for $T_c=250$ K (*2*) and in La_2CuO_4[22] for $T_c=450$ K (*3*).

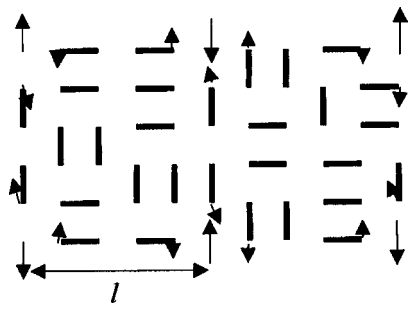

FIG. 6. Schematic representation of a quasilattice of singlet pairs of spins (segments) and spinons (arrows).

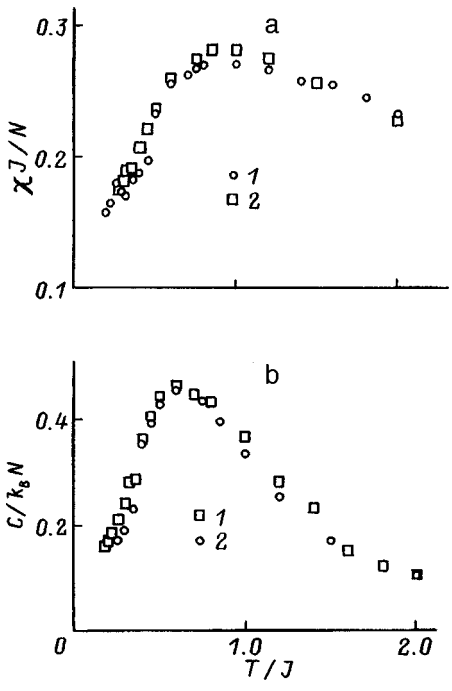

FIG. 8. Susceptibility $\chi J/N$ (a) and specific heat C/k_BN (b) calculated in the present work (*1*) and in Ref. 16 (*2*) as a function of temperature.

$\langle S^z(0)S^z(r=1)\rangle$, and the magnetic susceptibility are virtually temperature independent in the interval $T_N<T<T_c$.

The results obtained explain well the experimental data on the magnetization and the neutron scattering intensity in the quasi-two-dimensional compounds $Sr_2CuO_2Cl_2$,[27] La_2CuO_4,[23], and Er_2CuO_4.[24] The experimental values of the sublattice magnetization for $Sr_2CuO_2Cl_2$ and La_2CuO_4 are, respectively, $\sigma=0.42\mu_B$ and $\sigma=0.44\mu_B$. The exchange anisotropy in these compounds is of the order of $\Delta\sim10^{-4}$ and MC calculations give $\sigma=0.45\mu_B$. The very small decrease of the sublattice magnetization could be due to a covalence effect. The neutron scattering intensity $S(k=0)(k=\pi-q)$ in these compounds is essentially temperature independent above the Néel temperature up to some temperature $T_c/T_N=1.5-2.1$. For Er_2CuO_4, magnetic and resonance investigations[25,26] give a Néel temperature $T_N=165$ K, while neutron diffraction measurements give $T_N=(250-265)$ K.[24] The normalized magnetic structure factors — the experimental factor $S(Q,T)/S(Q,T=250\text{ K})$ and the theoretical factor $S(Q,T)/S(Q,T=0.4\text{ J})$ — qualitatively agree in the interval $(0.7-1)T/T_c$ (Fig. 7c). Taking account of the exchange anisotropy, as done in Fig. 7b, will improve the agreement with experiment. The magnitude of the exchange in Er_2CuO_4 can be estimated as $J\approx630$ K from the temperature T_c. For La_2CuO_4 the normalized intensity $S(Q,T)/S(Q,T=450\text{ K})$ agrees well with the MC results (Fig. 7c). This is probably due to the weaker exchange anisotropy, since the temperature interval between T_N and T_c decreases with increasing anisotropy. The magnitude of the exchange for La_2CuO_4, estimated from T_c, is $J\approx1125$ K, while the value estimated from an approximation of the correlation radius in the interval $T/J=0.26-0.46$ by the function $1/\xi=0.25T^{0.35}/\exp(1302/T)$ gives $J\approx1302$ K (Fig. 6c). An independent value of the exchange can also be obtained from the Néel temperature $T_N=2/\ln(11/\Delta)$ and $J=1160$ K.

These estimates of the exchange fall near the values 900 and 1500 K obtained on the basis of different theoretical and experimental methods. For example, the exchange values obtained from the function $1/\xi(T)$ determined using a nonlinear σ model and the normalization group or quantum MC method are $J=1175$[4] and 1450 K,[16] respectively. The exchange anisotropy $\Delta\sim0.003$ and sublattice magnetization $\sigma\approx0.56$ can be estimated from the Néel temperature $T_N=165$ K for Er_2CuO_4. It is desirable to perform for this compound more careful neutron diffraction measurements to determine the site moment. We note that the MC calculations are in good agreement with experiment in the temperature range of existence of singlets and spinons for $\Delta=0.003$: $(T_N/T_c)^{MC}=0.62$ and $(T_N/T_c)^{ex}=0.66$. The objective of this work was not only to determine a more accurate value for the exchange but also to investigate the temperature dependence of the magnetic structure factor and the correlation radius. In the compound, above the Néel temperature, the magnetic structure can be represented in the form of singlet pairs and spinons (solitons). Singlets make the main contribution to the magnetic structure factor while spinons, whose density decreases exponentially with increasing temperature, make the main contribution to the correlation radius.

Summarizing the results obtained in this paper, we can draw the following conclusions. There is no long-range antiferromagnetic order in the ground state in a two-dimensional isotropic Heisenberg model. The exchange anisotropy dependence of the sublattice magnetization of an anisotropic antiferromagnet is logarithmic: $1/\sigma=1+0.13(1)\ln(1/\Delta)$. At low temperatures, $T/J<0.4$, the magnetic static factor $S(Q)$ is essentially temperature-independent, while the correlation radius varies exponentially. This could be due to the existence of singlets, which make the main contribution to $S(Q)$, and the temperature-excited spinons, which give an exponential behavior of the correlation radius. The sublattice magnetization, correlation radius, and static magnetic structure factor above the Néel temperature in Er_2CuO_4, La_2CuO_4, and $Sr_2CuO_2Cl_2$ are described well by the $2D$ Heisenberg model with spin $S=1/2$.

[1] P. W. Anderson, Mater. Res. Bull. **8**, 153 (1973).
[2] E. J. Neves and J. F. Peres, Phys. Lett. A **114**, 331 (1986).
[3] I. Affleck, T. Kennedy, E. H. Lieb, and H. Tasaki, Commun. Math. Phys. **115**, 477 (1988).
[4] S. Chakravarty, B. I. Halperin, and D. R. Nelson, Phys. Rev. B **39**, 2344 (1989).
[5] F. Wilczek and A. Zee, Phys. Rev. Lett. **51**, 2250 (1983).
[6] P. B. Wiegmann, Phys. Rev. Lett. **60**, 821 (1988).
[7] Yu. A. Izyumov, M. I. Katsnel'son, and Yu. N. Skryabin, *Magnetism of Collectivized Electrons*, Fizmatlit, Moscow (1994), 368 pp.
[8] E. Lieb, T. Schultz, and D. Mattis, Ann. Phys. **16**, 407 (1961).
[9] P. Horsch and W. Von der Linden, Z. Phys. B **72**, 181 (1988).
[10] S. Tang and J. E. Hirsch, Phys. Rev. B **39**, 4548 (1993).
[11] J. Richter, Phys. Rev. B **47**, 5794 (1993).
[12] P. Vries and H. D. Raedt, Phys. Rev. B **47**, 7929 (1993).
[13] H. J. Schulz, T. A. Ziman, and D. Poilblang, J. de Phys. **6**, 675 (1996).
[14] J. D. Reger and A. P. Young, Phys. Rev. B **37**, 5978 (1988).
[15] R. A. Sauerwein and M. J. de Oliveira, Phys. Rev. B **49**, 5983 (1994).
[16] M. S. Makivic and H. Q. Ding, Phys. Rev. B **43**, 3562 (1991).
[17] D. V. Dmitirev, V. Ya. Krivnov, V. N. Likhachev, and A. A. Ovchinnikov, Fiz. Tverd. Tela (St. Petersburg) **38**, 397 (1996) [Phys. Solid State **38**, 219 (1996)].
[18] C. Gros, R. Joint, and T. M. Rice, Z. Phys. B **68**, 425 (1987).
[19] E. Manousakis and R. Salvador, Phys. Rev. Lett. **61**, 1210 (1989).
[20] D. C. Mattis and C. J. Pan, Phys. Rev. Lett. **61**, 463 (1988).
[21] D. A. Huse and V. Elser, Phys. Rev. Lett. **60**, 2531 (1988).
[22] C. Keimer, B. Birgerneau, R. J. Cassnh, A. Endoh, C. Y. Greven, M. Kastner, and M. A. Shirane, Z. Phys. B **91**, 373 (1993).
[23] Y. Endoh, K. Yaamada, R. J. Birgenau, D. R. Gabbe, H. P. Jennssen, and M. A. Kastner *et al.*, Phys. Rev. B **37**, 7443 (1988).
[24] T. Chatopadhyaya and J. W. Lynn, N. Rosov *et al.*, Phys. Rev. B **49**, 9944 (1994).
[25] É. I. Golovenchits, S. L. Ginsburg, V. A. Sanina, and A. V. Babinskiĭ, Zh. Éksp. Teor. Fiz. **107**, 1641 (1995) [J. Exp. Theor. Phys. **80**, 915 (1995)].
[26] A. V. Babinskiĭ, E. I. Golovenchits, N. V. Morozov, V. A. Sanina, and L. M. Sapozhnikova, Fiz. Tverd. Tela (Leningrad) **34**, 60 (1992) [Sov. Phys. Solid State **34**, 31 (1992)].
[27] M. Greven, R. J. Birgenean, Y. Endoh, M. A. Kastner, M. Matsuda, and G. Shirane, Z. Phys. B **96**, 465 (1995).
[28] R. Claessen and R. Manzke *et al.*, Phys. Rev. B **39**, 7316 (1989).
[29] T. Freltoft, Phys. B **37**, 137 (1988).
[30] S. Molna, A. Torressen, and D. Kaiser *et al.*, Phys. Rev. B **37**, 3762 (1988).
[31] G. Shirane, Y. Endoh, and R. J. Birgeneau *et al.*, Phys. Rev. Lett. **59**, 1613 (1987).
[32] H. Raedt and A. Lagendijk, Phys. Rep. **127**, 233 (1985).
[33] S. S. Aplesnin, Fiz. Tverd. Tela (St. Petersburg) **38**, 1868 (1996) [Phys. Solid State **38**, 1031 (1996)].

Translated by M. E. Alferieff

Critical slowing of local fluctuations near the paraelectric-incommensurate phase transition in Rb_2ZnCl_4

M. P. Trubitsyn, V. I. Pastukhov, and T. M. Bochkova

Dnepropetrovsk State University, 320625 Dnepropetrovsk, Ukraine
(Submitted June 11, 1998)
Fiz. Tverd. Tela (St. Petersburg) **41**, 122–125 (January 1999)

A study is reported of the anomalous broadening of Mn^{2+} EPR lines on the high-temperature side of the paraelectric-incommensurate phase transition in Rb_2ZnCl_4 crystals. It is shown that the resonant-line broadening is inhomogeneous and due to the contribution of low-frequency fluctuations corresponding to the central peak in the elementary-excitation spectrum. The data obtained have permitted us to obtain the critical correlation-length exponent $\nu = 0.64 \pm 0.02$ corresponding to the $3d\,XY$ model of Heisenberg. © *1999 American Institute of Physics.* [S1063-7834(99)02501-0]

It is known that the dynamic properties of crystalline materials take on a relaxational nature in the vicinity of structural phase transitions, which becomes evident in the appearance of the central peak in vibrational spectra. Investigation of the critical dynamics near structural phase transitions had benefited considerably from the use of radiospectroscopical methods, in particular EPR.[1–3] Many crystals reveal near the transition point anomalous broadening and a change in the resonant-line shape caused by the critical slowing in the order-parameter dynamics. Structural distortions induced by the transition entail, as a rule, changes in the EPR spectrum, which for the low-temperature phase can be described by a spin Hamiltonian

$$\mathcal{H} = \mathcal{H}_0 + \mathcal{H}' . \tag{1}$$

The first term in Eq. (1), $\mathcal{H}_0$, determines the state of the paramagnetic center in the high-temperature phase, while $\mathcal{H}'$, considered as a perturbation, includes spin operators responsible for the transition-induced change in site symmetry.[4] The parameters of the spin operators in $\mathcal{H}'$ depend on the magnitude of structural displacements in the paramagnetic center environment. The appearance of a nonvanishing local-order parameter below the transition point gives rise to a temperature-induced shift of the EPR signal position. The fluctuations in the local order parameter responsible for the dynamic part of $\mathcal{H}'$ contribute to the width and affect the shape of resonant lines. Within the approach made in terms of Eq. (1), resonant-line broadening in the phase-transition region may be due to contributions of two types.[5] The first contribution, δH_S, is determined by the diagonal matrix elements of the spin Hamiltonian $\mathcal{H}'$ and the spectral density of fluctuations $J(0)$ at zero frequency. The second contribution to linewidth, δH_{NS}, comes from the off-diagonal matrix elements of $\mathcal{H}'$ and the spectral density $J(\omega_{\rm res})$ at the resonant frequency $\omega_{\rm res} \sim 10^{10}$ Hz. It was shown[5] that in the case where the characteristic fluctuation frequencies Ω exceed considerably the fluctuation-induced linewidth ω_1, the spectral profile is a Lorentzian with a width $(\delta H_S + \delta H_{NS})$. In the limit of slow fluctuations, $\Omega \ll \omega_1$, the line shape can be described by a convolution of a Lorentzian with off-diagonal width δH_{NS} with a Gaussian, whose width is determined by the diagonal component δH_S.[5]

1. EXPERIMENTAL RESULTS

This paper reports an EPR study of Mn^{2+} centers in rubidium tetrachlorozincate, which belongs to a family of A_2BX_4 isomorphic compounds.[6] At $T_i = 303$ K, Rb_2ZnCl_4 crystals undergo a transition form the high-temperature paraelectric (symmetry group D_{2h}^{16}-*Pnam*, $b > a > c$) to incommensurate phase with the onset of structural modulation described by the wave vector $q_i = (\frac{1}{3} - \delta)\, a^*$.[7,8]

The samples were prepared from Czochralski-grown single crystals.[9] The measurements were performed on a standard *X*-range radiospectrometer. The sample temperature was controlled to within 0.1 K by heating in liquid-nitrogen vapor.

The high-field hyperfine line group ($M_S = 3/2 \leftrightarrow 5/2$) was measured with the samples cooled to approach T_i from above. Figure 1 presents experimental spectra for two orientations of the external magnetic field **H** relative to the crystallographic axes. One readily sees that for $\mathbf{H} \| \mathbf{a}$ the hyperfine sextet does not undergo any noticeable changes near T_i^+ (Fig. 1a). Deflecting **H** from the **a** axis in the (010) plane by 7° affects considerably the temperature dependence of the spectral profile, which starts to broaden as $T \to T_i^+$ (Fig. 1b). Note that analysis of the spectra obtained is complicated by superposition of adjacent hyperfine components, whose widths (~ 3.2 mT) are comparable to the hyperfine splitting (~ 7.5 mT).

Broadening of Mn^{2+} EPR lines in Rb_2ZnCl_4 crystals in the vicinity of T_i was reported earlier.[10] The treatment of experimental data was based on a deconvolution procedure excluding from consideration the hyperfine multiplication of the spectrum, which is insensitive to structural changes, by direct and inverse Fourier transformation.[10] It appears that this approach has a certain drawback. The peak in the Fourier transform of the experimental sextet corresponding to

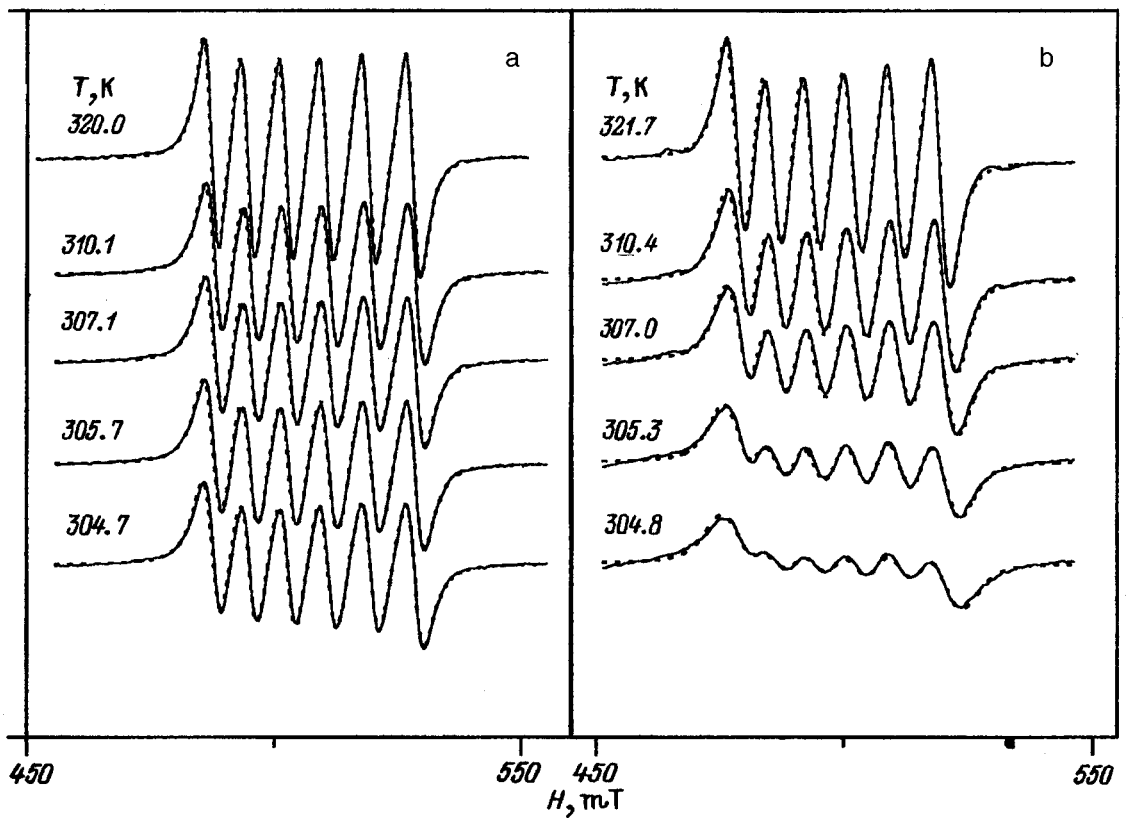

FIG. 1. A part of an EPR spectrum of $Rb_2ZnCl_4:Mn^{2+}$ crystals corresponding to the $M_S=3/2\leftrightarrow 5/2$ hyperfine group obtained slightly above $T_i=304.4$ K. (a) $\mathbf{H}\|\mathbf{a}$; (b) $\angle\mathbf{H},\mathbf{a}=7°$, $\mathbf{H}\perp\mathbf{b}$. Dashed lines present calculated spectra obtained by convolution of a Lorentzian and a Gaussian function.

the hyperfine-structure periodicity is broadened because of a finite number of components in the group and of their not being equidistant within one electronic transition. Accordingly, the single line obtained by deconvolution is considerably distorted. Therefore deconvolution does not yield adequate information on spectral line shape and does not permit one to isolate the critical contribution to linewidth and to investigate its temperature dependence near the transition point.

This work deals with a simulation of the experimental hyperfine-sextet shape by convolution of a Lorentzian with a Gaussian, $\int L[(H-H_C)/\delta H_L]\cdot G[(H_C-H_0)/\delta H_G]\,dH_C$. This approach enabled determining the homogeneous, δH_L, and inhomogeneous, δH_G, contributions to linewidth and to reach a good agreement of the calculated with experimental spectra (Fig. 1).

Figure 2 displays the temperature dependence of the width of the hyperfine component in the high-field group $M_S=3/2\leftrightarrow 5/2$ for three orientations of the external magnetic field. The width was determined as the distance between the extrema in the derivative of the absorption line. The slight increase in the linewidth for $T\to T_i^+$ observed for the main orientation $\mathbf{H}\|\mathbf{a}$ is seen to transfer to a clearly pronounced anomalous broadening, whose magnitude grows with deviation of **H** from the **a** axis. The results of the simulation showed that the critical contribution to linewidth is associated with the increase of the Gaussian component δH_G, whereas the behavior of the Lorentzian δH_L does not exhibit any anomalies in the vicinity of the transition point.

2. DISCUSSION OF RESULTS

As shown earlier,[9,11] Mn^{2+} centers substitute for the zinc ions in the $ZnCl_4$ tetrahedra. In the paraphase, active centers have local symmetry C_S with multiplicity $k_M=2$ and lie in the (**a**,**b**) plane. The orientational relations of the EPR fine

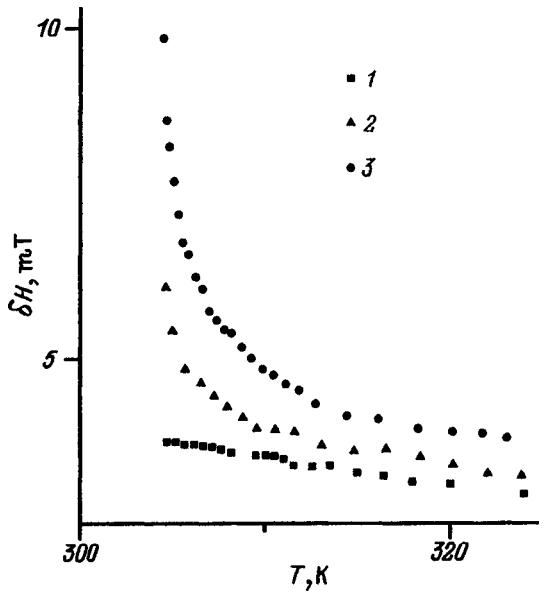

FIG. 2. Temperature dependence of the width of a hyperfine $M_S=3/2\leftrightarrow 5/2$ component for the following external magnetic-field orientations: *1* — $\mathbf{H}\|\mathbf{a}$, *2* — $\angle\mathbf{H},\mathbf{a}=3.5°$, *3* — $\angle\mathbf{H},\mathbf{a}=7°$, $\mathbf{H}\perp\mathbf{b}$.

structure are adequately described by a rhombic spin Hamiltonian $\mathcal{H}_0$ with parameters $g=2.004$, $|B_2^0|/g\beta=16.01$ mT, and $|B_2^2|/g\beta=9.10$ mT calculated for the magnetic axis arrangement $\angle\mathbf{Z},\mathbf{a}=\pm5°$, $\angle\mathbf{X},\mathbf{b}=\pm5°$, and $\mathbf{Y}\|\mathbf{c}$.[9] As the crystal transfers to the incommensurate phase, the $(\mathbf{a},\mathbf{b})$ symmetry plane undergoes local distortion (although the symmetry group of the modulated phase remains macroscopically unchanged due to spatial averaging of periodic distortions along the modulation axis), and the center positions correspond to group C_1. Hence the perturbation spin Hamiltonian $\mathbf{H}'$ in Eq. (1) contains equivalent spin operators corresponding to triclinic symmetry and can be recast in the form retaining the most essential terms[4]

$$\mathcal{H}'=B_2^1O_2^1+C_2^1\tilde{O}_2^1. \tag{2}$$

In the case where the external magnetic field lies in the $(\mathbf{a},\mathbf{b})$ plane or is perpendicular to it, the diagonal matrix elements of the type $\langle M_S|\mathcal{H}'|M_S\rangle$ vanish. For $\mathbf{H}\|\mathbf{a}$, the linewidth δH (Fig. 2) and its Gaussian component δH_G do not exhibit any noticeable features near T_i^+. For misorientations $\angle\mathbf{H},\mathbf{a}=3.5$ and $7°$, $\mathbf{H}\perp\mathbf{b}$ magnetic field distorts the local symmetry, thus lifting the forbiddenness of the diagonal matrix elements of spin Hamiltonian $\mathcal{H}'$ (2). Accordingly, for $T\to T_i^+$ one observes in an experiment anomalous line broadening (Fig. 2) caused by the growth of the inhomogeneous component δH_G.

The data obtained show that the anomalous broadening has an inhomogeneous character and is determined by the diagonal matrix elements of the spin Hamiltonian $\mathcal{H}'$. According to Ref. 5, such a behavior of the width is associated with a growth of the spectral density of zero-frequency fluctuations, $J(0)$. To be exact, the characteristic frequency of the fluctuations contributing to the broadening should be substantially lower than the measuring frequency, which is of the order of the linewidth in the rigid-lattice case, $\sim10^7$ Hz.[12] The critical contribution can be extracted from the Gaussian component using the relation

$$\delta H_{\rm cr}(T)=[\,\delta H_{\rm G}^2(T)-\delta H_{\rm bgr}^2]^{1/2}, \tag{3}$$

where $\delta H_{\rm bgr}$ is the inhomogeneous background component originating from noncritical static contributions. Thus the temperature dependence $\delta H_{\rm cr}(T)$ should be considered within a quasistatic approximation where the critical width approaches a finite value $\delta H^{\max}$ at the transition point[13]

$$\delta H_{\rm cr}=\delta H^{\max}[\,1-C\tau^{\nu}\arctan(C^{-1}\tau^{-\nu})\,]^{1/2}. \tag{4}$$

In Eq. (4), the small pair-correlator critical exponent η is neglected, and the following notation is introduced: $C=k_0a/\pi$, $k=k_0\tau^{\nu}=\xi^{-1}$ is the inverse correlation length, ν is the corresponding critical exponent, $\tau=(T-T_i)/T_i$ is the reduced temperature, and a is the unit cell parameter. Replacing the inverse tangent in Eq. (4) by $\pi/2$, which is valid near T_i, we obtain

$$\delta H_{\rm cr}=\delta H^{\max}[\,1-(\pi/2)C\tau^{\nu}\,]^{1/2}. \tag{5}$$

Obviously enough, for $\tau\to0$ the critical contribution to the width $\delta H_{\rm cr}$ tends to $\delta H^{\max}$ at the transition point. As one goes away from T_i, in the limit as $\tau\to\infty$, the inverse tangent can be expanded in a series, and Eq. (4) transforms to

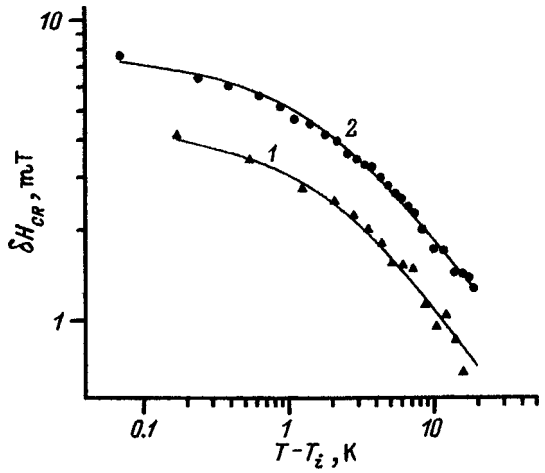

FIG. 3. Log-log plot of the critical contribution to the linewidth $\delta H_{\rm cr}$ *vs* $(T-T_i)$. *1* — $\angle\mathbf{H},\mathbf{a}=3.5°$, *2* — $\angle\mathbf{H},\mathbf{a}=7°$, $\mathbf{H}\perp\mathbf{b}$. Solid lines were drawn using Eq. (4).

$$\delta H_{\rm cr}=\frac{1}{\sqrt{3}}\,\delta H^{\max}C^{-1}\tau^{-\nu}. \tag{6}$$

The experimental relations of the critical width derived from oblique magnetic-field measurements by means of Eq. (3) are displayed in Fig. 3 on a log-log scale. The background widths used are $\delta H_{\rm bgr}=1.35$ mT ($\angle\mathbf{H},\mathbf{a}=3.5°$) and $\delta H_{\rm bgr}=1.48$ mT ($\angle\mathbf{H},\mathbf{a}=7°$). The solid lines in Fig. 3 are plots of Eq. (4). The transition point $T_i=304.4$ K was determined independently from the resonant-line splitting into a singular spectrum.[14] One readily sees that relation (4) derived in quasistatic approximation offers a good fit to the experimental relations and predicts the following critical contributions to linewidth at T_i: $\delta H^{\max}=4.48$ mT ($\angle\mathbf{H},\mathbf{a}=3.5°$) and $\delta H^{\max}=7.93$ mT ($\angle\mathbf{H},\mathbf{a}=7°$).

It is known that the local order parameter for Mn^{2+} centers can be related to the rotation angle of the tetrahedral groups $ZnCl_4$,[11] and that EPR spectra are most sensitive to tetrahedron rotations about the **b** axis[15]. The extrapolated values of $\delta H^{\max}$ and the above parameters of the spin Hamiltonian $\mathcal{H}_0$ permit one to estimate the rms fluctuation of the tetrahedron turn at the transition point: $\langle\delta\alpha^2\rangle^{1/2}=3.0°$ for $\angle\mathbf{H},\mathbf{a}=3.5°$ and $\langle\delta\alpha^2\rangle^{1/2}=2.7°$ for $\angle\mathbf{H},\mathbf{a}=7°$. These values are in a good agreement with x-ray diffraction measurements[7].

The average slope of the experimental relations for $T-T_i\geqslant7$ K (Fig. 3) is determined, according to Eq. (6), by the critical exponent of the correlation length, and for both relations $\nu=0.68\pm0.05$ for $\angle\mathbf{H},\mathbf{a}=3.5°$ and $\nu=0.64\pm0.02$ for $\angle\mathbf{H},\mathbf{a}=7°$. These values coincide within experimental error with the value of ν in the Heisenberg three-dimensional model for the two-component order parameter ($3dXY$ model), whose universality class comprises incommensurate crystals of the potassium selenate family.[16] The value of the fitting parameter $C=k_0a/\pi$ used in Eq. (4) permits one to estimate the ratio of the correlation length ξ_0 at $T=0$, which is a measure of the range of the forces responsible for the transition, to the cell parameter, $\xi_0/a\sim0.01$

($a \sim 10$ Å). This value turns out to be substantially smaller than could be expected considering the dimensions of the rigid structural blocks, the $ZnCl_4$ tetrahedra, and the characteristic distances between them, $\sim 2-3$ Å. The reason for such a small estimate for ξ_0 may lie in the need to take into account the anisotropy of correlated motions in the vicinity of T_i,[13] which results in a change of the dispersion relation and introduction of new parameters into the expression of the type (4).

To sum up, our EPR study of Mn^{2+} ions in Rb_2ZnCl_4 crystals near $T_i = 304.4$ K has shown that the resonant-line broadening is due to quasistatic order-parameter fluctuations with frequencies below the frequency analog of the background width δH_{bgr}. Thus the anomalous contribution to EPR linewidth can be associated with the presence of the central peak in the vibrational spectrum of Rb_2ZnCl_4, which yields an upper estimate for its width ~ 40 MHz. Because in the case of Mn^{2+} EPR the local order parameter corresponds to rotation of the tetrahedral complexes $ZnCl_4$, the data obtained offer a possibility of estimating the rms fluctuation of the rotation angle near the transition point.

An analysis of the behavior of the fluctuation contribution to EPR linewidth permits estimating the critical correlation-length exponent $\nu = 0.64 \pm 0.02$, which supports, within experimental error, the nonclassical character of the critical properties of Rb_2ZnCl_4 crystals corresponding to the Heisenberg $3d\,XY$ model.

[1] K. A. Müller and J. C. Fayet, in *Structural Phase Transitions II*, edited by K. A. Müller and H. Thomas (Springer, Berlin, 1991), V. 45, p. 1.
[2] K. A. Müller, in *Dynamical Critical Phenomena and Related Topics*, Lecture Notes in Physics (Springer, Berlin, 1979), V. 104, p. 210.
[3] R. Blinc, Ferroelectrics **20**, 121 (1978).
[4] S. A. Al'tshuler and B. M. Kozyrev, *Electronic Paramagnetic Resonance in Intermediate-Group Compounds* [in Russian] (Nauka, Moscow, 1972).
[5] G. F. Reiter, W. Berlinger, K. A. Müller, and P. Heller, Phys. Rev. B **21**, 1 (1980).
[6] A. U. Sheleg and V. V. Zaretskii, in *Incommensurate Phases in Dielectric Materials* (North-Holland, Amsterdam, 1986), p. 367.
[7] K. Itoh, A. Hinasada, H. Matsunaga, and E. Nakamura, J. Phys. Soc. Jpn. **52**, 664 (1983).
[8] K. Gesi and M. Iizumi, J. Phys. Soc. Jpn. **46**, 697 (1979).
[9] T. M. Bochkova, O. E. Bochkov, S. A. Flerova, and M. P. Trubitsyn, Fiz. Tverd. Tela (Leningrad) **26**, 2170 (1984) [Sov. Phys. Solid State **26**, 1315 (1984)].
[10] A. Kaziba, M. Pezeril, J. Emery, and J. C. Fayet, J. Phys. Lett. (Paris) **46**, L387 (1985).
[11] M. Pezeril, J. Emery, and J. C. Fayet, J. Phys. Lett. (Paris) **41**, L499 (1980).
[12] A. Abragam, *The Principles of Nuclear Magnetism* [Clarendon Press, Oxford, 1961; IL, Moscow, 1963], 551 pp.
[13] Th. von Waldkirch, K. A. Müller, and W. Berlinger, Phys. Rev. B **7**, 1052 (1973).
[14] R. Blinc, Phys. Rep. **79**, 331 (1981).
[15] J. J. L. Horikx, A. F. M. Arts, and H. W. de Wijn, Phys. Rev. B **37**, 7209 (1988).
[16] A. D. Bruce and R. A. Cowley, *Structural Phase Transitions* [Taylor & Francis, London, 1981; Mir, Moscow, 1984], 407 pp.

Translated by G. Skrebtsov

Microwave absorption in a $Y_1Ba_2Cu_3O_{7-x}$ single crystal near the superconducting transition

M. K. Aliev, G. R. Alimov, T. M. Muminov,*) B. A. Olimov, Kh. I. Turkmenov, and I. Kholbaev

Scientific-Research Institute of Applied Physics, Tashkent State University, 700095 Tashkent, Uzbekistan

L. I. Leonyuk

M. V. Lomonosov Moscow State University 119899 Moscow, Russia

R. F. Rumi

Institute of Materials Science, Scientific and Industrial Association ''Fizika–Solntse'' 700084 Tashkent, Uzbekistan

(Submitted January 27, 1998)
Fiz. Tverd. Tela (St. Petersburg) **41**, 14–17 (January 1999)

$Y_1Ba_2Cu_3O_{7-x}$ single crystals are investigated near $T_c \approx 92$ K in fields $0 < H \leqslant 9$ kOe using a modified ESR spectrometer. The temperature modulation method is used for the first time, together with the traditional magnetic modulation method, to detect microwave responses in single crystals. Superconducting-transition peaks shifted relative to one another in temperature and differing in shape are observed in the temperature dependence of the corresponding signals $\partial R/\partial H$ and $\partial R/\partial T$ (R — microwave absorption). The evolution of these peaks as a function of the field and the angle θ between **H** and the **c** axis of the single crystal is traced. It is shown that the difference in the temperature dependences of the derivatives $\partial R/\partial H$ and $\partial R/\partial T$ is due to the broadening of the superconducting transition characteristic of HTSCs. © *1999 American Institute of Physics.* [S1063-7834(99)00301-9]

It is well known that the superconducting transition in high-temperature superconductors (HTSCs), in contrast to low-temperature superconductors, undergoes pronounced broadening with increasing external magnetic field. This property of HTSCs is the main obstacle to determining the temperature dependence of the upper critical field $H_{c_2}(T)$ by traditional methods.[1] For example, on account of this broadening the lines of constant resistance $H_\delta(T)$ measured by the resistance method are strongly dependent on the resistance level $\delta = \rho/\rho_n$ (ρ_n — resistivity in the normal state), and for this reason they cannot be identified with the line of the upper critical field $H_\delta(T)$. It should be noted that the mechanism of broadening of the transition in HTSCs has still not been definitely established and is the subject of unabated attention from investigators.[2–8]

As shown in Refs. 8–13, a peak near the superconducting transition is observed in the temperature dependence of the microwave response detected in HTSCs using an ESR spectrometer with magnetic modulation. The signal measured in the process is the field derivative of the absorption — $\partial R/\partial H$. In this connection, it was noted in Refs. 10 and 12 that, if the derivatives $\partial R/\partial H$ and $\partial R/\partial T$ near the superconducting transition in HTSCs possess the same temperature dependence, as happens in low-temperature superconductors, then their ratio can be used to determine $dH_{c_2}(T)/dT$, characterizing the slope of the line of the upper critical field in the phase plane (H,T).

In the present paper we report the first data on the temperature dependence of both the derivative $\partial R/\partial H$ and the derivative $\partial R/\partial T$ for a Y–Ba–Cu–O single crystal. The results of our investigations show that for HTSCs the assumption that the temperature dependences of $\partial R/\partial H$ and $\partial R/\partial T$ are of the same character near a superconducting transition is untenable. It is shown that this is due to the broadening of the superconducting transition in a magnetic field.

1. EXPERIMENTAL PROCEDURE

A modified SE/X-2543 RADIOPAN ESR spectrometer ($\nu \approx 9$ GHz, $P_{\max} = 130$ mW) with a TE_{102} resonator with $Q = 5000$ was used in the experiment. The measurements were performed in a constant mangetic field in the range $0 < H \leqslant 9$ kOe. For weak magnetic fields, Helmholtz coils ($H_{\max} = 880$ Oe) were used. The coils were placed, together with the resonator, inside a magnetic screen which suppressed the earth's field by more than a factor of 100.

The temperature regulation system that we developed, based on heating of the sample with a light beam, makes it possible to modulate the temperature of the sample with frequency 80 Hz. Near $T \sim 90$ K the system characteristics are as follows:[14] the rms instability of the temperature in the samples does not exceed 0.06 K in 5 min; the temperature gradient in the sample is ~ 0.01 K/min; the relaxation time of the system is 1–10 s; and, the modulation amplitude of the sample temperature is $10^{-2} - 10^{-1}$ K.

Single crystals with the composition $Y_{0.99}Ba_{2.00}Cu_{2.89}O_{7-x}$, grown from $3Y_2O_3 + 25BaCuO_3$

+ 72CuO melt, were investigated. The initial charge was heated to 1100 °C in a ZrO_2:Y crucible at a rate of 2–5 °C/h and then cooled to room temperature at the same rate. The composition of the crystals was determined by x-ray microanalysis. The unit cell parameters obtained from the x-ray data are $a=3.85$ Å , $b=3.89$ Å , and $c=11.74$ Å . The single crystals consisted of thin wafers with thickness $d\sim 0.03$ mm (along the **c** axis) and up to 1 mm in size in the (**a**,**b**) plane. A well-developed twin structure was observed in the samples. The twinning boundaries formed a system of parallel lines (with period $\sim 2\mu$m), making an angle of 45° with the natural faces of the crystal.

The standard (for ESR spectrometers) field geometry $\mathbf{H}\perp\mathbf{H}_1$ (**H** — constant field, $\mathbf{H}_1$ — microwave field) was used in the experiment (inset in Fig. 2). The measurements were conducted for orientations of the single crystal $\mathbf{c}\perp\mathbf{H}_1$. The angle θ between **c** and **H** could be varied by rotating the single crystal around the direction $\mathbf{H}_1$ and was set to within $\pm 1.0°$.

The microwave absorption signal was detected by the synchronous detection method: at 100 kHz — by modulating the magnetic field (the maximum modulation amplitude $h_{\max}=10$ Oe) and at 80 Hz by modulating the temperature of the sample. It should be noted that a direct measurement of the temperature-modulation amplitude is in itself a complicated technical problem. For this reason, here we confine ourselves to noting that, according to the estimates made in Ref. 14, this amplitude has a definite value in the interval $10^{-2}-10^{-1}$ K and can vary near the superconducting transition by not more than 10%. Since this amplitude is much less than the transition width, the corresponding signal can be interpreted as the derivative $\partial R/\partial T$. All measurements were performed with constant microwave power, -17 dB.

2. EXPERIMENTAL RESULTS AND DISCUSSION

Samples for which the measured signals had the simplest structure — single peaks in the temperature dependences $\partial R/\partial H$ and $\partial R/\partial T$ — were selected for the investigations. The so-called low-field signals were absent in all samples.[15,16] This guaranteed that the temperature dependence of the measured signals was due only to the superconducting transition. It is also important to note that no effects due to irreversibility of the observed signals were observed in the experimental samples.

Five samples from the same series, which differed only by their dimensions in the (**a**,**b**) plane, were investigated. The experimental results reduce to the following laws common to all samples and demonstrated in Figs. 1–3 for one of the samples. The most important law is that the temperature dependences of the derivative $\partial R/\partial H$ is qualitatively different from that of $\partial R/\partial T$: As one can see from Fig. 1, the peaks of $\partial R/\partial H$ and $\partial R/\partial T$ are shifted relative to one another in temperature and the $\partial R/\partial H$ peak is wider and more asymmetric than the $\partial R/\partial T$ peak and has a pronounced low-temperature tail. The different behavior of the peaks with increasing external field is also seen in Fig. 1: The $\partial R/\partial H$ peak drops off more rapidly in amplitude and shifts more rapidly in the direction of low temperatures than the $\partial R/\partial T$ peak.

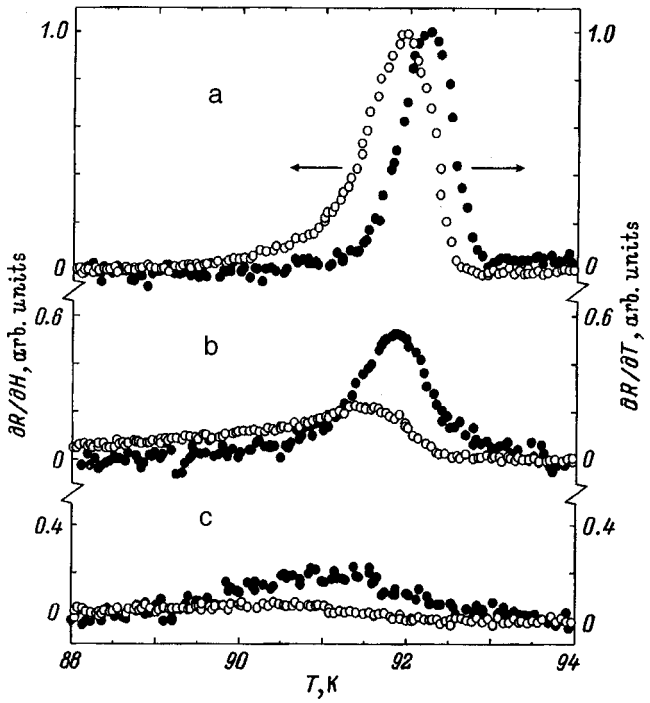

FIG. 1. Temperature dependences of the derivatives $\partial R/\partial H$ and $\partial R/\partial T$ for $\theta=0$ and different values of H. $H=20$ kOe (a), 2 kOe (b), and 9 kOe (c).

We established the following concerning the asymptotic behavior of the peaks in the limit $H\to 0$. Below $H=20$ Oe the amplitude of the $\partial R/\partial H$ peak remained constant with decreasing field (within the limits of experimental accuracy), while the peak became more symmetric, approaching in shape the $\partial R/\partial T$ peak but its position remaining unchanged in the process. However, the $\partial R/\partial T$ peak itself did not change in any way right down to the lowest field used in our experiment ($10^{-3}-10^{-2}$ Oe).

Here we call attention to a specific difficulty arising in measurements of the derivative $\partial R/\partial H$ in zero fields. To detect the corresponding signal ΔR we employed the highest field modulation amplitudes for which the proportionality $\Delta R\sim(\partial R/\partial H)h$ still holds (h — modulation amplitude of the external magnetic field). As special tests showed, the latter requirement reduced to the well-known restriction $h<H$. The need to decrease the modulation amplitude as $H\to 0$ made it impossible for us to perform satisfactory measurements of the temperature dependence of $\partial R/\partial H$ in fields $H<2.5$ Oe (at $H=1$ Oe the signal ΔR was at the noise level). For this reason, our assertion that the amplitude and the position of the $\partial R/\partial H$ peak remain unchanged as $H\to 0$ should be taken with this stipulation.

The $\partial R/\partial H$ and $\partial R/\partial T$ peaks also behaved differently as a function of the angle θ between the directions of the field **H** and the **c** axis of the single crystal.

In weak fields, $H\leqslant 20$ Oe, the $\partial R/\partial T$ peak remained essentially constant as the angle θ increased from 0 to 90°, while the $\partial R/\partial H$ peak changed substantially (Fig. 2): The amplitude of the $\partial R/\partial H$ peak decreased monotonically, dropping by approximately a factor of 10 at $\theta=90°$, and the

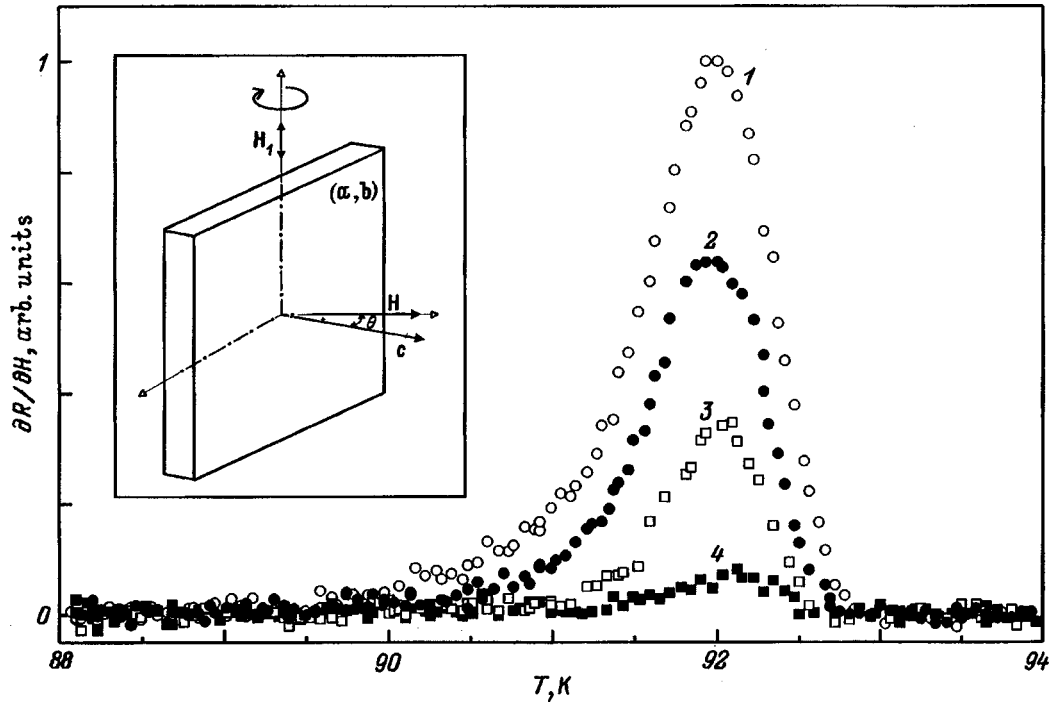

FIG. 2. Evolution of the temperature dependence of the derivative $\partial R/\partial H$ at $H=20$ Oe as a function of the angle θ: *1* — 0°, *2* — 50°, *3* — 70°, *4* — 90°. Inset: Geometry of the experiment.

peak shifted by a small amount in the direction of high temperatures.

The opposite picture was observed in sufficiently strong fields: As the angle θ increased, the amplitude of the $\partial R/\partial T$ peak changed strongly, as shown in Fig. 3, while the amplitude of the $\partial R/\partial H$ peak decreased very little. The widths of both peaks as a function of the angle θ decreased in the range from 0 to 90°, while the maxima shifted in the direction of high temperatures by approximately 1 K at $H=9$ kOe.

We note that the differences, examined above, in the strong- and weak-field anisotropy of the peaks are due to the fact that the decrease in the amplitudes as well as the shift of the peaks in the direction of low temperatures as the field

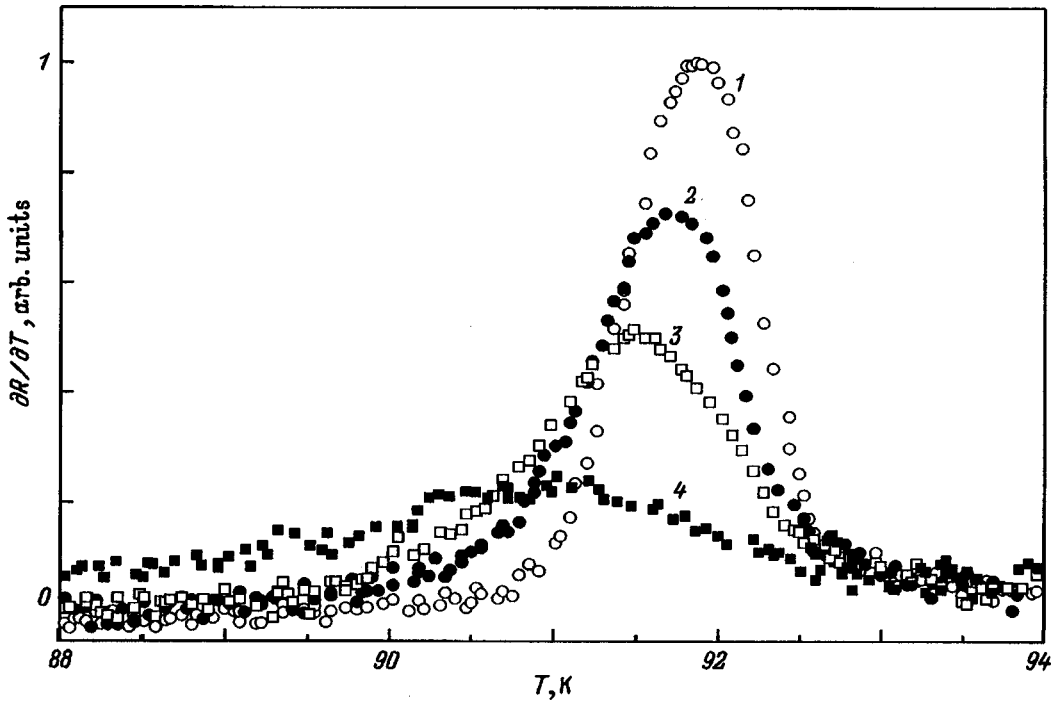

FIG. 3. Evolution of the temperature dependence of the derivative $\partial R/\partial H$ at $H=9$ kOe as a function of the angle θ: *1* — 90°, *2* — 80°, *3* — 70°, *4* — 0°.

increases from zero values slow down as θ increases. For example, at $H=9$ kOe the amplitudes of the peaks for $\theta=90°$ decreased by less than 20%, while their shift did not exceed 0.2 K.

We begin our discussion of the experimental results with the following remark. In the general case, the absorption $R(H,T)$ as a function of two variables satisfies the relation

$$\partial R/\partial T=-(dH_r(T)/dT)(\partial R/\partial H), \quad (1)$$

where the function $H_r(T)$ is determined from the equation

$$R(H_r(T),T)=r=\text{const}$$

and describes in the phase plane (H,T) a line of constant absorption, passing through the point of interest in the plane. Near the superconducting transition the line of constant absorption is usually interpreted as the curve of the upper critical field $H_{c_2}(T)$. This interpretation is possible only if the slope dH_r/dT depends weakly on the absorption level r in the temperature interval of the transition for fixed H [otherwise the lines $H_r(T)$ corresponding to different values of r would diverge in the phase plane and there would be an uncertainty in identifying $H_r(T)$ as $H_{c_2}(T)$]. This condition holds well for low-temperature superconductors and, as follows from Eq. (1), the temperature dependences of $\partial R/\partial H$ and $\partial R/\partial T$ should have the same form. We note that this is possible only if the curve of R versus T shifts as a whole as the field H is varied.

As one can see from Fig. 1, the superconducting-transition peaks observed in the temperature dependence of the derivatives $\partial R/\partial H$ and $\partial R/\partial T$ in our experimental single crystal differ appreciably in shape and, what is important, they are shifted relative to one another in temperature. According to Eq. (1), this means that the slope dH_r/dT is very nonuniform in the temperature interval of the transition and therefore it should depend strongly on the absorption level. Therefore the relative temperature shift of the peaks in each plot in Fig. 1 itself attests to broadening of the superconducting transition with increasing magnetic field. We emphasize that a comparative analysis of the $\partial R/\partial H$ and $\partial R/\partial T$ peaks makes it possible to observe the broadening of the transition even in weak magnetic fields, where the temperature would have to be measured with a much higher accuracy in order for this effect to be directly observable. This suggests that our results can be used to check the existing theoretical models explaining the broadening of transitions in HTSCs.

It is our pleasant duty to thank B. Yu. Sokolov for helpful discussions and I. R. Mikulin for assisting in the preparation of the temperature system.

[a)]E-Mail: muminov@iaph.silk.glas.apc.org

[1] E. Z. Meĭlikhov and V. G. Shapiro, Sverkhprovodimost', **4**(8), 1437 (1991).
[2] Y. Yeshurun and A. P. Malozemoff, Phys. Rev. Lett. **60**, 2202 (1988).
[3] M. Tinkham, Phys. Rev. Lett. **61**, 1658 (1988).
[4] T. T. M. Palstra, B. Batlogg, R. B. van Dover, L. F. Schneemeyer, and J. V. Waszczak, Phys. Rev. B **41**, 6621 (1990).
[5] K. H. Lee and D. Stroud, Phys. Rev. B **46**, 5699 (1992).
[6] H. A. Blackstead, Phys. Rev. B **47**, 11 411 (1993).
[7] H. A. Blackstead and G. A. Kapustin, Physica C **219**, 109 (1994).
[8] H. A. Blackstead, D. B. Pulling, M. Paranthaman, and J. Brynestad, Phys. Rev. B **51**, 3783 (1995).
[9] K. Moorjani, J. Bohandy, F. J. Adrian, B. F. Kim, R. O. Shull, C. K. Chiang, L. J. Swartzendruber, and L. H. Bennett, Phys. Rev. B **36**, 4036 (1987).
[10] B. F. Kim, J. Bohandy, K. Moorjani, and F. J. Adrian, J. Appl. Phys. **63**, 2029 (1988).
[11] M. K. Aliev, Ya. Vavryshchuk, S. P. Volosyanyĭ, T. M. Muminov, and I. Kholbaev, Fiz. Tverd. Tela (Leningrad) **31**(9) 254 (1989) [Sov. Phys. Solid State **31**, 1621 (1989)].
[12] D. Shaltiel, H. Bill, A. Grayevsky, A. Junod, D. Lovy, W. Sadowski, and E. Walker, Phys. Rev. B **43**, 13 594 (1991).
[13] S. G. L'vov, Yu. I. Talanov, R. I. Khasanov, and V. A. Shustov, Sverkhprovodimost' **6**(6), 1175 (1993).
[14] M. K. Aliev, G. R. Alimov, T. M. Muminov, B. A. Olimov, B. Yu. Sokolov, R. R. Usmanov, and I. Kholbaev, Prib. Tekh. Éksp., No. 5, 152 (1996).
[15] A. A. Romanyukha, Yu. N. Shvachko, and V. V. Ustinov, Usp. Fiz. Nauk **161**(10), 37 (1991) [Sov. Phys. Usp. **34**, 862 (1991)].
[16] M. K. Aliev, G. R. Alimov, T. M. Muminov, B. A. Olimov, and I. Kholbaev, Fiz. Tverd. Tela (St. Petersburg) **38**, 3535 (1996) [Phys. Solid State **38**, 1926 (1996)].

Translated by M. E. Alferieff

Motion of a planar domain wall in the ferroelectric–ferroelastic gadolinium molybdate

B. Ya. Shur,* E. L. Rumyantsev, V. P. Kuminov, A. L. Subbotin, and E. V. Nikolaeva

Institute of Physics and Applied Mathematics, Ural State University, 620083 Ekaterinburg, Russia
(Submitted June 17, 1998)
Fiz. Tverd. Tela (St. Petersburg) **41**, 126–129 (January 1999)

The lateral motion of a planar domain wall (PDW) in an electric field and the spontaneous rotation of the wall in the initial position after the field is switched off were investigated in the improper ferroelectric–ferroelastic gadolinium molybdate $Gd_2(MoO_4)_3$, using optical visualization and measurement of the switching currents. The characteristic behavior found for the PDW is attributed to the delay of the volume screening of the depolarizing fields. It is shown that the dependence of the motion of the PDW on the switching duration in an ac field is due to the redistribution of the screening charges. © *1999 American Institute of Physics.* [S1063-7834(99)02601-5]

Ferroelectrics–ferroelastics are the best model materials for studying such elementary processes in the evolution of domain structures as the motion of planar domain walls (PDWs). Just as in any ferroelastics, in these materials PDWs exist in a stable manner in a wide range of actions and can be visualized because the domains have different optical characteristics and, just as in any ferroelectrics, the position of a PDW can be changed by applying an electric field. This makes it possible to investigate the dynamics of PDWs in detail by recording the switching currents and determining optically the instantaneous positions of PDWs with high spatial and temporal resolution. The improper ferroelectric–ferroelastic gadolinium molybdate $Gd_2(MoO_4)_3$ (GMO), whose physical properties and domain structure have been studied fairly well,[1–5] were chosen for the investigations.

In previous work it was noted that the velocity of a PDW when the wall is displaced from its initial position and returns there after the field is switched off is nonuniform.[1,3,4,6–8] It was established that these features depend on the intensity and duration of the field as well as on the temperature and past history. Screening of depolarizing fields was used to explain the observed effects.[6–9]

In the present work the characteristic features of the motion of a PDW near the initial (equilibrium) position is studied in detail for the example of GMO.

1. EXPERIMENT

GMO single crystals were Czochralski grown from melt by pulling in the [001] direction. Rectangular $0.39\times2\times7$ mm wafers were cut out perpendicular to the polar axis, and the lateral faces were oriented parallel to the allowed orientations of the PDWs. The thickness chosen ensured maximum contrast when visualizing the PDWs. All faces of the wafers were ground and polished using diamond paste. Transparent In_2O_3:Sn electrodes were deposited on the polar faces by reactive sputtering. Samples with one PDW, which were cantilevered from the substrate on the side with the smaller face (Fig. 1), were investigated. Gaps in the electrodes prevented the PDW from vanishing (the gaps limited the range of motion).

The apparatus based on a polarized-light microscope (Fig. 2) made it possible to detect simultaneously sequences of instantaneous domain configurations under cyclic switching and the corresponding switching currents. The experimental sample *1* was secured to the microscope stage. Stroboscopic lighting *2* was used to detect the instantaneous domain configurations. The repetition frequency of the light pulses (duration less than 1 μs) was equal to the frequency of the field, which made it possible to visualize, using a delay unit *4*, any stage of the evolution of the domain structure. An incandescent lamp *3* served as the source of light for observing the static domain structures. Switching was accomplished with an ac voltage with frequency 30–100 Hz and amplitude up to 300 V, varying according to a sinusoidal or linear law. The switching currents and instantaneous domain configurations were recorded with an IBM PC and a vcr. The error in determining the instantaneous positions of the PDW did not exceed 1 μm.

The continuous and reproducible motion of a PDW under cyclic switching made it possible to use stroboscopic lighting to the determine instantaneous position of the wall. The following features of the motion of the PDW were established: 1) A displacement from the initial position starts when the external field exceeds a certain amplitude (the start field E_{st}); 2) the maximum displacement Δx_{max} depends on the amplitude of the ac field; and, 3) after the field is switched off, the PDW spontaneously returns to the initial position.

The following series of experiments were performed: 1) The displacement of the PDW as a function of time was measured — $\Delta x(E(t))$; 2) series of measurements of $\Delta x_{max}(E_A)$ with the field amplitude E_A increased and decreased by discrete amounts were perforend; and, 3) Δx_{max} was measured as a function the number of switching cycles with fixed field amplitude.

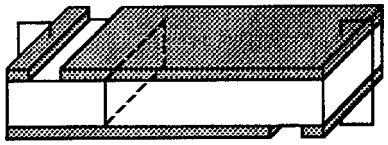

FIG. 1. Configuration of the electrodes and the initial position of the PDW.

2. VOLUME SCREENING EFFECTS

It is well known that the motion of domain walls in ferroelectrics is due to near-wall nucleation, whose probability is determined by the local field $E_{\rm loc}$, averaged over a volume of the order of the size of a nucleus.[9,10] The field $E_{\rm loc}$ is determined by the potential difference U between the electrodes and by the depolarizing field $E_{\rm dep}$ (produced by bound charges) and the screening fields. The contribution of the external screening field $E_{\rm escr}$ (due to redistribution of the charge on the electrodes) and the bulk screening field $E_{\rm bscr}$ produced by the bulk charges[11,12] can be singled out as

$$E_{\rm loc}(r,t)=E_{\rm ex}-[E_{\rm dep}(r,t)-E_{\rm escr}(r,t)-E_{\rm bscr}(r,t)]$$
$$=E_{\rm ex}-\Delta E_{\rm loc}(r,t), \tag{1}$$

where $E_{\rm ex}=U/d$ is the external field and d is the thickness of the plate.

The depolarizing field retards the PDW and the screening decreases its influence. The time constant $\tau_{\rm escr}$ of the external screening is determined by the parameters of the external circuit and is ordinarily small (less than 1 μs). However, after the external screening is completed, a residual depolarizing field $E_{\rm dr}$ due to the presence of surface dielectric layers of thickness L is present in the bulk:[12,13]

$$E_{\rm dr}=E_{\rm dep}-E_{\rm escr}=2LP_S[\varepsilon_L\varepsilon_0(d-2L)+2\varepsilon_b\varepsilon_0L]^{-1}$$
$$\approx 2LP_S(\varepsilon_L\varepsilon_0 d)^{-1}, \tag{2}$$

where P_S is the spontaneous polarization and ε_L and ε_b are the permittivities of the surface layer and volume, respectively. The compensation of $E_{\rm dr}$ occurs by means of screening in the interior of the ferroelectric due to redistribution of charge carriers and polarization of dipole defects.[11,12,14] The adequately long lifetime of the PDW in a stationary state without an external field (in GMO $\tau_{\rm bscr}\approx 10^4$ s at $T=300$ K) results in complete screening in the bulk

$$E_{\rm dr}-E_{\rm bscr}\approx 0. \tag{3}$$

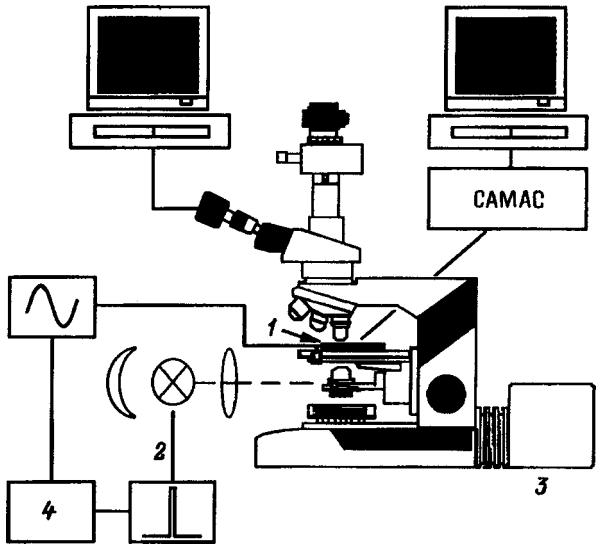

FIG. 2. Arrangment of the measuring apparatus. *1* — Sample, *2* — stroboscopic lamp, *3* — incandescent lamp, *4* — delay unit.

3. MOTION OF A PDW

A linear field dependence of the velocity of a PDW[1,3]

$$v(E_{\rm ex})=\mu(E_{\rm ex}-E_{\rm st}), \tag{4}$$

where μ is the mobility of the PDW, is observed experimentally in a wide range of fields and temperatures in GMO.

To explain the characteristic features of the motion of a PDW displaced from its initial position, we shall examine the change in $E_{\rm loc}$ that determines the velocity of the wall. As the wall moves, the depolarizing field produced by the bound charges in the bulk changes. There is enough time for the external screening to compensate this change partially, but there is not enough time for the bulk screening charges to be redistributed. As a result, $E_{\rm loc}$ is changed by the total residual depolarizing field $E_{\rm dr}$ and the field produced by bulk screening charges that compensated the polarizing field in the initial position (memory effect). Let the PDW be displaced from its initial position by the amount Δx. Then the spatial distribution of the charges can be represented in the form of two strips of width Δx with effective surface charge density

$$\sigma=LP_Sd^{-1}\varepsilon_b\varepsilon_L^{-1}(1+k), \tag{5}$$

where k is the degree of screening $(-1<k<1)$.

Introducing the parameter k makes it possible to take the past history into account: For the first displacement from a completely screened state $k=1$, prolonged cyclic switching decreases k, and $k=-1$ if the PDW stays in the displaced position for a sufficiently long time. In the general case, as a result of cyclic switching, the screening charge decreases nonuniformly in space in the interval of displacements $0<\Delta x<\Delta x_{\rm max}$.

It is easy to see that in this case the field on the PDW can be determined as function of the displacement as

$$\Delta E_{\rm loc}(\Delta x)=\sigma(\varepsilon_b\varepsilon_0)^{-1}F(\Delta x/d), \tag{6}$$

$$F(\Delta x/d)=(1/\pi)[2\tan^{-1}(\Delta x/d)+(\Delta x/d)\ln(1+d^2/\Delta x^2)].$$

In this approximation, the start field $E_{\rm st}$ depends on the displacement,

$$E_{\rm st}=\Delta E_{\rm loc}(\Delta x)-E_{\rm th}, \tag{7}$$

where $E_{\rm th}$ is the threshold field required to form a nucleus.[6,7] This also explains the observed stopping of the PDW.

Then the expression for the velocity of the PDW is

$$v(E_{\rm ex},\Delta x)=\mu[E_{\rm ex}-\Delta E_{\rm loc}(\Delta x)-E_{\rm th}]. \tag{8}$$

Neglecting bulk screening, the PDW stops at a displacement by $\Delta x_{\rm max}$ from the initial position:

$$v(E_{\rm ex},\Delta x_{\rm max})=0. \tag{9}$$

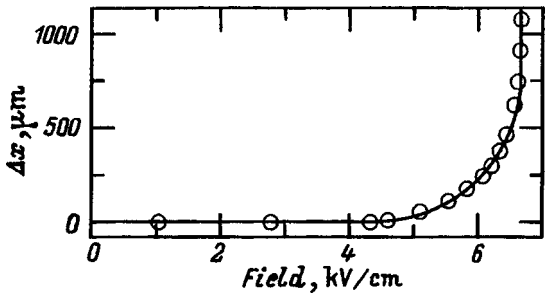

FIG. 3. Trajectory of the PDW. The experimental points are fit by the function (11).

A relation between E_{ex} and Δx_{max} can be obtained from this condition:

$$E_{ex}-P_S L(1+k)(\varepsilon_L\varepsilon_0 d)^{-1}F(\Delta x_{max}/d)-E_{th}=0. \quad (10)$$

This relation is also applicable for incomplete bulk screening.

The parameters E_{th} and k can be determined by fitting the function (10) to the experimental results $\Delta x_{max}(E_{ex})$. In addition, the motion of the PDW in a varying field can be described using the relation

$$v(t)=d\Delta x(t)/dt=\mu[E_{ex}-\Delta E_{loc}(\Delta x)-E_{th}]. \quad (11)$$

As a result, the mobility of a PDW can be determined from measurements of the time-dependence of the displacement.

4. DISCUSSION

The mobility of a PDW (at room temperature $\mu=1.9\times10^{-6}$ m^2/V·s) was determined by analyzing the motion of the wall (Fig. 3).

The relation (10) with $E_{th}=5.6$ kV/cm gives a good fit of $\Delta x_{max}(E)$ in the interval from 10 to 1500 μm (Fig. 4a), obtained by successively increasing the field amplitude by discrete amounts (in the first series of measurements).

It should be noted that small (but measurable) displacements $\Delta x_{max}<10$ μm can also be observed for $E<5.6$ kV/cm (Fig. 4b). This effect can be attributed to the influence of the spatial dependence of the degree of screening of the depolarizing fields near the initial position of the PDW.

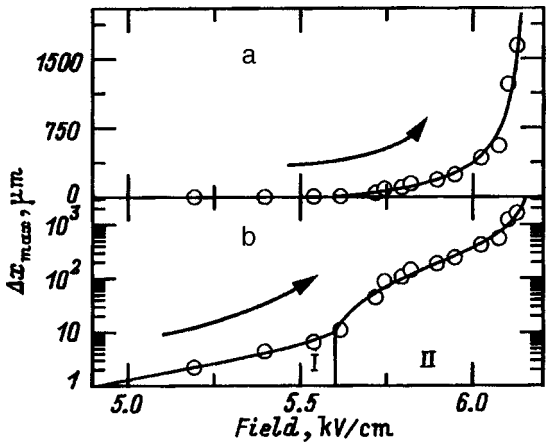

FIG. 4. Field dependence of Δx_{max} with increasing field amplitude. The arrow shows the direction of variation of the field amplitude. The experimental points are fit by the relation (10).

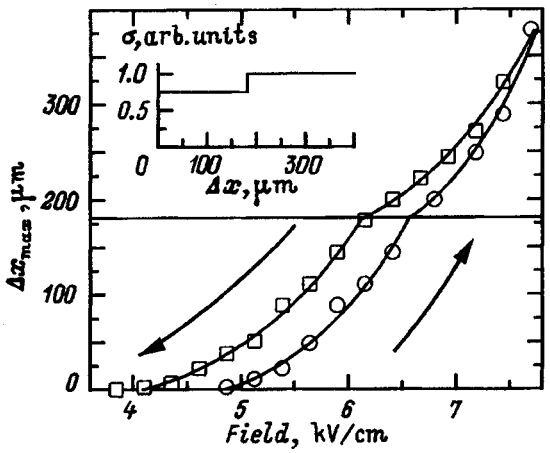

FIG. 5. Field dependence of Δx_{max} with increasing and subsequently decreasing field amplitude. The experimental points are fit by the relations (12) and (13). Inset: Spatial distribution of the charge density of bulk screening with increasing field amplitude.

To study the influence of the past history on $\Delta x_{max}(E)$ the sample was switched cyclically for a long period of time in a field with constant amplitude and fixed maximum displacement Δx_{max}. Then, in a series of measurements performed with both increasing and decreasing field amplitude kinks were observed in the dependence $\Delta x_{max}(E_{ex})$ at $\Delta x_{max}=\Delta x_{max1}$ (Fig. 5).

To explain the characteristic features let us assume that with prolonged cyclic motion of a PDW in the displacement interval $0<\Delta x_{max}<\Delta x_{max1}$ the surface charge density of bulk screening decreases and $\sigma(\Delta x)$ changes abruptly at the limit of the interval. Then, a complicated function is used to fit the experimental results:

$$E_{ex}=P_S L(1+k_1)(\varepsilon_L\varepsilon_0 d)^{-1}F(\Delta x_{max}/d)+E_{th}, \quad (12)$$

for $\Delta x_{max}<\Delta x_{max1}$ and

$$E_{ex}=P_S L(\varepsilon_L\varepsilon_0 d)^{-1}\{(1+k_1)F(\Delta x_{max}/d) + (1+k_2)F[(\Delta x_{max}-\Delta x_{max1})/d]\}+E_{th}. \quad (13)$$

for $\Delta x_{max}>\Delta x_{max1}$.

The spatial distribution (relief) of $\sigma(\Delta x)$ (Fig. 5, inset) can be determined from the results of the fit.

The large hysteresis in the displacements (Fig. 5) (increase of the displacements with the same field amplitude, obtained with a discrete increase of the field amplitude as compared with measurements with increasing amplitude) can be explained by a change in the relief $\sigma(\Delta x)$ in the course of prolonged measurements.

To investigate the kinetics of the change in $\sigma(\Delta x)$ the dependence of the maximum displacement Δx_{max} on the number of successive switching cycles with a fixed field amplitude was measured by integrating the switching currents. The results obtained can be fit satisfactorily by a power-law function (Fig. 6), characteristic for nonexponential relaxation processes.

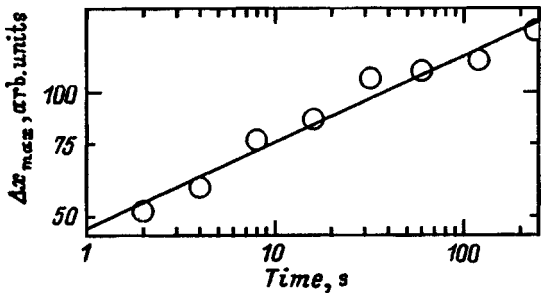

FIG. 6. Maximum displacement of PDW versus the cyclic switching time.

The comprehensive investigations of the dynamics of PDWs in GMO showed that the motion of the PDW and the change is the motion as a result of cyclic switching can be described systematically by taking into account the kinetics of the bulk screening of the depolarizing fields. The proposed approach is general and can be used to analyze the kinetics of the domain structure in other ferroelectric materials.

These investigations were supported in part by the Russian Fund for Fundamental Research (Grant No. 96-02-19588).

*E-Mail: Vladimir.Shur@usu.ru

[1] A. Kumada, Ferroelectrics **3**, 115 (1972).
[2] A. N. Alekseev, M. V. Zlokazov, and I. V. Osipov, Izv. Akad. Nauk SSSR, Ser. Fiz. **47**, 465 (1983).
[3] A. Kumada, Phys. Lett. A **30**, 186 (1969).
[4] R. B. Flippen, J. Appl. Phys. **46**, 1068 (1975).
[5] V. Ya. Shur, V. V. Letuchev, E. L. Rumyahtsev, and T. B. Charikova, Zh. Tekh. Fiz. **55**(8), 1666 (1985) [Sov. Phys. Tech. Phys. **30**, 971 (1985)].
[6] V. Ya. Shur, V. P. Kuminov, A. L. Gruverman, and E. V. Kopylova, Izv. Akad. Nauk SSSR, Ser. Fiz. **53**(7) 1403 (1989).
[7] V. Ya. Shur, A. L. Gruverman, V. P. Kuminov, and N. A. Tonkachyova, Ferroelectrics **111**, 197 (1990).
[8] V. Ya. Shur, V. V. Letuchev, E. L. Rumyantsev, and T. B. Charikova, Fiz. Tverd. Tela (Leningrad) **28**, 2829 (1986) [Sov. Phys. Solid State **28**, 1583 (1986)].
[9] V. Ya. Shur and E. L. Rumyantsev, Ferroelectrics **191**, 319 (1997).
[10] V. Ya. Shur, in *Ferroelectric Thin Films: Synthesis and Basic Properties. Ferroelectricity and Related Phenomena series*, edited by C. A. Paz de Araujo, J. F. Scott, and G. W. Taylor, Gordon & Breach Science Publ., 1996, Vol. 10, Chap. 6, p. 153.
[11] V. Ya. Shur, Yu. A. Popov, and N. V. Korovina, Fiz. Tverd. Tela (Leningrad) **26**(3), 781 (1984) [Sov. Phys. Solid State **26**, 471 (1984)].
[12] V. M. Fridkin, *Ferroelectrics–Semiconductors*, Nauka, Moscow (1976), 408 pp.
[13] M. E. Drougard and R. Landauer, J. Appl. Phys. **30**, 1663 (1959).
[14] P. V. Lambeck and G. H. Jonker, Ferroelectrics **22**, 729 (1978).

Translated by M. E. Alferieff

LATTICE DYNAMICS. PHASE TRANSITIONS

Interaction of long-wavelength excitations in crystals

A. A. Anik'ev and D. E. Edgorbekov

Khudzhand State University, 735700 Khudzhand, Tadzhikistan
(Submitted March 13, 1998)
Fiz. Tverd. Tela (St. Petersburg) **41**, 130–133 (January 1999)

The conditions of resonance interaction of phonons for a scalar model of a crystal in the region of the initial linear section of the dispersion curve of acoustic phonons are investigated using two-particle Green's functions. © *1999 American Institute of Physics.* [S1063-7834(99)02701-X]

A linear dispersion law for acoustic phonons is ordinarily used to calculate the interaction spectra of various elementary excitations interacting with phonons at low momenta. In addition, the thermodynamic characteristics of the crystals are obtained, as a rule, on the basis of the density of states of acoustic phonons calculated in the Debye approximation or a combined Einstein and Debye approximation for the dispersion law. The initial linear phonon dispersion law becomes restructured as a result of the interaction of various types of excitations with acoustic phonons. The deviation of the dispersion law of acoustic phonons from a linear law at low momenta is observed, for example, in strongly anisotropic crystals,[1] in the presence of a high concentration of heavy impurities, and so on. It has been shown in Refs. 2–5 that a radical restructuring of the phonon spectrum can also occur in the case of the phonon-phonon interaction with formation of coupled or resonance states of phonons in crystals. In Ref. 5 it was conjectured that weakly coupled phonon states should always exist in crystals, since special points in the space of wave vectors satisfying general conditions can always be found on the phonon dispersion curves.

In the present paper we investigate the conditions of resonance interaction of phonons for a scalar model of a crystal[6] in the region of the initial linear section of the dispersion curve of acoustic phonons. We shall use the method of two-particle Green's functions (GFs) at room temperature.[3] We must calculate the two-phonon density of states of acoustic phonons taking account of interaction processes and the dispersion law for the excitations obtained. In the ''ladder'' approximation for the GFs, we write the solution of the Bethe–Salpeter equation in the momentum representation in the form[3]

$$G_2(\mathbf{k},\omega)=\frac{2\pi(\mathbf{k},\omega)}{1-\frac{1}{2}\lambda_4\pi(\mathbf{k},\omega)}, \tag{1}$$

where λ_4 is the fourth-order phonon-phonon interaction constant, the function $\pi(\mathbf{k},\omega)$ is the convolution of two single-phonon GFs

$$\pi(\mathbf{k},\omega)=\frac{i}{(2\pi)^4}\int G_1^0(\mathbf{k},\omega)G_1^0 \times(\mathbf{k}-\mathbf{k}_1,\omega-\omega_1)d\omega_1 d\mathbf{k}_1. \tag{2}$$

The Green's function $G^0(\mathbf{k}_1,\omega)$ for free phonons is taken in the form

$$G^0(\mathbf{k},\omega)=\frac{\omega_0(\mathbf{k})}{2}\left\{\frac{1}{\omega-\omega_0(\mathbf{k})+i\delta}-\frac{1}{\omega+\omega_0(\mathbf{k})-i\delta}\right\} \tag{3}$$

with the dispersion law $\omega_0(\mathbf{k})=s|\mathbf{k}|$ for the acoustic phonons. The two-phonon density of states is determined by the imaginary part of the GF (1)

$$\rho_2(\mathbf{k},\omega)=-\frac{1}{\pi}\operatorname{Im}G_2(\mathbf{k},\omega)=-\frac{2\operatorname{Im}\pi(\mathbf{k},\omega)}{|1-\frac{1}{2}\lambda_4\pi(\mathbf{k},\omega)|^2}. \tag{4}$$

The dispersion law for two-phonon excitations is determined by the equation

$$1-\frac{1}{2}\lambda_4\pi(\mathbf{k},\omega)=0. \tag{5}$$

One can see from the relations (4) and (5) that to investigate the excitation spectra with interaction it is necessary to calculate the function $\pi(\mathbf{k},\omega)$ and find the functions (4) and (5) for various values of λ_4. After substituting the expression (3) into Eq. (2) and integrating over ω_1, we have for the case of interacting phonons with total momentum $k=0$ from one dispersion branch

$$\pi(\varepsilon)=\frac{2s_0}{(2\pi)^2 4s}\int_0^{k_m}\frac{d^3dk}{\varepsilon-k^2+i\delta}. \tag{6}$$

Here $\varepsilon=\omega^2/4s^2$ and the integration extends to some momentum k_m cutting off the linear dispersion law. In the Debye model $k_m=k_0$ and $sk_0=\omega_0$. We rewrite Eq. (6) in the form

$$\pi(\varepsilon)=\frac{2s}{(2\pi)^2 4s_0^2}\int_0^{k_m}\frac{k^3dk}{\varepsilon-k^2}-i\frac{2s}{4\pi 4s_0^2}\int k^3\delta(\varepsilon-k^3)dk. \tag{7}$$

Integrating Eq. (7) gives

$$\operatorname{Re}\pi(\varepsilon')=\frac{(2\omega_{\max})^2}{8\pi^2(2s)^2}\left(1+(\varepsilon')^2\ln\left|\frac{(\varepsilon)^2-1}{(\varepsilon')^2}\right|\right), \tag{8}$$

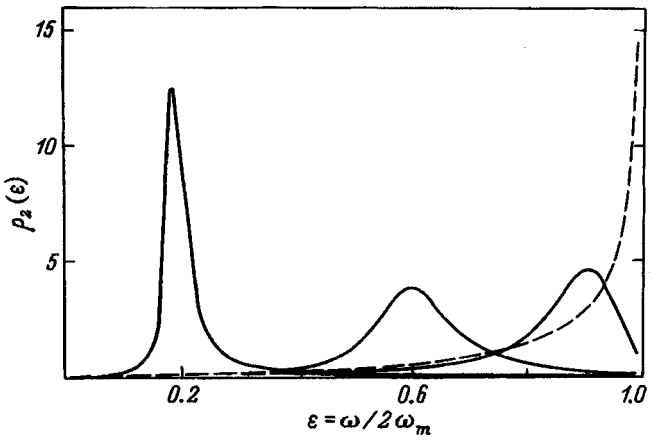

FIG. 1. Density of states of acoustic phonons with a Debye dispersion law.

$$\mathrm{Im}\,\pi(\varepsilon') = -\frac{(2\omega_{\max})^2}{8\pi^2(2s)^3}(\varepsilon')^2. \tag{9}$$

Here $\varepsilon' = \omega^2/2sk_m$ corresponds to the upper limit of the two-phonon acoustic spectrum. The unperturbed two-phonon density of states is determined from Eqs. (9) and (4) with $\lambda_4 = 0$

$$\rho_2^0(\omega) = \frac{\omega^2}{8\pi^2(2s)^3} = \frac{3V_0}{(2\omega_0)^3}\omega^2, \tag{10}$$

where the maximum value $\omega_m = \omega_0 = (6\pi^2/V_0)^{1/3}\cdot s$ corresponds to the Debye frequency ω_0. The density of states (10) is shown in Fig. 1 (dashed line). The two-phonon density of states, taking account of the interaction, is determined by the relations (4), (8), and (9). Solutions exist only for negative values of the renormalized coupling constant $\lambda_4' = (2\omega_m)^2/8\pi^2(2s)^3\lambda_4$. The change occurring in the density of states spectra when the interaction is switched on is shown in Fig. 1 (solid lines) for $\lambda_4 = -0.1$, $\lambda_4 = -0.2$, and $\lambda_4 = -0.3$. One can see that as the coupling constant λ_4 increases, a peak due to a resonance state of the phonons appears in the spectrum. The intensity of this peak increases rapidly and the peak itself shifts toward the low-frequency limit of the spectrum. In Eq. (7) the integration was performed formally over momenta from $k = 0$ to $k = k_m$. This is legitimate only for infinite bodies. In the case of a real crystal with a finite volume, we must integrate from a value $k = k_0$, $k_0 = V^{-1/3}$, where V is the volume of the crystal. In this case the expression (8) becomes

$$\mathrm{Re}\,\pi(\omega) = -\frac{(k_m - k_0)^2}{8\pi^2 2s}\left(1 + \frac{\omega^2}{2s^2(k_m - k_0)^2}\ln\frac{\dfrac{\omega^2}{2sk_m^2} - 1}{\dfrac{\omega^2}{2sk_0^2} - 1}\right). \tag{11}$$

Nonetheless, the equation (11) does not change the results in principle, since we employed an approximation in which the coupling constant λ_4 does not depend on the momentum. For long-wavelength excitations, the vertex describing phonon–phonon scattering should be proportional to the momentum, since in the limit $k \to 0$ scattering does not occur in a uniform medium.[7] For phonons with a linear dispersion law, the case studied here, a coupled phonon state cannot exist outside the two-phonon band.

1. ACOUSTIC PHONONS WITH A NONLINEAR SECTION ON THE DISPERSION CURVE

Let us now assume that the dispersion law of acoustic phonons is $\omega(\mathbf{k}) = s_0|\mathbf{k}| - a|\mathbf{k}|^3$ $(a > 0)$. The function $\pi(\rho, \omega)$ for nonzero total momentum $\mathbf{p}$ can be written as

$$\pi(\mathbf{p},\omega) = \frac{1}{(2\pi)^3}\int d\mathbf{k}\left\{\frac{1}{\omega - \omega(\mathbf{k}) - \omega(\mathbf{p}-\mathbf{k}) + i\delta} - \frac{1}{\omega + \omega(\mathbf{k}) + \omega(\mathbf{p}-\mathbf{k}) - i\delta}\right\}. \tag{12}$$

Let us transform the expression in braces, introducing the new wave vector $\mathbf{q} = \mathbf{p}/2 - \mathbf{k}$. Then Eq. (12) assumes the form $(\varepsilon = \omega - 2\omega_0(\mathbf{p}))$

$$\pi(\mathbf{p},\omega) = \frac{1}{(2\pi)^2}\int_0^{\Lambda}\frac{k^2 dk}{\varepsilon + 3apk^2}. \tag{13}$$

Here the integration extends up to a maximum value Λ_m, where the chosen dispersion law is satisfied. From Eq. (4) we have for the dispersion law of such phonons

$$1 - \frac{\lambda_4\Lambda}{(2\pi)^2 3ap}\left[1 - \left(\frac{\varepsilon}{3ap\Lambda}\right)^{1/2}\tan^{-1}\left(\frac{3ap\Lambda}{\varepsilon}\right)^{1/2}\right] = 0. \tag{14}$$

Expanding the function $\tan^{-1}x$ in a power series in x for $x > 1$ $(\varepsilon \approx 0)$ we have for the dispersion law

$$\omega(\mathbf{p}) = 2(s\mathbf{p} - a|\mathbf{p}|^3) + \frac{2\pi}{3}\lambda_4\Lambda^3. \tag{15}$$

Therefore, for $\mathbf{p} = 0$, the branch of the coupled state terminates at a nonzero frequency $\omega = \frac{2\pi}{3}\lambda_4\Lambda^3$, which is determined by the coupling constant λ_4 and the maximum value of the wave number Λ. It is obvious from Eq. (15) that the branch of the coupled state exists for arbitrarily small values of λ_4 and, for $\lambda_4 = 0$, the dispersion law (15) transforms into the initial dispersion law.

2. ACOUSTIC PHONONS IN STRONGLY ANISOTROPIC CRYSTALS

In strongly anisotropic crystals, the dispersion law of acoustic phonons on even one branch can be different for directions along the symmetry axis and in a plane perpendicular to it. For example, for complicated crystals the dispersion law of the transverse acoustic phonon branch can be approximated by the relation[8]

$$\omega^2(\mathbf{k}) = s_\perp^2 k_\perp^2 + ak_\perp^4 + b\sin^4\frac{k_\parallel a}{2}, \tag{16}$$

where $k_\parallel$ and $k_\perp$ are the projections of the wave vector on a local-order axis and on a plane perpendicular to it, $s_\perp$ is the sound speed in the layer, b is the sound speed in the direction

of the anisotropy axis, and the coefficient a is determined by the force constants of the interatomic interaction within a layer. The first two terms determine the dispersion law of acoustic phonons within a layer, and $s_\perp \ll a$,[8] while the last term describes the dispersion law of acoustic phonons in the direction of the anisotropy axis. We shall investigate the conditions for coupling of acoustic phonons satisfying the dispersion law (16), retaining only the first term in the expansion of the sine on the right-hand side. To find the dispersion branch of the coupled state we shall determine the solution of Eq. (4) with the function $\pi(\mathbf{p},\omega)$ given by Eq. (12), taking into account only the first term in braces. We introduce the vector $\mathbf{q}=\mathbf{p}/2-\mathbf{k}$ and direct the vector $\mathbf{p}$ along the sixfold axis. Let $\varepsilon=2\omega_0(\mathbf{p}/2)-\omega$, where $\omega_0(\mathbf{p}/2)=bp_\parallel^2+cp_\parallel^4+\ldots$. We obtain

$$\pi(\mathbf{p},\omega)=-\frac{1}{(2\pi)^2}\int\frac{q_\perp dq_\perp dq_\parallel}{\varepsilon+s_\perp^2q_\perp^2+bq_\parallel^2+aq_\perp^4}. \tag{17}$$

Integrating over $q_\parallel$ gives

$$\pi(\mathbf{p},\omega)=-\frac{1}{8\pi}\int_0^\Lambda\frac{q_\perp dq_\perp}{(\varepsilon+s_\perp^2q_\perp^2+aq_\perp^4)^{1/2}}. \tag{18}$$

The integration in Eq. (17) must be cut off at the upper limit at some $q_{\max}=\Lambda$. For $\varepsilon<s_\perp^4/4a$ we obtain[8]

$$\pi(\mathbf{p},\omega)=-\frac{1}{16\pi s_\perp^2\sqrt{1-\dfrac{4a\varepsilon}{s_\perp^4}}}\times\ln\left|\frac{[s_\perp^2\delta(2-\frac{1}{2}\delta)/4a\Lambda^2]+2-\frac{1}{2}\delta}{[s_\perp^2\delta(2-\frac{1}{2}\delta)/4a\Lambda^2]+\frac{1}{2}\delta}\right|. \tag{19}$$

Here we have introduced

$$\delta=4a\varepsilon/s_\perp^4 \quad (\varepsilon\approx 0).$$

Since $a\gg s_\perp^2$, the dispersion law of excitations near the threshold for the formation of a resonance state $\varepsilon\approx 0$ can be represented as

$$1+\frac{\lambda_4(1+\frac{1}{2}\delta)}{16\pi s_\perp^2}\ln\left|\frac{4-\delta}{\delta}\right|=0. \tag{20}$$

It is evident from this relation that near the threshold the coupling constant must be negative. The dispersion law will have the form

$$\omega(\mathbf{p})=2\omega_0\left(\frac{\mathbf{p}}{2}\right)-\frac{s_\perp^4}{4a}\left(4+\frac{64\pi s_\perp^2}{3\lambda_4}\right)^{1/2}, \tag{21}$$

where $\omega_0(\mathbf{p}/2)$ is determined by the relation (16). Therefore, for momentum $p=0$ the frequency has a nonzero value

$$\omega=\frac{s_\perp^4}{2a}\left(1+\frac{16\pi s_\perp^2}{3\lambda_4}\right)^{1/2}. \tag{22}$$

A branch of the coupled state appears for some threshold value λ_4 determined by the relation $|\lambda_4|\geqslant 16\pi s_\perp^2/3$. The frequency ω $(p=0)$ increases with $|\lambda_4|$.

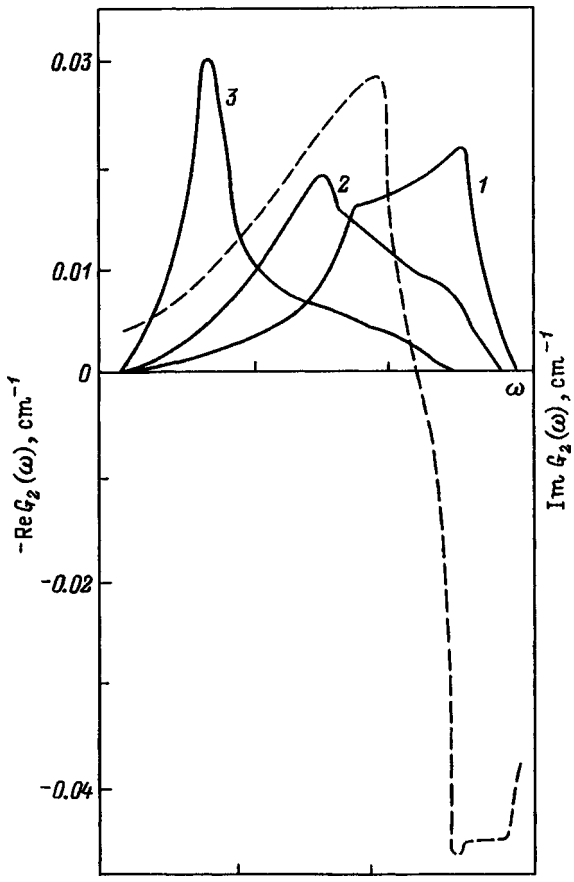

FIG. 2. Acoustic two-phonon density of states for various values of the four-phonon interaction constant. $\lambda_4=-0.1$ (*1*), -0.2 (*2*), and -0.3 (*3*). Dashed line — unperturbed density of states.

3. ACOUSTIC PHONONS WITH A SINUSOIDAL DISPERSION LAW FOR A SCALAR MODEL OF A CRYSTAL

Thus far we have investigated the dispersion law obtained for acoustic phonons by expanding the more general dispersion law, which for a scalar model of a crystal can be expressed in the form

$$\omega(\mathbf{k})=\omega_m^2\sin^2\frac{\mathbf{k}a}{2}, \tag{23}$$

in powers of a small momentum. Here ω_m is the maximum frequency at the limit of the Brillouin zone with $k=\pi/a$ and a is the lattice constant. To calculate the density of states of acoustic phonons with the dispersion law (23) we shall employ the definition (12) of the function $\pi(\mathbf{p},\omega)$ taking account of both terms in the propagator in braces. We obtain for the total momentum of two phonons $p=0$

$$\pi(\omega)=\frac{2\omega_m}{(2\pi)^2}\int\frac{\left|\sin\dfrac{\mathbf{k}a}{2}\right|d\mathbf{k}}{\omega^2-4\omega_m^2\sin\dfrac{\mathbf{k}a}{2}+i\delta}. \tag{24}$$

Separating the real and imaginary parts, we have

$$\mathrm{Re}\,\pi(\varepsilon)=\frac{1}{\pi^2 a^3\omega_m}\int_0^{\pi/2}\frac{z^2 dz\sin z}{\varepsilon^2-\sin^2 z},\quad \begin{cases} z=\dfrac{ka}{2}, \\ \varepsilon=\omega/2\omega_m \end{cases} \tag{25}$$

$$\mathrm{Im}\,\pi(\varepsilon)=-\frac{1}{\pi a^3\omega_m}\frac{(\sin^{-1}|\varepsilon|)^2}{\sqrt{1-\varepsilon^2}}. \tag{26}$$

The integral in Eq. (25) diverges at the upper limit, and it is impossible to calculate it analytically. Therefore we calculated the integral numerically for values of ε in the interval 0–0.99 with step $\Delta z=2\times10^{-5}\pi$. Next, the computed values of $\pi(\varepsilon)$ were substituted into the relation (4) and the two-phonon density of states was calculated taking into account the interaction of the acoustic phonons. For $\lambda_4=0$ the unperturbed part of the density of states is determined by Eq. (26) divided by π. In Fig. 2 the dashed line shows the density of states $\rho_2^0(\varepsilon)$ with the dispersion law (23). As one can see from Eq. (25), $\mathrm{Re}\,\pi(\varepsilon)$ is negative for all values of ε in the interval $(0;1)$, which corresponds to a two-phonon frequency interval with limits 0 and $2\omega_m$. For this reason, the solutions of Eq. (5) exist only for negative values of the anharmonicity constant λ_4. The solid lines in Fig. 2 show the two-phonon density of states $\rho_2(\varepsilon)$ for different values of λ_4: $-0.1,-0.2,-0.3$. One can see from Fig. 2 that the resonance interaction of phonons radically changes the initial two-phonon density of states. In the low-frequency section of the spectrum, an anomalously sharp peak appears with increasing coupling constant, while on the high-frequency edge of the band the density of states drops to zero smoothly. Apparently, these features of the spectrum of acoustic phonons are also general features for the interaction of phonons with other elementary excitations, for example, defects, crowdions, electrons, and so on. One indication of this could be the density of states of acoustic phonons, reconstructed from tunneling measurements in superconducting metals — lead, mercury, and niobium. The reconstructed spectrum has a clear ''anti-Debye'' form with a sharp peak in the low-frequency section of the spectrum.[9,10] This raises the problem of investigating the effect of interactions of phonons with other excitations having close energies on the conditions of formation of coupled and hybrid phonon states and on the form of the phonon dispersion law. The examples studied above show that, for phonons with a linear dispersion law in a scalar model of a lattice, coupled states do not arise outside the two-phonon band. The presence of strong anisotropy improves the coupling conditions. Together with the initial dispersion law, a branch of a coupled state with $\lambda_4 \geqslant 16\pi s_\perp^2/3$ arises in the spectrum.

[1] R. M. Nicklew and H. G. Smith, Phys. Rev. **39**, 4951 (1972).
[2] M. H. Cohen and J. Rivalds, Phys. Rev. Lett. **23**, 1378 (1969).
[3] A. Zavadowski and J. Rivalds, Phys. Rev. Lett. **24**, 1111 (1970).
[4] J. Rivalds and A. Zavadowski, Phys. Rev. B **2**, 1178 (1970).
[5] L. P. Pitaevskiĭ, Zh. Éksp. Teor. Fiz. **70**, 738 (1976) [Sov. Phys. JETP **43**, 382 (1976)].
[6] A. A. Anikev, V. S. Gorelik, and B. S. Umarov, Fiz. Tverd. Tela (Leningrad) **26**, 2772 (1984) [Sov. Phys. Solid State **26**, 1679 (1984)].
[7] A. A. Abrikosov, L. P. Gor'kov, and I. E. Dzyaloshinskiĭ, *Methods of Quantum Field Theory in Statistical Physics* [Prentice-Hall, Englewood Cliffs, N. J., 1963; Fizmatgiz, Moscow, 1962], p. 426.
[8] A. M. Kosevich, *The Physical Mechanics of Real Crystals*, Naukova Dumka, Moscow (1962), p. 105.
[9] E. Burstein and S. Lundqvist, *Tunneling Phenomena in Solids* [Plenum Press, N. Y., 1969; Mir, Moscow, 1973], p. 421.
[10] W. Buckel, *Superconductivity*, Mir, Moscow (1975), p. 316.

Translated by M. E. Alferieff

On an adiabatic invariant in the thermodynamics of solids

V. L. Gilyarov and A. I. Slutsker

A. F. Ioffe Physicotechnical Institute, Russian Academy of Sciences, 194021 St. Petersburg, Russia

L. A. Laĭus

Institute of High-Molecular Compounds, Russian Academy of Sciences 199004 St. Petersburg, Russia
(Submitted July 2, 1998)
Fiz. Tverd. Tela (St. Petersburg) **41**, 134–136 (January 1999)

A thermodynamic invariant in the form of the ratio of a vibrational frequency in an anharmonic solid to the temperature in adiabatic processes is derived. The adiabatic invariance established is used to derive in a simple manner an expression for the temperature change due to elastic adiabatic loading of solids (Kelvin's equation). © *1999 American Institute of Physics.* [S1063-7834(99)02801-4]

The concept of an adiabatic invariant was introduced for mechanical systems.[1] Specifically, for a harmonic oscillator, the invariant amounts to the constancy of the ratio of the vibrational energy of an oscillator to its vibrational frequency with the frequency changing adiabatically (in this case, slowly).[1] The existence of a thermodynamic adiabatic invariant is not obvious. In the present paper this matter is elucidated for anharmonic solids.

The thermodynamic properties of solids are often described, to a first approximation, in a model of independent harmonic oscillators. If the oscillators all have the same characteristic frequency, the Einstein model obtains. However, if the interatomic interaction is taken into account in a harmonic approximation (see, for example, Ref. 2), one arrives at a thermodynamic model of a solid as a phonon gas. Neither case takes account of effects due to the anharmonicity of the interatomic interaction.

These effects are included when the approximations considered are used as zeroth order approximations in more general models. In the simplest case, taking the phonon frequencies to be strain-dependent, we arrive at the Grüneisen theory of anharmonic effects in crystals (quasiharmonic approximation).[2] More accurate approximations are obtained by using the variational theorem of statistical physics[3] as the starting point to construct self-consistent approximations of various types — self-consistent harmonic,[4,5] pseudoharmonic,[6,7] or self-consistent Einstein.[8] We emphasize that the oscillator model plays a key role in all of these cases.

In the present paper we employ a self-consistent Einstein approximation to construct an adiabatic invariant of a solid — a quantity that remains constant in an adiabatic (isoentropic) process.

We start with the expression for the free energy of an ensemble of harmonic oscillators[3]

$$F_0 = kT\sum_n \ln\left(2\sinh\frac{\hbar\omega_n}{2kT}\right). \tag{1}$$

The entropy S_0 of the system is

$$S_0 = -\left(\frac{\partial F}{\partial T}\right)_V = k\sum_n (x_n \coth x_n - \ln(2\sinh x_n)). \tag{2}$$

In these expressions k is Boltzmann's constant, T is the absolute temperature, ω_n is the characteristic frequency of the n-th oscillator, and $x_n = \hbar\omega_n/2kT$. If the oscillators have the same characteristic frequency, summation over n is replaced by a simple multiplication by the number of oscillators in the system. The entropy depends on the parameter x alone.

The condition of adiabaticity is that the entropy is constant. This holds for $x = \text{const}$, whence

$$\frac{\omega}{T} = const, \tag{3}$$

i.e. the ratio of the fundamental frequency (or energy of zero-point vibrations) to the temperature remains invariant for an ensemble of harmonic oscillators.

Evidently, for the model of a solid as an ensemble of harmonic oscillators it is difficult to find a real possibility of varying the frequency of the spectrum by some action applied to the body. However, a change in temperature due to heating (or removal of heat) is inconsistent with adiabaticity. For this reason, for a harmonic solid an adiabatic invariant in the form (3) is more of symbolic (important as a reference) significance.

The behavior of an anharmonic solid is of great practical interest, since in the frequency spectrum such a solid can change under adiabatic conditions.

Let us consider an anharmonic atomic chain in a self-consistent Einstein approximation.[8] The thermodynamic properties of such a system are determined using an auxiliary system (with index 0), which is taken to be the ensemble of harmonic oscillators considered above. The force constants (or frequencies) of these oscillators are determined by the self-consistency variational equations. The free energy of a uniform chain, calculated using the variational theorem,[3] in the nearest-neighbors approximation is

$$F \approx F_0 + \langle U - U_0 \rangle_0$$
$$= F_0 + (N-1)\psi(T,\Delta a) - \frac{\hbar\omega}{4}\coth\frac{\hbar\omega}{2kT}. \quad (4)$$

Here F_0 is determined by the expression (1), U is the potential energy of the system, U_0 is the potential energy of the auxiliary (Einstein) system, ψ is the softened pair-interaction potential (interatomic potential averaged over the states of the auxiliary system), $\Delta a = a\varepsilon$ is the average displacement of an atom from its equilibrium position a, and ε is the relative deformation of the bonds. Averaging is performed over the states of the auxiliary system. We obtain for the entropy per atom (for $N \gg 1$)

$$S = S_0 - \psi_T' + \frac{\hbar^2\omega^2}{8kT}\frac{1}{\sinh^2 x}. \quad (5)$$

Using the Fourier expansion of the softened potential it can be shown that its temperature derivatives are related with the coordinate derivatives as

$$\psi_T' = \frac{\hbar^2}{4mkT^2}\frac{1}{\sinh^2 x}\,\psi''_{\Delta a}. \quad (6)$$

Here

$$\phi = m\omega^2 = 2\psi''_{\Delta a} \quad (7)$$

is the self-consistent force constant. Indeed, the softened potential can be represented by the following chain of equalities:

$$\psi(T,a_n) = \langle \varphi(a_n + u_n - u_{n-1})\rangle_0 = \int \varphi(q)\exp(iqa_n) \times \langle \exp(iq(u_n - u_{n-1}))\rangle_0 dq$$
$$= \int \varphi(q)\exp(iqa_n) \times \exp\left(-\frac{q^2}{2}(\langle u_n^2\rangle_0 + \langle u_{n-1}^2\rangle_0)\right) dq. \quad (8)$$

The last equality was obtained in Ref. 9. For a spatially uniform chain, in Eq. (8) there is no dependence on the index n. The mean-square vibrational amplitude of an atom is determined by the expression[10]

$$\langle u^2\rangle_0 = \frac{\hbar}{m\omega}\coth x. \quad (9)$$

Substituting the expression (9) into Eq. (8) and performing the differentiation, it is not difficult to obtain Eqs. (6) and (7).

Substituting the expression (6) into Eq. (5) for the entropy, we find

$$S = S_0 + \frac{\hbar^2}{8mkT^2}\frac{1}{\sinh^2 x}[m\omega^2 - 2\psi''_{\Delta a}]. \quad (10)$$

The self-consistency condition (7) gives $S = S_0$, i.e. the entropy is identical to the expression (2), which was obtained in a purely harmonic limit. This is related to the fact that the expression for the entropy, with no dynamical analog, does not contain any parameters associated with the details of the interatomic interaction. This circumstance makes it possible, when studying the adiabatic (isoentropic) behavior of an anharmonic system, to extend to such a system the condition of constant entropy in the form of the relation (3). Thus we arrive at the important conclusion that an adiabatic invariant in the form (3) exists for anharmonic systems. The validity of the expression (3) for the invariant is also confirmed by the condition that, in quantum mechanics, the population of the energy levels of oscillators does not change with an adiabatically slow variation of the state of the system.[11] This is due to the fact that the population of the levels is determined only by the factor x_n introduced above, and the condition of a constant population is once again related with the constancy of this factor.

We shall use the expression obtained above for the invariant to find a relation between the temperature and strain of an adiabatically loaded solid, i.e., to describe the thermoelastic effect. To find this relation, expression (7) must be substituted into the expression for the adiabatic invariant (3). This requires an explicit expression for the interaction potential. It can be shown[12] that, for a potential with cubic anharmonicity of the form

$$\varphi(\varepsilon) = \frac{f}{2}(a\varepsilon)^2 - \frac{g}{3}(a\varepsilon)^3,$$

expression (7) becomes

$$\phi = 2(f - 2ga\varepsilon).$$

Substituting this expression into Eq. (3) we obtain

$$\frac{T_2}{T_1} = \sqrt{\frac{f - 2ga\varepsilon_2}{f - 2ga\varepsilon_1}}. \quad (11)$$

Assuming the temperature change and the deformations to be small and expanding Eq. (11) we find

$$\frac{\Delta T}{T} \cong -\frac{g}{f}a\varepsilon_f, \quad (12)$$

where $\varepsilon_f = \varepsilon_2 - \varepsilon_1$ and $\Delta T = T_2 - T_1$.

Expression (12) can be easily reduced to the well-known Kelvin equation for the thermoelastic effect. Indeed, the mechanical stress in the atomic chain under study is determined by the relation $\sigma = f\varepsilon_f/a$, the linear thermal expansion coefficient is $\alpha \simeq gk/af^2$,[13] and the specific heat per degree of freedom is $c = k/a^3$. Then we obtain approximately

$$\frac{\Delta T}{T} \cong -\frac{g}{f}a\varepsilon_f \cong -\frac{\alpha}{c}\sigma,$$

which is the Kelvin equation.

In summary, an adiabatic invariant makes it possible to derive simply and quickly an expression for describing the behavior of a system of oscillators in adiabatic processes.

This work was supported by the Russian Fund for Fundamental Research (No. 96-03-32467a).

[1] L. D. Landau and E. M. Lifshitz, *Mechanics* [Pergamon Press, N. Y.; Nauka, Moscow, 1965], 204 pp.
[2] L. A. Girifalco, *Statistical Physics of Materials* [Wiley, N. Y., 1973; Mir, Moscow, 1975], 382 pp.

[3] R. Feynman, *Statistical Physics*, Mir, Moscow (1978), 407 pp.
[4] N. S. Gills, N. R. Werthamer, and T. R. Koehler, Phys. Rev. **165**, 951 (1968).
[5] A. K. Kugler, Ann. Phys. **53**, 133 (1969).
[6] N. M. Plakida and T. Siklos, Phys. Lett. A **67**, 342 (1978).
[7] N. M. Plakida and T. Siklos, Phys. Status Solidi **33**, 103 (1969).
[8] T. Matsubara and K. Kamiya, Prog. Theor. Phys. **58**, 767 (1977).
[9] A. Maradudin, E. Montroll, and J. Weiss, in *Solid State Physics*, Suppl. 3 [Academic Press, N. Y., 1963; Mir, Moscow, 1965], 383 pp.
[10] V. L. Gilyarov, V. A. Petrov, R. Kh. Sabirov, and A. S. Luk'yanenko, Fiz. Tverd. Tela (Leningrad) **28**, 1332 (1986) [Sov. Phys. Solid State **28**, 750 (1986)].
[11] L. D. Landau and E. M. Lifshitz, *Quantum Mechanics* [Pergamon Press, N. Y.; Nauka, Moscow, 1989], 768 pp.
[12] V. L. Gilyarov and A. B. Pakhomov, Fiz. Tverd. Tela (Leningrad) **23**, 1569 (1981) [Sov. Phys. Solid State **23**, 919 (1981)].
[13] Ya. I. Frenkel, *Kinetic Theory of Liquids* [Clarendon Press, Oxford, 1946; Nauka, Moscow, 1975], 460 pp.

Translated by M. E. Alferieff

The invar effect and phase transitions in Cs_2ZnI_4 crystals

B. Sh. Bagautdinov and V. Sh. Shekhtman

Institute of Solid-State Physics, Russian Academy of Sciences, 142432 Chernogolovka, Moscow District, Russia

(Submitted May 29, 1998)
Fiz. Tverd. Tela (St. Petersburg) **41**, 137–142 (January 1999)

An *in situ* x-ray diffraction study of Cs_2ZnI_4 crystals performed in the 4.2–300 K temperature range is reported. The lattice parameter measurements have revealed three anomalies corresponding to phase transitions. The thermal expansion coefficient along the **c** axis was found to vanish in the region of incommensurate and commensurate modulated phases, 120–96 K (the invar effect). A possible crystallographic model relating modulated atomic displacements to the invar effect is discussed. © *1999 American Institute of Physics.* [S1063-7834(99)02901-9]

It is known that crystals having an incommensurate (IC) phase can exhibit specific anomalies in the temperature dependence of thermal expansion up to the vanishing of the thermal-expansion coefficient (TEC) in certain directions. This feature, called the invar effect, was observed in the IC phase in proustite Ag_3AsS_3,[1] tin selenohypodiphosphate $Sn_2P_2Se_6$,[2] and thiourea $SC(NH_2)_2$ (Refs. 3,4). The nature of this interesting phenomenon remains unclear to this day, which stimulates further investigations of the behavior of the lattice parameters of IC crystals with temperature.[5] This accounts for the interest in compounds of the A_2BX_4 family (A $=$Rb, K, Cs, . . . , B$=$Zn, Co, Hg, . . . , X$=$Cl, Br, I, . . .) which comprises most of the dielectric crystals having an IC phase known at present.[6] Cs_2ZnI_4 belongs structurally to the β-K_2SO_4 type; its room-temperature lattice parameters $a=10.84$ Å, $b=8.29$ Å, $c=14.45$ Å and the space group *Pnma* were determined in Ref. 7. Note that like many crystals of the A_2BX_4 family, the lattice parameters of Cs_2ZnI_4 are in a pseudohexagonal relation: $c\approx b\sqrt{3}$. It was established that, at high temperatures, compounds of the β-K_2SO_4 type are characterized (sometimes virtually) by the hexagonal group $P6_3/mmc$.[8]

Phase transitions in Cs_2ZnI_4 crystals have been a subject of a number of studies. Dielectric,[9,10] NMR,[11] x-ray diffraction,[12] and dilatometric[13] measurements revealed that below room temperature Cs_2ZnI_4 undergoes the following sequence of phase transitions: $Pnma\,(Z=4,\ T_i=120\ \mathrm{K})$ IC $(T_c=108\ \mathrm{K})\ P2_1/m\ (Z=8)$ [or $P2_1/n(T=96\ \mathrm{K})\ P\bar{1}\ (Z=4)$]. Optical and calorimetric measurements revealed additional anomalies near 104 K, so that another sequence following this transition was proposed c.f. Refs. 14 and 15: $Pnma\,(Z=4,\ T_i=117\ \mathrm{K})$ IC $T_c=108\ \mathrm{K}\ P2_1/n\ (Z=8,\ T_1=104\ \mathrm{K})\ P\bar{1}\ (Z=4,\ T_2=96\ \mathrm{K})\ P\bar{1}\ (Z=4)$. A thermodynamic description of the IC phase in Cs_2ZnI_4 can be found in Refs. 16 and 17.

Note that the structural aspects of phase transformations in Cs_2ZnI_4 have not been well studied. No systematic investigation of the temperature dependence of lattice parameters, which is a sensitive indicator of phase transitions, has been carried out thus far for Cs_2ZnI_4. A complete structural analysis of the phases has not been made, the nature of the modulations has not been established, and the phase-transition sequence and the space group of the monoclinic phase ($P2_1/m$ or $P2_1/n$) still remain unclear. This stimulated our comprehensive x-ray diffraction investigation of single-crystal Cs_2ZnI_4 within a broad temperature range, down to the helium temperature.

1. EXPERIMENT

Cs_2ZnI_4 samples were grown from water solution at 313 K.[11] Measurements of temperature dependences were carried out on single-crystal, optically transparent (100), (010), and (001) cuts measuring $2.0\times1.5\times0.3$ mm; a helium cryostat manufactured by IFTT RAS enabled maintaining the temperature to within 0.1 K.[18] The measurements were performed on a SIEMENS D500 diffractometer adapted to two-circle studies of single crystals with Cu $K\alpha$ radiation. The interplanar distances were determined from the centers of gravity of the Bragg reflections (12,0,0) (diffraction angle $\theta\approx58.6°$), (0,10,0) ($\theta\approx69.6°$), and (0,0,18) ($\theta\approx71°$) obtained by $2\theta/\theta$ scanning. The reflection indices relate to the axes of the original *Pnma* phase. Using reflections with large diffraction angles enabled a relative accuracy of not worse than 1.5×10^{-4}. Each scan of the reflection profile was preceded by holding the sample for $\sim$10 min at the given temperature. The reciprocal-lattice configuration analysis was done by scanning in the (a^*b^*0), ($0b^*c^*$), and (a^*0c^*) planes. The program of scanning over undistorted reciprocal space (q scanning) made use of the previously measured crystal-lattice parameters.

2. RESULTS AND DISCUSSION

A. Measurements of temperature dependences

The room-temperature lattice parameters of the Cs_2ZnI_4 crystal were $a=10.835(9)$ Å, $b=8.310(3)$ Å, and $c=14.469(5)$ Å. In accordance with the *Pnma* space group, one observed extinction of the reflections corresponding to the glide-reflection planes a ($hk0;\ h=2n+1$) and n ($0kl;\ k+l=2n+1$). Figure 1 presents temperature depen-

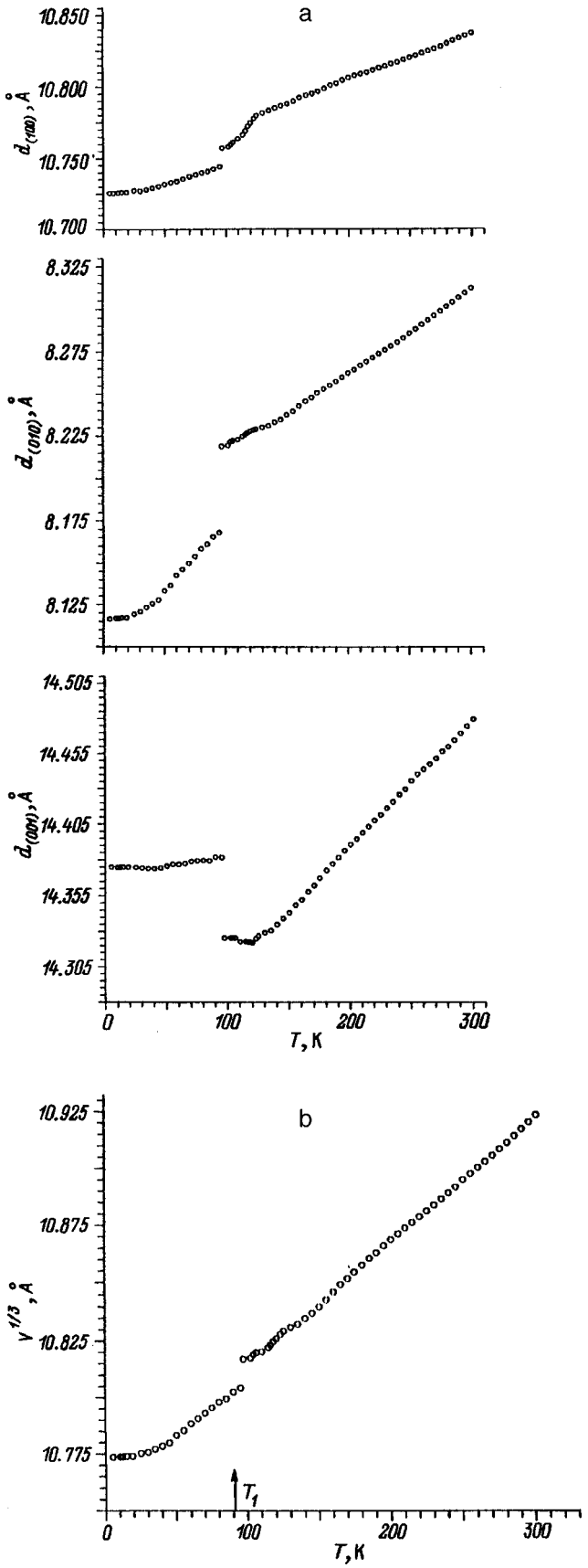

FIG. 1. Temperature dependences of (a) interplanar distances d_{100}, d_{010}, d_{001} and of (b) the unit cell volume of Cs_2ZnI_4. The measurements were made in the heating regime.

TABLE I. Thermal expansion coefficient within the temperature intervals of four low-temperature Cs_2ZnI_4 phases ($\times 10^{-5}$ K^{-1}).

Temperature interval	α_{100}	α_{010}	α_{001}
Pnma 300–120 K	3.1	5.5	6.2
Incommensurate 120–108 K	9.7	6.1	≈0
*P*21/*m* 108–97 K	4.2	4.97	≈0
P-1 96–20 K	2.0	7.06	0.52

dences of the interplanar distances $d(T)$ for the directions [100], [010], and [001]. The TEC values corresponding to the regions of existence of the observed phases were determined by graphical differentiation of the $d(T)$ curves (Table I). Consider the observed temperature-induced effects one by one.

Within the region extending from room temperature to 120 K, one observes close to linear variation of the cell pa-

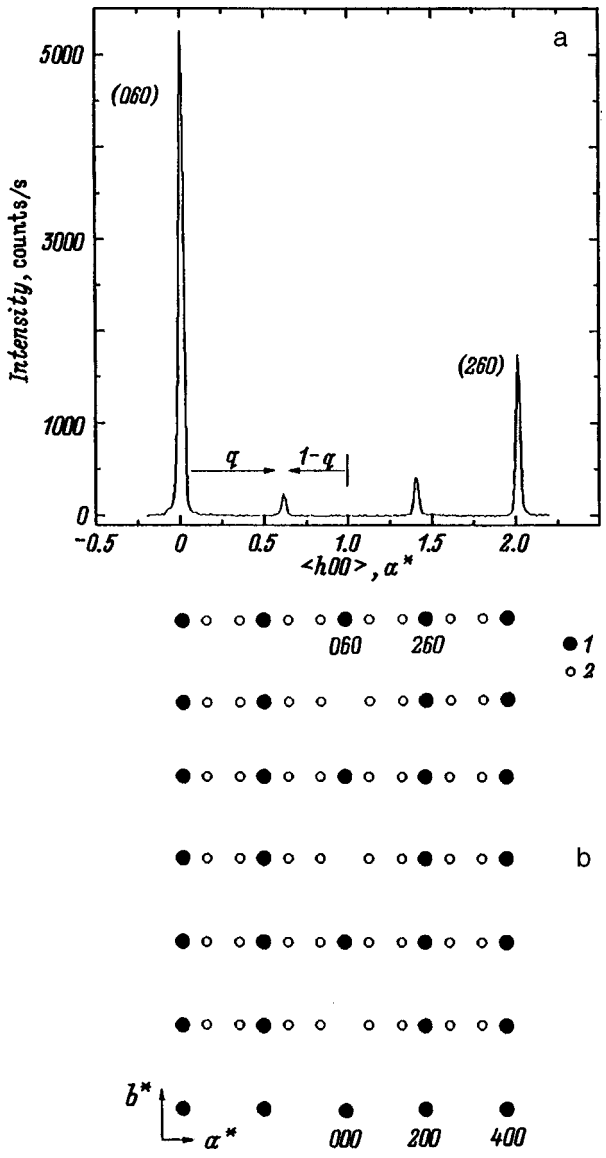

FIG. 2. Position of the Bragg and satellite reflections in the IC phase region: (a) between the (060) and (260) Bragg reflections; (b) schematically on the (a^*b^*0) plane, *1* — Bragg reflections, *2* — satellites.

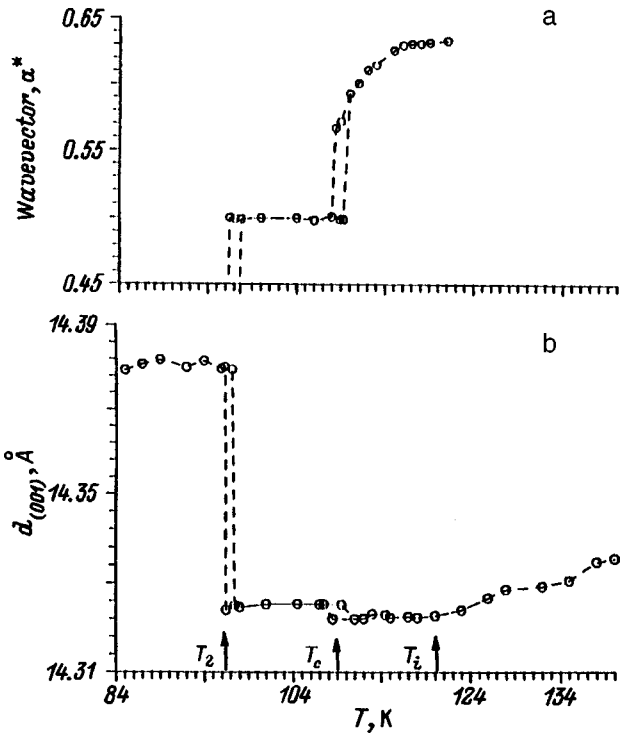

FIG. 3. Temperature dependence of the modulation wave vector (a) and the invar interval of interplanar distance d_{001} (b).

rameters along the a, b, and c axes. An analysis of the systematic reflection absences showed that the above-mentioned conditions for the *Pnma* phase are upheld throughout the temperature range covered. No diffraction features which would support the existence of a phase transition proposed in Ref. 19 have been observed at ~ 270 K.

The normal-IC phase transition at $T_i = 120$ K is signaled by breaks in the $d\,(T)$ curves and jumps in the TEC, which is in agreement with this transition being second order. The modulation of the structure within the 120–108 K interval is identified by the appearance of satellite reflections in the (a^*b^*0) plane.[12] The satellite positions can be described by a wave vector $\mathbf{q}=(1/2+\delta)\mathbf{a}^*$ in the enlarged Brillouin zone or by $1-\mathbf{q}=(1/2-\delta)\mathbf{a}^*$ in the normal zone (Fig. 2). Figure 3a displays the temperature dependence $q\,(T)$ indicating the incommensurability of the modulations. In the IC phase region, the extinction conditions for Bragg reflections do not differ from those for the original *Pnma* phase, with the additional reflections, first-order satellites, grouped around the positions of the forbidden *hk0* reflections with $k=2n+1$ (Fig. 2b). In the four-dimensional representation, this corresponds to the *hk0m* condition with $k+m=2n$, which is a specific feature of the superstructural group $P\,(Pnma)$:$(\bar{1}ss)$ characteristic of the IC phase in the A_2BX_4 family.[20] The vanishing of the TEC along the c axis ($\alpha_{001}\approx 0$) appears remarkable; the invar effect is observed throughout the region of incommensurate and commensurate modulations (Fig. 3).

The IC phase transforms at 108 K to modulated commensurate monoclinic. One can see in Fig. 3b a small jump in the c parameter, and this lock-in transition is first order, which becomes manifest in the coexistence of incommensurate and commensurate modulations in the hysteresis region.[12] The appearance at the transition to the monoclinic phase of the (0,0,11) and (0,1,10) Bragg reflections, which are forbidden for the $0kl$ glide-reflection plane n when $k+l=2n$, is seen in Fig. 4. An analysis of the conditions for extinctions within the 108–96 K interval showed that there is only one such condition, namely, $0k0$ with $k=2n+1$. It

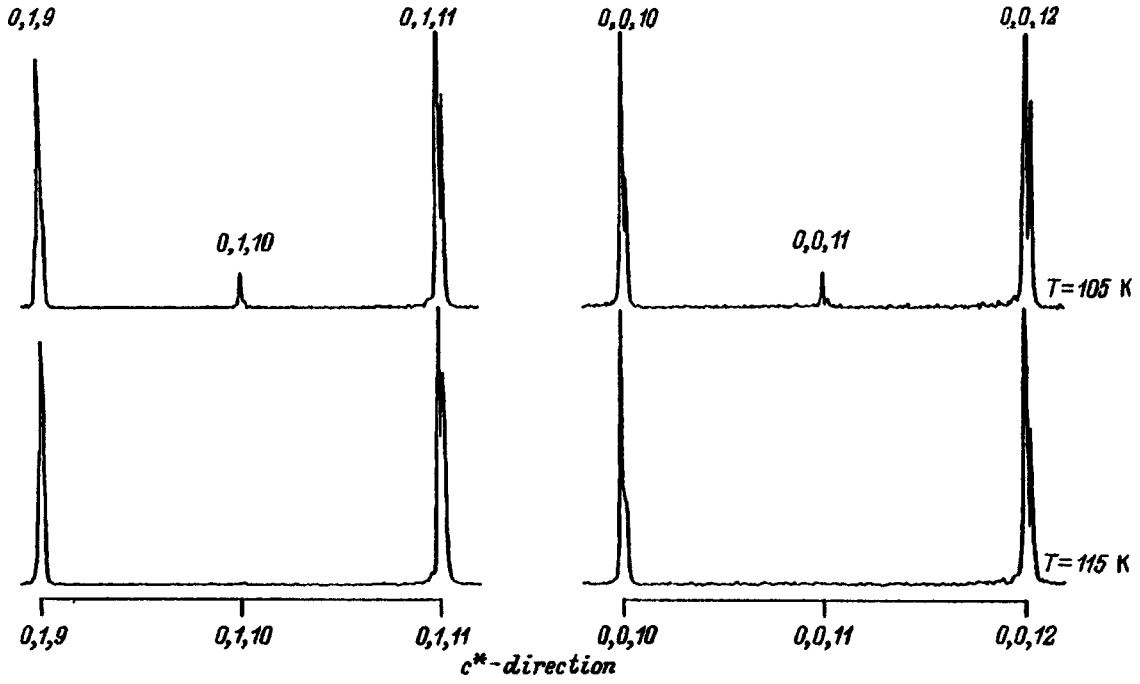

FIG. 4. Analysis of the extinction conditions by scanning in the $(0b^*c^*)$ plane at the temperatures of the incommensurate and commensurate monoclinic phases.

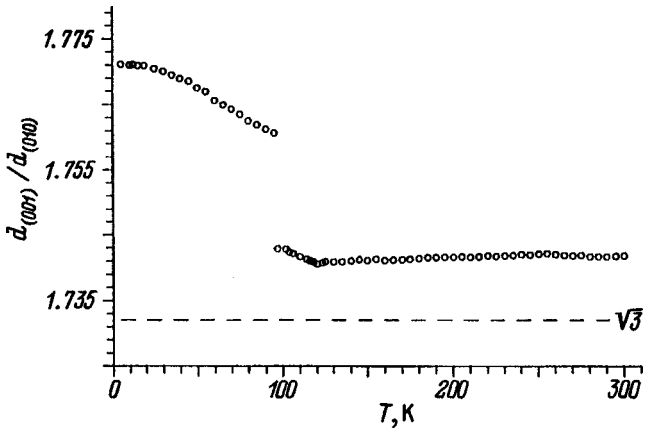

FIG. 5. Temperature dependence of the d_{001}/d_{010} ratio.

indicates two possible space groups for the monoclinic phase, namely, $P12_1/m1$ or $P12_11$. Because no polar properties were revealed in Cs_2ZnI_4 by dielectric measurements,[9,10] one should accept the centrosymmetric space group $P12_1/m1$. We have not observed any features in TEC in the vicinity of 104 K or 101 K, where anomalies in physical properties were quoted in Refs. 14,15.

The first-order phase transition to the triclinic phase $P\bar{1}$ at 96 K is accompanied by a volume compression by 0.1% (Fig. 1b). Here all the three parameters undergo jumps, namely, the *a* and *b* parameters contract, and the *c* parameter expands. The transition exhibits a temperature hysteresis $\Delta T \approx 1.3$ K. As seen from Fig. 5, the deviation of c/b from $\sqrt{3}$ increases at the phase transitions, i.e., the structural rearrangements are accompanied by noticeable distortions of the pseudohexagonal character of the orthorhombic lattice.

B. On the crystallographic characteristics of the modulated phases

The modulation in Cs_2ZnI_4 crystals is characterized by the following crystallographic data: wave vector direction $\mathbf{q} \| [100]$ and the plane of polarization of the atomic displacement wave coincides with (001).[12] Information on the invar effect observed in the $d_{001}(T)$ dependence appears to be an important experimental finding. Let us compare now the orientational characteristics of the modulations and of the invar effect in Cs_2ZnI_4 with data available for other compounds (Table II). According to Table II, the direction of the wave vector **q** in real space for each crystal determines the zone axis $\mathbf{J}_{mnp}$ to which the atomic displacement (polarization) plane is related. The normal to this plane corresponds to the interplanar distance, which remains constant under varying temperature. To put it in simpler words, the ''invar direction'' is perpendicular both to the atomic-displacement wave plane and to the wave vector. The model of the observed lattice anomalies can be based, in our opinion, on competition between static displacements of atoms under modulation and their thermal vibrations. We start from the assumption that thermal expansion of atomic bonds in a crystal, both in modulated and normal state, is determined by the anharmonic part of the atomic interaction potential. As the amplitude of thermal vibrations increases during heating, the component aligned with the atomic bond increases its length, and the components acting in transverse directions affect the tilt of these bonds. The geometry of atomic displacements in the modulated wave can give rise to additional anisotropic contributions to the TEC.

As seen from Fig. 6, the projection of the interatomic bond on the normal to the displacement-wave plane (i.e. the interplanar distance) can remain constant during heating due

TABLE II. Orientational characteristics of the modulations and of the invar direction.

Compound, temperature interval of IC phase	Space group, lattice parameters	Wave-vector direction		Atom displacement plane	Zero TEC plane
		in reciprocal space	in crystal space		
Cs_2ZnI_4 [12], 120–108 K	*Pnma*, $a=10.84$ Å, $b=8.31$ Å, $c=14.47$ Å	$(1-\delta)a^*/2$	[100]	(001)	(001)
$CS(NH_2)_2$ [4], 202–169 K	*Pnma*, $a=7.655$ Å, $b=8.537$ Å, $c=5.520$ Å	δb^*	[010]	(001)	(001)
$Sn_2P_2Se_6$ [2], 220–193 K	$P2_1/c$, $a=6.83$ Å, $b=7.70$ Å, $c=11.72$ Å, $\beta=124.5°$	$-\delta_1 a^* + \delta_2 c^*$	[100]	(001)	(001)
$Cs_3Sb_2I_9$ [21], 78–72 K	$P-3m1$, $a=8.435$ Å, $b=10.390$ Å	$(1/2-\delta)a^* + c^*/2$	[100]	no data	(001)
As_3AsS_3 [1], 60–48 K	$R-3m1$, $a=10.82$ Å, $b=8.69$ Å	$(1-\delta)a^*/3 + (1-\delta)c^*/3$	[001] (principal direction)	no data	(100)

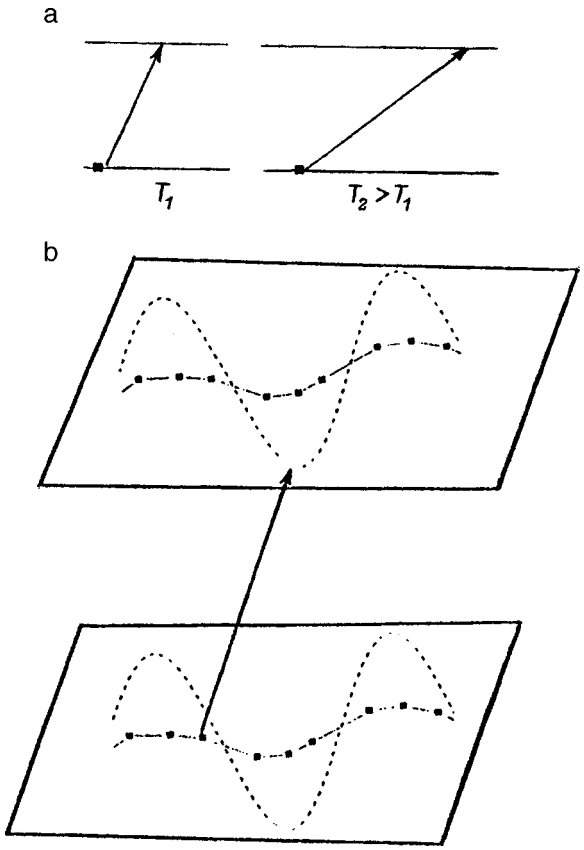

FIG. 6. Schematic explanation of the invar effect in the modulated phase. (a) Compensation of the elongation of a bond by an increase of its tilt; (b) increase in bond tilt as a result of static modulated atom displacements with different amplitudes.

to the elongation of the bonds being compensated by an increase in their tilt. This appears possible in the IC phase, because static displacements of chemically unlike atoms in a modulated state differ in amplitude while having the same wavelength. As a result, the bond tilts in the direction perpendicular to the polarization plane increase. For instance, in Rb_2ZnCl_4, a compound structurally close to Cs_2ZnI_4, the displacement amplitude of the Rb^+ cations is nearly three times smaller than that of the Cl^- anions.[22] In β-K_2SO_4–type crystals, the increase in bond tilt compensating the bond elongation is $\approx 3°$. Considered from this standpoint, it appears natural to expect observation of the invar properties in the direction perpendicular to the polarization plane, as this indeed occurs in the cases given in Table II. Comprehensive structural studies of atomic displacements at several temperatures within the IC phase are planned to test the model.

Thus we have determined the temperature dependence of the (100), (010), and (001) interplanar distances along the a, b, and c axes of the original normal phase, refined the phase-transition sequence and space group $P2_1/m$ for the monoclinic phase of the crystals, and discussed a possible crystallographic model of the invar effect in incommensurate phases. The results of the work show that standard $d(T)$ measurements using Bragg reflections can be used to advantage in determination of the atomic displacement plane in a modulation wave. The discussed sequence has thus far been confirmed for a limited number of crystals presented in Table II. It would apparently be useful to proceed with TEC measurements for zone planes with the same wave-vector direction.

The authors owe their thanks to I. P. Aleksandrova for the crystals and to I. M. Shmyt'ko for providing the helium cryostat for the study.

[1] S. S. Khasanov and V. Sh. Shekhtman, Ferroelectrics **67**, 371 (1986).
[2] T. K. Parsamyan and V. Sh. Shekhtman, Fiz. Tverd. Tela (Leningrad) **31**, No. 5, 69 (1989) [Sov. Phys. Solid State **31**, 759 (1989)].
[3] H. Futama, J. Phys. Soc. Jpn. **17**, 434 (1962).
[4] I. M. Shmyt'ko, B. Sh. Bagautdinov, and V. K. Magataev, Fiz. Tverd. Tela (St. Petersburg) **38**, 2223 (1996) [Phys. Solid State **38**, 1224 (1996)].
[5] V. L. Pokrovskiĭ and L. P. Pryadko, Fiz. Tverd. Tela (Leningrad) **29**, 1492 (1987) [Sov. Phys. Solid State **29**, 853 (1987)].
[6] H. Z. Cummins, Phys. Rep. **185**, 211 (1990).
[7] D. E. Scaife, Austral. J. Chem. **24**, 1315 (1971).
[8] K. S. Aleksandrov, Kristallografiya **38**, 128 (1993) [Sov. Phys. Crystallogr. **38**, 67 (1993)].
[9] K. Gesi, J. Phys. Soc. Jpn. **50**, 3535 (1981).
[10] F. Shimizu, T. Anzai, S. Savada, and M. Takashige, Ferroelectrics **185**, 301 (1996).
[11] I. P. Aleksandrova, S. V. Primak, E. V. Shemetov, and A. I. Kruglik, Fiz. Tverd. Tela (Leningrad) **33**, 1344 (1991) [Sov. Phys. Solid State **33**, 758 (1991)].
[12] B. Sh. Bagautdinov and I. P. Aleksandrova, Solid State Commun. **90**, 817 (1994).
[13] S. V. Mel'nikova and S. V. Primak, Phase Transit. **36**, 191 (1991).
[14] D. P. Billesbach and F. G. Ullman, Phys. Rev. B **46**, 5073 (1992).
[15] J. Díaz-Hernández, M. J. Tello, J. M. Igartua, I. Ruiz-Larrea, T. Breczewski, and A. López-Echarri, J. Phys.: Condens. Matter **7**, 7481 (1995).
[16] J. J. Melero, J. Bartolomé, R. Burriel, I. P. Aleksandrova, and S. Primak, Solid State Commun. **95**, 201 (1995).
[17] A. E. Jacobs, J. Phys.: Condens. Matter **8**, 517 (1996).
[18] V. V. Borovikov, L. S. Kruts, G. S. Med'ko, A. A. Novomlinskiĭ, G. A. Ryazankin, and I. M. Shmyt'ko, Preprint IFTT AN SSSR, Chernogolovka (1984).
[19] O. P. Lamba, M. B. Patel, S. Ram, P. Chand, and H. D. Bist, Solid State Commun. **50**, 321 (1984).
[20] P. M. de Wolff, T. Janssen, and A. Janner, Acta Crystallogr., Sect. A: Cryst. Phys., Diffr., Theor. Gen. Crystallogr. **37**, 625 (1981).
[21] M. S. Novikova, B. Sh. Bagautdinov, I. P. Aleksandrova, and M. Blomberg, Solid State Commun. (in press).
[22] A. Hedoux, D. Grebille, J. Jaud, and G. Godefroy, Acta Crystallogr., Sect. B: Struct. Sci. **45**, 370 (1989).

Translated by G. Skrebtsov

Phase transitions in the $(Cs_{1-x}Rb_x)_2ZnI_4$ system

A. A. Sukhovskiĭ, V. V. Lisin, I. P. Aleksandrova, and V. N. Voronov

A. V. Kirenskiĭ Institute of Physics, Siberian Branch of the Russian Academy of Sciences, 660036 Krasnoyarsk, Russia

J. J. Melero

Saragossa University, 50009 Saragossa, Spain
(Submitted June 22, 1998)
Fiz. Tverd. Tela (St. Petersburg) **41**, 143–147 (January 1999)

$(Cs_{1-x}Rb_x)_2ZnI_4$ crystals were grown by two different methods with Rb concentrations varying from $x=0$ to 2.5%. ^{127}I NQR and calorimetric measurements showed that crystals grown by the Bridgman technique contain residual impurities ($\sim 0.5\%$) for all x. While $x=0$ crystals grown from solution do not contain detectable impurities, they allow incorporation only of a low Rb concentration, not above 0.5%. A transition-temperature–concentration (x) phase diagram has been constructed for Bridgman-grown crystals from NQR data. Rb doping shifts the normal-incommensurate and incommensurate-ferroelastic phase-transition points toward higher temperatures with different rates. The $P2_1/m \leftrightarrow P1$ first-order transition shifts toward lower temperatures. The region of low Rb concentrations lies closest to the critical point.
 [S1063-7834(99)03001-4]

Studies of defect interaction with incommensurate (IC) structure belong to an independent and well-developed area in the physics of aperiodic systems. While this subject includes several phenomena occurring only in IC modulated crystals, each such investigation starts from the assumption that the phase diagram of the system within a certain interval of impurity concentrations x is known.

We are reporting a ^{127}I NQR and calorimetric study of the $(Cs_{1-x}Rb_x)_2ZnI_4$ system within the Rb concentration region $x=0-0.025$. There are several publications on the phase transitions in undoped Cs_2ZnI_4 (Refs. 1–6) and symmetry measurements in the phase transition sequence[2]

$$Pnma\ (Z=4) \leftrightarrow IC \leftrightarrow P2_1/m\ (Z=8) \leftrightarrow P1\ (Z=4).$$

The phase-transition temperatures of crystals grown from solution, as determined under cooling, are $T_i=120.5$ K for the normal-IC phase transition, $T_{c1}=108$ K for the lock-in transition, and $T_{c2}=96$ K for the low-temperature first-order transition.

Interestingly, the coefficient ratio $\beta_2/\beta_1=0.44$ (Ref. 3) of the thermodynamic potential describing the phase transition sequence in the theoretical model of Cs_2ZnI_4 is characteristic of the so-called strong-anisotropy case, where the system is close to the Lifshits-type critical point[7]. Doping a crystal is one of the ways to bring the system to a singular point on the phase diagram and to study it. Unfortunately, predicting the direction of doping-induced displacement of a system in complex structures is virtually impossible; it is established experimentally and is one of the goals pursued in phase diagram studies.

1. EXPERIMENT

A. Crystal growing

Crystals of undoped Cs_2ZnI_4 were grown previously from water solution. This method was employed also to grow doped crystals, but we did not succeed in increasing the Rb concentration in solution-grown crystals above $x=0.005$. The Bridgman method was employed to prepare crystals with higher Rb concentrations. The crystals were grown in quartz ampoules in an argon ambient. The starting reagents were purified by repeated recrystallization. Crystals with Rb content $x=0$, 0.0011, 0.005, 0.01, and 0.025 were obtained. The rubidium content for small concentrations (up to $x=0.005$) was determined by plasma absorption analysis, and for high x, by x-ray fluorescence. It was established that the Rb concentrations in grown boules coincide within experimental error with those in the starting charge.

B. NQR

For conveniency in comparison, Fig. 1 reproduces the data of Ref. 2 obtained for an undoped Cs_2ZnI_4 crystal grown from water solution. The temperature dependences of the NQR frequencies at the lock-in transition (T_{c1}) exhibit breaks which permit determination of the transition point T_{c1} to within ~ 0.5 K. The normal-IC phase-transition point (T_i) is determined to within 1–2 K because of a partial overlap of the lines belonging to the normal and IC phases, which is associated with the presence of transition precursor clusters above T_i.

Figure 2 presents temperature dependences of the ^{127}I NQR frequencies for a solution-grown crystal with Rb concentration $x=0.0018$. Even such a low concentration of the Rb impurity affects strongly the shape of the ^{127}I NQR spec-

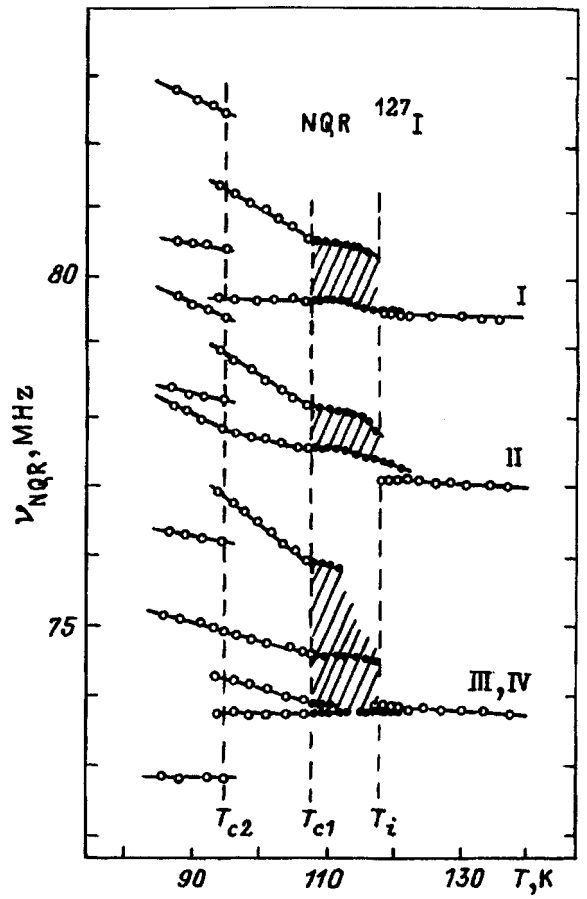

FIG. 1. Temperature dependence of NQR frequencies in solution-grown Cs_2ZnI_4 (from data of Ref. 1).

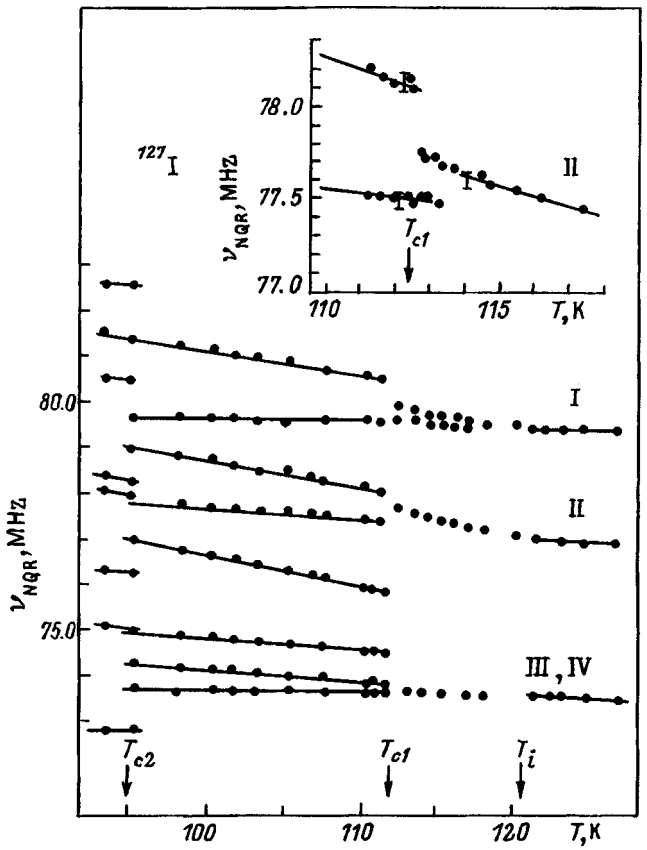

FIG. 2. Temperature dependence of NQR frequencies in solution-grown $(Cs_{1-x}Rb_x)_2ZnI_4$ ($x=0.0018$). Inset: region near T_{c1} for the spectrum component II.

trum in the IC phase compared to the undoped Cs_2ZnI_4. The undoped crystal exhibits an anomalous line shape characteristic of one-dimensional modulation, namely, a continuum frequency distribution bounded on both sides by peaks. A characteristic feature of Cs_2ZnI_4 is that, just below T_i, one of the side singularities is suppressed and is barely seen against the background. This singularity grows, however, in intensity with decreasing temperature, so that at approximately 5 K below T_i the spectrum takes on the shape typical of the IC phase.[2] In the doped crystal, the second singularity remains suppressed throughout the temperature region of existence of the IC phase. The only feature left in the spectrum from the IC continuum is one asymmetrical side singularity. Above T_i, the clusters, transition precursors, disappear in doped crystals. However in this case one also cannot determine the transition temperature to better than 1 K, because there is an interval near the transition where the line becomes washed out by noise as a result of the specific behavior of nuclear quadrupole relaxation.

The lines of the third phase become discernible against the background below T_i, with their intensity reaching a maximum within ~ 0.5 K. A region has been found where the residual peaks of the IC phase and the C-phase lines coexist (~ 0.5 K, see inset in Fig. 2). While the transition at T_{c1} appears more clearly pronounced first order than that in the undoped crystal, this observation should be checked in studies of the temperature dependences of the wave vector q_δ, which yield a more complete information on the character of a lock-in transition. The transition temperatures for the solution-grown, doped ($x=0.0018$) crystal are, within experimental errors, $T_i=121.0\pm 1$ K, $T_{c1}=112.0\pm 0.5$ K, and $T_{c2}=95.0\pm 0.5$ K.

The temperature dependences of NQR frequencies for Bridgman-grown crystals with Rb concentrations $x=0$, 0.001, 0.005, 0.01, and 0.025 were obtained in the region from 170 to 110 K. Figures 3 and 4 present the temperature dependences of the frequency for the spectrum component II for the lowest, $x=0$, and maximum, $x=0.025$, Rb concentrations. Similar dependences obtained for the intermediate concentration region follow the behavior shown in Figs. 3 and 4, if one takes into account the shift of the transition points along the temperature scale with Rb concentration.

Note that the spectrum of the undoped crystal grown by the Bridgman technique resembles not that of the ''pure,'' solution-grown Cs_2ZnI_4 but rather the spectrum of the crystal with a low Rb concentration ($x=0.0018$). The phase-transition point T_{c1} is shifted toward higher temperatures to become 112.0 ± 0.5 K. While the shift in T_i is just at the experimental accuracy limit, it nevertheless is seen clearly (121.6 K). A comparison of crystals with close Rb concentrations, $x=0.0018$ and $x=0.0011$, grown by the two different methods shows that the transition points T_i and T_{c1} in the Bridgman-pulled crystal are shifted noticeably toward higher

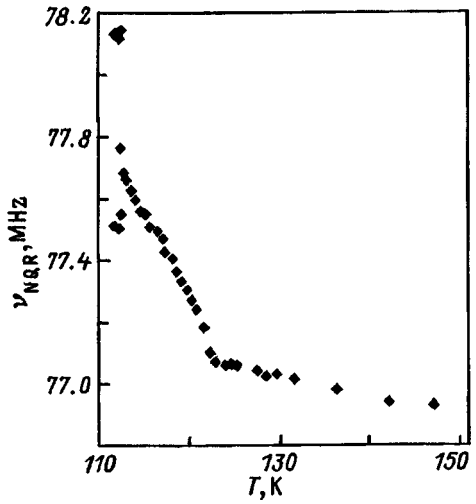

FIG. 3. Temperature dependence of NQR frequencies in Bridgman-grown Cs_2ZnI_4 ($x=0$).

temperatures. The dependence of the first-order transition temperature T_{c2} on x was derived from the jump in frequency of component I at the transition. The Rb concentration $\sim 2.5\%$ is the upper limit for NQR studies of the $(Cs_{1-x}Rb_x)_2ZnI_4$ system. In addition to the NQR lines of this crystal being broadened substantially already in the initial phase, weak broad lines not characteristic of the rhombic phase of Cs_2ZnI_4 appear in the spectrum.

The transition temperatures obtained for the above-mentioned Rb concentrations from the temperature dependences of the NQR frequencies are given in Table I.

C. Calorimetric data

Calorimetric data were obtained for solution-grown crystals with the minimum concentration $x=0.0018$ (Fig. 5). The measurements were performed on a SinkuACC-1VL calorimeter within the 80–300 K temperature region. The

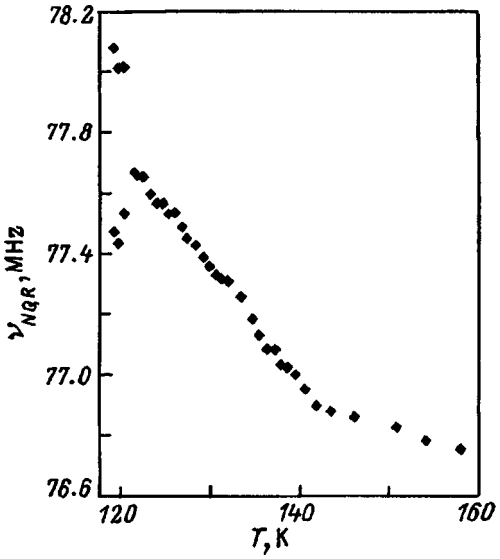

FIG. 4. Temperature dependence of NQR frequencies in solution-grown $(Cs_{1-x}Rb_x)_2ZnI_4$ ($x=0.025$).

TABLE I. Phase-transition temperatures for $(Cs_{1-x}Rb_x)_2ZnI_4$ derived from the temperature dependences of NQR frequencies.

Growth method	Rb concentration, x	T_i, K	T_{c1}, K	T_{c2}, K
Melt	0.0	120.0±1.0	108.0±0.5	96.0±0.5
Melt	0.0	121.6±1.0	112.7±0.5	96.3±0.5
Melt	0.0018	121.0±1.0	112.0±0.5	95.0±0.5
Melt	0.0011	124.5±1.0	115.0±0.5	95.3±0.5
Melt	0.005	127.6±1.0	115.0±0.5	92.4±0.5
Melt	0.01	131.2±1.0	117.5±0.5	90.3±0.5
Melt	0.025	142.0±1.0	120.6±0.5	?(<78 K)

samples were 0.1-mm thick plates coated by black carbon paste to improve heat absorption. The conditions of heat capacity recording are similar to those described in Ref. 3. For $x=0.0018$, the anomaly corresponding to the transition at T_i is observed at the same (within experimental error) temperature of 117.0 ± 0.08 K as in the undoped, solution-grown crystal[3]. The anomaly is slightly washed out compared to the data quoted in Ref. 3, which is seen from the decrease by a few percent of the height of the step in the heat capacity curve corresponding to T_i. The anomaly at T_{c1} (the lock-in transition) is washed out strongly and is substantially lower, but its peak is observed to lie at the same temperature as in pure Cs_2ZnI_4. The first-order transition $P2_1/m \leftrightarrow P_1$ at T_{c2} is shifted down by 0.4 K, and the heat capacity anomaly decreased somewhat in height.

2. DISCUSSION OF RESULTS

Figure 6 presents the phase diagram constructed from NQR data for Bridgman-grown crystals in the transition-temperature–concentration x coordinates. As x increases, the phase-transition points T_i and T_{c1} shift toward higher temperatures, and T_{c2} moves rapidly to lower temperatures.

The region of existence of the IC phase in the phase diagram expands somewhat with increasing impurity concentration. Because the IC phase region should become more narrow as one approaches the Lifshits-type critical point, one may conclude that Rb doping of Cs_2ZnI_4 moves the system away from the singular critical point.

The NQR line shape of Bridgman-grown undoped crystals in the IC phase is in agreement with the spectra of solution-grown crystals with a low Rb concentration. Besides, a comparison of the transition points of undoped crystals grown by the two above methods reveals a shift of the transition temperatures in melt-grown crystals toward higher temperatures for T_i and T_{c1}, and in the opposite direction, for T_{c2}, with respect to pure Cs_2ZnI_4 grown from solution. Melt-grown crystals contain apparently residual impurities in amounts of $0.2-0.4\%$.

Doping results characteristically in a change of the NQR line shape in the IC phase already at the lowest Rb concentration $x=0.0018$ studied. A possible explanation of this observation lies in the presence of order-parameter fluctuations near T_i in the case of a quadratic relation between the resonant frequency and the order parameter, which is valid for the spectrum component II. It was shown, in particular, that

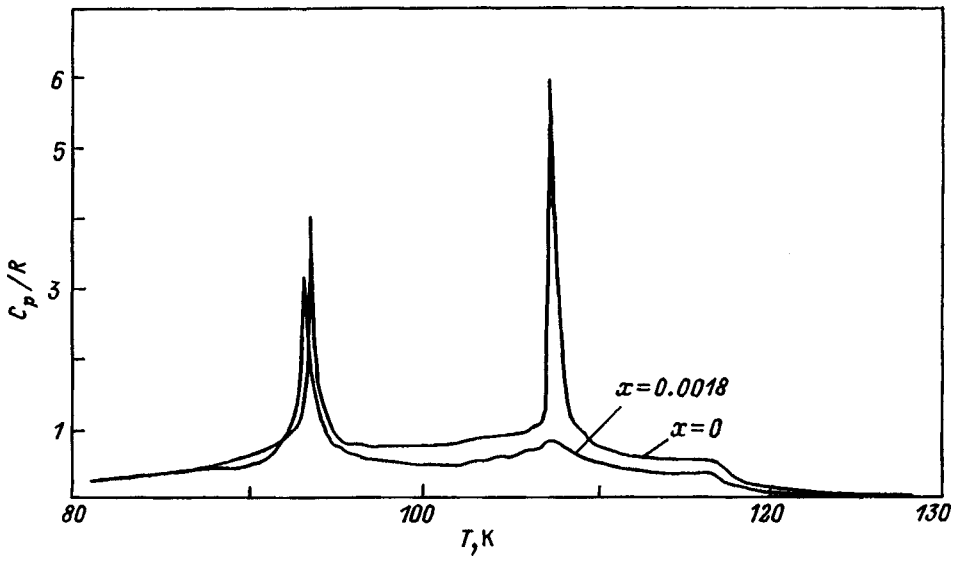

FIG. 5. Temperature dependence of the heat capacity of solution-grown $(Cs_{1-x}Rb_x)_2ZnI_4$ ($x=0$ and 0.0018).

the effect of amplitude fluctuations on the intensity of high-frequency (for Cs_2ZnI_4) side peaks depends essentially on damping, which is characterized by coefficient γ of the dissipation function $[\gamma(\eta_1^2+\eta_2^2)/2]$.[1,6] It is this effect that brings about suppression of the temperature-dependent continuum singularity near T_i in pure Cs_2ZnI_4. If the damping is strong, $\gamma\sim 0.1$,[1] the temperature-dependent side peak can become suppressed to become unobservable against the noise throughout the IC phase interval. Thus the doping-induced change in the spectrum of the IC phase can originate from an increase in fluctuation damping caused by incorporation of the impurity. One cannot exclude also such a ''static'' reason for the variation of the line shape as the onset of several metastable states with fixed values of q_δ. This uncertainty could be removed by studying the temperature dependences of wave vectors q_δ for different impurity concentrations. This requires independent and fairly complex x-ray diffraction measurements which we are planning to perform.

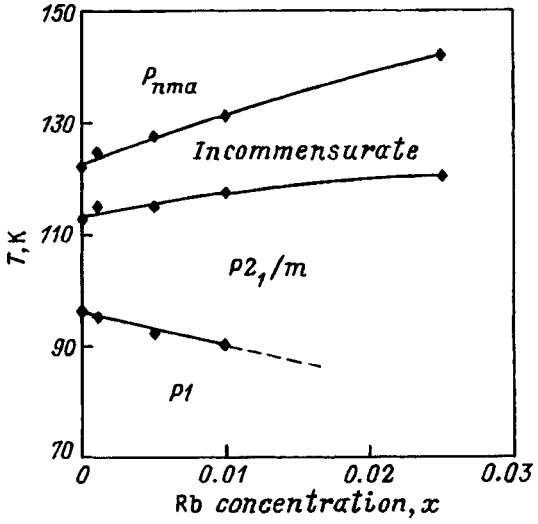

FIG. 6. Phase diagram of the $(Cs_{1-x}Rb_x)_2ZnI_4$ system.

We conclude with the results of a calorimetric study. The fact that even the lowest Rb concentration results in an extremely strong washing out of the thermal anomaly at T_{c1} is apparently a consequence of the well-known formation near the lock-in transition in doped crystals of several modulations having a fairly broad region of coexistence on the side of the IC phase. Note that the peak of the T_{c1} anomaly in the $x=0.0018$ case does not shift with respect to its position in the undoped crystal (Fig. 5), whereas the corresponding transition point derived from NQR data lies higher by 4 K. The fact that the real transition point in doped crystals, rather than coinciding with the thermal-anomaly peak, may sometimes lie substantially higher in temperature was shown, e.g., in Ref. 8.

Support of the Krasnoyarsk Territory Science Foundation (Grant 5F0100) is gratefully acknowledged.

[1] I. P. Aleksandrova, B. Sh. Bagautdinov, J. Bartolomé, R. Burriel, J. Melero, M. A. Popov, and S. V. Primak, Ferroelectrics **169**, 115 (1995).
[2] I. P. Aleksandrova, S. V. Primak, E. V. Shemetov, and A. I. Kruglik, Fiz. Tverd. Tela (Leningrad) **33**, 1344 (1991) [Sov. Phys. Solid State **33**, 758 (1991)].
[3] J. J. Melero, J. Bartolomé, R. Burriel, I. P. Aleksandrova, and S. V. Primak, Solid State Commun. **95**, 201 (1995).
[4] B. Sh. Bagautdinov and I. P. Aleksandrova, Solid State Commun. **90**, 817 (1994).
[5] I. P. Aleksandrova, K. Parlinsky, R. Currat, C. Vettier, and G. Eckold, Ferroelectrics **143**, 17 (1993).
[6] M. A. Popov, I. P. Aleksandrova, and S. V. Primak, JETP Lett. **59**, 485 (1994).
[7] D. G. Sannikov, in *Incommensurate Phases in Dielectrics* (Elsevier, Amsterdam, 1986), edited by R. Blinc and A. P. Levanyuk, Vol. 1, Ch. 2.
[8] J.-G. Yoon, Y. J. Kwag, Y.-S. Cho, and S.-I. Kwun, J. Phys. Soc. Jpn. **62**, 327 (1993).

Translated by G. Skrebtsov

Clusters in the model ferroelastic Hg_2Cl_2

Yu. F. Markov

A. F. Ioffe Physicotechnical Institute, Russian Academy of Sciences, 194021 St. Petersburg, Russia

K. Knorr

Universität des Saarlandes, Saarbrücken, Germany

(Submitted July 9, 1998)
Fiz. Tverd. Tela (St. Petersburg) **41**, 148–152 (January 1999)

The critical fluctuations induced by a ferroelastic phase transition and corresponding to the soft *TA* mode at the *X* point at Brillouin zone boundary have been studied in the model crystal Hg_2Cl_2 within a broad temperature and wave-vector range. Anisotropic diffuse x-ray scattering maxima associated with order-parameter fluctuations and nucleation of low-temperature orthorhombic clusters in the high-temperature tetragonal matrix have been found to exist at these points. New information has been obtained on the temperature dependence of the susceptibility and correlation length, cluster shape and anisotropy, and the critical exponents.
 [S1063-7834(99)03101-9]

The mercurous halides Hg_2Hal_2 (Hal=Cl, Br, I) are isomorphic at room temperature and have a specific crystal structure consisting of parallel chains of linear Hal–Hg–Hg–Hal molecules, weakly bound to one another and forming a body-centered tetragonal lattice D_{4h}^{17} with two molecules per unit cell.[1] The chain-like structure of these crystals gives rise to a very strong anisotropy in their physical properties, in particular, to a strong elastic anisotropy. For example, Hg_2Cl_2 crystals exhibit a transverse (TA) sound velocity $V_{[110]}^{[110]}=347$ m/s, a record-low characteristic among solids, a record-high birefringence $\Delta n=+0.66$, and a very high acousto-optic coupling ($M_2=640\times10^{-18}$ s^3/g for the *TA* wave[2]). These crystals are used to advantage in acoustic delay lines, acoustic filters, polarizers etc.

When cooled, these crystals undergo improper ferroelastic phase transitions ($D_{4h}^{17}\rightarrow D_{2h}^{17}$) at $T_c=186$ K (Hg_2Cl_2) and $T_c=144$ K (Hg_2Br_2). These transitions are induced by condensation of the slowest (TA) mode (see above) at the zone-edge *X* point of the tetragonal paraphase and are accompanied for $T\leqslant T_c$ by a doubling of the unit cell, a $X\rightarrow\Gamma$ transition in the zone, onset of spontaneous strain, and nucleation of ferroelastic domains.[3] Crystals of mercurous halides possess a very simple crystal structure and clearly pronounced phase-transition effects, and, hence, serve as model objects for basic studies of structural phase transitions.

This work reports a high-precision x-ray diffraction study of phase transition effects at various high-symmetry reciprocal-lattice points performed within a broad temperature range (10–300 K) including $T_c=186$ K (Hg_2Cl_2). The interest was focused at the *X* points at zone boundary. Bragg reflections at these points in the tetragonal phase (D_{4h}^{17}) are forbidden by selection rules and should appear in the low-temperature orthorhombic phase (D_{2h}^{17}) as a result of the phase transition, unit-cell doubling, and the $X\rightarrow\Gamma$ transfer in the Brillouin zone. At the same time, in the high-temperature phase, one can sometimes observe low-intensity diffuse reflections at zone boundary (in our case, at the *X* points), which are associated with spatial and temporal order-parameter fluctuations giving rise to nucleation of low-temperature clusters. Recently, studies of diffuse scattering have been carried out on the model perovskites $SrTiO_3$, $KMnF_3$, and $RbCaF_3$, which undergo displacive phase transitions from the cubic to tetragonal phase induced by soft-mode condensation at the zone-boundary *R* point. X-ray diffraction experiments revealed two length scales, the well-known one, short, and a new one, long, corresponding to the broad and a very narrow diffuse-scattering maximum, respectively.[4]

We are presenting here new information on the temperature dependence of diffuse (broad) reflections at the *X* points of the Brillouin zone, on clusters of the orthorhombic phase in the tetragonal matrix, and on the variation with temperature of their shape and size and of the critical exponents. Attempts to observe the narrow component in x-ray diffuse scattering from Hg_2Cl_2 crystals did not meet with success.

1. EXPERIMENTAL TECHNIQUE

The x-ray studies were performed on a two-circle diffractometer using copper-anode $K\alpha$ radiation. The low-temperature measurements were made with a Cryogenics closed-cycle cryostat providing a good temperature stabilization (≈0.1 K). The samples were $3\times3\times3$-mm high-quality mercurous chloride crystals cleaved along the (110) and $(1\bar{1}0)$ planes and cut in the (001) plane. Prior to measurements, the samples were etched for a short time in an aqua regia solution in distilled water. All measurements were made on the {110} faces.

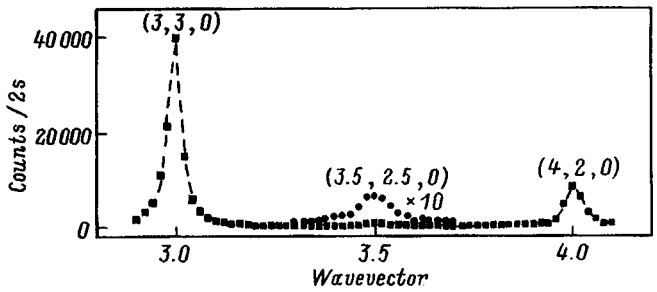

FIG. 1. Fundamental Bragg reflections (3,3,0) and (4,2,0) and the diffuse maximum at the zone X point (3.5,2.5,0) obtained in an extended $\Gamma-X-\Gamma$ scan at $T=200$ K.

2. EXPERIMENTAL RESULTS AND DISCUSSION

We studied the temperature dependence of diffuse scattering at the various Brillouin-zone X points with moderate indices h and k and $l=0$ [primarily the (3.5,2.5,0) and (2.5,1.5,0) points] of the reciprocal lattice. It should be noted that working with high h and k indices results in a low intensity of the corresponding diffuse reflections, while small h and k entail a lower resolution and a substantial increase of background scattering in the X-ray spectra and of experimental errors.

Figure 1 presents $T=200$ K a typical extended scan through the reciprocal-lattice (or Brillouin zone) points $\Gamma-X-\Gamma$ $(3.5+\eta, 2.5-\eta, 0)$ with the Bragg and a diffuse reflection at the X point (3.5, 2.5, 0). This scan coincides in direction with the soft TA-wave propagation in Hg_2Cl_2 crystals. This $\Gamma-X-\Gamma$ scan permits one to observe, besides the diffuse maximum, very strong fundamental (Bragg) even $(h+k+l=2n)$ reflections (3,3,0) and (4,2,0) allowed for the bcc tetragonal (D_{4h}^{17}) lattice of Hg_2Cl_2 crystals. The odd $(h+k+l=2n+1)$ Bragg reflections are forbidden by the selection rules for this structure, but an extended scan in the $ZE-X-EZ$ direction $(3.5+\eta, 2.5+\eta, 0)$ performed in the vicinity of T_c revealed broad low-intensity (3,2,0) and (4,3,0) maxima, which could be induced by a phase transition, as well as by structural imperfections, including defects (these low-intensity odd reflections are not shown in the figures).

The above-mentioned diffuse (3.5, 2.5, 0) reflections (maxima) can be seen in Fig. 2 in scans made in two mutually perpendicular directions, $\Gamma-X-\Gamma$ and $ZE-X-EZ$, at various temperatures $T\geqslant T_c$. The integrated intensity and amplitude of these reflections increase upon cooling, as one approaches T_c, and their FWHM decreases. The profile of

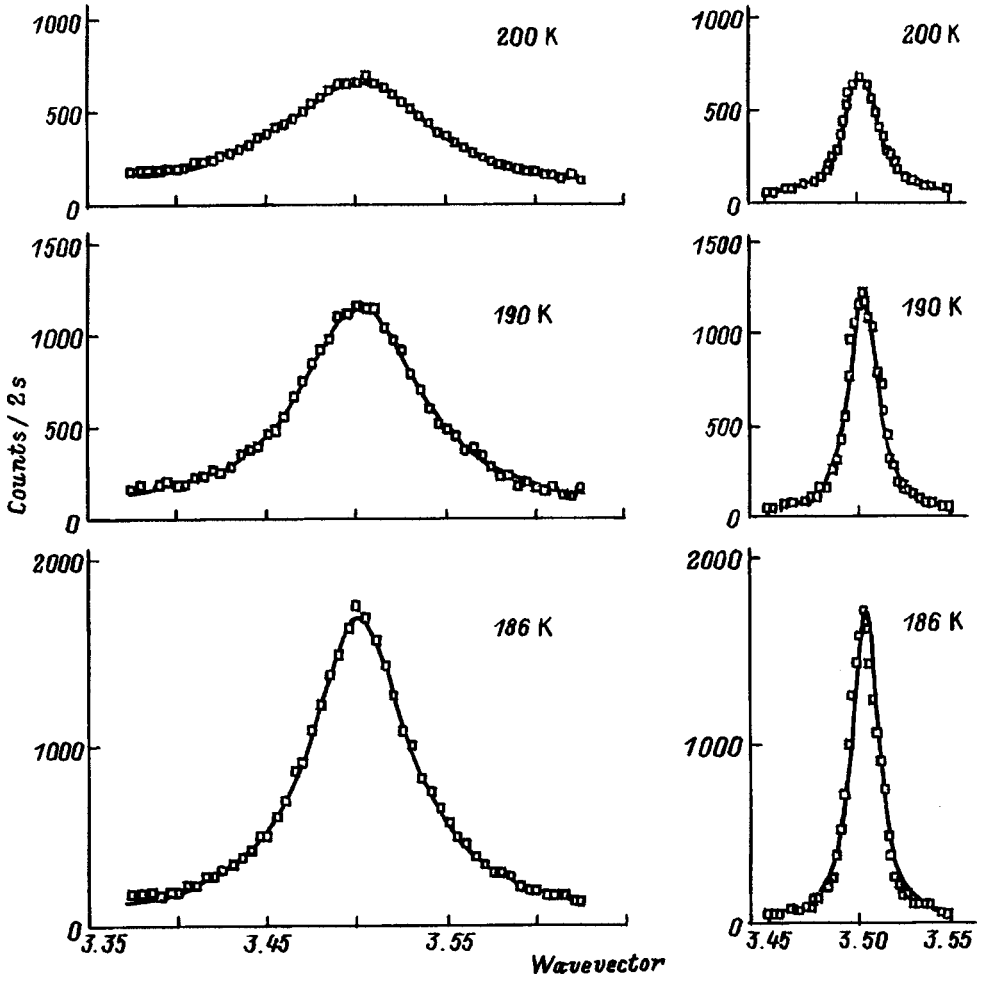

FIG. 2. Diffuse maxima (3.5,2.5,0) obtained in $\Gamma-X-\Gamma$ (left-hand part) and $ZE-X-EZ$ (right-hand part) scans at different temperatures $T\geqslant T_c$ (points — experiment, solid lines — Lorentzians).

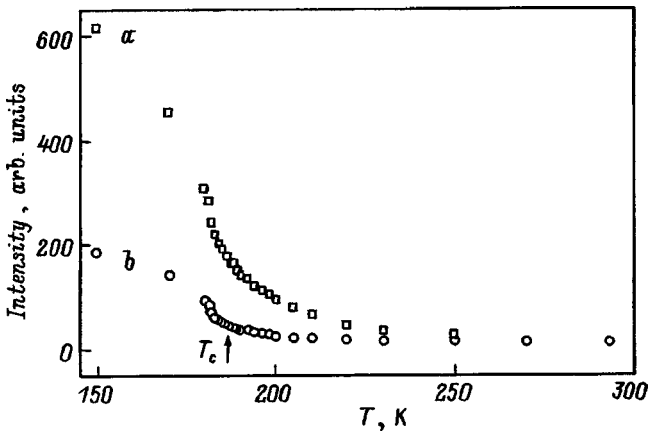

FIG. 3. Temperature dependences of the integrated intensities of diffuse scattering at the zone-boundary X point (3.5,2.5,0) obtained in (a) Γ-X-Γ and (b) $ZE-X-EZ$ scans.

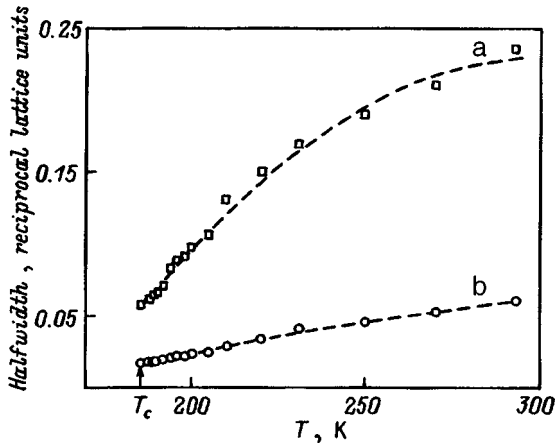

FIG. 4. Temperature dependences of the FWHM of diffuse reflections at the zone-boundary X point (3.5,2.5,0) obtained in (a) $\Gamma-X-\Gamma$ and (b) $ZE-X-EZ$ scans (points — experiment, dashed lines are drawn to aid the eye).

these reflections can be fit well to a Lorentzian (the solid lines in Fig. 2):

$$I(\mathbf{K})=A\Delta^2/[\Delta^2+4(\mathbf{K}-\mathbf{K}_x)^2], \tag{1}$$

where A is the reflection intensity (amplitude), $\mathbf{K}$ and $\mathbf{K}_x$ are the wave vectors, and Δ is the FWHM.

This data treatment permits one to derive with a high accuracy the main parameters (amplitude, FWHM, integrated intensity etc.) of these reflections. The large FWHM of these diffuse reflections obtained in $\Gamma-X-\Gamma$ scans originates primarily from interaction with the soft TA mode (wave) in the vicinity of the zone X point, which has small dispersion ($\lambda_1=8$ meV$^2\cdot$Å^2) in this direction compared to the large dispersion ($\lambda_2=255$ meV$^2\cdot$Å^2) of this TA mode seen along $ZE-X-EZ$.[5]

The temperature dependences of the integrated intensities of the Hg_2Cl_2 diffuse reflections are shown in Fig. 3. One observes up to room temperature broad low-intensity maxima at the zone X points, and their comparison with the nearest Bragg reflections (see, e.g., Fig. 1) permits one to estimate the amount of the orthorhombic phase in the tetragonal paraphase matrix, which at room temperature is about 0.1%. Cooling from room temperature reveals a slow rise in diffuse-reflection intensity with a sharp anomaly (increase) near T_c and a subsequent slowing down of this rise under further cooling (for $T<T_c$). It should be pointed out that the temperature dependence of integrated intensity at $T=T_c$ does not exhibit any jumps, thus confirming the continuity of the phase transition under study. For $T\leqslant T_c$, the phase transition and the associated unit-cell doubling and $X\rightarrow\Gamma$ transition in the Brillouin zone transform the diffuse reflections at the X points to the fundamental Bragg reflections allowed in x-ray scattering. The behavior of the integrated intensity of these reflections for $T<T_c$ in displacive transitions is directly related to the temperature dependence of the order parameter. In our case the order parameter corresponds to oppositely directed shift of the centers of gravity of the nearest Hg_2Cl_2 molecules in the adjacent (110) planes along [110].[3] Quantitative investigation of the temperature dependence of the order parameter, while being an interesting problem, would require special high-precision measurements, which were outside the scope of the present investigation.

Figure 4 displays the temperature dependence of the diffuse-reflection FWHM. One readily sees that the FWHM depends here strongly on temperature, decreasing by a few times when cooled from room temperature to $T=T_c$ (186 K). Below T_c it remains approximately constant, which is primarily due to a phase-transition–induced transformation of these reflections to fundamental reflections, whose FWHM usually depends weakly on temperature, and, to a lower extent, on the resolution being limited by the x-ray diffractometer response function. It is well known that the correlation length, the most essential parameter characterizing structural phase transitions, is inversely proportional to the FWHM of a diffuse maximum

$$\xi=2/\Delta, \tag{2}$$

where ξ is the correlation length, Δ is the FWHM, and the factor two in this relation is accounted for by the need of using one half of the FWHM.

The correlation length can actually be identified with the size of the clusters. Thus we can derive the size of the clusters and their temperature dependence from the measured FWHM relation. The correlation lengths measured in our experiment in two directions differ obviously by a few times. At room temperature, the correlation lengths are, accordingly, 70 and 250 Å for the $\Gamma-X-\Gamma$ and $ZE-X-EZ$ directions. As one approaches T_c under cooling, these dimensions increase monotonically by a few times and reach several thousand Å, to become comparable to the wavelength of visible light.

The dependence of inverse correlation length on reduced temperature t can be written

$$\Delta\sim t^{\nu}, \tag{3}$$

where $t=T-T_c/T_c$ is the reduced temperature, and ν is the critical exponent.

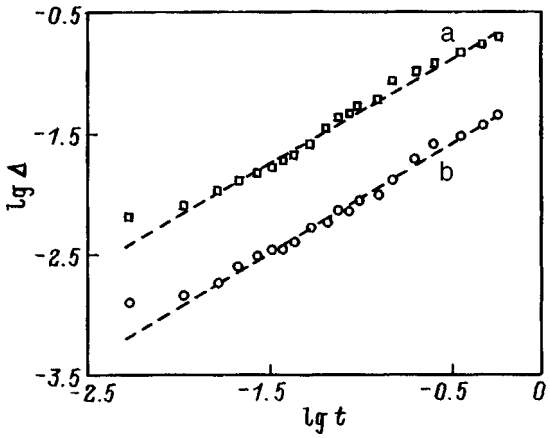

FIG. 5. Log-log plot of the inverse correlation length Δ *vs* reduced temperature t. (a) $\Gamma-X-\Gamma$ scan, (b) $ZE-X-EZ$ scan; points — experiment, dashed lines - linear approximation.

In order to determine the critical exponent ν, the experimental relation of Fig. 4, after subtraction of the background, which is the FWHM of the reflections for $T \leqslant T_c$, was plotted on a log-log scale (see Fig. 5). The experimental points of these relations were fit to straight lines, and their slopes yielded the average values of the critical exponents, 0.85 ± 0.1 and 0.90 ± 0.1, for the $\Gamma-X-\Gamma$ and $ZE-X-EZ$ directions, respectively. The difference between these values lies within experimental error. It should be pointed out that as one approaches T_c, these exponents decrease slightly to reach ~ 0.5 in the immediate vicinity of T_c.

An important characteristic of diffuse x-ray scattering is the diffraction-maximum amplitude. By simulating the profile of these maxima with a Lorentzian we were able to derive the temperature dependence of the amplitude (static susceptibility), which resembles that of the integrated intensity. We may recall that

$$A \sim t^{-\gamma}, \tag{4}$$

where A is the amplitude (intensity at reflection maximum), t is the reduced temperature, and γ is the critical exponent.

Figure 6 plots on a log-log scale this relation, for which

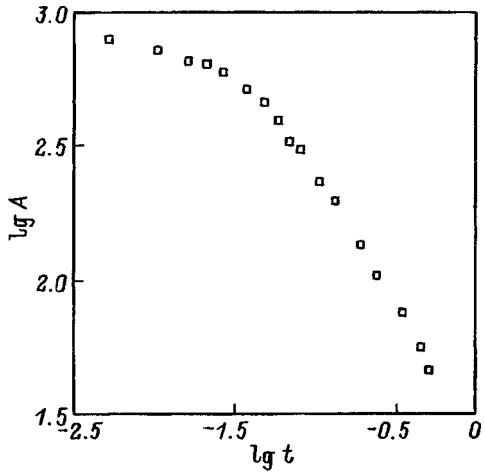

FIG. 6. Log-log plot of the diffuse-maximum amplitude A *vs* reduced temperature t.

the critical exponent γ was determined. From room temperature down to $T \cong 195$ K, γ remains practically constant, 1.0 ± 0.1 (the values obtained in the two orthogonal scans used in the work are naturally equal). As one approaches $T_c = 186$ K under further cooling, the critical exponent γ decreases monotonically. This experimental observation, reliably established, appears strange, because it implies that in the immediate vicinity of T_c the growth of the amplitude of the diffuse maxima slows down.

All the above results relate to x-ray investigation of the broad diffuse component. We also made an attempt to detect close to T_c the second, more narrow component in Hg_2Cl_2, which has recently been observed in perovskites [$SrTiO_3$, $RbCaF_3$, $KMnF_3$ (Ref. 4)] using the rotating anode or high-power synchrotron radiation, high-quality single crystals, and very good resolution. Our attempt, however, failed, which can probably be attributed to poorer parameters of our experiment.

3. DISCUSSION

The studies carried out on Hg_2Cl_2 single crystals showed that the soft *TA* mode undergoes condensation at the zone-boundary *X* point, and that the phase transition is accompanied by unit-cell doubling in the basal plane and an $X \rightarrow \Gamma$ transition in the Brillouin zone. The monotonic increase of the integrated intensity of diffusion reflections and the absence of any jumps at $T = T_c$ is not at odds with the model[6] of continuous ferroelastic phase transition in the vicinity of the tricritical point. The observed and studied diffuse scattering at high temperatures is primarily associated with the nucleation of static clusters. At the same time as one approaches T_c under cooling, the dynamic effects connected with spatial and temporal order-parameter fluctuations will increase, which should become manifest in an increasing contribution of dynamic clusters to diffuse scattering. It is certainly the latter effect that is observed, but we did not succeed in separating the static and dynamic contributions. Besides this reason (interaction with the *TA* soft mode at the zone-boundary *X* point), the large anisotropy in the correlation length revealed in two orthogonal directions, $\Gamma-X-\Gamma$ and $ZE-X-EZ$, can be due also, although to a lesser extent, to some elastic anisotropy near the surface of these crystals (the average x-ray penetration depth is about 5 μm). It appears natural to relate the nucleation of static clusters to the presence in the crystals under study of various growth-induced defects, for instance, dislocations, residual elastic-stress fields, point defects etc. We may recall that these crystals exhibit a very strong dependence (increase) of the phase-transition temperature T_c on hydrostatic and uniaxial pressure, 43.8 and 103 K/kbar, respectively,[7] which means that defects capable of generating in their vicinity elastic-stress fields can initiate nucleation of the low-temperature orthorhombic phase even at room temperature. It should be added that the criterion of the minimum of elastic and surface energy makes nucleation of a ferroelectric phase in the paraphase matrix in the form of extended, small-radius cylinders or very thin platelets preferable. Optical studies[8] and calculations made for Hg_2Cl_2 crystals argue for the forma-

tion of nuclei only in the form of platelets parallel to {110}, with their cross section being characterized by two different dimensions, thickness and width, along the [110] and $[1\bar{1}0]$ directions. It is this anisotropy (different correlation lengths) that was observed in our x-ray scans along the $\Gamma-X-\Gamma$ and $ZE-X-EZ$ directions (see Fig. 4).

It appears interesting to compare the critical exponents obtained in this work with those of the above-mentioned perovskites, which undergo first-order phase transitions with soft-mode condensation at the zone-boundary R point. The average values of the critical exponent ν derived from the temperature dependence of the inverse correlation length in Hg_2Cl_2 crystals are 0.85 and 0.90 for the $\Gamma-X-\Gamma$ and $ZE-X-EZ$ scans, respectively. These values are slightly larger than the corresponding parameters of the perovskite crystals [$\nu=0.62$ for $KMnF_3$, 0.64 for $RbCaF_3$, and 0.83 for $SrTiO_3$ (Ref. 4)].

The critical exponent γ describing fairly well the temperature dependence of the amplitude (susceptibility) of diffuse reflections from room temperature down to $\sim$195 K, is approximately constant and equal to 1.0. It can be compared with the same parameters for $KMnF_3$ (1.19), $RbCaF_3$ (1.34), and $SrTiO_3$ (1.40). A slowing down of the rise in reflection amplitude (Fig. 6) and correlation length (Figs. 4 and 5) in Hg_2Cl_2 near T_c (for $(T>T_c)$ was observed to occur earlier in perovskite crystals but did not find an adequate explanation.[4] This phenomenon near T_c is apparently induced by the onset of cluster interaction, because the content of the ferroelastic phase in the paraphase matrix of Hg_2Cl_2 at these temperatures constitutes already a few percent, making it a mixed heterophase crystal. It may be that the latter conclusion is valid only for near-surface regions in the crystal.

The authors consider it a pleasure to thank A. A. Kaplyanskiĭ and A. P. Levanyuk for fruitful discussions.

Partial support of RFRF-DFG (Grant 96-02-00138) and Russian Fundamental Research Foundation (Grant 98-02-16144) is gratefully acknowledged.

[1] H. Mark and J. Steinbach, Z. Kristallogr. **64**, 78 (1926).
[2] *Proceedings of the 2nd International Symposium on Univalent Mercury Halides* (Trutnov, ČSFR, 1989).
[3] A. A. Kaplyanskiĭ, Yu. F. Markov, and Č. Barta, Izv. Akad. Nauk SSSR, Ser. Fiz. **43**, 1641 (1979).
[4] S. R. Andrews, J. Phys. C: Solid State Phys. **19**, 3721 (1986); U. J. Nicholl and R. A. Cowley, *ibid.* **20**, 3417 (1987); A. Gibaud, R. A. Cowley, and P. W. Mitchell, *ibid.* **20**, 3849 (1987).
[5] J. P. Benoit, G. Hauret, and J. Levebvre, J. Phys. (France) **43**, 641 (1982).
[6] M. E. Boiko, Yu. F. Markov, V. S. Vikhnin, A. S. Yurkov, and B. A. Zadokhin, Ferroelectrics **130**, 263 (1992).
[7] A. A. Kaplyanskiĭ, Yu. F. Markov, V. Yu. Mirovitskiĭ, and N. N. Stepanov, Fiz. Tverd. Tela (Leningrad) **27**, 223 (1985) [Sov. Phys. Solid State **27**, 133 (1985)].
[8] Č. Barta, A. A. Kaplyanskiĭ, Yu. F. Markov, and V. Yu. Mirovitskiĭ, Fiz. Tverd. Tela (Leningrad) **24**, 875 (1982) [Sov. Phys. Solid State **24**, 493 (1982)].

Translated by G. Skrebtsov

LOW-DIMENSIONAL SYSTEMS. SURFACE PHYSICS

Photoluminescence of thin amorphous-nanocrystalline silicon films

V. G. Golubev, A. V. Medvedev, A. B. Pevtsov, A. V. Sel'kin, and N. A. Feoktistov

A. F. Ioffe Physicotechnical Institute, Russian Academy of Sciences, 194021 St. Petersburg, Russia
(Submitted May 22, 1998)
Fiz. Tverd. Tela (St. Petersburg) **41**, 153–158 (January 1999)

Photoluminescence spectra of thin hydrogenated-silicon films having mixed amorphous-nanocrystalline phase composition have been studied. Fabry-Perot interference was found to affect strongly the shape of the spectra. An analysis of the spectra made with inclusion of interference corrections shows that only one emission band forms in the 0.6–1.0 μm region due to carrier recombination at centers of the same type. © *1999 American Institute of Physics.* [S1063-7834(99)03201-3]

The optical and electrical properties of nanoscale semiconductor crystallites are presently attracting considerable interest, because, on the one hand, these objects exhibit very strong size-quantization effects, and on the other, these materials may provide a basis for development of novel opto-electronic devices.[1,2] In particular, observation of intense visible emission at room temperature from low-dimensional silicon structures[3–5] offers a possibility of constructing injection-type light-emitting devices compatible with silicon-based opto-electronic integrated circuits. Among nanoscale objects of this type are thin silicon films with a mixed amorphous-nanocrystalline composition obtained by PE CVD.[6–8] This method permits control within a broad range the size of crystallites and their volume fraction, is only weakly sensitive to substrate choice, and is compatible with standard silicon technology.

A number of experimental studies reported that photoluminescence (PL) spectra of heterophase silicon films contain, as a rule, several emission bands. Some authors associate them with various types of emitting centers present in films.[9–14] It should, however, be borne in mind that a thin hydrogenated silicon film on a polished substrate is close in optical properties to the Fabry-Perot etalon so that it can exhibit interference effects which may affect substantially the shape of PL spectra.[15] For certain relations between the refractive index and film thickness, the number of interference maxima in the spectral region under study can be limited to two or three broad peaks capable of masking the true PL spectrum. Hence, when investigating the emitting properties of such objects, one should first exclude the simplest cause for the appearance of an additional structure in PL spectra, namely, interference.

1. EXPERIMENT

The films with mixed amorphous-nanocrystalline composition were grown by PE CVD. To stimulate nanocrystallite formation, the layers were deposited from silane diluted strongly ($>95\%$) by hydrogen. The films thus produced had the following parameters: thickness 0.6–0.8 μm, refractive index 2.2–2.8, absorption coefficient at the pump argon-laser wavelength (488 nm) about 10^4 cm^{-1}, and gap width 1.9–2.1 eV. The volume fraction of the crystallites and their average diameter, derived from numerical processing of the Raman spectra of films and, particularly, from the conditions of deposition, could be varied within 0–40% and 30–50 Å, respectively.

PL measurements were performed both at liquid-nitrogen and room temperature. The laser radiation power did not exceed 40 mW. The spectra were measured with an MDR-23 monochromator. Within the 0.6–1.0 μm region, the PL spectra were recorded by a FÉU-62 PM photomultiplier. The film transmission was measured in the 0.7–1.6 μm range by a germanium photodiode.

The PL measurements were carried out with the film facing the monochromator slit, and the pump laser beam traversing the sample from the side of the quartz substrate. After this, the optical transmission spectrum was recorded with the sample in the same position. The thickness and refractive index of the film were derived from the interference structure of the transmission spectrum in the IR region.

Figure 1 presents a typical PL spectrum (with the laser beam directed along the sample surface normal) after correction for the response function of the measurement system. A characteristic feature is the presence of several maxima. These spectra lie in the PL region expected both from the nanocrystallites[16] and from the amorphous matrix. A comparison of the PL and transmission spectra revealed, however, that the extrema of both spectra lie at the same wavelengths, which argues for the interference origin of the many-peak PL. Thus, in order to determine the true PL spectrum, one has to exclude first of all its modulation by interference.

2. THEORY

The emergence of Fabry-Perot interference in the emission spectra of epitaxial films (in the case of ZnSe) was discussed in Ref. 17, which proposed also the corresponding

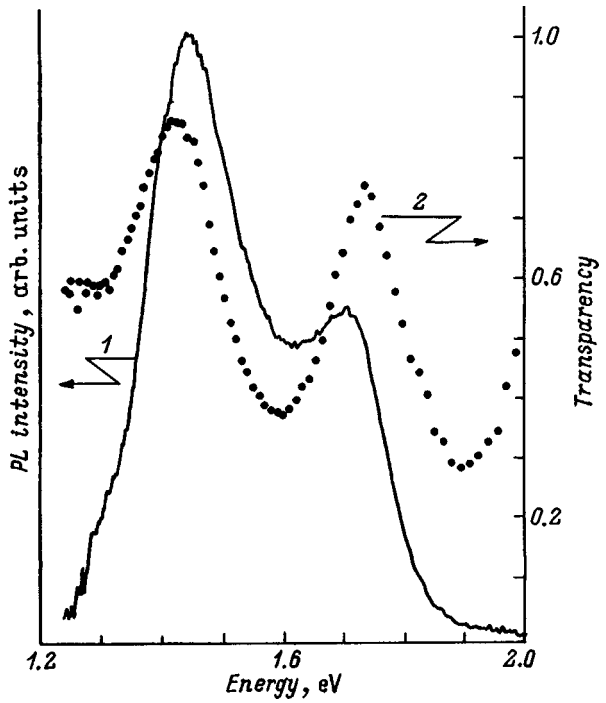

FIG. 1. (*1*) Experimental PL spectrum of an amorphous-nanocrystalline film and (*2*) transmission spectrum measured at the point where the emission spectrum was obtained. $T=77$ K.

expression for the intensity of the radiation leaving the film. This expression was derived[17] by the method (see, e.g., Ref. 18, Ch. 4) involving summation of partial electric-field amplitudes undergoing multiple reflection from the layer boundaries, which was applied to the case of field sources inside the film. Unfortunately, the validity of the relations of Ref. 17 is limited to the cases where the emitted light propagates nearly normally to the inner film surface and one can thus neglect light absorption at the emitted frequency. At the same time studies of luminescence spectra for arbitrary radiation escape angles and within the spectral region where absorption cannot be considered small may also be of interest.

Straightforward application of the approach in Ref. 17 to obtain a more general expression for radiation intensity with inclusion of oblique light propagation in a film is impossible if the relations connecting the electric field amplitudes at the boundaries of each elementary emitting layer are unknown. These relations are determined by the orientation of the elementary emitters, which can be prescribed, for example, by the density vector of the extraneous polarization current **j**. Then the problem of light emission will reduce to finding the electromagnetic field at the outer (emitting) film surface from the given currents **j** inside the film which, in their turn, are determined by the external excitation source.

We shall start with Maxwell's equations formulated for the frequency Fourier components of the fields

$$\operatorname{curl}\mathbf{E}(\mathbf{r};\omega)=ik_0\mathbf{B}(\mathbf{r};\omega)\,, \tag{1}$$

$$\operatorname{curl}\mathbf{B}(\mathbf{r};\omega)=-ik_0\mathbf{D}(\mathbf{r};\omega)+4\pi/c\,\mathbf{j}(\mathbf{r};\omega)\,, \tag{2}$$

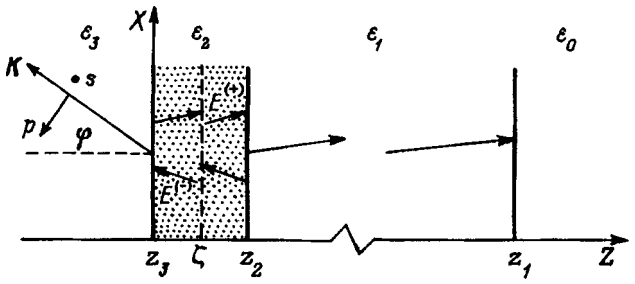

FIG. 2. Schematic diagram of the four-layer planar structure under study.

where **E** is the electric field vector, and **D** and **B** are the electric and magnetic induction vectors, respectively ($k_0=\omega/c$ is the wave vector of light in vacuum, c is the velocity of light, and ω is frequency).

Consider the solution of this system for a four-layer planar structure depicted schematically in Fig. 2. In accordance with our experimental conditions, the structure consists of a thin emitting film, $z_3<z<z_2$, of thickness L_2 and a thick substrate, $z_2<z<z_1$, of thickness L_1, which are sandwiched between transparent semi-infinite layers $z>z_1$ and $z<z_3$. We shall denote the dielectric permittivity of the layer to the left (right) of the interface z_j by ε_j (ε_{j-1}), with $\varepsilon_3=\varepsilon_0$. In accordance with Fig. 2, it is assumed that the z axis is perpendicular to the interfaces of the structure, and that the radiation of frequency ω is detected at an angle φ in the $z<z_3$ medium in the direction lying in the xz plane. In this case the wave vectors **K** of normal waves contributing to the emission in this geometry have the same tangential components, $K_y=0$ and $K_x=\sqrt{\varepsilon_0}\,k_0\sin(\varphi)$, for all waves.

In view of the translational symmetry of the problem along the xy plane, one can transfer conveniently by Fourier transformation to the $(\mathbf{K}_\parallel,z;\omega)$ field representation, where $\mathbf{K}_\parallel(K_x,K_y)$ is a two-dimensional wave vector in a plane parallel to the interfaces. We shall understand subsequently by the quantities $\mathbf{F}(z)$ the amplitudes $\mathbf{F}(K_\parallel,z;\omega)$ of fields **F** ($\mathbf{F}=\mathbf{E},\mathbf{B},\mathbf{D},\mathbf{j}$) and consider the response $\tilde{\mathbf{F}}(z,\zeta)$ ($\tilde{\mathbf{F}}=\tilde{\mathbf{E}},\tilde{\mathbf{B}}$) of the system to a singular polarization current $\mathbf{j}(\zeta)\cdot\delta(z-\zeta)$ localized in the $z=\zeta$ plane. In these conditions, the total current $\mathbf{j}(z)=\int d\zeta\,\mathbf{j}(\zeta)\,\delta(z-\zeta)$ excites in the structure a field $\mathbf{F}(z)=\int d\zeta\,\tilde{\mathbf{F}}(z,\zeta)$.

Direct integration of Eqs. (1) and (2) over the thickness of the infinitely thin layer containing the singular-current plane $z=\zeta$, made taking into account that the tangential components of fields **E** and **B** do not go to infinity anywhere, yields a system of boundary conditions

$$\tilde{B}_y(\zeta+0,\zeta)-\tilde{B}_y(\zeta-0,\zeta)=-(4\pi/c)j_x(\zeta)\,, \tag{3}$$

$$\tilde{E}_x(\zeta+0,\zeta)-\tilde{E}_x(\zeta-0,\zeta)=(4\pi/c)(n_x/\varepsilon_2)j_z(\zeta)\,, \tag{4}$$

$$\tilde{B}_x(\zeta+0,\zeta)-\tilde{B}_x(\zeta-0,\zeta)=(4\pi/c)j_y(\zeta)\,, \tag{5}$$

$$\tilde{E}_y(\zeta+0,\zeta)-\tilde{E}_y(\zeta-0,\zeta)=0\,, \tag{6}$$

where $n_x=K_x/k_0$. Note that boundary conditions (3) and (4) correspond to the p wave polarization, and conditions (5) and (6), to s polarization. At all points $z\neq\zeta$ corresponding to the

interfaces z_1, z_2, and z_3, the standard continuity conditions for the tangential components of the fields $\tilde{\mathbf{E}}(z,\zeta)$ and $\tilde{\mathbf{B}}(z,\zeta)$ are met.

The above full system of boundary conditions relates the amplitudes of the waves depicted schematically in Fig. 2 by inclined arrows and permits one to express the electric field $\tilde{\mathbf{E}}(z_3-0,\zeta)$ at the outer interface z_3 of the structure through the extraneous current density $\mathbf{j}(\zeta)$. It is assumed that at the z_2 interface one can neglect the contribution due to the waves reflected from the z_1 interface because of the large substrate thickness L_1.

Setting $z_3=0$, we obtain for the p and s components $\tilde{\mathbf{E}}_\sigma$ ($\sigma=p,s$) of the field $\tilde{\mathbf{E}}(-0,\zeta)$ (see Fig. 2)

$$\tilde{E}_p(-0,\zeta)=G_{px}j_x+G_{pz}j_z, \quad \tilde{E}_s(-0,\zeta)=G_{sy}j_y, \tag{7}$$

where

$$G_{px}=\frac{(4\pi/c)\sqrt{\varepsilon_0}n_{2z}}{\varepsilon_0 n_{2z}+\varepsilon_2 n_{0z}}\,\frac{\Phi(\zeta-L)+r_{21}^p\Phi(L-\zeta)}{\Phi(-L)+r_{32}^p r_{21}^p\Phi(L)}, \tag{8}$$

$$G_{pz}=\frac{(4\pi/c)\sqrt{\varepsilon_0}n_x}{\varepsilon_0 n_{2z}+\varepsilon_2 n_{0z}}\,\frac{\Phi(\zeta-L)-r_{21}^p\Phi(L-\zeta)}{\Phi(-L)+r_{32}^p r_{21}^p\Phi(L)}, \tag{9}$$

$$G_{sy}=-\frac{(4\pi/c)}{n_{2z}+n_{0z}}\,\frac{\Phi(\zeta-L)+r_{21}^s\Phi(L-\zeta)}{\Phi(-L)+r_{32}^s r_{21}^s\Phi(L)}, \tag{10}$$

$r_{ij}^\sigma=(\nu_i^\sigma-\nu_j^\sigma)/(\nu_i^\sigma+\nu_j^\sigma)$ is the reflection coefficient of σ polarized light at the interface separating two semi-infinite media i and j ($i,j=0,1,2,3$) for the light passing from medium i into medium j, $\nu_j^p=\varepsilon_j/n_{jz}$, $\nu_j^s=-n_{jz}$, $n_x=\sqrt{\varepsilon_0}\sin(\varphi)$, $n_{jz}=\sqrt{\varepsilon_j-n_x^2}$ ($\mathrm{Im}\, n_{jz}\geqslant 0$), $\Phi(z)=\exp(ik_0 n_{2z}z)$, and $L=L_2$.

To calculate the light intensity $J^\sigma(\omega,\varphi)$ emitted at a frequency ω in σ polarization and emerging at an angle φ, one has to specify the statistical behavior of random extraneous currents $\mathbf{j}(\zeta)$ by prescribing appropriately the correlation function $\langle j_\alpha(\zeta)j_\beta^*(\zeta')\rangle$ ($\alpha,\beta=x,y,z$). Assuming the currents excited at different points ζ and ζ' to be fully statistically independent and excited isotropically, this function can be presented in the form

$$\langle j_\alpha(\zeta)j_\beta^*(\zeta')\rangle=\mathcal{F}(\omega,\zeta)\,\delta_{\alpha\beta}\delta(\zeta-\zeta'), \tag{11}$$

where the angular brackets $\langle\ldots\rangle$ denote statistical, including orientational, averaging over the ensemble of random-current realizations.

The dependence of the $\mathcal{F}$ function on light frequency ω determines the true (without taking into account Fabry-Perot interference) spectral profile $S(\omega)$ of the radiation, and its dependence on ζ is related to the spatial distribution $J_0(\zeta)$ of luminescence excitation sources inside the sample. Assuming $\mathcal{F}(\omega,\zeta)\propto S(\omega)\cdot J_0(\zeta)$, we obtain for the measured radiation intensity

$$J^p=S(\omega)\int_0^L d\zeta J_0(\zeta)(|G_{px}(\omega,\zeta)|^2+|G_{pz}(\omega,\zeta)|^2), \tag{12}$$

$$J^s=S(\omega)\int_0^L d\zeta J_0(\zeta)|G_{sy}(\omega,\zeta)|^2. \tag{13}$$

Equations (8)–(10), (12), and (13) are actually the solution of the formulated problem, and they permit one to take into account the effect of Fabry-Perot interference when treating experimental luminescence data. Note that the method proposed here reduces to finding the electrodynamic Green's functions determining the fields at the outer boundary of layer 2. A full Green's function system applicable to a three-layer planar structure was described in Ref. 19 and used to solve the problem of light reflection with inclusion of singular perturbations in dielectric permittivity at interfaces.

3. RESULTS AND DISCUSSION

Taking into account the experimental conditions of interest here (optical excitation from the side of the substrate), we shall prescribe the source spatial-distribution function in the form

$$J_0(\zeta)\propto\exp(k_0(\zeta-L)), \tag{14}$$

where coefficient k_0^{-1} has the meaning of effective diffusion depth of photogenerated carriers trapped by the emitting centers. Coefficient k_0 should be equal or larger in order of magnitude than the light extinction coefficient at the pump frequency.

Integration in Eqs. (12) and (13), made with due account of Eq. (14), yields the following expressions for the p and s PL component intensities

$$J^p=\frac{S(\omega)(|n_{2z}|^2+n_x^2)}{|\varepsilon_2\cos\varphi+\sqrt{\varepsilon_0}n_{2z}|^2}\left(I_1+|r_{21}^p|^2 I_2+2|r_{21}^p|\frac{|n_{2z}|^2-n_x^2}{|n_{2z}|^2+n_x^2}I_3^p\right)\Big/\,\Delta_L^p, \tag{15}$$

$$J^s=\frac{S(\omega)}{|n_{2z}+\sqrt{\varepsilon_0}\cos\varphi|^2}(I_1+|r_{21}^s|^2 I_2+2|r_{21}^s|I_3^s)/\Delta_L^s, \tag{16}$$

where

$$\Delta_L^\sigma=|\Phi(-L)+r_{02}^\sigma r_{21}^\sigma\Phi(L)|^2;$$

$$I_1=\frac{1-\exp(-(\varkappa_0-\varkappa_2)L)}{\varkappa_0-\varkappa_2}, \quad I_2=\frac{1-\exp(-(\varkappa_0+\varkappa_2)L)}{\varkappa_0+\varkappa_2},$$

$$I_3^\sigma=\frac{1}{\varkappa_0^2+q^2}\{e^{-\varkappa_0 L}[q\sin(\Delta_{21}^\sigma+qL)-\varkappa_0\cos(\Delta_{21}^\sigma+qL)]-q\sin\Delta_{21}^\sigma+\varkappa_0\cos\Delta_{21}^\sigma\};$$

$$\varkappa_2=2k_0\,\mathrm{Im}\, n_{2z}, \quad q=2k_0\,\mathrm{Re}\, n_{2z},$$

$$\Delta_{21}^\sigma=\arg(r_{21}^\sigma), \quad \sigma=p,s. \tag{17}$$

Integral I_1 determines the contribution of the $E^{(-)}$ waves (see Fig. 2) emitted by the sources directly toward the outer boundary of layer 2, and I_2 takes into account the $E^{(+)}$ waves, which were initially emitted toward the inner layer interface but reversed the propagation direction after a single reflection from this interface. Integral I_3^σ describes the mutual interference of the $E^{(-)}$ and $E^{(+)}$ waves. The interference arising in multiple traversal of waves through layer 2

and their multiple reflection from the outer and inner boundaries of this layer is characterized by the interference denominators Δ_L^σ in Eqs. (15) and (16).

Note that the interference denominator Δ_L^σ enters explicitly the expression for the energy transmission coefficient of the whole structure (Fig. 2)

$$T^\sigma = |\Phi_1(L_1) t_{01}^\sigma t_{12}^\sigma t_{20}^\sigma|^2 / \Delta_L^\sigma, \tag{18}$$

where $\Phi_1(L_1) = \exp(i\mathbf{k}_0 n_{1z} L_1)$, and $t_{ij}^\sigma = 1 + r_{ij}^\sigma$ are amplitude transmission coefficients at the interface separating the two semi-infinite media i and j. If integrals I_3^σ in Eqs. (15) and (16) can be neglected, and the dispersion in the frequency region of interest is negligible, then the interference structure in the PL spectrum, as seen from a comparison of (18) with Eqs. (15) and (16), is fully determined by that of the transmission coefficient T^σ.

It should also be pointed out that the corrections n_x^2 for the p component intensity entering Eq. (15) describe the contribution to emission by harmonic oscillators vibrating along the Z axis of the structure. Assuming $n_x^2 \ll |\varepsilon_2|$ and $\mathrm{Im}\,\varepsilon_2 = 0$ makes Eqs. (15) and (16) equivalent to the expressions derived in Ref. 17. If the radiation emerges normal to the film surface, Eqs. (15) and (16) yield the same result, as this should be expected.

For our amorphous-nanocrystalline silicon films of thickness $L \approx 0.7\,\mu$m, the extinction coefficient of pump light at the wavelength $\lambda = 488$ nm is about 10^4 cm^{-1}, and the refractive index of the material, 2.2–2.8. In these conditions, the integral I_3^σ in Eqs. (15) and (16), which contributes to interference, is small compared to I_1 and I_2 within the wavelength interval of interest, and the spectrum of an excited center is primarily modulated by the interference structure of the film transmission spectrum. Hence, by dividing the PL spectrum by the transmission spectrum, one can exclude the interference effect in the emission spectrum of the recombination center. This is illustrated by Fig. 3 presenting the original PL spectrum under normal ($\varphi \approx 0°$) emergence of radiation (curve *1*), the result of its division by the transmission spectrum (curve *2*, points), and approximation of the spectrum obtained in this way by a Gaussian (solid line 2).

As follows from Eqs. (15) and (16), the observed interference pattern in the original PL spectrum is due to the frequency dependence of the interference denominator Δ_L^σ. The structure of the expression for Δ_L^σ shows that the amplitude of oscillations in Δ_L^σ is determined by the reflection coefficients r_{02}^σ and r_{21}^σ. For the p component ($\sigma = p$), these coefficients become small at emergence angles close to the Brewster angle φ_B. In this case [see Eq. (17)] the interference effect turns out to be insignificant.

Figure 4 shows PL spectra calculated using Eq. (15) as functions of the radiation emergence angle φ for the p polarization. The $S(\omega)$ function was calculated based on the parameters of the Gaussian approximating the PL spectrum in Fig. 3. As seen from curve *3* in Fig. 4, the interference pattern of the spectrum does indeed disappear at $\varphi = \varphi_B \equiv \arctan\sqrt{\varepsilon_2}$. The PL spectra measured at the escape angles of the p polarized luminescence used in Fig. 4 are displayed in Fig. 5. One observes a good correlation between the theoretical (Fig. 4) and experimental (Fig. 5) data. Thus to exclude interference effects in the PL of thin films, it is sufficient to measure the spectra in p polarized light at luminescence escape angles near φ_B without invoking investigation of transmission spectra.

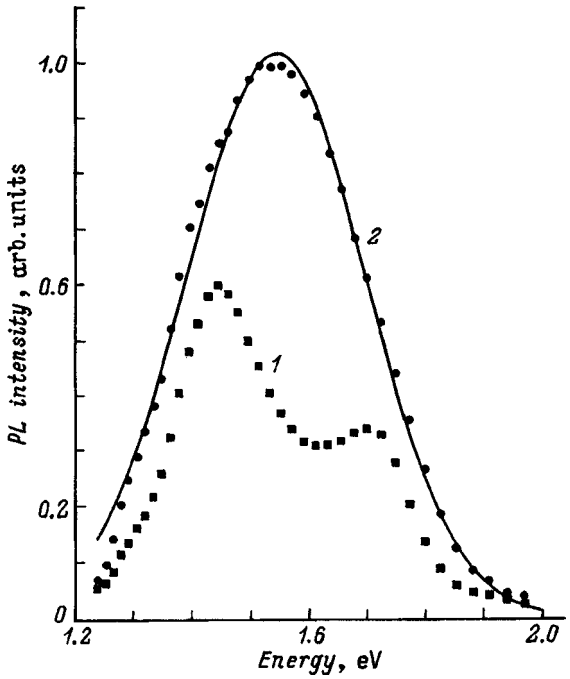

FIG. 3. (*1*) Experimental PL spectrum and (*2*) reconstructed spectrum (points) obtained by division of spectrum *1* by the transmission spectrum. $T = 77$ K. Solid line *2* is the reconstructed spectrum approximated by a Gaussian with $E_{\max} = 1.52$ eV and FWHM = 0.3 eV.

The above analysis permits a conclusion that the true PL spectrum of the films studied here is associated with one type

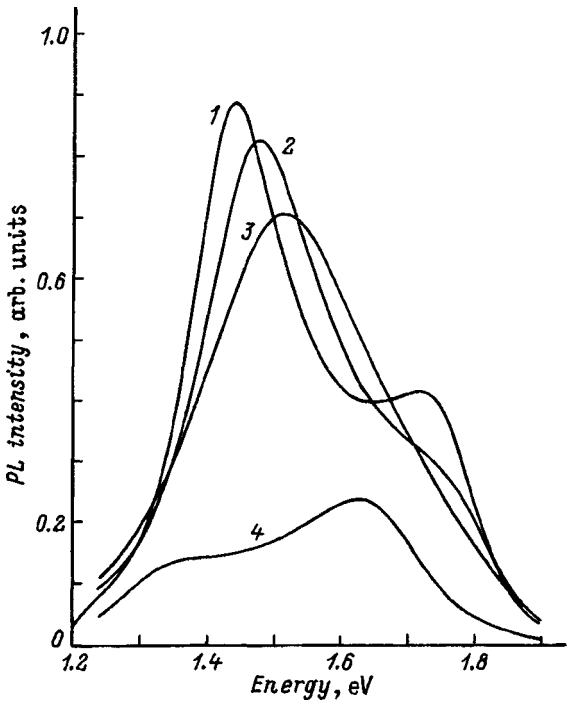

FIG. 4. Theoretical p-polarized PL spectra obtained at different radiation emergence angles φ(°): *1* — 0; *2* — 45; *3* — 66 (Brewster angle); *4* — 82.

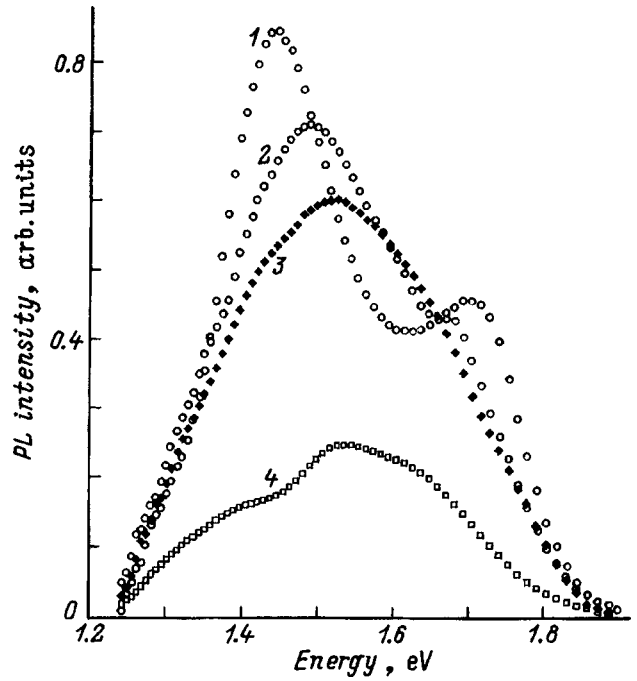

FIG. 5. Experimental *p*-polarized PL spectra obtained at different radiation emergence angles $\varphi(°)$: *1* — 0; *2* — 45; *3* — 66 (Brewster angle); *4* — 82. $T=77$ K.

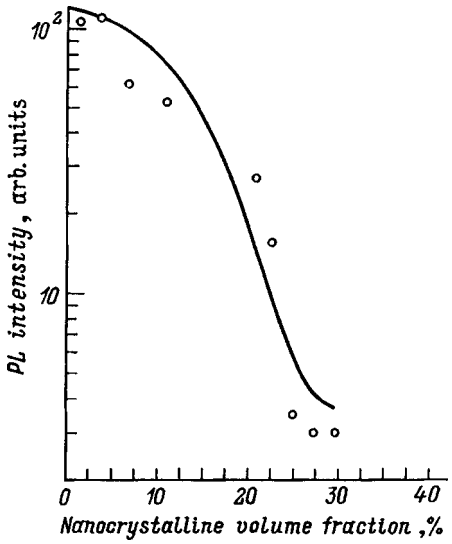

FIG. 6. PL intensity vs volume fraction of nanocrystallites. $T=77$ K.

of recombination centers producing the emission line about 1.5 eV with a FWHM of ~ 0.3 eV. Our measurements established that the position of the PL peak was practically independent of the size and volume fraction of nanocrystallites, which varied depending on the deposition technology employed, in the ranges of 30–50 Å and 0–40%, respectively. Thus the observed emission is apparently not connected with electron-hole pair recombination inside nanocrystallites. The comparatively weak temperature quenching of the PL (the signal decreased by less than two orders of magnitude while the film temperature increased from the nitrogen to room temperature) does not permit one to relate the PL seen in the experiments to recombination via the tails in the density of localized states, as is characteristic of conventional bulk amorphous silicon. On the other hand, in view of the high porosity of the films (which is implied by the relatively small refractive index) one cannot exclude a substantial effect from localized surface states in pores on the radiative recombination of carriers.

A recombination mechanism involving excitons localized at pore surfaces and nanocrystallite interfaces has been proposed.[20–22] Note that the films studied by us exhibited fast (ns-scale) PL kinetics. This suggests that an exciton-like mechanism of radiative recombination operates also in amorphous-nanocrystalline silicon films investigated in this work.

The above procedure of finding the true luminescence spectrum was used by us also to study the dependence of integrated PL intensity on the volume fraction of nanocrystallites in films with mixed amorphous-nanocrystalline composition (Fig. 6). The sharp drop in PL intensity observed to occur with increasing volume fraction of the nanocrystalline phase can be associated with the formation of extended nanocrystalline clusters.[23] Localization of photoexcited carriers in the regions of the film where a noticeable fraction of nanocrystallites underwent clusterization is hardly likely. This increases substantially the probability of their transfer to nonradiative states, which results in the PL decay. As seen from Fig. 6, the PL signal disappears when the volume fraction of the nanocrystalline phase is about 25%.

Note that obtaining thin films with no interference altogether would require special technological procedures, for instance, grinding the quartz substrate, which may, in particular, interfere with crystallite nucleation and affect the film properties. Therefore it appears expedient to measure transmission and PL spectra from the same point on the film surface, which will permit reconstruction of the true luminescence spectrum in the cases where the film parameters allow the onset of interference.

In very thin films ($L<0.4\,\mu$m), only one interference maximum may form in the spectral region under study. Its position and width are extremely sensitive to small variations in thickness and refractive index of the film, which may vary from one sample lot to another, as well as in the subsequent processing of the samples. One should not overlook this point when discussing possible microscopic mechanisms of PL spectrum formation.

Thus investigation of the PL of thin hydrogenated amorphous-nanocrystalline silicon films has revealed a strong effect of Fabry-Perot interference on the spectral shape. Analytic expressions for emission-band shape including interference corrections have been derived. It has been shown that the true luminescence spectrum in a film–transparent-substrate system allowing PL excitation from the side of the substrate can be reconstructed by straightforward division of the PL spectrum by the experimental transmission spectrum of the sample under study. An analysis of spectra made with inclusion of interference corrections showed that only one emission band due to carrier recombination at centers of the same type forms within the 0.6–1.0 μm interval. The film PL was found practically to disappear

when the volume fraction of the nanocrystalline phase rises above ~25%.

The authors owe sincere thanks to V. A. Kosobukin for fruitful discussions.

Partial support of the ''Physics of Solid-State Nanostructures'' Program (Grants 95-1001 and 96-1012), of the Russian Fund for Fundamental Research (Grants 96-02-16933, 97-02-18138, and 98-02-17350), and INCO-COPERNICUS Project PL87-8104 is gratefully acknowledged.

[1] L. Brus, Appl. Phys. A **53**, 465 (1991).
[2] C. Weisbuch, Optoelectron., Devices Technol. **8**, 523 (1993).
[3] L. T. Canham, Appl. Phys. Lett. **57**, 1046 (1990).
[4] Y. Kanemitsu, Phys. Rev. B **48**, 4883 (1993).
[5] T. Toyama, Y. Kotani, H. Okamoto, and H. Kida, Appl. Phys. Lett. **72**, 1489 (1998).
[6] A. T. Voutsas, M. K. Hatalis, J. Boyce, and A. Chiang, J. Appl. Phys. **78**, 6999 (1995).
[7] Ch. Yin, X. Liu, and Y. He, J. Appl. Phys. **75**, 797 (1994).
[8] X. Liu, S. Tong, L. Wang, G. Chen, and X. M. Bao, J. Appl. Phys. **78**, 6193 (1995).
[9] H. Z. Song, X. M. Bao, N. S. Li, and X. L. Wu, Appl. Phys. Lett. **72**, 356 (1998).
[10] K. Kim, M. S. Suh, T. S. Kim, C. J. Woun, E. K. Suh, Y. J. Shin, K. E. Lee, H. J. Lee, M. H. An, and H. Rwu, Appl. Phys. Lett. **69**, 3908 (1996).
[11] J. F. Du, T. Wan, and B. Zhou, in *Solid State Phenomena* **44-46**, Pt. I, edited by H. Neber-Äschbacher (Scitec Publ. Ltd, Zürich, 1995), p. 283.
[12] L. Sh. Liao, X. M. Bao, X. Q. Zheng, N. Sh. Li, and N. B. Min, Appl. Phys. Lett. **68**, 850 (1996).
[13] M. Nogami and Y. Abe, Appl. Phys. Lett. **65**, 2545 (1994).
[14] X. Zhao, O. Schoenfeld, J. Kusano, Y. Aoyagi, and T. Sugano, Jpn. J. Appl. Phys., Pt. 2 **33**, L649 (1994).
[15] A. M. Danishevskiĭ, V. Latinis, M. M. Mezdrogina, and E. I. Terukov, Zh. Éksp. Teor. Fiz. **104**, 4031 (1993) [JETP **77**, 944 (1993)].
[16] C. Delerue, G. Allan, and M. Lannoo, Phys. Rev. B **48**, 11024 (1995).
[17] Th. Weber, H. Stolz, W. von der Osten, M. Heuken, and K. Heime, Semicond. Sci. Technol. **10**, 1113 (1995).
[18] R. M. A. Azzam and N. M. Bashara, *Ellipsometry and Polarized Light* [North-Holland, Amsterdam, 1977; Mir, Moscow, 1981], 584 pp.
[19] V. A. Kosobukin and A. M. Samsonov, Zh. Tekh. Fiz. **54**, 19 (1984) [Sov. Phys. Tech. Phys. **29**, 10 (1984)]; FTI Preprint No. 806 (1983).
[20] D. J. Wolford, J. A. Reimer, and B. A. Scott, Appl. Phys. Lett. **42**, 369 (1983).
[21] D. J. Wolford, B. A. Scott, J. A. Reimer, and G. B. Bradley, Physica B **117-118**, 920 (1983).
[22] S. Furakawa and N. Matsumoto, Solid State Commun. **48**, 539 (1983).
[23] V. G. Golubev, V. Yu. Davydov, A. V. Medvedev, A. B. Pevtsov, and N. A. Feoktistov, Fiz. Tverd. Tela (St. Petersburg) **39**, 1348 (1997) [Phys. Solid State **39**, 1197 (1997)].

Translated by G. Skrebtsov

Photocurrent resonances in short-period AlAs/GaAs superlattices in an electric field

V. L. Al'perovich,* A. S. Terekhov, V. A. Tkachenko, and O. A. Tkachenko

Institute of Semiconductor Physics, Siberian Branch of the Russian Academy of Sciences, 630090 Novosibirsk, Russia;
Novosibirsk State University, 630090 Novosibirsk, Russia

N. T. Moshegov, A. I. Toropov, and A. S. Yaroshevich

Institute of Semiconductor Physics, Siberian Branch of the Russian Academy of Sciences, 630090 Novosibirsk, Russia
(Submitted June 9, 1998)
Fiz. Tverd. Tela (St. Petersburg) **41**, 159–164 (January 1999)

The photocurrent was measured as a function of the external electric field in short-period AlAs/GaAs superlattices for various photon energies. Transport resonances, whose positions do not depend on the photon energy, were observed in these dependences together with optical resonances due to interband transitions in Wannier–Stark levels. It is shown that the transport resonances are due to tunneling of photoelectrons from the *p*-GaAs contact region into the first level in GaAs wells located 2–5 lattice periods from the contact layer. © *1999 American Institute of Physics.* [S1063-7834(99)03301-8]

It is known that an external electric field F should lead to localization of electron wave functions in an ideal crystal and decomposition of quasicontinuous energy bands into a ''Wannier–Stark ladder'' — a series of equidistant levels with spacing $\Delta E = eaF$, where a is the lattice period and e is the electron charge.[1] In ordinary semiconductor crystals, for realistic uniform electric fields $F \leqslant 10^5$ V/cm, ΔE is small compared to the width of the levels, which is determined by scattering processes. This makes it impossible to observe the Wannier–Stark ladder experimentally. Semiconductor superlattices have turned out to be good objects for investigating Stark states. The period a of the superlattice, the width of the minibands, and therefore the distance ΔE between the Stark levels can be fixed independently by varying the thickness and composition of individual layers during the epitaxy process. Wannier–Stark quantization has been observed experimentally in Refs. 2–4. Further investigations have shown that not only Stark localization, but also delocalization of electron wave functions as a result of Zener resonance tunneling with the participation of Wannier–Stark states, occur with increasing field.[5–8] In Refs. 5 and 6, Zener tunneling of electrons in superlattices was studied on the basis of anticrossing of the lines of optical transitions in Wannier–Stark levels belonging to minibands with different numbers. Zener tunneling with participation of Wannier–Stark states is likewise manifested in the first and second applied voltage derivatives of the current-voltage characteristics of the dark current.[7,8] Another resonance effect appears in the form of a series of peaks observed in plots of the photocurrent versus the external electric field.[7] The position of these peaks did not depend on the photon energy, so that they could not be explained by optical transitions in Wannier–Stark levels. In Ref. 7 it was suggested that the photocurrent peaks are due to the competition between transport and recombination of photoexcited charge carriers. However, the experimental data were inconsistent with the hypothesis of tunneling between Stark levels belonging to different electron and hole minibands. To investigate further the mechanisms of electron transport in short-period superlattices and to determine the microscopic nature of the observed resonances, in the present work the external field dependences of the photocurrent were measured in a wide range of photon energies, including in the region where tunneling resonance dominate over optical transitions in Wannier–Stark levels. It is shown that the experimental data can be explained well by resonance tunneling of photoelectrons from the *p*-GaAs contact layer to the first size-quantization level in GaAs layers of the superlattice.

1. EXPERIMENTAL PROCEDURE

The experimental samples consisted of p–i–n diodes, whose undoped i regions contained short-period superlattices $(\mathrm{AlAs})_m/(\mathrm{GaAs})_n$ with $m=3-5$, $n=10-13$ monolayers (ML) and $N=30-50$ periods. The samples were grown by molecular-beam epitaxy (MBE) on GaAs (100) substrates.[9,10] The superlattice was separated from the substrate by a strongly doped $\sim 1\,\mu$m thick n^+-GaAs buffer layer, which was used as the bottom contact. A 0.2 μm thick p^+-GaAs contact layer was grown on top of the superlattice. The details of the procedure used to grow the superlattices and to monitor their structural perfection are described in Refs. 9 and 10. Mesostructures with a diameter of ~ 1 mm and ohmic contacts to the n and p layers were fabricated on the initial epitaxial structures (Fig. 1a). The measurements of the spectra of the barrier photocurrent arising between the contacts when the structure is illuminated were conducted at 4.2 K using the automated apparatus described in Ref. 10.

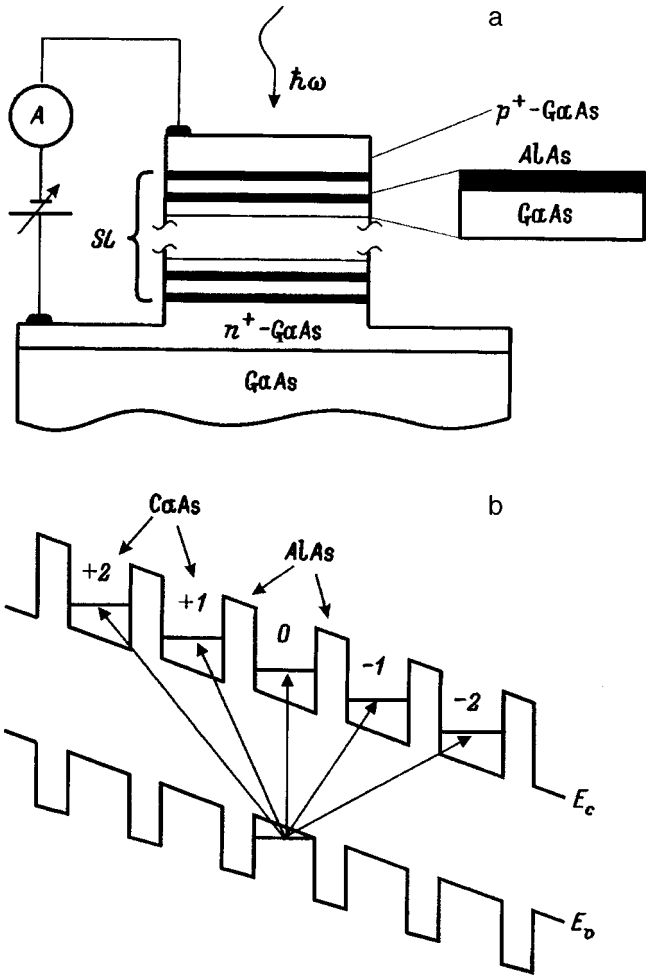

FIG. 1. a) Mesa structure based on a p–i–n diode with a (AlAs)/(GaAs) superlattice (SL) with an undoped i-region and the scheme for measuring the photocurrent. b) Energy diagram of a fragment of the superlattice in an electric field and the optical interband transitions between Wannier–Stark levels of the valence and conduction bands.

2. RESULTS AND DISCUSSION

The energy diagram of the semiconductor superlattice in an electric field F is shown schematically in Fig. 1b. The electric field takes the size-quantization levels in individual GaAs wells, where the levels form a miniband in the absence of a field $F=0$, out of resonance. As a result, the miniband decomposes into a system of equidistant Wannier–Stark energy levels, and the electron and hole wave functions become localized in individual quantum wells.[2–4] The arrows in Fig. 1b show possible channels of optical transitions, direct and indirect in space, between Wannier–Stark levels in the valence and conduction bands. Indirect optical transitions are possible as a result of tunneling of electrons from neighboring wells into the central well (which lies at the position of the well for a photohole). The thresholds $\hbar\omega_n$ of such interband transitions are described by the following relation:

$$\hbar\omega_n=\hbar\omega_0+neaF, \tag{1}$$

where $n=0,\pm1,\pm2,\ \ldots$. enumerates the junctions and $\hbar\omega_0$ is the energy of the fundamental (vertical) transition between hole and electron size-quantization levels.

Figure 2 shows the photocurrent spectrum measured with zero external bias in the built-in electric field of the p–i–n structure. A series of transitions in Wannier–Stark levels, right up to large numbers $n=-5$, is observed in the spectrum. This attests to the high quality of the superlattices investigated. Nonetheless, as shown in Ref. 10, even in the best of the experimental superlattices, together with a monotonic variation of the thickness of the levels over the area of the epitaxial structure, small-scale protuberances of the order of 1 ML high and $\leqslant 10$ nm in lateral size are present on the heteroboundaries. It should be noted that Wannier–Stark transitions are observed in the form of clear peaks and not thresholds, as was expected from the one-electron model of optical transitions. These peaks are due to the production of

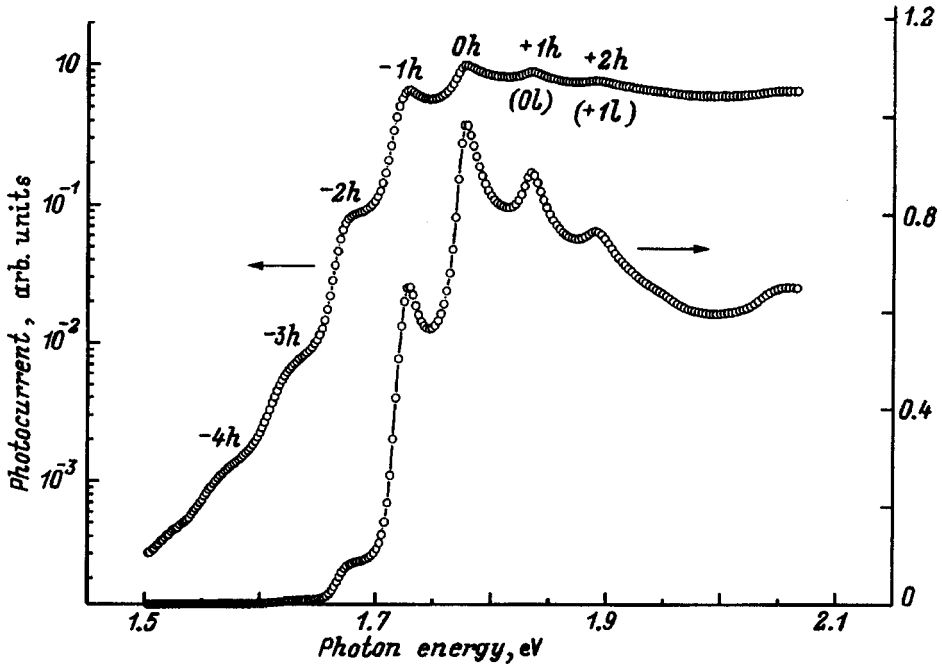

FIG. 2. Photocurrent spectrum of a $[(AlAs)_3(GaAs)_{11}]\times30$ superlattice, measured with zero reverse bias, in the built-in electric field of a p–i–n structure. The peaks $0h,\pm1h,\pm2h,\ \ldots$ correspond to optical transitions from heavy hole (h) levels to Wannier–Stark levels in the conduction band, the peaks $0l,+1l$ correspond to optical transitions from light-hole levels (l). The spectrum is constructed in linear (right-hand scale) and logarithmic (left-hand scale) scales in order to determine the optical transitions to Wannier–Stark levels with large numbers n. $T=4.2$ K.

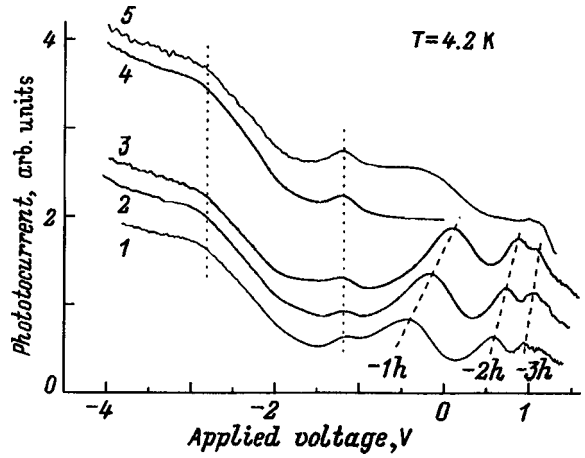

FIG. 3. Photocurrent versus applied voltage curves measured in a $[(AlAs)_3(GaAs)_{11}]\times 30$ superlattice for different photon energies. $\hbar\omega$ (eV): *1* — 1.71, *2* — 1.72, *3* — 1.73, *4* — 1.96, *5* — 1.78. The dashed lines connect peaks corresponding to optical resonances — spatially indirect phototransitions to Wannier–Stark levels $-1h, -2h$, and $-3h$. The vertical dotted lines show the transport photocurrent resonances due to tunneling of photoelectrons along Wannier–Stark levels. In contrast to the optical resonances, the position of the transport resonances does not depend on the photon energy.

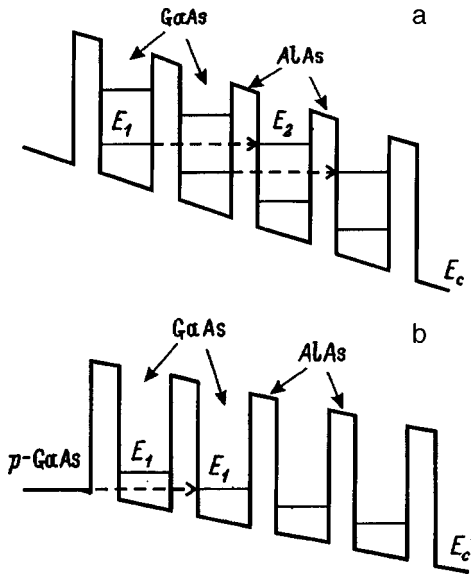

FIG. 4. a) Energy band diagram of a one-dimensional superlattice, illustrating a tunneling resonance with $k=2$ between the first E_1^e and second E_2^e quantization levels of electrons in the GaAs layers. b) Same for resonance tunneling of photoelectrons from the *p*-GaAs contact layer to the first level E_1^e in the second well ($n=2$).

bound electron-hole pairs — excitons.[11] As the transition number n increases, the distance between the electrons and holes partipating in an optical transition decreases, the Coulomb interaction becomes weaker, and the excitonic peaks therefore become less intense and gradually convert into steps.

Spatially indirect optical transitions among Wannier–Stark levels can be observed not only in the spectral curves of the photocurrent (Fig. 2) but also in the curves of the photocurrent J_{pc} versus the external bias U, measured for different photon energies. This follows from Eq. (1) and the fan diagram for the transition energies $\hbar\omega_n(U)$ shown in Fig. 5 of Ref. 10. Indeed, for fixed photon energy below the energy $\hbar\omega_0$ of the main transition Wannier–Stark levels corresponding to the numbers $n=-1,-2,-3,\ldots$ should appear in the curve of the photocurrent versus the reverse bias. The curves $J_{pc}(U)$ measured in a $[(AlAs)_3(GaAs)_{11}]\times 30$ superlattice for different photon energies in the range $\hbar\omega=1.71-1.96$ eV are shown in Fig. 3. The dashed lines connect peaks corresponding to optical resonances — spatially indirect transitions of electrons in Wannier–Stark levels $-1h$, $-2h$, and $-3h$ with absorption of photons. In accordance with Eq. (1), the positions of the optical resonances depend on the photon energy.

Together with optical resonances, peaks, whose positions do not depend on the photon energy, are also observed in the curves of the photocurrent versus the bias U (see Fig. 3). We observed such stationary peaks (''transport resonances'') in all of the superlattices investigated, both at low ($T=4.2$ K) and room temperatures. The transport resonances could be due to Zener tunneling of electrons and holes between quantum-size levels belonging to different wells and originating from minibands with different numbers.[5–7] The condition for observing transport resonances has the form

$$E_2^{e,l,h}-E_1^{e,l,h}=keF_ka, \tag{2}$$

where $E_1^{e,l,h}$ and $E_2^{e,l,h}$ are the centers of the first and second minibands of electrons (e), light holes (l), and heavy holes (h), k is the number of the tunneling resonance, equal to the number of the barriers through which the particle tunnels, and $F_k=(E_g-U_k)/Na$ and U_k are the resonance values of the electric field and applied voltage. Figure 4a shows schematically the tunneling of electrons through two barriers ($k=2$) from the first to the second size-quantization level. When the resonance condition (2) is satisfied, the increase in the photocurrent could be due to an increase in the probability of extraction of electrons or holes from the superlattice. However, the previously obtained experimental data[7] were inadequate to confirm or reject the assumption that electrons and holes tunnel in the bulk of the superlattice between Wannier–Stark levels originating from different minibands.

To determine the microscopic nature of the transport resonances we performed detailed measurements of the dependences $J_{pc}(\hbar\omega,U)$ in a wide range of photon energies, including $\hbar\omega<\hbar\omega_0$, where transport resonances are most clearly observed. A series of curves $J_{pc}(U)$ is shown in Fig. 5. Transport resonances with numbers $k=2-5$ can be seen in this series. Here, the interference from optical resonances could be decreased by making an appropriate choice of the photon energy range. Similar curves were measured on different mesa structures fabricated from the same epitaxial structure with a $[(AlAs)_3/(GaAs)_{11}]\times 50$ superlattice. Curves of $(E_g-U_k)^{-1}$, the reciprocal of the total voltage drop on the superlattice, versus the number k of the tunneling resonance are shown in Fig. 6 for three mesa structures. Here U_k is the reverse bias for which a photocurrent peak corresponding to electron tunneling through k barriers is observed. To determine more accurately the position of the resonance $k=5$, which is not as pronounced in the curves $J_{pc}(U)$, the

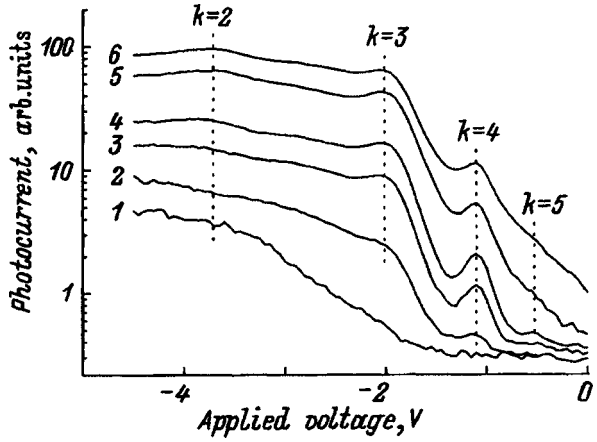

FIG. 5. Photocurrent J_{pc} versus the bias U curves measured for different photon energies. $\hbar\omega$ (eV): *1* — 1.494, *2* — 1.503, *3* — 1.512, *4* — 1.521, *5* — 1.550, *6* — 1.590. Tunneling resonances with $k=2-5$, whose position does not depend on the photon energy, appear in the curves $J_{pc}(U)$.

experimental curves were differentiated. Least-squares straight lines were drawn through the experimental points. The difference of the slopes of the curves on different mesa structures is due to the monotonic variation of the period of the superlattice over the area of the epitaxial structure.[10] The dependence shown by the squares corresponds to the nominal values of the barrier and well thicknesses, i.e. 3 ML for AlAs layers and 11 ML for GaAs layers. If it is assumed that tunneling in the bulk of the superlattice occurs between Stark levels originating from the first and second minibands, then according to Eq. (2) the difference between these levels $E_2-E_1\approx 230\pm 5$ meV can be determined from the slope of the experimental curve. This value was compared with a numerical calculation of the energy spectrum of a $(AlAs)_3/(GaAs)_{11}$ superlattice by the effective-mass method. The computational details are described in Ref. 10. The electron

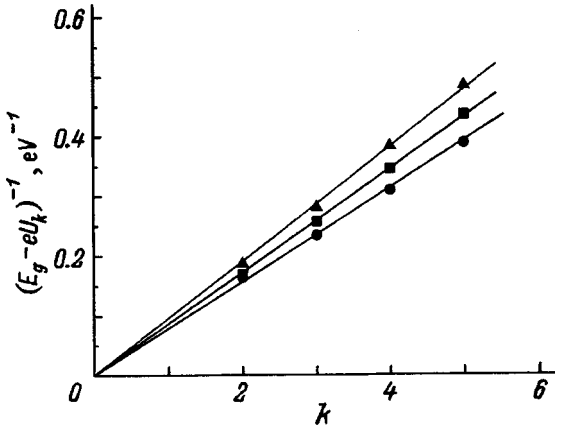

FIG. 6. $(E_g-U_k)^{-1}$, the reciprocal of the total voltage drop in the superlattice, versus the number k of the tunneling resonance. The measurements were performed on three different mesa structures of a $[(AlAs)_3/(GaAs)_{11}]\times 50$ superlattice. U_k — reverse bias for which a photocurrent peak corresponding to tunneling of electrons through k barriers is observed. The straight lines are least-squares fits of the experimental points. The difference in the slopes of the curves for different mesa structures is due to the monotonic variation of the superlattice period over the area of the epitaxial structure.[10]

and hole effective masses as well as the height of AlAs barrier were varied within the values presented in the literature, so that the computed energies $E_g+E_1^e+E_1^h$ and $E_g+E_1^e+E_1^l$ of the vertical interband transitions agreed with experiment to within $\sim 1-2$ meV. The computed values are as follows: for electrons $E_1^e=205$ meV, $E_2^e-E_1^e=540$ meV; for light holes $E_1^l=130$ meV, $E_2^l-E_1^l=395$ meV; and, for heavy holes $E_1^h=70$ meV, $E_2^h-E_1^h=200$ meV. One can see that the experimental value of the difference E_2-E_1 determined from the slope of the curve in Fig. 6 does not agree with the calculations for light particles (electrons and light holes), while the tunneling of heavy holes through several barriers is unlikely to occur. Therefore the hypothesis of resonance tunneling between Stark levels of the first and second miniband in the bulk of the superlattice is not confirmed.

We assumed that the experimentally observed transport resonances are due to tunneling of photoelectrons from the *p*-GaAs contact region to the ground size-quantization level E_1^e in the GaAs layers adjoining the contact. This process is apparently the ''bottleneck'' for transport of electrons produced in the contact region through the superlattice. Next, electrons with a high probability (as compared with the probability of tunneling out of the contact) descend the Stark ladder, losing energy, and are collected by the *n*-GaAs collecting contact. The process of resonance tunneling from the contact to the level E_1^e through two AlAs barriers is illustrated in Fig. 4b. In contrast to Eq. (2), the resonance condition for the case shown has the form $E_l^e=keF_ka$. The energy of the level $E_1^e\approx 230\pm 5$ meV, determined from the slope of the experimental curves in Fig. 6, corresponds approximately to the computed value 205 meV.

An additional experimental confirmation of the mechanism leading to the formation of transport resonances due to tunneling from the contact region is the increase of the relative role of these resonances with decreasing photon energy. Indeed, on account of the exponential decay of the probability of indirect transitions to Wannier–Stark levels with increasing number n, the intensity of optical transitions in the bulk of the superlattice decreases rapidly with decreasing photon energy in the region $\hbar\omega<\hbar\omega_0$. At the same time, on account of photoelectron generation in the contact region, transport resonances are observed clearly in the curves $J_{pc}(U)$ right up to photon energies $\hbar\omega\sim E_g^{GaAs}=1.52$ eV — the band gap in GaAs. According to Fig. 5, as the photon energy decreases further $\hbar\omega<E_g^{GaAs}$, the resonance peaks gradually vanish because the number of photoelectrons generated in the contact region decreases. Surprisingly, a transport resonance with number $k=4$, which is separated by a deep minimum from the less pronounced resonances $k=2$ and $k=3$, is most pronounced in the curves $J_{pc}(U)$. The reason for such nonmonotonic behavior of the width and amplitude of resonances as a function of the number k is unclear. It could be that the broadening of the transport resonances with low numbers is determined by the wings of the optical resonances. In addition, it is evident from Fig. 5 that another, wider maximum, whose nature has not yet been established accurately, appears between the transport resonances $k=2$ and $k=3$. The wide maximum could be due to electron tunneling through an interfacial state arising on the

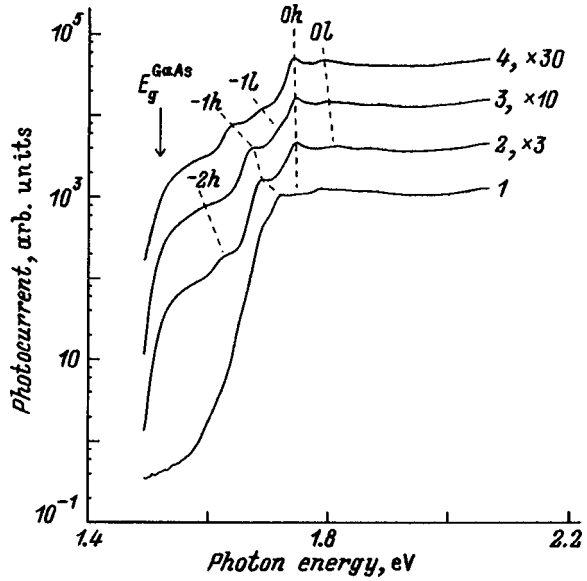

FIG. 7. Photocurrent spectra of a $[(AlAs)_3/(GaAs)_{11}]\times 30$ superlattice measured with various reverse biases. U (V): *1* — 0, *2* — 1.7, *3* — 2.5, *4* — 4.0. The arrow shows the band gap in GaAs. The remaining notation is the same as in Fig. 2.

boundary of the superlattice and *p*-GaAs contact layer as a result of the penetration of the electric field into *p*-GaAs. To clarify these questions it is necessary to perform and compare with experiment a calculation of the energy spectrum and transport properties of a finite superlattice taking into account the real variation of the potential at the interface. The results of such a comparison will be presented in a separate paper.

Figure 7 shows the spectral curves of the photocurrent $J_{pc}(\hbar\omega)$ of a $[(AlAs)_3/(GaAs)_{11}]\times 50$ superlattice, measured for various bias voltages U. Together with optical transitions in Wannier–Stark levels for $\hbar\omega > 1.6$ eV, interband transitions in the *p*-GaAs contact layer with a clear threshold in the photon energy $\hbar\omega \approx 1.52$ eV, close to the band gap in gallium arsenide at $T = 4.2$ K, appear in the spectra. Holes photogenerated in n^+-GaAs apparently do not make a large contribution to the photocurrent; in the opposite case, the threshold for optical transitions should be observed at $\hbar\omega \approx 1.55$ eV because of a large Moss–Burshteĭn shift in strongly doped *n*-GaAs. A direct observation of a current due to photoelectrons generated in the *p*-GaAs layer confirms the proposed interpretation of the transport resonances. The contribution of the contact region to the photocurrent, determined from the spectra in Fig. 7, agrees with the amplitude of the resonance peaks observed in the curves $J_{pc}(U)$. It should be noted that transport resonances were not observed in the curves $J_{pc}(U)$ presented in Ref. 5 because of the presence of additional ~100 nm thick AlGaAs blocking barriers, which prevented tunneling of photoexcited charge carriers from the contact regions into the superlattice. This fact also agrees with the proposed explanation of the transport resonances.

In summary, under the conditions of Wannier–Stark localization, the transport resonances in the curves of the photocurrent of short-period AlAs/GaAs superlattices as a function of the external electric field are due to tunneling of photoelectrons from the *p*-GaAs contact region into the ground size-quantization level E_1^e of electrons in GaAs wells adjoining the contact.

In conclusion, we note that the observation of transport resonances makes it possible to determine independently the position of the electron ground state E_l^e. Together with the experimental energies of the interband vertical optical transitions, this makes it possible to determine separately the energies of electron, heavy-hole, and light-hole levels and therefore to determine more accurately the parameters of the energy spectrum of short-period superlattices.

This work was supported in part by the Russian Fund for Fundamental Research (Grant No. 96-02-19060), the State Program ''Surface atomic structures'' (Grant No. 95-2.4), and the Scientific-Technical Program ''Physics of solid-state nanostructures'' (Grant No. 98-1102).

*E-Mail: alper@thermo.isp.nsc.ru

[1] G. H. Wannier, Phys. Rev. **117**, 432 (1960).
[2] E. E. Mendez, F. Agullo-Rueda, and J. M. Hong, Phys. Rev. Lett. **60**, 2426 (1988).
[3] P. Voisin, J. Bleuse, C. Bouche, S. Gaillard, C. Alibert, and A. Regreny, Phys. Rev. Lett. **61**, 1639 (1988).
[4] K. Fujiwara, H. Schneider, R. Chingolani, and K. Ploog, Solid State Commun. **72**, 935 (1989).
[5] H. Schneider, H. T. Grahn, K. von Klitzing, and K. Ploog, Phys. Rev. Lett. **65**, 2720 (1990).
[6] R. P. Leavitt and J. W. Little, Phys. Rev. B **41**, 5174 (1990).
[7] V. L. Alperovich, V. A. Haisler, A. S. Jaroshevich, N. T. Moshegov, A. S. Terekhov, A. I. Toropov, and V. A. Tkachenko, Surf. Sci. **267**, 541 (1992).
[8] H. Nagasawa, K. Murayama, M. Yamaguchi, M. Morifuji, C. Hamaguchi, A. Di Carlo, P. Vogl, G. Böhm, G. Tränkle, and G. Weimann, Solid-State Electron. **40**, 245 (1996).
[9] N. T. Moshegov, L. V. Sokolov, A. I. Toropov, A. K. Bakarov, A. K. Kalagin, and V. V. Tichomirov, Inst. Phys. Conf. Ser. N 145. Ch. 2, 97 (1996).
[10] V. L. Al'perovich, N. T. Moshegov, V. V. Popov, A. S. Terekhov, V. A. Tkachenko, A. I. Toropov, and A. S. Yaroshevich, Fiz. Tverd. Tela (St. Petersburg) **39**, 2085 (1997) [Phys. Solid State **39**, 1864 (1997)].
[11] F. Agullo-Rueda, J. A. Brum, E. E. Mendez, and J. M. Hong, Phys. Rev. B **41**, 1676 (1990).

Translated by M. E. Alferieff

POLYMERS. LIQUID CRYSTALS

Structures and thermoelectric convection in cholesteric liquid crystals

E. D. Eĭdel'man

Chemical-Pharmaceutical Institute, St. Petersburg, Russia
(Submitted July 3, 1998)
Fiz. Tverd. Tela (St. Petersburg) **41**, 165–170 (January 1999)

The possibilities for excitation of electromagnetic field structures and convection cells, i.e., temperature and velocity structures, in a thermotropic cholesteric liquid crystal in the presence of flow are studied. Estimates are made and possible experiments for observing such structures are discussed. A special thermoelectric effect is investigated as the cause of these excitations — the influence of a heating-induced change in the pitch of the cholesteric helix of the molecules on the permittivity and the electric conductivity of the material. © *1999 American Institute of Physics.* [S1063-7834(99)03401-2]

In thermotropic cholesteric liquid crystals (cholesterics, or CLCs), in many cases the formation (excitation) of structures different from those arising in nematic substances can form (be excited).[1] The structures which arise resemble the convection cells produced by the thermoelectric effect when a thin layer (thickness $h<0.1$ mm) of a liquid semiconductor is heated,[2] whereas in a number of cases thermotropic cholesterics exhibit high thermoelectric power, thereby exhibiting the properties of liquid semiconductors.[3]

These differences are due to the existence of a vector associated with the direction of the axis of the CLC molecules. The magnitude of this vector $2\pi/q$ is determined by the reciprocal of the pitch q of the helix, which depends strongly on the temperature T.[4] Even for ''small'' heatings $A=|\nabla T|$, such that $hA/T\ll 1$, on account of a ''large'' change in the pitch $h|\nabla q|/1\gg 1$ it is possible that

$$\left|\frac{d\ln q}{d\ln T}\right|\frac{hA}{T}\geqslant 10^2\frac{hA}{T}\geqslant 1. \tag{1}$$

A large change in the pitch of the helix on heating results in a strong temperature dependence of the characteristics of a CLC (for example, the permittivity ε_{ik}, conductivity σ_{ik}, viscosity ν_{ik}, thermal diffusivity $\varkappa_{ik}$, and others).

The temperature dependence of the anisotropic parts of the electric characteristics of the medium (ε_a and σ_a) is observed as a new thermoelectric effect arising in the presence of current flow.[5] The influence of this effect on the conditions of excitation of instabilities in the presence of a flow (heat and charge) will be examined below. The existence of anisotropic parts of the dissipative quantities (ν_a and $\varkappa_a$) affects the possibility of rotations of the director **n** and gives effects which are characteristic of all media, transmitting not only hydrostatic compression but also twist.

It is more convenient to construct a quantitative theory of this phenomenon for thermotropic nematic liquid crystals (see, for example, Ref. 6). The dissipation anisotropy is neglected in what follows.

1. EFFECT OF ELECTROPHORETIC FORCES. FORMULATION OF THE PROBLEM

The existence of a temperature dependence of the reciprocal of the pitch $q(T)$ of the helix in a cholesteric leads to a force $E_iE_k\nabla\varepsilon_{ik}$. The electric field E_i consists of a thermoelectric field $\gamma\nabla T_0$ (γ — thermoelectric power) and a field due to small deviations $E_1=-\nabla\varphi$. We shall construct a theory of the excitation of structures (convection) by this force.

Let us consider a cholesteric layer with axes of the molecular helices (x axis) parallel to the surface of the layer. (The case where the molecular axes (direction of the director) are perpendicular to the surface of the layer (z axis) can be treated similarly.) The components of the permittivity tensor in the plane of the layer can be written

$$\varepsilon_{ik}=\varepsilon\delta_{ik}+(\varepsilon_a)_{ik}, \tag{2}$$

where the components of the anisotropic part of the tensor are

$$(\varepsilon_a)_{ix}=0;\quad (\varepsilon_a)_{zy}=0.5\Gamma\varepsilon\sin(2qx);$$
$$(\varepsilon_a)_{zz}=-(\varepsilon_a)_{yy}=0.5\Gamma\varepsilon\cos(2qx). \tag{3}$$

The quantity Γ characterizes the degree of anisotropy. We note that the tensors of other characteristics of the cholesteric can be written identically (substituting the letters σ,ν, and $\varkappa$ for ε).

The possibilities of excitation can be understood qualitatively by comparing the electrophoretic force with dissipation. This can be done similarly to the manner in which the buoyancy force is equated to the dissipation (see, for example, Ref. 7) so that their ratio provides a criterion for excitation of convection — the Rayleigh number $\mathcal{R}$. However, in the present case such a comparison will not give an excitation criterion. The problem is that the new force is a rapidly oscillating quantity; it varies strongly over short distances q^{-1}, comparable in magnitude to the size of a cholesteric molecule. The macroscopic excitation effect is there-

fore determined only after averaging, which contributes a large factor to the excitation condition. This factor can be written in different ways, for example (in order of decreasing magnitude)

$$\frac{A}{q^2}\frac{dq}{dT}, \quad \frac{Ah}{q}\frac{dq}{dT}, \quad Ah^2\frac{dq}{dT} \tag{4}$$

and cannot be ''picked up'' in a qualitative analysis. It turns out that the excitation criterion for thermoelectric convection can be written as

$$\mathcal{E}_c=\frac{\varepsilon\gamma^2h^5A^4}{\rho\nu\varkappa q}\left(\frac{dq}{dT}\right)^2=\mathcal{E}\frac{A^2h^3}{q}\left(\frac{dq}{dT}\right)^2, \tag{5}$$

where $\mathcal{E}$ is a dimensionless parameter, a number characterizing excitation in an isotropic medium (in a liquid semiconductor[2]). One can see from this relation that the product of the last two expressions in Eqs. (4) appears in the criterion, while the large factor itself has not appeared. We note that the factor dq/dT appeared squared in the number $\mathcal{E}_c$, i.e. the influence of the temperature dependence of the pitch of the helix on the excitation of structures is independent of whether or not this quantity increases or decreases with rising temperature.

Let us now formulate the problem. We shall assume that at equilibrium the cholesteric is electrically neutral, i.e. we neglect the charge fluctuations arising in a thermoelectric field. The effect of small deviations arising in a thermoelectric field from electrical neutrality would lead to effects similar to those investigated for liquid semiconductors.[2] This effect can be taken into account by substituting $\pm\mathcal{R}+\mathcal{E}k^2$ for the Rayleigh number $\mathcal{R}$ in the final results. The signs are determined by the direction of the heating. The upper sign corresponds to heating from below and the lower sign corresponds to heating from above; the squared wave number k^2 will be determined below. In addition, since the pitch of the helix is, as already emphasized, strongly temperature-dependent, small deviations of the pitch of the helix on account of other factors will be neglected. Then we can set

$$q=q_0\pm zA\frac{dq}{dT}+\frac{dq}{dT}q_1, \tag{6}$$

i.e. we assume that $A=|dT_0/dz|$, and there is no heating along the layer.

These approximations make it possible to neglect the effect of a change in the pitch of the helix on the director and to assume that for the anisotropic liquid under study the components of the director are

$$n_z=\cos(qx), \quad n_x=0, \quad n_y=\sin(qx). \tag{7}$$

In this approximation, the director equation need not be included in the system of equations (in the geometry where the axes of the helices are oriented in the direction of heating, this would be necessary). This form of the director corresponds to the form chosen above [see Eqs. (2) and (3)] for the coordinate dependences of the electrical characteristics of the medium. In accordance with Eqs. (2) and (3), using Eq. (7) we obtain $\varepsilon_{ik}=\varepsilon\delta_{ik}+\varepsilon\Gamma n_in_k$, which agrees completely with the expansions that are ordinarily used (see, for example, Ref. 4).

The system of equations of electrohydrodynamics of CLCs consists of the standard continuity equation $\nabla\cdot\mathbf{v}=0$ and the heat transfer equation $(\partial/\partial t-\varkappa\Delta)T_1=\mp v_zA$ as well as the equation expressing electrical neutrality

$$\partial(\varepsilon_{ik}E_k)/\partial x_i=0 \tag{8}$$

and the equation of motion (g is the acceleration of gravity)

$$\rho\left(\frac{\partial}{\partial t}-\nu\Delta\right)\mathbf{v}-\rho\mathbf{g}+\nabla p=-0.5E_iE_k\nabla\varepsilon_{ik}, \tag{9}$$

which, in order to find the excitation criteria, must be linearized with respect to small deviations of the density $\rho_1=\rho-\rho_0$, pressure $p_1=p-p_0$, and the characteristics of the electric field. These equations take account of the fact that the medium is at rest at equilibrium. After linearizing, the variables must be eliminated in the standard manner, expressing them in terms of the potential φ.

The nonlinear equation obtained in the standard manner must be averaged. Indeed, we are interested in the excitation of structures and convections on the scale $h\gg q^{-1}$. For this reason, averaging must be performed over the scale q^{-1}, i.e.,

$$\langle f\rangle=\frac{q}{2\pi}\int_0^{2\pi/q}f\,dx \tag{10}$$

must be calculated for all parts of the equation obtained after elimination of the variables. In this procedure, the small deviations (i.e., φ) and their derivatives are replaced by average values. The condition $qh\gg1$, separating the scales, makes it possible to replace the convolutions (integrals of products) by derivatives of average quantities (constants on the microscale q^{-1}). Averaging yields an equation with a constant coefficient, in which terms which are not small with respect to the parameter qh must be retained. The solution of the equation will be a superposition of the solutions proportional to

$$\exp\left(-i\omega\frac{t}{h^2/\nu}+ik_x\frac{x}{h}+ik_z\frac{z}{h}\right), \tag{11}$$

where the y dependence of fluctuating quantities is neglected for simplicity. The wave number $k^2=k_x^2+k_z^2$ (in our case $k^2=k_\perp^2+k_z^2$) is determined by the dimensionless projections, the projection along the layer $k_x=2\pi h/\lambda$ (λ is the size of the structure along the layer) being a real quantity by virtue of the translational symmetry characteristic of the geometry of a layer that is infinite in this direction; k_z is, generally speaking, a complex quantity, which must be determined by solving a boundary-value problem. It is assumed below that k_z is real. This is sufficient to obtain qualitative results. The reality of k_z must be assured by substituting the corresponding boundary conditions. These conditions are of the ''free isothermal boundaries'' type.[7] If the equation contains only even z derivatives, then $k_z=\pi$. Finally, the frequency $\omega=\omega'+i\omega''$ is, as always, determined by the conditions leading to the appearance of an instability.

Omitting complicated calculations, we immediately present the excitation condition

$$[(i\omega-k^2)(i\omega\mathcal{P}-k^2)k^2\mp\mathcal{R}k_x^2]k^2 = \mathcal{E}_c\left[-ik_z^2k_x+2Ahk_xk_z\frac{\partial}{\partial T}\left(\ln\frac{dq}{dT}\right)\right]. \quad (12)$$

This equation is written in a dimensionless form, and it contains together with the numbers $\mathcal{R}$ and $\mathcal{E}_c$ the Prandtl number $\mathcal{P}=\nu/\varkappa$.

We emphasize once again that the terms standing on the right-hand side in this equation are due to the special thermoelectric effect which is characteristic for thermotropic cholesterics and arises because of the temperature dependence of the pitch of the helix of a cholesteric. This effect is comparable to ordinary Rayleigh convection, while other mechanisms of excitation and the forces influencing them are assumed to be included in the Rayleigh number $\mathcal{R}$ characterizing this convection.

2. ANALYSIS OF THE EFFECT OF ELECTROPHORETIC FORCES ON THE EXCITATION OF INSTABILITY

Separating the real and imaginary parts in Eq. (12) we find that the instability ($\omega''=0$) arises under Rayleigh (possibly, altered) conditions, not aperiodically ($\omega'=0$), but rather oscillating with frequency (in a dimensionless form)

$$\omega=\frac{k_z^2k_x}{k^6(1+\mathcal{P})}\mathcal{E}_c. \quad (13)$$

Therefore, in contrast to thermoelectric convection arising in liquid semiconductors[2] the effect due to the temperature dependence of the pitch of the cholesteric helix does not change the excitation threshold, but instead influences the character of the growth of small deviations of all variables. Aperiodic growth, characteristic under ordinary conditions (including isotropic liquid semiconductors), is meaningless in cholesterics. Growth in cholesterics occurs in an oscillatory manner. The excitation conditions for Rayleigh convection are well known:[7] Cellular motion can arise only with heating from below and $k_\perp^2/k_z^2=1/2$,

$$k_z=\pi, \quad \mathcal{R}=27\pi^4/4.$$

Using these conditions and the values of the parameters in the liquid ($\varkappa\simeq\nu\simeq10^{-6}$ m^2/s) and the values of the characteristics of the medium which are usually used for liquid semiconductors,[3] i.e. at room temperature $T=300$ K and for values characteristic for CLCs[4] — $\beta T\simeq0.1$ (β — thermal expansion coefficient), $q^{-1}\simeq10^{-7}$ m, $d\ln q/d\ln T\simeq10^2$ (possibly even 10^3), and $\Gamma=0.1$ — we find from the equation for the frequency of oscillatory growth (in a dimensionless form)

$$\omega=\frac{\nu}{h^2}\frac{27\pi^4}{4\sqrt{2}}\Gamma^2\left(\frac{d\ln q}{d\ln T}\right)^2\frac{qh}{(\beta Ah)^2}\left(\frac{\varkappa\nu}{gh^3}\right)^4\frac{\varepsilon\gamma^2}{\rho\beta h^2(\varkappa+\nu)} \quad (14)$$

that with layer thickness $h\simeq0.1$ cm the frequency $\omega\simeq1-10$ Hz depends very strongly ($\sim h^{-15}$) on the layer thickness. For this reason, for thicknesses of the liquid layer $h>0.1$ cm growth is actually aperiodic.

The frequency does not become ''catastrophically'' high with decreasing layer thickness, i.e. just as in liquid semiconductors the excitation mechanism changes.[2] The frequency of the oscillations becomes

$$\omega=4\pi^2\Gamma^2qh\left(\frac{d\ln q}{d\ln T}\right)^2\frac{\rho\varkappa\nu}{\varepsilon\gamma^2A^2h^2}\frac{\varkappa\pi^3}{\nu+\varkappa}\frac{\nu}{h^2}. \quad (15)$$

Estimates with the same parameters of the medium as above give $\omega\simeq10-100$ Hz with $h\simeq0.01$ cm, and the dependence on the layer thickness is weak (inversely proportional).

It is also easy to find the change in the excitation conditions. We obtain

$$\pm\mathcal{R}+\mathcal{E}k^2=\frac{k^2}{k_\perp^2}(k^4-\omega^2\mathcal{P}). \quad (16)$$

The standard condition (found in Ref. 2) is obtained from Eq. (16) by setting $\omega=0$.

In thick layers ($h>0.1$ cm) an instability is possible only in the case of heating from below (upper sign in Eq. (16)), and substituting the frequency (13) into Eq. (16) we find the excitation condition in the form

$$\frac{k^6}{k_\perp^2}=\mathcal{R}+\frac{k_z^4}{k^{10}}\mathcal{I}_c, \quad (17)$$

where $\mathcal{I}_c=\mathcal{E}_c\mathcal{P}/(1+\mathcal{P})$ is also a dimensionless quantity.

It is of interest to examine a case where the new effect dominates. Minimizing with respect to $w=k_\perp^2/k_z^2$, we find that the instability occurs for $w=1/7$ (instead of the usual $w=1/2$). Thus, under these conditions there arises a motion with cells which are much more strongly extended (by the factor 3.5) along the layer (along the axes of the helix). Substituting $k_z=\pi$ and $k_x=\pi/\sqrt{17}$ we find that in this case motion arises for $\mathcal{I}_c>160$ with heating $A\geqslant10^2$ K/cm, which is not small. It is found that $A\sim h^{-5/4}$, and not h^{-4} as in the Rayleigh problem. Now, comparing the terms on the right-hand side in the excitation condition (17), we find that the new effect predominates over the Rayleigh effect only in sufficiently thin layers $h<10^{-2}$ cm. But in such layers the main excitation mechanism is not buoyancy but rather a thermoelectric lift mechanism. The excitation condition for it is also the condition (17) but with $\mathcal{E}k^2$ substituted for $\mathcal{R}$. Using the relation $\mathcal{I}_c=\mathcal{E}^4h^2/h_c^2$ we obtain

$$h_c=\frac{1}{q}\frac{\varepsilon\gamma^2\Gamma^2T^2}{\rho\nu\varkappa}\frac{\nu}{\nu+\varkappa}\left(\frac{d\ln q}{d\ln T}\right)^2, \quad (18)$$

the critical thickness of a cholesterin layer that separates the scales. Estimates show that $h_c\simeq0.01$ cm. The standard mechanisms of excitation of cellular motion (including the thermoelectric mechanism, for which the range of thicknesses is, however, quite narrow) predominate for $h>h_c$. For $h<h_c$ a new excitation mechanism should dominate in the CLC. The main force driving this mechanism is the electrophoretic force.

The mutual effects of Rayleigh and electrophoretic or thermoelectric and electrophoretic mechanisms on each other can be studied by eliminating $\mathcal{I}_c$ from Eq. (17). This can be done in the same manner in which the influence of Rayleigh and thermoelectric mechanisms on one another in liquid semiconductors was studied in Ref. 2. However, it is pointless to do this because there are no experimental data. For the same reason, there is no need to solve boundary-value problems in order to calculate the ranges of the parameters corresponding to the limits of the stability zones with more realistic boundary conditions than ''free and isothermal'' conditions.

As is well known,[7] boundary conditions cannot ''in principle'' suppress the qualitative possibility of an instability. It can be concluded that in a real experiment field and velocity structures should arise on heating in some region of parameters in the CLC, especially in thin layers.

3. EXCITATION OF STRUCTURES BY AN ELECTRIC CURRENT

We shall now study the possibility of excitation of instability by an electric current in CLC (see Ref. 5 for the general assumptions). We note that a cholesteric is characterized by the special temperature dependence of the conductivity tensor $\sigma_{ik}=\sigma\delta_{ik}+\Gamma\sigma n_i n_k$ on account of the temperature dependence of the pitch of the helix. Therefore everything said above concerning the form of the temperature dependence of the permittivity transfers to the temperature dependence of the conductivity. Of course, the analysis here refers to cases where the cholesteric exhibits quite strongly the properties of a conductor. Such substances do exist.[4]

Thus, let an electric current with density $\mathbf{j}_0$, produced by external factors, flow (x axis oriented along the axes of the helix and along the layer, z axis oriented across the layer) in the direction of the y axis in a cholesteric. In accordance with Ohm's law and Maxwell's equations, this means that electric $\mathbf{E}$ and magnetic $\mathbf{H}$ fields are present in such a medium, and $\sigma_{ik}E_k=\nabla_i\times\mathbf{H}$ and $\nabla\times\mathbf{E}=-\mu\partial\mathbf{H}/\partial t$ (μ — absolute magnetic permeability). The properties of the CLC are manifested in the conductivity tensor σ_{ik}, whose components are determined exactly by the Eqs. (2) and (3) with σ substituted for ε. When a current flows, Joule heat j_iE_i is released. This alters the equation of heat transfer, which must now be written in the form

$$\left(\frac{\partial}{\partial t}-\varkappa\Delta\right)T=\frac{\mathbf{j}\cdot\mathbf{E}}{\rho C_p}. \tag{19}$$

Here C_p is the specific heat of the cholesteric. Convective heat transfer, which under the conditions of the problem at hand is weak, is neglected in this equation. Of course, the thermal diffusivity in the CLC is a tensor quantity of the same form as σ_{ik}, but here we neglect the dependence of $\varkappa$ on the pitch of the helix in order to distinguish the effect under study. More accurate (and more complicated) calculations show that this approximation is justified.

The qualitative picture of the appearance of instabilities is as follows. A fluctuation change in temperature and a corresponding change in the pitch of the helix result in a small change in the conductivity. The fluctuation change of the conductivity in the presence of an external current results in changes in the electric and magnetic fields. If the energy stored in the field increases in the process by a larger amount than the work performed to overcome dissipation, then structure formation is possible.

The excitation problem is formally very similar to the problem discussed in Sec. 1. We obtain from Maxwell's equations and the equation of heat transfer a linearized system with respect to T_1 and H_{1x} (it is sufficient to take in H_1 one component, along the x axis and then average over the small scale q^{-1}). The excitation condition replacing Eq. (12) will have the form

$$k^2+\frac{\gamma_0^2\Gamma h^2}{2\sigma\chi}\frac{1}{q}\frac{dq}{dT}=0, \tag{20}$$

where $\chi=\rho C_p\varkappa$ is the thermal conductivity. From the excitation condition $\omega''=0$ it also follows that $\omega'=0$, i.e., instability arises aperiodically.

Proceeding now to an analysis of the condition obtained, we note first that structures are possible only if the reciprocal of the pitch of the helix q decreases with increasing temperature, i.e. $dq/dT<0$. Such cholesteric materials do exist.[4] When current flows in such media, structuring of the electric and magnetic fields (possibly against the background formed by the fields existing in the stationary state) occurs and the structures of temperature change form.

Structures with period (repetition length) $\lambda\simeq h$ require a current

$$j>j_c=\frac{2\pi}{h}\left(\frac{\sigma\chi}{|\Gamma/qdq/dT|}\right)^{1/2}. \tag{21}$$

Using the conductivity $\sigma=10^{-4}$ Sm/m (which corresponds to $10^6\ \mathrm{s}^{-1}$ in the Gaussian system) and $\chi\simeq 500$ J/(K·s) (see Ref. 4), as well as the parameters already used above for cholesteric liquid crystals, we find that structures with $\lambda\simeq 1$ cm can be obtained by passing a current $j_c\simeq 200\ \mathrm{A/cm}^2$.

4. FORMATION OF STRUCTURES IN CLCS IN AN EXTERNAL ELECTRIC FIELD

Ordinarily, an external field E_0 does not lead to steady-state structures, i.e., it does not lead to a spatially periodic distribution of the deviation of T_1 from the average temperature T_0.[8] This is explained by the fact that the Joule heating time of the medium $t\simeq\rho C_p\delta T/(\sigma E_0^2)$, where δT is the temperature difference between the points studied, should be shorter than the buildup time of such structures (after they appear), i.e., shorter than ω^{-1}. Instabilities with aperiodic growth, for example, such as that studied in Sec. 3, formally always satisfy this condition. The instability studied in Secs. 1–2, however, build up in an oscillatory manner, and for them the satisfaction of the condition $\tau<\omega^{-1}$ is not obvious. For this reason, we shall examine the effect of the temperature dependence of the pitch of the helix on the state of the CLC taking account the dielectric (the tensor ε_{ik}) and conductivity (the tensor σ_{ik}) properties. Such a model corresponds better to real cholesterics, which are, as a rule, liquid semiconductors.[4]

Thus, let us consider a CLC in an external electric field E_0. It is obvoius qualitatively that the main reason for the appearance of temperature fluctuations under isothermal equilibrium conditions, just as Sec. 3, is a change in the pitch of the helix. When the dimensions change, the conditions of motion of such a molecule change so that a change in temperature $T_1 = q_1(dq/dT)^{-1}$ appears. As mentioned above repeatedly, the same change in the pitch also renders the tensor characteristics anisotropic. The coordinate dependence in the anisotropic part, which gives the coefficient in the direction perpendicular to the direction of the helices, is the same for all tensors (see Eq. (3)), but the degree of anisotropy $\Gamma_\varepsilon, \Gamma_\sigma$, and $\Gamma_\varkappa$ is different (the indices correspond to the coefficient whose anisotropy is given by the corresponding quantity).

The anisotropic part of the permittivity tensor determines the possible small deviations of the electric field $\mathbf{E}_1 = -\nabla\varphi$. Now, $\Delta\varphi$ can be found from Eq. (8) and then, using the heat transfer Eq. (19), the anisotropy can be taken into account as done in Sec. 3.

It is found that if the external field $\mathbf{E}_0$ is directed perpendicular to a layer (along the z axis), then such a field does not influence the heat flux. However, if $\mathbf{E}_0$ is directed along a layer (along the y axis, like the current $\mathbf{j}_0$ in Sec. 3), then the heat flux depends only on the conductivity and does not depend on the permittivity ε_{ik}, which confirms the model adopted above in the analysis of the excitation of instability by current flow. In this case, performing the same calculations as in Secs. 1 or 3, we find that the dimensionless number determining the excitation condition is

$$\mathcal{I} = \frac{\sigma E_0 \Gamma_\sigma}{4\chi q^3}\frac{dq}{dT}, \tag{22}$$

corresponding to the dimensionless number from the condition (20) with h replaced by q^{-1}.

To obtain a strict solution, the solution for the averaged nonlinear equations must be sought in the form of a Fourier series with $k_m = m\pi/(Lq)$, where L is the pitch of the helix of the molecules, determined earlier by the condition $Lq = \pi$, and $m = 1, 2, 3, \ldots$ are integers. Substituting this solution into the corresponding equation, multiplying by $\sin(k_n zq)$ (or $\cos(k_n zq)$) and integrating, we obtain an infinite system of equations for the coefficients c_m (or b_m). For $n = m$ we obtain the excitation condition. The corresponding equation of Sec. 3 becomes $\mathcal{I} + k^2 = 0$, identical to the excitation condition (20).

For $n \neq m$ we obtain the equation

$$c_m(k_m^2 + \mathcal{I}) + \sum_{m\neq n} c_n \mathcal{I} B_{mn} = 0, \tag{23}$$

where $B_{nm} \sim (k_m \pm k_n)^{-1}$ are decreasing numbers of order 1.

Therefore we obtain that in an external field structures are excited if

$$E_0 > E_c \simeq \left(B\frac{\chi T q^2}{\sigma|\Gamma_\sigma|}\left|\frac{d\ln T}{d\ln q}\right|\right)^{1/2}, \tag{24}$$

where B is simply one of the numbers B_{mn}. Now, it is easy to estimate from the heat transfer equation

$$\omega \geqslant t^{-1} = \frac{\sigma E_0^2}{\chi}\left[\frac{d\ln\sigma}{d\ln T} - \frac{d\ln\varepsilon}{d\ln T}\frac{(\mathbf{k}\cdot\mathbf{E}_0)^2}{k^2 E_0^2}\right] - \varkappa k^2. \tag{25}$$

Using the field determined by the relation (24), the dominant term in this formula will be the term containing $d\ln\sigma/d\ln T$.

We note that the condition $E_0 > E_c$ (Eq. (24)) is completely compatible with the well-known[4] condition that the pitch of the helix be independent of the electric field, which can be written as $E_0 < qh(G/(\varepsilon|\Gamma_\varepsilon|))^{1/2}$, where G is the twist modulus of the liquid crystal. Both conditions are compatible if

$$\frac{\sigma G q^2 h^4}{\chi\varepsilon T}\left|\frac{d\ln q}{d\ln T}\right| \gg 1. \tag{26}$$

Estimates with the parameters of the medium used above (typical value $G \simeq 10^6$ Pa) show that all conditions are satisfied for field structures with dimensions $\lambda \simeq h \simeq 1$ cm for $E_0 > 10^5$ V/m.

I thank I. V. Ioffe for fruitful discussions.

[1] E. I. Kats and V. V. Lebedev, *Dynamics of Liquid Crystals*, Nauka, Moscow (1988).
[2] E. D. Eĭdel'man, Zh. Éksp. Teor. Fiz. **103**, 1633 (1993) [J. Exp. Theor. Phys. **76**, 802 (1993)].
[3] M. Kastler, *Liquid Semiconductors*, Mir, Moscow (1980).
[4] W. de Jeu, *The Physical Properties of Liquid-Crystal Substances*, Mir, Moscow (1982).
[5] L. É. Gurevich and I. V. Ioffe, Zh. Éksp. Teor. Fiz. **61**, 1133 (1971) [Sov. Phys. JETP **34**, 1151 (1972)].
[6] E. D. Eĭdel'man, Fiz. Tverd. Tela (St. Petersburg) **37**, 162 (1995) [Phys. Solid State **37**, 86 (1995)].
[7] S. Chandrasekhar, *Hydrodynamic and Hydromagnetic Stability*, University Press, Oxford (1961).
[8] M. K. Bologa and A. B. Berkov, *Electroconvective Heat Transfer in Dispersed Systems*, Shtiinitsa, Kishinev (1989).

Translated by M. E. Alferieff

Effect of Li doping on the critical temperature and glass formation in the Bi–Sr–Ca–Cu–O system

M. P. Volkov, B. T. Melekh, V. I. Bakharev, N. F. Kartenko, N. V. Matykin, and Yu. N. Filin

A. F. Ioffe Physicotechnical Institute, Russian Academy of Sciences, 194021 St. Petersburg, Russia
(Submitted June 16, 1998)
Fiz. Tverd. Tela (St. Petersburg) **41**, 18–21 (January 1999)

A study has been made of the glass-forming ability, structure, and superconducting properties of $Bi_{2.2}Sr_{1.8}Ca_{1.05}Cu_{2.15}Li_xO_y$ and $Bi_{2.2}Sr_{1.8}Ca_{1.05}Cu_{2.15-x}Li_xO_y$ $(x=0;0.3;0.5;0.7)$. The compounds were melted by rf at $T=1300-1500\,^{\circ}C$. Rapid quenching produces glassy alloys whose glass-forming ability is the highest when lithium is substituted for copper. Glass annealing at 700–800 °C results in the formation of the HTSC phase 2212 with a critical temperature of up to 91 K. In lithium-doped samples the HTSC phase forms at lower temperatures and shorter anneals and it depends on the cooling rate following the anneal. The composition and properties of the 2212 phase depend nonmonotonically on the anneal time. The lattice parameter *C* of the 2212 phase increases with increasing lithium content. © *1999 American Institute of Physics.* [S1063-7834(99)00401-3]

1. Superconductivity in the Bi–Sr–Ca–Cu–O system is observed in the compositions $Bi_2Sr_2CuO_x$ (phase 2201, $T_c=10-20$ K), $Bi_2Sr_2CaCu_2O_x$ (phase 2212, $T_c=80-90$ K), and $Bi_2Sr_2Ca_2Cu_3O_x$ (phase 2223, $T_c=100-110$ K). Obtaining the 2223 phase with the highest critical temperature requires a complex and long annealing procedure and is very sensitive to even small deviations from stoichiometry and preparation conditions. The 2212 phase is less sensitive to deviations from stoichiometry and does not require long anneals, but its critical temperature is close to the liquid-nitrogen boiling point, which may become an obstacle to the use of this phase in applications. Therefore raising the T_c of this phase by a few degrees Kelvin by appropriate doping appears desirable. Alkali metals are promising candidates for cation substitution in the 2212 phase, because the ionic radii in the Li–Cs series range from 0.73 to 1.81 Å, and those of the cations in the 2212 phase are (in Å): Bi – 1.17, Sr – 1.4, Ca – 1.26, and Cu – 0.87. Doping with alkali metals should change also the carrier concentration, because their valence state is +1.

2. A number of studies dealt with the effect of alkali-metal incorporation on the structure and superconducting properties of the 2212 phase. It was found that doping with alkali metals lowers the melting point and the formation temperature of the 2212 phase, the effect being the strongest in the case of lithium incorporation. The temperature of complete melting for undoped stoichiometric materials is 905 °C, and it decreases as part of the strontium in the starting composition is replaced by lithium, namely, to 864 °C for $Sr_{0.8}Li_{0.2}$ and to 737 °C for $Sr_{0.55}Li_{0.45}$, and when lithium substitutes for copper, it comes down to 860 °C for $Cu_{0.8}Li_{0.2}$ and to 745 °C for $Cu_{0.55}Li_{0.45}$.[1] Direct observation of a $Cu_{1.2}Li_{0.8}$ single-crystal sample yielded 720 and 870 °C for its temperatures of partial and complete melting, respectively.[2] The anneal temperature most favorable for the formation of the 2212 phase is 820–840 °C for undoped samples, for $Cu_{1.8}Li_{0.2}$ the optimum $T_{ann}=740\,^{\circ}C$, and for $Cu_{1.2}Li_{0.8}$, $T_{ann}=710-720\,^{\circ}C$ it can be added that single-phase samples of the latter composition form in as short an anneal time as 12 h.[3]

There is experimental evidence that lithium doped into the 2212 phase substitutes for copper in the lattice. A study was made of samples of two types, with lithium added to the stoichiometric 2212 composition and with lithium substituting for a part of strontium or copper in the starting composition.[4] It was found that single-phase samples form only under partial substitution of copper. In all other cases, except for the 2212, other copper-containing phases appeared, which argues for lithium occupying copper sites in the lattice. At the same time there are reports of single-phase samples prepared by partial substitution of lithium for strontium.[5] Some authors pointed out an increase of the lattice constant *C* with increasing lithium concentration,[4,6,7] while other studies[8,9] did not find this correlation. Grains in lithium-doped $Bi_2Sr_2CaCu_2O$ ceramics were reported to be larger in size.[9]

Doping with alkali metals, primarily with lithium, increases the critical temperature (T_c) of the 2212 phase compared to undoped samples. The highest critical temperature of this phase (91–92 K) is reached at an optimum carrier concentration. Undoped 2212 samples prepared by standard technology turn out usually to be overdoped, and in order to reach the highest critical temperature, the samples have to be annealed additionally in an inert atmosphere, which reduces the carrier concentration. Lithium doping results apparently in close to optimal carrier concentration and, accordingly, in higher T_c. For instance, in a study of starting (undoped) samples with $T_c(R=0)=91$ K the $T_c(R=0)$ was increased to 92–94 K by simultaneously substituting lead for part of the bismuth and alkali-metal doping.[10] In another study,[4] by replacing copper in standard undoped 2212 ceramic with

$T_c(R=0)=76$ K by lithium (Cu:Li=1.45:0.7, or 0.8) one succeeded in obtaining a single-phase 2212 sample with $T_c=91$ K. It was found that an increase in the content of lithium being substituted for strontium resulted in an increase of the critical temperature $T_c(R=0)$ from 69 K for an undoped sample to 94 K for $x=0.6$ in $Sr_{2-x}Li_x$.[5] Single crystals of the 2212 phase with the copper partially replaced by lithium had a transition temperature of 93 K for $Cu_{1.8}Li_{0.2}$ and 92 K for $Cu_{1.9}Li_{0.1}$.[11] A study of the 2212+Li single crystals yielded $T_c(R=0)=89$ K for 1.4%Li, 92 K for 3%Li, and 93 K for 13%Li.[12] Thus despite some discrepancy in measurements one may conclude that incorporation of lithium or substitution of lithium for cations in the 2212 phase results in a rise of the critical temperature.

3. The $Bi_{2.2}Sr_{1.8}Ca_{1.05}Cu_{2.15}Li_xO_y$ and $Bi_{2.2}Sr_{1.8}Ca_{1.05}Cu_{2.15-x}Li_xO_y$ ($x=0;0.3;0.5;0.7$) compounds studied in this work were prepared by annealing their amorphous parents. Annealing from the amorphous phase has certain advantages, namely, the metallic components are distributed uniformly throughout the sample and the phase formation reactions proceed faster so that this method does not require such prolonged anneals as in solid-state synthesis. The melts were produced by cold-crucible rf melting.[13,14] OSCh-grade Bi_2O_3, CuO, $SrCO_3$, $CaCO_3$, and Li_2CO_3 were used as starting compounds. The $T=1300-1500\,^\circ$C melts were poured into massive wedge-, cone-, or disk-shaped molds, which resulted in different sample cooling rates. The glassy state was identified from the characteristic pitted fracture surface, the absence of any lines in diffraction patterns, the presence of characteristic temperatures (softening, crystallization) in DSC curves, and from the electrical resistivity of the samples. The glass-forming ability of the melts was estimated from the thickness of homogeneous glass (which did not contain crystalline inclusions).

The curves in Fig. 1 relating the thickness of the glasses obtained to composition permit a conclusion that the best glass-forming ability is observed in alloys where lithium was substituted for copper. The glass thickness increases with lithium concentration. For instance, glass samples up to 4 mm thick were obtained for the $x=0.7$ composition, which is substantially in excess of the available data for bismuth-containing HTSC systems, including the system[15] with BaO substituted for CaO. The glasses thus prepared were annealed at 700–800 °C. The change in sample weight due to oxygen being absorbed in the course of annealing is the larger, the higher is the lithium content and the longer is the anneal time.

A study was made of the temperature dependence of the resistivity of annealed samples by the standard four-probe method. The contacts were attached to samples with a paste based on finely dispersed silver. The superconducting phase in lithium-doped samples forms after a comparatively short anneal in a process depending on the rate of the subsequent cooling. The superconducting properties of the samples thus obtained likewise depend strongly on the rate of cooling after the anneal. This is seen from Fig. 2 for samples annealed at $T=700\,^\circ$C for seven h, but with different cooling rates, namely, the samples cooled slowly together with the furnace exhibit a higher resistivity, semiconducting character of its temperature dependence, and a lower critical temperature, whereas those quenched rapidly by taking them out of the furnace and letting them cool in air are characterized by lower resistivity, metallic conduction, and higher critical temperatures.

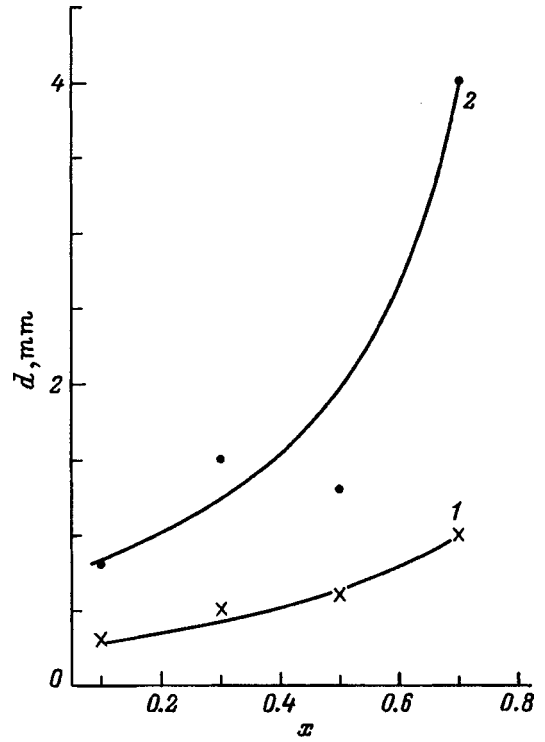

FIG. 1. Thickness d of prepared glasses *vs* lithium concentration x in the alloys. *1* — $Bi_{2.2}Sr_{1.8}Ca_{1.05}Cu_{2.15-x}Li_xO_y$, *2* — $Bi_{2.2}Sr_{1.8}Ca_{1.05}Cu_{2.15}Li_xO_y$.

The content and properties of the 2212 superconducting phase depend nonmonotonically on the anneal time, which is

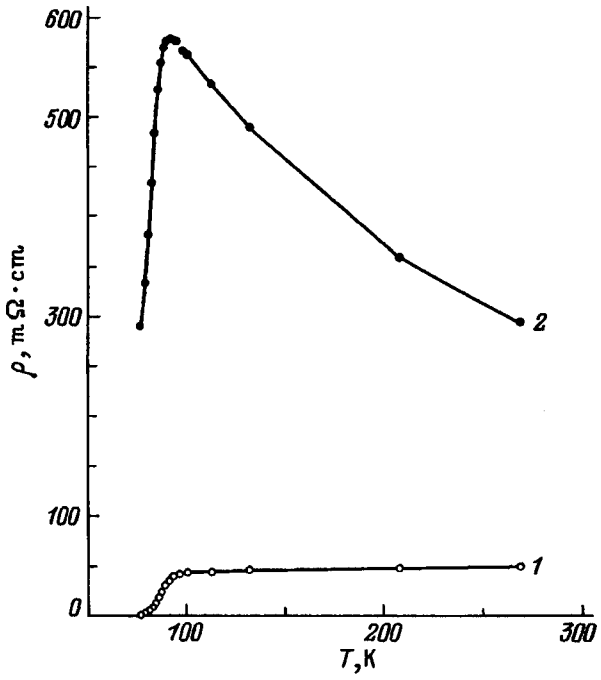

FIG. 2. Temperature dependence of the resistivity of samples annealed at 700 °C for seven h. Cooling: *1* — slow, *2* — fast.

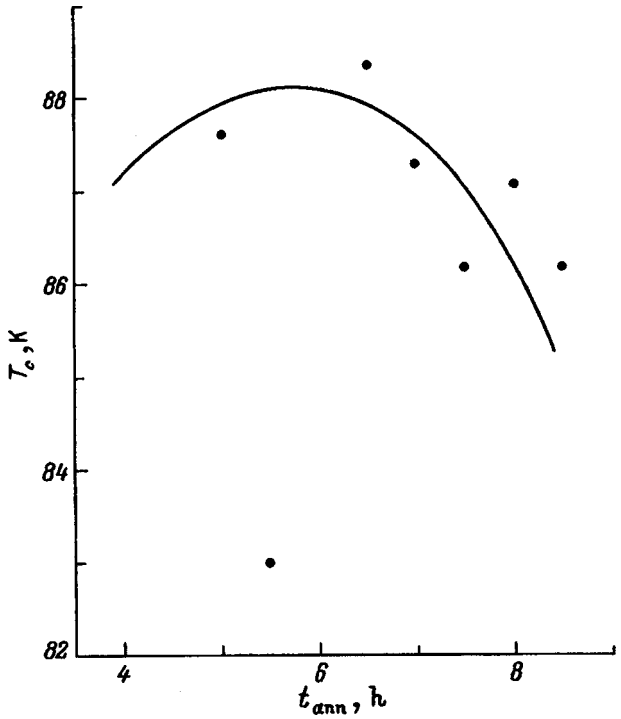

FIG. 3. Critical temperature of the 2212 phase in samples with lithium content $x=0.7$ *vs* anneal time at 700 °C.

shown in Fig. 3 for the critical temperature T_c. X-ray diffraction showed the quenched samples to be completely amorphous, without any crystalline inclusions. After five h of annealing, the samples contain several crystalline phases, viz. 50% 2212 phase, up to 10% 2201 phase, and up to 40% nonsuperconducting phases, in particular, CuO, $SrCO_3$, and an unidentified Li–Ca–Bi phase. Increasing the anneal duration to 6–6.5 h improves the quality of the 2212 phase, and its content rises to 60%. As the anneal time increases still more, the content of the 2212 phase starts to decrease, and the Cu_2SrO_3 phase appears.

4. The results of our study can be summed up as follows.

(i) Incorporation of lithium in a Bi-based HTSC lowers the formation temperature of the superconducting 2212 phase and reduces noticeably the anneal time in the case of an amorphous parent as well. This may be due to the lithium-induced decrease of the temperature of partial melting of this material. Note that a low-melting-point eutectic with $T_{melt}=690\,°C$ forms in the $Bi_2O_3-Li_2O$;

(ii) The critical temperature of the samples is close to the maximum value observed in the 2212 phase at an optimum carrier concentration. The samples obtained by standard ceramic technology are usually overdoped. To bring the carrier concentration to an optimum, they have to be annealed for a long time in an oxygen-free ambient. The carrier concentration in lithium-containing samples is apparently close to the optimum, which is supported by the influence of the rate of cooling from the anneal temperature on the critical temperature. If a sample has an optimum carrier concentration, its fast cooling should result in a high critical temperature, while slow cooling will favor saturation by oxygen, an increase of carrier concentration and, hence, a decrease of the critical temperature and a growth of normal resistivity. This is exactly what is observed experimentally (Fig. 2). Similar to Ref. 4, our samples exhibit an increase of the lattice constant C with lithium content. The C parameter of the 2212 phase in a $Cu_{1.45}Li_{0.7}$ sample with $T_c=87.5$ K is 30.83 Å, for $Cu_{1.7}Li_{0.3}$ with $T_c=86$ K it is 30.77 Å, and for a sample with $T_c=82$ K it is 30.7 Å.

(iii) The decrease of the critical temperature observed to occur for long anneal times (Fig. 3) could be due to sample oversaturation by oxygen and a deviation of the carrier concentration from the optimum value, but one would have seen then a growth of resistivity with decreasing temperature which would depend only weakly on the cooling rate. The samples studied by us, even those prepared under long annealing, followed a metallic behavior of resistivity with temperature (under rapid cooling from the anneal temperature). The chosen anneal temperature $T_{ann}=700\,°C$ was apparently below the optimum favoring the formation of the 2212 phase in the presence of lithium ($T_{ann}=710-720\,°C$, Ref. 3). It may be conjectured that at this anneal temperature formation of other crystalline phases (Li–Ca–Bi, Cu_2SrO_3) is thermodynamically preferable, and that this process occurs partially at the expense of destruction of the 2212 phase as well.

Support of the Russian Fund for Fundamental Research (Grant 96-02-17848) and of the Ministry of General and Professional Education (''Fundamental Research in Power Production and Electrical Engineering'') is gratefully acknowledged.

[1] J. Schwartz and S. Wu, Physica C **190**, 169 (1991).
[2] H. Hoshizaki, S. Kawabata, N. Kawahara, E. Enami, T. Shinohara, and T. Imura, J. Cryst. Growth **121**, 53 (1992).
[3] T. Kawai, T. Horiuchi, K. Mitsui, K. Ogura, S. Takagi, and S. Kawai, Physica C **161**, 561 (1989).
[4] T. Horiuchi, T. Kawai, K. Mitsui, K. Ogura, and S. Kawai, Physica C **168**, 309 (1990).
[5] C. Engkagul, K. Eaiprasertsak, J. Laksanaboonsong, K. Treechairusme, N. Chaichit, S. Leelaprute, N. Chiengpratoom, and I. M. Tang, Physica C **181**, 63 (1991).
[6] N. A. Flescher, J. Manassen, P. Coppens, P. Lee, Y. Gao, and S. G. Greenbaum, Physica C **190**, 367 (1991).
[7] S. X. Dou, H. K. Liu, W. M. Wu, W. X. Wang, C. C. Sorrell, R. Winn, and N. Savvides, Physica C **172**, 295 (1990).
[8] A. Britton and B. McBreen, Czech. J. Phys. **46**, 1495 (1996).
[9] S. Moehlecke, C. H. Westphal, M. S. Torikachvili, J. A. Davis, and I. C. L. Torriani, Physica C **211**, 113 (1993).
[10] I. B. Bobylev, V. N. Morycheva, M. G. Lyubimov, B. P. Romanov, F. B. Nasyrov, and L. V. Zherdeva, Sverkhprovodimost' (KIAE) **5**, 2056 (1992).
[11] T. Horiuchi, K. Kitahama, T. Kawai, S. Hontsu, K. Ogura, I. Shigaki, and Y. Kawate, Physica C **185-189**, 629 (1991).
[12] T. Horiuchi, K. Kitahama, and T. Kawai, Physica C **221**, 143 (1994).
[13] B. T. Melekh, M. P. Volkov, and N. F. Kartenko, in *Abstracts II International Conference HTSC Materials Science* (Khar'kov, 1995), p. 103.
[14] B. T. Melekh, A. A. Andreev, N. F. Kartenko, A. B. Pevtsov, V. A. Trepakov, and Yu. N. Filin, Izv. Akad. Nauk SSSR, Neorg. Mater. **18**, 1620 (1982).
[15] Yu. N. Filin, B. T. Melekh, and N. F. Kartenko, in *Abstracts III All-Union Conference HTSC* (Khar'kov, 1991), Vol. III, p.116.

Translated by G. Skrebtsov

INSTRUCTIONS TO AUTHORS

Fiz. Tverd. Tela (St. Petersburg)

[S1063-7834(99)03501-7]

The Editor of the journal ''Physics of the Solid State'' requests that authors who submit articles for publication follow the rules listed below.

Articles prepared without regard for these rules will not be accepted for consideration by the Editor. Articles with unimportant deviations from the rules will be sent back to the authors for revision; the submission dates of such articles will include the corresponding date of receipt of the corrected manuscript.

1. Articles that are the result of work carried out at institutions should be submitted by the corresponding institutions.

2. This journal prints both original articles and assigned reviews on various topics in solid-state physics. Two copies of the article must be sent for editing, typed using 12 or 14 point font sizes, double-spaced on one sided of the page. Margins should be no less than 4 cm from the left-hand edge. Handwritten inserts are not permitted. All pages must be numbered. The e-mail address (if there is one) should stand to the left and above the title. The article title and the author's names should be followed by the full name of the institution submitting the work and its location (mailing code, city, country). The abstract should come immediately before the text of the article, and should not simply repeat either the introduction or the conclusion of the latter. When the article is prepared on a computer, the setup parameters (line spacing, font size, etc.) should be chosen such that the article looks like a typewritten manuscript.

3. The article should be as brief as possible consistent with clarity of presentation. Intermediate expressions or calculations should not be included in the article. Authors should avoid repeating data tables, plots, and figure captions in the text of the article, and also presenting numerical results in the form of tables and plots at the same time. Articles can be divided up in two different ways: a) Sections with no subtitles should be labeled with the numbers 1,2,3,..., starting with the beginning of the article; b) When subtitles are used, numbers are omitted for the first and last sections (labeled ''Introduction'' and ''Conclusions'').

Designations, symbols, and units of measurement of physical quantities should conform to the International SI system of units (GOST 9867-61). Other systems of units that are commonly accepted in physics (Gaussian, etc.) are also permitted. **Dimensions of quantities must be transcribed using Latin letters.**

All abbreviations used by the authors must be explained in the text.

4. *Figures.* Authors must use a minimum number of figures, with a minimum of detail. Supplementary information should be placed in the captions.

All figures must have captions, which are listed on a separate page. These captions should contain no graphic elements (circles, crosses, etc.).

Black-and-white photographs should be on white glossy (*not* ''birch'') paper with a backing, without defects. Paper clips are not to be used. Photos are not to be glued on. Photos in the second copy should not have number or letter designations; only the illustrations should have them. On the back of photos write ''top,'' bottom'' with a soft pencil.

Notations and dimensions of quantities in figures should be given in Latin-letter transcription (*a*, *b*, *c*, cm, Oe, eV).

5. *Tables.* Tables should be printed on separate pages. Each table should have a header. Units of measurement for the quantities listed must be indicated. Photocopied tables are not acceptable.

6. *Equations and notations.* **All notations and labels must be given in Latin transcription.** Equations must be written large, with lots of space, and legibly. Special attention must be paid to subscripts and superscripts. Numbering of equations should be continuous throughout the article (not by section).

The first copy of the paper must include callouts of all equations and notations, according to common editorial practice:

—Greek letters are called out with a red line beneath.

—Vectors are called out with a boldface black line beneath (not an arrow on top!)

—Italic letters are encircled by a green line.

—Gothic letters by a yellow line;

—Lower-case and upper-case letters with the same shapes are indicated as follows: lower case letters have two lines above them, upper case two lines below. The lines should be made with a plain pencil. Sub- and superscripts are indicated by ''hands'' (drawn with a pencil). In order to distinguish the letter Σ from the sign of summation Σ, the latter should not be marked with a red line. The marks for the letters *e* and *l* should be somewhat exaggerated in order to avoid confusion.

In equations within the text of the article (not placed on a separate line), division should be indicated by a diagonal line, and exp should be used to denote the exponential function.

Avoid long and cumbersome mathematical expressions:

7. References. These belong on a separate page. The rules for preparing bibliographical entries are as follows:

—For books: initials and surnames of the authors, complete title of book, publisher, place of publication, year of printing, volume or issue. If a specific page is cited, the page number should appear after the year of publication thus: p. 54 (for ''see p. 54'').

—For journal articles: initials and surnames of **all** authors, title of journal, volume and issue number, first page of the article, and year of publication. For example:

1. E. Ya. Glushko, FTT **30**, *6*, 95 (1989).
2. V. J. Emery, Phys. Rev. B **14**, *3*, 2989 (1976).
3. L. D. Landau and E. M. Lifshits, Kvantovaya Mekhanika. Nauka, M. (1989), 768 c.

The numbering of references should strictly correspond to the order of their citation in the text.

8. A translation of the title of the article into English, together with English equivalents of special terms, is desirable.

The Editor requests that authors take particular care in preparing articles for publication, as it is not possible to send out author proofs at this time.

SEMICONDUCTORS AND INSULATORS

Utilization of the compound SnTe as a standard in tin-119 Mössbauer spectroscopy

D. Baltrunas*)

Institute of Physics, 2600 Vil'nyus, Lithuania
(Submitted May 18, 1998)
Fiz. Tverd. Tela (St. Petersburg) **41**, 22–23 (January 1999)

Experimental data from an investigation of the variation of isomeric shifts in the homogeneity region of tin telluride show that this compound does not meet the requirements for reference compounds. © *1999 American Institute of Physics.* [S1063-7834(99)00501-8]

It is well known that Mössbauer isomeric shifts are usually given relative to some compound (for example, the source). Such reference compounds for isomeric shifts in tin were proposed in Ref. 1. Certain requirements for these compounds are also listed there. One of the most important is that the reference compound should be easy to prepare in pure form and it should exist as a single phase under the experimental conditions. Moreover, the compound should not show any unresolved hyperfine interactions. Tin telluride is among the compounds listed. Although this compound is one of the tin compounds that has been investigated most by Mössbauer spectroscopy, the large variance in the experimental isomeric shifts is surprising: from 3.35 mm/s (Ref. 2) up to 3.54 mm/s (Ref. 3) with an error $\Delta\delta = \pm 0.03$ mm/s. The reasons for such a variance in δ have not been discussed in the literature.

Investigations of solid solutions based on tin telluride[4] raised the possibility that the isomeric shifts depend on the stoichiometric composition. It is known that tin monotelluride is characterized by a substantial deviation from stoichiometry (the maximum in the melting curves in the system Sn–Te corresponds to 50.4 at.% Te) and it has a wide (50.1–50.8 at.% Te at 550 °C) unilateral range of homogeneity.[5] The influence of the deviation from stoichiometry has been investigated in several works (see, for example, Ref. 3), but no changes were observed in the Mössbauer spectra. One possible reason could be that the accuracy of the measurements of isomeric shifts is inadequate.

The samples used in the investigations were prepared by direct melting together of highly pure elements in evacuated quartz ampuls using vibrational mixing. After holding at 1200 K, the samples were quenched in ice water and then annealed at 773 K for 300 h and quenched once again. The compositions of the experimental samples in Sn–Te system corresponded to a tellurium content of 49.9–51.5 at.%. The samples were synthesized with a 0.05 at.% Te step. The limits of the homogeneity range, according to microprobe analysis, were 50.1–50.9 at.%. The Mössbauer spectra were measured at room temperature with a NP–255 Mössbauer spectrometer. The compound $CaSnO_3$ served as the source. The thickness of the samples was 0.5 mg/cm^2 according to the ^{119}Sn isotope. All spectra consisted of single lines, whose width varied somewhat as a function of the composition. The experimental data on the isomeric shifts are presented in Fig. 1. One can see that the curve of δ versus the concentration Te contains a section where the isomeric shift decreases rectilinearly; this section coincides with the region homogeneity. The figure explains the reason for the variance in the experimental isomeric shifts observed in published works. The reasons for the variations of δ are explained in Ref. 6. Thus, the experimental data on the isomeric shifts show that tin telluride does not meet the requirements for reference compounds.

Tin telluride also does not meet another requirement — unresolved hyperfine interactions can also appear in it. It is known that a ferroelectric phase transition can occur in this compound as a function of temperature.[5] It has been investigated repeatedly by Mössbauer spectroscopy, especially near the temperature of liquid nitrogen, but the published data are very contradictory. Some authors (see, for example, Refs. 7 and 8) observed broadening of the Mössbauer line at the temperature of liquid nitrogen, while others rejected this.[3] Thus, there is no concensus concerning the presence of a quadrupole interaction (broadening of the spectral line) at liquid-nitrogen temperature. We have called attention to the fact that the phase transition temperature depends on the charge-carrier (hole) density.[5,9] According to these works, an increase in the hole density decreases the phase transition

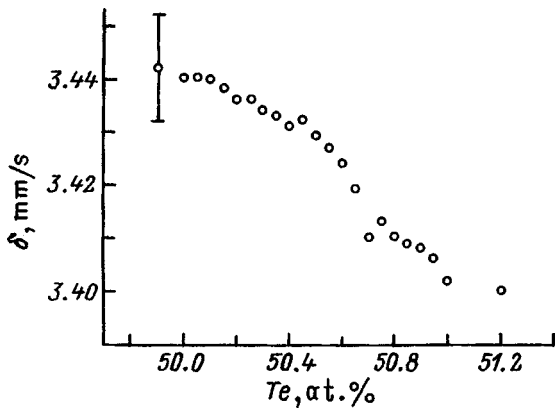

FIG. 1. Isomeric shift δ versus the Te content in the system Sn–Te.

TABLE I. Line width W_{exp} for SnTe versus the charge-carrier (hole) density p and temperature of the sample.

	W_{exp}, mm/s	
p, cm^{-3}	80 K	300 K
2.5×10^{20}	0.89±0.02	0.75±0.02
7.9×10^{20}	0.84±0.02	0.79±0.02

temperature. It can be inferred that the disagreement between the published results is due to the difference in the charge-carrier density in the experimental samples. To check this supposition, two tin telluride samples with hole densities $p_1=2.5\times10^{20}$ cm^{-3} and $p_2=7.9\times10^{20}$ cm^{-3} were investigated. According to the data of Ref. 9, the first sample should have a rhombohedral structure at liquid-nitrogen temperature.

It is known that the effective thickness of the absorber increases with decreasing temperature, broadening the spectal line.[10] To rule out this effect, the width of the line was extrapolated to zero absorber thickness. For comparison, the room-temperature spectra were also measured. The results obtained are presented in Table I. It should be noted that the parasitic vibrations arising in the cryostat when nitrogen boils can produce some line broadening. An estimate showed that this gives an error of not more than 0.03 mm/s.

One can see from Table I that the broadening of the Mössbauer line at liquid-nitrogen temperature is approximately 0.1 mm/s. This shows unequivocally that the lattice symmetry is lowered as a result of a ferroelectric phase transition and it shows the pesence of a quadrupole interaction.

In conclusion, I thank E. I. Rogacheva for providing the samples.

*)E-Mail: bdalius@ktl.mii.lt

[1] J. G. Stevens, Hyperfine Interact. **13**, 221 (1983).
[2] V. V. Chekin, A. P. Vinnikov, and O. P. Balkashin, Fiz. Tverd. Tela (Leningrad) **9**, 2992 (1967) [Sov. Phys. Solid State **9**, 2354 (1967)].
[3] V. A. Varnek, L. N. Mazalov, Yu. G. Sidorov, Yu. O. Kanter, and V. I. Mashchanov, Izv. Akad. Nauk SSSR, Neorg. Mater. **16**, 931 (1980).
[4] D. Baltrūnas, Phys. Status Solidi B **204**, 811 (1997).
[5] L. E. Shelimova, V. N. Tomashik, and V. I. Grytsiv, *Phase Diagrams in Semiconductor Materials Science: Systems Based on the Chalcogenides Si, Ge, Sn, and Pb*, Nauka, Moscow (1991), 368 pp.
[6] S. Motiejūnas, D. Baltrūnas, N. Gečiauskaite, and K. Makariūnas, Phys. Status Solidi B **154**, 341 (1989).
[7] B. I. Boltaks, S. I. Bondarevskiĭ, P. P. Seregin, and V. T. Shipatov, Fiz. Tverd. Tela (Leningrad) **11**, 1839 (1969) [Sov. Phys. Solid State **11**, 1483 (1969)].
[8] Sh. Sh. Bashkirov, I. A. Dobryakov, A. B. Liberman, and S. S. Tsarevskiĭ, Kristallografiya **30**, 1016 (1985) [Sov. Phys. Crystallogr. **30**, 592 (1985)].
[9] E. I. Slyn'ko, A. G. Khandozhko, S. D. Letyuchenko, and K. D. Tovstyuk, in *Abstracts of Reports at the 11th All-Union Conference on the Physics of Ferroelectrics*, Kiev, 1986, Vol. 1, p. 263.
[10] V. F. Masterov, F. S. Nasredinov, S. A. Nemov, and P. P. Seregin, Fiz. Tverd. Tela (St. Petersburg) **38**, 2973 (1996) [Phys. Solid State **38**, 1625 (1996)].

Translated by M. E. Alferieff

Thermal conductivity of gallium sulfide

M. A. Alzhdanov, M. D. Nadzhafzade, and Z. Yu. Seidov*)

Institute of Physics, Azerbaĭdzhan Academy of Sciences, 370143 Baku, Azerbaĭdzhan
(Submitted May 22, 1998)
Fiz. Tverd. Tela (St. Petersburg) **41**, 24–25 (January 1999)

The results of investigating of the thermal conducitivity of a GaS single crystal in directions parallel and perpendicular to the *c* axis in the temperature interval 5–300 K are reported. The investigations show that the degree of anisotropy of the thermal conductivity of GaS decreases with temperature. © *1999 American Institute of Physics.* [S1063-7834(99)00601-2]

The strong anisotropy of interatomic interactions in lamellar crystals gives rise to a variety of specific properties. The phonon spectrum of strongly anisotropic materials has been repeatedly investigated theoretically, but there is no unequivocal interpretation of the experimental data. The specific features of the phonon spectra of such crystals are reflected in the behavior of the heat capacity, thermal expansion, and thermal conductivity.

In the present work we investigated the thermal conductivity of a lamellar GaS crystal in the temperature interval 5–300 K. In Ref. 1, where the specific heat of gallium monosulfide is studied at low temperature, it is shown that flexural waves with a quadratic dispersion law play the main role in the behavior of $C_p(T)$ at low temperatures. A quasiflexural mode was later observed in the phonon spectrum of GaS by neutron diffraction.[2] Thus it is doubtless of scientific interest to study the influence of structural anisotropy on the thermal conductivity of this compound.

The thermal conductivity was measured by the steady-state method.[3] The temperature gradient was measured with copper–constantan and Cu–Cu+Fe thermocouples. The thermocouples were calibrated with respect to platinum and germanium resistance thermometers. The thermocouples were indium-soldered to the sample. Adiabatic screens, whose temperature was regulated automatically, were used to prevent any heat losses by lateral radiation. The error in the measurements of the thermal conductivity did not exceed 5%. Reference measurements of the thermal conductivity in crystal quartz cut parallel to the *c* axis agree with published data. Single-crystal GaS samples were cut in the form of a 0.10–0.15 cm^2 and 2–2.5 cm long parallelepiped.

Figure 1 shows the temperature dependences of the thermal conductivity in directions perpendicular ($\varkappa_\perp$) and parallel ($\varkappa_\parallel$) to the principal axis *c* of a hexagonal GaS crystal. The thermal conductivity of GaS above 100 K has been studied in Ref. 4. Our room-temperature data agree satisfactorily with the results obtained in Ref. 4. As one can see from the figure, the temperature dependences $\varkappa_\perp(T)$ and $\varkappa_\parallel(T)$ have a maximum at 24 and 20 K, respectively. We note that the electronic part can be neglected, i.e. in the experimental temperature interval heat is transferred by phonons. At room temperature the degree of thermal conductivity anisotropy reaches $\varkappa_\perp/\varkappa_\parallel \sim 9$. the degree of anisotropy decreases with temperature, and is approximately 3 at 20 K and ~ 1.7 at liquid-helium temperatures. At low temperatures (below the maximum in the region of boundary scattering) the temperature dependence of $\varkappa$ in gallium sulfide satisfies the power law $\varkappa_\perp \sim T^{2.4\pm0.1}$ and $\varkappa_\parallel \sim T^{2.1\pm0.1}$. In the same temperature range the temperature dependence of the heat capacity has the form given in Ref. 1 for GaS. Above the maximum the thermal conductivity of GaS can be expressed as $\varkappa_\perp \sim T^{-0.7}$ and $\varkappa_\parallel \sim T^{-1.1}$ in a wide temperature interval 60–300 K.

We note that the temperature variation of $\varkappa_\parallel$ is somewhat different in different samples. This is probably due to the difficulty of cutting out and orienting the samples in the [001] direction. The $\varkappa_\parallel$ data were obtained by averaging measurements for two samples.

It is known[5] that in lamellar crystals, including GaS, the acoustic phonons can be treated approximately as if they belong to three separate frequency branches $\omega_l \sim k, \omega_t \sim k$, and $\omega_c \sim k^2$. The phonons belonging to the *l* and *t* branches correspond to longitudinal and transverse in-plane atomic displacements. The *c* branch pertains to out-of-plane modes.

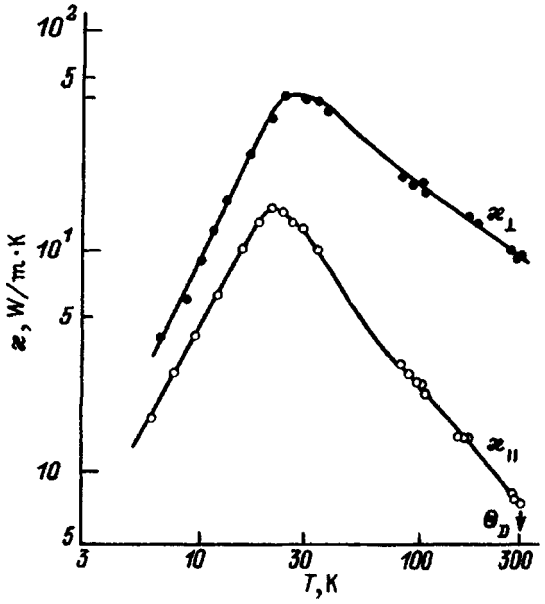

FIG. 1. Temperature dependence of the thermal conductivity of gallium sulfide parallel ($\varkappa_\parallel$) and perpendicular ($\varkappa_\perp$) to the *c* axis. The arrow marks the Debye temperature.

The difference between $\varkappa(T)$ and $C_p(T)$ at low temperatures (below 20 K) for GaS is probably due to the difference in the contributions of *c*, *l*, and *t* phonons to the thermal conductivity and heat capacity.

*)E-Mail: seidov@lan.ab.az

[1] K. K. Mamedov, M. A. Aldzhanov, I. G. Kerimova, and M. I. Mekhtiev, Fiz. Tverd. Tela (Leningrad) **19**(5), 1471 (1977) [Sov. Phys. Solid State **19**, 857 (1977)].
[2] B. M. Powell, S. Jaudl, J. L. Brebner, and J. Levy, J. Phys. C **10**, 3039 (1977).
[3] M. A. Aldzhanov, K. K. Mamedov, A. B. Abdullaev, and S. A. Aliev, Fiz. Tverd. Tela (Leningrad) **27**(1), 284 (1985) [Sov. Phys. Solid State **27**, 174 (1985)].
[4] G. D. Guseinov, A. I. Rasulov, E. M. Kerimov, and M. Z. Ismailov, Phys. Lett. **22**, 562 (1966).
[5] A. M. Kosevich, *The Physical Mechanics of Real Crystals*, Naukova Dumka, Kiev (1981), 327 pp.

Translated by M. E. Alferieff

Heat conductivity and the Lorentz number of the $Sm_{1-x}Gd_xS$ ''black'' phase

A. V. Golubkov, L. S. Parfen'eva, I. A. Smirnov

A. F. Ioffe Physicotechnical Institute, Russian Academy of Sciences, 194021 St. Petersburg, Russia

H. Misiorek, J. Mucha, and A. Jezowski

Institute for Low-Temperature and Structural Research, 53529 Wrocław, Poland
(Submitted May 28, 1998)
Fiz. Tverd. Tela (St. Petersburg) **41**, 26–29 (January 1999)

Measurement of the heat conductivity and electrical resistivity of two $Sm_{1-x}Gd_xS$ compositions with $x=0.1$ and 0.14 is reported within the 80–300 K interval. An analysis of experimental data on the electronic component of heat conductivity permits a conclusion that the *d* subband of ''heavy'' carriers in the conduction band of these materials lies above the *s* ''light''-carrier subband. © *1999 American Institute of Physics.* [S1063-7834(99)00701-7]

Intense investigation of the physical properties of the SmS–GdS solid-solution system started in 1972.[1] Since then, an enormous number of publications dealing with $Sm_{1-x}Gd_xS$ have appeared, but many aspects of the physical phenomena occurring in this system still remain unclear.

Strangely enough, there are still no studies of the heat conductivity $\varkappa$ of $Sm_{1-x}Gd_xS$, although this parameter is needed for thermodynamic calculations, while data on the electronic component of the heat conductivity ($\varkappa_e$) would provide information on position of the *d* and *s* subbands in the conduction band of $Sm_{1-x}Gd_xS$.[2–6] Literature is dominated presently by two directly opposed viewpoints concerning the latter.[5,7–11]

We are reporting here heat conductivity measurements made within the 80–300 K interval for two $Sm_{1-x}Gd_xS$ compositions ($x=0.1$ and 0.14) corresponding to the so-called ''black'' phase of this system.

Prior to discussing the results obtained, consider the main characteristics of the $Sm_{1-x}Gd_xS$ system and the possibilities suggested by an analysis of the behavior of the Lorentz number for compounds with a complex band structure.

1. $Sm_{1-x}Gd_xS$ undergoes an isostructural (NaCl-NaCl) first-order phase transition at $x=0.16$, from a strongly degenerate semiconductor (or bad metal) to the metal, where samarium ions are in the state of homogeneous mixed valence ($Sm^{+2.6}$).[12,13] The phase transition (occurring at $x=0.16$) changes strongly the lattice constant: $a_{x<0.16}\sim 5.85$ Å, and $a_{x>0.16}\sim 5.68$ Å.[14,15] Within the $x=0-0.16$ compositional interval, the samples are black (the ''black'' phase), and after the phase transition they acquire a yellowish tint (the ''golden'' phase) for $x>0.16$.

2. The conduction band of SmS, GdS, and the $Sm_{1-x}Gd_xS$ black phase is derived from the ''heavy,'' *d*, and ''light,'' *s*, subbands. Their mutual position (i.e. which of them lies lower or higher in energy) became a subject for debate in literature.[5,9,11]

3. Substances whose conduction (or valence) band is derived from subbands with heavy and light carriers coupled by interband interaction exhibit an unusual behavior of the Lorentz number L ($\varkappa_e=LT/\rho$, where ρ is the electrical resistivity, and T is the temperature).[1)] An analysis of the temperature dependence $L(T)$ permits a conclusion on the mutual position of the heavy and light subbands in the material under study.[2–6,10]

The purpose of the work was (i) To study the magnitude and temperature dependence of the heat conductivity for a number of $Sm_{1-x}Gd_xS$ black-phase compositions, and (ii) To refine the conduction-band structure of the $Sm_{1-x}Gd_xS$ black phase.

GdS and SmS were synthesized from elements.[16] The material obtained was used to prepare fused polycrystalline or single-crystal $Sm_{1-x}Gd_xS$ samples of a given composition. The preparation and melting of the samples were carried out in air-tight tantalum containers[17] in an induction furnace. The loss of material was reduced to a minimum due to reliable sealing of the containers in which the melting and annealing of the samples were performed.

We measured the lattice constant *a* at 300 K and the heat conductivity and electrical resistivity of $Sm_{1-x}Gd_xS$ (for $x=0.1$ and 0.14) within the 80–300 K temperature interval. X-ray diffraction measurements used instrument and Cu*a* DRON-2 radiation. The $\varkappa$ and ρ were measured on a setup similar to the one described in Ref. 18.

The results of the measurements are presented in Figs. 1–4. The values of *a* for the compositions with $x=0.1$ and 0.14 were found to coincide with literature data[15] (Fig. 1), which confirms that the melting of samples did not entail any loss of material.

Figure 2 presents experimental data on $\varkappa_{\text{tot}}$. For the studied compositions

$$\varkappa_{\text{tot}}=\varkappa_{\text{ph}}+\varkappa_e, \tag{1}$$

where $\varkappa_{\text{ph}}$ is the lattice component of the heat conductivity. The electrical resistivity $\rho(T)$ is shown graphically in Fig. 3. For both compositions, the $\rho(T)$ relation has a metallic character.

We used Eq. (1) to calculate $\varkappa_{\text{ph}}(T)$ under the assumption that $\varkappa_e$ obeys the Wiedemann-Franz law

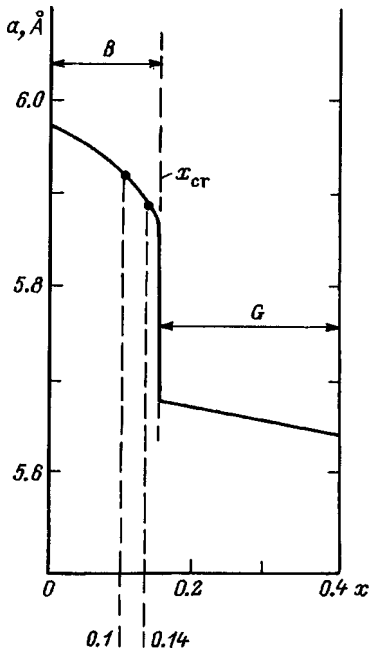

FIG. 1. Lattice constant of $Sm_{1-x}Gd_xS$ *vs* composition. Solid curve — after Ref. 15; points — this experiment for the $x=0.1$ and 0.14 compositions; *B* and *G* — regions of the black and golden phase, respectively; x_{cr} — the critical Gd concentration at which the phase transition occurs.

$$\varkappa_e = L\rho/T, \tag{2}$$

and the Lorentz number $L=L_0=2.45\times10^{-8}$ WΩ/K^2, which is valid for metals and strongly degenerate semiconductors under elastic carrier scattering.[4,6]

Figure 4 displays the lattice heat resistance $W_{ph}(T)=1/\varkappa_{ph}(T)$ calculated from Eqs. (1) and (2) for $Sm_{1-x}Gd_xS$ with $x=0.1$ (*1*) and 0.14 (*2*). By theory,[4,6] for $T\gtrsim\Theta/3$ (Θ is the Debye temperature)[2)]

$$W_{ph}=AT+W_{ph}. \tag{3}$$

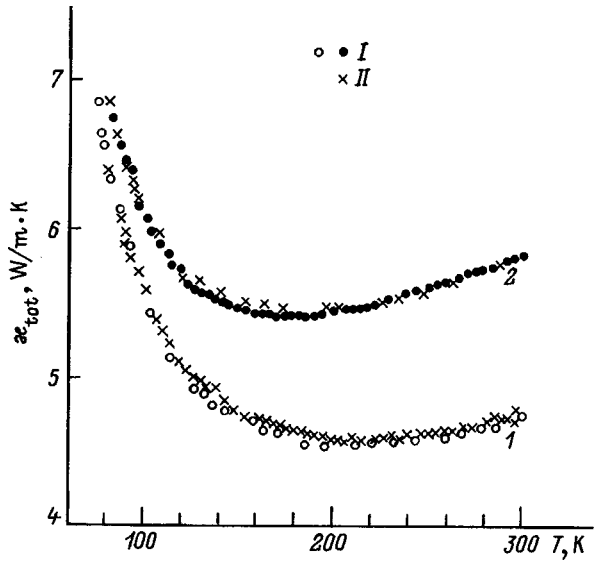

FIG. 2. Temperature dependence of the total heat conductivity $\varkappa_{tot}$ for $Sm_{1-x}Gd_xS$ samples with $x=0.1$ (*1*) and 0.14 (*2*). I — heating cycle, 80 to 300 K, II — cooling cycle, 300 to 80 K.

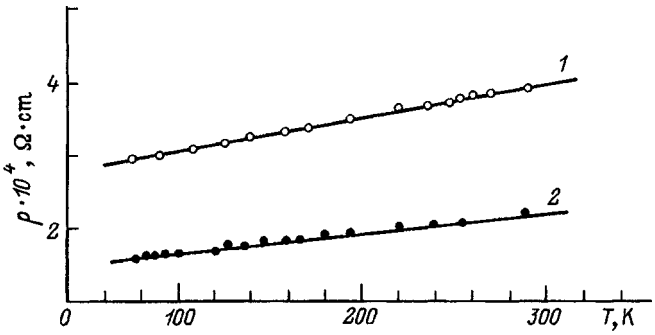

FIG. 3. ρ *vs* T plot for $Sm_{1-x}Gd_xS$ with $x=0.1$ (*1*) and 0.14 (*2*).

For pure samples W_{ph}^0, the residual heat resistance, is zero, and for defective (or doped) crystals, $W_{ph}^0\neq0$. The latter case applies directly to our samples.

It was found that, for $Sm_{1-x}Gd_xS$ with $x=0.1$ and 0.14, relation (3) holds only within the 160–300 K interval. For $T<160$ K, $W_{ph}(T)$ deviates noticeably from (3) toward smaller values. This effect is not seen in stoichiometric SmS samples and compositions within the SmS homogeneity region (Fig. 4, curves *3* and *4*).[5,10,20]

$W_{ph}(T)$ may deviate from a linear relation because a wrong assumption of $L(T)$ in Eq. (2) would affect $\varkappa_e(T)$ and, hence, $W_{ph}(T)$. In order for $W_{ph}(T)$ to remain linear down to 80 K, L must be larger than L_0 ($L>L_0$) within the 160–80 K interval.

We shall assume $W_{ph}(T)$ to obey Eq. (3) within the whole temperature region from 80 to 300 K for both compositions, $x=0.1$ and 0.14. Taking into account Eqs. (1) and (2), $L(T)$ will now take on the values shown in Fig. 5a. Under what conditions could L become larger than L_0? We made an attempt at explaining this effect in terms of interband interaction of heavy (d) and light (s) carriers in the subbands making up the conduction band in $Sm_{1-x}Gd_xS$.[2,5,6,10] Within the above model, L can be larger or smaller than L_0, depending on the energy positions of the Fermi level (E_F) and the d and s subbands.[2,5,10] In these conditions, a noticeable difference between L and L_0 is observed only when the heavy-carrier subband (within which E_F lies) is higher than the light-carrier one (see Fig. 5b). For the opposite position of the above subbands, $L\approx L_0$.[5,10]

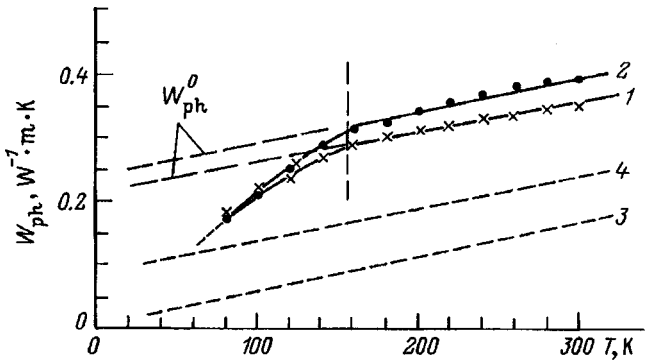

FIG. 4. Lattice heat resistance of $Sm_{1-x}Gd_xS$ *vs* temperature for $x=0.1$ (*1*) and 0.14 (*2*). Curves *3* and *4* are, respectively, plots of $W_{ph}(T)$ for SmS and $Sm_{1.015}S$ (data from Refs. 10 and 20). W_{ph}^0 — residual lattice heat resistance.

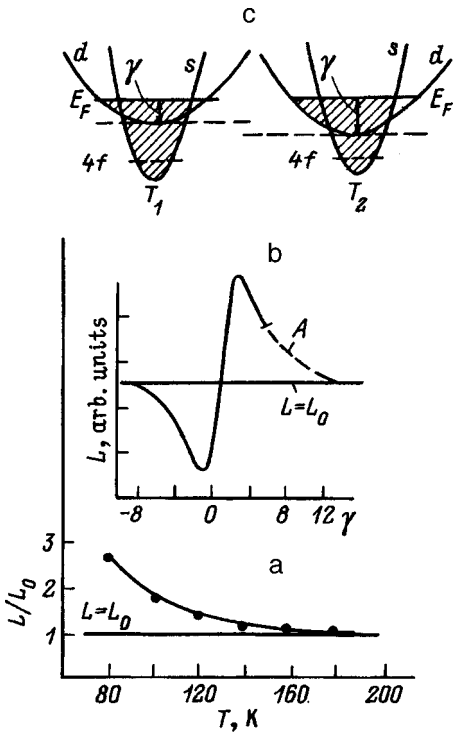

FIG. 5. (a) Experimental $L/L_0\,(T)$ ratio for $Sm_{0.86}Gd_{0.14}S$; (b) $L\,(\gamma)$ relation drawn schematically for the case of a complex band structure in the presence of interband interaction between heavy and light carriers[2,10] under the condition that the Fermi level E_F lies in the heavy-carrier subband, and that the latter is above the light-carrier subband; $\gamma=(E_F-\varepsilon_0)/kT$; ε_0 is the position of the heavy-carrier band bottom; (c) band structures for the $Sm_{1-x}Gd_xS$ black phase drawn schematically for different temperatures ($T_2>T_1$).

Our experimental relation $L\,(T)$ shown in Fig. 5a is in agreement with the model displayed in Fig. 5c and can relate to region *A* in Fig. 5b. As shown in Refs. 5 and 21, the *d* subband in SmS lowers in energy with increasing temperature at a rate $\sim 1\times 10^{-4}$ eV/K. Such a behavior could be expected for the *d* subband in $Sm_{1-x}Gd_xS$.

Thus we have estimated the magnitude of $\varkappa$ for a number of $Sm_{1-x}Gd_xS$ black-phase compositions and shown that the heavy *d* subband located in the conduction band of the $Sm_{1-x}Gd_xS$ black phase lies above the light *s* subband in energy.

The authors express their gratitude to N. F. Kartenko for x-ray diffraction measurements of the samples.

The work was carried out within bilateral agreements of the Russian Academy of Sciences, on the one side, and of the Polish Academy of Sciences and DFG.

[1)]We shall consider this effect in more detail when discussing the obtained experimental results.
[2)]for SmS and GdS, $\Theta/3\sim 80$ K. Ref. 19.

[1] A. Jayaraman, E. Bucher, P. D. Dernier, and L. D. Longinotti, Phys. Rev. Lett. **31**, 700 (1973).
[2] N. V. Kolomoets, Fiz. Tverd. Tela (Leningrad) **8**, 997 (1966) [Sov. Phys. Solid State **8**, 799 (1966)].
[3] N. A. Erasova and V. I. Kaĭdanov, Fiz. Tekh. Poluprovodn. **2**, 34 (1968) [Sov. Phys. Semicond. **2**, 26 (1968)].
[4] V. S. Oskotskiĭ and I. A. Smirnov, *Defects in Crystals and Heat Conductivity* [In Russian] (Nauka, Leningrad, 1972), 159 pp.
[5] E. V. Shadrichev, L. S. Parfen'eva, V. I. Tamarchenko, O. S. Gryaznov, V. V. Sergeeva, and I. A. Smirnov, Fiz. Tverd. Tela (Leningrad) **18**, 2380 (1976) [Sov. Phys. Solid State **18**, 1388 (1976)].
[6] I. A. Smirnov and V. I. Tamarchenko, *Electronic Conduction in Metals and Semiconductors* [In Russian] (Nauka, Leningrad, 1977), 151 pp.
[7] V. V. Kaminskiĭ, A. A. Vinogradov, V. A. Kapustin, and I. A. Smirnov, Fiz. Tverd. Tela (Leningrad) **20**, 2721 (1978) [Sov. Phys. Solid State **20**, 1571 (1978)].
[8] V. V. Kaminskiĭ and A. V. Golubkov, Fiz. Tverd. Tela (Leningrad) **21**, 2805 (1979) [Sov. Phys. Solid State **21**, 1615 (1979)].
[9] I. A. Smirnov and V. S. Oskotskiĭ, Usp. Fiz. Nauk **124**, 241 (1978) [Sov. Phys. Usp. **124**, 117 (1978)].
[10] V. S. Oskotskiĭ and I. A. Smirnov, in *Rare-Earth-Based Semiconductors* [in Russian], edited by V. P. Zhuze and I. A. Smirnov (Nauka, Leningrad, 1977), 108 pp.
[11] O. V. Farberovich, Fiz. Tverd. Tela (Leningrad) **21**, 3434 (1979) [Sov. Phys. Solid State **21**, 1982 (1979)].
[12] V. A. Shaburov, A. I. Egorov, G. A. Krutov, A. S. Ryl'nikov, A. E. Sovestnov, and O. I. Sumbaev, Zh. Éksp. Teor. Fiz. **68**, 326 (1975) [Sov. Phys. JETP **41**, 158 (1975)].
[13] A. I. Egorov, E. V. Petrovich, Yu. P. Smirnov, A. E. Sovestnov, O. I. Sumbaev, and V. A. Shaburov, Izv. Akad. Nauk SSSR, Ser. Fiz **40**, 395 (1976).
[14] A. Jayaraman, P. Dernier, and L. D. Longinotti, Phys. Rev. B **11**, 2783 (1975).
[15] M. Onashi, T. Kaneko, H. Yoshida, and S. Abe, Physica B **86–88**, 224 (1977).
[16] A. V. Golubkov, T. B. Zhukova, and V. M. Sergeeva, Izv. Akad. Nauk SSSR, Neorg. Mater. **2**, No. 11, 77 (1966).
[17] A. V. Golubkov and V. M. Sergeeva, Preprint, Institute of Metal Physics, USC AS SSSR (1977).
[18] A. Jezowski, J. Mucha, and G. Pompe, J. Phys. D **20**, 1500 (1987).
[19] A. V. Golubkov, E. V. Goncharova, V. P. Zhuze, G. M. Loginov, V. M. Sergeeva, and I. A. Smirnov, *Physical Properties of Rare-Earth Chalcogenides* [in Russian] (Nauka, Leningrad, 1973), 304 pp.
[20] V. P. Zhuze, E. V. Goncharova, N. F. Kartenko, T. I. Komarova, L. S. Parfeneva, V. M. Sergeeva, and I. A. Smirnov, Phys. Status Solidi A **18**, 63 (1973).
[21] B. Batlogg, J. Schoenes, and P. Wachter, Phys. Lett. A **49**, 13 (1974).

Translated by G. Skrebtsov

Structural perfection of GaN epitaxial layers according to x-ray diffraction measurements

R. N. Kyutt, V. V. Ratnikov, G. N. Mosina, and M. P. Shcheglov

A. F. Ioffe Physicotechnical Institute, Russian Academy of Sciences, 194021 St. Petersburg, Russia
(Submitted June 5, 1998)
Fiz. Tverd. Tela (St. Petersburg) **41**, 30–37 (January 1999)

Two- and three-crystal diffractometric study of the structural perfection of GaN epitaxial films grown on sapphire, GaAs, and SiC substrates is reported. The diffraction intensity distributions around the reciprocal-lattice points are shown to be extended in the direction parallel to the surface, which is connected with the anisotropy of the local strain fields in the layers. A comprehensive analysis is made of the broadening for several reflection orders measured in three geometries, namely, Bragg, symmetric Laue, and grazing-angle diffraction. The five independent components of the microdistorsion tensor δe_{ij}, as well as the average coherent-scattering lengths in two directions, τ_z and τ_x, have been obtained. It is shown that for most samples the components responsible for reflection broadening along the surface are noticeably larger, i.e. $\delta e_{xx} > \delta e_{zz}$, and $\delta e_{zx} > \delta e_{xz}$, as well as $\tau_z > \tau_x$. All tensor components are related to a specific dislocation type. Electron microscopy of the samples revealed a high density of pure edge and pure screw dislocations extending normal to the interface, and which provide a dominant contribution to e_{xx} and e_{zx}, respectively. © *1999 American Institute of Physics.* [S1063-7834(99)00801-1]

Structural studies of GaN epitaxial layers by x-ray diffraction methods have been the subject of a large number of experimental works.[1–8] X-ray diffractometric studies deal mostly with three problems, viz. (i) measurement of the lattice parameters of single crystals and films;[1,2] (ii) determination of the symmetry and orientation of GaN films grown on different substrates and of the part played by the substrate orientation;[3,4] and (iii) investigation of the structural perfection of films[5–8].

Some publications present a comprehensive analysis of the halfwidths of reflections in various orders, both symmetric and asymmetric, measured in Bragg geometry. It was shown that the broadening of Bragg reflections originates primarily from dislocation-induced distortions of the reflecting planes. Intensity contours extended along the normal to the diffraction vector were traced to misorientation of the mosaic blocks.[7] By contrast, another study[8] suggests that small lateral dimensions of coherent scattering regions provide a dominant contribution to the angular width of symmetric reflections. This conclusion accords with the presently accepted model of a columnar structure for GaN films. The structure of GaN layers is characterized by an anisotropy in microstrain fields, which becomes manifest in a large difference between the halfwidths of symmetric and asymmetric Bragg reflections.[6]

This work demonstrates the possibilities of using various x-ray diffraction geometries to obtain a better insight into the structural perfection of gallium nitride films grown on different substrates.

1. TECHNIQUES

The study focuses on construction and analysis of a two-dimensional x-ray diffraction intensity distribution around various reciprocal lattice points (RLP). In a general case, a film with lattice parameters different from those of the substrate is characterized by distortion tensor components e_{ij}, where one considers film atom displacements relative to substrate lattice sites, and both deformation and rotations can take place. The average values of the e_{ij} components determine the position of an RLP of the film with respect to the like substrate site

$$\Delta \mathbf{H}_i = -\sum \langle e_{ij} \rangle \mathbf{H}_j . \tag{1}$$

Besides macrostrains caused by uniformly distributed structural defects and impurities, the layer undergoes microdistortions originating from displacement fields around structural defects. They can be described by rms fluctuations $\langle \delta e_{ij} \rangle$ of the components of the average distortion. Microdistortions affect the shape of the RLPs by causing their extension and the broadening of the corresponding diffraction intensity contours. Note also that, in contrast to the average distortion components, here only the absolute values of microstrains have any significance. In this case we exclude the existence of macrogradients, i.e., of a nonuniform distribution of defects in the film, since the latter would bring about asymmetry in the diffraction peaks.

In a general case, the distortion tensor can be decomposed into a symmetric strain tensor ε and an antisymmetric rotation tensor ω. The diagonal components ε_{ii} relate to compression and tension, and the off-diagonal ones, ε_{ij}, to shear. Most studies of the broadening of diffraction peaks discriminate only between the diagonal and off-diagonal microdistortion terms, and assume the former to be due to microdilatation, and the latter, to microrotations. GaAs–Si was the first epitaxial system for which this was shown to be not

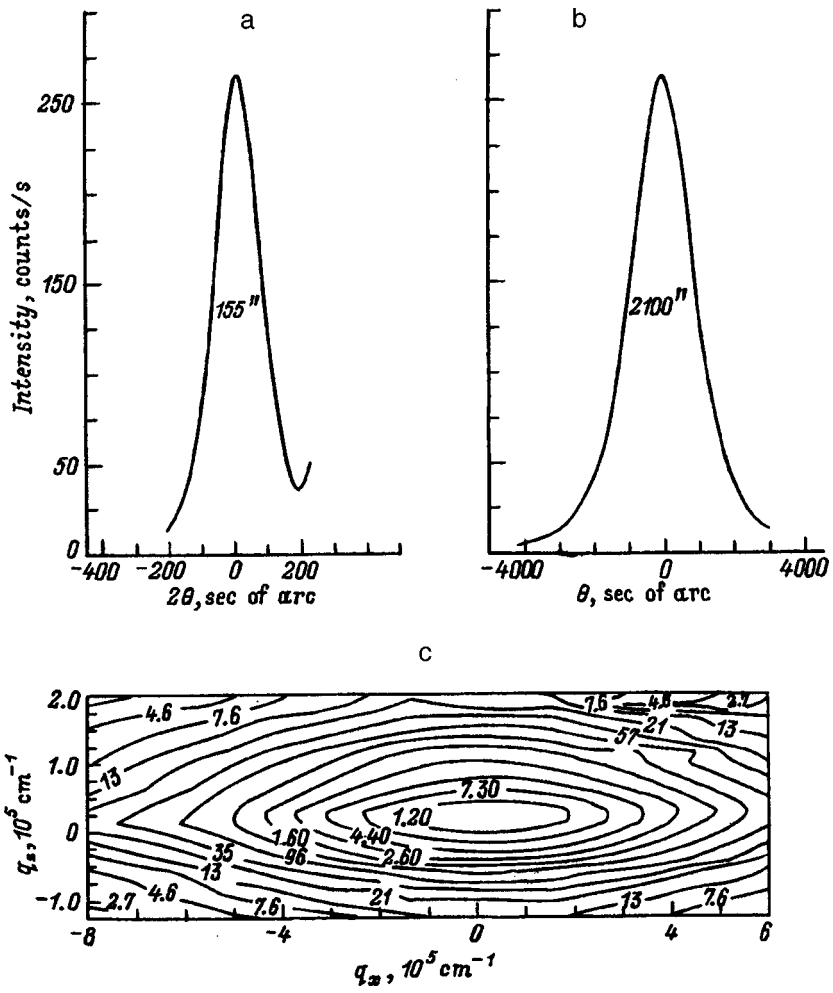

FIG. 1. Three-crystal (a) $\theta-2\theta$ and (b) θ scans and (c) intensity distribution around a reciprocal-lattice point for the (0002) symmetric Bragg reflection from a GaN film on *c*-plane sapphire (sample 2).

true, in fact, the experimental values of δe_{xz} and δe_{zx} did not coincide.

Strain is not the only factor accounting for diffraction peak broadening. The shape of an RLP is affected also by the limited size of the coherent-scattering regions. One of the problems in diffraction analysis lies in separation of these contributions. In x-ray diffraction measurements this can be done because the microdistortion components broaden only the reflections which have the corresponding component of vector **H**

$$\delta q_i = \langle \delta e_{ji} \rangle H_j , \tag{2}$$

and the limitation of a dimension in a particular direction affects all RLPs in the same direction

$$\delta q_i = 1/\tau_i . \tag{3}$$

The relation between coordinates in q space and angular broadening depends on the way in which the latter is measured (the scanning mode). For an RLP scanned in the direction of the diffraction vector ($\theta-2\theta$ scanning) $\delta w = \delta q_H/(k \cos\theta_B)$, and for perpendicular scanning (θ scan) $\delta w = \delta q_\perp / H$. Here q_H and $q_\perp$ are the projections of vector **q** which are parallel and perpendicular to the diffraction vector **H**, respectively. Thus in order to separate the contributions due to microdistortion and size effect one can use the different dependence of broadening on the Bragg angle.[5,9,10]

Because the (0001) basal plane is isotropic, the distortion tensor can be described by five independent components. Thus in a general case we have to define seven structural parameters, namely, five components of microdistortion and two, of grain dimensions. A diffractometer set-up with an analyzer (a narrow slit in front of the counter in the two-crystal arrangement or the third crystal in the three- crystal one) permits obtaining two RLP scans for one chosen reflection, perpendicular to the diffraction vector by θ scanning and parallel to **H** by $\theta-2\theta$ scanning. Thus one actually measures two halfwidths of these cross sections, i.e. two independent quantities for determining the parameters of interest.

To obtain the distortion-tensor components, one has to measure several x-ray reflections with differently oriented reciprocal-lattice vectors. Symmetric reflections, for which vector **H** is directed along one of the x,y,z axes, are an optimum. In this case, as can be seen from Eq. (1), the e_{ij} components are found directly. In the symmetric Bragg geometry, the diffraction vector is aligned with the surface normal, and one measures the projections of vector ΔH on the z and x (or y) axes, where z is oriented along the normal, and x (y) is parallel to the film plane. In symmetric Laue diffraction, **H** is along x, and one measures ΔH_x and ΔH_z. In coplanar diffraction geometry (with the surface normal and

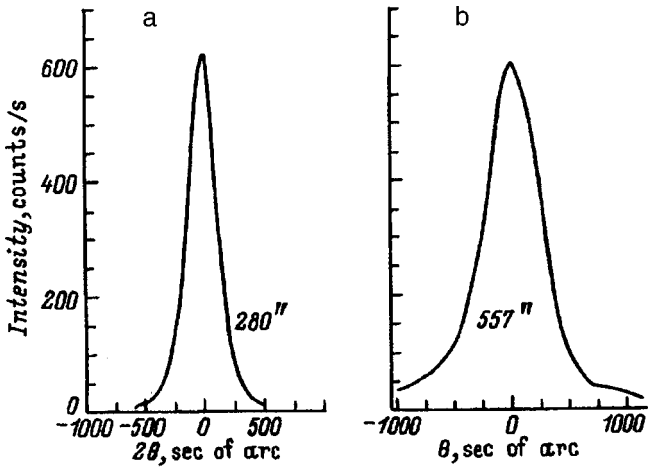

FIG. 2. Three-crystal (a) $\theta-2\theta$ and (b) θ scans of the $11\bar{2}0$ Laue reflection from sample 2 [GaN/(0001) sapphire].

diffraction vector lying in the same scattering plane) one cannot measure the e_{xy} and e_{yx} components (the so-called φ and χ scans used in many studies provide much lower resolution than measurements performed in the scattering plane). The missing quantities can be found using grazing noncoplanar diffraction geometry with the diffraction vector along x or y, and the scattering plane almost parallel to the surface.[11]

In this work, a three-crystal diffractometer was used in θ and $\theta-2\theta$ scans for the following reflections from GaN films: symmetric Bragg reflections 0002 and 0004, symmetric Laue reflections 1120, 2240, 1010, and 2020, and 1120 in grazing geometry.

Besides, two-crystal curves (with the detector window wide open) were measured for the 1124 asymmetric Bragg reflections ($\theta_B=50.2°$, $\varphi=39.2°$) at grazing incidence and reflection.

The diffraction analysis presented here was conducted for several GaN epitaxial films grown on different substrates, viz. sapphire (r and c planes), GaAs, and SiC. The layers were grown by different methods and varied in thickness from 0.5 to 6 μm.

2. RESULTS

We present below the results of diffraction measurements made on several typical GaN films. Figure 1 illustrates the intensity distribution around the RLP 0002 for a symmetric Bragg reflection and the corresponding scans along and perpendicular to the diffraction vector ($\theta-2\theta$ and θ scans) obtained on one of the samples studied. The intensity contours are extended in the direction perpendicular to **H**, a shape typical of relaxed epitaxial systems. The 1120 reflection curves obtained for the same sample in symmetric Laue geometry are shown in Fig. 2.

The FWHMs measured in two directions in different geometries are given in Table I for the first two reflection orders. As one crosses over to higher orders, the reflection width in the θ scans remains nearly constant, while for the $\theta-2\theta$ curves it increases proportionately to the tangent of the Bragg angle. It thus follows that the main contribution to reflection broadening comes from strains, as is the case also with most strongly mismatched epitaxial structures with μm-thick films. Note also that the halfwidths of the maxima obtained in θ and $\theta-2\theta$ scans in transmission mode are nearer to one another than in the Bragg case. As a result, the intensity distribution contours in Laue geometry approach closer the spherical shape than those obtained in the Bragg arrangement (Fig. 1).

A characteristic feature of these films was the smaller width of the diffraction curves obtained in asymmetric geometry at grazing incidence compared to those measured for the same reflection under grazing scattering (Fig. 3). This should be the case for the RLP extended in a direction parallel to the surface. In these conditions, if one uses a two-crystal arrangement with a widely open detector window and with the intensity integrated in a direction nearly parallel to the surface (at grazing incidence) or perpendicular to it (at grazing reflection), the observation band intersects the intensity distribution along the shorter section in the first case, and along the longer one, in the second, as shown in the insets to Fig. 3a and 3b. Because for the 1124 asymmetric reflection the diffraction vector has nearly equal components H_x and H_z (parallel and perpendicular to the surface, respectively), such a diffraction pattern can be accounted for by an anisotropy in either the microdistortion components or the coherent lengths, $\delta e_{zx} > \delta e_{xz}$, $\delta e_{xx} > \delta e_{zz}$, $\tau_x < \tau_z$.

The components were derived directly from the halfwidths of the symmetric reflections obtained in the Bragg and Laue geometries. The results are presented in Table II. We see that the dilatation component of the macrostrain δe_{xx}

TABLE I. FWHM of θ and $\theta-2\theta$ x-ray diffraction scans for symmetric Bragg and Laue reflections and of two-crystal curves for asymmetric Bragg and grazing-angle reflections (in arcsec).

Sample No.	Substrate	0020–Cu Ka, (Bragg)		1120-Mo Ka, (Laue)		1124-asym		1120-graz
		w_θ	$w_{\theta-2\theta}$	w_θ	$w_{\theta-2\theta}$	$\gamma_0<\gamma_h$	$\gamma_0>\gamma_h$	
1	*c*-sap	835	72	257	103	360	1460	1440
2	*c*-sap	1850	75	557	282	577	2550	–
3	*c*-sap	310	18	128	25	190	433	660
4	*c*-sap	1820	195			1360	2290	–
5	GaAs	1745	95	–	–	735	2120	2700
6	SiC	85	25			135	180	–

Note: The FWHM values for sample 4 grown on *r*-plane sapphire are for the symmetric $11\bar{2}0$ and asymmetric $30\bar{3}0$ Bragg reflections. For sample 3, the $10\bar{1}0$ reflection was measured in symmetric Laue geometry.

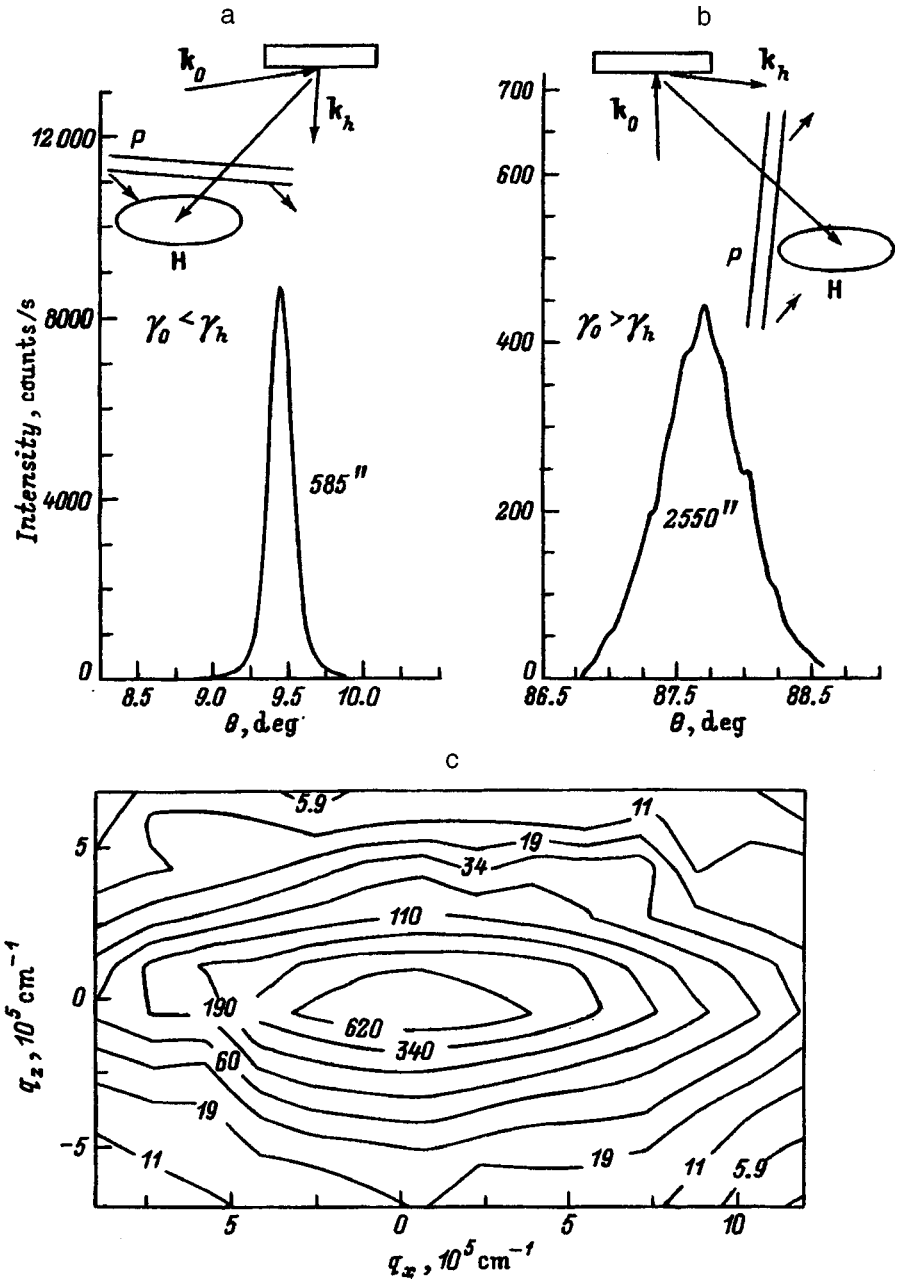

FIG. 3. Asymmetric Bragg reflections obtained (a) under grazing incidence, $11\bar{2}4$, and (b) under grazing reflection, $11\bar{2}\bar{4}$, and (c) intensity distribution around the $11\bar{2}4$ reciprocal-lattice point for a GaN/Al_2O_3 sample. The insets show the geometry of measurements and the relative positions of the observation band (P) and of the reciprocal-lattice point, the arrows identify the direction of P-band displacement under θ scanning.

is indeed substantially larger than δe_{zz}, i.e. that local variations in interplanar distance for the planes perpendicular to the surface are considerably larger than those for the planes parallel to the interface. We see also from Table II that the off-diagonal components are in the opposite relation, $\delta e_{zx} > \delta e_{xz}$, which means that the planes parallel to the surface undergo larger macromisorientations than those perpendicular to it.

TABLE II. Microdistortion components and dimensions of the coherent-scattering regions in GaN films.

Sample No.	δe_{zz}, 10^{-4}	δe_{zx}, 10^{-4}	δe_{xx}, 10^{-4}	δe_{xz} 10^{-4}	δe_{xy}, 10^{-4}	τ_z, nm	τ_x, nm
1	5.1	20.1	12.3	6.3	34.0	640–2300	430–3800
2	5.1	43	29	12.2	–	440–1100	190–1840
3	1.4	7.5	45	3.1	11.5	3440	1860
5	7.1	42.3	<50	<18	57	2170–35000	780–5000

In the grazing diffraction geometry, only reflection $11\bar{2}0$ was measured by the two-crystal arrangement. Because the dimensions of the coherent scattering regions contribute very little to broadening, the reflection width is determined by two parameters, namely, the dilatation, δe_{xx}, and orientation, δe_{xy}, components. Since the first of them was derived from Laue measurements, one determines the average micromisorientations of atomic planes around the c axes after subtraction of the corresponding contribution from the total FWHM.

As for the dimensions of the coherent-scattering regions, they contribute noticeably less to the total diffraction-peak width than the microdistortion components. Therefore their

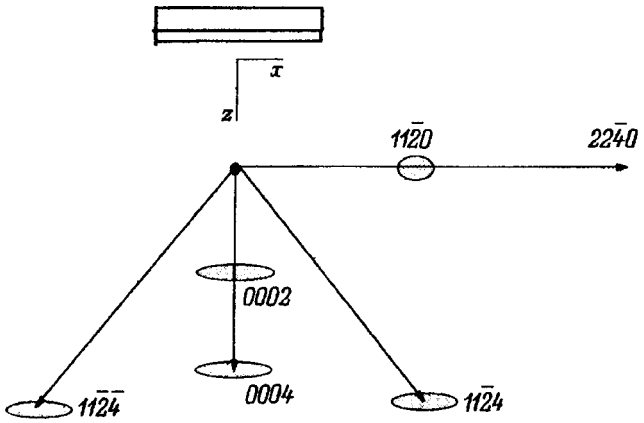

FIG. 4. Relative position and shape of the reciprocal-lattice points of the reflections used in the study of GaN films on (0001) sapphire.

determination from the angular dependence of the halfwidths on Bragg angle depends critically on the way in which one adds the broadenings due to different contributions, namely, linearly, $w=w_e+w_\tau$, or quadratically, $w^2=w_e^2+w_\tau^2$. The first approach, as is well known, corresponds to convolution of two Lorentzians, and the second, to that of two Gaussians. Therefore Table II presents the upper and lower limits on the values of τ_x and τ_z obtained, respectively, from the first and second relations. It should be pointed out that the latter appear more realistic, which is in accord with the fact that most diffraction calculations made for crystals with randomly distributed dislocations yield a Gaussian-shaped broadened diffraction line.

The RLP shape obtained from an analysis of the halfwidths of all the measured reflections is shown schematically in Fig. 4. The intensity distribution for all measured reflections is extended in the direction parallel to the surface. In symmetric Bragg geometry, this results from the large component due to misorientation of the reflecting planes parallel to the surface. If the coherent-scattering regions in a layer underwent only microrotations, all RLPs would be extended along the normal to the **H** vector, and this is what is observed in most experiments performed on other epitaxial systems[12,13] and is supported by theoretical calculations[14]. As for the shape observed with the GaN films studied by us, it can be accounted for only by assuming the presence of both dilatational and orientational components of microdistortion.

3. DISCUSSION OF RESULTS

As seen from Table II, microdistortion on both parallel and perpendicular atomic planes has anisotropic components in all samples, irrespective of the substrate material. This trend fails sometimes only for films grown on SiC, which exhibit a better structural perfection (and are characterized by the most narrow curves). This anisotropy in the microdistortion components can be explained within simple dislocation models. If one has pure edge dislocations, which are normal to the interface and whose Burgers vector is parallel to the latter, they should provide the major contribution to the δe_{xx} and δe_{xy} components while not affecting the z indexed ones. For pure screw dislocations, the displacements perpendicular to the interface are directed along z and vary as one moves away from the dislocation lines. Such dislocations give rise to shear strain with a δe_{zx} component and distort only the atomic planes parallel to the surface. The δe_{xz} component can be associated with the rotation of grains (blocks) produced by the dislocation network at the interface. (Obviously enough, these microrotations provide the same contribution to δe_{zx} as well, but, as seen from Table II, it is much smaller than the pure shear component.) The quantity δe_{zz} is the smallest of all deformation parameters responsible for the broadening of diffraction maxima. It can be dominated both by fluctuations in nonstoichiometry of the film composition and by dislocations parallel to the interface. Besides, any deviation from the ideal dislocation structure, i.e., a twist of the dislocation lines or their nucleation at points other than at the interface, will distort the above relation between the dislocations themselves and the microdistortion components.

The results obtained here are in qualitative agreement with the theory[15] of Krivoglaz developed for x-ray scattering by crystals having randomly distributed dislocations, by which the diffraction intensity distribution around RLPs in the case of a system of straight dislocations has the shape of disks oriented perpendicular to the dislocation line, and the width of the Gaussian distribution in the other two directions depends on the product $(\mathbf{H}\cdot\mathbf{b})$, where **b** is the Burgers vector. Based on this model, the extension of the diffraction distributions parallel to the surface observed by us argues unambiguously for the dislocation ensemble consisting predominantly of straight dislocations perpendicular to the interface.

As for a quantitative determination of dislocation density ρ from the x-ray diffraction-line broadening, the various theoretical models developed[15–17] for randomly distributed straight dislocations predict proportionality of the line width (in q units) to the quantity $Hb\sqrt{\rho}$, where H is the length of the reciprocal-lattice vector (for the given direction of **H**). The quantitative relation between the halfwidth and the density contains, however, two more factors, which are associated with the direction of the **H** and **b** vectors and the so-called external and internal radii taken as limits of integration over the dislocation ensemble. The diffraction vector of the reflections studied by us was parallel to the corresponding Burgers vector, which leaves an uncertainty with the second factor only; this uncertainty is aggravated by the fact that we deal here not with bulk crystals considered by Krivoglaz and Wilkens but rather with thin epitaxial layers. Therefore we can offer only a rough estimate of the dislocation density of $2\times10^8-10^9$ cm^{-2} for the best sample (No. 3), and $6\times10^9-3\times10^{10}$ cm^{-2} for the film on GaAs. This density is probably approximately the same for screw and edge dislocations, because the smaller magnitude of the corresponding microdistortion component in the second case (Table II) is due to the smaller length of the Burgers vector. The correlation in the dislocation distributions should also affect the estimate of ρ. The large magnitude of the δe_{xy} component (see Table II) may be connected, in particular, with possible ordering of like perpendicular edge dislocations.

A comparison of the samples in parameters of their defect structure shows that the observed features and, hence, the dislocation structures are the same for different samples, irrespective of the degree of structural perfection (the reflection halfwidths ranged over more than an order of magnitude). Most likely, this suggests that the presence of extended pure screw and pure edge dislocations is a characteristic feature of GaN films having hexagonal structure, irrespective of the growth technique and conditions chosen.

Although the grain sizes are determined from our experiments with not high enough accuracy, one can nevertheless maintain that the transverse dimensions of the coherent-scattering regions in all samples are smaller than the size along the normal. This speaks in favor of the columnar structure observed repeatedly in GaN films.

On the whole, electron microscope observations of both planar samples and cross sections coincide with the results of x-ray diffraction measurements. Figure 5a, 5b and 5c displays electron microscope images of a sample grown on GaAs. The plan view (Fig. 5a) shows grains 0.2–0.3 μm in size, and dislocations in between, normal to the surface, seen as dark and bright points. The type of the extended dislocations was derived from cross sectional images obtained from different reflections. One clearly sees screw dislocations with the Burgers vector $\mathbf{b}=[0001]$ (Fig. 5b) and pure screw with the Burgers vector of the type $\mathbf{b}=\frac{1}{3}[11\bar{2}0]$ (Fig. 5c). These dislocation types were observed to occur in GaN films by other researchers as well.[18,19] As already pointed out, it is this dislocation configuration that should be responsible for the large e_{zx} and e_{xx} components.

The microdistortion components presented in Table II were derived from symmetric reflections obtained in Laue geometry. Measurements in transmission geometry are possible naturally only for films grown on weakly absorbing substrates, such as sapphire, silicon, and silicon carbide. This method is inapplicable to structures on GaAs. To find the parameters of interest in this case, one has to use asymmetric Bragg diffraction, which is conventionally employed in studies of structural perfection of epitaxial systems. As already mentioned, it does not yield as unambiguous values of the deformation parameters as the former approach, because the number of factors acting on the reflection FWHM in asymmetric geometry is twice that met in the case of a symmetric arrangement, and their rigorous separation is a much more complex problem requiring knowledge of strain distribution functions in the film. For epitaxial gallium nitride films, however, measurement of asymmetric Bragg reflections, as seen from Table I and Fig. 2, offers a fast way to reveal anisotropy in microdistortion parameters and, hence, to estimate the density of edge and screw dislocations responsible for this anisotropy.

One should bear in mind that the regions of an epitaxial film involved efficiently in scattering are different in different measurement geometries. In Laue geometry it is practically the whole thickness of the film, while in the Bragg arrangement the radiation penetration depth is determined by photoelectric absorption, so that the upper layers, which lie closer to the surface, provide a larger contribution to diffracted intensity. In the case of grazing diffraction, information is collected only from a thin near-surface film layer. All

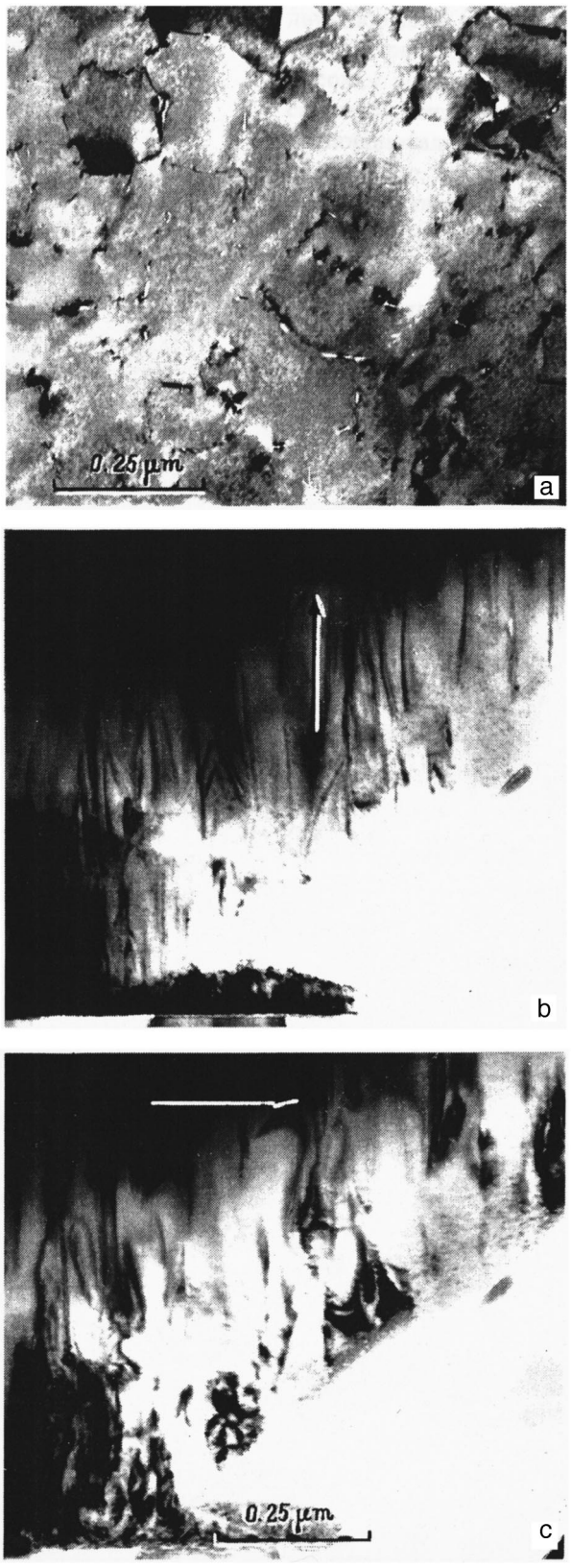

FIG. 5. Electron microscope images of a GaN film grown on GaAs. (a) plan view, (b) and (c) cross sections with diffraction vector (b) $\mathbf{g}=[0002]$ and (c) $\mathbf{g}=[1120]$.

this may be of considerable significance if the epitaxial film is thick ($>5-10\,\mu$m), and defects are distributed nonuniformly through the film thickness. The samples studied in this work had a GaN layer about $1-2\,\mu$m thick, which is less than the penetration depth in symmetric Bragg geometry. Hence both Bragg and Laue diffraction involve the whole thickness of the epitaxial film, and the comparative analysis carried out in this study is valid even if the defect structure varies in depth. And it is only in the case of grazing diffraction geometry that the δe_{xy} component found relates to the surface layer (about 0.1-μm thick) and, generally speaking, may not coincide with the layer-averaged value.

Thus we have performed a comprehensive analysis of x-ray diffraction reflections from GaN epitaxial layers in different measurement geometries, determined the microdistortion components and the size of the coherent-scattering regions, and revealed an asymmetry in local displacement fields around defects, which was also related to the configuration of dislocations in the layers.

Support of the Russian Fund for Fundamental Research (Grant 96-02-16907a) is gratefully acknowledged.

[1] M. Leszczynski, T. Suski, P. Perlin, H. Teisseyre, I. Grzegory, M. Bockowski, J. Jun, S. Porowski, and J. Major, J. Phys. D **28**, A149 (1995).
[2] C. Kim, I. K. Robinson, J. Myoung, K. Shim, M.-C. Yoo, and K. Kim, Appl. Phys. Lett. **69**, 2358 (1996).
[3] T. D. Moustakas, T. Lei, and R. J. Molnar, Physica B **185**, 36 (1993).
[4] D. Kapolnek, X. H. Wu, B. Heying, S. Keller, B. P. Keller, U. K. Mishra, S. P. DenBaars, and J. S. Speck, Appl. Phys. Lett. **67**, 1541 (1995).
[5] T. Lei, K. F. Ludwig, Jr., and T. D. Moustakas, J. Appl. Phys. **74**, 4430 (1993).
[6] B. Heying, X. H. Wu, S. Keller, Y. Li, D. Kapolnek, B. P. Keller, S. P. DenBaars, and J. S. Speck, Appl. Phys. Lett. **68**, 643 (1996).
[7] W. Li, P. Bergman, I. Ivanov, W.-X. Ni, H. Amano, and I. Akasa, Appl. Phys. Lett. **69**, 3390 (1996).
[8] R. Stoommer, T. Metzger, M. Schuster, and H. Göbel, Nuovo Cimento D **19**, 465 (1997).
[9] R. N. Kyutt, L. M. Sorokin, T. S. Argunova, and S. S. Ruvimov, Fiz. Tverd. Tela (St. Petersburg) **36**, 2700 (1994) [Phys. Solid State **36**, 1473 (1994)].
[10] R. N. Kyutt and T. S. Argunova, Nuovo Cimento D **19**, 267 (1997).
[11] R. N. Kyutt, T. S. Argunova, and S. S. Ruvimov, J. Appl. Crystallogr. **28**, 700 (1995).
[12] W. C. Marra, P. Eisenberger, and A. Y. Cho, J. Appl. Phys. **50**, 6927 (1979).
[13] E. Koppensteiner, A. Schuh, G. Bauer, V. Holy, G. P. Watson, and E. A. Fitzgerald, J. Phys. D **28**, A114 (1995).
[14] V. M. Kaganer, R. Köhler, M. Schmidbauer, R. Opitz, and B. Jenichen, Phys. Rev. B **55**, 1793 (1997).
[15] M. A. Krivoglaz, *Theory of X-Ray and Thermal Neutron Scattering by Real Crystals* [Plenum Press, New York, 1969; Nauka, Moscow, 1967].
[16] M. Wilkens, Krist. Tech. **11**, 1159 (1976).
[17] L. P. Ryaboshapka, Zavod. Labor. No. 5, 26 (1981).
[18] W. Qian, M. Skowronski, M. De Graef, K. Doverspike, L. B. Rowland, and D. K. Gaskill, Appl. Phys. Lett. **66**, 1252 (1995).
[19] A. Sakai, H. Sunakawa, and A. Usui, Appl. Phys. Lett. **71**, 2259 (1997).

Translated by G. Skrebtsov

Erbium in silicon carbide crystals: EPR and high-temperature luminescence

P. G. Baranov, I. V. Ilyin, E. N. Mokhov, A. B. Pevtsov, and V. A. Khramtsov

A. F. Ioffe Physicotechnical Institute, Russian Academy of Sciences, 194021 St. Petersburg, Russia
(Submitted June 18, 1998)
Fiz. Tverd. Tela (St. Petersburg) **41**, 38–40 (January 1999)

Erbium ions have been incorporated for the first time in bulk 6*H*-SiC crystals during growth, and they were unambiguously identified from the ^{167}Er EPR hyperfine structure. High-temperature luminescence of erbium ions at a wavelength of 1.54 μm has been detected. The observed luminescence exhibits an increase in intensity with increasing temperature. The observation of Er luminescence in 6*H*-SiC offers a promising potential for development of semiconductor light-emitting devices at a wavelength within the fiber-optics transparency window. [S1063-7834(99)00901-6]

Rare-earth-doped semiconductors are attracting an ever increasing interest due to their potential use as light-emitting diodes or lasers. Because the luminescence is produced in intra-4*f* transitions, the crystal-field effects are very weak, and the luminescence is practically independent of the semiconductor material. Of particular interest is erbium, because the $^4I_{13/2} \rightarrow {}^4I_{15/2}$ intra-4*f* transition observed at 1.54 μm is at the minimum of absorption of silicon-based optical-fiber systems. Photoluminescent properties of rare-earth (RE) elements in III–V systems (see Ref. 1 and references therein) and silicon[2] have been a subject of many publications.[3]

The main problem is presently the low luminescence yield, particularly at room temperature. The luminescence quenching decreases with increasing semiconductor gap width. This factor becomes particularly essential when assessing the potential of Si:Er-based devices, because it is believed that a high luminescence yield is, in principle, impossible in this system.[4] Incorporation of erbium ions in wide-gap materials like silicon carbide could be a promising approach, because such systems can be matched to silicon-based devices. Besides, semiconductor technology based on the silicon carbide itself presently finds ever increasing application. Erbium luminescence at 1.54 μm was observed in ion-implanted SiC.[5] The maximum depth of erbium penetration was 0.3 μm. To our knowledge, all attempts at detecting these ions by EPR in ion-implanted layers and, thus, at establishing the structure of the luminescencing centers failed. The reason for this is that ion implantation permits one to obtain only a very thin doped layer, which makes EPR measurements very difficult. The difference in structure between the defects in ion-implanted layers and bulk material adds another problem. Besides, ion implantation permits doping with impurities which cannot be introduced into the semiconductor during growth, i.e. when the system is in a non-equilibrium state. This point can be illustrated by an EPR study of erbium-oxygen complexes (Er^{3+} surrounded by six oxygens) in silicon.[6] A 2-μm thick oxygen-enriched layer was obtained by solid-state recrystallization of an epitaxial amorphous layer produced by ion implantation of erbium into silicon. One cannot exclude the possibility that what was observed were actually EPR spectra of erbium pairs, because one could not detect the hyperfine (hf) structure of the spectra. We believe that only by solving the problem of incorporation of isolated Er^{3+} ions in bulk SiC material during growth (as far as we know, for Si this problem still remains unsolved) can make this material promising for application in opto-electronic devices.

This work reports on a successful solution of the problem of incorporating single Er^{3+} ions (i.e. ions that do not form impurity clusters such as erbium pairs etc.) in bulk 6*H*-SiC crystals grown by the sandwich sublimation method. Preliminary results of EPR studies of Er^{3+} ions in 6*H*-SiC:Er crystals were presented in Ref. 7.

1. EXPERIMENTAL TECHNIQUES

The samples were bulk erbium-doped 6*H*-SiC crystals grown by the sublimation sandwich technique[8] in vacuum at 1850–1900 °C. Metallic erbium placed in a tantalum container served as the impurity source during the growth. Because of the presence of nitrogen donors, the crystals thus grown had *n*-type conduction. Using a tantalum container permitted reducing the nitrogen donor concentration to 10^{16} cm^{-3}.

EPR spectra were measured in the *X* range (9.3 GHz) within the 4–300 K temperature region. The samples were 3×4 mm platelets about 1 mm thick, with their plane being perpendicular to the hexagonal axis *c* of the crystal. The luminescence was excited with He–Cd (325 nm), Ar (488 nm), and Kr (647.1 nm) lasers. The luminescence was studied at 77 and 300 K.

2. RESULTS OF THE EXPERIMENTS: EPR

The EPR spectra measured in 6*H*-SiC:Er crystals consisted of many anisotropic lines, whose positions varied with orientation within the magnetic-field range of 50 to 800 mT. Spectra of two types of centers with qualitatively different angular behavior were observed. The first type comprised seven axially symmetric centers, with the symmetry axis along the hexagonal direction in the crystal (*c* axis). Three centers with orthorhombic EPR spectra belong to the second type.

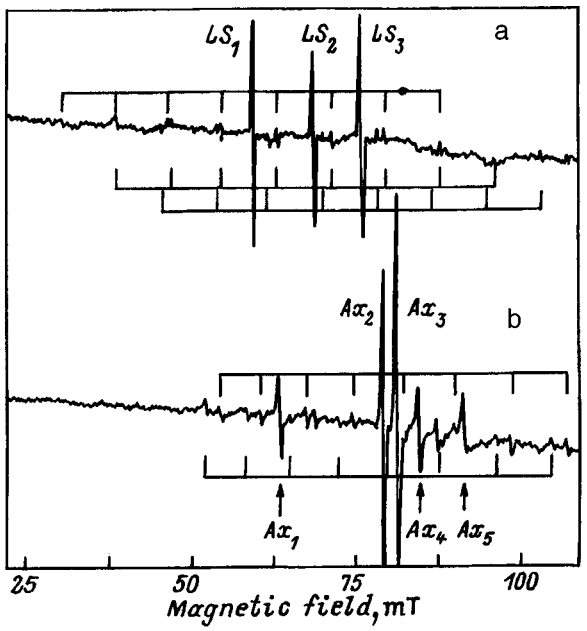

FIG. 1. EPR spectra of a 6*H*-SiC:Er crystal measured in the $\mathbf{B}\|c$ and $\mathbf{B}\perp c$ orientations at (a) 12 K and (b) 15 K at a frequency of 9.3 GHz.

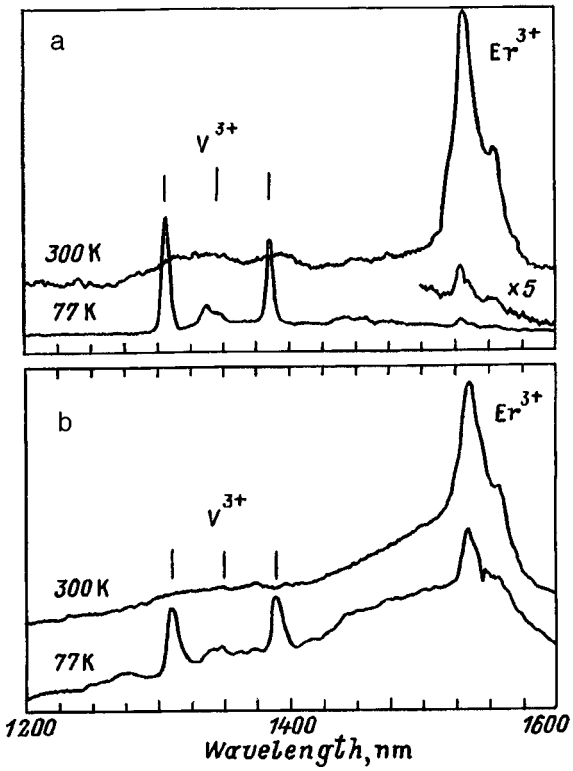

FIG. 2. Luminescence spectra of a 6*H*-SiC:Er crystal measured under excitation with (a) Ar laser (488-nm wavelength) at two temperatures, 77 K (10-mV gain) and 300 K (1-mV gain), and (b) Kr laser (647.1 nm) at 77 and 300 K.

All EPR spectra can be described by a spin Hamiltonian

$$H=\mu_B \mathbf{BgS}+\mathbf{SAI}, \tag{1}$$

where $S=1/2$, $I=7/2$ (the nuclear spin of ^{167}Er), μ_B is the Bohr magneton, and **g** is the g tensor. The first term describes the interaction of the electron spin with external magnetic field, the second relates to the hf interaction of the electron spin with the ^{167}Er nuclear spin, and **A** is the corresponding tensor (this term is zero for even erbium isotopes). The hf structure was measured reliably for three centers with orthorhombic symmetry and two axially symmetric centers. For three centers with orthorhombic symmetry, which are denoted here by LS_1, LS_2, and LS_3, the local axis z coincides with one of the six Si–C directions, and does not coincide with the c axis. The x and y axes lie in the plane perpendicular to the z axis, and the former is in one of the $\{11\bar{2}0\}$ planes. The spin-Hamiltonian parameters were found to be as follows: for the LS_1 centers — $g_X=12.2$, $g_Y=3.35$, and $g_Z=1.5$; for LS_2 — $g_X=10.6$, $g_Y=6.16$, and $g_Z=1.26$; and for LS_3: $g_X=9.25$, $g_Y=7.2$, and $g_Z=1.45$. Direct identification of erbium ions was made possible by observation of the hf structure in the spectra due to the interaction with the ^{167}Er nucleus. Erbium has one stable odd isotope, ^{167}Er (natural abundance 22.8%), with a nuclear spin $I=7/2$, so that the spectrum must consist of one strong central line and eight weak satellites of equal intensity. Their intensity should be about 3% of the central-line amplitude. Figure 1 shows EPR spectra obtained for two crystal orientations, $\mathbf{B}\|c$ and $\mathbf{B}\perp c$, at 12 and 15 K, respectively. The EPR spectra of the LS_1, LS_2, and LS_3 centers and their hf structure are seen in the $\mathbf{B}\|c$ orientation. We also obtained hf constants of the structure, and they are given here only for the LS_1 centers: $A_X=450\times10^{-4}$ cm^{-1}, $A_Y=123.5\times10^{-4}$ cm^{-1}, and $A_Z=55.4\times10^{-4}$ cm^{-1}.

Besides orthorhombic Er^{3+} centers, we detected in the 100–600-mT magnetic-field region EPR signals of axial symmetry, with the hexagonal axis c as the g tensor axis. The spectrum shown in Fig. 1 and obtained in the $\mathbf{B}\perp c$ orientation is seen to have five lines denoted by Ax_1, Ax_2, Ax_3, Ax_4, and Ax_5. Such spectra can be described by the same axially symmetric Hamiltonian (1). We shall consider only the two centers denoted by Ax_2 and Ax_3, because they produced the strongest lines, and their hf structure was reliably established (Fig. 1). For the Ax_2 centers, $g_\|=1.073$, $g_\perp=8.284$, $A_\|=290\times10^{-4}$ cm^{-1}, $A_\perp=38\times10^{-4}$ cm^{-1}, and for the Ax_3 centers, $g_\|=1.164$, $g_\perp=8.071$, $A_\|=285\times10^{-4}$ cm^{-1}, and $A_\perp=41\times10^{-4}$ cm^{-1}.

One observed also an intense, strongly anisotropic EPR spectrum characterized by axial symmetry with $g_\|=0.77$ and $g_\perp=3.5$, which we denoted by Ax_6. The EPR linewidth of the Ax_6 center is almost an order of magnitude larger than those of the above spectra. Although we did not detect the ^{167}Er hf structure in this spectrum, it may be conjectured to be also due to the erbium impurity.

3. LUMINESCENCE

We studied also the luminescence of the crystals where the above ^{167}Er EPR spectra were observed. The visible and near-IR luminescence produced by interband excitation exhibits lines typical of *n*-type 6*H*-SiC crystals with a low nitrogen concentration. Figure 2a,b shows luminescence spectra excited by photons of energy considerably lower than

the 6*H*-SiC band gap by means of lasers operating at 488 and 647.1 nm, respectively. The luminescence spectra were taken for two temperatures, 77 and 300 K. One sees in both panels strong luminescence lines, with their wavelengths practically coinciding in both cases. The long-wavelength line intensity increases strongly with increasing temperature, and this line is typical of the $^4I_{13/2} \rightarrow {}^4I_{15/2}$ $4f$ intrashell transition in the Er^{3+} ion. The three additional luminescence lines whose intensity, in contrast to the Er^{3+} emission line, grows with decreasing temperature, correspond in position[9] to vanadium lines in 6*H*-SiC. Vanadium is the usual residual impurity in silicon carbide.

4. DISCUSSION OF RESULTS

A comparison of the RE ionic radii with the radii of silicon and carbon suggests that erbium occupies silicon sites in SiC. Our studies of the hf structure of EPR spectra showed unambiguously that these spectra are produced by single erbium ions which are not bound in impurity clusters (Er–Er pairs etc.). We believe that three of the axial centers are due to erbium substituting for silicon in the lattice sites. Orthorhombic Er^{3+} centers have a more complex structure and include another defect in the carbon site near an erbium ion. It may be conjectured that the Er^{3+} ion forms a complex with one oxygen atom or a carbon vacancy in such a way that the line connecting them coincides with one of the Si–C bonds while not coinciding in direction with the hexagonal *c* axis for orthorhombic centers. Some of the axial centers may also be connected with erbium-containing complexes.

The main problem lies in establishing the excitation mechanism for the strong erbium-ion luminescence, as well as the intense growth in luminescence intensity with increasing temperature, a phenomenon which may play a decisive role in possible future applications. The efficiency of direct excitation of erbium is usually low and, therefore, our experiments to apparently reveal absorption by defects and impurities with subsequent excitation transfer to Er^{3+} ions. A good candidate for this process could be, in particular, vanadium, whose luminescence lines are also effectively excited in the crystal. We used excitation at two wavelengths in our experiments to obtain supportive evidence for the assumption that absorption by vanadium may be involved in excitation of the erbium luminescence.

The authors owe sincere thanks to W. J. Choyke, G. Pensl, Yu. A. Vodakov, V. F. Masterov, and V. G. Golubev for fruitful discussions.

Partial support of the Russian Fund for Fundamental Research (Grant 98-02-18241) is gratefully acknowledged.

[1] V. F. Masterov, Fiz. Tekh. Poluprovodn. **27**, 1435 (1993) [Semiconductors **27**, 791 (1993)].
[2] J. Michel, J. L. Benton, R. F. Ferrante, D. C. Jacobson, D. J. Eaglesham, E. A. Fitzgerald, Y.-H. Xie, J. M. Poate, and L. C. Kimerling, J. Appl. Phys. **70**, 2672 (1991).
[3] A. Polman, J. Appl. Phys. **82**, 1 (1997).
[4] W. Jantsch and H. Przybylinska, in *Proceedings of the 23rd International Conference Physics of Semiconductors* (Berlin, 1996), edited by M. Scheffler and R. Zimmermann (World Scientific, Singapore), p. 3025.
[5] W. J. Choyke, R. P. Devaty, L. L. Clemen, and M. Yoganathan, Appl. Phys. Lett. **65**, 1668 (1994).
[6] J. D. Carey, J. F. Donegan, R. C. Barklie, F. Priolo, G. Franzò, and S. Coffa, Appl. Phys. Lett. **69**, 3854 (1996).
[7] P. G. Baranov, I. V. Ilyin, and E. N. Mokhov, Solid State Commun. **103**, 291 (1997).
[8] Yu. A. Vodakov, E. N. Mokhov, M. G. Ramm, and A. D. Roenkov, Krist. Tech. **5**, 729 (1979).
[9] M. Kunzer, H. D. Müller, and U. Kaufmann, Phys. Rev. B **48**, 10846 (1993).

Translated by G. Skrebtsov

Electronic structure of semiconductor solutions of cadmium chalcogenides

B. V. Gabrel'yan, A. A. Lavrent'ev, and I. Ya. Nikiforov

Don State Technical University, 344010 Rostov-on-the-Don, Russia*
(Submitted June 22, 1998)
Fiz. Tverd. Tela (St. Petersburg) **41**, 41–43 (January 1999)

The electronic structure of the semiconductor solid solutions CdS_xSe_{1-x} $x=(0, 0.17, 0.33, 0.5, 0.67, 0.83, 1.0)$ is investigated. The experimental x-ray and x-ray-induced electronic spectra of sulfur in CdS are compared with computed spectra. The calculations are performed using the *FEFF* (Version 7) program and a package of programs that implements a cluster version of the local-coherent-potential approximation. The effect of an electron vacancy in the 1*s* level on the x-ray absorption spectrum is investigated. The band gap as a function of the anion concentration in the solution is estimated. © *1999 American Institute of Physics.* [S1063-7834(99)01001-1]

The solid solutions CdS_xSe_{1-x} with different concentrations x are of interest in connection with the possibility of varying continuously the physical characteristics of these semiconductors. This creates a potential for practical applications of such solutions, for example, in frequency-tunable lasers. Although there is a large number of works on methods for preparing the solid solutions CdS_xSe_{1-x},[1,2] the electronic-energy structure of these solutions has been studied very little, especially in the region of unoccupied states, i.e. in the conduction band. In the present work we investigated the local electronic densities of states in the solid solutions CdS_xSe_{1-x} as a function of the sulfur concentration ($x=1$, 0.83, 0.67, 0.5, 0.33, 0.17, 0). In addition, the influence of a core hole in the *K* level on the electronic states is investigated. The calculations are performed using the *FEFF* (Version 7) program[3] for free states and by the local coherent potential (LCP) method, used many times for semiconductors[4] and solid solutions,[5] for free and occupied states. This enabled us to compare the results obtained in the total multiple scattering (MS) approximation and in the high-order multiple scattering approximation, using the Rehr–Albers algorithm (*FEFF* program).

The *FEFF* (Version 7) program, authored by Zabinsky, Rehr, and Ankudinov,[3,6,7] is based on the high-order multiple scattering (MS) approximation. In this approximation, a single-electron calculation of the effective cross section for x-ray photoabsorption is calculated in the dipole approximation using Fermi's golden rule taking the core vacancy into account.

A cluster version of the local-coherent-potential approximation was proposed by Gyorffy[8,9] and employs the Green's functions apparatus to calculate the local partial electronic densities of states. A description of this approximation and a comparison with the coherent potential approximation and the average *t* matrix are given in Ref. 10.

In the present work, the substitutional solid solutions CdS–CdSe having the cubic sphalerite lattice are studied. The lattice parameter for the solutions was determined using Vegard's law

$$a_x = x a^{\mathrm{CdS}} + (1-x) a^{\mathrm{CdSe}},$$

where x is the sulfur concentration in the anionic sublattice of the solution, a^{CdS} is the lattice constant of ''pure'' CdS,[11] and a^{CdSe} is the lattice constant of ''pure'' CdSe.[11] The local-coherent-potential method presupposes a specific scattering potential of an atom placed at the center of a cluster, while all other scatterers can be ''effective.'' For the solutions studied in the present work this means that, besides the central atom, the other atoms of both sulfur and selenium are replaced by the same interstitial scattering *t* matrix of the form

$$t_{\mathrm{eff}}(E) = x t^{\mathrm{S}}(E) + (1-x) t^{\mathrm{Se}}(E).$$

The crystal potentials in the calculations of the occupied states (valence band) were constructed according to the scheme used in Ref. 12. The following scheme was used for the free states (XANES region). The crystal potentials of Cd and S of ''pure'' CdS and the potentials of Cd and Se in ''pure'' CdSe but with lattice constant a_x (in both cases) were calculated for a chosen value of x using the *FEFF* (Version 7) program. Next, it is assumed that in the solution the scattering potentials $V^{\mathrm{Cd}}, V^{\mathrm{S}}$, and V^{Se} are

$$V^{\mathrm{Cd}} = x V^{\mathrm{Cd}}_{\mathrm{CdS}} + (1-x) V^{\mathrm{Cd}}_{\mathrm{CdSe}}, \quad V^{\mathrm{S}} = V^{\mathrm{S}}_{\mathrm{CdS}},$$

$$V^{\mathrm{Se}} = V^{\mathrm{Se}}_{\mathrm{CdSe}}.$$

Next, the local partial electronic densities of states for all components of the compound were calculated in the standard (for the local coherent potential approximation) manner taking account of the S and Se concentrations.

In Fig. 1, the experimental x-ray photoelectron spectra in CdS from Ref. 13 (curve *1*), our *K* x-ray emission spectra (curve *2*) and absorption spectra (curve *3*) of sulfur in CdS (the experimental details are described in Ref. 4) are compared with the theoretical *K* absorption spectrum (curve *4*), calculated using the program *FEFF* (Version 7), and the computed LCP density of free *p* states in sulfur using the same potential from *FEFF* (Version 7), taking into account an electron vacancy in the *K* level (curve *5*), and the density

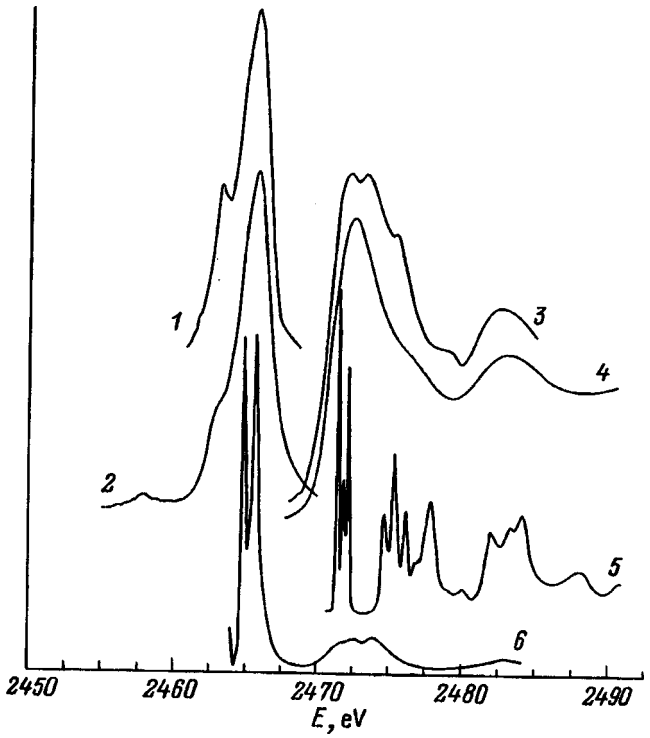

FIG. 1. Results of investigations of the valence band top and conduction band bottom in CdS, *1* — x-ray photoelectron spectrum (XPS),[13] *2* — x-ray *K* emission band of S, *3* — x-ray *K* absorption spectrum of S, *4* — computed x-ray *K* absorption spectrum of sulfur (*FEFF* (Version 7)), *5* — density of free *p* states of S taking account of the core vacancy, *6* — density of *p* states in S.

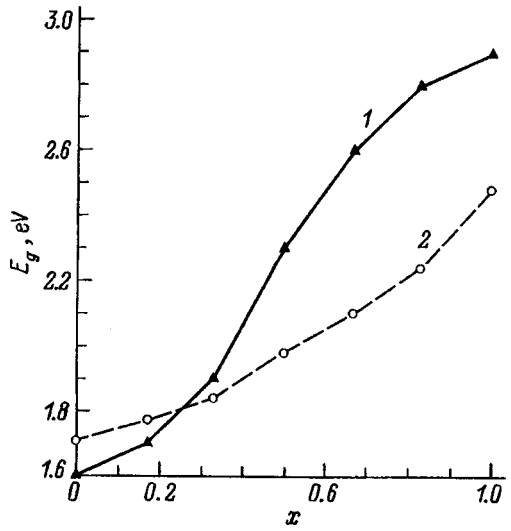

FIG. 2. Band gap E_g versus the sulfur concentration x in the anionic sublattice in the solid solutions CdS_xSe_{1-x}. *1* — Calculation, *2* — experiment.[2]

of occupied and unoccupied *p* states of S in CdS (curve *6*), calculated using a potential constructed by the scheme described in Ref. 12. The *FEFF* (Version 7) *K* absorption spectrum of sulfur (curve *4*) reproduces well the position and shape of the main peaks in the experimental spectrum, but a number of low-intensity elements of the fine structure on the high-energy side of the first principal peaks of the experimental spectrum (curve *3*) could not be obtained in this calculation. The numerous details of the density of free *p* states of S (curve *5*), calculated in the total multiple scattering approximation, agrees quite well with the characteristic features of the experimental spectrum.

The calculations showed that the presence of a hole in a *K* level does not greatly influence the form of the free *p* states of sulfur and gives only a very small ($\sim$0.3 eV) shift of the positions of the characteristic peaks in the direction of lower energies.

The curves of the density of free *p* states in S and Se for the solid solutions have close shapes and maxima at close energies with concentration-dependent intensity indicating substantial mixing of free *p* states of S and Se in all of the solutions investigated.

To estimate the band gaps in the solid solutions CdS_xSe_{1-x} it is necessary to know the total electronic densities of states in the valence and conduction bands. The computational results for the total densities of states for pure CdS and CdSe and their solid solutions showed that the density of states has a distinct region which drops off essentially to zero. This region was used to estimate E_g. This region is smaller in pure CdSe than in pure CdS, and its energy correlates well with the experimental data of Ref. 2. As one can see from Fig. 2, the difference between the computed and experimental values of E_g is 0.25 eV on the average, while E_g in the solution cannot be determined by simple linear interpolation (similar to Vegard's law) on its values for pure CdS and CdSe, as the calculations and experiment showed.

*E-Mail: root@sintez.rnd.su

[1] Yu. A. Varvas, M. É. Al'tosar, M. T. Nyches, and T. L. Kukk, Tr. Tallin. Politekhn. Instituta (1969). A. c. 3.
[2] I. B. Midetskaya, G. S. Oleĭnik, L. D. Budennaya *et al.*, *Physicochemical Principles of the Synthesis of Single Crystals of II–VI Semiconductor Solid Solutions*, Naukova Dumka, Kiev (1986), 160 pp.
[3] S. I. Zabinsky, J. J. Rehr, and A. Ankudinov *et al.*, Phys. Rev. B **52**, 2995 (1995).
[4] A. A. Lavrent'ev, I. Ya. Nikiforov, A. B. Kolpachev, and B. V. Gabrel'yan, Fiz. Tverd. Tela (St. Petersburg) **38**, 2347 (1996) [Phys. Solid State **38**, 1291 (1996)].
[5] V. V. Ilyasov and I. Ya. Nikiforov, Fiz. Tverd. Tela (St. Petersburg) **39**, 211 (1997) [Phys. Solid State **39**, 185 (1997)].
[6] J. J. Rehr and R. C. Albers, Phys. Rev. B **41**, 8139 (1990).
[7] J. Mustre de Leon, J. J. Rehr, S. I. Zabinsky, and R. C. Albers, Phys. Rev. B **44**, 4146 (1991).
[8] B. L. Gyorffy and M. J. Stott, in *Band Structure Spectroscopy of Metals and Alloys*, edited by D. Fabian (London–New York, 1973), pp. 385–403.
[9] D. House, B. L. Gyorffy, and G. M. Stocks, J. de Phys. **35**, C4-81 (1974).
[10] I. Ya. Nikiforov and E. V. Stern, in *Proceedings of the 9th Annual Symposium ''Electronic Structure of Metals and Alloys,''* Gaussig, GDR (1979), pp. 141–149.
[11] A. V. Novoseleva and V. B. Lazarev [Eds.], *Handbook of the Physicochemical Properties of Semiconductor Materials*, Nauka, Moscow, (1979), 340 pp.
[12] G. V. Vol'f, V. V. Dyakin, and V. P. Shirokovskiĭ, Fiz. Met. Metalloved. **38**, 949 (1974).
[13] L. Ley, R. A. Pollak, F. R. McFeely, S. P. Kowalczyk, and D. A. Shirley, Phys. Rev. B **9**, 600 (1974).

Translated by M. E. Alferieff

Characteristic features of the photoconductivity and spin conversion of electron-hole pairs in doped amorphous molecular semiconductors in the dye absorption region

N. A. Davidenko

T. Shevchenko Kiev State University, 252033 Kiev, Ukraine

A. A. Ishchenko

Institute of Organic Chemistry, Ukrainian Academy of Sciences, 253094 Kiev, Ukraine

(Submitted July 1, 1998)
Fiz. Tverd. Tela (St. Petersburg) **41**, 44–48 (January 1999)

The photoconductivity of doped poly-*N*-epoxypropylcarbazole films in the absorption region of a cationic polymethine dye is observed to increase when the BF_4^- ion is replaced by Cl^- and I^-. The effect of a magnetic field on the photoluminescence is investigated at room temperature. The photoconductivity is studied as a function of the electric field intensity and wavelength of light. The dependence of the photoconductivity on the nature of the anion can be explained by a change in the probability of intercombination conversion in ionic and electron-hole pairs.
 [S1063-7834(99)01101-6]

Amorphous molecular semiconductors (AMSs) with visible-range photoconductivity are used as electrographic, holographic, and electroluminescence recording media.[1,2] In this connection, a basic requirement for AMSs is high photoconductivity. It has been shown[3,4] that in the poly-*N*-epoxypropylcarbazole (PEPC) based dye-doped AMSs used in practice charge-carrier photogeneration consists of two stages: photogeneration of electron-hole pairs (EHPs) and external electric field and temperature stimulated dissociation of EHPs on free current carriers. However, it has been established experimentally that the EHP photogeneration efficiency depends strongly on the choice of dye (Dye^+An^{-1}), consisting of, for example, for a cationic dye, of an organic color (light absorbing) cation Dye^+ and an inorganic anion An^{-1}. Thus far attention has been devoted mainly to the choice of Dye^+, initiating EHP photogeneration, while the role of the noncolor counterion in these processes has been neglected. In the present work we investigated the influence of An^{-1} in a cationic polymethine dye on the photoconductivity of PEPC films in the absorption region of the dye.

1. EXPERIMENTAL SAMPLES AND PROCEDURE

The dye 1, 3, 3, 1′, 3′, 3′-hexamethylindocarbocyanine (*HIC*) with three different An^{-1} were used for the investigations. The structural formulas of PEPC and the molecule HIC^+An^- are displayed in Fig. 1, where *Cz* is a carbazole chromophore. The cation and anion of the dye are in the form of an ionic pair, and their position relative to one another is determined by the polarity of the medium.

The experimental samples were prepared either in the form of structures having a free surface — quartz substrate — PEPC + 0.5–5 mol % HIC^+An^- or in the form of a sandwich structure quartz — SnO_2–PEPC + 0.5–5 mol % HIC^+An^-–Al. The AMS films were prepared by pouring onto substrates solutions of the initial components in dichloroethane and drying in a drying oven at temperature +75 °C. Aluminum electrodes were deposited on the AMS films by thermal sputtering in a vacuum chamber. The thickness of the AMS films was $L=0.5-1\,\mu$m, while the Al films were 300–350 Å thick.

To achieve our objective we determined the influence of the type of An^{-1} on the photoabsorption and photoluminescence spectra of AMS films, the photocurrent in the sandwich-structure samples irradiated by light from the absorption region of the dye, and the ratio of the singlet (n_1) and triplet (n_3) EHP densities.

The optical spectra of the absorption coefficient (κ) and the photoluminescence intensity (I_{PL}) of the AMS films were measured on samples having a free surface, using the KSVIP-23 spectroscopic–computational system.

The quasistationary photocurrent density (j_1) was measured in the photoresistance regime using a storage oscillograph with samples of the sandwich structure irradiated on the SnO_2 electrode side by monochromatic light with wavelengths $\lambda_1=511$, 546, 578, and 633 nm from the absorption region of HIC^+An^-. The λ_1 light source was an incandescent lamp with interference light filters. The intensity (I_1) of the λ_1 light was varied with neutral light filters. The intensity of the external electric field was varied in the range $E=4\times10^7-2\times10^8$ V/m.

The samples having a free surface were also used to measure the effect of an external magnetic field on I_{PL}. The magnetic field intensity produced between the two poles of the electromagnet in a RÉ-1306 radiospectrometer was varied in the range $H=0-6$ kOe. An optical arrangement with fiber-optic cables was used in these measurements. To analyze the results, the ratio $\delta I_{PL}=\{I_{PL}(H)-I_{PL}(0)\}/I_{PL}(0)$, where $I_{PL}(H)$ and $I_{PL}(0)$ are the intensity of photoluminescence with and without a field, respectively, was calculated.

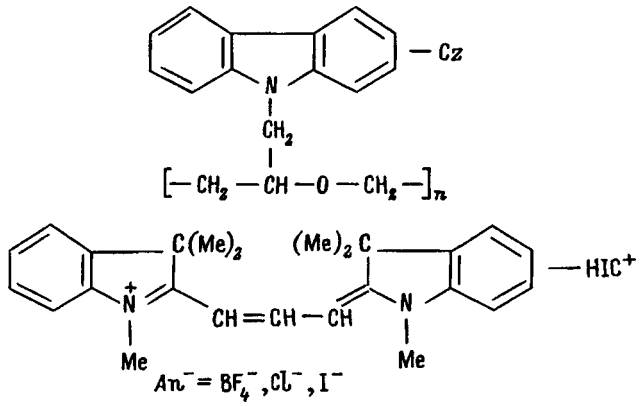

FIG. 1. Structural formulas for the PEPC molecule and the dye molecule HIC^+An^-.

To determine the ratio of n_1 and n_3, besides measurements of the effect of a magnetic field on $I_{PL,}$ we also use the method proposed in Refs. 5 and 6 for determining the change in photoconductivity of an AMS in the absorption region of the dopants with simultaneous photogeneration of triplet excitons. It is known that triplet excitons catalyze $S-T$ conversion of EHPs.[7,8] For this reason, photogeneration of triplet excitons increases the photoconductivity due to the dissociation of singlet EHPs in AMSs and decreases the photoconductivity due to dissociation of triplet excitons. In the present work, just as in Refs. 5 and 6, samples of the sandwich structure were irradiated with λ_1 light, and for exciton photogeneration the structures were irradiated with light with wavelength $\lambda_2=365\mp2$ nm (the wavelength of the λ_2 light does not fall in the absorption region of *HIC* and lies near the red absorption edge of PEPC, where efficient photogeneration of triplet excitons occurs[9]). The intensity of the λ_2 light was varied in the range $I_2=0.05-0.2$ W/m^2 with light filters. When a sample was irradiated with λ_1 or λ_2 light, a quasistationary photocurrent j_1 or j_2, respectively, was recorded. When a sample was irradiated simultaneously with λ_1 and λ_2 light, a quasistationary photocurrent j_3 was recorded. To analyze the results, the ratio of the photocurrents $\delta j=j_3/(j_1+j_2)$ was calculated and the dependences of j_1 and δj on E, λ_1, and l_1 were determined. The ratio n_1 and n_3 in photogenerated EHPs was estimated, just as in Refs. 5 and 6, from the amount by which δj differs from 1: if $\delta j>1$ or $\delta j<1$, then photogeneration produces more singlet or triplet EHPs, respectively. All measurements in the present work were performed at room temperature.

2. EXPERIMENTAL RESULTS

The electronic absorption spectra of the AMS PEPC + HIC^+An^- in the wavelength range $\lambda>400$ nm have a narrow intense band with vibrational structure on the short-wavelength edge of the spectrum (Fig. 2). This band is characteristic for polymethine dyes. As the dye concentration in PEPC increases, absorption near the vibrational maximum increases more strongly than near the main maximum, and a bathochromic shift of the spectrum and a decrease of intensity are observed in the photoluminescence spectra. These features of the electronic spectra attest to the appearance of *H* aggregates of dyes, absorbing light at shorter wavelengths than nonassociated molecules.[10] Substituting Cl^- and I^- for An^{-1} with BF_4^- produces a hypsochromic shift of the electronic spectra.

All experimental sandwich samples exhibited photoconductivity when irradiated with λ_1 light. The plots of j_1 versus E are linear in the coordinates $\log j_1$ versus $E^{1/2}$ (Fig. 3), the tangent of the slope angle of these plots being the same for all samples. This makes it possible to represent j_1 as a function of E by the analytical expression $j_1(E)\sim\exp\times\{-(W_{0PH}-\beta E^{1/2})/k_BT_{eff}\}$, similar to the expression for the photoconductivity in AMS as a function of E and T.[3,11] Here W_{0PH} is the activation energy of photogeneration at $E=0$; k_B is Boltzmann's constant; T_{eff} is calculated from the expression $T_{eff}^{-1}=T^{-1}-T_0^{-1}$, where $T_0=490\mp20$ K for PEPC based AMSs. From the tangent of the slope angle of the straight lines in Fig. 3 we find that the coefficient of proportionality $\beta=(4.6\mp0.2)\times10^{-5}$ eV·V$^{-1/2}$·m$^{1/2}$ and is close to the corresponding values measured in other PEPC-

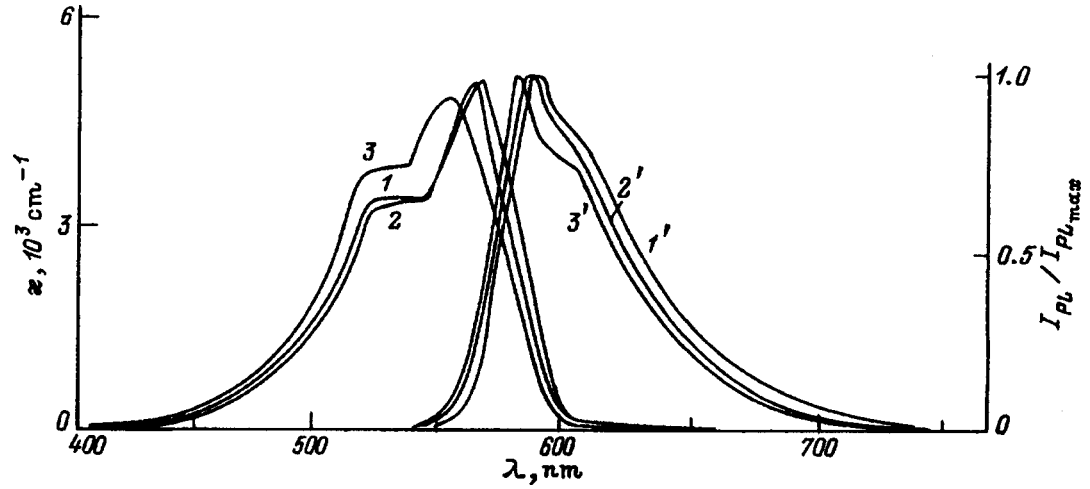

FIG. 2. Optical absorption spectra (*1–3*) and photoluminescence spectra (*1′–3*) of the PEPC + 1 mol % HIC^+An^- films with the anion BF_4^- (*1, 1′*), Cl^- (*2, 2′*), and I^- (*3, 3′*).

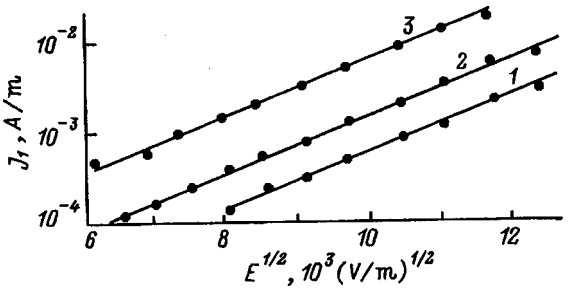

FIG. 3. $\log j_1$ vesus $E^{1/2}$ in Al–PEPC + 1 mol % HIC^+An^-–SnO_2 samples with the anion BF_4^- (*1*), Cl^- (*2*), I^- (*3*). $L=1\,\mu$m, $\lambda_1=546$ nm, $I_1=12$ W/m^2.

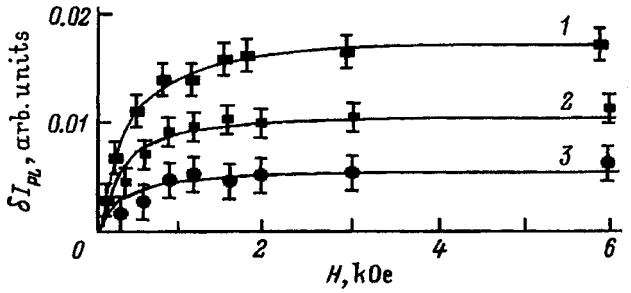

FIG. 5. δI_{PL} versus H for the PEPC + 1 mol % HIC^+An^- films with the anion BF_4^- (*1*), Cl^- (*2*), I^- (*3*). $\lambda_1=633$ nm.

based AMSs as well as to the theoretical value of the Poole–Frenkel constant.

In samples with equal L and the same absorbed λ_1 light intensity, the density j_1 for samples with Cl^- and I^- is several times higher than in samples with the BF_4^- anion (Fig. 3). Measurements of δj versus E and λ_1 established that δj decreases with increasing E and, for samples with Cl^- and I^- substituted for BF_4^-, but it increases with λ_1. Plots of δj versus λ_1 are displayed in Fig. 4.

Under our experimental conditions, an appreciable magnetic field effect on I_{PL} was observed only for $\lambda_1=633$ nm, while for other values of λ_1 we were not able to distinguish the change in I_{PL} in a magnetic field against the FÉU noise background. Figure 5 shows plots of δI_{PL} versus H for $\lambda_1=633$ nm. As H increases up to $H=1$ kOe, the intensity of the photoluminescence of PEPC + HIC^+An^- films increases, while I_{PL} decreases very little for $1<H<6$ kOe. Such features of the effect of H on I_{PL}[12,13] show that, when films are irradiated with λ_1 light, a portion of I_{PL} is determined by geminate recombination of the charges of singlet EHPs.

3. DISCUSSION

There are several possible reasons why the photoconductivity of PEPC + HIC^+An^-[1] films increases when Cl^- and I^- are substituted for An^- BF_4^-. We shall discuss the most important ones.

1) For An^- from the series indicated, the electron localization radius (α_n) on the anion in a dye molecule increases,

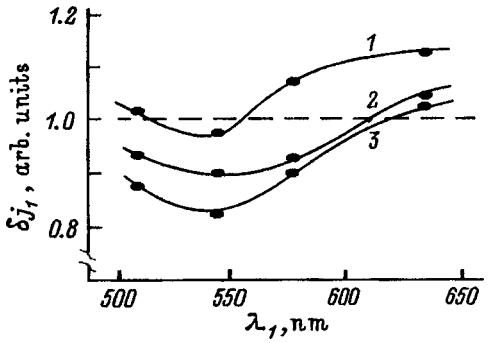

FIG. 4. δj_1 vesus λ_1 in Al–PEPC + 1 mol % HIC^+An^-–SnO_2 samples with the anion BF_4^- (*1*), Cl^- (*2*), I^- (*3*). $L=1\,\mu$m, $I_2=0.1$ W/m^2, $E=1.2\times10^8$ W/m.

and when an EHP dissociates the mobile hole charge (the hole localization radius on a carbazole chromophore (*Cz*) in PEPC $\alpha_p=1.1$ Å[13,14]) overcomes with high probability the Coulomb attraction of the delocalized electron. This mechanism of the influence of electron delocalization on the quantum yield of photogeneration of charge carriers was considered in Refs. 3, 14, and 15; it is especially strongly manifested in AMSs where the photogeneration centers are intermolecular charge transfer complexes. However, in the An^- series studied here, α_n should be larger for BF_4^- than for I^-, as follows from the values of the van der Waals radii.[16] Therefore the electrostatic interaction energy between An^- and Cz^+ should increase in the An^- series considered and, therefore, the EHP dissociation probability should decrease.

2) For An^- in the series indicated, the effect of traps for mobile holes decreases. Indeed, in all samples investigated with constant E the current density j_1 decreases with increasing L and I_1, as is characteristic for carrier-trap controlled photoconductivity in AMSs. Such traps can be dye aggregates in which the ionization energy of the upper occupied orbitals can be less than the ionization energy of the sample orbital of the carbazole chromophore *Cz*. However, it is evident from Fig. 2 that when the An^- BF_4^- is replaced by Cl^- and I^-, the intensity of the short-wavelength absorption band characterizing the absorption by *H* aggregates increases. This indicates that the concentration of *H* aggregates in AMS films is higher with I^- than with BF_4^-. Therefore the density of hole traps should be higher in AMSs with I^-, which does not agree with our experimental data.

3) For An^- from the series indicated, the density of dissociating EHPs increases as a result of an increase in the $S-T$ conversion rate and the transition of singlet EHPs into triplet pairs. The measurements of δj and δI_{PL} versus λ_1 and H for the An^- series investigated (Figs. 4 and 5) show that such a mechanism of an increase in photoconductivity is possible. According to Refs. 7 and 8, the decrease in δj as An^- changes attests to an increase in the fraction of dissociating photogenerated triplet EHPs. Figure 4 also shows that δj decreases with λ_1, so that the fraction of triplet EHPs increases with decreasing λ_1. The latter agrees with the results of previous investigations of the effect of a magnetic field on the photoconductivity of doped AMSs:[3,17] As the photon energy in the absorption region of photogeneration centers increases, the probability of photogeneration of triplet EHPs increases. Evidently, for the same reason we could

not observe an effect of the magnetic field on I_{PL} for $\lambda_1 < 633$ nm and we obtained δI_{PL} curves only for $\lambda_1 = 633$ nm (Fig. 5).

In nonpolar media, such as PEPC, polymethine dyes are found in the form of ionic pairs and their associates.[10] The dependence of the spectroscopic-luminescence characteristics of 1–3 dyes in PEPC on the nature of the anion (Fig. 1) attests to the fact that these pairs are predominantly contact pairs. In such pairs, even a noncolor counterion is capable of influencing the deactivation of their excited electronic states.[18] On the basis of the external ''heavy'' atom effect, in which the spin-orbit interaction increases in the halogen series from F to I, it can be expected to increase when the dye 1 is replaced by the dyes 2 and 3. In turn, this should increase the rate of singlet–triplet conversion of charged pairs and increase the concentration of long-lived triplet EHPs, whose dissociation in an electric field gives rise to an increase of the photoconductivity.[3]

In summary, the increase in the photoconductivity of the AMSs, investigated here, when the An^- BF_4^- is replaced by Cl^- and I^- is due mainly to an increase in the fraction of triplet EHPs as a result of an increase in the $S-T$ conversion probability. This makes it possible to refine our physical understanding of the process of photogeneration of charge carriers in accordance with a two-stage photogeneration model.[1,3,4] At the first stage of photogeneration, after a dye molecule absorbs a photon with energy $h\nu$, an EHP with the hole localized on the carbazole chromophore *Cz* in PEPC and the electron localized in the dye molecule is formed. If the dye consists of an organic cation Dye^+ and an inorganic anion An^{-1}, then the EHP photogeneration process can be represented by the scheme

$$Cz + {}^1(Dye^+An^-)_0 \xrightarrow{h\nu} Cz + {}^{1,3}(Dye^+An^-)_1 \rightarrow Dye^{\cdot} + {}^{1,3}(An^- \ldots Cz^+), \quad (1)$$

where it is indicated that the EHP^{1,3} $(An^- \ldots Cz^+)$ can be in a singlet spin state (S) as well as in one of three triplet spin states (T_0, T_-, T_+).[12,13]

At the second stage of photogeneration, the charges in an EHP either recombine as a result of a hole returning to the photoregeneration center or they separate as a result of holes hopping along *Cz*. Ordinarily, the unexcited ground state $^1(Dye^+An^-)$ of an ionic pair of the dye is a singlet state and the rate constant (k_1) for recombination of singlet EHPs is higher than the rate constant (k_3) for recombination of triplet EHPs. As the intensity E of the external electric field and temperature T increase, the EHP dissociation rate (k_η) increases. Recombination and dissociation of EHPs are competing processes, and whether one predominates over the other depends on k_1, k_3, and k_η and on the EHP $S-T$ conversion rate k_{ST}, since often $k_{ST} > k_1, k_\eta, k_3$. For example, for PEPC based AMSs, where the photoregeneration centers are intermolecular charge-transfer complexes or compounds with intramolecular charge transfer, $k_{ST} = 10^9 - 10^8$ s^{-1}, $k_1 = 10^8 - 10^7$ s^{-1}, $k_\eta = 10^7 - 10^5$ s^{-1}, $k_3 < 10^3$ s^{-1}.[3]

According to the photoregeneration scheme (1), in an external electric field the mobile hole moves away from an electron localized on An^-. In a zero magnetic field the magnetic interactions[12,13] and nonmagnetic spin-exchange interactions[19,20] of an electron and hole with the radical $Dye^{\cdot}$ initiate $S-T$ conversion of EHPs. For this reason, its rate depends on the nature of An^-. For photoregeneration of EHPs from a singlet excited state $^1(Dye^+An^-)_1$ of the dye, an increase of k_{ST} with an appropriate substitution for An^- stimulates an increase in the density of triplet EHPs and an increase in the density of free charge carriers.

[1] A. N. D'yakonov, *The Chemistry of Photographic Materials*, Moscow (1989), 270 pp.
[2] D. Neher, M. Remmers, and V. Cimrova, in *Electrical and Related Properties of Organic Solids*, edited by R. W. Muss, Kluwer Academic Publishers, Netherlands (1997), pp. 79–99.
[3] N. G. Kuvshinskiĭ, N. A. Davidenko, and V. M. Komko, *The Physics of Amorphus MOlecular Semiconductors*, Lybid', Kiev (1994), 176 pp.
[4] N. A. Davidenko, N. G. Kuvshinsky, V. G. Syromyatnikov, and L. N. Fedorova, Adv. Mater. Opt. Electron. **7**, 207 (1997).
[5] N. A. Davidenko and N. G. Kuvshinskiĭ, Fiz. Tverd. Tela (St. Petersburg) **39**, 1020 (1997) [Phys. Solid State **39**, 916 (1997)].
[6] N. A. Davidenko and N. G. Kuvshinsky, Adv. Mater. Opt. Electron. **7**, 255 (1997).
[7] V. L. Berdinskiĭ and A. L. Buchachenko, Kinetika; Kataliz. **37**, 659 (1996).
[8] A. L. Buchachenko and V. L. Berdinsky, J. Phys. C **100**, 18 292 (1996).
[9] A. Undzenas, Yu. Grazhulyavichus, and Ya. Urbanaviche, Litov. Fiz. Sb. **21**, 106 (1981).
[10] A. A. Ishchenko, *Structure and Spectroscopic-Luminescence Properties of Polymethine Dyes*, Naukova Dumka, Kiev (1994), 232 pp.
[11] M. Pope and C. E. Swenberg, *Electronic Processes in Organic Crystals*, Clarendon Press, Oxford (1982), 725 pp.
[12] A. L. Buchachenko, R. Z. Sagdeev, and K. M. Salikhov, *Magnetic and Spin Effects in Chemical Reactions*, Nauka, Novosibirsk (1978), 296 pp.
[13] E. L. Frankevich, in *Electronic Processes in Organic Molecular Crystals. Transport, Capture, Spin Effects*, edited by E. L. Silinysh, Riga (1992), 363 pp.
[14] N. G. Kuvshinsky, N. A. Davidenko, V. V. Reshetnjak, L. I. Savransky, and V. L. Sheptun, Chin. Phys. Lasers **165**, 323 (1990).
[15] N. G. Kuvshinsky, N. A. Davidenko, and V. V. Reshetnyak, Mol. Phys. **69**, 933 (1990).
[16] A. Gordon and R. A. Ford, *The Chemist's Companion: A Handbook of Practical Data, Techniques, and References* [Wiley, N. Y. (1972); Mir, Moscow (1976)], 541 pp.
[17] N. A. Davidenko and N. G. Kuvshinsky, J. Inf. Rec. Mat. **22**, 149 (1994).
[18] M. I. Demchuk, A. A. Ishchenko, V. P. Mikhailov, and V. I. Avdeeva, Chem. Phys. Lett. **144**, 99 (1988).
[19] A. L. Buchachenko, V. L. Berdinsky, and N. J. Turro, Chem. Phys. Lett. **242**, 43 (1996).
[20] A. L. Buchachenko and V. L. Berdinskiĭ, Izv. Akad. Nauk. SSR, Ser. Khi. **9**, 1646 (1995).

Translated by M. E. Alferieff

Rapid luminescence saturation of the Mn^{2+} $3d$ shell in the $Cd_{1-x}Mn_xTe$ dilute magnetic semiconductor with a high manganese concentration

V. F. Agekyan, N. N. Vasil'ev, and A. Yu. Serov

Institute of Physics, St. Petersburg State University, 198904 Petrodvorets, St. Petersburg, Russia
(Submitted June 9, 1998)
Fiz. Tverd. Tela (St. Petersburg) **41**, 49–53 (January 1999)

The dependence of manganese-ion intracenter-luminescence intensity on optical excitation level has been studied in the $Cd_{1-x}Mn_xTe$ dilute magnetic semiconductor with $0.4<x<0.7$. It is shown that the intracenter luminescence saturates due to effective nonlinear quenching already at low excitation levels. Mechanisms are proposed which can provide nonlinear quenching and offer a qualitative explanation for the temperature dependence of the luminescence saturation in samples with different manganese concentrations. © *1999 American Institute of Physics.* [S1063-7834(99)01201-0]

Spectroscopic investigation of dilute magnetic semiconductors (DMS), solid solutions of Group II–VI semiconductors with an iron-group magnetic component, and the corresponding low-dimensional systems, has been actively pursued during the recent two decades (see, e.g., reviews Refs. 1–3). These materials are characterized by a high concentration of localized magnetic moments originating from the unfilled $3d$ shell of iron-group ions. This results in strong ion-ion and carrier-ion exchange interactions causing giant magnetic splitting of excitonic levels, the magnetic polaron effect, and formation of antiferromagnetic pairs and magnetic-ion clusters.

The most popular DMS compound is $Cd_{1-x}Mn_xTe$ due to its good technological properties, the highest possible magnetic moment of the manganese $3d$ shell, and favorable parameters of the parent crystal CdTe. For magnetic component concentrations $x>0.4$, the gap width $E_g(x)=(1.55+1.5x)$ eV (at $T=77$ K) becomes larger than the threshold energy $E_t=2.15$ eV for the intracenter optical transitions in the $Mn^{2+}3d$ shell. This makes possible observation in the absorption spectrum of a band system corresponding to transitions in the manganese ion in a tetragonal crystal field. These transitions from the ground state $^6A_1(S)$ to excited states $^4T_1(G)$, $^4T_2(G)$, $^4A_1(G)$, and $^4E(G)$ (Fig. 1) are intercombination type (the $3d$-shell spin moment decreases from 5/2 to 3/2), and therefore the absorption coefficient in the bands is one to two orders of magnitude smaller than that for transitions from the valence to conduction band, even with 50% Cd replaced by manganese. As a result of the relaxation in the excited Mn^{2+} ion leading to considerable Stokes losses, the maximum of the broad Mn^{2+} intracenter-luminescence band lies near 2.0 eV, i.e., below E_t by 0.15 eV. The kinetic studies[4,5] of this band established that the decay time τ_0 is about 2×10^{-5} s and exhibits for $T<60$ K a frequency dependence within the band profile by increasing toward lower energies.

Thus there are two channels of light absorption and emission in DMSs, the conventional interband type with the Wannier exciton fixed to $E_g(x)$ and an intraionic one (involving excitation of the $Mn^{2+}3d$ shell with the threshold E_t), between which energy transfer can occur. The process of energy transfer from nonthermalized Wannier excitons to the manganese $3d$ ions was studied, in particular, in the $Zn_{1-x}Mn_xTe$ wide-gap DMS.[6] The dominant direction of energy transfer in $Cd_{1-x}Mn_xTe$ is determined by the relative magnitude of $E_g(x)$ and E_t, so that the interband exciton luminescence decays rapidly as x is increased above 0.4. The redistribution of emission between these channels can be affected not only by varying properly the solid-solution composition but by external factors as well (magnetic field, hydrostatic pressure), which likewise change the relation between E_t and the Wannier exciton energy E_{1s}, which is close to $E_g(x)$.[7,8]

In crystals having a high manganese concentration studied in the present work ($0.4<x<0.7$), practically all Mn^{2+} ions are interconnected in an infinite cluster within which energy is transferred from one excited ion to another. This transfer can be considered as motion of a Frenkel-type exciton among lattice sites occupied by manganese ions. Excitation of a Mn^{2+} ion reduces the $3d$ shell moment to nearly one half, which weakens substantially the exchange interaction of the excited ion with free carriers (Wannier excitons) and neighboring ions. Thus, if one succeeds in exciting a large enough fraction of the manganese ions by optical pumping, a noticeable photoinduced change in the magnetic properties of the DMS will occur. This will affect, in particular, the dynamics of formation and size of magnetic polarons.[9] The decrease of the magnetic moment, produced by $3d$-shell excitation and weakening the indirect exchange interaction, should act also on the rate of Frenkel exciton migration among the Mn^{2+} ions. All this relates equally both to bulk DMSs and to superlattices and quantum-well structures of the type $CdTe/Cd_{1-x}Mn_xTe$ with a high manganese concentration in the barrier layers. These considerations have initiated the present study of the dependence of the Mn^{2+} intraionic luminescence properties in $Cd_{1-x}Mn_xTe$ on the level of optical excitation, both selective into the $Mn^{2+}3d$ shell and above the interband transition edge. This dependence was found to be nontrivial in our earlier work.[10] This study may also help in understanding the photo- and electroluminescent properties of a broad class of II–VI wide-gap materials activated by iron-group ions.[1)]

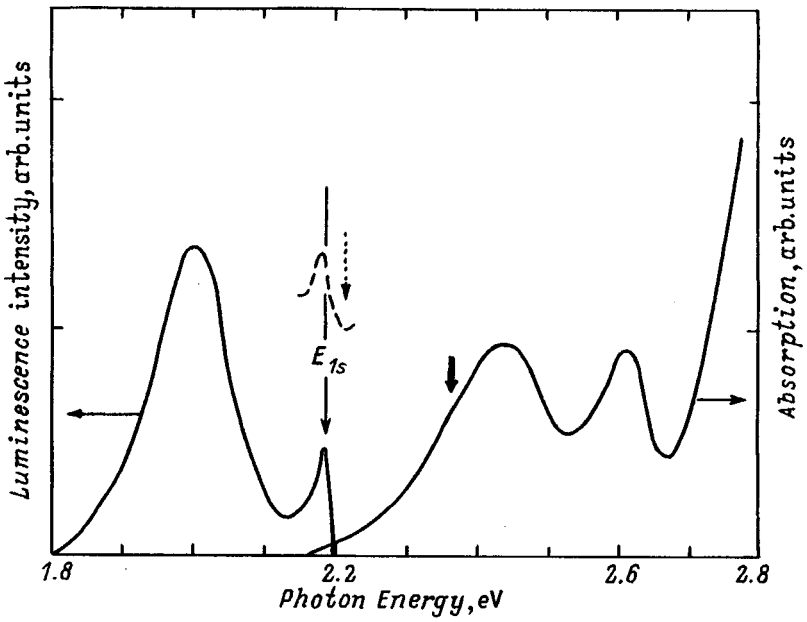

FIG. 1. Right — $Cd_{0.3}Mn_{0.7}Te$ absorption spectrum: $Mn^{2+}3d$ intrashell transition bands ${}^6A_1-{}^4T_1$ and ${}^6A_1-{}^4T_2$, whose position is practically independent of manganese concentration and temperature, and interband transition edge. Left — $Cd_{0.6}Mn_{0.4}Te$ luminescence spectrum: intracenter band ${}^4T_1-{}^6A_1$ and the Wannier exciton E_{1s}. Dashed arrow shows the structure of the Wannier exciton E_{1s} in the reflectance spectrum of $Cd_{0.6}Mn_{0.4}Te$ obtained at 77 K, with the dotted arrow identifying the short-wavelength shift of this structure with the temperature lowered to 4 K. The solid arrow refers to the pump-photon energy of the Nd^{3+}:YAG-laser second harmonic.

1. EXPERIMENTAL

$Cd_{1-x}Mn_xTe$ crystals with x varying from 0.4 to 0.7 were grown by a modified Bridgman technique. The crystals were pumped by the second and third harmonics of a Nd^{3+}:YAG laser with a pulse width $\tau_{ex}=0.12\,\mu s$ and pulse repetition frequency of 1 kHz. The number of $h\nu_0=2.35$-eV second-harmonic photons in a pulse was 4×10^{13}, and the maximum excitation level was 5 kW/cm^2. A cw Ar ion laser was used to probe luminescence at low excitation levels. The luminescence was usually measured in the cw mode.

2. RESULTS AND THEIR DISCUSSION

None of the samples studied revealed any substantial difference between the saturation curves obtained at different points within the Mn^{2+} intraionic-luminescence band profile in the 4–77 K interval, and therefore we shall present in what follows data relating only to the maximum of the 2.0-eV band. Figures 2–4 display intraionic-luminescence saturation curves measured on $Cd_{1-x}Mn_xTe$ samples with $x=0.4$, 0.5, 0.6, and 0.7 under pulsed excitation within a broad excitation-level range J_{ex} (second harmonic) at 4 and 77 K. The luminescence is seen to saturate in all samples excited by the third harmonic as well (photon energy 3.51 eV). Studies carried out under weak cw excitation show that the band saturates already at J_{ex} on the order of a few W/cm^2.

For comparison, we measured the dependence of the intensity of exciton interband luminescence peaking at E_{1s} on excitation level in a $Cd_{0.7}Mn_{0.3}Te$ crystal, where $E_{1s}<E_t$ and, hence, there is no intracenter luminescence at all. At low pumping levels this dependence is superlinear, it becomes linear at higher excitations and does not change up to the maximum value of J_{ex} used in the experiment. Thus there is no saturation of the interband exciton luminescence. This result correlates with theory predicting superlinear dependence of interband luminescence for weak excitations when one takes into account the trapping of nonequilibrium carriers at defect or impurity levels, and a linear one for higher pumping, where the impurity channel saturates. The significance of impurity levels in $Cd_{1-x}Mn_xTe$ DMSs grown by the Bridgman technique is supported by the efficient excita-

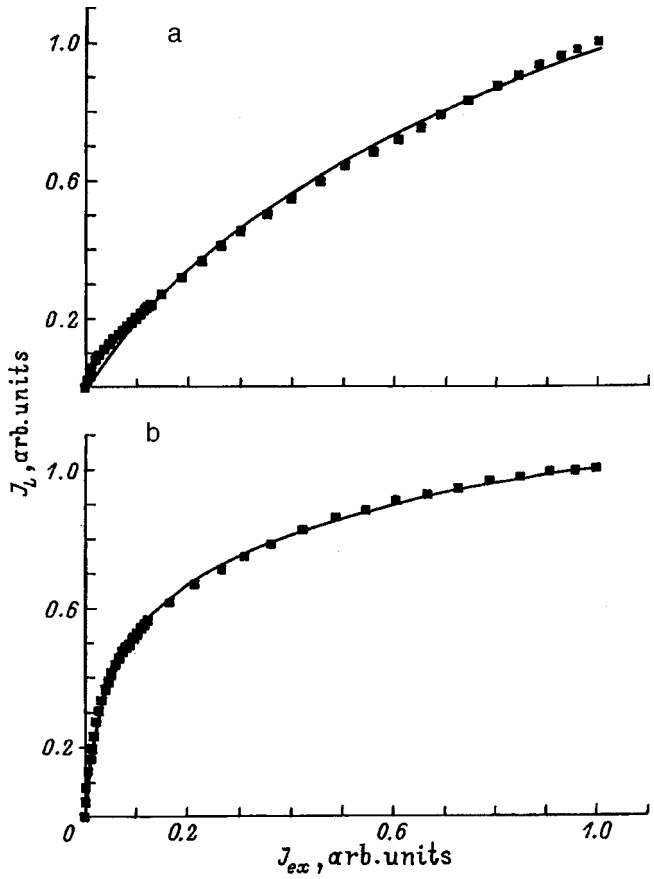

FIG. 2. Intracenter luminescence intensity of Mn^{2+} ions in $Cd_{0.6}Mn_{0.4}Te$ *vs* pulsed excitation intensity by the Nd^{3+}:YAG-laser second harmonic at (a) 77 K and (b) 4 K. Solid lines are plots of Eq. (1) with the β parameter equal to 42 (a) and 112 (b), and J_{ex} normalized to unity. The $J_{ex}=1$ level in Figs. 2–4 corresponds to a pump density of 5 kW/cm^2.

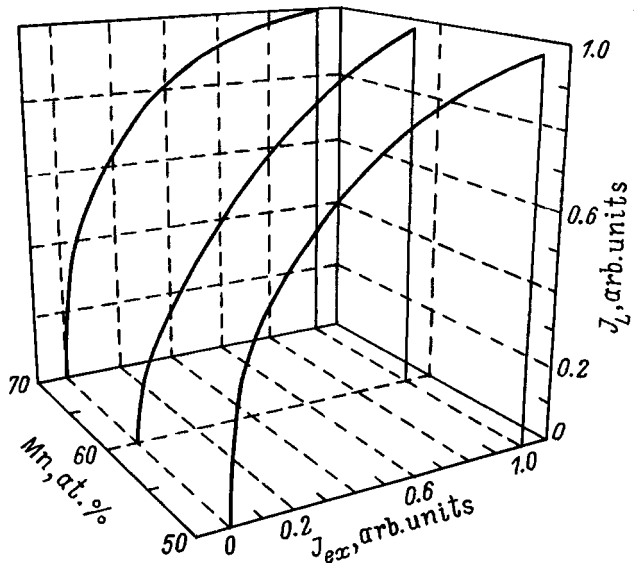

FIG. 3. Intracenter luminescence intensity of Mn^{2+} ions in $Cd_{1-x}Mn_xTe$ with $x=0.5, 0.6$, and 0.7 vs pulsed excitation intensity by the Nd^{3+}:YAG-laser second harmonic at 77 K.

tion at low temperatures of luminescence, both intracenter and interband, in $x=0.4$ samples by a helium-neon laser with photon energy of 1.96 eV, which is lower than E_t and $E_g(0.4)$.[8] Under such excitation, the dependence of the Wannier exciton luminescence intensity on J_{ex} is quadratic. Because J_{ex} is too low to produce two-photon excitation, this experimental result should be interpreted as two-stage excitation of electrons and holes through impurity levels.

As seen from Figs. 2–4, at 4 K the Mn^{2+} luminescence saturation sets in the fastest in the $x=0.4$ sample, while within the $0.5<x<0.7$ interval the saturation occurs more slowly and depends only weakly on x. Heating up a sample from 4 to 77 K slows down strongly the luminescence saturation for $x=0.4$ while accelerating it for $x=0.5-0.7$.

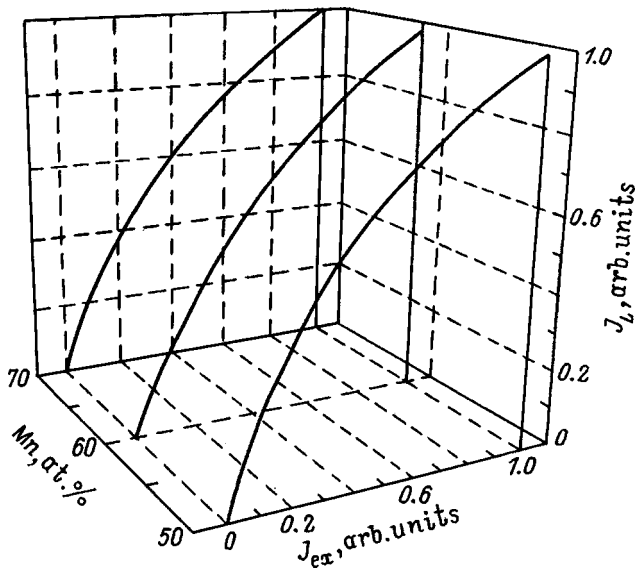

FIG. 4. Intracenter luminescence intensity of Mn^{2+} ions in $Cd_{1-x}Mn_xTe$ with $x=0.5, 0.6$, and 0.7 vs pulsed excitation intensity by the Nd^{3+}:YAG-laser second harmonic at 4 K.

In $Cd_{1-x}Mn_xTe$ with $x>0.5$, the maximum number of Mn^{2+} ions that can simultaneously reside in excited state can be readily estimated because one knows the ion concentration (10^{22} cm^{-3}), the absorption coefficient α in the manganese bands at the pump frequency (10^2 cm^{-1}), the lifetime of the Mn^{2+} ion in excited state τ_0, and the characteristics of optical excitation (when operating in the pulsed regime, one knows the number of photons per laser pulse, whose duration is much shorter than τ_0, and the pulse separation which exceeds substantially τ_0). The α parameter for $Cd_{0.6}Mn_{0.4}Te$ has a different meaning, namely, it characterizes the efficiency of the process consisting in the excitation of interband transitions with subsequent transfer of this excitation to the Mn^{2+} ions. Estimates show that even if every absorbed photon is expended in the final count in promoting the Mn^{2+} ion from the ground to the $^4T_1(G)$ excited state, saturation should be observable already after only a small fraction of the manganese ions present in a crystal layer about α^{-1} thick have become excited.

Luminescence saturation at low excitation levels can occur if, as a result of inhomogeneous broadening, monochromatic light excites selectively only a small fraction of ions, and migration of the excitations is strongly limited (below 60 K, a Frenkel exciton can change during its lifetime only two or three sites[4]). In $Cd_{1-x}Mn_xTe$ solid solutions with x from 0.4 to 0.7, random potentials associated with fluctuations of local values of x and various defects should produce a noticeable inhomogeneous broadening of the Mn^{2+} levels. In principle, all this assumes selectivity of excitation and its efficient localization. The complex systems of excited Mn^{2+} levels split by the exchange and crystal fields, however, overlap strongly for ions acted on by different local fields. Moreover, the phonon-initiated migration of excitation among manganese ions in $Cd_{1-x}Mn_xTe$ becomes strongly enhanced above 60 K,[4] which, if considered within the above conditions of rapid saturation, should favor its temperature-induced suppression. At the same time, experiment yields an opposite result, namely, for all samples (except $Cd_{0.6}Mn_{0.4}Te$, which will be dealt with later on) saturation at 77 K is much more efficient than that at 4 K.

Saturation of the Mn^{2+} intraionic luminescence can result from nonlinear quenching by the following sequences. After the already excited ion has captured one more Frenkel exciton, its energy is expended in raising the ion to a still higher excited state, thus reducing the quantum yield of the luminescence in the 2.0-eV band. This assumes a faster luminescence saturation at high temperatures, where the migration of Frenkel excitons is strong. Another possible mechanism involves absorption of the second photon by an already excited Mn^{2+} ion during a laser pulse. Here the high oscillator strength of the dipole-allowed optical transition from the excited $^4T_1(G)$ state to a still higher state may become an important factor. In this case the photon-capture cross section by an excited ion exceeds by far that by an unexcited ion involving an intercombination transition from the ground state $^6A_1(S)$ to G-type excited states.

Consider now the relation describing the saturation of manganese intraionic luminescence with inclusion of the mechanisms of its nonlinear quenching. During a laser pulse

$\tau_{ex} \ll \tau_0$ long, the excited manganese-ion concentration n increases

$$dn/dt = \alpha J_{ex}/h\nu_0 .$$

At the end of the pulse, the excited-ion concentration becomes

$$n_0 = \alpha \tau_{ex} J_{ex}/h\nu_0 .$$

After the end of the pump pulse, i.e., starting from the moment $t = \tau_{ex}$, the ion system begins to relax to ground state

$$dn/dt = -wn - qn^2 ,$$

$$w = (1/\tau_0 + w_d) .$$

Here the rate of linear relaxation w is a sum of that of radiative recombination $1/\tau_0$ and of nonradiative relaxation w_d, which is determined, in particular, by the probability for a Frenkel exciton migrating among the Mn^{2+} ions to encounter the quenching centers, such as iron ions etc. Parameter q determines the efficiency of nonlinear quenching by above mechanisms. Setting as the initial condition $n|_{t=0} = n_0$, we have

$$n(t) = w \exp(-wt)/q[(w/qn_0 + 1) \times \exp(-w\tau_{ex}) - \exp(-wt)] .$$

Because the linear relaxation rate is not faster than $1/\tau_0$, it is in order of magnitude not less than 10^5 s^{-1}, i.e., $w\tau_{ex} \ll 1$, so that $\exp(-w\tau_{ex})$ differs very little from unity. In the cw mode of luminescence measurement, one determines experimentally an integrated value proportional to

$$\int_0^\infty n(t)dt = q^{-1}\ln(1 + qn_0/w) ,$$

and, thus, the dependence of the luminescence intensity on excitation level can be written

$$J_L = J_0 \ln(1 + \beta J_{ex}) , \quad (1)$$

where $\beta = \alpha q n_0/wh\nu_0$ is a parameter characterizing the luminescence saturation rate. Figure 2 compares the experimental data on luminescence saturation with relation (1) using β as a fitting parameter.

Consider now in more detail the difference between the cases of $x = 0.4$ and $x = 0.5-0.7$. For $x > 0.5$, the second harmonic of the Nd^{3+}:YAG laser excites only $Mn^{2+}3d$ intrashell transitions, because the photon energy $h\nu_0$ is less than the energy $E_g(x)$ of the interband transition and of the associated Wannier-exciton level E_{1s}. For $x = 0.4$, however, E_{1s} becomes approximately equal to E_t, and both these energies are less than $h\nu_0$, so that light will now directly pump predominantly the interband transitions, for which the absorption coefficient is two orders of magnitude larger than that for intraionic intercombination transitions. Under these conditions, Wannier excitons will form in a thin near-surface layer, and they will promote manganese ions to the $^4T_1(G)$ excited state through resonant energy transfer. The inverse process cannot operate because of the fast energy relaxation of this excited state to equilibrium in a time of the order of 10^{-11} s (the Stokes losses). As seen from Fig. 1, the Wannier exciton level in our $x = 0.4$ sample coincides exactly at 77 K with the threshold of the $Mn^{2+}3d$ intrashell transitions. Cooling $Cd_{1-x}Mn_xTe$ from 77 to 4 K practically does not affect the position of the intraionic absorption bands, but E_g increases. As a result, the Wannier exciton level E_{1s} in $Cd_{0.6}Mn_{0.4}Te$ shifts from the low-energy edge of the first absorption band of Mn^{2+} toward its maximum (Fig. 1). The density of Mn^{2+} electronic states at the new position of E_{1s} is substantially higher, which accelerates resonant energy transfer from Wannier excitons to Mn^{2+} ions. It is this factor that is apparently dominant, and saturation of intracenter luminescence in $Cd_{0.6}Mn_{0.4}Te$ is achieved faster with decreasing temperature.

In samples with $0.5 < x < 0.7$, $E_g(x) > h\nu_0$, which makes possible direct excitation of the $Mn^{2+}3d$ intrashell transition and for which case the excitation efficiency is only weakly temperature dependent. At the same time the temperature-induced enhancement of Frenkel-exciton migration among manganese ions makes their encounter with already excited Mn^{2+} ions more probable, thus accelerating the luminescence saturation. As for the concentration dependence of the saturation rate of the Mn^{2+} luminescence within the $0.5 < x < 0.7$ interval, it is determined by such concentration-dependent factors as the rate of excitation migration among manganese ions and the magnitude of the solid-solution fluctuation potentials.

Thus the most probable reason for the Mn^{2+} luminescence saturation observed in $Cd_{1-x}Mn_xTe$ DMSs with $x = 0.4-0.7$ is the nonlinear quenching associated with migration of Frenkel-type excitons and photon absorption by already excited manganese ions. The experimentally observed very rapid saturation of the Mn^{2+} luminescence in DMSs requires a comprehensive analysis of the efficiency of the above mechanisms.

[1)] The energy level system of the $Mn^{2+}3d$ shell and its optical manifestations were studied comprehensively in the weakly-doped ZnS:Mn^{2+} wide-gap semiconductor (see, e.g., Refs. 11 and 12).

[1] O. Goede and W. Heimbrodt, Phys. Status Solidi B **146**, 11 (1988).
[2] J. K. Furdyna, J. Appl. Phys. **64**, R29 (1988).
[3] P. A. Wolff, *Semiconductors and Semimetals*, Vol. 25, edited by J. K. Furdyna and J. Kossut (Academic Press, London, 1988).
[4] E. Müller, W. Gebhardt, and V. Gerhardt, Phys. Status Solidi B **113**, 209 (1982).
[5] V. F. Agekyan, Yu. V. Rud', and R. Schwabe, Fiz. Tverd. Tela (Leningrad) **29**, 1685 (1987) [Sov. Phys. Solid State **29**, 970 (1987)].
[6] D. Some and A. V. Nurmikko, Phys. Rev. B **48**, 4418 (1993).
[7] V. F. Agekyan, Fan Zung, and S. V. Pogarev, Fiz. Tverd. Tela (Leningrad) **29**, 3312 (1987) [Sov. Phys. Solid State **29**, 1900 (1987)].
[8] V. F. Agekyan and Fan Zung, Fiz. Tverd. Tela (Leningrad) **30**, 3150 (1988) [Sov. Phys. Solid State **30**, 1812 (1988)].
[9] D. R. Yakovlev and K. V. Kavokin, Comments Condens. Matter Phys. **18**, 51 (1996).
[10] F. F. Agektan and Fan Zung, Fiz. Tverd. Tela (Leningrad) **27**, 1216 (1985) [Sov. Phys. Solid State **27**, 732 (1985)].
[11] W. Busse, H.-E. Gumlich, B. Meissner, and D. Theis, J. Lumin. **12/13**, 693 (1976).
[12] H.-E. Gumlich, J. Lumin. **23**, 73 (1981).

Translated by G. Skrebtsov

Orientation-dependent Faraday effect in thin films of porous silicon

M. E. Kompan* and I. Yu. Shabanov

A. F. Ioffe Physicotechnical Institute, Russian Academy of Sciences, 194021 St. Petersburg, Russia

Ya. Salonen

Turku University, Turku, Finland
(Submitted July 14, 1998)
Fiz. Tverd. Tela (St. Petersburg) **41**, 54–56 (January 1998)

[S1063-7834(99)01301-5]

According to a recent analytical review, the stream of papers on porous silicon is comparable to that on the fundamental problem of high-temperature superconductivity.[1] This is due in no small part to the ''inexhaustibility'' of this material, whose unusual properties are of interest for the most diverse disciplines in physics, chemistry, and technology.

The present paper calls attention to another group of properties of this material that investigators have essentially ignored up to now — the magnetic properties of porous silicon (*P*Si). Only a few works on this subject exist. As happens for porous silicon, the authors of the various works arrive at opposite conclusions. This is understandable in that the general term ''porous silicon'' encompasses the entire class of materials which differ among each other not only by the composition and the characteristics of quantum-size elements (''wires'') but also by the structure and the topology of the material at the mesoscopic level. However, disagreements should not serve as a basis for rejecting the investigations.

The result of two works suggest that *P*Si and its closest analog, obtained in an electric discharge, possess special magnetic properties. In the first one a SQUID magnetometer was used to detect a magnetic moment and hysteresis of magnetization of *P*Si in an external magnetic field.[2] In the second one a magnetic field dependence with characteristic hysteresis was observed in the intensity of luminescence for a modification of silicon treated with a spark discharge.[3] The difference between the samples and the fragmentary nature of the information in Ref. 3 make it impossible to analyze the results of Refs. 2 and 3 and to compare them with our experimental results. However, these works motivated the present investigation, and taken together with our work they provide sufficient proof that porous silicon possesses nontrivial magnetic properties. (We note that at the same time in a large number of works, including in works specially devoted to this question, for example, Ref. 4, no peculiarities were found in the magnetic properties of *P*Si.)

Our choice of the Faraday effect for characterizing the magnetic properties of *P*Si is due to the fact that this effect is more directly related with magnetization than is the luminescence intensity and, at the same time, in contrast to SQUID, it excludes the detection of magnetic moments of ancillary particles and adsorbates.

1. EXPERIMENTAL TECHNIQUE AND SAMPLES

The experimental samples were free films of porous silicon, less than 1 cm in width, secured in a rigid plastic holder. The samples were obtained by etching [100] wafers of *n*-type silicon with resistivity $0.015-0.025\ \Omega$/cm in a 1:1 mixture of 38% hydrofluoric acid and absolute alcohol, using anodic bias of the sample relative to the etching solution and simultaneously illuminating with light from a halogen lamp the sample undergoing etching. The etch current density was 75 mA/cm^2. The current density increased by an order of magnitude after 6–10 min of etching. This caused the free film of porous silicon to separate from the parent crystal. The samples were of the order of 0.05 mm thick, which gave an optical transmission of about 1/3, close to the optimal value for Faraday rotation experiments, at wavelength 6328 Å . This same value, 0.05 mm, was used to estimate the relative rotation of the plane and the polarization in the experimental *P*Si samples.

A block diagram of the apparatus used to investigate the magnetic rotation of the polarization plane is displayed in Fig. 1. The light source was a 2 mW He–Ne laser (*1*) with an additional light polarizer (*2*). A 3.8 kG magnetic field was produced with a laboratory electromagnet (*3*), whose design made it possible to transmit light along the field lines into the gap. The signal corresponding to the angle of rotation of the polarization plane was detected using a differential scheme, thereby eliminating spurious signals due to the variation of the intensity of the laser. After passing through the sample (*4*), the light beam passed through a special polarizing prism (*5*) that split the beam into two beams polarized orthogonally with respect to one another and at an angle of 45° with respect to the initial beam. The rotation of the polarization plane in the sample increases the intensity of one beam and decreases the intensity of the second beam. The difference electric signal proportional to the rotation angle was extracted off the diagonal of the bridge, where two photodetectors (*6*, *7*), which recorded the intensity of each beam at the exit of the splitting prism, were connected. The detection sensitivity to the rotation angle for transparent samples was 10^{-4} rad.

The samples could rotate in the gap between the poles. The rotation axis was also the direction of polarization of the transmitted light. This reduced the possible depolarization

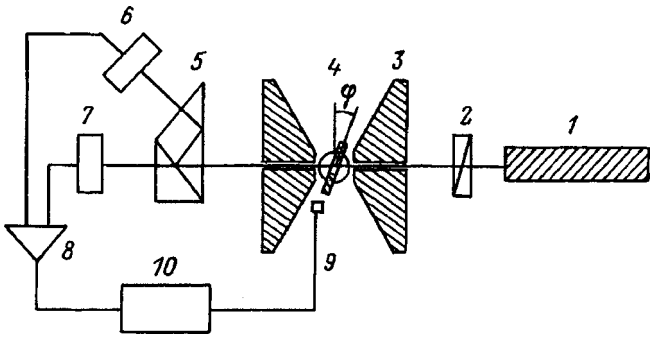

FIG. 1. Block diagram of the apparatus for measuring Faraday rotation. *1* — He–Ne laser, *2* — polarizer, *3* — electromagnet, *4* — sample, *5* — polarizing prism–beam splitter, *6,7* — photodetectors, *8* — differential amplifier, *9* — magnetic field sensor, *10* — detection unit.

accompanying rotations of the sample to a minimum. The experiments were performed at room temperature.

2. EXPERIMENTAL RESULTS AND DISCUSSION

The experiments showed the existence of a substantial Faraday effect in the experimental samples of porous silicon. The signal due to the rotation of the polarization plane with normal incidence of light on the film in the range of fields employed corresponded to a Verdet constant of 0.15″/G·cm. A saturated solution of iron chloride has a comparable Verdet constant — 0.2″/G·cm (Ref. 6). The rotation angle depended linearly on the applied magnetic field.

The dependence of the Faraday rotation on the rotation angle of the sample was unusual (deviations of the normal to the surface from the direction of the magnetic field lines). As shown in Fig. 2, for porous silicon the signal decreases to the noise level of the apparatus for rotation angles of the sample of the order of 30°. At the same time, the same dependence for a standard diamagnetic material is of a completely different character: The rotation signal from the quartz plate even increased somewhat as the plate turned in the field. Thus, two facts — the substantial magnitude of the effect and the anomalous angular dependence — are unusual and require explanation.

3. DISCUSSION

Since the experiments were designed from the onset to obtain independent data on the unusual magnetic properties of porous silicon, and taking account of Refs. 2 and 3, it is natural to attempt an interpretation of the results in terms of the magneto-optics of a ferromagnetic material.

All the basic facts of this paper can be easily interpreted in these terms. The linear dependence of the rotation angle on the intensity of the applied field is a shape effect: In a field applied in a direction normal to the film surface, the effective magnetic permeability of a thin film should be 1. This means that for such a film the characteristics of the magnetization in the normal direction will be the same as for a nonmagnetic material, as was observed. The quite large Faraday rotation is probably due to the concentration of magnetic centers.

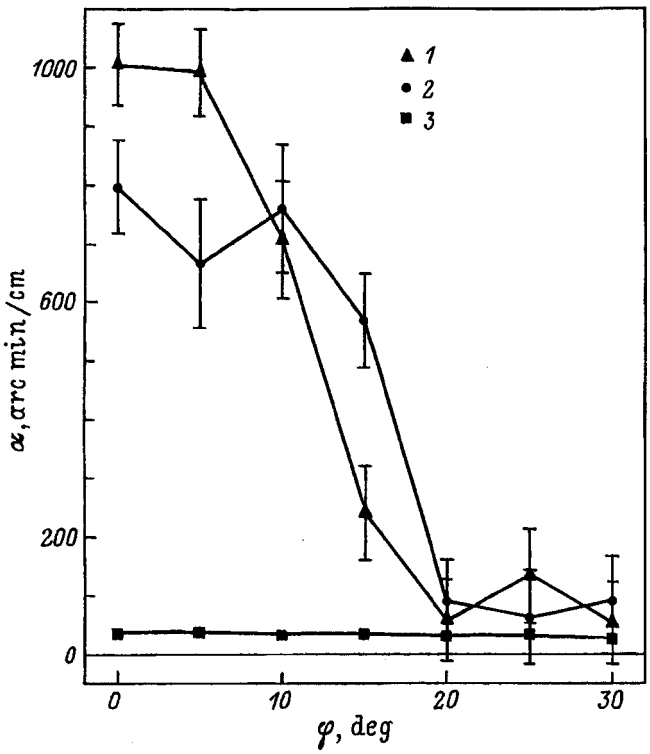

FIG. 2. Rotation angle α of the polarization plane in a 3.5 kG magnetic field versus the rotation angle φ of the sample relative to the direction of the field lines for free films of porous silicon (*1* — *P*Si film No. 1, *2* — *P*Si film No. 2) and a fused quartz plate (curve *3*).

The anomalous polarization dependence could be due to a superposition of diamagnetic and ferromagnetic (or paramagnetic) mechanisms. It can be shown that if the Faraday rotation of the material is due the sum of the diamagnetic and magnetic contributions and if the Verdet constants of these contributions have different signs, then for some angle of rotation of the sample in a field the diamagnetic and magnetic contributions should compensate one another. This is easy to understand qualitatively. As explained above, even a high magnetic permeability is not manifested for light incident in the normal direction. As the film rotates, the field in the film plane starts to increase, since the magnetic permeability in the film plane is high. However, for small angles of rotation this is not manifested in the Faraday effect, since on account of refraction the light will propagate in the film in a direction almost normal to the surface and the component of the light in the direction of the field will be almost zero. However, at some angle of rotation of the sample the paramagnetic and diamagnetic contributions will be almost equal in magnitude. For a diamagnetic material whose magnetic permeability is isotropic and close to 1 there should be no such effect — as is observed experimentally (Fig. 2).

The assumption used in the explanation that the signs of the Verdet constants are different for the dia- and paramagnetic (ferromagnetic) contributions corresponds to the typical situation — see, for example, Refs. 5 and 6.

We emphasize that we cannot draw any conclusions about the observation of ferromagnetism in *P*Si on the basis of our experiments. Our data show only a substantial Faraday effect with a Verdet constant of the order of 0.15″/G·cm

and a substantial magnetic permeability in the film plane.

In summary, a magneto-optic Faraday effect was observed in films of porous silicon. A number of characteristics of this effect can be easily explained assuming that this material is ferromagnetic. Together with the results of Refs. 2 and 3, this would seem to be quite probable. However, the many works in which no magnetism in porous silicon was observed should not be overlooked. More complicated models, not requiring any assumptions about ferromagnetic order, for interpreting the experimental data are possible. However, it is clear from the existing results that the magnetic properties of porous silicon are not trivial and require further study.

*E-Mail: kompan@solid.pti.spb.su

[1] Vera Parkhutic, in *International Conference on Porous Semiconductors. Extended Abstracts*, Majorka, 1998, Abstract P2-23, p. 232.
[2] R. Laiho, E. Lahderanta, L. Vlasenko, and M. Afanasiev, J. Lumin. **57**, 197 (1993).
[3] R. E. Hummell, M. E. Stora, N. Shepherd, and S. Yu., in *International Conference on Porous Semiconductors (PSST-98). Extended Abstracts*, Majorka, 1998, Abstract O-42, p. 76.
[4] C. Y. Perry, F. Lu, F. Namavar, N. Kalhoran, and R. Soret, Appl. Phys. Lett. **60**, 3117 (1992).
[5] D. I. Sivukhin, *Optics*, Nauka, Moscow (1985), 751 pp.
[6] G. W. C. Kaye and T. H. Laby, *Tables of Physical and Chemical Constants* [London, 1941; Inostr. Lit., Moscow, 1949], 299 pp.

Translated by M. E. Alferieff

Electronic structure of lithium tetraborate $Li_2B_4O_7$ crystals. Cluster calculations and x-ray photoelectron spectroscopy

A. Yu. Kuznetsov,*) A. V. Kruzhalov, I. N. Ogorodnikov, and A. B. Sobolev

Ural State Technical University, 620002 Ekaterinburg, Russia

L. I. Isaenko

Institute of Single Crystals, Siberian Branch of the Russian Academy of Sciences, 630058 Novosibirsk, Russia

(Submitted June 17, 1998)
Fiz. Tverd. Tela (St. Petersburg) **41**, 57–59 (January 1999)

The results of an investigation of the electronic structure of lithium tetraborate crystals using experimental (x-ray photoelectron spectroscopy) and theoretical (quantum-chemical modeling) methods are reported. The experimental spectrum of the valence-band states of the crystal lies 2–15 eV below the Fermi level and is due primarily to boron-oxygen groups (B_4O_9). The quantum-chemical calculations were performed self-consistently, using the standard variant of the scattered-wave method in the model of a cluster embedded in a lattice of point charges. The data obtained on the partial contribution of the model densities to the one-electron spectrum of the $[B_4O_9]^6$ cluster make it possible to interpret the fine structure of the experimental spectrum of the valence-band states.
[S1063-7834(99)01401-X]

Lithium tetraborate $Li_2B_4O_7$ (LTB) possesses a combination of physical properties which are important for practical applications, and it finds wide application in various fields of science and technology. For example, it is a promising material for piezotechnology, acoustoelectronics,[1] and nonlinear optics.[2] In addition, Mn- or Cu-activated $Li_2B_4O_7$ crystals are widely used as tissue-equivalent thermoluminescence dosimeters.[3] Their undisputed advantages are high radiation-optical hardness, wide transmission band, and mechanical strength. Investigations of the electronic structure of LTB are a topical problem which is important for practical applications, because the fundamental properties of LTB that are responsible for the characteristic processes leading to the dissipation of excitation energy and nonlinear-optical phenomena are still not completely understood. At the present time only isolated works on the electronic structure of lithium tetraborate exist.[4]

Our objective in the present work is to study the electronic structure of $Li_2B_4O_7$ crystals using experimental (x-ray photoelectron spectroscopy — XPS) and theoretical (quantum-chemical modeling) methods.

1. EXPERIMENTAL OBJECTS AND METHODS

The $Li_2B_4O_7$ crystals were Czochralski grown from stoichiometric melt using up to 200 cm^3 platinum crucibles. After the recrystallized reactant of pure-grade $Li_2B_4O_7$ and the required holding period, the temperature was lowered to the melting point 917 °C. The crystals were grown on seeds with different orientation and a pulling velocity of up to 3 mm/day and rotational speed of the order of 20 rpm. For a 15-day growth period, the typical dimensions of the $Li_2B_4O_7$ crystals were 35×40 mm in diameter and up to 70 g in mass. The XPS investigations of freshly cleaved samples were conducted in an ESCALAB MK II spectrometer using a nonmonochromatic Mg $K\alpha_{1,2}$ source. The vacuum in the analyzer chamber was maintained at 10^{-8} Pa. The binding energy was determined to within ± 0.1 eV. The electric charging of the surface of the samples was estimated according to the $C\ 1s$ (284.6 eV) line.

The quantum-chemical calculations were performed self-consistently on the basis of the standard variant of the scattered-wave method[5] in the model of a cluster embedded in a lattice of point charges.[6] The embedding Coulomb potential was constructed taking into account the translational invariance of the entire crystal. The exchange potential was chosen in a local form in accordance with the exchange-correlation energy density proposed in Ref. 7. The radii of the muffin-tin spheres touched one another, and the outer sphere was chosen from the condition that the muffin-tin spheres of the peripheral ions of the cluster touch. Since we were interested only in the filled states, the localizing potential was chosen in the form of a Watson-sphere potential, whose charge was equal in magnitude and opposite in sign to that of the cluster. Harmonics up to $L=1$ for the inner ions of a cluster and $L=4$ for the outer sphere were included in the partial-wave expansion.

Lithium tetraborate crystals belong to the space group $I4_1cd$ and possess 104 atoms per unit cell. The main crystal motif of LTB are boron-silicon complexes (B_4O_9), consisting of two planar trigonal (BO_3) and two tetrahedral (BO_4) groups. The lithium atoms are localized at interstices.[8]

The debatable aspect of the cluster model is the choice of a cluster. The anionic group $[B_4O_9]^{6-}$ (Fig. 1) was chosen as the fragment modeling the ideal crystal; the coordinate

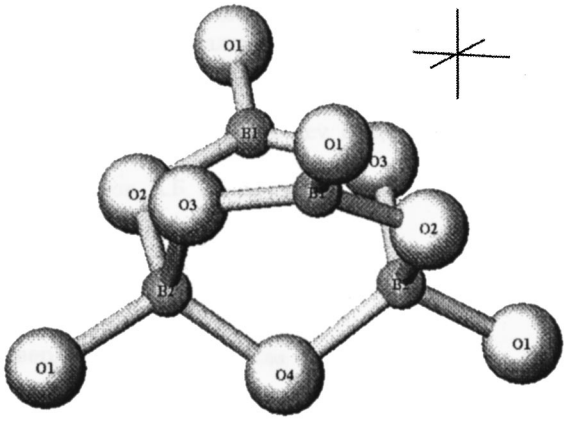

FIG. 1. Basic crystallographic motif of an $Li_2B_4O_7$ crystal — boron-oxygen complex (B_4O_9).

origin was placed on the O(4) atom. The model cluster possessed local C_1 symmetry. In a previous work, we obtained satisfactory results in calculations of low-symmetry clusters[9] in oxide crystals. This was the methodological basis for using a cluster model in the present case. In Ref. 10 it is shown that lithium in LTB crystals stabilizes the framework structure of the crystal, and its makes only a negligible contribution to the formation of the valence band (VB) of the crystal. This justifies the choice of a $[B_4O_9]^{6-}$ cluster to describe the structure of the valence-band top.

2. RESULTS AND CONCLUSIONS

The XPS spectrum of $Li_2B_4O_7$ crystals is displayed in Fig. 2a. It consists of two subbands. The band with three characteristic peaks 2–15 eV below the Fermi energy E_f corresponds to the VB states of the crystal. The peak near 25 eV below E_f corresponds to O 2*s* quasicore states. We also obtained the values of the binding energies of the core levels — 55.7, 192.4, and 531.8 eV for Li 1*s*, B 1*s*, and O 1*s*, respectively. The XPS investigations of the surface layer of LTB (3–5 nm), including using ionic cleaning of the surface layer, showed that the elemental composition found from the ratio of the core lines, taking account of the photoionization cross sections, agrees with the formula composition. Analysis of the data on elemental composition and on the binding energies of the core levels[11] shows that there are no compounds of a nonstructural character in the surface layer.

Let us analyze the computational results for the single-electron energies of the molecular orbitals of a $[B_4O_9]^{6-}$ cluster in comparison with our XPS data (Fig. 2a). The total and partial model densities of states of a $[B_4O_9]^{6-}$ cluster are presented in Figs. 2b–2e (the results shown included a Gaussian modification of the linewidth). The computational results agree satisfactorily with the experimental data on both the shape and energy position of the lines. We shall analyze separately the band in the XPS spectrum in the energy range 2–15 eV below E_f. This band belongs to the VB of an ideal crystal (Fig. 2a), peaks *A*, *B*, and *C*). We shall perform the analysis in comparison with the partial contributions of the VB states for the cluster $[B_4O_9]^{6-}$ to the resulting single-electron spectrum (Fig. 2c–2e). The complicated

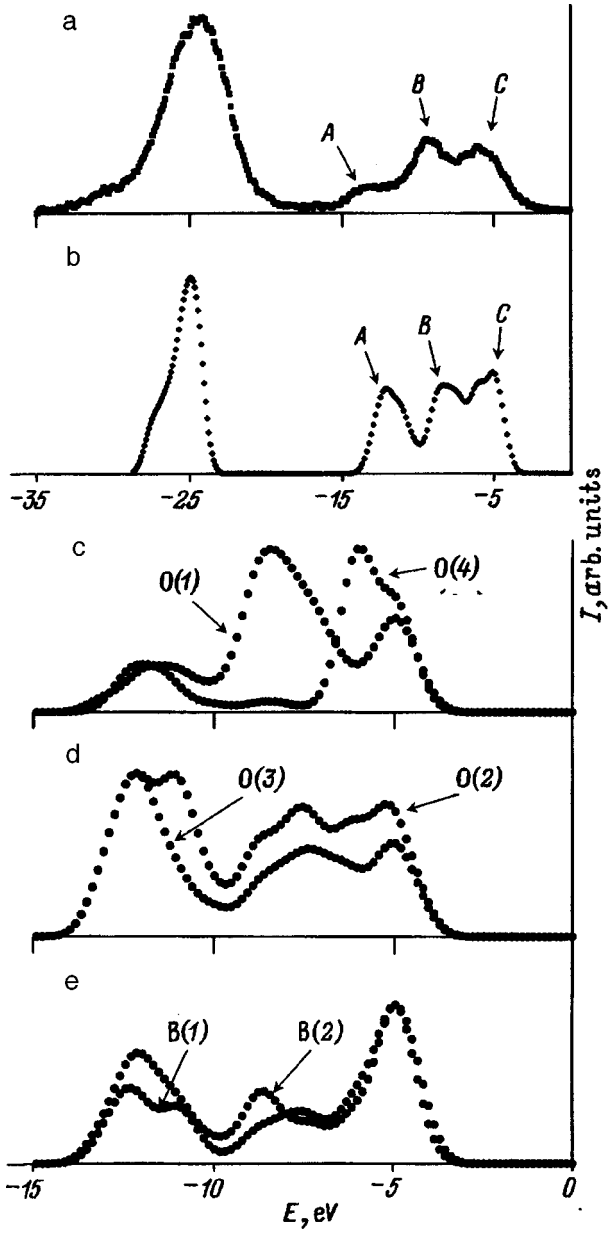

FIG. 2. X-Ray photoelectron spectrum of $Li_2B_4O_7$ (a), model one-electron densities of states of a $[B_4O_9]^{6-}$ cluster (b), O(1) and O(4) atoms (c), O(2) and O(3) atoms (d), and B(1) and B(2) atoms (e).

shape of the density of states obtained in the cluster calculation is due to the existence of different types of oxygen bonds ($2p$ molecular orbitals of the π and σ type, bonding and antibonding), which form with different angular dependences of the wave functions of a $[B_4O_9]^{6-}$ cluster and nonequivalence of oxygen atoms in a cluster (four nonequivalent positions). Evidently, the presence of several peaks in the XPS spectrum of the VB states in the crystal can be explained by both the crystallographic and specific crystal-chemical role of various oxygens in the formation of the framework structure of the crystal as a whole.[10] The oxygen atoms O(2) and O(3) in the complex (B_4O_9) join each B(1) triangle with two B(2) tetrahedra, which have an O(4) atom in common. The structural complexes form a framework structure by generalization of the O(1) atoms. According to

the data presented in Fig. 2d, the O(2) and O(3) atoms have similar partial densities of states and make a large contribution to the formation of the peak *A* in the valence band (Fig. 2a and 2b). The partial densities of states presented in Fig. 2c attest to a large contribution of O(1) atoms to the formation of the peak *B* and O(4) atoms to the peak *C* in the valence band. It should also be noted that according to our data the boron atoms make only a negligible contribution to the formation of the VB of the crystal.

Thus, the following conclusions can be drawn from our experimental and theoretical investigations of the electronic structure of the lithium tetraborate crystals.

1) The x-ray photoelectron spectrum of the VB of the LTB crystal lies 2–15 eV below the Fermi level and is due primarily to the boron-oxygen groups (B_4O_9).The XPS investigations showed that there are no compounds of nonstructural character in the surface layer; the elemental composition is identical to the formula composition. The XPS spectra obtained reflect the electronic structure of the $Li_2B_4O_7$ single crystal itself.

2) The calculations performed agree well with the experimental data from XPS investigations. This shows that cluster models based on the local density functional approximation can be used in theoretical investigations of the electronic structure of this crystal.

3) The data obtained on the partial contribution of model densities to the one-electron spectrum of the cluster $[B_4O_9]^{6-}$ permit interpreting the fine structure of the experimental spectrum of the VB states. Specifically, it can be concluded that anions playing a specific crystal-chemical role in the formation of the framework structure of the crystal as a whole make substantially different contributions to the density of states of the crystal.

This work was supported by the program INCO COPERNICUS (Grant IC15CT960721) and Grants 98-03-33195a from the Russian Fund for Fundamental Research.

We are grateful to M. V. Kuznetsov and O. I. Yakovleva for assisting in this work.

*)E-mail: kay@dpt.ustu.ru

[1] A. S. Bhalla, L. E. Cross, and R. W. Whatmore, Jpn. J. Appl. Phys. **24**, *Suppl. 24–2*, 727 (1985).
[2] R. Komatsu, T. Sugawara, K. Sassa, N. Sarukura, Z. Liu, S. Izumida, Y. Segawa, S. Uda, T. Fukuda, and K. Yamanouchi, Appl. Phys. Lett. **70**, 3492 (1997).
[3] D. R. Vij [Ed.], *Thermoluminescent Materials*, PTR Prentice-Hall, Inc. (1993), 452 pp.
[4] Ya. V. Burak, Ya. O. Dovgiĭ, and I. V. Kityk, Fiz. Tverd. Tela (Leningrad) **31**, 275 (1989) [Sov. Phys. Solid State **31**, 1634 (1989)].
[5] K. H. Johnson, Adv. Quantum Chem. **7**, 143 (1973).
[6] A. B. Sobolev, A. Yu. Kuznetsov, I. N. Ogorodnikov, and A. V. Kruzhalov, Fiz. Tverd. Tela (St. Petersburg) **36**, 1517 (1994) [Phys. Solid State **36**, 829 (1994)].
[7] S. H. Vosko, L. Wilk, and M. Nusair, Can. J. Phys. **58**, 1200 (1980).
[8] S. V. Radaev, L. A. Muradyan, L. F. Malakhova, Ya. V. Burak, and V. I. Simonov, Kristallografiya **34**, 1400 (1989) [Sov. Phys. Crystallogr. **34**, 842 (1989)].
[9] A. Yu. Kuznetsov, A. B. Sobolev, A. N. Varaksin, and O. A. Keda, Phys. Status Solidi B **204**, 701 (1997).
[10] R. H. French, J. W. Ling, F. S. Ohuchi, and C. T. Chen, Phys. Rev. B **44**, 8496 (1991).
[11] V. I. Nefedov, *Handbook of X-Ray Spectroscopy of Chemical Compounds*, Khimiya, Moscow (1984), 256 pp.

Translated by M. E. Alferieff

Quasiequilibrium states of solid solutions

M. A. Zakharov

Novgorod State University 173003 Novgorod, Russia
(Submitted February 9, 1998; resubmitted June 23, 1998)
Fiz. Tverd. Tela (St. Petersburg) **41**, 60–63 (January 1999)

A phenomenological theory of quasiequilibrium states of solid solutions with at least three components is constructed under the assumption that the atomic mobilities of the components differ in order of magnitude. The short-range parts of the interatomic interactions are taken into account by introducing atomic self-volumes. The long-range parts of the potentials are taken into account in the effective-field approximation. The equations for the quasiequilibrium components in the solutions are derived neglecting the mobility of the least mobile component. It is shown that, for a nonuniform distribution of this component, the nonequilibrium critical temperature ceases being unique within the sample and acquires a local character. In consequence, opposing processes occur in the system in the temperature interval between $T_c^{\min}$ and $T_c^{\max}$ — homogenization in some sections and formation of interphase boundaries in others. © *1999 American Institute of Physics.* [S1063-7834(99)01501-4]

Real physical systems of the solid solution type are, as a rule, strongly nonequilibrium. Specifically, nonequilibirum in solid solutions occurs if the maximum relaxation time in the system is longer than or of the order of the time elapsed from the moment the thermodynamic conditions have changed. In this respect the intermediate (quasiequilibrium) states of solid solutions with more than two components are of interest. A characteristic feature of multicomponent solutions is the hierarchy of atomic mobilities of the various components.[1,2] For an N-component system this makes it possible to introduce a set of characteristic times τ_1, τ_2, $\ldots$, τ_{N-1}, playing the role of relaxation times and related by a system of inequalities of the form $\tau_1 \ll \tau_2 \ll \ldots \ll \tau_{N-1}$. The significance of these characteristic times lies in the following.

The process whereby the system passes from a nonequilibrium into an equilibrium state occurs in stages. First, the distribution of the two highest-mobility components evolves, making their chemical potentials constant in space. Let τ_1 be the corresponding relaxation time. The less mobile components play the role of a ''medium.'' At the next stage with characteristic time τ_2 the evolution of the third (with respect to the mobility) component must be taken into account. The first two components, having the highest mobility, likewise become redistributed, their chemical potentials remaining constant in the process, while the less mobile components continue to play the role of the medium, and so on.

We shall call quasiequilibrium states of the system those states in which some components are distributed in space so that their chemical potentials are constant. Only some conditions of thermodynamic equilibrium are thereby satisfied in quasiequilibrium states, specifically, the conditions that can be reached in a relaxation time shorter than the time elapsed from the last change in the external thermodynamic parameters.

The quasiequilibrium states of solutions will be analyzed on the basis of a generalized lattice model[3] that takes account of the possible differences between the self-volumes of the components (volume effects) — on account of these differences the concept of a crystal lattice and the probability of occupation of lattice ''sites'' by different components become poorly defined. Correspondingly, the method of static concentration waves, which was proposed in Ref. 4 in the absence of volume effects in homogeneous solutions, needs to be generalized. The extension to the case of inhomogeneous solutions (neglecting volume effects) was done in Ref. 5 (see also Ref. 6).

1. GENERALIZED LATTICE MODEL AND EQUILIBRIUM STATES OF SOLUTIONS

We shall assume that the interatomic potentials in condensed systems can be divided into two parts: a) a short-range repulsive part, preventing atoms from approaching close to one another and taken into account below by introducing atomic self-volumes ω_i, and b) a long-range part, which can be taken into account in the mean-field approximation.

Such a phenomenological separation of the potentials into long and short ranges was evidently first introduced by van der Waals in his famous equation of state. The correct first-principles separation for one-dimensional model systems was done in Refs. 7–9.

Following Ref. 3, we introduce the local particle-number density $n_i(\mathbf{r})$ and the self-volume ω_i of a particle ($i=1,2,\ldots,m$, where m is the number of components in the system). If the self-volumes of all components of the system are the same, then it is possible to introduce the idea of a solid solution as a lattice whose sites are occupied with definite probabilities by the atoms of the components. We note that for homogeneous solutions the corresponding probabilities are given by the relations

$$P_i=\frac{n_i}{\Sigma_j n_j}. \tag{1}$$

For solid solutions there is a correlation in the arrangement of the atoms — two atoms cannot occupy the same lattice site, similar to the Pauli principle in coordinate space. Accordingly, in Ref. 10 a one-component distribution function is postulated in the form of a Fermi function

$$N(\mathbf{r})=[\exp\{-\beta\mu+\beta\Phi(\mathbf{r})\}+1]^{-1}, \tag{2}$$

where $\Phi(\mathbf{r})$ is the total potential produced at an atom at the site $\mathbf{r}$ by all other atoms, $\beta=1/T$, and μ is the chemical potential. We note that aside from a function of the type (2) there exist infinitely many other functions satisfying the ''Pauli principle.''

Instead of the postulate (2), we shall assume that the densities of the components are related by the relation

$$\sum_{i=1}^{m}\omega_i n_i(\mathbf{r})=1, \tag{3}$$

called in what follows the close-packing condition. This relation takes account of the strong repulsion of particles at short distances and, specifically, the upper limit on the densities

$$n_i(\mathbf{r})\leqslant\frac{1}{\omega_i}. \tag{4}$$

The Helmholtz free energy $F=F_0-TS$ for a system with m components can be written as follows in the regular-solution approximation:

$$F=F_0+T\sum_{i=1}^{m}\int n_i(\mathbf{r})\ln\left(\frac{n_i(\mathbf{r})}{n(\mathbf{r})}\right)dV, \tag{5}$$

where the integration extends over the entire volume V of the system, F_0 is the configuration part of the free energy, and

$$n(\mathbf{r})=\sum_{i=1}^{m}n_i(\mathbf{r}) \tag{6}$$

is the total particle number density.

We shall find the local chemical potential of the i-th component:

$$\mu_i(\mathbf{r})=\left(\frac{\delta F}{\delta n_i(\mathbf{r})}\right)_{n_j(\mathbf{r})}=\varphi_i(\mathbf{r})+T\ln\left(\frac{n_i(\mathbf{r})}{n(\mathbf{r})}\right), \tag{7}$$

where

$$\varphi_i(\mathbf{r})=\left(\frac{\delta F_0}{\delta n_i(\mathbf{r})}\right)_{n_j(\mathbf{r})}. \tag{8}$$

The condition that the i-th component is in chemical equilibrium (its chemical potential is constant) at a constant temperature gives, taking account of Eq. (7),

$$\varphi_i(\mathbf{r})+T\ln\left(\frac{n_i(\mathbf{r})}{n(\mathbf{r})}\right)=C_i, \tag{9}$$

where C_i are constants.

The configuration part of the free energy in the self-consistent field approximation taking account of only pair interactions is related with the distribution of the components as

$$F_0=\frac{1}{2}\sum_{i,j=1}^{m}\int\int V_{ij}(\mathbf{r}''-\mathbf{r}')n_i(\mathbf{r}'')n_j(\mathbf{r}')dV''dV', \tag{10}$$

where V_{ij} is the long-range part of the interatomic potentials. Hence we find $\varphi_i(\mathbf{r})$ as

$$\varphi_i(\mathbf{r})=\sum_{j=1}^{m}\int V_{ij}(\mathbf{r}-\mathbf{r}')n_j(\mathbf{r}')dV'. \tag{11}$$

Substituting the expression (11) into Eq. (9) we find

$$\sum_{j=1}^{m}\int V_{ij}(\mathbf{r}-\mathbf{r}')n_j(\mathbf{r}')dV'+T\ln\left(\frac{n_i(\mathbf{r})}{n(\mathbf{r})}\right)=C_i. \tag{12}$$

This system of nonlinear integral equations describes the equilibrium distributions of the components in solutions.

The situation is different in the case of quasiequilibrium distributions. Equations of the type (12) hold for components in a state of intermediate equilibrium, while the densities of less mobile components are fixed.

We shall consider ternary systems as a simple illustration.

2. QUASIEQUILIBRIUM STATES OF TERNARY SOLUTIONS AND THE LOCAL CRITICAL TEMPERATURE

The distribution of the components in a ternary system is given by the local particle number densities $n_1(\mathbf{r},t)$, $n_2(\mathbf{r},t)$, and $n_3(\mathbf{r},t)$. We shall enumerate the components in order of decreasing atomic mobilities.

On the time scale $\tau\sim\tau_1$ the distribution of the third (least mobile) component remains essentially unchanged ($n_3(\mathbf{r},t)\approx n_3(\mathbf{r},0)\equiv f_3(\mathbf{r})$) and the first two components arrive into a state of quasiequilibrium

$$\mu_i=\sum_{j=1}^{3}\int V_{ij}(\mathbf{r}-\mathbf{r}')n_j(\mathbf{r}')dV'+T\ln\left(\frac{n_i(\mathbf{r})}{n(\mathbf{r})}\right)=C_i,$$

$$(i=1,2). \tag{13}$$

Hence

$$n_1(\mathbf{r})=\frac{1-\omega_3 f_3(\mathbf{r})}{\omega_1}\left[\frac{\omega_2}{\omega_1}\exp\left(\frac{A_2(\mathbf{r})-A_1(\mathbf{r})}{T}\right)+1\right]^{-1},$$

$$n_2(\mathbf{r})=\frac{1-\omega_3 f_3(\mathbf{r})}{\omega_2}\left[\frac{\omega_1}{\omega_2}\exp\left(\frac{A_1(\mathbf{r})-A_2(\mathbf{r})}{T}\right)+1\right]^{-1} \tag{14}$$

where

$$A_1(\mathbf{r})=C_1-\sum_{j=1}^{3}\int V_{1j}(\mathbf{r}-\mathbf{r}')n_j(\mathbf{r}')dV',$$

$$A_2(\mathbf{r})=C_2-\sum_{j=1}^{3}\int V_{2j}(\mathbf{r}-\mathbf{r}')n_j(\mathbf{r}')dV'. \tag{15}$$

The relations (14) have a form similar (but not identical, because of volume effects) to the ''Fermi distribution'' (2).

The system of equations (14) extends the equations for the equilibrium distribution of the components in a binary system[11] to the case of a quasiequilibrium distribution of two components in a medium with a low-mobility third component.

In a binary system, phase separation can occur under well-known conditions[11] which are an extension of the Gor'skiĭ–Bragg–Williams criterion. Phase separation can also occur in ternary systems, but under quasiequilibrium conditions (i.e., with a fixed nonequilibrium distribution of the third component) the corresponding phenomena will likewise be nonequilibrium. Since it plays the role of an external field influencing a phase transition, a third component with a nonuniform distribution has a different effect at different points of the system. Specifically, the critical temperatures of a pseudobinary system with two mobile components and a fixed third component are different at different points of the system.

We shall confine ourselves to two simple particular cases: a) a uniform distribution of the third component and b) a nonuniform distribution of the third component with a scale of nonuniformity r_0 much larger than the range r_1 of the longest-range interatomic potential.

Let us consider the first particular case — a uniform distribution of the third component in the system: $f_3(\mathbf{r}) = f_3 =$ const. The branch point of the solutions of a system of two nonlinear equations, which corresponds to a phase transition in a quasibinary system, can be found by analyzing the system of equations (14). Separation of the initial homogeneous medium into two phases, each of which is described by the corresponding branch of the solution of the system (14), occurs below the critical temperature. These branches correspond to the same densities of the low-mobility component and different compositions relative to the first and second components.

To find the critical temperature we shall represent the local concentrations in the form

$$n_1(\mathbf{r}) = n_1^0 + \delta n_1(\mathbf{r}), \quad n_2(\mathbf{r}) = n_2^0 + \delta n_2(\mathbf{r}), \tag{16}$$

where $\delta n_1(\mathbf{r})$ and $\delta n_2(\mathbf{r})$ are infinitesimal deviations of the local particle number densities of the components from their equilibrium values n_1^0 and n_2^0, respectively. Then

$$\delta n_1(\mathbf{r}) = \alpha_1 \left\{ \int [V_{21}(\mathbf{r}-\mathbf{r}') - V_{11}(\mathbf{r}-\mathbf{r}')]\,\delta n_1(\mathbf{r}')\,dV' + \int [V_{22}(\mathbf{r}-\mathbf{r}') - V_{12}(\mathbf{r}-\mathbf{r}')]\,\delta n_2(\mathbf{r}')\,dV' \right\},$$

$$\delta n_2(\mathbf{r}) = \alpha_2 \left\{ \int [V_{11}(\mathbf{r}-\mathbf{r}') - V_{21}(\mathbf{r}-\mathbf{r}')]\,\delta n_1(\mathbf{r}')\,dV' + \int [V_{12}(\mathbf{r}-\mathbf{r}') - V_{22}(\mathbf{r}-\mathbf{r}')]\,\delta n_2(\mathbf{r}')\,dV' \right\}, \tag{17}$$

where

$$\alpha_1 = \left(\frac{1-\omega_1 n_1^0 - \omega_3 f_3}{1-\omega_3 f_3} \right) \frac{n_1^0}{T}, \tag{18}$$

$$\alpha_2 = \left(\frac{1-\omega_2 n_2^0 - \omega_3 f_3}{1-\omega_3 f_3} \right) \frac{n_2^0}{T}, \tag{19}$$

We note that the equations in the system (17) are not independent, but rather they are coupled by the relation $\delta n_1(\mathbf{r})\omega_1 = -\delta n_2(\mathbf{r})\omega_2$, in agreement with the close-packing condition (3).

We introduce

$$K_{11}(\mathbf{r}-\mathbf{r}') = V_{21}(\mathbf{r}-\mathbf{r}') - V_{11}(\mathbf{r}-\mathbf{r}'),$$
$$K_{12}(\mathbf{r}-\mathbf{r}') = V_{22}(\mathbf{r}-\mathbf{r}') - V_{12}(\mathbf{r}-\mathbf{r}'),$$
$$K_{21}(\mathbf{r}-\mathbf{r}') = V_{11}(\mathbf{r}-\mathbf{r}') - V_{21}(\mathbf{r}-\mathbf{r}'),$$
$$K_{22}(\mathbf{r}-\mathbf{r}') = V_{12}(\mathbf{r}-\mathbf{r}') - V_{22}(\mathbf{r}-\mathbf{r}'). \tag{20}$$

Fourier transforming the system (17) we obtain

$$\delta\tilde{n}_1(\mathbf{k}) = \alpha_1 \tilde{K}_{11}(\mathbf{k})\,\delta\tilde{n}_1(\mathbf{k}) + \alpha_1 \tilde{K}_{12}(\mathbf{k})\,\delta\tilde{n}_2(\mathbf{k}),$$
$$\delta\tilde{n}_2(\mathbf{k}) = \alpha_2 \tilde{K}_{21}(\mathbf{k})\,\delta\tilde{n}_1(\mathbf{k}) + \alpha_2 \tilde{K}_{22}(\mathbf{k})\,\delta\tilde{n}_2(\mathbf{k}), \tag{21}$$

where the overtilda donotes a Fourier transform.

At the branch point the system of integral equations (17) possesses a nontrivial solution, so that

$$\det(\alpha_i \tilde{K}_{ij}(\mathbf{k}) - \delta_{ij}) = 0. \tag{22}$$

The maximum temperature at which this condition holds is the critical temperature and is determined by the relation

$$T_c = \frac{n_1^0 n_2^0}{1-\omega_3 f_3} \max_{\{\mathbf{k}\}} \{\omega_2[\tilde{V}_{21}(\mathbf{k}) - \tilde{V}_{11}(\mathbf{k})] + \omega_1[\tilde{V}_{12}(\mathbf{k}) - \tilde{V}_{22}(\mathbf{k})]\}. \tag{23}$$

We note that the critical temperature T_c does not depend on V_{13} and V_{23} — the pair-interaction potentials of the particles of the first two components with a low-mobility third component. This is due to the assumption that the atoms of the third component are distributed uniformly.

We note that the standard Gor'skiĭ–Bragg–Williams condition for phase separation is obtained hence with $\omega_1 - \omega_2$ and $f_3 = 0$

$$\min_{\{\mathbf{k}\}} [\tilde{V}_{11}(\mathbf{k}) + \tilde{V}_{22}(\mathbf{k}) - 2\tilde{V}_{12}(\mathbf{k})] < 0. \tag{24}$$

We now proceed to the second case — a nonuniform distribution of the third component with an inhomogeneity scale r_0 much larger than r_1 — the longest range of the interatomic potentials. Then f_3 in Eq. (23) must be replaced by $f_3(\mathbf{r})$.

Accordingly, the critical temperature determined by the expression (3) becomes local

$$T_c = T_c(\mathbf{r}). \tag{25}$$

We note that this temperature is not the temperature of an equilibrium phase transition, since the system has not reached complete thermodynamic equilibrium: The chemical potential of the third component depends on the coordinates.

We introduce

$$T_c^{\min}=\min_{\{\mathbf{r}\}} T_c(\mathbf{r}) \quad \text{and} \quad T_c^{\max}=\max_{\{\mathbf{r}\}} T_c(\mathbf{r}), \tag{26}$$

the maximum and minimum local critical temperatures. Then, for $T_c^{\min}<T<T_c^{\max}$, in the spatial regions where $T_c(\mathbf{r})<T$ the system becomes homogenized with respect to the first two components, and the opposite process — formation of microphase interfaces — occurs in the regions where $T_c(\mathbf{r})>T$.

In summary, in a ternary system having substantially different relaxation times, nonequilibrium phase transitions can materialize in the corresponding quasibinary systems. There exists a finite temperature interval, determined by the degree of nonuniformity of the least mobile component, where opposing processes occur simultaneously in the system — homogenization and formation of microphase interfaces.

In conclusion, we shall say a few words about the possibilities of further investigations of quasiequilibrium states of ternary solid solutions on the basis of a generalized lattice model. It is of interest to study the kinetics of such processes — we have in mind estimating the relaxation times τ_1 and τ_2, on the one hand, and studying the temporal evolution of the spatial distributions of the components of the ternary system. Moreover, the case where complete equilibrium of the system is reached, which by analogy with (13) can be described by a system of three nonlinear integral equations of the form $\mu_i=C_i(i=1,2,3)$, is interesting. These questions will be examined in the next paper.

I thank A. I. Olemskiĭ for a discussion of this work and for helpful remarks.

[1] B. S. Bokshteĭn, S. Z. Bokshteĭn, and A. A. Zhukhovitskiĭ, *The Thermodynamics and Kinetics of Diffusion in Solids*, Metallurgiya, Moscow (1974), 280 pp.
[2] B. Ya. Lyubov, *Diffusion Processes in Inhomogeneous Media* Mir, Moscow, (1981), 296 pp.
[3] A. Yu. Zakharov and S. V. Terekhov, Fiz. Met. Metalloved. **95**(2), 261 (1985).
[4] M. A. Krivoglaz and A. A. Smirnov, *The Theory of Alloys Undergoing Ordering*, GIFML, Moscow (1958), 336 pp.
[5] A. I. Olemskiĭ, Fiz. Met. Metalloved. **51**(5), 917 (1981).
[6] A. A. Katsnel'son and A. I. Olemskiĭ, *Microscopic Theory of Inhomogeneous Structures*, Moscow State University Press Moscow, (1987), 336 pp.
[7] M. Kac, G. E. Uhlenbeck, and P. C. Hemmer, J. Math. Phys. **4**, 216 (1963).
[8] G. E. Uhlenbeck, P. C. Hemmer, and M. Kac, J. Math. Phys. **4**, 229 (1963).
[9] P. C. Hemmer, M. Kac, and G. E. Uhlenbeck, J. Math. Phys. **5**, 60 (1964).
[10] A. G. Khachaturyan, *The Theory of Phase Transformations and the Structure of Solid Solutions*, Nauka, Moscow (1974), 384 pp.
[11] A. Yu. Zakharov and S. V. Terekhov, in *Mathematical Problems of Chemical Thermodynamics*, Nauka, Novosibirsk, (1985) p. 173.

Translated by M. E. Alferieff

DEFECTS, DISLOCATIONS. PHYSICS OF STRENGTH

Diffusion processes near triple joints of special grain boundaries

N. M. Vlasov and V. A. Zaznoba

State Scientific–Research Institute of the Scientific and Industrial Association ''Luch'', 142100 Podol'sk, Moscow Region, Russia*
(Submitted June 4, 1998)
Fiz. Tverd. Tela (St. Petersburg) **41**, 64–67 (January 1999)

Diffusion processes are studied near triple joints of special grain boundaries, whose dilatation field is modeled by a wedge disclination. An exact analytic solution of the diffusion equation in the stress field produced by the structural defect considered is obtained. The results of the theoretical analysis are used to determine the concentration field of point defects near triple joints of special grain boundaries in a polycrystal. © *1999 American Institute of Physics.* [S1063-7834(99)01601-9]

Special grain boundaries of a polycrystal possess minimal surface energy. This is due to the fact that atoms at coinciding sites of the crystal lattice produce negligible distortions. The largest lattice distortions arise at triple joints of special grain boundaries. They are caused, as a rule, by the orientational dependence of the elastic and thermophysical properties of the grain material. For this reason, the triple joints of special grain boundaries are powerful stress concentrators. They appear for the following basic reasons. Neighboring grains near triple joints possess different orientation. It is known[1] that the tensile yield stress in single crystals is strongly orientation-dependent. Thus, the yield point of zinc crystals in tension varies by a factor of six as the orientation changes. For this reason, neighboring grains deform differently under an external load. This results in the appearance of stresses near the triple joint of special grain boundaries. The anisotropy of Young's modulus and the linear expansion coefficient under force and temperature loads is also accompanied by the appearance of stresses near triple joints. The maximum stresses occur near the vertex of a joint since, as the distance from the vertex increases, the stresses decrease because of compensation by stresses with the opposite sign produced by a neighboring triple joint. Rotational modes of plastic deformation near the rotation axis are also stress concentrators. Triple joints of ordinary and special grain boundaries serve as such an axis. Special grain boundaries are chosen for the analysis of diffusion processes because the activation energy of diffusion along special grain boundaries is essentially the same as for diffusion in the bulk. However, in ordinary grain boundaries, the activation energy of impurity diffusion as well as of intrinsic point defects along grain boundaries is lower.

The plastic flow of a polycrystal is a self-consistent process: The deformation of each grain depends on the deformation of the surrounding grains. The stress field can also be self-consistent. The latter means that the stress system must be self-balanced, i.e. there are no volume changes in the material caused by the stresses. Mathematically, this is expressed in the form $\int_V \sigma_{ll} dV = 0$, where σ_{ll} is the trace of the tensor of normal stresses. For ternary joints of grain boundaries it can be assumed that only tensile stresses are present near some boundaries and compressive stresses are present near other boundaries. The distribution of triple joints of grain boundaries over a qualitative characteristic of a strained state is quite arbitrary, but integrally the volume of a polycrystal does not dependent on stress concentrators.

If a polycrystal is placed in a temperature field, then thermal stresses arise because of the linear expansion coefficients are different along the orientation directions of the grains. These stresses are highest near triple joints of grain boundaries. In this case, regions of compression and tension are present because of the simultaneity of the deformation (it is assumed that the continuity of the material is not destroyed). The existence of such regions near triple joints of grain boundaries makes possible different diffusion processes: the formation of impurity atmospheres, the formation of porosity, the growth of precipitates of a new phase, the separation of a flux of radiation-induced point defects, and so on. Therefore, there is a need to study the effect of a stress field generated by triple joints of special grain boundaries on some of the processes mentioned. This is the objective of the present work.

The stress field near a triple joint of special grain boundaries is modeled by a wedge disclination.[2] If the rotation vector of the wedge disclination conforms to the rotational symmetry of the crystal, then such disclinations are said to be perfect. Ordinarily, such a rotation angle is 60 and 90°. However, near triple joints the rotation angle can be small and may not conform to the rotational symmetry of the crystal. Such disclinations are said to be partial. For a perfect disclination there are no distinguished surfaces because of the conditions of the rotational symmetry of the crystal. For partial disclinations, the presence of a disclination destroys the identity of the atomic structure and distinguished surfaces with disrupted structure appear. Such surfaces model special grain boundaries. In what follows, to study the diffu-

sion processes near triple joints of special grain boundaries we shall consider a model of a given structural imperfection — a wedge disclination.

The diffusion redistribution of impurity atoms near a wedge disclination was first considered in Refs. 3–6. Following these works, we write the binding energy of a point defect with a wedge disclination in the form

$$V=A\ln\left(\frac{r}{R}\right),\quad A=\frac{4\mu\omega(1+\nu)\varepsilon r_1^3}{3(1-\nu)},$$

where μ is the shear modulus of the material, ν is Poisson's ratio, ω is the modulus of the disclination rotation vector, ε is the relative difference of the linear sizes of the matrix and impurity atoms, r_1 is the radius of a matrix atom, and R is the outer radius of the disclination. Since the potential V diverges logarithmically as $r\to 0$, we introduce the concept of the nucleus of a wedge disclination with a characteristic size of several interatomic distances. Triple joints of grain boundaries are randomly distributed in the volume of the polycrystal with the condition that their stress fields far from the vertices of joints compensate one another. This is a consequence of the combined deformation of the grains and absence of discontinuities in the material. This prevents the potential V from diverging in the limit $R\to\infty$. We note that R is arbitrary, and the dilatation field at this boundary can be different from zero. However, near the vertex of a triple joint, where diffusion processes are most intense, the expression presented describes quite correctly the binding energy of a point defect to a triple joint of special grain boundaries.

The diffusion of point defects near a wedge disclination can be described by an equation for non-steady-state diffusion in a force field with appropriate initial and boundary conditions

$$\frac{1}{D}\frac{\partial C}{\partial t}=\Delta C+\frac{\nabla(C\nabla V)}{kT},$$

$$C(r,0)=C_0,\quad C(R,t)=C_0,\quad C(r_0,t)=C_{\rm eq},$$

where D is the diffusion coefficient of point defects, k is Boltzmann's constant, T is the absolute temperature, C_0 is the average density of point defects, $C_{\rm eq}$ is the equilibrium concentration of point defects at the disclination nucleus, and r_0 is the radius of the disclination nucleus.

Initially, the concentration of point defects near a wedge disclination is equal to the average concentration C_0. The same concentration is maintained at $r=R$. Physically, this means that as point defects migrate toward a disclination nucleus, point defects from a disclination of an opposite sign appear at the boundary $r=R$. We shall illustrate this for a specific example. Let the dilatation be positive near a wedge disclination (tensile stresses), and let neighboring dislocations possess negative dilatation (compressive stresses). Then the impurity atoms that expand the crystal lattice are predominantly attracted toward disclinations with positive dilatation and are repelled from the disclinations with negative dilatation. In the process, a constant concentration C_0 is maintained at the boundary $r=R$. A similar situation holds for interstitial atoms under irradiation. Vacancies and impurity atoms, whose ionic radius is less than the corresponding radius of the matrix atoms, migrate toward sinks with negative dilatation and away from disclinations with positive dilatation. A constant average concentration C_0 is also maintained at the boundary $r=R$. The boundary condition at $r=r_0$ means that an equilibrium concentration of point defects is established there instantaneously and is henceforth maintained during the entire time of their diffusion redistribution

$$C_{\rm eq}=C_0\exp\left(-\frac{V}{kT}\right)=C_0\left(\frac{R}{r}\right)^{\alpha},\quad \alpha=\frac{A}{kT}.$$

The binding energy of a point defect with a wedge disclination is a logarithmic function of the coordinates. Such a dependence makes it possible to write down quite simply and elegantly the diffusion equation in a force field as

$$\frac{1}{D}\frac{\partial C}{\partial t}=\frac{\partial^2 C}{\partial r^2}+\frac{1+\alpha}{r}\frac{\partial C}{\partial r},$$

$$C(r,0)=C_0,\quad C(R,t)=C_0,\quad C(r_0,t)=C_{\rm eq}.$$

This problem can be solved analytically for an arbitrary value of $\alpha=A/kT$. The dimensionless parameter α characterizes the ratio of the binding energy of a point defect with a disclination to the thermal kinetic energy. If $\alpha\ll 1$, then the drift of point defects toward a disclination nucleus can be treated as a small perturbation of the main diffusion flux. For $\alpha\gg 1$ the drift of point defects predominates, and for $\alpha\simeq 1$ the contribution of the stress field of a disclination to diffusion is comparable to diffusion under a concentration gradient.

Next, we shall study for specific examples the kinetics of accumulation of impurity atoms, interstitial atoms, and vacancies near a wedge disclination. First, we shall estimate α. For the system Fe–C ($r_1=1.40\times10^{-10}$ m, $\nu=0.29$, $\mu=8.3\times10^4$ MPa, $\varepsilon=0.2$, $kT=10^{-20}$ J, and $\omega=0.1$ rad) $\alpha=1$. The value $\omega=0.1$ rad for the disorientation angle with the formation of special grain boundaries is entirely reasonable. Let an impurity atmosphere consisting of atoms that expand the crystal lattice be formed near a positive ($\omega<0$) wedge disclination. Then for $\alpha=-1$ the problem of determining the concentration field of the impurity atoms reduces mathematically to solving the equation

$$\frac{1}{D}\frac{\partial C}{\partial t}=\frac{\partial^2 C}{\partial r^2},$$

$$C(r,0)=C_0,\quad C(R,t)=C_0,\quad C(r_0,t)=C_{\rm eq}=C_0\frac{R}{r_0}.$$

The solution of this problem gives the concentration distribution of impurity atoms near a triple joint of special grain boundaries as modeled by a positive wedge disclination

$$\frac{C-C_0}{C_{\rm eq}-C_0}=\frac{\frac{R}{r_0}-\frac{r}{r_0}}{\frac{R}{r_0}-1}-\frac{2}{\pi}\sum_{n=1}^{\infty}\frac{\sin\left[\frac{\pi n\left(\frac{r}{r_0}-1\right)}{\frac{R}{r_0}-1}\right]}{n}\times\exp\left[-\frac{\pi^2n^2Dt}{\left(\frac{R}{r_0}-1\right)^2r_0^2}\right].$$

This expression was obtained taking into account the stress field of a wedge disclination in the diffusion equation and in the boundary condition. If the effect of the stress field of a wedge dislocation is taken into account only in the boundary condition, then the corresponding problem is formulated mathematically as

$$\frac{1}{D}\frac{\partial C}{\partial t}=\frac{\partial^2C}{\partial r^2}+\frac{1}{r}\frac{\partial C}{\partial r},$$

$$C(r,0)=C_0,\quad C(R,t)=C_0,\quad C(r_0,t)=C_{\rm eq}.$$

The solution of this problem describes the kinetics of the formation of an impurity atmosphere neglecting the stress field of the disclination in the diffusion equation

$$\frac{C-C_0}{C_{\rm eq}-C_0}=\frac{\ln\left(\frac{R}{r}\right)}{\ln\left(\frac{R}{r_0}\right)}+\pi\sum_{n=1}^{\infty}\frac{J_0\left(\frac{\mu_nR}{r_0}\right)J_0(\mu_n)Z_0\left(\frac{\mu_nr}{r_0}\right)}{J_0^2(\mu_n)-J_0^2\left(\frac{\mu_nR}{r_0}\right)}\times\exp\left(\frac{\mu_n^2Dt}{r_0^2}\right),$$

where

$$Z_0\left(\frac{\mu_nr}{r_0}\right)=N_0\left(\frac{\mu_nR}{r_0}\right)J_0\left(\frac{\mu_nR}{r_0}\right)-J_0\left(\frac{\mu_nR}{r_0}\right)N_0\left(\frac{\mu_nr}{r_0}\right),$$

μ_n are the roots of the equation

$$J_0(\mu)N_0\left(\frac{\mu R}{r_0}\right)-J_0\left(\frac{\mu R}{r_0}\right)N_0(\mu)=0,$$

and $J_0(\mu)$ and $N_0(\mu)$ are Bessel functions of the first and second kind, respectively.

In the steady state, the ratio of the dimensionless concentrations of the impurity atoms for these cases is

$$\frac{(R-r)\ln\left(\frac{R}{r_0}\right)}{(R-r_0)\ln\left(\frac{R}{r}\right)},$$

which for $r_0<r<R$ is always larger than 1. Physically, this means that the dilatation field near a wedge disclination ''confines'' more impurity atoms.

Next, we shall consider the kinetics of accumulation of interstitial atoms and vacancies near a triple joint of special grain boundaries. An atmosphere consisting of interstitial atoms is formed if the vertex of the joint (disclination nucleus) is not a perfect sink for interstitial atoms. However, if the dislocation nucleus is a perfect sink for interstitial atoms, then, because the motion of edge dislocations is nonconservative, the center of the wedge disclination is displaced and relaxation of stresses occurs near it. The problem of determining the concentration field of interstitial atoms near a wedge disclination is identical to the problem considered above. However, the physical meaning of the boundary condition at $r=r_0$ is different. For interstitial atoms, $C_{\rm eq}$ at $r=r_0$ is the equilibrium concentration with respect to the nonconservative motion of dislocations. The diffusion flux of vacancies is directed into the zone of compressive forces of a negative ($\omega>0$) wedge disclination. The boundary condition at $r=r_0$ signifies in this case an equilibrium of vacancies with respect to the nonconservative motion of dislocations. The vacancies change the crystal structure near a positive wedge disclination and do not accumulate in pores. The situation resembles the suppression of swelling of a material as a result of vacancy migration into compressed regions near precipitates of a new phase.

Finally, we shall consider the case where pore nuclei with characteristic size r_0 are present at the center of a triple joint of special grain boundaries (negative wedge disclination). The compressive stress field is equivalent to a pressure near the pore. Since the compressive stress field is distributed nonuniformly and is maximum at the pore boundary, the diffusion flux of vacancies is directed toward that location. The oppositely directed flux of interstitial atoms allows pores to grow in size. To determine the vacancy concentration field, $C_{\rm eq}$ for $r=r_0$ should be interpreted as the equilibrium vacancy concentration at a pore boundary, determined by the relation

$$C_{\rm eq}|_{r=r_0}=C_0\ \exp\left[\frac{\Omega}{kT}\left(\frac{\gamma}{r_0}+P_{EP}-P_0\right)\right],$$

where Ω is the atomic volume, γ is the surface stress (the pore nucleus is assumed to be cylindrical), P_{EP} is the external pressure, and P_0 is the internal pressure of the gas in a pore. It is assumed that the slow growth of a pore is accompanied by rapid adjustment of the vacancy concentration field. Then the rate of change of the pore radius is given by

$$\frac{dr_0}{dt}=-\Omega D\left(\frac{\partial C}{\partial r}-\frac{C}{kT}\frac{\partial V}{\partial r}\right)_{r=r_0}=\Omega D\frac{C_{\rm eq}}{r_0}+\frac{(C_{\rm eq}-C_0)\Omega D}{(R-r_0)}\times\left[1+2\sum_{n=1}^{\infty}\exp\left[-\frac{\pi^2n^2Dt}{\left(\frac{R}{r_0}-1\right)^2r_0^2}\right]\right]$$

(the concentration and drift vacancy fluxes are oppositely directed).

For $Dt/r_0^2\gg1$ the rate of change of the pore radius is found from the expression

$$\frac{dr_0}{dt}=\frac{\Omega D(RC_{eq}-r_0C_0)}{r_0(R-r_0)}.$$

The corresponding value of $\frac{dr_0}{dt}$ in this approximation, neglecting the dilatation field of the wedge disclination in the diffusion equation, gives

$$\frac{dr_0}{dt}=\frac{\Omega D(C_{eq}-C_0)}{r_0\ln\left(\frac{R}{r_0}\right)}.$$

Their ratio

$$\frac{\left(\frac{R}{r_0}C_{eq}-C_0\right)\ln\left(\frac{R}{r_0}\right)}{(C_{eq}-C_0)\left(\frac{R}{r_0}-1\right)}$$

for arbitrary R/r_0 is always greater than 1, i.e. the rate of change of the pore radius, taking account of the dilatation field of the wedge disclination in the diffusion equation, exceeds the corresponding rate neglecting the dilatation field. Physically, this is due to the fact that taking into account the dilatation field is equivalent to effective vacancy sources near the wedge disclination.

The triple joints of special grain boundaries with tensile and compressive stress fields are distributed randomly in the material. In these stress fields the diffusion fluxes of radiation defects separate; vacancies migrate into the compression region, while interstitial atoms migrate into the tension region. Near the vertices of triple joints the dislocation structure of the material becomes rearranged and swelling is thereby suppressed. A strict description of this process reduces to solving a system of diffusion equations for vacancies and interstitial atoms, taking account of their production under irradiation and recombination accompanying migration. However, the solution of this problem does not greatly change the qualitative picture of diffusion processes for vacancies and interstitial atoms near the triple joints of special grain boundaries.

*E-Mail: luch@atis.kiae.su

[1] R. W. Honeycombe, *Plastic Deformation of Metals*, Mir, Moscow (1972), 403 pp.
[2] V. A. Likhachev and R. Yu. Khaĭrov, *Introduction to the Theory of Disclinations*, Leningrad University Press, Leningrad (1975), 183 pp.
[3] N. M. Vlasov and B. Ya. Lyubov, Fiz. Met. Metalloved. **40**, 1162 (1975).
[4] B. Ya. Lyubov and N. M. Vlasov, Fiz. Met. Metalloved. **47**, 140 (1979).
[5] N. M. Vlasov and B. Ya. Lyubov, Dokl. Akad. Nauk SSSR **259**(2), 348 (1981) [Sov. Phys. Dokl. **26**, 693 (1981)].
[6] A. E. Romanov and G. G. Samsonidze, Pis'ma Zh. Tekh. Fiz. **14**(14), 1339 (1988) [Sov. Tech. Phys. Lett. **14**, 585 (1988)].

Translated by M. E. Alferieff

MAGNETISM AND FERROELECTRICITY

Characteristic features of the extrinsic electric resistance in ferromagnets with low carrier density

V. A. Gavrichkov*) and S. G. Ovchinnikov

L. V. Kirenskiĭ Institute of Physics, Siberian Branch of the Russian Academy of Sciences, 660036 Krasnoyarsk, Russia

(Submitted April 10, 1998)
Fiz. Tverd. Tela (St. Petersburg) **41**, 68–76 (January 1999)

Switching from simple semiconductors to more complicated chemical compositions, we encounter mainly nonstoichiometric or undoped compounds. Combined with other characteristic features of *d(f)* compounds, this can lead, together with the ordinary scattering by spin disorder in magnetic semiconductors, to an unusual impurity contribution to the total scattering of carriers even in intrinsic semiconductors. A unique scheme for calculating the energy structure of the conduction-band bottom of a ferromagnetic semiconductor and the temperature and field dependences of the impurity contribution to the resistivity is proposed on the basis of a model Hamiltonian. The computed magnetoresistance ratio is negative and has a maximum near T_c. A qualitative comparison is made between the results and the experimental temperature dependences of the Hall mobility and magnetoresistance ratio in the ternary semiconductor *n*-$HgCr_2Se_4$, which is nonstoichiometric with respect to the chalcogen. To identify previously unobserved temperature oscillations of the resistance, a careful analysis is made of the low-temperature part of the resistance using the relations obtained. [S1063-7834(99)01701-3]

1. Many compounds, which according to bond type are intermediate ion-covalent compounds, form extended concentration regions with their own components, often of the berthollide type.[1] This is facilitated by the characteristic features of the electronic shell structure of transition, rare-earth, and actinide elements. Interestingly, in these cases the effects due to nonstoichiometry and strong Coulomb correlations are present at the same time. In turn, in such compounds stoichiometry is only a special case or it is unattainable, if the ordinate of the compound corresponding to the highest degree of ordering of the ions falls outside the range of existence of these phases. Nonstoichiometry in semiconductor compounds is of special interest. In such compounds the main cation is a *d* element, since transition-element compounds form the largest group of semiconductors.[2,3]

We are interested in compounds of $d(f)$ elements, at whose Fermi level there is a contribution not only from diffuse *sp* states, which form wide bands, but also from more localized *d(f)* states, which form narrow bands. Ordinarily, in a two-band model it is not difficult to calculate the transport relaxation time, using Fermi's golden rule to calculate the probabilities of quantum transitions. But for substances with quite strong localization of the *d(f)* electrons the electronic correlations make it impossible to use a simple two-band model, since the correlations renormalize not only the parameters of the carrier dispersion law in a narrow band (the bandwidth and the effective mass) but also the hybridization parameters of the states of the wide and narrow bands. Such materials include compounds with variable valence, heavy fermions, and magnetic semiconductors. The discovery of giant magnetoresistance in the perovskites $La_{1-x}(Ca,Sr,Pb,Ba)_xMnO_y$[4] drew additional attention to this problem, since the microscopic mechanism of giant magnetoresistance is still not clear.

The carrier dispersion laws in magnetically ordered substances depend on both temperature and magnetic field on account of the exchange interaction. This makes an additional contribution to the temperature and field dependences of the electric resistance. Many physical properties of conducting magnets can be described in the narrow-band *s–d(f)* model,[2,3] where the carrier is a spin polaron — a quasiparticle, whose motion is similar to that of an ''irregular spin $S \pm 1/2$ on the background formed by a lattice of regular spins S.'' This model is applicable when the *d(f)* electrons are well localized and their contribution to the density of states at the Fermi level is zero. This naive picture is unsuitable in the case of partial delocalization of *d(f)* electrons, where narrow *d* bands must be taken into account together with strong electronic correlations and hybridization with the more diffuse *sp* states. A synthesis of the *s–d(f)* model and Anderson's periodic model makes it possible to do this, and we shall use it below to calculate the temperature and field dependences of the resistance. The computational results will be compared with the experimental data for the magnetic semiconductor *n*-$HgCr_2Se_4$.

The paper is organized as follows. In Sec. 2 the electronic structure of a degenerate semiconductor is described in the periodic Anderson model taking into account *s–d* ex-

change and scattering by impurities and intrinsic defects. In Sec. 3 the electrical conductivity is calculated. In Sec. 4 the experimental results pertaining to the present calculation are briefly listed and compared with the relations obtained.

2. Let us consider a multielectron model of a magnetic semiconductor taking into account the real multielectronic orbital structure of the $3d$ states.[5] Following this model, the Hamiltonian can be written as a superposition of the periodic Anderson model and the *sd* exchange model

$$H=H_0+H_1+H_2+H_3;$$

$$H_0=\sum_{\mathbf{k}\sigma}\xi_{\mathbf{k}}c^+_{\mathbf{k}\sigma}c_{\mathbf{k}\sigma}+\sum_{\mathbf{f}}\left[(E_n-n\mu)\sum_{\gamma}X^{\gamma\gamma}_{\mathbf{f}}+(E_{n+1}-(n+1)\mu)\sum_{\Gamma}X^{\Gamma\Gamma}_{\mathbf{f}}\right];$$

$$H_1=\sum_{\mathbf{f}}\left\{-J\sigma_{\mathbf{f}}S_{\mathbf{f}}+V\sum_{\sigma}(c^+_{\mathbf{f}\sigma}d_{\mathbf{f}\sigma}+\text{h.c.})\right\}. \qquad (1)$$

Here $c_{\mathbf{k}\sigma}$ is the operator annihilating a c electron with momentum $\mathbf{k}$, spin σ, and energy $\xi_{\mathbf{k}}=\varepsilon_{\mathbf{k}}-\mu$, measured from the chemical potential μ. It is assumed that the c band is formed mainly by the $4s$ states of the magnetic ion. $X^{pq}_{\mathbf{f}}=|\mathbf{f}p\rangle\langle\mathbf{f}q|$ are Hubbard operators, describing the transition of a magnetic ion at a lattice site $\mathbf{f}$ from a localized state $|q\rangle$ into a state $|p\rangle$; E_n and E_{n+1} are the energies of the ground state configurations d^n and d^{n+1} of the magnetic ion; the indices γ and Γ refer to the orbital degeneracy of these terms; $S_{\mathbf{f}}$ and $\sigma_{\mathbf{f}}$ are the spin operators of the d ion and c conduction electrons; V and J are hybridization and exchange interaction parameters of the c and d electrons. The signal-electron operators $d_{\mathbf{f}\sigma}$ can be expressed in terms of the Hubbard operators in the standard manner as $d_{\mathbf{f}\sigma}=\Sigma_{pq}\langle p|d_{\mathbf{f}\sigma}|q\rangle X^{pq}_{\mathbf{f}}$. For specific calculations we shall consider only the d^3 and d^4 configurations. This makes it possible to compare the results with experimental data on the semiconductor $HgCr_2Se_4$, where the $^4A_2$ ground state of the Cr^{3+} ion is orbitally nondegenerate and corresponds to spin $S=3/2$. When the ''extra'' electron (current carrier) is transported along the multielectronic $^4A_2$ states, $Cr^{2+}(d^4)$ ions are formed. For chromium, the energies of the terms $^3T_1(d^4)$ and $^5E(d^4)$ can compete with one another, attesting to the possible presence of two types of donor single-particle excitations of different symmetry with energies $E(^3T_1)-E(^3A_2)$ and $E(^5E)-E(^3A_2)$ in this compound. Here we shall confine ourselves to the latter case, although the method described below for calculating the linear response makes it possible, where it is important to do so, to take into account the excited states of Cr^{2+} and Cr^{4+} (for the valence band), as done in Ref. 5 in a calculation of absorption coefficients. If ^5E is the ground state of the Cr^{2+} ion,

$$d_{\mathbf{f}\uparrow}=X^{1.5}_{\mathbf{f}}+\frac{\sqrt{3}}{2}X^{2.6}_{\mathbf{f}}+\frac{1}{\sqrt{2}}X^{3.7}_{\mathbf{f}}+\frac{1}{2}X^{4.8}_{\mathbf{f}};$$

$$d_{\mathbf{f}\downarrow}=X^{4.9}_{\mathbf{f}}+\frac{\sqrt{3}}{2}X^{3.8}_{\mathbf{f}}+\frac{1}{\sqrt{2}}X^{2.7}_{\mathbf{f}}+\frac{1}{2}X^{1.6}_{\mathbf{f}},$$

where the superscripts enumerate states of the Cr^{3+} and Cr^{2+} ions:

$$Cr^{3+}:|1\rangle=\left|S=\frac{3}{2};S_z=\frac{3}{2}\right\rangle;\quad |2\rangle=\left|\frac{3}{2};\frac{1}{2}\right\rangle;$$

$$|3\rangle=\left|\frac{3}{2};-\frac{1}{2}\right\rangle;\quad |4\rangle=\left|\frac{3}{2};-\frac{3}{2}\right\rangle;$$

$$Cr^{2+}:|5\rangle=|2,2\rangle;\quad |6\rangle=|2;1\rangle;$$

$$|7\rangle=|2;0\rangle;\quad |8\rangle=|2;-1\rangle;\quad |9\rangle=|2;-2\rangle.$$

The operators $d_{\mathbf{f}\sigma}$ in this representation are quasi-Fermi operators. This is because the highest excited states of chromium are neglected, and it corresponds to the single-electron transition $^2A_2\leftrightarrow{}^5E$. We also call attention to the existence of similar concepts in the theory of defects in semiconductors, referring to ''local population levels.''[6] The presence of a hybridization term in the Hamiltonian is due to the possible entanglement of the c and d states by the distant coordination spheres (trigonal corrections to the crystal field in the case of $HgCr_2Se_4$). Of the different processes responsible for electron scattering by impurities, we take into account in out calculation the standard potential scattering of carriers in c states and fluctuations of the energies of the d level

$$H_2=\sum_{\mathbf{kpfq}}p_{l\mathbf{f}}\Delta_1(\mathbf{k}-\mathbf{q})e^{-i\mathbf{f}\cdot(\mathbf{k}-\mathbf{q})}c^+_{\mathbf{k}\sigma}c_{\mathbf{q}\sigma}+\sum_{\mathbf{f}\sigma}p_{2\mathbf{f}}\Delta_2(\mathbf{f})d^+_{\mathbf{f}\sigma}d_{\mathbf{f}\sigma}. \qquad (2)$$

Here $p_{1\mathbf{f}}$ and $p_{2\mathbf{f}}$ are projection operators, equal to 0 in the absence of impurities and 1 in the nearest-neighbor environment of an impurity atom or defect. The second term in H_2 presumes random fluctuations of the crystal field without a change in symmetry of the field. We chose the form of the Hamiltonian H_2 describing the interaction with impurities so as to illustrate the characteristic features of potential scattering and multicomponent semiconductors.

Depending on the specific physical situation the following are possible: independent fluctuations of the impurity parameters $p_{1\mathbf{f}}\cdot p_{2\mathbf{f}}=0$ or correlated fluctuations $p_{1\mathbf{f}}\cdot p_{2\mathbf{f}}=p_{\mathbf{f}}$. We turn to the first case, which we shall identify below with the presence of intrinsic defects in the sublattices of both the A cations and the B anions. For the system of equations for the two-time Green's functions not averaged over the impurities

$$G_{11}=\langle\langle c_{\mathbf{k}\sigma}|c^+_{\mathbf{k}\sigma}\rangle\rangle,\quad G_{22}=\langle\langle d_{\mathbf{k}\sigma}|d^+_{\mathbf{k}\sigma}\rangle\rangle,$$

$$G_{12}=\langle\langle c_{\mathbf{k}\sigma}|d^+_{\mathbf{k}\sigma}\rangle\rangle$$

is obtained in the standard manner[7]

$$G_{11}(\mathbf{k},\mathbf{k}')=G^{(0)}_{11}\delta_{\mathbf{k}\mathbf{k}'}+G^{(0)}_{11}\sum_{\mathbf{fq}}p_{1\mathbf{f}}\Delta_1(\mathbf{k}-\mathbf{q})e^{i\mathbf{f}\cdot(\mathbf{q}-\mathbf{k})}\times G_{11}(\mathbf{q},\mathbf{k}')+G^{(0)}_{12}\sum_{\mathbf{fq}}p_{2\mathbf{f}}\Delta_{2\mathbf{f}}e^{i\mathbf{f}\cdot(\mathbf{q}-\mathbf{k})}G_{21}(\mathbf{q},\mathbf{k}'),$$

$$G_{21}(\mathbf{k},\mathbf{k}')=G_{21}^{(0)}\delta_{\mathbf{k}\mathbf{k}'}+G_{21}^{(0)}$$

$$\times\sum_{\mathbf{fq}} p_{\mathbf{f}1}e^{i\mathbf{f}\cdot(\mathbf{q}-\mathbf{k})}\Delta_1(\mathbf{k}-\mathbf{q})G_{11}(\mathbf{q},\mathbf{k}')$$

$$+G_{22}^{(0)}\sum_{\mathbf{fq}} p_{2\mathbf{f}}\Delta_{2\mathbf{f}}e^{i\mathbf{f}\cdot(\mathbf{q}-\mathbf{k})}G_{21}(\mathbf{q},\mathbf{k}'). \quad (3)$$

The second pair of equations is obtained by interchanging the indices $1\leftrightarrow 2$. Here the initial Green's functions describe the *c* and *d* states in the generalized Hartree–Fock approximation:

$$G_{11}^{(0)}=\frac{E-\Omega}{(E-\tilde{\xi}_{\mathbf{k}})(E-\Omega)-K_\sigma V^2},$$

$$G_{12}^{(0)}=\frac{\sqrt{K_\sigma}V}{(E-\tilde{\xi}_{\mathbf{k}})(E-\Omega)-K_\sigma V^2},$$

$$G_{22}^{(0)}=\frac{K_\sigma(E-\tilde{\xi}_{\mathbf{k}})}{(E-\tilde{\xi}_{\mathbf{k}})(E-\Omega)-K_\sigma V^2}, \quad (4)$$

and $\Omega=E_4-E_3-\mu$ is the transition energy between the terms of the d^4 and d^3 configurations, $\tilde{\xi}_{\mathbf{k}}=\xi_{\mathbf{k}}-\sigma J\langle S_z\rangle$, $K_\sigma=\langle d_{\mathbf{k}\sigma}^+ d_{\mathbf{k}\sigma}+d_{\mathbf{k}\sigma}d_{\mathbf{k}\sigma}^+\rangle=1/4(5/2+2\sigma\langle S_z\rangle)$,[5] $\sigma=\pm 1/2$, and $\langle S_z\rangle$ is the average spin of the Cr^{3+} ion. The spectrum of the bands $E_{\mathbf{k}\sigma}^+$ can be represented by the expression

$$E_{\mathbf{k}\sigma}^+=\frac{1}{2}(\tilde{\xi}_{\mathbf{k}}+\Omega\pm\sqrt{(\tilde{\xi}_{\mathbf{k}}-\Omega)^2+4K_\sigma V^2}).$$

We call attention to the fact that strong correlations not only determine the energy of a localized *d* level Ω but they also renormalize the hybridization. In the case of no correlations $K_\sigma=1$ and hybridization is determined by the parameter *V*. On account of the restrictions imposed on the Hilbert space by strong correlations, $K_\sigma=1$ and the effective hybridization $VK_\sigma^{1/2}$ depends on both *T* and *H* as a result of $\langle S_z\rangle$, and it is different for the spin subbands.

The functions (4) make it possible to construct a plot of the density of states at the conduction-band bottom of the semiconductor. Figure 1 shows a plot of the density of states obtained under the assumption of a semielliptic density of states for the initial *c* band:

$$g_0(\varepsilon)=\frac{2}{\pi W}\left[1-\left(\frac{\varepsilon}{W}\right)^2\right]^{1/2},$$

where *W* is the width of the initial *c* band.

As is well known, in the band theory the influence of magnetic order reduces to splitting of the spin subbands. In our approach the amplitude Ω of the *d* peak, corresponding to the one-electron transition $^2A_2\leftrightarrow{}^5E$, changes without a change in energy of the *d* states. Since in a semiconductor with a completely filled valence band and empty conduction band, the band contribution to the magnetization is $\langle\sigma_i\rangle=0$. Shifts of the peak Ω are possible only as a result of Heisenberg exchange, but they are of the order of $T_c\approx 0.01$ eV and much less than the *sd* exchange interaction, which is responsible for the spin splitting of the *c* band. The difference in the temperature behavior of the density of *c* and *d* states is the

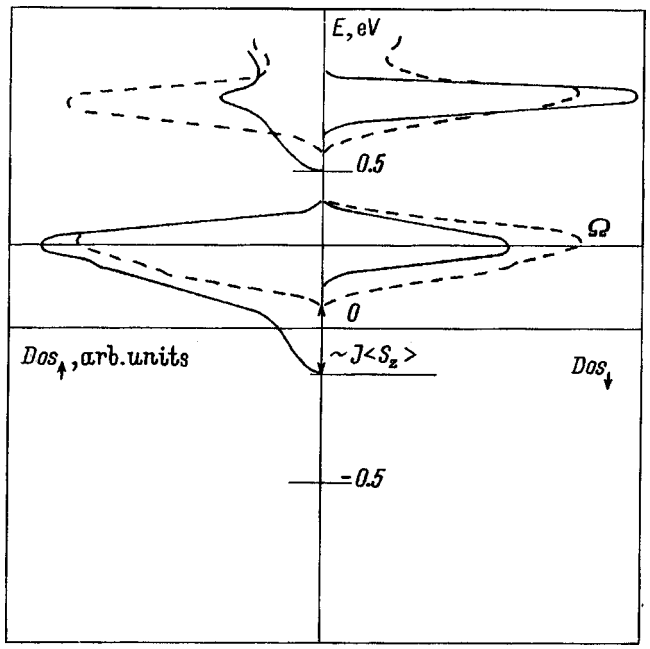

FIG. 1. Density of states near the conduction-band bottom of the compound $HgCr_2Se_4$[5] for $T=4.2$ (solid line) and 300 K (dashed line). The symbol Ω denotes the initial *d* level: $E(^5E)-E(^3A_2)\mu$.

key for further understanding, and for this reason we shall explain in greater detail the physical reasons for this and our approach to the compound $HgCr_2Se_4$. In the paraphase, as one can easily understand, all states $|i\rangle(i=1-4)$ of the Cr^{3+} ion which differ by the spin projection are equally likely. However, as temperature decreases, in the ferrophase the state $|1\rangle$ with maximum spin projection $S_z=3/2$ is predominantly populated, and the single-particle density of *d* states loses symmetry to spin flip, since $d_{\mathbf{f}\uparrow}^+$ and $d_{\mathbf{f}\downarrow}^+$ acting on the same initial state $|1\rangle$ place carriers in completely different four-particle (d^4) states $|5\rangle$ and $|6\rangle$, respectively. The differences between the multielectron states can lead to a zero density of states in the limit $T\rightarrow 0$ K for a carrier with one of the spin projections, as happens, for example, in the case of $^3T_1$ symmetry of the ground state for Cr^{2+} (Fig. 1). We note that in our approach it is not necessary to introduce a giant spin splitting of the *d* bands, which still cannot describe the presence of a large spin on the Cr^{3+} ion in the paraphase (the Curie–Weiss law). Similar features of the density of states are also observed in other magnetic semiconductors — both ferromagnetic and antiferromagnetic.[8]

To perform the configurational averaging, we shall employ an impurity diagram technique.[7] We shall average each term in the series of the system (3) using the rules

$$\left\langle\sum_{\mathbf{f}} Z_{\mathbf{f}}p_{i\mathbf{f}}e^{i\mathbf{f}\cdot(\mathbf{k}'-\mathbf{k})}\right\rangle=c_i Z\delta_{\mathbf{k}\mathbf{k}'};\quad i=1,2,$$

where c_1 and c_2 are the concentrations of defects of the first and second kinds. Intersecting plots were dropped when writing the corresponding equations. This is valid only for a degenerate semiconductor $\langle\mu\rangle\hbar/\tau$, where the Fermi level lies in the conduction band and the substitution KT $\Leftrightarrow\mu$

makes sense. As a result, the solution of these equations for the average Green's functions G_{11} and G_{12} has the form

$$G_{11}^{\sigma}(\mathbf{k},E)=\left\{ E-\tilde{\xi}_{\mathbf{k}}+\frac{i}{2\tau_1^{\sigma}}\,\mathrm{sign}(\tilde{E}) - \frac{K_{\sigma}V^2}{E-\Omega+\dfrac{i}{2\tau_2^{\sigma}}\dfrac{(K_{\sigma}V)^2}{(E-\Omega)^2}\,\mathrm{sign}(\tilde{E})}\right\}^{-1},$$

$$G_{22}^{\sigma}(\mathbf{k},E)=K_{\sigma}\left\{ E-\Omega+\frac{i}{2\tau_2^{\sigma}}\frac{(K_{\sigma}V)^2}{(E-\Omega)^2}\mathrm{sign}(\tilde{E}) - \frac{K_{\sigma}V^2}{E-\tilde{\xi}_{\mathbf{k}}+\dfrac{i}{2\tau_1^{\sigma}}\,\mathrm{sign}(\tilde{E})}\right\}^{-1}. \qquad (5)$$

Here $(\tau_i^{\sigma})^{-1}=c_i g_0^{\sigma}\int d\omega|\Delta_i(\theta)^2|/4\pi$; $\tilde{E}=E-K_{\sigma}V^2/(E-\Omega)$, g_0^{σ} is the density of states in the initial c band at the Fermi level. The Green's functions (5) have a two-band structure. For a degenerate semiconductor, the contribution of the top band $E_{\mathbf{k}\sigma}^{+}$ can be neglected and a single-pole expression can be used:

$$G_{11}^{\sigma}(\mathbf{k},E)=\frac{u_{\mathbf{k}\sigma}^2}{D_{\mathbf{k}\sigma}};\quad G_{22}^{\sigma}(\mathbf{k},E)=\frac{K_{\sigma}v_{\mathbf{k}\sigma}^2}{D_{\mathbf{k}\sigma}};$$

$$G_{12}^{\sigma}(\mathbf{k},E)=\frac{u_{\mathbf{k}\sigma}^2 v_{\mathbf{k}\sigma}\sqrt{K_{\sigma}}}{D_{\mathbf{k}\sigma}};$$

$$D_{\mathbf{k}\sigma}=E-E_{\mathbf{k}\sigma}^{-}+i\left(\frac{u_{\mathbf{k}\sigma}^2}{2\tau_1^{\sigma}}+\frac{K_{\sigma}v_{\mathbf{k}\sigma}^2}{2\tau_d^{\sigma}}\right)\mathrm{sign}(E). \qquad (6)$$

$u_{\mathbf{k}\sigma}^{+}$ and $v_{\mathbf{k}\sigma}^2$ determine the probability of finding a carrier quasiparticle in the lowest conduction band $E_{\mathbf{k}\sigma}$ in the c and d relaxation channels

$$u_{\mathbf{k}\sigma}^2=\frac{\partial E_{\mathbf{k}\sigma}^{-}}{\partial\tilde{\xi}_{\mathbf{k}}}=\frac{(\Omega-E_{\mathbf{k}\sigma})}{(E_{\mathbf{k}\sigma}^{+}-E_{\mathbf{k}\sigma}^{-})};\quad v_{\mathbf{k}\sigma}^2=1-u_{\mathbf{k}\sigma}^2;$$

$$(u_{\mathbf{k}\sigma}v_{\mathbf{k}\sigma})^2=\frac{K_{\sigma}V^2}{(E_{\mathbf{k}\sigma}^{+}-E_{\mathbf{k}\sigma}^{-})^2},$$

$\dfrac{1}{\tau_d^{\sigma}}=\dfrac{K_{\sigma}v_{\mathbf{k}\sigma}^2}{u_{\mathbf{k}\sigma}^2}\dfrac{1}{\tau_2^{\sigma}}$ is the effective relaxation rate of a carrier in a d channel. Specifically, when the Ω level lies far below the c band of the diffuse states $u_{\sigma}^2|_{\mathbf{k}=\mathbf{k}_F}\to 0$ and in accordance with the high density of states at Ω level, the effective relaxation rate $\dfrac{1}{\tau_d^{\sigma}}\to\infty$.

In the limit $\Omega\to\infty$, where an unoccupied d level lies high above the Fermi energy, for $E_{\mathbf{k}\sigma}\to\tilde{\xi}_{\mathbf{k}}$, $v_{\mathbf{k}\sigma}^2\to 0$ and the Green's function G_{11} assumes the standard form for the single-band model

$$G_{11}^{\sigma}(\mathbf{k},E)=\left(E-\tilde{\xi}_{\sigma}+\frac{i}{2\tau_{\sigma}}\mathrm{sign}(E)\right)^{-1}. \qquad (7)$$

We do not discuss here the specific form of the dispersion relation $\xi_{\mathbf{k}}$, since the further calculations concerning the conductivity will make it possible to leave it in the general form. In what follows, we shall consider the particular case of a quadratic dispersion law near the bottom of the initial c band, and we shall present the conductivity formula corresponding to this case.

3. The dispersion laws of the hybridized $E_{\mathbf{k}\sigma}^{+}$ bands can give the impression that the problem of calculating the electrical conductivity reduces to the standard problem for a simple two-band model. Then it would be possible to use Fermi's golden rule to calculate the probabilities of quantum transitions and to write down easily the transport relaxation time. In the present problem, there is one circumstance that makes it necessary to use a more complicated computational method in terms of the Green's function, specifically, the localization of d electrons on account of the strong electronic correlations. Strong correlation effects result in a renormalization of the hybridization parameter $V^2\to K_{\sigma}V^2$, where K_{σ} is determined by the magnetization and depends on both temperature and the applied magnetic field. The renormalized hybridization parameter appears in the effective relaxation time. In all other respects, the picture is indeed similar to the model of two bands for quasiparticles with band structure, depending on the carrier density, temperature, and magnetic field.

On account of the initial atomic description of the *3d* states appearing in the lower conduction band $E_{\mathbf{k}\sigma}$, the width of the initial d band is 0, and conduction in this band occurs by charge transfer along c states. The expression for the current density can be written in the form[7]

$$j_{\alpha}(\mathbf{q},\nu)=-\frac{e^2}{2c}\sum_{\mathbf{k}\sigma}\int\frac{dE}{2\pi}\rho_{\alpha}^{\sigma}(\mathbf{k},\mathbf{k}+\mathbf{q}) \times\prod_{\beta}^{\alpha}(\mathbf{k}+\mathbf{q},\mathbf{k},E+\nu,E)A^{\beta}(\mathbf{q},\nu), \qquad (8)$$

$$\prod_{\beta}^{\sigma}(\mathbf{k}+\mathbf{q},\mathbf{k},E+\nu,E)=\sum_{p}\langle G_{11}^{\sigma}(\mathbf{k},\mathbf{p},E)\rho_{\beta}^{\sigma}(\mathbf{p},\mathbf{p}+\mathbf{q}) \times G_{11}^{\sigma}(\mathbf{k}+\mathbf{q},\mathbf{p}+\mathbf{q},E+\nu)\rangle, \qquad (9)$$

where $A^{\beta}(\mathbf{q},\nu)=i\nu E^{\beta}(\mathbf{q},\nu)/c$, $\rho_{\alpha}^{\sigma}(\mathbf{k},\mathbf{k}+\mathbf{q})=\dfrac{\partial\tilde{\xi}_{\mathbf{k}}}{\partial\mathbf{k}_{\alpha}}+\dfrac{\partial\tilde{\xi}_{\mathbf{k}+\mathbf{q}}}{\partial(\mathbf{k}+\mathbf{q})_{\alpha}}$, and $E(\mathbf{q},\nu)$ is the intensity of the external electromagnetic field. The vertex part (9) can be found in a ladder approximation from the system of equations

$$\prod_{11}^{\sigma}(\mathbf{k},E+\nu,E)=\frac{\partial\tilde{\xi}_{\mathbf{k}}}{\partial\mathbf{k}}\{G_{11}^{\sigma}(\mathbf{k},E)G_{11}^{\sigma}(\mathbf{k},E+\nu) \times(1+\Lambda_{11}^{\sigma}(E,\nu))+G_{12}^{\sigma}(\mathbf{k},E) \times G_{21}^{\sigma}(\mathbf{k},E+\nu)\Lambda_{22}^{\sigma}(E,\nu)\},$$

$$\prod_{22}^{\sigma}(\mathbf{k},E+\nu,E)=\frac{\partial\tilde{\xi}_{\mathbf{k}}}{\partial\mathbf{k}}\{G_{21}^{\sigma}(\mathbf{k},E)G_{12}^{\sigma}(\mathbf{k},E+\nu)\times(1+\Lambda_{11}^{\sigma}(E,\nu))+G_{22}^{\sigma}(\mathbf{k},E)\times G_{22}^{\sigma}(\mathbf{k},E+\nu)\Lambda_{22}^{\sigma}(E,\nu)\},\tag{10}$$

where, confining our attention to the normal skin effect $\nu(q)\ll 1/\tau$, we have introduced the notation

$$\mathbf{k}\Lambda_{ii}^{\sigma}(E,\nu)=\frac{c_i}{2\pi}\int|\Delta_i(\mathbf{k}-\mathbf{k}')|^2\Pi_{ii}^2(\mathbf{k}',E+\nu,E)d\mathbf{k}'.\tag{11}$$

Since in our model the impurity potential Δ_2 does not depend on the momentum, the integration over angles leads to $\Delta_{22}=0$, so that a transport relaxation time does not arise for *d* states. For *c* electrons the transport relaxation time is

$$\tau_{tr}^{-1}=c_1 g_0^{\sigma}\int d\Omega|\Delta_1(\theta)|^2(1-\cos(\theta))/4\pi.$$

As a result, we have for the statistical conductivity

$$\sigma=e^2\sum_{\sigma}g_0^{\sigma}\int\frac{d\Omega}{4\pi}\left(\frac{\partial\tilde{\xi}_{\mathbf{k}}}{\partial\mathbf{k}}\right)^2 u_{\mathbf{k}\sigma}^2\tau_{\mathrm{eff}}^{\sigma}|_{\mathbf{k}=\mathbf{k}_F},\tag{12}$$

where the effective relaxation rate (all labels referring to the momenta on the Fermi surface are dropped in what follows)

$$(\tau_{\mathrm{eff}}^{\sigma})^{-1}=\frac{u_{\sigma}^2}{\tau_{tr}}+\frac{K_{\sigma}v_{\sigma}^2}{\tau_d}.\tag{13}$$

In the particular case of a quadratic dispersion law for the *c* band

$$\sigma=\frac{e^2}{m}\sum_{\sigma}n_{\sigma}u_{\sigma}^2\tau_{\mathrm{eff}}^{\sigma},\tag{14}$$

where $n_{\mathrm{eff}}^{\sigma}=n_{\sigma}u_{\sigma}^2$ is the effective density of carriers with spin σ, which occupy *c* states with the effective mass *m* and rate $\partial\xi_{\mathbf{k}}/\partial\mathbf{k}$ characteristic of the latter. The effective relaxation rate (13), in agreement with Mathiessen's rule, is additive in the relaxation rates τ_{tr}^{-1} and $(\tau_d^{\sigma})^{-1}$ with weights u_{σ}^2 and $K_{\sigma}v_{\sigma}^2$. They are simply the probability with which the carrier participates in scattering by the corresponding potential for the *c* and *d* states. The main individual features of the material, such as the chemical composition, symmetry, and lattice constant, strongly influence the conductivity in this relation through the position of the *d* level relative to the conduction-band bottom and the effective hybridization parameter, and therefore via the u_{σ}^2 and v_{σ}^2 coefficients. Moreover, since the u_{σ}^2 and v_{σ}^2 coefficients depend on temperature, the conductivity also turns out to be temperature-dependent.

To study the case of completely correlated impurities $p_{f1}\times p_{f2}=p_f$, we added diagrams where the dashed line connects different impurity vertices.

As a result, solving the system in the standard manner, we obtain for the conductivity the expression (14) but with a renormalized relaxation time

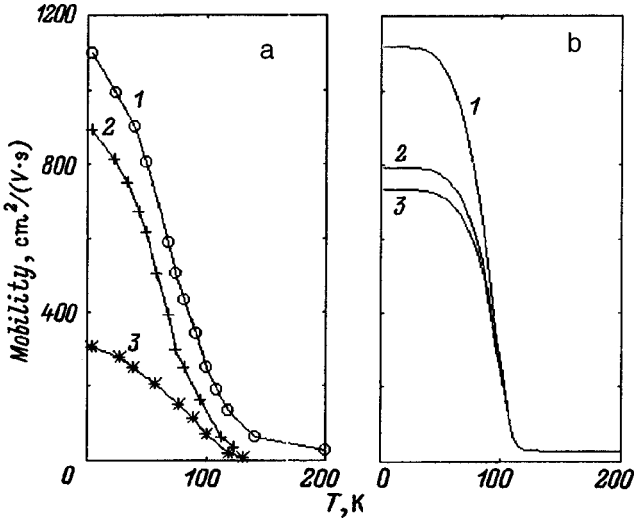

FIG. 2. Temperature dependence of the mobility for $HgCr_2Se_4$ with different carrier density. a — Experiment,[17] b — theory. $n=5\times10^{18}$ cm^{-3} (*1*), 1.23×10^{18} (*2*), and 1.4×10^{17} cm^{-3} (*3*).

$$(\tau_{\mathrm{eff}}^{\sigma})_{tr}^{-1}=\frac{cg_0^{\sigma}}{u_{\sigma}^2}\int\frac{d\Omega}{4\pi}|u_{\sigma}^2\Delta_1(\theta)+K_{\sigma}v_{\sigma}^2\Delta_2|^2\times(1-\cos(\theta)),$$

$$c=c_1=c_2.\tag{15}$$

The latter relation attests to the fact that the arrangement of the impurities strongly influences the relaxation rate. If Eq. (13) describes scattering of carriers under the condition that the impurities or defects are distributed randomly, then for a correlated arrangement of impurities or defects the interference of electronic waves, scattered by different impurity atoms (defects), becomes important.

4. The conductivity of the semiconductor *n*-$HgCr_2Se_4$ has been investigated in detail in a series of works.[9–12] In what follows, we shall briefly sketch the experimental situation, and we shall discuss its possible interpretation. Figure 2a shows the typical temperature dependences of teh Hall mobility for different $HgCr_2Se_4$ samples. The mobility in the paraphase is 10–30 cm^2/V·s. As temperature decreases, the mobility increases strongly (approximately from $T_c\sim110$ K), reaching values of the order of 1200 cm^2/V·s at $T=4.2$ K for $n\sim5\times10^{18}$ cm^{-3}.[9] Starting approximately at 2×10^{18} cm^{-3}, the carrier density at low temperatures and up to 200 K remains virtually constant, in agreement with our initial assumption that the object of our calculation is a degenerate semiconductor.

In this way, the mobility increases by two orders of magnitude in the temperature interval ~100 K. A magnetic field shifts the mobility versus temperature curve as a whole in the direction of higher temperatures. As a consequence, a large negative magnetoresistance ratio, displayed in Fig. 3a, with a peak near T_c is observed.

Such dependences in magnetically ordered substances ordinarily are attributed to scattering of carriers by spin disorder.[10,11] As correctly noted in Ref. 9, the absence of a minimum in the mobility versus temperature curve at the

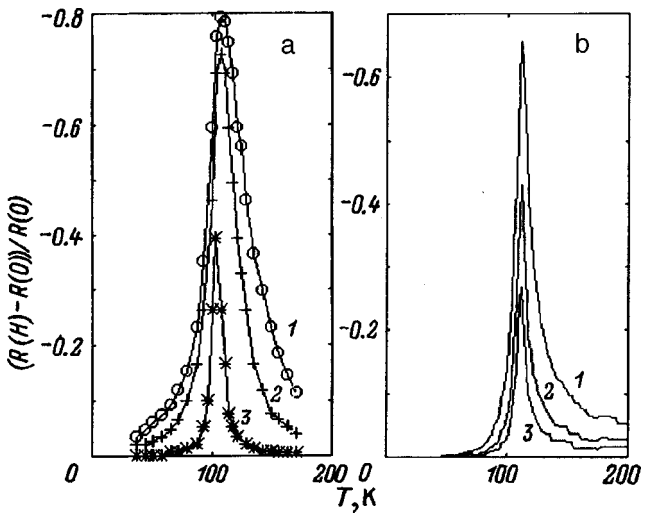

FIG. 3. Temperature dependence of the magnetoresistance ratio for $HgCr_2Se_4$. a — Experiment,[17] b — theory. $H=10.2$ (*1*), 5.6 (*2*), and 1 kOe (*3*).

point T_c, associated with increasing diffusion through spin disorder with increasing temperature, casts doubt on the existence of the standard mechanism of scattering of carriers by spin disorder in this compound. We also mention that the increase in the mobility by two orders of magnitude up to values characteristic for widegap semiconductors attests to serious temperature changes in the semiconductor band structure itself. As an acceptable mechanism, the authors of Ref. 9 proposed a mechanism of carrier scattering by spin disorder in a narrow band of *d* states, the nature of the band, just as in our case, being associated with the states of Cr^{2+}. However, the $1/T$ relation presented for the mobility in Ref. 9, with no features at T_c, appears to be incorrect for this scattering mechanism. Moreover, it has long been known for transition-metal alloys (the Mott model[13]) that the residual impurity scattering may be temperature-dependent,[14] so that it cannot be neglected when identifying the real scattering mechanism according to the temperature dependence. This is also supported by the unusual, for semiconductors, dependence of the mobility on the defect density. The highest mobility occurs in the sample obtained at the highest excess mercury vapor pressure, and hence with the highest content of uncompensated Se vacancies. Since the high-temperature part of the mobility is essentially independent of the defect density, the presence of defects increases the temperature-dependent part of the mobility.

An alternative to the generally accepted explanation could be the presence of a record-high ''red'' shift of the optical absorption edge in $HgCr_2Se_4$.[15] For a semiconductor gap $E_g(300\ \mathrm{K})\approx 0.8$ eV, the shift reaches 0.5 eV and $E_g(4.2\ \mathrm{K})\approx 0.3$ eV, which attests to a large rearrangement of the lower conduction band (Fig. 1). Together with the restructuring of the spectrum and the density of states, the carrier scattering mechanisms change: impurity and phonon.[14] Just as in the case of transition-metal alloys, we can encounter a situation where the spin disorder scattering mechanism will compete with the impurity scattering mechanism among the *d* states, which exhibits an analogous temperature dependence. Even though they are different in nature, these mechanisms nonetheless have different concentration dependences, which ultimately makes it possible to identify the predominant presence of one of them in the experimental material.

For a specially undoped *n*-$HgCr_2Se_4$ sample, the carrier scattering is due to vacancies among the anions and the *A* cations. The Se vacancies lead to both the standard potential scattering and scattering by fluctuations of the crystal field as a result of energy shifts of the *d* level. The Hg-cation vacancies apparently influence the *d* levels very little, since they are located in the second coordination sphere. At the same time they act as scattering centers for carriers undergoing the standard potential scattering. For Se vacancies the second term in Eq. (2) is most important because of the strong localization of the *d* states, and all other defects give rise mainly to carrier scattering in the channel for ordinary potential scattering by the potential Δ_1. Defects in the Se and Hg sublattice can be distributed differently. We shall assume that these defects are distributed independently, and we shall employ the results of a calculation with uncorrelated impurities (13) and (14). These relations contain, together with the parameters $V=0.15$ eV, $J=0.8$ eV, and $\Omega=-0.25$ eV (Ω is measured from the bottom of the initial *c* band in the paraphase)[5] two unknown parameters μ_S and μ_d:

$$\sigma = e\sum_{\sigma} n_\sigma u_\sigma^2 \mu_{\mathrm{eff}},$$

$$\mu_{\mathrm{eff}} = \frac{e}{m}\left(\frac{u_\sigma^2}{\tau_{tr}} + \frac{K_\sigma v_\sigma^2}{\tau_d}\right)^{-1} = \left(\frac{u_\sigma^2}{\mu_s} + \frac{K_\sigma v_\sigma^2}{\mu_d}\right)^{-1}. \qquad (16)$$

At low temperatures ($T\to 0$) the *c* band of the diffuse states drops below the Ω level as a result of the *sd* exchange interaction (Fig. 1), and for this reason the fraction of carriers in the *c* states is high: $u_\sigma^2\to 1$ and $\mu_{\mathrm{eff}}\to\mu_s\sim 1/c_1$. As temperature increases, the action of the *sd* exchange interaction on the *c* band becomes weaker ($\langle S_z\rangle\to 0$), causing the band to rise above the Ω level. In the process, the carriers pass into current-free *d* states, and their fraction in the *c* states $u_\sigma^2\to 0$. Therefore, in the paraphase for $T\gg T_c$ $\mu_{\mathrm{eff}}\to\mu_d/K_\sigma \sim 1/c_2$. Hence $\dfrac{\mu_s}{\mu_d}\approx\dfrac{\mu_{\mathrm{eff}}(T\to 0)}{K_\sigma\mu_{\mathrm{eff}}(T\gg T_c)}$. According to the experimental data, this ratio is approximately 100. The quantity μ_s was determined from the absolute value of $\mu_{\mathrm{eff}}(4.2\ \mathrm{K})$ for $n\sim 5\times 10^{18}$ cm^{-3} and was found to be ~ 2000 cm^2/V·s. Next, the temperature dependence $\mu_{\mathrm{eff}}(T)$ shown in Fig. 2b (solid line) was calculated. We shall assume that the role of the excess mercury vapor reduces to simply decreasing the number of Hg vacancies, the number Se vacancies remaining constant and equal to 10^{19} cm^{-3}. Then the temperature dependences for samples with a different carrier density can be easily calculated (Fig. 2b).

Characteristically, μ_{eff} is always less than the parameter μ_s. Thus, it follows from Eq. (16) that as $u_\sigma^2\to 0$ (the *d* level drops much below the bottom of the *c* band) $\mu_{\mathrm{eff}}\to 0$. This signifies that all carriers are in the *d* scattering channel, and in accordance with the high density of *d* states their contribution to the mobility is minimal. In the intermediate case $u_\sigma^2\sim v_\sigma^2$ the effective mobility $\mu_{\mathrm{eff}}\sim\mu_d$ and scattering by

fluctuations of the d levels makes the main contribution to the carrier scattering. Finally, only in the limit $v_\sigma^2 \to 0$, when the d level $\Omega \to \infty$, we have $\mu_{\text{eff}} \sim \mu_s$, i.e. the parameter μ_s is the maximum possible mobility that can occur if the d level were located infinitely high above the bottom of the c band. Then the carriers undergo mainly the standard potential scattering. We note also that for u_σ^2, $v_\sigma^2 \neq 0$, in the limit $\mu_s \to \infty$, we obtain from Eq. (16)

$$\sigma = \sum_\sigma en_\sigma u_\sigma^2 \mu_\sigma^*, \quad \mu_\sigma^* = \frac{\mu_d}{K_\sigma v_\sigma^2}, \tag{17}$$

i.e. the conductivity is finite even with an infinitely long free path of carriers in c states. This effect is due for carrier scattering by the fluctuation potential Δ_2 of the crystal field.

The computed value of the magnetoresistance ratio $(R(H)-R(0))/R(0)$ as a function of temperature is shown in Fig, 3b (solid line). One can see that, just as in the case of scattering by critical fluctuations of the magnetization, a large negative magnetoresistance with a maximum at $T \sim T_c$ occurs near the Curie temperature. However, these features of the magnetoresistance are due to potential scattering by impurities or defects, as well as by the magnetic field induced redistribution of carriers over different scattering channels. A direct consequence of these results is that the simple estimate of the form $\rho = \rho(H=0) - \rho(H \to \infty)$ is incorrect for determining the contribution of only the scattering of current carriers by spin disorder to the resistance of the semiconductor. The computed mechanism of magnetoresistance is observed, in complete agreement with experiment, in the form of a uniform shift (without a large change in shape) of the conductivity versus temperature curve in the direction in higher temperatures in a magnetic field.

The concentration dependence of the mobility is of special interest. As the density of defects among the nonmagnetic cations increases, the effective mobility μ_{eff} of the current carriers increases from 300 $\text{cm}^2/\text{V}\cdot\text{s}$ at $n \sim 1.4 \times 10^{17}$ cm^{-3} up to 1850 $\text{cm}^2/\text{V}\cdot\text{s}$ at $n \sim 10^{19}$ cm^{-3}.[9] It can be inferred that this is due to processes, continuing at this defect density, that lead to the formation of an impurity conduction band and therefore to drawbacks in the simplified treatment of a degenerate semiconductor as a metal with KT simply replaced by μ. It is also possible that as the mercury vapor pressure increases, the defect concentration c_1 in the Hg cation sublattice decreases, and $\mu_{\text{eff}}(\sim 1/c_1)$ at low temperatures, where scattering of carriers occurs mainly in the standard potential scattering channel, intensifies. In turn, the Se vacancy concentration c_2 remains constant, but only at high temperatures $(T \gg T_c)$ $\mu_{\text{eff}} \sim 1/c_2$.

In strong magnetic fields, where Landau quantization occurs for itinerant electrons, unusual quantum oscillations of the magnetization and resistance are observed in n-$HgCr_2Se_4$.[16] A theoretical description of the magnetization was given in Ref. 17 on the basis of the same model as the one in the present paper. As one can see from Eq. (4), the conduction-band bottom shifts in proportion to $\langle S_z \rangle$, while the chemical potential is pinned near the d level Ω. For this reason, the effective chemical potential, measured from the band bottom and determining the phase of the oscillating part

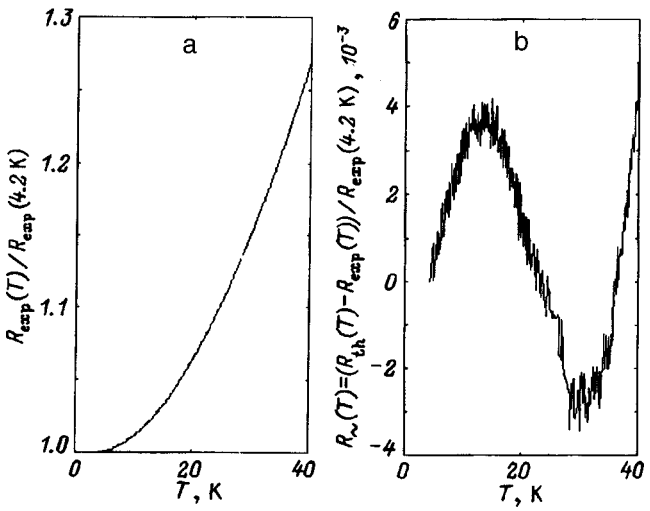

FIG. 4. Experimental temperature dependence of the electrical resistance for n-$HgCr_2Se_4$ in a 60 kOe field (a) and oscillating part of the resistance $R_\sim(T)$ (b).

of the thermodynamic potential, the magnetization, and the resistance, acquires strong field and temperature dependences, in contrast to the weak T^2/ε_F corrections in the Fermi-liquid theory. As a result, the quantum oscillations of the magnetization and resistance which are observed in an external magnetic field are no longer periodic as functions of the reciprocal of the field.[16] Similarly, as the temperature varies, crossings of the chemical potential with the Landau levels can occur. Such crossing can lead to temperature quantum oscillations, observed thus far only for the magnetization.[18]

To single out the oscillating part in the temperature dependence of the resistance, it is necessary to subtract the monotonic dependence, not associated with Landau quantization, specifically, the resistance $R_{th}(T)$ determined by Eq. (15), from the experimental curve $R_{\text{exp}}(T)$ (Fig. 4a[16]). The temperature dependence appearing in Eq. (14) was found on the basis of the spin-wave theory

$$\langle S_{\acute{E}} \rangle = 3/2 - at^{3/2} Z_{3/2}(x) - bt^{5/2} Z_{5/2}(x) - ct^{7/2} Z_{7/2}(x), \tag{18}$$

$t = T/4\pi IS$, $x = 2\mu_B H/T$. The parameters in the expansion (18) a, b, and c were determined by fitting the experimental data on the temperature dependence of the magnetization using a simplex method. The results are $a = 0.8499$, $b = -0.5545$, and $c = 0.1294$. The theoretical temperature dependence $R_{th}(T)$ obtained in this manner describes the temperature dependence of the resistance neglecting Landau quantization. The oscillating part of the resistance $R_\sim(T) = R_{\text{exp}}(T) - R_{th}(T)$ is shown in Fig. 4b, where indeed a single period of the oscillations is observed, just as for the magnetization.[18] The relative amplitude of the oscillations of the electrical resistance is small because of the smallness of the carrier density itself, but, as it turned out, it is approximately five times greater than the magnitude of the magnetization oscillations.

In conclusion, we note that the potential impurity scattering mechanism acquires such unusual, for the practice of

multicomponent compounds, temperature and field dependences because of a characteristic combination of several factors, the initial ones being the breakdown of the stoichiometric laws and the presence of transition elements in the chemical composition of the semiconductor. Such a combination could be the first indication of a substantial impurity contribution to the resistance in a semiconductor with temperature and field dependences that are similar to those calculated here.

We thank A. D. Balaev for providing the low-temperature dependence of the resistivity of *n*-$HgCr_2Se_4$ in a 60 kOe field.

This work was supported by the Russian Fund for Fundamental Research (Grant No. 96-02-16075) and the Krasnoyarsk Krai Science Foundation (Grant No. 7F0175).

*)E-Mail: gav@iph.krasnoyarsk.su

[1] N. N. Sirota, *Physicochemical Nature of Phases with Variable Composition*, Nauka i Tekhnika, Minsk (1970), 231 pp.
[2] S. Metfessel and D. C. Mattis, *Magnetic Semiconductors, Handbuch der Physic*, Springer-Verlag, N. Y. (1968), 562 pp.
[3] É. L. Nagaev, *Physics of Magnetic Semiconductors*, Nauka, Moscow (1979), p. 127.
[4] R. von Helmholt, J. Wecker, B. Holzapfel, L. Shultz, and K. Samwer, Phys. Rev. Lett. **71**, 2331 (1993); S. Jin, T. H. Tiefel, M. Mc. Cormack, R. A. Fasthnacht, R. Ramesh, and L. H. Chen, Science **264**, 413 (1994).
[5] V. A. Gavrichkov, S. G. Ovchinnikov, M. Sh. Erukhimov, I. S. Édel'man, and M. Sh. Erukhimov, Zh. Éksp. Teor. Fiz. **90**, 1275 (1986) [Sov. Phys. JETP **63**, 744 (1986)]; V. A. Gavrichkov, S. G. Ovchinnikov, and M. Sh. Erukhimov, Fiz. Tverd. Tela (Leningrad) **29**, 527 (1987) [Sov. Phys. Solid State **29**, 298 (1987)].
[6] M. Lanoo and J. Bourgoin, *Point Defects in Semiconductors I, Theoretical Aspects*, Springer Series in Solid-States Science 22. Springer-Verlag, N. Y. (1981), 264 pp.
[7] A. A. Abrikosov, L. P. Gor'kov, and I. E. Dzyaloshinskiĭ, *Methods of Quantum Field Theory in Statistical Physics* [Prentice-Hall, Englewood Cliffs, N. J., 1963; Gostekhizdat, Moscow, 1962].
[8] S. G. Ovchinnikov, Phase Transit. **36**, 15 (1991).
[9] A. Selmi, *Galvanomagnetic Properties of the Semiconductor* $HgCr_2Se_4$, Diplome de Doctoeur (in French), University of P.-M. Curie, 1979, pp. 61–71; A. Selmi *et al.*, J. Appl. Phys. **57**, 3216 (1985); A. Selmi *et al.*, J. Magn. Magn. Mater. **66**, 295 (1987).
[10] N. Koguchi, K. Masumoto, and J. Phys. Chem. Solids **41**, 1279 (1980).
[11] B. A. Gizhevskiĭ, A. A. Samokhvalov *et al.*, Fiz. Tverd. Tela (Leningrad) **26**, 2647 (1984) [Sov. Phys. Solid State **26**, 1604 (1984)].
[12] V. K. Chernov, V. A. Gavrichkov, N. B. Ivanova, G. S. Veĭst, and Yu. V. Boyarshinov, Fiz. Tverd. Tela (Leningrad) **28**, 289 (1986) [Sov. Phys. Solid State **28**, 159 (1986)].
[13] N. F. Mott, Proc. Phys. Soc. **47**, 571 (1935); Proc. Roy. Soc. A **153**, 368 (1936); N. F. Mott, K. W. H. Stevens Philos. Mag. **2**, 1364 (1957); B. R. Coles Adv. Phys. **7**, 40 (1958).
[14] J. Frank and F. Blatt, *Physics of Electronic Conduction in Solids*, Mc Graw–Hill Book Co., N. Y. (1968), 470 pp.
[15] T. Arai and M. Wakaki *et al.*, J. Phys. Soc. Jpn. **34**, 68 (1973).
[16] A. D. Balaev, V. V. Val'kov, V. A. Gavrichkov, N. B. Ivanova, S. G. Ovchinnikov, and V. K. Chernov, Usp. Fiz. Nauk **167**, 1016 (1997); A. D. Balaev, V. A. Gavrichkov, S. G. Ovchinnikov, V. K. Chernov, T. G. Aminov, and G. G. Shabunina, Zh. Éksp. Teor. Fiz. **113**, 5 (1998), at press [J. Exp. Theor. Phys. **86**, 1026 (1998)].
[17] V. V. Val'kov and D. Dzebisashvili, Zh. Éksp. Teor. Fiz. **111**, 654 (1997) [J. Exp. Theor. Phys. **84**, 360 (1997)].
[18] S. G. Ovchinnikov, V. K. Chernov, A. D. Balaev, N. B. Ivanova, V. A. Levshin, and B. P. Khrustalev, JETP Lett. **62**, 642 (1995).

Translated by M. E. Alferieff

Spin fluctuations and Curie temperature in the compounds R_2M_{17} with nonmagnetic elements

V. I. Grebennikov and S. A. Gudin

Institute of Metal Physics,) Ural Branch of the Russian Academy of Sciences, 620219 Ekaterinburg, Russia*
(Submitted April 20, 1998)
Fiz. Tverd. Tela (St. Petersburg) **41**, 77–83 (January 1999)

The magnetic properties of materials for permanent magnets based on binary compounds R_2M_{17} (R=Y, Sm; M=Fe, Co), also including additions of the nonmagnetic elements N, Al, and Si, are investigated a the theory of dynamical fluctuations of the electronic spin density. It is shown that the Curie temperature is determined by the ratio of the exchange splitting energy (proportional to the magnetization at $T=0$) and the rms value of the fluctuations (proportional to the local spin susceptibility). The fluctuations are much larger in iron compounds than in cobalt alloys. This results not only in quantitative differences in their characteristics but also in a qualitatively different change in the properties of these materials on nitriding. © *1999 American Institute of Physics.* [S1063-7834(99)01801-8]

When nonmagnetic elements N, Al, and Si are introduced into the intermetallic rare-earth compounds R_2M_{17} used as permanent magnets, unusual changes occur in the properties of the compounds.[1,2] For example, the addition of 2.9 nitrogen atoms per formula unit to the compound Sm_2Fe_{17} increases the Curie temperature T_c from 389 to 746 K. A similar increase is observed in the compound Y_2Fe_{17} with nitrogen, aluminum, and silicon. The corresponding quantities are presented in Table I. We also note that a very large increase of the saturation magnetization M_0 at $T=0$ compared with the initial binary alloy is observed in the compound $Y_2Fe_{17}N_{2.6}$.

Ordinarily, such effects are attributed to an increase in the lattice constant and a change in the value of the exchange integrals with increasing distance between the iron atoms.[3] However, the lattice parameters both increase (Al, N) and decrease (Si),[2] while T_c increases in both cases. Conversely, T_c in Sm_2Co_{17} decreases from 1189 to 811 K when 2.7 nitrogen atoms are added.

In Ref. 4 the spin-polarized electron density of states (EDS) were calculated for the compounds mentioned and attempts were made to calculate the Curie temperature on the basis of the Mohn–Wohlfarth spin-fluctuation theory.[5] The quantitative results were unsatisfactory, though the tendency for T_c to increase with added nitrogen was correctly portrayed. The same theory was used for quantitative interpretation of the experimental results obtained in Ref. 2 for the system Y_2Fe_{17} where, together with the magnetic measurements, other properties of the alloys, specifically, the specific heat, were investigated.

Later,[6] the systems Sm_2Fe_{17} and Sm_2Co_{17} were investigated using the theory of localized Heisenberg magnetic moments with exchange integrals obtained in band calculations.[7]

It seems to us that fluctuations of the spin density of collectivized electrons dominate in all of the compounds named above. In the present paper we study the quanitative effect of spin fluctuations (SFs) on the magnetic properties of the compounds (2)–(17) using a fluctuation approach.[8,9]

The investigation is based on the following idea. The intraatomic repulsion u of electrons leads to two basic effects: (1) exchange splitting $\pm V_0$ of the energy of states having different spin projections and (2) fluctuations $\langle \Delta V^2 \rangle$ of the exchange field on an atom — both as a result of thermal excitations and, generally speaking, as a result of zero-point (at $T=0$) SFs. The first effect (mean field) leads to ordering of the spin moments of the atoms, while the second effect (fluctuations), conversely, gives rise to disordering. The ratio of the two characteristic quantities determines the magnetic properties of metallic magnets. The introduction of nonmagnetic elements ordinarily decreases the exchange splitting, but fluctuations weaken at the same time. The combined effect of these two opposing factors has the effect that the Curie temperature increases in some cases (Fe) and decreases in other cases (Co). Similar changes can also occur with the magnetization M_0 at $T=0$ — as a result of zero-point fluctuations. The increase in the degree of band filling from iron to cobalt likewise results in similar suppression of fluctuations.

Comparing M_0 and T_c in pure iron and its compounds shows that SFs play a larger role in the latter. This is also indicated by the large value of the low-temperature specific heat $\gamma=C/T$, which is three times larger than the value obtained using standard estimates from the electronic density of states at the Fermi level.[2]

1. CHARACTERISTIC FEATURES OF SPIN FLUCTUATIONS IN R_2M_{17}

A detailed description of the derivation of the basic equations of the electron spin density fluctuations method and the approximations employed in the process is given in Refs. 8 and 9. However, there are a number of new features in the problem considered in the present paper. In previous

TABLE I. Magnetic properties and characteristics of fluctuations in the compounds Y–Fe, Sm–Fe, and Sm–Co.

Composition	M_0, μ_B/form.unit	T_c^{exp}, K	T_c, K	V_0, eV	a	β
Y_2Fe_{17}	34.0	309	312	0.97	18.9	1.00
$Y_2Fe_{17}Al_{1.9}$	31.7	384	353	0.82	15.7	0.97
$Y_2Fe_{17}Si_{1.9}$	31.8	430	391	0.81	14.4	0.96
$Y_2Fe_{17}N_{2.6}$	40.3	694	777	1.10	9.6	0.92
Sm_2Fe_{17}	36.9	389	390	1.10	14.8	0.88
$Sm_2Fe_{17}N_{2.9}$	36.5	746	630	0.95	9.8	0.80
Sm_2Co_{17}	26.3	1189	1188	0.74	4.9	0.90
$Sm_2Co_{17}N_{2.7}$	23.4	811	876	0.52	4.8	0.83

work, a single ''nonmagnetic'' EDS was taken as the initial density, and the polarized densities of states at $T=0$ were obtained simply by splitting it by the amount $\pm V_0$ for states with opposite spins. Here we shall formulate the equations starting from the spin-polarized EDS obtained in calculations by the spin density functional method[4,6] [the corresponding curves $\nu_+^0(\varepsilon)$ and $\nu_-^0(\varepsilon)$ differ not only with respect to position but also shape (Fig. 1)]. In addition, characteristic features arise because of the need to take into account the s–p states of the nonmagnetic atoms. The corresponding altered equations used in the calculations are presented in the Appendix.

In the text below we shall confine ourselves to very simple approximation relations, which are required to discuss the basic results obtained in the full calculation.

The mean-square fluctuating field is determined by the dynamic spin susceptibility χ

$$\langle \Delta V_{jq\omega_n}^2 \rangle = \frac{T}{2} \frac{u^2 \chi_q^j(\omega_n)}{(1-u\chi_q^j(\omega_n))}. \tag{1}$$

Here T is the temperature in energy units, u is the intratomic electron repulsion constant, q is the wave number, $\omega_n = 2\pi nT$ is the thermodynamic frequency (energy), and $j = x, y, z$ are the spatial components of the vectors. The z axis is directed along the average magnetization. It was shown in previous work[10] that the effect of a random field is determined mainly by its integral characteristic — the fluctuations of the field at a lattice site

$$\zeta^j = \sum_n \{\langle \Delta V_{jq\omega_n}^2 \rangle\}, \tag{2}$$

where the braces denote averaging over the wave vectors of the Brillouin zone. In what follows, to simplify the equations, we shall drop the vector indices. We shall express the estimate for the quantity (2) as

$$\zeta = \frac{\pi U^2 T^2}{6D} \left\{ \frac{\beta\varphi}{\lambda^2} \right\},$$

$$\lambda = 1 - U\beta\chi(0), \quad \varphi = \mathrm{Im}\,\chi(\varepsilon)/\varepsilon, \quad \varepsilon \to 0. \tag{3}$$

The average value $\overline{V} \equiv \langle V \rangle$ of the exchange field is proportional to the average spin polarization (moment) s^z of one state

$$\overline{V} = -Us^z. \tag{4}$$

Here

$$D = R/N_a, \quad U = Du, \quad \beta = R_d/R, \tag{5}$$

R is the number of electronic states per formula unit per spin, and R_d is the number of electronic states forming the local susceptibility, which we shall determine according to the number N_{ad} of d-type atoms: $R_d = 5N_{ad}$; N_a is the total number of atoms per formula unit and D is the number of electronic states per atom. All quantities in Eqs. (3) and (4) are given per electronic state in order to distinguish clearly the dependence on the number of states R.

According to the relations presented in the Appendix, the spin polarization s^z and the local susceptibility χ and φ are determined by the Fermi integrals of the single-site Green's function $g_s = g_s(\varepsilon; \overline{V}, \zeta)$, which can be calculated using the known electronic density of states $\nu_s^0(\varepsilon)$ at $T=0$ taking into account scattering of electrons by the fluctuating exchange field. Thus Eqs. (3) and (4) form a closed system of equations. The interaction constant U is determined from the initial (at $T=0$) condition

$$s^z(U) = s_0 = M_0/2R, \tag{6}$$

which because of the absence of fluctuations at $T=0$ is identical to the equation obtained in the Stoner–Wohlfarth mean-field theory. The quantity $2R$ is simply the total area under the two curves of the polarized density of states.

The equations were obtained in the following model. It is assumed that the uniform magnetization, or the average polarization s^z, is formed by all states in a band, both s and d type, while the response to a fluctuating field at a site, or the local susceptibility χ, is determined only by the d states. This model was constructed under the assumption that fast s electrons are scattered by the entire cluster of atoms inside which the field fluctuations are averaged. Such electrons ''see'' only the uniform mean field and for this reason do not contribute to the local susceptibility. This results in an effec-

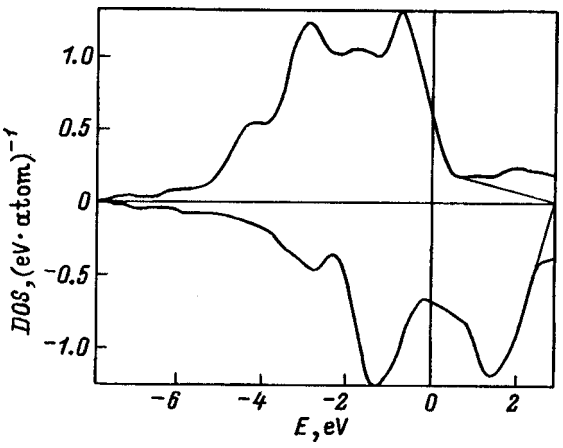

FIG. 1. Separation (by the straight line segments) of a closed zeroth density of states from the EDS of Sm_2Fe_{17} obtained in a band calculation.[6] The energy e is measured from the Fermi level.

tive renormalization of the susceptibility χ, calculated according to the total EDS, which is given by the coefficient β — the relative weight of the d states.

We now introduce a quantity characterizing the rate of growth of the rms value of the field fluctuations with temperature, or the temperature coefficient of the fluctuations,

$$a=\left(\sum_j \zeta^j\right)^{1/2} \Big/ T\cong \text{const}(T). \tag{7}$$

The quantity a is almost temperature-independent in the ferromagnetic region, since the electronic characteristics vary quite little because an increase in fluctuations is ordinarily compensated by a decrease in the mean field,

$$\overline{V^2}+2\sum_j \zeta^j\cong \text{const}(T)=V_0^2. \tag{8}$$

The equation (8) is actually a consequence of the approximate conservation of the atomic magnetic moments, since $\langle V^2\rangle = U^2\langle s^2\rangle$. The factor 2 in Eq. (8) appears because the quantity ζ determines equally both the chaotic part of the SFs and the correlated, long-wavelength part. The Curie temperature is determined by setting to zero the average magnetization or, in other words, $\overline{V}(T_c)=0$. Therefore we obtain from Eqs. (7) and (8) the estimate

$$T_c\cong V_0/2a, \tag{9}$$

where V_0 and a are calculated at $T=0$, i.e. according to the zeroth EDS.

According to Ref. 11, the low-temperature specific heat $C=\gamma T$ (per atom) is determined by the equation $\gamma=\gamma_f+\gamma_e$,

$$\gamma_f=\frac{\pi k_B^2 U}{3}\sum_j\left\{\frac{\beta\varphi}{\lambda}\right\},\quad \gamma_e=\frac{\pi^2}{3}k_B^2\overline{\nu}, \tag{10}$$

where γ_f and γ_e are the contributions of the SFs and the Fermi excitations, respectively, while $\overline{\nu}=D(\nu_+(\mu)+\nu_-(\mu))$ is the density of states at the Fermi level μ.

As one can see from Eqs. (3), (7), and (10), $a\propto\gamma_f$. Therefore an inverse dependence of T_c on γ is expected in magnets with a large low-temperature specific heat (larger than the contribution of the single-particle excitations).

Equation (3) indicates another feature. In substances with strong fluctuations (the magnetization is large and the Curie temperature is relatively low) a large change in T_c with a weak variation of the electronic characteristics of the system is likely. Indeed, in this case the denominator λ is close to zero, so that a small correction to the interaction U, the weight β of the d states, or the static local susceptibility χ (the latter is proportional to the number of holes in a band) can lead to a sharp increase or decrease of the SFs and correspondingly the Curie temperature. In high-T_c magnets the fluctuations of weaker and the denominator λ in Eq. (3) is far from zero, so that a in Eq. (9) is quite stable and the changes in T_c follow the changes in the initial exchange splitting or zeroth magnetization, $V_0\propto M_0$.

2. MODEL FOR DESCRIBING TERNARY COMPOUNDS

The number of atoms N_a and correspondingly the number of electrons N_e per formula unit increase when additional elements are introduced into the initial compound. In addition, the magnetic moment M_0 at $T=0$, which we take from the experimental data, ordinarily changes. The shape of the EDS curve of the alloy likewise changes. The new EDS is calculated for some alloys but not for others. So as not to introduce an additional uncertainty associated with the distortion of the EDS and the separation from it of the energy range that is important for magnetic properties, where the interaction of the electrons can be described by a single intraatomic interaction constant U (and not a function depending on the wave number or energy), we shall assume that the form of the density of states remains unchanged and the same as in the starting material when nonmagnetic atoms are added. In the process, let the number of states per formula unit R simply increase by the amount

$$\Delta R=R\Delta N_e/N_e. \tag{11}$$

In this case, the band filling $n_0=N_e/R$ does not change, but, as one can see from Eq. (5), the fraction $\Delta\beta=-\beta\Delta N_e/N_e$ of the states forming the local susceptibility decreases. This suppresses the fluctuations (under otherwise the same conditions). The initial (at $T=0$) value of the spin polarization s_0 changes according to Eq. (6), which can lead to a corresponding change in the effective interaction U and splitting V_0.

3. RESULTS

1) *Initial data.* The experimental value of the zero-temperature magnetization M_0 (in Bohr magnetons per formula unit), the number of electrons N_e, and the spin-polarized density of states $\nu_s^{0R}(\varepsilon)$ (from band calculations) are taken as the input data.

Curves of the EDS for Sm_2Fe_{17}, taken from Ref. 6, are displayed in Fig. 1. The densities of states contain a large pronounced contribution from the 3d states and to the right of it a tail formed by the states of other bands, extending, generally speaking, to arbitrarily distant energies. Since we are confining ourselves to an energy-independent interaction, we must single out the states lying in a bounded energy interval, where the matrix element of the exchange interaction is described by the constant u, i.e. we must close the band. The corresponding cutoff is eyeballed, as shown in Fig. 1 by straight line segments.

Of course, such a procedure is arbitrary to a certain extent and affects the results of the subsequent calculation. For this reason we give the cut-off EDSs for the initial binary compounds and leave them unchanged in calculations of ternary alloys.

2) *Quantitative results.* After the above-described preliminary treatment of the EDS, the problem becomes uniquely defined, and the calculation follows the scheme described in the Appendix. The magnetization M, the reciprocal of the uniform susceptibility χ_0^{-1}, the specific heat, and the mean-square fluctuations of the field $\zeta^x+\zeta^y+\zeta^z$ are calculated as functions of the temperature T/T_c^{exp}. They are dis-

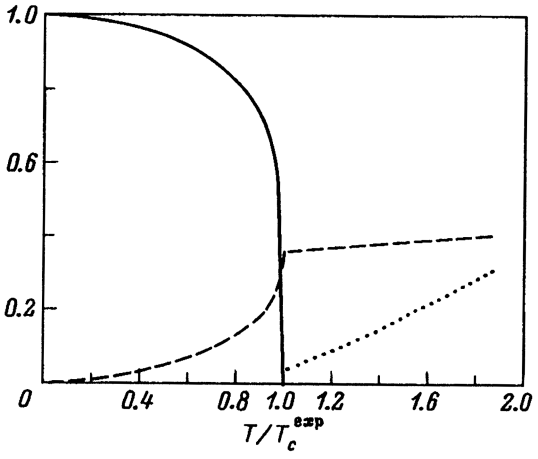

FIG. 2. Complete characteristics of Sm_2Fe_{17} as a function of temperature T/T_c^{exp}: the relative magnetization M/M_0 (solid line); square of the ratio of the field fluctuations to the magnitude of the exchange field at $T=0$, $(\zeta^x+\zeta^y+\zeta^z)/V_0^2$ (dashed line); the reciprocal of the uniform susceptibility χ^{-1} (per atom, in the units $k_B T_c^{exp}/\mu_B^2$) (dotted line).

played in Fig. 2 for Sm_2Fe_{17}. We note that in the course of the calculation a single-site Green's function, the decay of the single-electron states, the complex local susceptibility, the spatial spin correlation function, and so on are also found. This makes it possible to calculate the temperature dependence of the most diverse properties and characteristics of the system,[8,9] for example the photoemission and x-ray spectra of the valence band, the electrical resistance, the relaxation rate in NMR, the paramagnetic neutron scattering, the short-range magnetic order length, and others.

In the present paper we confine ourselves to the basic magnetic characteristics. The experimental values of the magnetization M_0^{exp} at $T=0$, the Curie temperature T_c^{exp}, the corresponding values of T_c obtained in the calculation, the exchange field V_0 (4), and the temperature coefficient a of the fluctuations (7) at $T=0$ are given in Table I. Renormalization of the local susceptibility β is determined using Eq. (5), and the Fe, Co, and Y in it are treated as d elements.

We compare first the binary compounds with one another. They all have approximately the same EDSs.[4,6] The band filling in Sm_2Co_{17} is greater than in the iron compounds, since the cobalt atom contains nine electrons while iron contains eight.

The exchange field V_0 depends directly on the magnetization M_0, as follows from Eqs. (4) and (6). Comparing the values of a characterizing the fluctuations, we can see that they differ quite substantially, so that the values of T_c also differ. The estimate (9) leads to the same result.

The fluctuations are strongest in Y_2Fe_{17} and weakest in Sm_2Co_{17}. This is easy to understand. The filling of the bands with electrons decreases the local susceptibility (χ is proportional to the number of unoccupied states in a band), which decreases fluctuations and correspondingly increases T_c.

Let us now consider the ternary compounds with respect to the starting binary compounds. The introduction of nonmagnetic elements ordinarily decreases the magnetization M_0 and the exchange energy V_0 ($Y_2Fe_{17}N_{2.6}$ is an exception; we shall discuss why below). However, T_c increases substantially in iron compounds, while in cobalt compounds, conversely, it decreasese. Turning to the a column, we can see that the nonmagnetic elements decrease the fluctuations. The value of a is smallest in SmCoN, and the magnetization decreases appreciably. The numerator in Eq. (9) decreases more strongly than the denominator, and ultimately T_c decreases. The fluctuations are much stronger in iron compounds, so that they control the change in T_c. Therefore the estimate (9) works everywhere.

TABLE II. Fluctuation and electronic contributions to the specific heat of the system Y–Fe.

Composition	γ_f, mJ $\cdot$mol$^{-1}\cdot$K^{-2}	γ_e, mJ $\cdot$mol$^{-1}\cdot$K^{-2}	$\gamma_f+\gamma_e$, mJ $\cdot$mol$^{-1}\cdot$K^{-2}	γ^{exp}, mJ $\cdot$mol$^{-1}\cdot$K^{-2}
Y_2Fe_{17}	125	55	180	215
$Y_2Fe_{17}Al_{1.9}$	115	65	180	186
$Y_2Fe_{17}Si_{1.9}$	106	66	172	150
$Y_2Fe_{17}N_{2.6}$	62	55	117	–

3) *Zero-point fluctuations.* We shall now discuss the increase in M_0 accompanying the addition of nitrogen to Y_2Fe_{17}, but now at a qualitative level, since our approach is specially adapted for describing only the thermal (low-energy) fluctuations, $\langle \Delta V^2 \rangle = 0$ at $T=0$. However, this does not mean that there are no SFs in the ground state. We simply neglected zero-point vibrations, making the assumption that they are taken into account in the initial calculation of the EDF by the spin density functional method. The initial equations of the theory of the dynamic fluctuating fields contains a contribution from zero-point fluctuations.[10] Moreover, the contribution can be calculated.[12] However, here we shall not go into the theory; we shall confine ourselves to the obvious assumption: If thermal fluctuations are large (a is large), then the zero-point fluctuations will also be large. Then the introduction of nitrogen will suppress not only thermal but also zero-point fluctuations. The latter increases M_0 in $Y_2Fe_{17}N_{2.9}$. We note that such an interpretation of the change in the magnetization is also applicable to other compounds. Nitrogen in Sm_2Fe_{17}, on the one hand, directly decreases the magnetization and, on the other, increases the magnetization indirectly by suppressing fluctuations. As a result, the effect of nitrogen on M_0 is almost completely compensated. Finally, in Sm_2Co_{17} fluctuations (including zero-point) are small, and ultimately nitriding decreases M_0.

The contributions of SFs, calculated from Eqs. (10), and the single-electron excitations to the temperature coefficient of the specific heat are presented in Table II together with the experimental values of Ref. 2 for the system Y–Fe. The fluctuation term γ_f decreases when nonmagnetic atoms are added to the same extent to which T_c increases in these compounds. The fluctuation contribution is greater than the electronic contribution γ_e, so that the measured quantity γ^{exp} is fully capable of characterizing the intensity of SFs in such a system. The quantitative agreement between the computed quantity $\gamma_f+\gamma_e$ and the experimental quantity γ^{exp} is not very good. The best quantitative results can be obtained by detailing the EDF of specific alloys and taking account of

the phonon enhancement, but we shall not do this, deliberately remaining within the simple model described above for ternary compounds, intended for determining the most general mechanisms leading to the manifestation of SFs.

We shall now summarize the results of this work. The effect of spin fluctuations on the main magnetic characteristics in materials used for permanent magnets based on the compounds R_2M_{17} with the addition of N, Al, and Si was studied. It was shown that the Curie temperature is determined by two factors: the exchange splitting energy of the spin states and the temperature coefficient of the fluctuations. The latter quantity is proportional to the local spin susceptibility, which in turn is determined by the hole density in the *d* band. Nonmagnetic elements added to the alloy suppress spin fluctuations. In iron compounds, where the SFs are large (T_c are relatively low, and the specific heat is high), this gives rise to a substantial increase of the Curie temperature. In cobalt alloys, the SFs are much weaker, so that the effect of nonmagnetic atoms on them is weaker, and the result is determined by the direct effect of the added elements on the magnetization, which decreases T_c. The calculations based on the theory of electron spin density fluctuations, using polarized densities of states, show quite good quantitative agreement with the experimental data. The extension of the above-formulated approach so as to take into account the zero-point SFs makes it possible to understand the influence of the latter on the zero-temperature saturation magnetization.

4. APPENDIX

Let the polarized densities of states $\nu_s^{0R}(\varepsilon)$, which depend on the energy ε, with spin projections $s=\pm$, the magnetization M_0 (in Bohr magnetons) at $T=0$, and the number of electrons $N_e=\Sigma N_{ei}N_{ai}$ (the sum over elements *i*, the number of atoms of which is N_{ai}, each atom containing N_{ei} valence electrons according to the periodic table) be known. All quantities are calculated per formula unit.

We shall find the number of states with fixed polarization and normalized to one state of the EDS

$$R_s=\int d\varepsilon\,\nu_s^{0R}(\varepsilon), \quad \nu_s^0(\varepsilon)=\nu_s^{0R}(\varepsilon)/R_s. \tag{A1}$$

In what follows, we shall require the single-site Green's function

$$G_s^0(\varepsilon)=\int d\varepsilon'\,\nu_s^0(\varepsilon')(\varepsilon-\varepsilon')^{-1},$$

$$\mathrm{Im}\,G_s^0(\varepsilon)=\pi\nu_s^0(\varepsilon). \tag{A2}$$

The average value $\langle V\rangle$ of the exchange field is proportional to the spin moment $D\langle s^z\rangle$ of an atom:

$$\langle V\rangle=-uD\langle s^z\rangle. \tag{A3}$$

The mean-square fluctuations of each vector component *x*, *y*, and *z* of the field at the site (2) is determined by the susceptibility

$$\zeta=\left\{\frac{u^2D\beta\chi_l T}{\pi\lambda_l t_q}\tan^{-1}\frac{\pi^2\varphi T}{6\chi_l\lambda_l t_q}\right\},$$

$$D=R/N_a, \quad \beta=R_d/R, \quad R=(R_++R_-)/2. \tag{A4}$$

Here *u* is the constant characterizing the interaction of electrons on an atom, *D* is the number of states per atom (and per spin), $\langle s^z\rangle$ is the spin moment of one electronic state, R_d is the number of *d* states, and *R* is the number of all states per formula unit, β is the fraction of *d* states forming the local susceptibility, which is studied in detail in the main text of the paper. The braces indicate averaging over the wave numbers *q* in the Brillouin zone. The quantities χ_l,φ, and t_q characterize the components of the zeroth (no electron-electron interaction) complex dynamic spin susceptibility $\chi_q(\varepsilon)$ with thermal energies ($\varepsilon\approx k_BT$) per state

$$\chi_q(\varepsilon)\cong\chi_q(1-i\varepsilon\varphi/\chi_q)^{-1}\cong\chi_q+i\varepsilon\varphi,$$

$$\chi_q\equiv\chi_q(0), \tag{A5}$$

$$\lambda_q=1-uD\chi_q=\lambda_l t_q=\lambda_0+(\lambda_l-\lambda_0)q^2/\{q^2\},$$

$$\lambda_l=1-uD\beta\chi_l. \tag{A6}$$

The latter equality (A6) gives the simplest isotropic interpolation of the nonuniform static susceptibility with respect to its value χ_0 (with zero wave number) and average value in the Brillouin zone or, in other words, with respect to the local susceptibility χ_l, describing the response to the exchange field acting per atom (inside a muffin-tin cell). The quantities χ_0,χ_l, and φ can be calculated, and the dependence on the wave number *q* is actually determined by the function t_q defined in Eq. (A6). The average value is $\{t_q\}=1$. Using it in Eq. (A4), we obtain the local-fluctuation theory limit.

We note that the expression (A4) for the fluctuations differs somewhat from that presented in Ref. 8. There the susceptibility was calculated from the second equality in Eq. (A5), while here the first equality, which gives the correct zero asymptotic in the limit $\varepsilon\to\infty$, is used. This ensures a strict passage to the static or high-temperature limit. For this, it is sufficient to make the substitution $\tan^{-1}\ldots\to\pi/2$ in Eq. (A4).

The average spin moment is determined by integrals of the single-site Green's function with the Fermi function

$$f(\varepsilon)=(\exp(\varepsilon-\mu)/T+1)^{-1},$$

$$\langle s^z\rangle=(n_+-n_-)/2, \quad n_s=\int\frac{d\varepsilon}{\pi}f(\varepsilon)\mathrm{Im}\,g_s(\varepsilon). \tag{A7}$$

The components of the susceptibility have the form

$$\chi_l^z=(\chi_l^+ +\chi_l^-)/2, \quad \chi_l^{\pm}=-\int\frac{d\varepsilon}{\pi}f(\varepsilon)\mathrm{Im}\,g_\pm^2(\varepsilon),$$

$$\chi_l^{x,y}=-\int\frac{d\varepsilon}{\pi}d\varepsilon f(\varepsilon)\mathrm{Im}(g_+(\varepsilon)g_-(\varepsilon)). \tag{A8}$$

Here $-f$ can be replaced by $1-f$, i.e. integration over the filled part of the band can be replace by the empty part.

The imaginary parts of the local susceptibility (A5) are actually determined by the squared EDS at the Fermi level,

$$\varphi_l^z=-\int\frac{d\varepsilon}{2\pi}\frac{\partial f}{\partial\varepsilon}((\mathrm{Im}\,g_+)^2+(\mathrm{Im}\,g_-)^2),$$

$$\varphi_l^{x,y} = -\int \frac{d\varepsilon}{\pi}\frac{\partial f}{\partial \varepsilon}\mathrm{Im}\, g_+(\varepsilon)\mathrm{Im}\, g_-(\varepsilon)$$

$$\cong \pi \nu_+(\mu)\nu_-(\mu). \tag{A9}$$

The static uniform susceptibility is found by numerically differentiating Eq. (A7)

$$\chi_0^z = \Delta\langle s^z\rangle/\Delta\langle V\rangle. \tag{A10}$$

The Green's function $g_s(\varepsilon;\langle V\rangle,\zeta)$ averaged over the field fluctuations is obtained from the zero-point function (A2) according to the equations

$$g_s(\varepsilon) = \sum_{s'=\pm} P_{ss'} G^0_{s'}(\varepsilon - \Delta\Sigma_s(\varepsilon) + s'(v - v_0)),$$

$$P_{ss'} = \frac{1}{2}\left(1 + ss'\frac{\langle V\rangle}{v}\right), \quad v = (\langle V\rangle^2 + \zeta^z + \zeta^x + \zeta^y)^{1/2},$$

$$\Delta\Sigma_s(\varepsilon) = \zeta^z g_s(\varepsilon) + (\zeta^x + \zeta^y) g_{-s}(\varepsilon). \tag{A11}$$

Here the coherent potential $\Delta\Sigma_s(\varepsilon)$ (in second order of perturbation theory) describes the scattering of electrons by the chaotic part of the fluctuating field, while the factors $P_{ss'}$ determine the contribution of long-wavelength fluctuations.

In the absence of fluctuations (at $T=0$)

$$g_s(\varepsilon) = G^0_s(\varepsilon + s(|\langle V\rangle| - v_0)). \tag{A12}$$

The energy shift ν_0 is determined from the requirement that the magnetization vanish for $\langle V\rangle = 0$,

$$\int \frac{d\varepsilon}{\pi} f(\varepsilon)\mathrm{Im}(G^0_+(\varepsilon - v_0) - G^0_+(\varepsilon + v_0)) = 0, \tag{A13}$$

which reflects the specific nature of the model with different null EDSs for two spin states. For one EDS curve, both functions in the integrand are identical at all energies and equal the nonmagnetic EDS.

We note that, if the polarization $\Delta\Sigma_s(\varepsilon)$ is neglected, then the symmetric component of the Green's function $g_0 = (g_+ + g_-)/2$ is

$$g_0(\varepsilon) = \frac{1}{2}\sum_{s'=\pm} G^0_{s'}[\varepsilon - \Delta\Sigma_0 + s'(v - v_0)]$$

$$\cong \frac{1}{2}\sum_{s'=\pm} G^0_{s'}(\varepsilon - \Delta\Sigma_0) \cong g_0(\varepsilon)_{T=0}, \tag{A14}$$

since $\nu \cong \mathrm{const} \cong \nu_0$. The latter equality obtains if $\Delta\Sigma_s(\varepsilon)$ is completely neglected.

Solution algorithm. Let $T=0$. We find the shift ν_0 from Eq. (A13). Next, we find $\langle V\rangle = V_0$ from the initial condition $\langle s^z\rangle(\langle V\rangle) = s_0 = M_0/2R$ using Eqs. (A7) and (A12), and the value of the interaction constant u from Eq. (A3).

Our system of equations contains only three unknown quantities: $\langle V\rangle, \zeta^x = \zeta^y$, and ζ^z. We fix the temperature T. Next, we give the starting values ζ of the fluctuations. Then the Green's function g_s is uniquely determined only by the quantity $\langle V\rangle$, which we find by solving Eq. (A3), for example, by the method of halving a segment. We calculate from Eq. (A4) new values of the components ζ. We repeat this procedure until complete matching with respect to ζ obtains. Of course, all operations are performed taking into account the conservation of the electron number $n_+ + n_- = n_0 = N_e/R$, which determines the chemical potential μ appearing in the Fermi function.

For simplicity, all specific calculations were performed with average components of the local susceptibility:

$$\chi_l^j \to \langle \chi_l\rangle = (\chi_l^x + \chi_l^y + \chi_l^z)/3.$$

*)E-Mail: transmet@ifm.e-burg.ru

[1] M. Katter, J. Wecker, C. Kuhrt, and L. Shultz, J. Magn. Magn. Mater. **114**, 35 (1992); Y. Otani, D. P. F. Hurley, H. Sun, and J. M. D. Coey, J. Appl. Phys. **69**, 5584 (1991).
[2] A. G. Kuchin, N. I. Kourov, Yu. V. Knyazev, N. M. Kleĭnerman, V. V. Serikov, G. V. Ivanova, and A. S. Ermolenko, Fiz. Met. Metalloved. **79**, 41 (1995); A. G. Kuchin, N. I. Kourov, Yu. V. Knyazev, N. M. Kleinerman, V. V. Serikov, G. V. Ivanova, A. S. Ermolenko, Phys. Stat. Sol. (A) **155**, 479 (1996).
[3] P. C. M. Gubbens, A. M. van der Kraan, T. H. Jacobs, and K. H. J. Buschow, J. Less-Common Met. **159**, 173 (1990).
[4] S. S. Jaswal, W. B. Yelon, G. C. Hadjipanayis, Y. Z. Wang, and D. J. Sellmyer, Phys. Rev. Lett. **67**, 644 (1991).
[5] P. Mohn and E. P. Wohlfarth, J. Phys. F **17**, 2421 (1987).
[6] R. F. Sabiryanov and S. S. Jaswal, Phys. Rev. Lett. **79**, 155 (1997).
[7] A. I. Liechtenstein, M. I. Katsnelson, V. P. Antropov, and V. A. Gubanov, J. Magn. Magn. Mater. **67**, 65 (1987).
[8] V. I. Grenennikov, Fiz. Tverd. Tela (St. Petersburg) **40**, 90 (1998) [Phys. Solid State **40**, 79 (1998)].
[9] V. I. Grebennikov and S. A. Gudin, Fiz. Met. Metalloved. **85**, 20 (1998).
[10] V. I. Grebennikov, J. Magn. Magn. Mater. **84**, 59 (1990); V. I. Grebennikov, Fiz. Met. Metalloved. **66**, 227 (1998).
[11] V. I. Grebennikov and N. I. Kourov, Fiz. Tverd. Tela (St. Petersburg) **39**, 1257 (1997) [Phys. Solid State **39**, 1116 (1997)].
[12] V. I. Grebennikov and O. B. Sokolov, J. Phys.: Condens. Mater. **4**, 3283 (1992); Phys. Status Solidi B **151**, 623 (1989); V. I. Grebennikov and O. B. Sokolov, Fiz. Met. Metalloved. **76**, 5 (1993).

Translated by M. E. Alferieff

Spin-glass and reentrant spin-glass states in iron sulfospinels having dilute *A* and *B* sublattices

A. I. Abramovich, L. I. Koroleva, and L. N. Lukina

M. V. Lomonosov Moscow State University, 119899 Moscow, Russia
(Submitted May 18, 1998)
Fiz. Tverd. Tela (St. Petersburg) **41**, 84–90 (January 1999)

The magnetic and electrical properties of new compounds having spinel structure $Fe_{1-x}Cr_{2(1-x)}Sn_{2x}S_4$ ($0.1 \leqslant x \leqslant 0.33$) (system 1), $Fe_{0.67}[Fe_{0.165}CrSn_{0.835}]S_4$, and $Fe_{0.67}[Fe_{0.33}Cr_{0.67}Sn]S_4$ has been studied. These compounds are *p*-type semiconductors with magnetic properties characteristic of the following magnetic-order types: ferrimagnetic (the $x=0.1$ composition of system 1), spin glass (the $x=0.33$ composition of system 1 and $Fe_{0.67}[Fe_{0.165}CrSn_{0.835}]S_4$), and reentrant spin glass (the $x=0.2$ composition of system 1 and $Fe_{0.67}[Fe_{0.33}Cr_{0.67}Sn]S_4$). For the spin-glass compositions, the dependence of the freezing temperature T_f, defined as the temperature of the maximum of initial magnetic susceptibility, on temperature and magnetic field obeys the Almeida-Thouless relation, and the dependence of T_f on magnetic-field frequency is a power-law function. For the spin-glass and reentrant spin-glass compositions, a large peak in the absolute value of negative isotropic magnetoresistance was found near T_f, which becomes as high as 15% in spin glasses and 30% in reentrant spin-glass compositions. In compositions with reentrant behavior, the activation energy of conductivity in the region of T_f was found to change by about two orders of magnitude. This experimental evidence suggests that the spin-glass–paramagnet (in spin glasses) and spin-glass–long-range magnetic-order transformations are actually phase transitions, and that the spin-glass region contains ferron-type ferromagnetic clusters. These are the first spin-glasses among the chalcospinels with magnetically active ions on the tetrahedral and octahedral sublattices.
 [S1063-7834(99)01901-2]

This work reports observation and a detailed investigation of the spin glass (SG) and reentrant spin-glass states in chromium-containing iron sulfospinels with dilute tetrahedral (A) and octahedral (B) sublattices. The spin-glass state has thus far been observed to set in in chalcospinels with magnetically active ions on one of the sublattices only. For instance, an SG state was described in $Ga_{2/3}Cr_2S_4$,[1] $Cu_{0.5}Me_{0.5}Cr_2Se_4$ (Me=In,Ga),[2] $Cu_{2/3}Ge_{1/3}Cr_2S_4$,[3] $CdCr_{2x}In_{2-2x}S_4$,[4] $ZnCr_{2x}Al_{2-2x}S_4$,[5] and $Zn_{1-x}Mn_xIn_2S_4$ (Ref. 6). It was of interest to learn whether the SG state can exist in chalcospinels with magnetically active ions present on both *A* and *B* sublattices. Because indirect intersublattice antiferromagnetic (AFM) exchange in spinels is considerably stronger than the intrasublattice one, the possibility of existence of the spin-glass state in such chalcospinels was far from obvious. For example, in the $FeCr_2S_4$ compound with normal-spinel structure, whose dilute compositions are studied in this work, the exchange integrals have the following values: $J_{Cr\text{-}Cr}=\pm 1$ K and $J_{Cr\text{-}Fe}=-10$ K.[7]

The SG state is dealt with in a large number of publications (see, e.g., reviews Refs. 8–12 and monographs Refs. 13 and 14). Some of the problems of fundamental importance remain, however, unsolved. It is unclear what is the nature of the SG state, and whether it is a new phase, as well as whether there exists a thermodynamic transition of the type SG-paramagnet (PM) or SG–long-range magnetic order (LRMO). Among spin glasses one presently classifies substances exhibiting a maximum in initial magnetic susceptibility at a temperature $T=T_f$ called usually the freezing temperature, dependence of magnetic properties for $T<T_f$ on thermomagnetic prehistory of the sample and time, and absence of long-range magnetic order, as shown by neutron diffraction measurements. Besides the true SGs, however, superparamagnets also possess the same properties. In contrast to true SGs, superparamagnets do not have a phase transition, and the cluster moments only become fixed at T_f, so that their freezing is a dynamically nonequilibrium phenomenon. In superparamagnets T_f, the temperature of the maximum in initial susceptibility measured in a magnetic field of frequency ω, depends on ω by the Arrhenius law:

$$1/\omega = 1/\omega_0 \exp[E/(kT_f)], \tag{1}$$

where $\omega_0 \approx 10^9$ s^{-1} is a frequency factor equal to the reciprocal minimum relaxation time, and E is the energy required to flip the cluster magnetic moment (for example, by thermal excitation). It was found that while practically all SGs known to date (except for the dilute AgMn alloy[15]) exhibit a frequency dependence of T_f, in most cases it differs somewhat from the Arrhenius relationship. The existence of a phase transition in real materials classifies among the SGs is discussed actively in the literature. No unambiguous answer to this question has, however, been obtained.

This work presents experimental evidence for the existence of SG-PM and SG-LRMO phase transitions in the

TABLE I. Main magnetic and electrical characteristics of the compounds studied.

Chemical formula	Θ, K	$M_{4.2K}$, μ_B	M_{sp}, μ_B	M_{ng}, μ_B	T_C, K	T_f, K	ρ, Ω·cm 80 K	ρ, Ω·cm 293 K
$Fe_{0.9}Cr_{1.8}Sn_{0.2}S_4$	−60	0.91	1.8	1.44	1.20		1100	31.9
$Fe_{0.8}Cr_{1.6}Sn_{0.4}S_4$	−76	0.52	1.6	1.28	87	65	4500	25.6
$Fe_{0.67}Cr_{1.33}Sn_{0.67}S_4$	−200	0.18	1.31	1.04		36	25×10^4	1082
$Fe_{0.67}[Fe_{0.33}Cr_{0.67}Sn]S_4$	35	0.22	0.65	0.52	110	60	2185	7.8
$Fe_{0.67}[Fe_{0.165}CrSn_{0.835}]S_4$	158	0.35	0.98	0.78		29	67.5	1.3

above materials, including agreement with dynamic scaling relations and some relations following from the mean-field theory, as well as features in the electric resistivity and magnetoresistance (MR) observed in the vicinity of these transitions. Besides, the large negative MR near T_f revealed in the materials under study implies that the SG phase contains ferron-type ferromagnetic (FM) clusters.[16]

1. SAMPLES AND EXPERIMENTAL METHOD

Polycrystalline samples of the $Fe_{1-x}Cr_{2(1-x)}Sn_{2x}S_4$ solid-solution system ($0.1\leqslant x\leqslant 0.33$) and the $Fe_{0.67}[Fe_{0.165}CrSn_{0.835}]S_4$ and $Fe_{0.67}[Fe_{0.33}Cr_{0.67}Sn]S_4$ compositions were prepared by solid-state technology from high-purity elements by Kesler and Filimonov (MGU, Chemical Dept.).[17] The corresponding mixture of starting elements was annealed repeatedly within the 800–1100 K interval (before each anneal it was ground, homogenized, and pressed into pellets) in quartz ampoules, which were evacuated to a 10 bar pressure before sealing.

The samples were characterized by x-ray diffraction analysis (with filtered Co $K\alpha$ radiation), as well as by ^{57}Fe Mössbauer (NGR) spectroscopy at 90 and 300 K. X-ray diffraction shows the samples to be single-phase spinel (space group Fd3m). The characteristic-distance method, which was used to advantage in studies of close-packed anion compounds,[18] showed[17] the Sn^{4+} ions to occupy only the octahedral sites. By combining this method with NGR it was found that the tetrahedral sites are occupied to various extents by Fe^{2+} ions.

^{57}Fe NGR spectra of the $Fe_{0.8}Cr_{0.6}Sn_{0.4}S_4$ composition were measured at $T=90$ and 300 K (see Fig. 2 in Ref. 17). Their $T=300$ K spectra were found to contain a clearly pronounced asymmetric doublet with a 1.0-mm/s quadrupole splitting, with the isomer shift corresponding to the tetrahedral Fe^{2+} ion (0.54 mm/s with respect to metallic Fe), which may be associated with a distorted tetrahedral environment of the iron ions and the onset of axial symmetry. This implies partial iron-ion and vacancy ordering in the tetrahedral sublattice, which results in a lowering of the true symmetry undetectable by x-ray diffraction analysis. These compounds were synthesized for the first time.

The magnetization was measured either ballistically with a multilayer superconducting solenoid, or with a vibrating-sample magnetometer in an electromagnet. The initial dc susceptibility was measured with a single-layer superconducting solenoid, and the magnetization curves obtained by the ballistic method were differentiated with respect to the field. An F5063 digital ferrometer was used to determine the magnetic susceptibility in weak ac magnetic fields. The paramagnetic susceptibility was studied with an electromagnetically compensated Faraday balance. The electrical resistance was determined by the four-probe method.

2. EXPERIMENTAL RESULTS AND THEIR DISCUSSION

A. Ferrimagnet–spin-glass transition in the $Fe_{1-x}Cr_{2(1-x)}Sn_{2x}S_4$ system ($0.1\leqslant x\leqslant 0.33$). Spin-glass state in $Fe_{0.67}[Fe_{0.165}CrSn_{0.835}]S_4$ and reentrant-spin-glass behavior in the $Fe_{0.67}[Fe_{0.33}Cr_{0.67}Sn]S_4$ composition

Table I presents the main magnetic and electrical characteristics of the compositions specified in the heading. Here Θ is the paramagnetic Curie point, T_C is the Curie temperature, $M_{4.2\,K}$ is the magnetic moment per formula unit derived from the magnetization at 4.2 K, M_{sp} and M_{ng} are theoretical magnetic moments per formula unit obtained from pure spin and neutron-diffraction values of the Fe^{2+} and Cr^{3+} moments, respectively, for antiferromagnetically (AFM) ordered moments on the *A* and *B* sublattices. (We assumed the Fe^{2+} and Cr^{3+} moments derived from neutron-diffraction measurements to be 4.2 and 2.9 μ_B, respectively.)

All the samples were found to be *p*-type semiconductors. As seen from the chemical formula of the $Fe_{1-x}Cr_{2(1-x)}Sn_{2x}S_4$ solid-solution system (1), an increase of *x* entails an increase in Fe^{2+} deficiency on the tetrahedral sublattice, accompanied by dilution of the octahedral sublattice by the Sn^{4+} diamagnetic ions. The $x=0.1$ composition of system (1) has magnetic properties typical of a ferrimagnet, namely, the paramagnetic susceptibility κ obeys the Néel law (Fig. 1), and the magnetization isotherms saturate in a field of 6 kOe both at $T=4.2$ K (Fig. 2) and at $77\leqslant T\leqslant 110$ K. At the same time the magnetic moment $M_{4.2\,K}$ is nearly one half M_{sp} and M_{ng} (Table I). The Curie temperature of this composition as determined from Belov-Arrott plots is 120 K. The underestimated magnitude of $M_{4.2\,K}$ is apparently due to the presence of magnetically disordered microregions. The disorder may be caused by bond frustration because of dilution of the *B* sublattice by the Sn^{4+} diamagnetic ions and the presence of vacancies on the *A* sublattice.

The magnetization isotherms of system 1 with $x=0.2$ and 0.33 do not saturate up to 35 kOe at 4.2 K (Fig. 2) and up to 10 kOe for $T\geqslant 77$ K. (We specify here the maximum fields in which the measurements were performed.) The paramagnetic susceptibility of these compositions obeys the Curie-Weiss relation (Fig. 1).

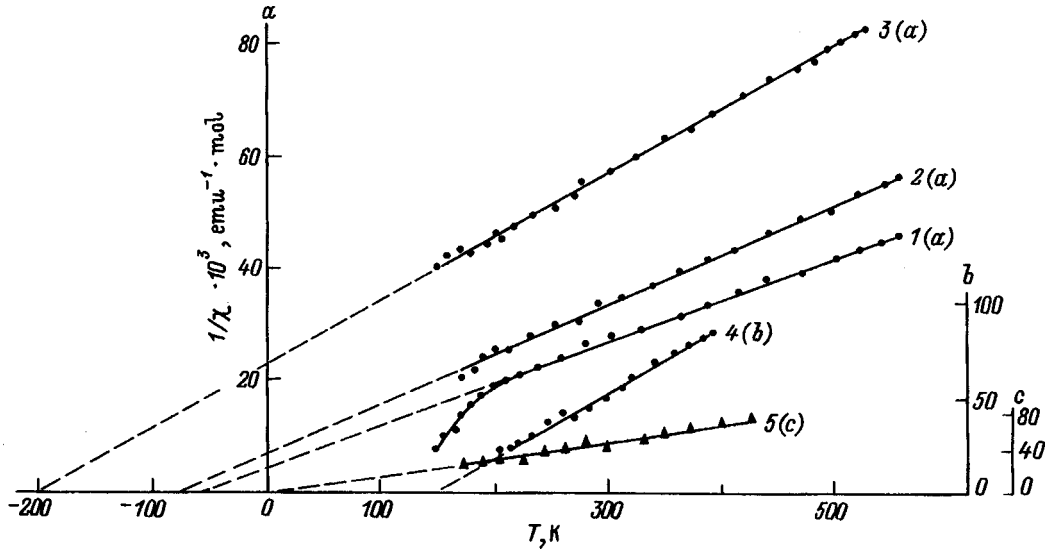

FIG. 1. Temperature dependence of inverse paramagnetic susceptibility $1/\chi$ for compositions of the $Fe_{1-x}Cr_{2(1-x)}Sn_{2x}S_4$ system with x: (*1*) 0.1, (*2*) 0.2, (*3*) 0.33, and for (*4*) $Fe_{0.67}[Fe_{0.165}CrSn_{0.835}]S_4$ and (*5*) $Fe_{0.67}[Fe_{0.33}Cr_{0.67}Sn]S_4$. The scales on the *a*, *b*, and *c* axes are different.

The temperature dependence of the initial magnetic susceptibility κ in dc and ac magnetic fields for the $x=0.2$ composition is shown graphically in Fig. 3. One readily sees that κ drops with decreasing temperature below $T_f=65$ K, which is characteristic of the reentrant spin-glass state. The Curie temperature $T_C=87$ K was derived from the maximum of curve *2* in Fig. 3. The dependence of magnetic properties below T_f on cooling conditions provided evidence for the existence of the SG state below T_f. For illustration, Fig. 4 presents temperature dependences of the thermoremanence of a sample cooled in a field $H=57.5$ Oe from $T>T_f$ down to $T=4.2$ K, and of the isothermal remanence of a sample zero-field cooled to 4.2 K. Below $T_f=65$ K these curves are seen to differ substantially. One observed also a shift of the hysteresis loop of the sample cooled in the above field down to 4.2 K along the H axis, whereas for the zero-field cooled sample the loop was symmetric.

The $x=0.33$ composition of system 1 exhibits magnetic properties characteristic of the SG state. For instance, the temperature dependence of the initial ac susceptibility (measurement frequency range $0.3\leqslant\omega\leqslant2$ kHz) has a maximum at T_f, which becomes suppressed already by a weak dc magnetic field applied parallel to the ac field (Fig. 5). The magnetization σ measured in a dc field $H=0.46$ Oe for $T\leqslant T_f$ depends on the cooling regime; indeed, the $\sigma(T)$ curve obtained on a sample field-cooled from $T>T_f$ to $T=4.2$ K lies considerably higher than that of the sample zero-field cooled to 4.2 K (the latter curve was taken by heating the sample, with the field turned on only for the period of measurement).

$Fe_{0.67}[Fe_{0.165}CrSn_{0.835}]S_4$ possesses magnetic properties similar to the ones which were measured on the $x=0.33$ composition of system 1 and are typical of the SG state. The magnetic properties of this composition are similar to those of the $x=0.2$ composition, which are characteristic of the reentrant SG behavior. The paramagnetic susceptibility of

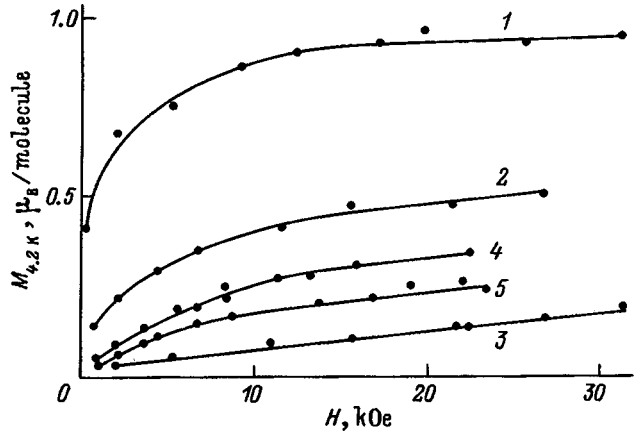

FIG. 2. Magnetic moment per formula unit $M_{4.2\,K}$ plotted against magnetic field H for 4.2 K for compositions of the $Fe_{1-x}Cr_{2(1-x)}Sn_{2x}S_4$ system with x: (*1*) 0.1, (*2*) 0.2, (*3*) 0.33, and for (*4*) $Fe_{0.67}[Fe_{0.165}CrSn_{0.835}]S_4$ and (*5*) $Fe_{0.67}[Fe_{0.33}Cr_{0.67}Sn]S_4$.

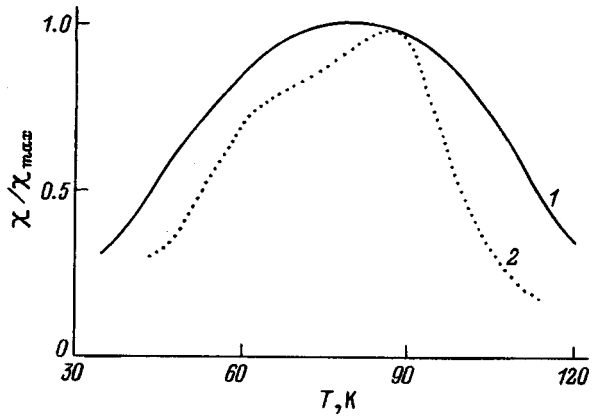

FIG. 3. Temperature dependence of the initial magnetic susceptibility χ of $Fe_{0.8}Cr_{1.6}Sn_{0.4}S_4$ normalized to its maximum value χ_{max} obtained in a dc magnetic field $H=30$ Oe (*1*), and in an ac magnetic field $H=0.3$ Oe of frequency $\omega=200$ Hz (*2*).

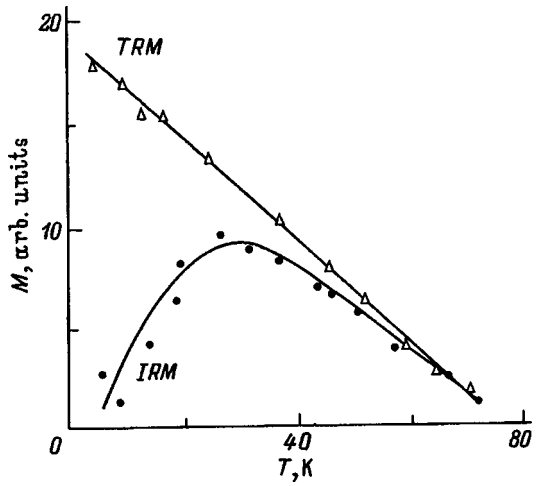

FIG. 4. Temperature dependence of the remanence of a $Fe_{0.8}Cr_{1.6}Sn_{0.4}S_4$ sample cooled in a field of 57.5 Oe from $T=90$ to 4.2 K (TRM curve) and zero-field-cooled (IRM).

the above compounds obeys the Curie-Weiss law (Fig. 1). Figure 2 displays the magnetization isotherms of these compositions obtained at 4.2 K. One sees that these curves do not saturate, and that the value of $M_{4.2\,\mathrm{K}}$ measured at $H=30$ kOe is much smaller than those of M_{sp} and M_{ng} listed in Table I.

B. Dynamics of spin-glass freezing

The SG compositions studied by us revealed a dependence of the freezing temperature, determined from the position of the maximum in the initial ac susceptibility, on the magnetic-field frequency ω. As already mentioned, the T_f temperature of almost all real materials classified among the SGs is frequency dependent. It was found, however, that the relaxation time τ in the region of the freezing temperature in

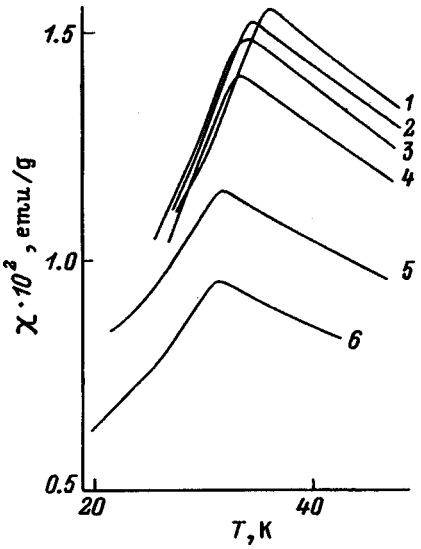

FIG. 5. Temperature dependence of the initial magnetic susceptibility χ of $Fe_{0.67}Cr_{1.33}Sn_{0.67}S_4$ in an ac magnetic field of frequency 500 Hz ($H=0.3$ Oe), and the effect on this dependence of a dc magnetic field H(Oe): (*1*) 0, (*2*) 10, (*3*) 20, (*4*) 35, (*5*) 50, and (*6*) 70. The dc magnetic field is applied parallel to the ac one.

SG materials grows faster than by the Arrhenius law (1) characteristic of superparamagnets, and in some cases follows the empirical Vogel-Fulcher relation[8]

$$\tau=1/\omega=\tau_0\exp[E/k(T-T_0)], \tag{2}$$

where $\tau_0\approx10^{-12}$ s is the minimum relaxation time, and E is a quantity with the dimension of energy. Because the relaxation time τ diverges at $T=T_0$, some researchers believed T_0 to be an SG-PM transition point. At the same time it is known that if a phase transition occurs at a temperature T^*, the relaxation time of magnetization fluctuations undergoes a critical slowing down at T^*, and that τ obeys a power law:[19]

$$\tau=\tau_0[T/(T-T^*)]^{z\nu}. \tag{3}$$

Here z is a dynamic exponent, and ν is the Edwards-Anderson critical correlation-length exponent. A Monte Carlo simulation of the Ising SG with $T^*\neq0$ (the $\pm J$ model, three-dimensional case) yielded $z\nu=7.2\pm1$.[20]

Binder and Young[21] proposed an alternative hypothesis assuming the SG-PM transition temperature to be zero. They obtained for τ the following relation, which was subsequently called the generalized Arrhenius law:

$$\ln(\tau/\tau_0)=T^{-z\nu}. \tag{4}$$

Binder and Young performed a Monte Carlo simulation of the Ising system within the $\pm J$ model and obtained $z\nu=2$ for the two-dimensional case and $z\nu=4$ for the three-dimensional one.

The $T(\omega)$ dependence obtained for a number of real SGs was compared with the three above relations, and a conclusion of the presence or absence of a phase transition in a given SG at a nonzero temperature was drawn depending on the actual relationship this dependence followed. We have performed a fitting of the $T(\omega)$ dependence to the relations (1)–(4) for the above new compounds where we detected an SG state, namely, for $Fe_{0.67}Cr_{1.33}Sn_{0.67}S_4$ and $Fe_{0.67}[Fe_{0.165}CrSn_{0.67}]S_4$. This was done by plotting the experimental relations (1)–(4) on a log-log scale, with the values of $1/\omega$ substituted in place of τ, and of T_f, for T in the Vogel-Fulcher and power-law expressions. The fitting parameters were T_0 in (2), T^* in (3), and τ_0 in (4). In the power-law and Vogel-Fulcher relations, we substituted for T_0 and T^* the freezing points, which were found from the maximum of the initial dc susceptibility, as well as several temperatures close to them. Next we selected the plots where the points fitted satisfactorily to straight lines, and the latter were used to determine τ_0 in the Arrhenius law, τ_0 and E in the Vogel-Fulcher relations, τ_0 and $z\nu$ in the power-law relation, and $z\nu$ in the generalized Arrhenius law. Table II presents the values of τ_0, $z\nu$, and E derived from the best fitting parameters chosen for each law. As seen from Table II, the $T(\omega)$ dependence fits best of all to the power law (3). The Vogel-Fulcher relation (3) yields an unrealistically small value of T_0, and the Arrhenius law (1) strongly underestimates τ_0. The generalized Arrhenius law (4) for the three-dimensional case yields an overestimated τ_0 as the best fit for $Fe_{0.67}Cr_{1.33}Sn_{0.67}S_4$, and an underestimated value of $z\nu$ for

TABLE II. Fitting of the $T_f(\omega)$ dependence to relations (1)–(4).

Composition	T_f, K	from the maximum in dc field (1)		Arrhenius law (4)		Generalized Arrhenius law (3)			Power law Vogel–Fulcher relation (2)		
		τ_0, s	E, meV	τ_0, s	zv	τ_0, s	zv	T^*, K	τ_0, s	E, meV	T_0, K
$Fe_{0.67}Cr_{1.33}Sn_{0.67}S_4$	35	5.3×10^{-27}	170.4	10^{-12}	2.5	1.9×10^{-10}	7.6	32	3.0×10^{-12}	23.3	23
				10^{-9}	3.8	2.0×10^{-11}	9.6	31	1.5×10^{-11}	20	24
						2.7×10^{-12}	11.7	30			
						7.2×10^{-12}	10.7	30.5			
$Fe_{0.67}[Fe_{0.165}CrSn_{0.835}]S_4$	31.2	2.4×10^{-27}	182.5	10^{-12}	2.9	6.7×10^{-11}	7.4	30	10^{-12}	21	22
				10^{-11}	3.6	2.0×10^{-11}	8.5	29.5	5×10^{-12}	17.6	23
				10^{-10}	3.9	4.0×10^{-12}	9.7	29	2.5×10^{-11}	14.4	24
						3.0×10^{-13}	12.2	28	2.5×10^{-11}		

$Fe_{0.67}[Fe_{0.165}CrSn_{0.835}]S_4$. The fact that $T(\omega)$ fits a power-law relation implies the existence of an SG-PM phase transition in the SGs under study.

C. The Almeida-Thouless relation for spin-glass compositions

Application of the mean-field theory to spin glasses showed the existence on the (H,T) plane of a line below which the Edwards–Anderson order parameter is unstable.[11] This is the so-called Almeida-Thouless line in the Ising model:

$$1-[T_f(H)/T_f(0)]\sim H^{2/3}. \tag{5}$$

Here $T_f(H)$ is the freezing temperature measured in a magnetic field H, and $T_f(0)$ is that determined in zero magnetic field. It was found that in a number of real SGs the $T_f(H)$ dependence obeys relation (5). These experiments were considered as evidence for the validity of the mean-field theory for these SGs and for the existence of the corresponding phase transition.[8–14]

In this work, we studied the effect of a dc magnetic field on the freezing temperature, determined from the maximum of the initial ac susceptibility χ, in the SG compositions $Fe_{0.67}Cr_{1.33}Sn_{0.67}S_4$ and $Fe_{0.67}[Fe_{0.165}CrSn_{0.835}]S_4$. Figure 5 shows for illustration the $\chi(T)$ relation obtained for the $Fe_{0.67}Cr_{1.33}Sn_{0.67}S_4$ composition, and how it is affected by application of a dc magnetic field H parallel to the ac one. As seen from Fig. 5, χ_{max} decreases with increasing dc field, and the maximum shifts toward lower temperatures. Figure 6 plots on a log-log scale the $\{1-[T_f(H)/T_f(0)]\}$ vs H relation obtained for the $Fe_{0.67}Cr_{1.33}Sn_{0.67}S_4$ composition. All experimental points are seen to fit satisfactorily onto a straight line, with a slope equal to 0.61, which is very close to the 2/3 exponent in the Almeida-Thouless relationship (5). This argues for the existence of SG-PM transitions in the above materials.

D. Magnetoresistance in the vicinity of the freezing temperature

Investigation of the temperature dependence of electrical resistivity ρ showed all compounds studied in this work to be semiconductors. The values of ρ for these compositions are presented in Table I. Seebeck coefficient measurements performed at $T=77$ and 293 K evidence p-type conduction in all the compositions.

The temperature dependence of magnetoresistance obtained for the SG and reentrant-SG compositions reveal features near the freezing temperature. For illustration, Figs. 7 and 8 plot the MR against temperature for various magnetic fields for the $Fe_{0.67}[Fe_{0.165}CrSn_{0.835}]S_4$ SG composition and for the $x=0.2$ composition of system 1 exhibiting reentrant-SG behavior. One readily sees that their MR is negative and, as shown by our measurements, isotropic. MR isotherms do not saturate up to the maximum fields of 30 kOe in which the measurements were made. As evident from Fig. 7, the absolute value of MR for the SG composition passes through a maximum near T_f, where it reaches $\sim15\%$ in a field of 30 kOe. In the reentrant SG composition, the absolute value of MR, $|\Delta\rho/\rho|$, at the maximum reaches a still larger value of 30% in 30 kOe (Fig. 8). This maximum is seen to be rounded off, wider than that for the SG composition, and to cover a temperature region including both $T_f=65$ K and $T_C=85$ K. The inset to Fig. 8 shows a log-log plot of the $\rho(T)$ dependence for the $x=0.2$ reentrant-SG composition of system 1; we readily see that in the vicinity of T_f the conduction activation energy E_a varies by about two orders of magnitude ($E_a=3.7\times10^{-4}$ eV in the SG region and 4×10^{-2} eV within the LRMO region). A similar

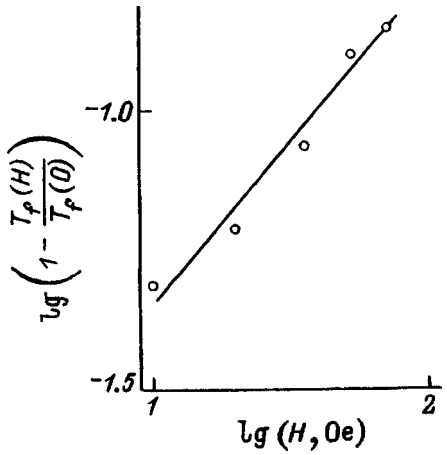

FIG. 6. A log-log plot of $\{1-[T_f(H)/T_f(0)]\}$ against H for the $Fe_{0.67}Cr_{1.33}Sn_{0.67}S_4$ composition.

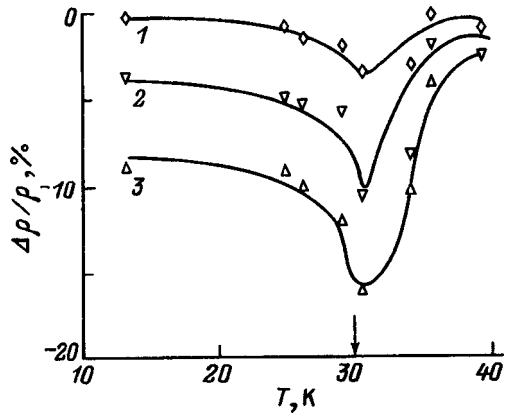

FIG. 7. Temperature dependence of the magnetoresistance of the $Fe_{0.67}[Fe_{0.165}CrSn_{0.835}]S_4$ composition obtained in magnetic fields (kOe): (*1*) 2, (*2*) 16, and (*3*) 33.

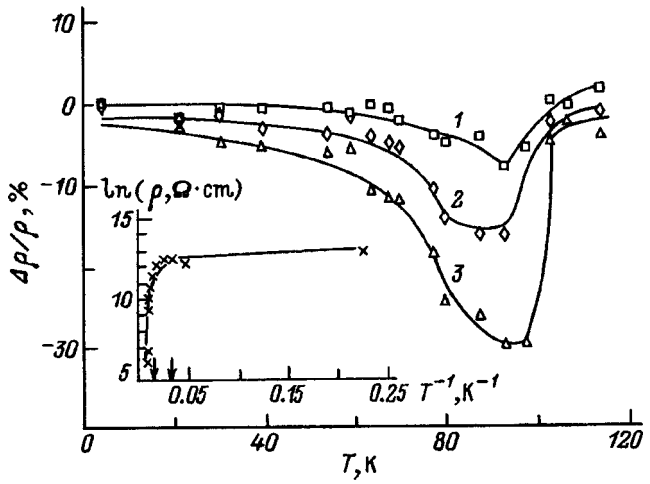

FIG. 8. Temperature dependence of the magnetoresistance of the $Fe_{0.8}Cr_{1.6}Sn_{0.4}S_4$ composition obtained in magnetic fields (kOe): (*1*) 2, (*2*) 17, and (*3*) 32. The inset plots ln ρ against $1/T$.

behavior of the MR and ρ was observed by us also for the $x=0.33$ SG composition of system 1, and for $Fe_{0.67}[Fe_{0.33}Cr_{0.67}Sn]S_4$ (reentrant SG behavior).

These features in the MR and electrical resistivity indicate that the spin system undergoes a significant rearrangement at T_f. A giant maximum in $|\Delta\rho/\rho|$ at T_f was observed earlier in $Cu_{0.5}Me_{0.5}Cr_2Se_4$ (Me=In,Ga) and $Cu_{2/3}Ge_{1/3}Cr_2S_4$.[22] It should be pointed out that MR measurements involve application across the sample of strong fields, in which the maximum or break in the susceptibility curves is, as a rule, suppressed. These features evidence a spin system rearrangement at T_f and should be considered as a direct argument for the existence of an SG-PM and SG-LRMO phase transition.

3. THE NATURE OF THE SPIN-GLASS STATE

Our experimental results presented in Sec. II attest to the existence of an SG state in $Fe_{0.67}Cr_{1.33}Sn_{0.67}S_4$ and $Fe_{0.67}[Fe_{0.165}CrSn_{0.835}]S_4$, and of a reentrant SG state, in $Fe_{0.8}Cr_{1.6}Sn_{0.4}S_4$ and $Fe_{0.67}[Fe_{0.33}Cr_{0.67}Sn]S_4$, with the transformations to the PM state in the former two, and to the LRMO state, in the latter two compositions being phase transitions. The main factor initiating the SG state in these compounds is the dilution of the *A* and *B* sublattices. The *A* sublattice is deficient in Fe^{2+} ions, and on the *B* sublattice the Fe^{2+} and Cr^{3+} ions are diluted by the diamagnetic ions Sn^{4+}. The percolation threshold in the spinel structure for an octahedral sublattice $p=0.401$,[23] and for a tetrahedral sublattice, $p=0.428$ (Ref. 24). In the SG compositions, the ratio of the number of magnetoactive ions to the total number of ions in the octahedral sublattice $p=0.665$ (the first composition), and for the tetrahedral sublattice in both compositions, $p=0.67$. These values are not substantially larger than the above threshold concentrations for the *A* and *B* sublattices. The Fe^{2+} and Cr^{3+} ions on the diluted *A* and *B* sublattices are randomly distributed over the corresponding sublattices, and although they are coupled through strong AFM superexchange *A-S-B* interactions, these bonds do not make up a periodic structure. As a result, long-range AFM order cannot set in among the moments located in the *A* and *B* sublattices, and the SG state occurs. These are the first SGs among the chalcospinels with magnetoactive ions on the *A* and *B* sublattices.

As pointed out in Subsect. D, the spin glasses under study exhibit a large maximum in $|\Delta\rho/\rho|$ in the vicinity of T_f. A giant maximum in $|\Delta\rho/\rho|$ near the magnetic ordering temperature is known to be characteristic of extrinsic magnetic semiconductors,[16] and it is usually associated with the presence of ferrons, i.e. FM microregions formed as a result of carrier self-trapping near impurities because of the corresponding gain in *s–d* exchange energy. External magnetic field destroys the ferrons, thus giving rise to a large negative MR. Ferrons can obviously exist also in a magnetic semiconductor diluted by nonmagnetic ions; if the dilution is strong enough, long-range magnetic order disappears, and an SG state sets in in the crystal, with some of the clusters present in such a cluster SG being of the ferron type. It is quite probable that this pattern is applicable to the SGs studied in this work as well.

The authors owe warm thanks to Ya. A. Kesler and D. S. Filimonov for preparation of the samples and their characterization.

Support of the Russian Fund for Fundamental Research (Grants 96-02-19684a and 96-15-96429) is gratefully acknowledged.

[1] K. P. Belov, L. I. Koroleva, N. A. Tsvetkova, Yu. F. Popov, I. V. Gordeev, Ya. A. Kesler, V. V. Titov, and A. G. Kocharov, JETP Lett. **31**, 87 (1980).
[2] L. I. Koroleva and A. I. Kuz'minykh, Zh. Éksp. Teor. Fiz. **84**, 1882 (1983) [Sov. Phys. JETP **57**, 1097 (1983)].
[3] L. I. Koroleva, T. V. Virovets, A. I. Abramovich, and Ya. A. Kesler, J. Magn. Magn. Mater. **115**, 311 (1992).
[4] E. Vincent, J. Hammann, and M. Alba, Solid State Commun. **58**, 57 (1986).
[5] M. Hamedoun, A. Wiedenmann, J. L. Dormann, M. Nogues, and J. Rossat-Mignod, J. Phys. C: Solid State Phys. **19**, 1783 (1986).
[6] J. J. Campo, F. Palacio, V. Sagredo, and G. Attolini, in *Proceedings of the International Conference Magn.* (Warsaw, 1994), p. 869.
[7] P. Gibart, J. L. Dormann, and Y. Pellerin, Phys. Status Solidi **36**, 187 (1969).
[8] K. H. Fischer, Phys. Status Solidi B **116**, 357 (1983).

[9] D. Chowdhury and A. Mookerjee, Phys. Rep. **114**, 1 (1984).
[10] C. Y. Huang, J. Magn. Magn. Mater. **51**, 1 (1985).
[11] K. Binder and A. Young, Rev. Mod. Phys. **58**, 801 (1986).
[12] S. L. Ginzburg, in *Proceedings of the XVI LNPI School*, edited by A. I. Okorokov (LNPI, Leningrad) (1982), p. 43.
[13] D. Chowdhury, *Spin Glasses and Other Frustrated Systems* (World Scientific, Singapore, 1986), 523 pp.
[14] H. Maletta and W. Zinn, in *Handbook on the Physics and Chemistry of Rare Earths*, edited by K. A. Gschneidner (North- Holland, Amsterdam), Vol. 12, 1 (1986).
[15] E. D. Dahlberg, M. Hardiman, R. Orbach, and J. Souletie, Phys. Rev. Lett. **42**, 401 (1979).
[16] E. L. Nagaev, *Physics of Magnetic Semiconductors* [in Russian] (Nauka, Moscow, 1979), 431 pp.
[17] D. S. Filimonov, Ya. A. Kesler, and K. V. Pokholok, Neorg. Mater. **32**, 930 (1996).
[18] Ya. A. Kesler, Neorg. Mater. **29**, 165 (1993).
[19] P. C. Hohenberg and B. I. Halperin, Rev. Mod. Phys. **49**, 435 (1977).
[20] A. T. Ogielski, Phys. Rev. B **32**, 7384 (1985).
[21] K. Binder and A. P. Young, Phys. Rev. B **29**, 2864 (1984).
[22] A. I. Abramovich, T. V. Virovets, and L. I. Koroleva, Phys. Lett. A **153**, 248 (1991).
[23] D. Fiorani, A. Gastaldi, A. Lapiccirella, S. Viticoli, and N. Tomassini, Solid State Commun. **32**, 831 (1979).
[24] M. K. Sykes, D. S. Gaunt, and M. Glenn, J. Phys. A **9**, 1705 (1976).

Translated by G. Skrebtsov

Calculation of the activation energy for surface self-diffusion of transition-metal atoms

S. Yu. Davydov

A. F. Ioffe Physicotechnical Institute, Russian Academy of Sciences, 194021 St. Petersburg, Russia
(Submitted June 25, 1998)
Fiz. Tverd. Tela (St. Petersburg) **41**, 11–13 (January 1999)

The cohesion-based approach developed earlier for describing the adsorptive properties of *d*-metal atoms on *d* substrates was used to calculate the self-diffusion on the (111) and (100) planes of fcc metals, and the (110) plane of bcc metals. The results of the calculation are compared with the data obtained by other researchers and with available measurements. © *1999 American Institute of Physics.* [S1063-7834(99)00201-4]

Mass transport over the surface of solids, or surface diffusion, is a key stage in many processes, such as, for instance, adsorption and desorption, heterogeneous catalysis and crystal growth, wetting etc.[1–4] The most important parameter of surface diffusion is its activation energy E_d. The activation energy E_d is derived experimentally from the temperature dependences of the diffusion coefficient D, which obeys the Arrhenius relation

$$D = D_0 \exp(-E_d/k_B T), \tag{1}$$

where D_0 is the preexponential factor. The temperature interval for measuring D with field-ion microscope is, as a rule, not large, because at low temperatures the diffusion is inhibited, and in the high-temperature range the adatoms detach from the microscope tip in too short a time. Therefore even small errors in D determination may result (and actually do result) in a large scatter of values of E_d and D_0 (see discussion of this problem in Ref. 5). Calculation of E_d is, in principle, an extremely complex problem, because its solution requires the knowledge of the surface energy relief of the substrate-adatom system. The approach most widely used presently in E_d calculations for metals is the embedded-atom method (EAM) (see Ref. 6 and references therein). EAM is based on the local density-functional approximation and representation of the total energy of a system as a sum of the so-called embedding energy (which depends only on the local electron density) and the short-range electrostatic energy, and it requires application of a fitting procedure to determine the characteristic parameters.[5,6] This method is also, however, not free of drawbacks and sometimes yields qualitatively wrong results.[7]

An approach based on the cohesion approximation to calculating the adsorptive properties of *d*-metal atoms adsorbed on *d* substrates, that permits calculating the surface-diffusion activation energy without any fitting has recently been proposed (see Ref. 8, referred to subsequently as Paper I). The results of E_d calculation for the diffusion of atoms of all transition (as well as rare-earth) metals on the W(110) surface have turned out to agree well enough with the available (surprisingly, very scarce) experimental data. It should also be pointed out that the method proposed in Paper I does not require computer calculations. We are going to use in this work the cohesion approximation to self-diffusion calculations.

1. COHESION APPROXIMATION

Based on the experimentally observed correlation between the adsorption energy of transition-metal atoms on W(110) and the cohesive energy of crystals made up of these atoms, Paper I proposed to describe the adsorption energy as the energy of cohesion of a ''renormalized atom,'' or adatom. It was shown also that in the case of transition-metal atoms adsorbed on *d* substrates one may neglect charge transport taking into account directly only the adatom interaction with the nearest-neighbor substrate atoms, whose number depends naturally on the surface structure and position of the adsorbed atom. We chose as a starting point the cohesion theory of Harrison and Wills[9], where the electron density of a metal is presented in the form of a superposition of quasi-free states and *d* states, with inclusion of their hybridization and electron-electron interaction described by the Thomas-Fermi formalism. The following expressions are obtained for the cohesive energy

$$E_{\mathrm{coh}} = E_s - E_b - E_c, \tag{2}$$

$$E_s = \frac{3}{4} Z_s \frac{\hbar^2 \pi^2}{m d^2}(1-a), \tag{3}$$

$$E_b = -\frac{1}{2} Z_d (1 - Z_d/10)(30.9)\sqrt{n}\,\frac{\hbar^2 r_d^3}{m d^5}, \tag{4}$$

$$E_c = Z_d n (11.40)\frac{\hbar^2 r_d^6}{m d^8}. \tag{5}$$

Here $Z_{s(d)}$ is the $s(d)$ band filling ($Z_s + Z_d = Z$, where Z is the number of valence electrons per atom), $a = \frac{4}{5}(3Z_s/2\pi)^{2/3}$ for fcc and hcp lattices, $a = \frac{6}{5}(3Z_s/4\pi)^{2/3}$ for a bcc structure, n is the number of nearest-neighbor atoms, d is the distance between the nearest neighbors in the crystal, r_d is the *d*-state radius, and m is the electronic mass. Equation (3) describes the contribution of quasi-free electrons to the cohesive energy, Eq. (4) that of the *d*-band, and (5) presents the shift of the center of gravity of the *d* band.

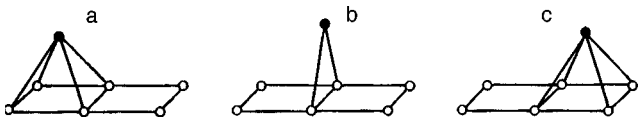

FIG. 1. Schematic presentation of diffusion. a – initial adatom position, b – position of the adatom crossing the boundary between adjacent surface cells (bridge diffusion), c – final position of the adatom.

Paper I considered the following simplified pattern of surface diffusion. It was assumed that the adsorption-bond length remains constant in the course of a hop from one surface cell to another (neighboring) cell. For a surface cell corresponding, for instance, to bcc(110) and fcc(100) structures, and a diffusion hop of an adatom over the boundary separating the neighboring cells, i.e. for bridge diffusion, this process is depicted schematically in Fig. 1 (here and in what follows the ground-state adatom is assumed to be at the cell center). In the initial and final stages of the hop (Fig. 1a and 1c) the adatom has four nearest neighbors and, hence, parameter n entering Eqs. (4) and (5) is $n_c=4$. At the moment of transition between the cells (Fig. 1b), $n=n_b=2$. In this case the surface-diffusion activation energy can be written

$$E_d=E_{\mathrm{coh}}(n_c)-E_{\mathrm{coh}}(n_b)\,, \tag{6}$$

or, taking into account Eqs. (2)–(5),

$$E_d=A\xi(Z_d/d^2)(1-Z_d/10-B\xi)\,, \tag{7}$$

where $\xi=(r_d/d)^3$, $A=69$, $B=2.52$, E_d is measured in eV, and d in Å.

For bridge diffusion ($n_c=3, n_b=2$) on the (111) surface of an fcc lattice, whose cell is an equilateral triangle, we obtain an expression similar to (7) but with $A=37.4$ and $B=2.32$. Note that if the diffusing adatom jumps into the adjacent cell not over its boundary but over another surface-cell atom, a process called atop diffusion[6] (for the case depicted in Fig. 1 this corresponds to the adatom jumping diagonally across the surface cell), the second term on the right-hand side of Eq. (6) should be replaced by $E_{\mathrm{coh}}(n_a=1)$. In the fcc (111) case we obtain Eq. (7) with $A=86.2$ and $B=2.02$.

Note that, in our approach to calculating the activation energy of surface diffusion, the contribution of quasi-free electrons E_s is disregarded.

TABLE I. Activation energy of surface self-diffusion E_d (in eV) for bridge diffusion on the (110) surface of a bcc substrate.

	E_d	
Adatom	Calculation from Eq. (7) $A=69$, $B=2.52$	Exp. Ref. 2
V	0.95	
Cr	1.23	
Fe	0.65	
Nb	1.12	
Mo	1.20	
Ta	1.19	
W	1.22	0.86, 0.87, 0.90

TABLE II. Activation energy of surface self-diffusion E_d (in eV) for bridge diffusion on the (111) surface of an fcc substrate.

	E_d		
Adatom	Calculation from Eq. (7) $A=37.4$, $B=2.32$	Theory	Exp.
Nr	0.11	0.056, 0.063 Ref. 5	0.33 Ref. 5
Cu	0.05	0.026, 0.044 Ref. 5	
Rh	0.26	–	0.16 Ref. 5
Pd	0.10	0.031, 0.059 Ref. 5	
Ag	0.04	0.059, 0.044 Ref. 5	
Ir	0.25	0.11 Ref. 6	0.22, 0.27 Ref. 6
Pt	0.06	0.007, 0.078 Ref. 5	0.25 Ref. 7
Au	0.00	0.021, 0.038 Ref. 5	

2. DISCUSSION OF RESULTS

The results of the calculation are presented in Tables I–IV. The distances between the nearest neighbors are given in Ref. 10, and the values of r_d, in Refs. 11 and 12. It was assumed that the adsorption-bond length d in the case of self-diffusion coincides with the distance between the nearest neighbors in the volume, i.e. we neglected relaxation effects. As in Paper I, we assumed $Z_s=1.5$ for the transition-metal s-band filling, and only for Cu, Ag, and Au the value $Z_s=2$ was chosen. Tables I–III list also the available experimental data, and tables II and III, EAM calculations[6] performed for two different potential functions.

The value of E_d calculated by us for bridge diffusion on the (110) bcc crystal plane (Table I) is of the order of 1 eV. The only exception is iron, whose self-diffusion barrier is two times lower. A comparison with experiment carried out for tungsten reveals that the calculated value of E_d exceeds by a factor 1.5 the experimental data. As shown in Paper I, the cohesion approximation applied to adsorption of $5d$ atoms on W(110) overestimates the values of both the adsorption energy and of E_d for the first half of the $5d$ series.

For bridge diffusion on the (111) surface of fcc crystals (Table II), our approach underestimates E_d, with the exception of Rh, for which E_d exceeds by a factor 1.5 the experimental values. Note that for ruthenium, $Z_d=7.5$. For nickel and palladium with $Z_d=8.5$ the theoretical value of E_d is three and eight times, respectively, lower than the observed one, and for Cu, Ag, and Au ($Z_d=9$) it is close to zero. It

TABLE III. Activation energy of surface self-diffusion E_d (in eV) for bridge diffusion on the (100) surface of an fcc substrate.

	E_d		
Adatom	Calculation from Eq. (7) $A=37.4$, $B=2.32$	Theory	Exp.
Ni	0.20	0.63, 0.68 Ref. 5	0.63Ref.5
Cu	0.01	0.38, 0.53 Ref. 5	
Rh	0.44	–	0.88Ref.5
Pd	0.15	0.71, 0.74 Ref. 5	
Ag	0.06	0.48, 0.48 Ref. 5	
Ir	0.40	1.58 Ref. 6	>1.02Ref.6
Pt	0.07	0.44, 1.25 Ref. 5	
Au	−0.03	0.64, 0.84 Ref. 5	

TABLE IV. Activation energy of surface self-diffusion E_d (in eV) for bridge diffusion on the (111) and (100) surfaces of an hcp substrate.

	E_d Calculation from Eq. (7)	
Adatom	$A=37.4$, $B=2.32$ (111)	$A=69$, $B=2.52$ (100)
Sc	0.21	0.12
Ti	0.37	0.67
Co	0.23	0.42
Y	0.25	0.45
Zr	0.45	0.80
Tc	0.56	0.98
Ru	0.44	0.77
Lu	0.29	0.52
Hf	0.49	0.87
Re	0.59	1.01
Os	0.45	0.75

thus follows that, for metals completing the *d* series, our approach should take into account some additional mechanisms of diffusion barrier formation. One of these could be the quasi-free electron contribution. For central elements in the *d* series, one apparently should take into account the relaxation, i.e., the variation of the adsorption-bond length.[7] It should be pointed out, however, that our results agree better with experiment than those obtained within the EAM approximation.[6] It can be added that a first-principles calculation performed for Pt yields $E_d=0.38$ eV,[7] which is 1.5 times the experimental value.

As for agreement of our calculations of bridge-type self-diffusion on the (100) plane of fcc crystals (Table III) with experiment, the trend here is the same as for the (111) plane, except that the calculated barrier for iridium is higher than suggested by measurements. Note that in this case the theory of Ref. 6 is in a substantially better accord with experiment. It should be stressed that both our approach (with the exception of Cu and Au) and EAM[6] yield higher values of E_d for the (100) than (111) surface.

The results of bridge-diffusion calculations for the (111) and (100) plane of hcp crystals are presented in Table IV. Unfortunately, we are not aware of any experimental data for these crystals. For all crystals except scandium, the values of E_d for the (100) plane are twice those for the (111) one.

We have calculated also the barrier height for atop self-diffusion on Ir(111). Our calculations yield $E_d=0.68$ eV, whereas the EAM model suggests[6] 1.43 eV. We know of no relevant experimental data.

Thus the model for calculating the activation energy of surface self-diffusion proposed in this work fits experimental data better for the (111) surface than the EAM approximation, but worse than the latter for the (100) plane. Viewed from the standpoint of our model, the underestimation of E_d for the (100) surface, as well as for metals in the second half of the *d* series, is due to the neglect of the part played by quasi-free *s* electrons. It would be of interest therefore to consider the diffusion of alkali metals on the surface of *d* metals, because there exists a wealth of experimental data.[3,4]

Support of the ''Surface Atomic Structures'' Program is gratefully acknowledged.

[1] A. G. Naumovets and Yu. S. Vedula, Surf. Sci. Rep. **4**, 365 (1985).
[2] T. T. Tsong, Rep. Prog. Phys. **51**, 759 (1988).
[3] R. Gomer, Rep. Prog. Phys. **53**, 917 (1990).
[4] E. S. Seebauer and C. E. Allen, Prog. Surf. Sci. **49**, 267 (1995).
[5] C. L. Liu, J. M. Cohen, J. B. Adams, and A. F. Voter, Surf. Sci. **253**, 334 (1991).
[6] C. M. Chang, C. M. Wei, and S. P. Chen, Phys. Rev. B **54**, 17083 (1996).
[7] P. J. Feibelman, J. S. Nelson, and G. L. Kellogg, Phys. Rev. B **49**, 10548 (1994).
[8] S. Yu. Davydov and S. K. Tikhonov, Surf. Sci. **371**, 157 (1997).
[9] J. M. Wills and W. A. Harrison, Phys. Rev. B **29**, 5486 (1984).
[10] Ch. Kittel, *Introduction to Solid State Physics* (Wiley, New York, 1971; Nauka, Moscow, 1978), 792 pp.
[11] J. M. Wills and W. A. Harrison, Phys. Rev. B **28**, 4363 (1983).
[12] W. A. Harrison, *Electronic Structure and the Properties of Solids* (Freeman, San Francisco, 1980; Mir, Moscow, 1983), 334 pp.

Translated by G. Skrebtsov

An analysis of the mechanism of Kerr effect enhancement in Mn/Dy/Bi

S. G. Ovchinnikov, L. V. Burkova, V. A. Seredkin, and V. Yu. Yakovchuk

L. V. Kirenskiĭ Institute of Physics, Siberian Branch of the Russian Academy of Sciences, 660036 Krasnoyarsk, Russia

(Submitted June 2, 1998)
Fiz. Tverd. Tela (St. Petersburg) **41**, 91–97 (January 1999)

A study is reported of the structural, magnetic, and magneto-optic properties of Mn/Dy/Bi films obtained by multilayer technology. The maximum Kerr rotation angle in such films is shown to be $\theta_k = 2.25°$. Possible reasons for such a large Kerr effect enhancement are considered, namely, an increase in the $6p-3d$ transition probability caused by symmetry distortion, polarization of the Bi$6p$ band, and a change in the density of states near the Fermi level. The latter reason has been analyzed by simulating the electronic structure of Mn/Dy/Bi through superposition of Dy levels on the MnBi band structure. This approach has revealed possible additional transitions which may be induced by the presence of a Dy buffer and could contribute to the Kerr magneto-optic effect.
[S1063-7834(99)02001-8]

MnBi polycrystalline films were one of the first materials[1] in which a large room-temperature Kerr effect ($\theta_k = 0.7°$) was observed[2]. Mn/Dy/Bi films, obtained presently by multilayer technology, exhibit, besides a reduction of mean crystallite size to 15 nm and an increased perpendicular anisotropy, a rotation angle of 2.25° (Ref. 3), which is of considerable interest from both scientific and applications standpoints. Experiment shows that incorporation into the bulk of the film of such impurities as Ti,[4] Zn, Te,[5] Sb,[6] V, Cr, Cu, Ni,[7] Ag, Au, In, Pt,[8] as well as of Dy,[9] results in degradation of the magneto-optic (MO) properties. While Al doping enhances the Kerr effect[8,10] up to 2°, it reduces at the same time the perpendicular anisotropy by one half. Using Sm, Ce, and Pr[11] as dopants permits one to obtain rotation angles of 2 to 2.5°, but the hysteresis loop rectangulatity ratio becomes less than unity.

Self-consistent calculations of the MnBi spin-polarized band structure, in which spin-orbit interaction was considered as a perturbation, showed that the main contribution to the MO effect should come from Bi$6p\downarrow \rightarrow$ Mn$3d\downarrow$ transitions.[12] Relativistic electronic-structure calculations made in the local density-functional augmented spherical-wave (LDA–ASW) approximation yield a spectral response of the Kerr effect in MnBi which agrees well with experiment.[13,14] Using this approach in an analysis of the microscopic nature of the Kerr effect in MnBi permitted one to relate its large values to a combination of the fairly large magnetic moment on Mn, a strong spin-orbit Bi coupling, which is believed to be ten times larger than that in $3d$ metals,[15] and a strong hybridization between the Mn d band and Bi p states[14]. A theoretic consideration[13,16] of the effect of impurities on the Kerr effect shows that their presence gives rise to a change in Mn magnetization and Bi spin-orbit coupling[16] and a redistribution of the density of states near the Fermi level and affects the hybridization,[13,16] while the magnitude of the MO effect depends to a considerable extent on the position of the impurity atoms in the MnBi cell (Ref. 13). The latter conclusion is consistent with cluster-model calculations[17]. An analysis of experimental data gives one grounds to assume that the relative significance of the above contributions to the Kerr effect is determined by the characteristics of the dopant.[8,11]

This work reports an investigation of the structural, magnetic, and magneto-optic properties of Mn/Dy/Bi films and analyzes the mechanism responsible for the considerable enhancement of the Kerr effect ($\theta_k = 2.25°$) observed in these films.

1. SAMPLES AND EXPERIMENTAL METHOD

Mn/Dy/Bi films were prepared by successive deposition of alternating Bi, Dy, Mn, Dy etc. layers on glass substrates at room temperature in a vacuum of 3×10^{-6} Torr.[18] Immediately after the deposition, the samples were annealed in a vacuum of 5×10^{-6} Torr at a temperature of 250–270 °C. The anneal times were chosen 60, 30, 15, and 7 min, depending on the thickness and number of layers.[19] The thicknesses of the Bi and Mn layers were chosen so as to satisfy the 1:1 atomic ratio, and varied within the 12.5–100-nm interval for Bi, and from 4 to 39 nm for Mn. The Dy layer thickness was varied from 3 to 40 nm.

The structural properties of the films were studied by transmission electron microscopy. The chemical composition and thickness of the samples were determined by spectral fluorescence analysis. Auger spectra permitted measuring the distribution of components through the thickness. Chemical bonding was derived from X-ray photoelectron (XPS) spectra. The saturation magnetization (M_s) and the perpendicular anisotropy constant (K_u) were measured with a torsion magnetometer. The polar Kerr-effect rotation (θ_k) and its spectral response were obtained from the side of the substrate at room temperature on a magneto-optic setup in fields of up to 16 kOe. The coercive force (H_c) was extracted from Kerr hysteresis loops.

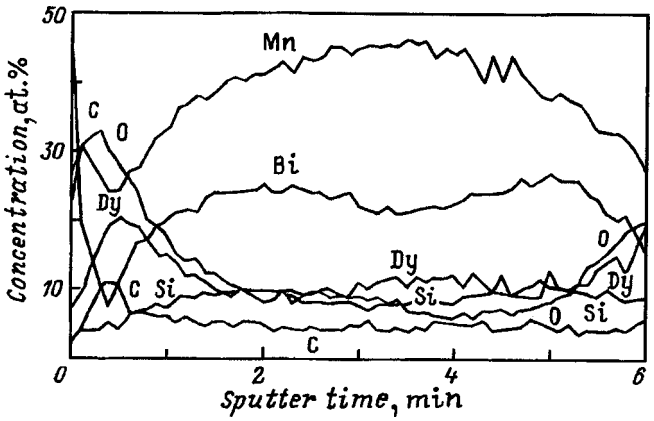

FIG. 1. Auger depth profile of a Mn/Dy/Bi film.

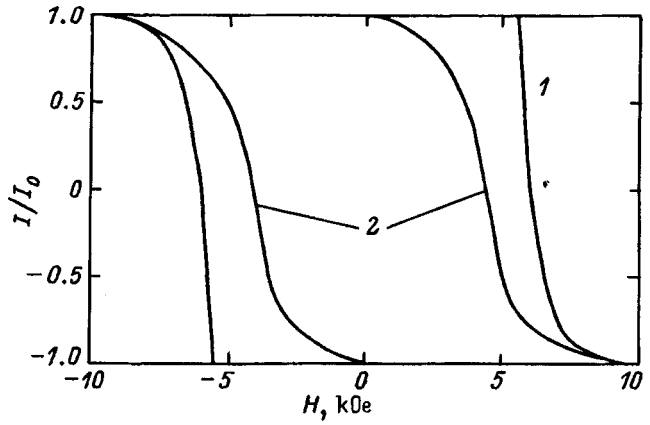

FIG. 2. Hysteresis loops of (*1*) Mn/Dy/Bi and (*2*) MnBi films.

2. EXPERIMENTAL RESULTS

The characteristics of Mn/Dy/Bi films optimized in thickness and number of layers in the starting condition were as follows: average crystallite size 15 nm, $H_c = 6$ kOe, $K_u = 1 \times 10^7$ erg/cm^3, and $\theta_k = 2.25°$ for $\lambda = 633$ nm. Before annealing, these films consisted of alternating Bi, Dy, and Mn layers of thickness 49.5, 5, and 17 nm, respectively, with the total number of layers being seven. They were annealed at 270 °C for 30 min.

A comparative analysis of the crystalline structure of these films and of MnBi films fabricated by standard technology[20] shows that the considerable decrease in crystallite size in the former is due to introducing Dy as a buffer. After annealing, MnBi films contain a lot of large crystallites 250–400 nm in size, with some of them measuring 1000–3000 nm. The average size of crystallites in structurally optimum Mn/Dy/Bi films decreases after annealing from 300 to 15 nm, i.e., by nearly two orders of magnitude compared to MnBi. The electron diffraction patterns of Mn/Dy/Bi films obtained before annealing show Bi, Dy, and Mn to be polycrystalline, with the average size of Bi and Mn crystallites about 300 nm, and that of Dy crystallites, an order of magnitude smaller. After the annealing, one observes besides the newly formed MnBi phase a small volume fraction of Mn and Bi as a free phase. Annealing reduces considerably the volume fraction of pure Dy, which may be due to its incorporation into the MnBi lattice. Formation of Dy compounds with oxygen and/or Mn oxide is also possible, which finds support in the presence of a $DyMnO_3$ reflection in the electron diffraction patterns and XPS spectra. These spectra reveal the presence of Bi and Mn in metallic state, and Dy, both in metallic and oxidized states.

Figure 1 shows an Auger depth profile of a Mn/Dy/Bi film showing that the distribution of each component is sufficiently uniform throughout the volume of the film. The enhanced content of oxygen and dysprosium in the near-surface and near-substrate regions can be attributed to a tendency characteristic of RE elements to migrate to the film surface and become oxidized there.[21]

A detailed analysis of the structural features of Mn/Dy/Bi compared with MnBi films permits a conclusion that multilayer technology favors formation of a fine-grained crystalline structure.[3] Doping with Dy by sandwiching the corresponding buffer layer favors a more uniform distribution of Dy atoms in the bulk of the film in the course of annealing and their incorporation in the crystal lattice, and there are grounds to assume that they preferably occupy intermediate positions in the MnBi cell and/or substitute for Bi,[11] but not for Mn (Ref. 4). One cannot exclude a possibility that a small fraction of Dy segregates to form a separate phase rather than entering a solid solution. If the content of the Dy dopant is small, this phase will apparently become distributed over MnBi grain boundaries, and for large contents pure Dy inclusions will appear.

Figure 2 presents a room-temperature hysteresis loop of a Mn/Dy/Bi film with optimum parameters. A comparison with the loop of a MnBi film obtained by us by standard technology indicates that a Dy buffer improves considerably the hysteresis-loop rectangularity ratio, which for all the Mn/Dy/Bi films is unity. Table I lists the magnetic and magneto-optic parameters of Mn/Dy/Bi films having different thicknesses and number of layers before anneal. Also presented are the parameters of MnBiDy and MnBi films fabricated by us using standard technology, and the relevant data available from the literature. As seen from Table I, the Kerr rotation angle for all Mn/Dy/Bi films is larger than that quoted for MnBi. The largest value θ_k was measured in the above-mentioned films with optimum parameters. The MO rotation in films prepared by us by conventional Dy doping at the equivalent percentage level is smaller, 0.35° (Table I). Figure 3 shows the spectral response of θ_k for Mn/Dy/Bi films, which is seen to peak around $\lambda = 633$ nm. This maximum is slightly shifted toward shorter wavelengths compared to the corresponding relation for MnBi films also displayed in the figure.

3. DISCUSSION OF RESULTS

Note the large Kerr rotation angle in Mn/Dy/Bi films, whose maximum value exceeds by 1.5 times the value obtained by us in MnBi films (Table I). As already mentioned, Kerr rotation depends on the spin-orbit coupling, magnetization, and density of states.[15] Our measurements showed that the magnetization of Mn/Dy/Bi films is about 30% less than that of our MnBi films. This may be due to a large extent to

TABLE I. Magnetic and magneto-optic properties of Mn/Dy/Bi, MnBiDy, and MnBi films.

Composition	Thickness			Total number of layers	Anneal time, min	H_c, kOe	M_s, G	$K_u \cdot 10^{-7}$, erg/cm^3	θ_k, deg
	Bi, nm	Mn, nm	Dy, nm						
Mn/Dy/Bi	49.5	17	5	3	30	2	485	1	1.5
Mn/Dy/Bi	49.5	17	20	3	60	5	–	–	1.4
Mn/Dy/Bi	50	18	4	7	30	1.6	520	1.2	1.9
Mn/Dy/Bi	104	39	5	3	60	4.7	320	0.7	1.0
Mn/Dy/Bi	49.5	17	5	7	30	6	330	1.4	2.25
MnBiDy		148			30	8			0.35
MnBi		148			60	3.5	400	1.4	1.3
MnBi [13]		148			300	0.8	620	20	0.7

the formation of a fine-grained crystalline structure.[17] Calculations suggest that incorporation of an impurity, e.g. Al, in MnBi results in a decrease in the spin-orbit coupling because of the impurity and Bi states becoming hybridized.[16] It thus appears hardly likely that the former two reasons could contribute to the increase of θ_k, and the explanation should be sought rather in a change of the electronic structure induced by the presence of a Dy buffer.

To picture more clearly the mechanism of Kerr effect enhancement, consider the MnBi band structure,[12] whose calculated density of states is shown in Fig. 4a–4c. We readily see that the Bi$6p\downarrow \rightarrow$ Mn$3d\downarrow$ optic transitions with energies of 1.5–2 eV have the highest probability. Quantitative calculations support this conclusion.[13,14] The calculated spectral response passes through a maximum at 1.8 eV, which agrees with both our (Fig. 3) and other available experimental data.

Phenomenological consideration identifies Kerr rotation with the off-diagonal term of the optical conductivity tensor[15]

$$\theta_k = \frac{4\pi}{\omega} \mathrm{Re}\left[\frac{\sigma_{xy}}{(1-(n+ik)^2)(n+ik)} \right], \qquad (1)$$

where $n+ik$ is the complex refractive index at frequency ω. Several microscopic-scale mechanisms can be proposed to account for the large Kerr effect in Mn/Dy/Bi films, which may lead to an increase of σ_{xy} in the presence of a Dy buffer:

1. As already mentioned, the large Kerr effect in MnBi may be due to the $6p-3d$ electronic transitions (see Fig. 4a–4c), whose matrix elements enter σ_{xy}. Incorporation of Dy atoms in the MnBi lattice may distort the symmetry and give rise to the associated increase in the $6p-3d$ transition probability, i.e., to an increase of the corresponding matrix elements. The symmetry is distorted when impurity atoms occupy intermediate positions in the MnBi cell.[13] As already pointed out, Dy atoms in Mn/Dy/Bi films have a higher probability to occupy intermediate positions, and this may be one

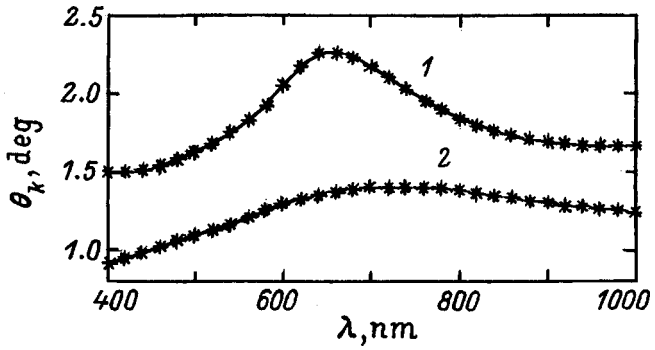

FIG. 3. θ_k dispersion relations for (*1*) Mn/Dy/Bi and (*2*) MnBi films.

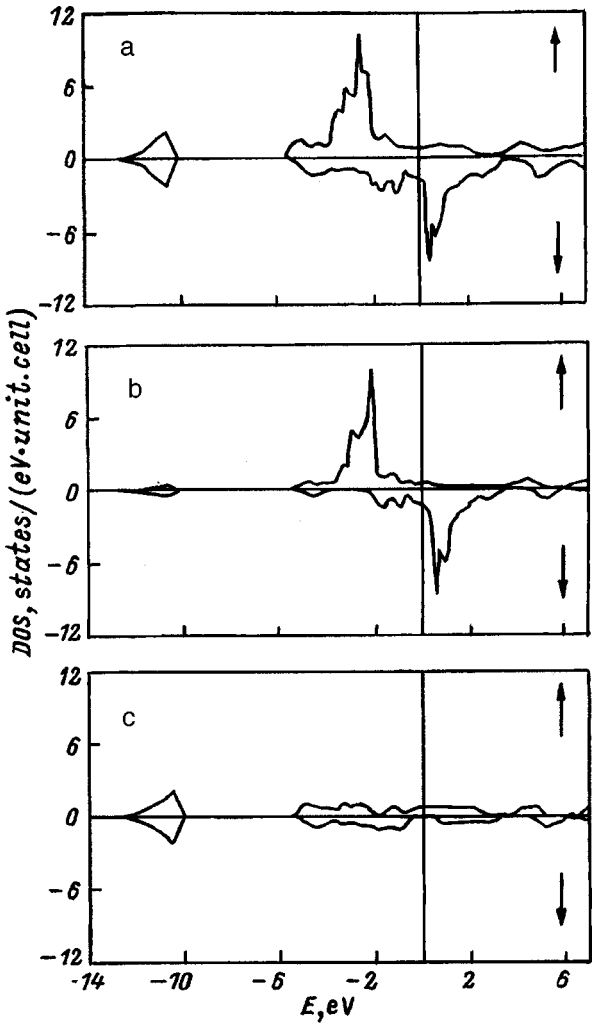

FIG. 4. MnBi densities of states.[12] (a) joint DOS, (b) density of Mn$3d$ states, (c) density of Bi$6p$ states. The vertical arrows in Figs. 4–6 refer to spin direction.

of the reasons for the enhanced Kerr effect. Our MnBiDy films prepared by codeposition of the components, the conditions favoring substitution of Dy atoms for Mn,[4] exhibit a substantially smaller θ_k (Table I).

2. The off-diagonal term of the optical-conductivity tensor can be expanded in terms depending on electron spin orientation[15]

$$\sigma_{xy}=\sigma_{xy}(\uparrow\uparrow)+\sigma_{xy}(\downarrow\downarrow)+\sigma_{xy}(\uparrow\downarrow)+\sigma_{xy}(\downarrow\uparrow)\,. \qquad (2)$$

A comparison of the energy dependences of these terms shows that transitions involving spin mixing yield an insignificant contribution, and calculations[13] suggest that the magneto-optic transition in MnBi is dominated by transitions from the $6p$ spin-down state of Bi to $3d$-Mn spin-down states. As seen from Fig. 4b, the Mn$3d$ band is totally polarized, and impurities should not affect it noticeably. An analysis of the electronic structure of MnBiAl films leads to the conclusion that Al doping gives rise to a considerable polarization of the Bi$6p$ band, i.e., to an increase in the number of $6p$ spin-down electrons and spin-up holes, and that this should enhance the MO effect.[17] Dysprosium in Mn/Dy/Bi films could act in this way. The mechanism underlying this interaction may be hybridization of the Dy$4f$ and $5d$ states with the Bi$6p$ states (Fig. 4b), which increases the density of states of Bi below the Fermi level, and this, in its turn, should result in an increase of the optical transition probability.

3. The discussion of the Kerr effect in Mn/Dy/Bi films can be facilitated by simulating the electronic structure of this system through superposition of Dy levels on the MnBi band structure. The RE *s* and *d* electrons in the compound form metallic bonds, whereas the $4f$ electrons can apparently be considered in a single-impurity approximation as an ensemble of isolated (disregarding hybridization with Mn and Bi) local terms. These terms can shift relative to those of the pure metal. According to XPS data, this shift depends on the percentage content of the RE element,[22] and for $Tb_{21}Fe_{79}$ amorphous films, for instance, is about 1 eV (Ref. 23). It is believed to be due to *d*-state hybridization between Fe and Tb.[23] The spectrum of $Tb_{21}Fe_{79}$ contains a low-energy maximum with a binding energy of 2–3 eV corresponding to Tb$4f$ electrons. For low binding energies, $E_b\approx 1-3$ eV, the density of states of the RE element is dominated by the $5d$ electrons (which is also supported by XPS data[24] for pure RE elements), which are responsible for the maximum in the optical conductivity $\sigma(\omega)$ at $\hbar\omega\approx 2$ eV.[25] Because RE $5d\rightarrow$Mn$3d$ transitions are forbidden by optical selection rules, *d* states of an RE element are insignificant from the standpoint of optical transitions.

The $4f$ electrons in Mn/Dy/Bi films are in the ferromagnetic matrix and can be magnetized by s–f exchange coupling. In this case, however, in contrast to pure RE elements, where intratomic s–f exchange interaction is dominant, $J_{s-f}\sim 1$ eV,[26] the $4f$ electronic spins interact also with the band electrons of Mn, and this interaction is an order of magnitude weaker. Therefore, one may neglect the exchange splitting of the $4f$ levels and present the Mn/Dy/Bi band-structure model as a superposition of the Dy density of states in Fig. 4a. Because of the lack of literature data on the density of states of Dy in a compound, one can use for this purpose the local density of states of Tb,[27] which was derived[23] directly from XPS and XPS^{-1} spectra for $Tb_{21}Fe_{79}$. This density of states, calculated taking into account the joint density-of-states function for ferromagnetic Gd,[28] is shown in Fig. 5a by dashed and dot-and-dash lines for the $4f$ and $5d$ electrons at $T=0$. The hybridization of the $4f$ and $5d$ electrons of Dy with the $3d$ electrons of Mn was taken into account. The case of parallel Dy and Mn spin orientation, i.e. $M_{\mathrm{Dy}}\uparrow\uparrow M_{\mathrm{Mn}}$, and $J_{df}>0$ was considered. It is assumed that there is no spin splitting of the Dy $5d$ band, or it is very small. Based on this model, Fig. 5a can permit us to find the additional transitions contributing to the Kerr effect enhancement that can be induced by incorporation of Dy. These transitions are listed in Table II. Figures 4 and 5a offer a possibility of making a rough estimate of the contributions due to these transitions. The transitions numbered 1, 4, 5, and 8 should not contribute, because the density of $6p$ states should already be involved in the transitions observed in MnBi, i.e., Bi$6p$–Mn$3d$. The intensity of transition 6 is extremely weak because of the low density of unoccupied spin-up Mn $3d$ states. The contributions due to the other transitions are of about the same order of magnitude. The above figures permit determining the limits on the energy of each transition, which are also given in Table II. By the transition energy ΔE one understands the difference between the energies of the final and initial states. The subscript *i* on

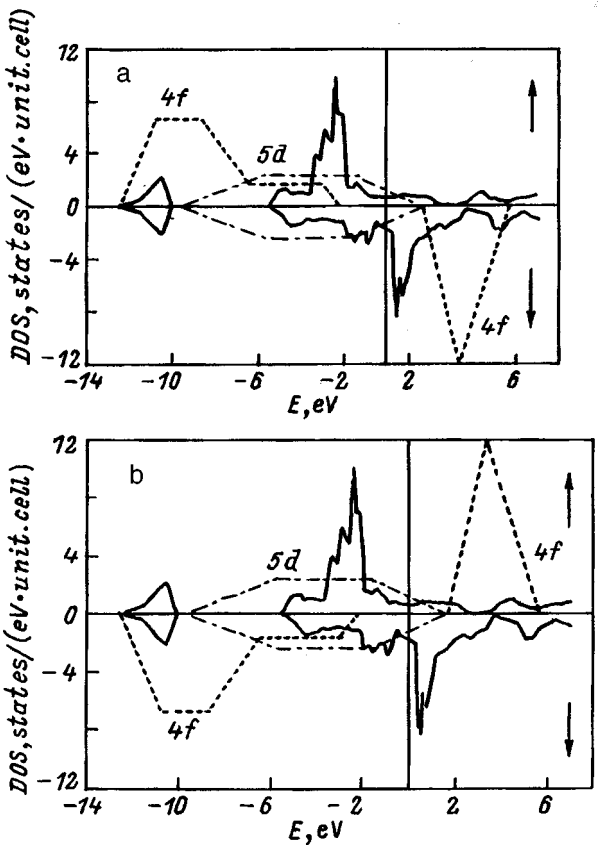

FIG. 5. Superposition of MnBi and Dy DOS for (a) parallel and (b) antiparallel Mn and Dy spin orientation.

TABLE II. Possible transitions in Mn/Dy/Bi films for parallel Dy and Mn spin orientation.

No. n/n	Possible transitions	Transition energy	Significant transition interval, nm
1	$5d\uparrow\rightarrow 6p\uparrow$	$\Delta E>0$	400–1000
2	$5d\downarrow\rightarrow 6p\downarrow$	$\Delta E>0$	400–1000
3	$6p\uparrow\rightarrow 5d\uparrow$	$0<\Delta E<E_{5d\uparrow}$	770–1000
4	$6p\downarrow\rightarrow 5d\downarrow$	$0<\Delta E<E_{5d\downarrow}$	770–1000
5	$4f\uparrow\rightarrow 6p\uparrow$	$\Delta E>E_{f\uparrow}$	400–860
6	$4f\uparrow\rightarrow 3d\uparrow$	$\Delta>E_{f\uparrow}$	400–860
7	$4f\uparrow\rightarrow 5d\uparrow$	$E_{f\uparrow}+E_{5d\uparrow}>\Delta E>E_{f\uparrow}$	400–860
8	$6p\downarrow\rightarrow 4f\downarrow$	$E_{f\downarrow}+\Delta E_{f\downarrow}>\Delta E>E_{f\downarrow}$	400–860
9	$3d\downarrow\rightarrow 4f\downarrow$	$E_{f\downarrow}+\Delta E_{f\downarrow}>\Delta E>E_{f\downarrow}$	400–860
10	$5d\downarrow\rightarrow 4f\downarrow$	$E_{f\downarrow}+\Delta E_{f\downarrow}>\Delta E>E_{f\downarrow}$	400–860

the energy identifies the edge of the density-of-*i*-states band closest to the Fermi level.

Table III presents similar data for the case of antiparallel Dy and Mn spin orientation. The corresponding density-of-states function is shown in Fig. 5b. One readily sees that the transitions labeled 1 and 4 do not contribute for the above-mentioned reason. The intensities of transitions 2, 3, 5, 7, 8, and 9 are of about the same order of magnitude, because the densities of the corresponding initial and final states differ insignificantly. Transition 10 may provide a noticeable contribution. Note also the $4f\downarrow\rightarrow 3d\downarrow$ transition, which may become strong under certain conditions.

The limits on the energies of possible transitions can be estimated quantitatively taking due account of the fact that the edges of the Dy$4f$ bands may differ from those presented in Fig. 5a and 5b for Tb. Published XPS data suggest that the maximum in the density of Dy$4f$ states in *RE*-Fe_2 lies closer to the Fermi level than that for Tb.[29] Tables II and III give the ranges for the contribution of possible transitions, which were determined under the assumption that the filled $4f$ band is shifted toward the Fermi level only by 1 eV compared to the diagram in Figs. 4 and 5a, i.e., $E_{f\downarrow}=-1.4$ eV, and the others, in accordance with the figure, are $E_{3d\downarrow}=0.3$ eV, $\Delta E_{3d\downarrow}=0.5$ eV, $E_{f\uparrow}=2.6$ eV, and $\Delta E_{f\uparrow}=3$ eV. Note also that this shift should be accompanied by about the same shift of the unfilled $4f$ band toward higher energies,[27] and vanishing of the contributions due to transitions terminating on unfilled $4f$ states.

TABLE III. Possible transitions in Mn/Dy/Bi films for antiparallel Dy and Mn spin orientation.

No. n/n	Possible transitions	Transition energy	Significant transition interval, nm
1	$5d\uparrow\rightarrow 6p\uparrow$	$\Delta E>0$	400–1000
2	$5d\downarrow\rightarrow 6p\downarrow$	$\Delta E>0$	400–1000
3	$6p\uparrow\rightarrow 5d\uparrow$	$0<\Delta E<E_{5d\uparrow}$	770–1000
4	$6p\downarrow\rightarrow 5d\downarrow$	$0<\Delta E<E_{5d\downarrow}$	770–1000
5	$4f\downarrow\rightarrow 6p\downarrow$	$\Delta E>E_{f\downarrow}$	400–860
6	$4f\downarrow\rightarrow 3d\downarrow$	$E_{f\downarrow}+E_{3d\downarrow}+\Delta E_{3d\downarrow}>\Delta E>E_{f\downarrow}+E_{3d\downarrow}$	560–730
7	$4f\downarrow\rightarrow 5d\downarrow$	$E_{f\downarrow}+E_{5d\downarrow}>\Delta E>E_{f\downarrow}$	400–860
8	$6p\uparrow\rightarrow 4f\uparrow$	$E_{f\uparrow}+\Delta E_{f\uparrow}>\Delta E>E_{f\uparrow}$	400–500
9	$3d\uparrow\rightarrow 4f\uparrow$	$E_{f\uparrow}+\Delta E_{f\uparrow}>\Delta E>E_{f\uparrow}$	400–500
10	$5d\uparrow\rightarrow 4f\uparrow$	$E_{f\uparrow}+\Delta E_{f\uparrow}>\Delta E>E_{f\uparrow}$	400–500

As seen from Table II, in the case of $M_{\mathrm{Dy}}\uparrow\uparrow M_{\mathrm{Mn}}$ the contributions due to possible transitions should be uniformly distributed within the 400–1000-nm wavelength range under consideration. The intensities of these transitions are of about the same order of magnitude, i.e., they can produce only a shift of the spectral curve as a whole toward higher values of θ_k and cannot give rise to the energy shift of the maximum observed for Mn/Dy/Bi, which, as in the case of MnBi, is provided by the Bi$6p\downarrow\rightarrow$ Mn$3d\downarrow$ transitions. The pattern for the $M_{\mathrm{Dy}}\downarrow\uparrow M_{\mathrm{Mn}}$ case is approximately the same. The relevant transition $4f\downarrow\rightarrow 3d\downarrow$, however, should contribute substantially within the wavelength interval determined by the width of the peak of unfilled Mn$3d\downarrow$ states, and it corresponds in this case to the interval of the observed maximum in the Kerr effect. There are unfortunately no data on the mutual orientation of the Dy and Mn spins, and the decrease in magnetization observed in Mn/Dy/Bi films cannot be considered as evidence for their antiparallel orientation, because it can be caused by a decrease in crystallite size.[17]

In Mn compounds with Dy one observes both ferromagnetic[30] and antiferromagnetic[31] spin ordering of these elements, with the magnetic properties depending to a considerable extent on interatomic distance[32]. It may be conjectured that ordering, similar to RE(Fe,Co)[33] compounds, varies from antiferromagnetic to ferromagnetic with increasing distance between the RE and Mn atoms. If Dy atoms occupy intermediate positions in the MnBi cell, the distance between the Mn and Dy atoms is larger than when they substitute for Bi atoms, i.e. in the second case antiferromagnetic ordering is more probable. As already mentioned, the Dy positions depend on the technology by which the Dy was incorporated, and, hence, the differences in the MO properties between Mn/Dy/Bi and MnBiDy films may be due to the fact that these films differ to a certain extent in the mutual ordering of Mn and Dy spins and in the corresponding contributions due to the above transitions.

For the case $M_{\mathrm{Dy}}\uparrow\uparrow M_{\mathrm{Mn}}$, if the unfilled $4f$ band is narrow enough, the maximum in the Kerr effect can be assigned to transitions to this band. The interval within which these transitions provide a contribution should be determined by the width of the peak of unfilled $4f$ states, so that, for instance, in the case of $E_{f\downarrow}=1.6$ eV corresponding to Fig. 6a and $\Delta E_{f\downarrow}\sim 0.8$ eV it extends from 520 to 770 nm. Hence such transitions may produce the maximum in θ_k observed exactly within this wavelength interval. Electronic structure calculations, which were carried out by means of the LMTO method localized to a maximum extent and were based on the atomic-sphere approximation and the recursive approach, showed that the position and width of the peak of unfilled $4f$ states in RE-TM amorphous films depend on the RE type.[34] It was shown also that variation of interatomic distance within 1 to 2% for the same atomic content shifts this peak by 0.3 eV. Hence there is a possibility of varying the width and position of the peak of unfilled $4f$ states by properly choosing the corresponding composition.

Figure 6a and 6b displays the densities of states calculated taking into account the spin splitting of the $5d$ band for

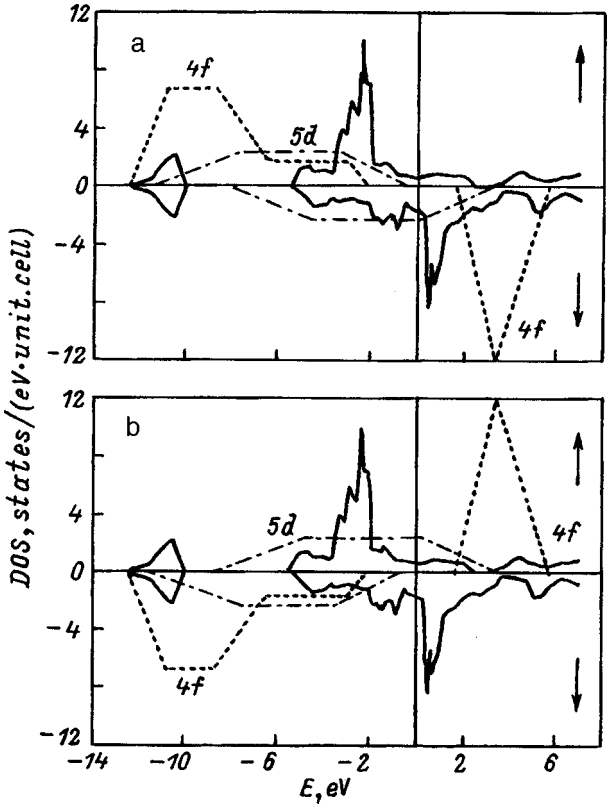

FIG. 6. Superposition of MnBi and Dy DOS with inclusion of the spin splitting of Dy5d band for (a) parallel and (b) antiparallel Mn and Dy spin orientation.

the $J_{\mathrm{MnDy}}>0$ and $J_{\mathrm{MnDy}}<0$ cases, respectively. Although splittings above 4 eV are not likely,[35] it is this limiting case that is depicted in the figure. An estimate of the intensity of the additional transitions shows that in the $M_{\mathrm{Dy}}\uparrow\uparrow M_{\mathrm{Mn}}$ case the transitions terminating on the $5d\uparrow$ state (transitions 3 and 7 in Table II) are no longer operative, as are also transitions 4 and 7 in Table III ending on the $5d\downarrow$ state in the $M_{\mathrm{Dy}}\downarrow\uparrow M_{\mathrm{Mn}}$ case. Because these transitions cover together the whole wavelength interval considered here, it can be assumed that the spectral curve undergoes a lowering as a whole in both cases, although there is a certain increase in intensity for transitions starting from the $5d\downarrow$ state (transition 10) in the first case and from the $5d\uparrow$ state in the second (transition 10). All the other transitions do not change.

A more detailed consideration made for the $M_{\mathrm{Dy}}\uparrow\uparrow M_{\mathrm{Mn}}$ case (Fig. 6a) shows that the effect of splitting depends on temperature. As the temperature increases, the $5d\uparrow$ band shifts toward the Fermi level and crosses it at a temperature $T=T^*$. For $T>T^*$, the transitions which disappeared because of the splitting, Bi6$p\uparrow\rightarrow$ Dy5$d\uparrow$ and Dy4$f\uparrow$ $\rightarrow$ Dy5$d\uparrow$, become operative again, to be accompanied by a growth in conductivity. A similar situation is observed in the $M_{\mathrm{Dy}}\downarrow\uparrow M_{\mathrm{Mn}}$ case (Fig. 6b), i.e., at $T=T^*$ the vanished transitions, $6p\downarrow\rightarrow 5d\downarrow$ and $4f\downarrow\rightarrow 5d\downarrow$, reappear, to give rise to an upward shift of the θ_k spectral response as a whole.

Thus the model proposed here permits a detailed analysis of the contribution to the MO effect due to additional transitions which may be induced by Dy doping. One may thus conclude that, if the filled Dy4f band in Mn/Dy/Bi films lies sufficiently close to the Fermi level, a maximum in the θ_k spectrum may appear only for antiparallel orientation of Dy and Mn spins, and it will be dominated by $4f\downarrow\rightarrow 3d\downarrow$ transitions. If the unfilled $4f$ band is very narrow and is located sufficiently close to the Fermi level, then a maximum may appear in the spectrum due to new transitions only in the parallel-orientation case. This maximum may be contributed by $6p\downarrow\rightarrow 4f\downarrow$, $3d\downarrow\rightarrow 4f\downarrow$, and $5d\downarrow\rightarrow 4f\downarrow$ transitions. As already pointed out, the shift of the unfilled $4f$ band toward the Fermi level should be accompanied by the corresponding shift of the edge of the filled $4f$ band toward higher binding energies,[27] and it is this band (i.e. the $4f\downarrow\rightarrow 3d\downarrow$ transitions) that will account for the maximum in the Kerr effect observed[13] in the short-wavelength region. The spin splitting of the $5d$ band lowers the θ_k spectral-response curve, which rises again with increasing temperature.

The present consideration of the reasons which may be responsible for the Kerr effect enhancement in Mn/Dy/Bi films is of a preliminary nature. Further structural studies of such films, as well as theoretical calculations taking into account different positions of Dy atoms in the MnBi cell, investigation of the optical and magneto-optic properties made within a broader wavelength range and for different temperatures, combined with XPS analysis, will offer a possibility of corroborating the influence of the above factors on the Kerr effect, as well as to determine quantitatively the contribution of each of them to its enhancement.

[1] H. J. Williams, R. C. Sherwood, F. G. Foster, and E. M. Kelley, J. Appl. Phys. **28**, 1181 (1957).
[2] K. Egashira and T. Yamada, J. Appl. Phys. **45**, 3643 (1974).
[3] L. V. Burkova, A. S. Parshin, V. A. Seredkin, and V. Yu. Yakovchuk, Avtometriya No. 2, 39 (1995).
[4] W. K. Unger, E. Wolfgang, H. Harms, and H. Haudek, J. Appl. Phys. **43**, 2875 (1972).
[5] H. Göbel, E. Wolfgang, and H. Harms, Phys. Status Solidi A **35**, 89 (1976).
[6] Y. J. Wang, J. X. Shen, and Q. Tang, J. Magn. Magn. Mater. **74**, 365 (1988).
[7] A. Katsui, A. Shibukawa, H. Terui, and K. Egashira, J. Appl. Phys. **47**, 5069 (1976).
[8] Y. Chen, C. P. Luo, Z. T. Guan, Q. Y. Lu, and Y. J. Wang, J. Magn. Magn. Mater. **115**, 55 (1992).
[9] A. Katsui, J. Appl. Phys. **47**, 4663 (1976).
[10] Y. J. Wang, J. Magn. Magn. Mater. **84**, 39 (1990).
[11] D. S. Dai, R. Y. Fang, P. Long, S. Zhang, T. J. Ma, C. Dai, and X. X. Zhang, J. Magn. Magn. Mater. **115**, 66 (1992).
[12] R. Coehoorn and R. A. de Groot, J. Phys. F **15**, 2135 (1985).
[13] J. Köhler and J. Kübler, J. Phys.: Condens. Matter **8**, 8681 (1996).
[14] P. M. Oppeneer, V. N. Antonov, T. Kraft, H. Eschrig, A. N. Yaresko, and A. Ya. Perlov, J. Appl. Phys. **80**, 1099 (1996).
[15] D. K. Misemer, J. Magn. Magn. Mater. **72**, 267 (1988).
[16] K. W. Wierman, J. X. Shen, R. D. Kirby, and D. J. Sellmyer, J. Appl. Phys. **75**, 6348 (1994).
[17] Z. Li, H. Luo, W. Lai, Z. Zeng, and Q. Zheng, J. Magn. Magn. Mater. **98**, 47 (1991).
[18] V. A. Seredkin, V. Yu. Yakovchuk, L. V. Burkova, and S. Z. Sklyuev, USSR Inventor's Certificate No. 1718273 (1992).
[19] M. Masuda, I. Izawa, S. Yoshino, S. Shiomi, and S. Uchiyama, Jpn. J. Appl. Phys. **26**, 707 (1987).
[20] D. Chen, J. Appl. Phys. **42**, 3625 (1971).
[21] R. B. van Dover, E. M. Gyorgy, R. P. Frankenthal, M. Hong, and D. J. Siconolfi, J. Appl. Phys. **59**, 1291 (1986).
[22] A. S. Andreenko and L. Zhanda, Fiz. Tverd. Tela (Leningrad) **30**, 1530 (1988) [Sov. Phys. Solid State **30**, 885 (1988)].

[23] G. A. N. Connell, S. J. Oh, J. Allen, and R. Allen, J. Non-Cryst. Solids **61-62**, 1061 (1984).
[24] P. O. Hedén, H. Löfgren, and S. B. M. Hagström, Phys. Rev. Lett. **26**, 432 (1971).
[25] N. Ahmed-Mokhtar, J. P. Petrakian, R. Philip, R. Fraisse, and B. Lazarides, Thin Solid Films **88**, 177 (1982).
[26] R. Ahuja, S. Auluck, B. Lohansson, and M. S. S. Brooks, Phys. Rev. B **50**, 5147 (1994).
[27] G. A. N. Connell, J. Magn. Magn. Mater. **54-57**, 1561 (1986).
[28] J. Sticht and J. Kübler, Solid State Commun. **53**, 529 (1985).
[29] V. V. Nemoshkalenko, V. N. Uvarov, S. V. Borisenko, A. I. Senkevich, and V. D. Borisenko, Metallofiz. Nov. Tekhnol. **17**, No. 10, 3 (1995).
[30] S. Labroo, N. Ali, and P. Robinson, J. Appl. Phys. **67**, 5292 (1990).
[31] K. Yoshimura, M. Shiga, and Y. Nakamura, J. Phys. Soc. Jpn. **55**, 3585 (1986).
[32] H. Wada, H. Nakamura, K. Yoshimura, M. Shiga, and Y. Nakamura, J. Magn. Magn. Mater. **70**, 134 (1987).
[33] K. N. R. Taylor and M. I. Darby, *Physics of Rare-Earth Solids* [Chapman and Hall, London, 1972; Mir, Moscow, 1974], 374 pp.
[34] H. Tanaka and S. Takayama, J. Appl. Phys. **67**, 5334 (1990).
[35] Yu. V. Knyazev and G. A. Bolotin, Fiz. Met. Metalloved. **58**, 1121 (1984).

Translated by G. Skrebtsov

Hall effect in microscopically inhomogeneous magnetic alloys

E. A. Mityushov

Ural State Technical University, 620002 Ekaterinburg, Russia

N. I. Kourov and Yu. P. Irkhin

Institute of Metal Physics, Ural Branch of the Russian Academy of Sciences 620219 Ekaterinburg, Russia*

(Submitted June 9, 1998)
Fiz. Tverd. Tela (St. Petersburg) **41**, 98–102 (January 1999)

A theory of the generalized conductivity for the normal component of the Hall effect is developed. It is shown that the normal Hall effect coefficient R_0 of microscopically inhomogeneous magnetic alloys $GdZn_xCu_{1-x}$, which at low temperatures consist of ferro-, antiferro-, and paramagnetic phases, can be described satisfactorily on the basis of an effective-medium theory. The experimentally observed relationship between the coefficient $R_0(x)$ and the resistivity $\rho(x)$ is obtained. © *1999 American Institute of Physics.* [S1063-7834(99)02101-2]

In Ref. 1, a scheme for studying the resistivity ρ of multiphase inhomogeneous systems is proposed and used to explain the anomalous behavior of the electrical properties of the alloys $GdZn_xCu_{1-x}$ with ferro-(F), antiferro-(A), and paramagnetic (P) regions. Specifically, the large magnetic component of ρ at $T=4.2$ K ($T \ll [T_c, T_N]$) and $x=0.45$ is attributed in Ref. 1 to the closeness of the system to the percolation threshold. According to Ref. 2, the Hall effect also changes in an unusual manner in the concentration range from the antiferromagnet GdCu ($T_N=142$ K) to the ferromagnet GdZn ($T_C=268$ K). It is natural to expect that the behavior of the galvanomagnetic properties of the alloys $GdZn_xCu_{1-x}$ is likewise determined by the peculiarities of the magnetic state in the transitional range of concentrations and can be described on the basis of an effective-medium theory.

For this reason, in the present work, we extended the theoretical method proposed in Ref. 1 to transport effects in a magnetic field H, and we employed the theoretical results so obtained to explain the experimental data on the normal Hall effect in $GdZn_xCu_{1-x}$.

1. EXTENSION OF THE THEORY TO THE HALL EFFECT

It is well known that the Hall effect in magnets is described by the relation

$$E_y=(R_0H_z+4\pi R_sM_z)J_x, \tag{1}$$

where E_y is the Hall emf, J_x is the current along the OX axis along which an electric field E_x is applied, H_z and M_z are, respectively, the magnetic field and magnetization along the OZ axis, and R_0 and R_s are, respectively, the normal and anomalous Hall coefficients.

In the present paper we confine our attention only to the simpler normal effect, for which R_0 is related mainly to the current-carrier density N, so that, for the simplest case

$$R_0=(Nec)^{-1}. \tag{2}$$

Conversely, R_s is well known to depend strongly on temperature and, according to theory (see, for example, Refs. 3–5) it is proportional to some power of the resistivity ρ^n, where n depends on the mechanism of charge-carrier scattering.

Just as in Ref. 1, we shall assume that the transport properties of the multiphase system under study can be described on the basis of the theory of generalized conductivity. $GdZn_xCu_{1-x}$ is a three-phase system, consisting of F, A, and P phases, the resistivity of one phase (specifically, the P phase) being much higher than that of the other phases — $\rho_P \gg \rho_A$ and ρ_F.[1)] This is not fundamental, but it greatly simplifies the calculations.

In the effective-medium approximation for the isotropic case, to the effective resistivity $\rho^*(x)=[\sigma^*(x)]^{-1}$ can be described by the expression[6]

$$(\rho^*)^{-1}=\frac{1}{4}[(3X_F-1)\sigma_F+(3X_A-1)\sigma_A] + \left\{ \frac{1}{16}[(3X_F-1)\sigma_F+(3X_A-1)\sigma_A]^2 + \frac{1}{4}(2-3X_p)\sigma_A\sigma_F \right\}^{1/2}. \tag{3}$$

Here σ_A and σ_F are the partial conductivities of the A and F phases with relative volumes X_A and X_F, while X_P is the relative volume of the P phase. Expression (3) holds in the limit $\sigma_P=\rho_P^{-1}\to 0$. The phase volumes X_i can be calculated for a random distribution of Zn and Cu ions using binomial coefficients. As follows from Ref. 1, the calculation of $\rho^*(x)$ using Eq. (3) gives good agreement with experiment.

Now, we must obtain an expression similar to Eq. (3) for the Hall coefficient R_0. To derive the expression for R_0 in the effective-medium approximation, two quantities must be averaged simultaneously: σ and R_0. In this case, we obtain two types of relations for the effective coefficient R_0^*:

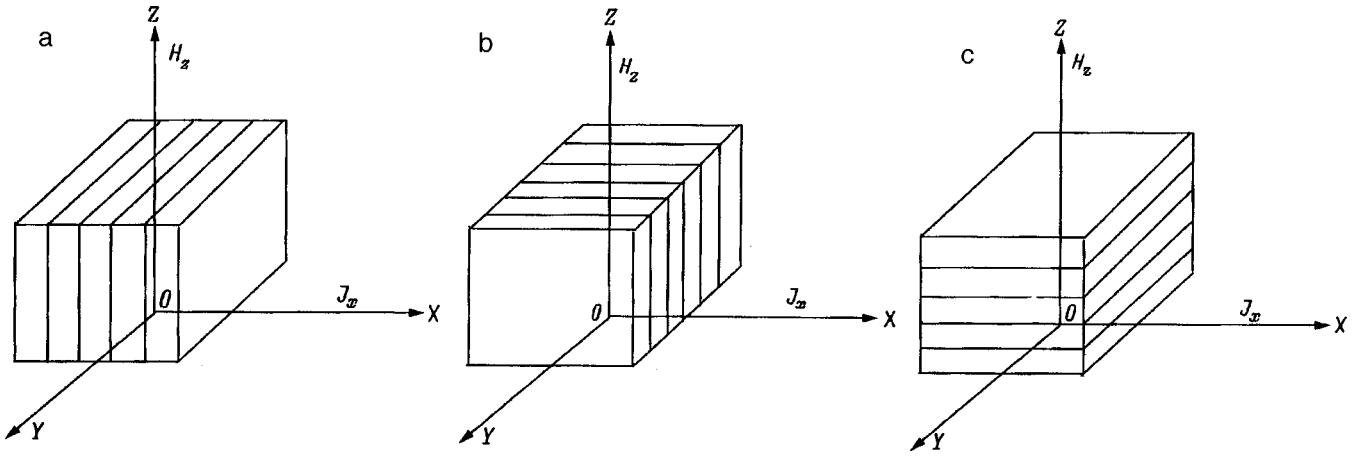

FIG. 1. Arrangement of the layers relative to the fields E_x and H_z.

$$R_0^*(\rho^*)=\rho^*\sum_i X_i R_0^i\sigma_i, \tag{4}$$

$$R_0^*(\rho^*)^2=(\rho^*)^2\sum_i X_i R_0^i(\sigma_i)^2. \tag{5}$$

Here R_0^i and σ_i are the partial values of R_0 and σ for the phases $i=$ F, A, and P, and ρ^* is calculated using Eq. (3).

The difference between the results (4) and (5) is due to the different method of averaging. This situation is well known in the theory of elasticity of microscopically inhomogeneous media, and it can arise when the direct and inverse tensors are averaged (for example, the tensors of the elastic moduli and compliances), which gives different results (see, for example, Ref. 7).

Different relations between R_0 and ρ can also arise as a result of the geometry of the phases (see, for example, Ref. 8, where a similar problem is studied for the particular case of two-phase systems). This situation can be illustrated for a multiphase layered structure with different arrangements of the layers relative to the external electric and magnetic field vectors $E=E_x$ and $H=H_z$, respectively. There are three variants of averaging.

1) The layers are arranged parallel to the YZ plane and perpendicular to the direction of the current $J_x=\sigma E_x$, as shown in Fig. 1a. In this case, J_x will be the same for all layers, and the effective resistivity

$$\rho^*=(\sigma^*)^{-1}=\sum_i \rho_i X_i, \tag{6}$$

$$E_x=\rho^* J_x, \quad \rho^*=\sum_i \rho_i X_i. \tag{7}$$

(The scheme where the resistances ρ_i are connected in series.) An emf

$$E_y^i=R_0^i J_x H_z \tag{8}$$

in the YZ plane will arise in each layer i. Averaging over an area with linear dimensions much larger than the layer thicknesses gives, in the effective-medium approximation, the macroscopic Hall field

$$E_y=\sum_i X_i E_y^i=\sum_i X_i R_0^i J_x H_z=R_0^* J_x H_z,$$

i.e.,

$$R_0^*=\sum_i X_i R_0^i=\overline{R_0}. \tag{9}$$

We note that in this case the effective coefficient R_0^* equals exactly the average value of the normal Hall effect coefficient $\overline{R_0}$.

2) The layers are arranged parallel to the XZ plane and perpendicular to the OY direction, i.e., parallel to the direction of the Hall emf E_y (see Fig. 1b). Here we have resistances ρ_i connected in parallel

$$(\rho^*)^{-1}=\sum_i X_i\rho_i^{-1}. \tag{10}$$

Each layer will give a Hall emf

$$E_y^i=R_0^i J_x^j H_z=R_0^i\sigma_i E_x H_z, \tag{11}$$

and to calculate the average we must average the product $R_0^i\sigma_i$, since now σ_i also depends on the number of layers (in contrast to Eq. (9), where only R_0^i is averaged). In the effective-medium approximation we have

$$E_y=R_0^*\sigma^* E_x H_z=\sum_i R_0^i\sigma_i X_i E_x H_z, \tag{12}$$

whence

$$R_0^*\sigma^*=\sum_i R_0^i\sigma_1 X_i$$

and

$$R_0^*=(\sigma^*)^{-1}\sum_i R_0^i\sigma_i X_i, \tag{13}$$

which gives Eq. (4). Here and below we shall employ an approximation with the substitution $(R_0\sigma)^*=R_0^*\sigma^*$, corresponding to the effective-medium theory.

3) The layers are parallel to the XY plane and perpendicular to the direction H_z, as shown in Fig. 1c. Then the conductivities in the OX direction must be added, kist as in the case 2, according to Eq. (10). Since the field is uniform in the direction of the OX and OY axes, $E_x^i = E_x$ and $E_y^i = E_y$. In the linear approximation in the field H, writing the standard (see, for example, Refs. 3 and 9) expressions for the currents J_x and J_y and taking account of the fact that $J_y = 0$, we obtain

$$J_x^i = \left(\frac{1}{\rho_i}\right) E_x + \left(\frac{R_0^i}{\rho_i^2}\right) H_z E_y, \tag{14}$$

whence averaging over areas in the YZ plane with linear dimensions greater than the layer thicknesses gives

$$J_x = \sum_i X_i J_x^i = \sum_i X_i \left(\frac{1}{\rho_i}\right) E_x + \sum_i X_i \left(\frac{R_0^i}{\rho_i^2}\right) H_z E_y.$$

Writing this expression in the effective-medium approximation

$$J_x = \frac{1}{\rho^*} E_x + \frac{R_0^*}{(\rho^*)^2} H_z E_y,$$

we find

$$\frac{R_0^*}{(\rho^*)^2} = \sum_i \frac{R_0^i X_i}{\rho_i^2}, \tag{15}$$

whence follows Eq. (5).

The derivation of Eqs. (13) and (15) for the particular case of layered structures does not rule out the fact that they can hold approximately in the general case also. Relation (15) can be obtained from the standard expression for the coefficient R_0 in the case of cubic symmetry (see, for example, Refs. 3 and 9)

$$R_0 = -\frac{\sigma_{yx}(H_z)}{\sigma_{xx}\sigma_{yy} - \sigma_{yx}\sigma_{xy}} \frac{1}{H_z}. \tag{16}$$

For $\sigma_{yx} \ll \sigma_{xx} = \sigma_{yy} = \sigma$ we have

$$R_0 = -\frac{\sigma_{yx}}{\sigma^2} \frac{1}{H_z},$$

and in the effective-medium approximation

$$R_0^* = -\left(\frac{\sigma_{yx}}{\sigma^2}\right)^* \frac{1}{H_z} = -\left(\frac{1}{\sigma^*}\right)^2 \sum_i X_i \sigma_{yx}^i \frac{1}{H_z}$$

$$= -\left(\frac{1}{\sigma^*}\right)^2 \sum_i X_i \sigma_i^2 \left(\frac{\sigma_{yx}^i}{\sigma_i^2}\right)\left(\frac{1}{H_z}\right).$$

Here we use the uncoupling $(\sigma_{yx}/\sigma^2)^* = \sigma_{yx}^*/(\sigma^*)^2$. Hence we obtain, using the expression for the Hall coefficient $R_0^i = -(\sigma_{yx}^i/\sigma_i^2)(1/H_z)$ in the i-th phase,

$$R_0^* = (\sigma^*)^{-2} \sum_i X_i R_0^i \sigma_i^2, \tag{17}$$

which is the same as Eq. (5).

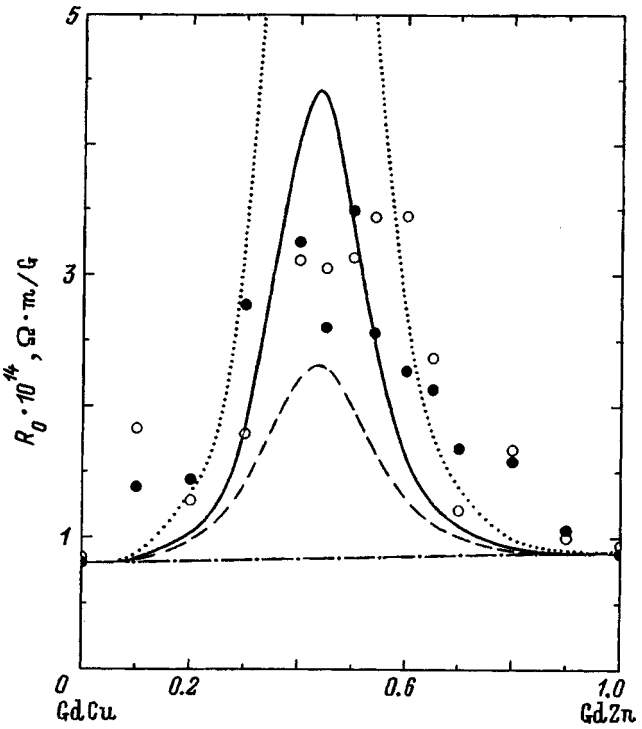

FIG. 2. Measured values of the normal Hall effect coefficient in the alloys $GdZn_xCu_{1-x}$ at temperature $T = 4.2$ K $\ll [T_N, T_c]$ in the region of the paraprocess according to Ref. 2 (filled circles) and from the coefficient in the linear function E_y/H versus M_z/H (open circles). Dashed line — computational results obtained with Eq. (4), dotted line — Eq. (5), dot–dash line — Eq. (9), and solid line — Eq. (18).

Therefore we arrive at a variety of formulas for the effective coefficients R_0^* which correspond to different approximations with uncoupling of the average values from products of the type $\overline{R_0\sigma}$ and $\overline{R_0\sigma^2}$ or which take account of the different geometry of the multiphase layered structure.

2. COMPARISON OF THEORY WITH EXPERIMENT

The concentration dependence of R_0 for the system of alloys $GdZn_xCu_{1-x}$ is displayed in Fig. 2 in the region of the transition between the single-phase F (in GdZn) and A (in GdCu) states at $T = 4.2$ K. One can see that R_0 depends quite strongly and nonmonotonically on the concentration x, reaching a maximum at $x \sim 0.5$ where the F, A, and P phases are present simultaneously. Such a dependence $R_0(x)$ is hard to explain according to Eq. (2), since the carrier density N in the system $GdZn_xCu_{1-x}$ cannot change so anomalously when univalent copper atoms are replaced by divalent zinc atoms, especially since R_0 has approximately the same value at the limits of the range studied: $R_0(x=0) = 0.81 \times 10^{-14}\Omega \cdot$m/G and $R_0(x=1) = 0.88 \times 10^{-14}\Omega \cdot$m/G.

The Hall effect in the system of intermetallides $GdZn_xCu_{1-x}$ was measured by a four-contact dc method. The experimental values of R_0 are presented in Fig. 2 for two types of analysis of the field dependences of the Hall voltage and magnetization. The filled circles show the values of R_0 obtained from the slope of the linear functions $E_y(H)$ and $M_z(H)$ in the region of the paraprocess by the method described in Ref. 2. The open circles are the values of $R_0(x)$

determined, using the expression (1), from the coefficient in the linear function E_y/H versus M_z/H. One can see from Fig. 2 that these two methods for analyzing the Hall effect and magnetization measurements give close values for R_0, even though the variance in the experimental data as a function of the concentration x is quite large.

Comparing the data presented in Fig. 2 and in Ref. 2 shows that the overall form of the experimental function $R_0(x)$ is the same as that of the curve $\rho(x)$. Therefore it is natural to attempt to explain the dependence $R_0(x)$ on the basis of the ideas presented above concerning the Hall effect in microscopically inhomogeneous media. Since there are no data on the geometry of the texture of the phases in the system $GdZn_xCu_{1-x}$, we perfomed calculations of $R_0(x)$ using different variants of the corresponding relations (4), (5), and (9) as well as a combination of these equations with the coefficients 1/3. The latter corresponds to equally probable evaluation of different methods of uncoupling (9), (13), and (17) or else the different geometry of the layers, as shown in Fig. 1,

$$R_0^*=\frac{1}{3}[\ \overline{R_0}+R_0^*(\rho^*)+R_0^*(\rho^{*2})]. \tag{18}$$

The computational results, together with the experimental data, are presented in Fig. 2.

It follows from Fig. 2 that (4), (5), and (9) do not agree with experiment for the concentration dependence of the coefficient R_0. At the same time, their combination (18) with the same statistical weights 1/3 agrees quite satisfactorily with experiment. Both the experimentally obtained dependence $R_0(x)$ and the theoretical curve $R_0^*(x)$ have maxima at $x=0.45$. However, it remains unclear whether the satisfactory description of the Hall effect in the alloys under study is due to the existence of a microscopically anisotropic texture with clusters forming a layered structure for which (as indicated above) there are three possible variants for arranging the layers relative to the current vector **J**, the Hall emf vector **E**, and the magnetic field vector **H** in the Hall effect geometry or whether the reason lies in the different variants of the effective-medium theory for a completely isotropic material and is due to different approximations for uncoupling the average values $\overline{R_0\sigma}$ and $\overline{R_0\sigma^2}$, characteristic for the theory of the Hall effect.

In this respect it is of interest to measure the coefficient R_0 in samples subjected to rolling or some other deformation that could produce a uniaxial anisotropy of microscopic inhomogeneities (or intensify the anisotropy as compared to the initial state). Further investigation of the theoretical aspect of this question is also of interest, i.e., clarifying the conditions under which the effective-medium theory is valid for the case when several physical quantities are averaged, including quantities which are not completely independent (in our case, R_0 and σ).

Physically, the maximum of $R_0(x)$ at $x=0.45$, just as for the resistivity $\rho(x)$, is due to the closeness of the system to the percolation threshold, which, according to Eq. (3), occurs at $X_p=\frac{2}{3}$. For R_0^*, averaging according to Eq. (18), this maximum is substantially smaller than for the case (5) and, conversely, it is larger than that obtained according to Eq. (4). Moreover, the maximum values of R_0^* using Eq. (18) are much larger than the values that can be obtained by standard averaging of the type (9), which gives for $R_0^*(x)$ a straight line without any maximum. We also note that the largest deviation of the theoretical dependence (18) from the experimental curve for the normal Hall effect is observed in the same concentration ranges as in the description of the resistivity of $GdZn_xCu_{1-x}$ alloys according to expression (3). This deviation could be due to the inaccuracy of the theoretical description of ρ^* for $\sigma_P\sim(\sigma_A$ and $\sigma_F)$ [Eq. (3) holds in the limit $\sigma_P=0$] or the fact that the layered structures and the real geometry of the phases do not correspond to the situation studied theoretically.

The method considered above for describing the Hall effect is based on the assumptions that the fields or fluxes are uniform in the microscopically inhomogeneous medium. A further refinement can be made by taking into account more accurately the effects due to the depolarization of the macroscopic field by individual phases by analogy with the methods used in the effective-medium theory.[6] However, even the simple method proposed in the present paper for describing the normal component of the Hall effect in microscopically inhomogeneous magnetic alloys makes it possible to understand the quite unusual interrelation, obtained experimentally in previous work,[2] between the coefficient $R_0(x)$ and the resistivity $\rho(x)$.

We thank V. V. Nikolaev for a helpful discussion.

*E-Mail: lowtemp@ifm.e-burg.su

[1)]We used the term paramagnetic P phase conditionally. Ordinarily, it is assumed that a spin-glass state occurs, together with A and F phases, in the transitional region in $GdZn_xCu_{1-x}$ alloys. This difference could be important for describing magnetic properties, but it appears to us that it should not strongly influence the scattering processes in transport effects. In this case, only the degree of spin disorder is important.

[1] Yu. P. Irkhin, Fiz. Tverd. Tela (St. Petersburg) **40**, 974 (1998) [Phys. Solid State **40**, 891 (1998)].
[2] N. I. Kourov, Fiz. Nizk. Temp. **16**, 749 (1990) [Sov. J. Low Temp. Phys. **16**, 441 (1990)].
[3] C. V. Hurd, *The Hall Effect in Metals and Alloys*, Plenum Press, New York (1972), 400 pp.
[4] Yu. P. Irkhin and V. G. Shavrov, Zh. Éksp. Teor. Fiz. **42**, 1233 (1962) [Sov. Phys. JETP **15**, 854 (1962)].
[5] Yu. P. Irkhin and Sh. Sh. Abel'skiĭ, Fiz. Tverd. Tela (Leningrad) **6**, 1635 (1964) [Sov. Phys. Solid State **6**, 1283 (1964)].
[6] E. A. Matyushov, P. V. Gel'd, and G. A. Adamesku, *Generalized Conductivity and Elasticity of Microscopically Inhomogeneous Heterogeneous Materials*, Metallurgiya, Moscow (1992), 144 pp.
[7] T. D. Shermergor, *Theory of Elasticity of Microscopically Inhomogeneous Media*, Nauka, Moscow (1977), 246 pp.
[8] G. N. Dul'nev and V. V. Novikov, *Transport Processes in Inhomogeneous Media*, Énergoatomizdat, Leningrad (1991), 246 pp.
[9] Yu. P. Irkhin and V. Yu.Irkhin, *Electronic Structure and Physical Properties of Transition Metals*, Ural State University Press, Sverdlovsk (1989), 115 pp.

Translated by M. E. Alferieff

Ferro- and antiferromagnetic ordering in $LaMnO_{3+\delta}$

A. N. Pirogov, A. E. Teplykh, V. I. Voronin, A. E. Kar'kin

Institute of Metal Physics, Ural Branch of the Russian Academy of Sciences, 620219 Ekaterinburg, Russia

A. M. Balagurov, V. Yu. Pomyakushin, V. V. Sikolenko

Joint Institute for Nuclear Research, 141980 Dubna, Russia

A. N. Petrov, V. A. Cherepanov, and E. A. Filonova

Ural State University, 620083 Ekaterinburg, Russia

(Submitted June 17, 1998)
Fiz. Tverd. Tela (St. Petersburg) **41**, 103–109 (January 1999)

A neutron diffraction study of the crystalline structure and magnetic state of $LaMnO_{3+\delta}$ samples with different deviations from oxygen stoichiometry has been made at 4.2 K. It is shown that annealing at reduced oxygen pressure is accompanied by transformation of the magnetic structure from ferromagnetic, with magnetic moments parallel to the *b* axis, to antiferromagnetic, with the wave vector $\mathbf{k}=0$ and the moments along the *a* axis (space group *Pnma*). A comparison of experimental with expected Mn ion moments suggests that magnetic order does not extend throughout the sample volume. Part of the Mn ions form magnetic clusters ~20 Å in size. © *1999 American Institute of Physics.* [S1063-7834(99)02201-7]

1. Investigation of the magnetic structure and properties of the lanthanum manganite $LaMnO_{3+\delta}$ was started in the 1950s.[1–4] The discovery of giant magnetoresistance in $La_{1-x}B_xMnO_{3+\delta}$ (B=Ca, Sr, Ba) has stimulated recently intense studies of the $LaMnO_{3+\delta}$ manganite.[5–7]

The off-stoichiometric manganite $LaMnO_{3+\delta}$ has vacancies on the cation sublattice and manganese ions with mixed $(+3, +4$, and, possibly, $+2)$ valence.[8] The vacancy concentration, the content of the Mn^{3+}, Mn^{4+}, and Mn^{2+} ions and, accordingly, the oxygen off-stoichiometry index δ are determined by external thermodynamic conditions. Manganites with $\delta>0$ are synthesized at relatively low temperatures and atmospheric pressure, while $\delta<0$ samples require high temperature (low oxygen pressure) for their preparation.

When studying the structural state and magnetic properties of $LaMnO_{3+\delta}$, one usually considers their dependence on Mn^{4+} content. If the content of Mn^{4+} ions exceeds 14%, structures with cubic, rhombohedral, or orthorhombic symmetry are obtained.[6] These structures are characterized by ferromagnetic ordering of Mn ion spins.[4] The data on the ferromagnetic state of the $LaMnO_{3+\delta}$ manganite were derived primarily from magnetic measurements. No neutron diffraction information on the orientation and magnitude of the magnetic moment of the Mn ion is available.

A lowering of the Mn^{4+} concentration in $LaMnO_{3+\delta}$ is accompanied by a decrease in magnetization and the onset of antiferromagnetic ordering. Within the 10–14% concentration interval, one observes simultaneously a ferromagnetic and an antiferromagnetic magnetic-moment component. Some authors[3,9] believe this to indicate the existence of a noncollinear magnetic structure, while others[2,4] draw a conclusion of the presence in the sample of two (ferro- and antiferromagnetic) phases.

For Mn^{4+} concentrations below 10%, an *A*-type antiferromagnetic order sets in.[3,7] There are reports[2,8] of antiferromagnetic $LaMnO_{3+\delta}$ compositions having monoclinic structure; at the same time Refs. 3, 7, and 10 suggest that the antiferromagnetic state is observed in orthorhombic manganite. While the diffraction patterns obtained in Ref. 8 were reported to be similar to those measured in another study[10], the conclusions drawn in these two investigations on the symmetry of the manganite structure are essentially different. There is still no consensus on the wave vector **k** of the antiferromagnetic structure in $LaMnO_{3+\delta}$; indeed, the opinions vary between $\mathbf{k}=[000]$ (Ref. 7) and $\mathbf{k}=2\pi/b[010]$ (Ref. 9).

The present work reports a neutron diffraction study of the crystal and magnetic structure of the $LaMnO_{3+\delta}$ manganite samples having different oxygen off-stoichiometries.

2. The starting compounds were the oxides La_2O_3 (99.99%) and Mn_2O_3 (ChDA grade) calcined preliminarily in air at 1373 and 1023 K, respectively. Samples *A* and *B* were synthesized in air within the 1123–1373 K interval in several stages, each followed by a thorough grinding. In the last stage of preparation (1373 K), the sample was annealed for 100 h and quenched. The $LaMnO_{3+\delta}$ powder was pressed into pellets, which were annealed in air for 4 h at 1573 K, with subsequent slow cooling to 973 K (*A* sample) and to 1023 K (*B* sample) and quenching. Sample *C* was obtained by annealing the *A* sample for 6 h at 1373 K in argon containing 310 Pa oxygen, with subsequent quenching in this environment.

Neutron diffraction measurements were carried out on D-3A (IWW-2M reactor, Zarechny) and FDWR (IBR-2 reactor, Dubna) diffractometers. The neutron diffraction patterns were processed using the FULLPROF code[11]. The symmetry analysis was performed with the MODY-2 code[12].

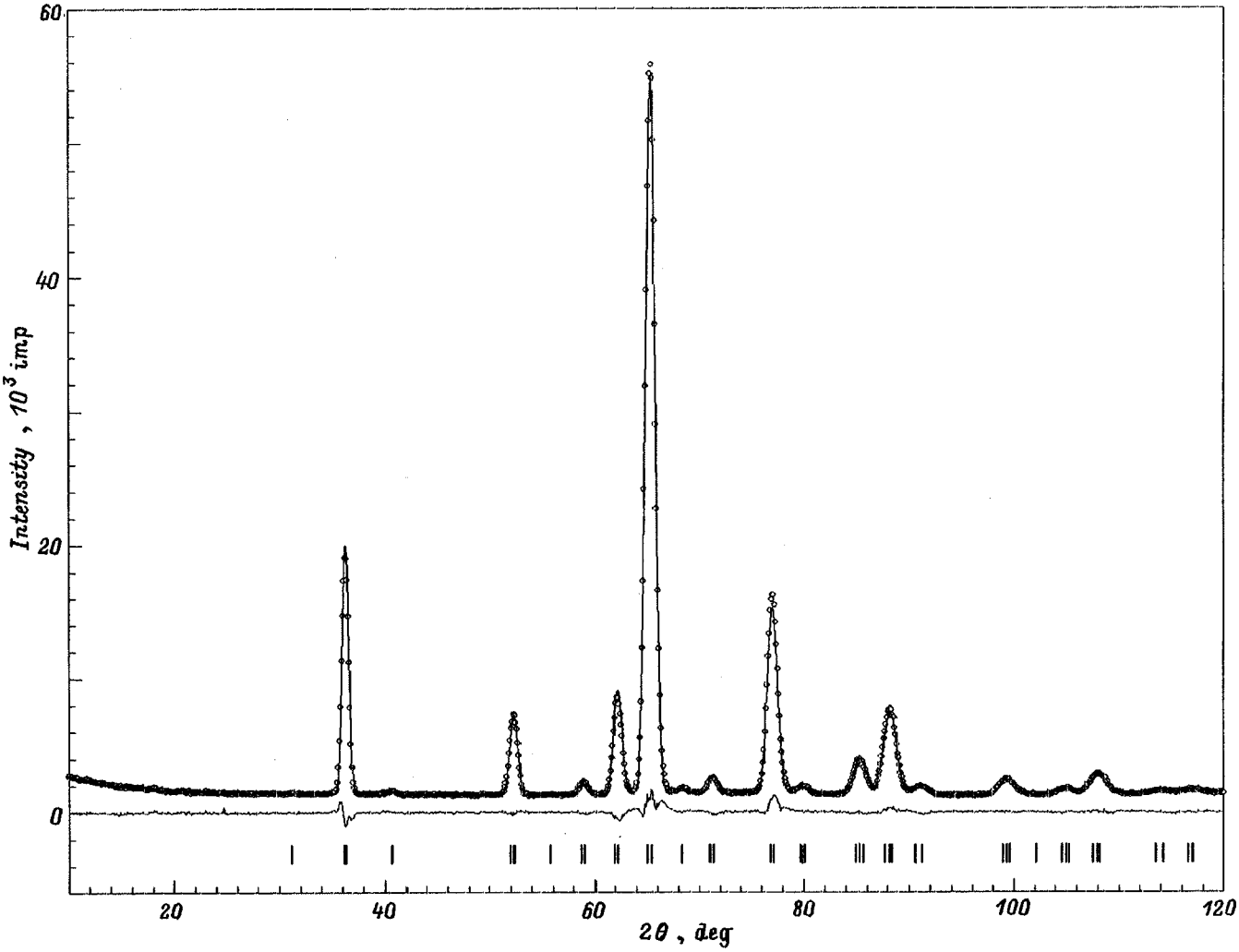

FIG. 1. Neutron diffraction pattern of sample *A* obtained at 4.2 K. Points — experiment, curve — calculation, shown below is the difference; vertical lines identify the angular positions of the reflections.

The magnetic ordering temperatures for samples *A* and *B* were derived from ac susceptibility data.

3. Figures 1–3 present neutron diffraction patterns obtained at 4.2 K for samples *A*, *B*, and *C* on the D-3A diffractometer. An analysis of the patterns showed sample *A* to have an orthorhombic lattice with parameters $a=5.474(1)$, $b=7.746(1)$, and $c=5.515(1)$ Å (space group $Pnma$). Because the nuclear and magnetic reflections coincided in angular position, the magnetic structure vector $\mathbf{k}=0$. Possible types of magnetic ordering with $\mathbf{k}=0$ in $LaMnO_{3+\delta}$ were studied by symmetry analysis of the magnetic structures.

Manganese ions occupy only one site, 4a, in the orthorhombic lattice. The $\mathbf{k}=0$ magnetic representation for this site can be written[13]

$$d_M=3\tau_1+3\tau_3+3\tau_5+3\tau_7,$$

where $\tau_1,\ldots,\tau_7$ are the irreducible representations of the $Pnma$ group.

Table I lists the basis functions of the irreducible representations (in the notation of International Tables for Crystallography) contained in the magnetic representation. One readily sees that the magnetic structures described by one irreducible representation are either collinear ferromagnets with one sublattice or two-sublattice collinear antiferromagnets with the spins oriented along one of the crystallographic axes. By properly mixing several representations, one can obtain noncollinear magnets and structures with spins canted at an angle to the crystal axes. Neutron diffraction patterns were calculated for different versions of mixing of irreducible representations and compared with the experimental pattern. The best agreement for the *A* sample ($R_{\mathrm{mag}}=2.8\%$) between the experimental and calculated patterns was obtained using the τ_3 representation. The magnetic structure of interest is a collinear ferromagnet with the moments aligned with the *b* axis. The magnetic moment μ_F of the Mn ion was found to be 3.4(1) μ_B. The coordinate parameters and site occupation numbers are listed in Table II. The Curie temperature of sample *A* is $T_c=142\pm5$ K.

The neutron diffraction pattern of sample *B* (Fig. 2) is basically similar to that discussed above, but it exhibits also at 4.2 K an additional reflection at $2\theta\approx17.7°$. As follows from its treatment, the magnetic and crystallochemical cells coincide, hence, vector $\mathbf{k}=0$. The parameters of the orthorhombic lattice of sample *B* are close to the ones obtained by us for sample *A*: $a=5.479(1)$, $b=7.764(1)$, and *c*

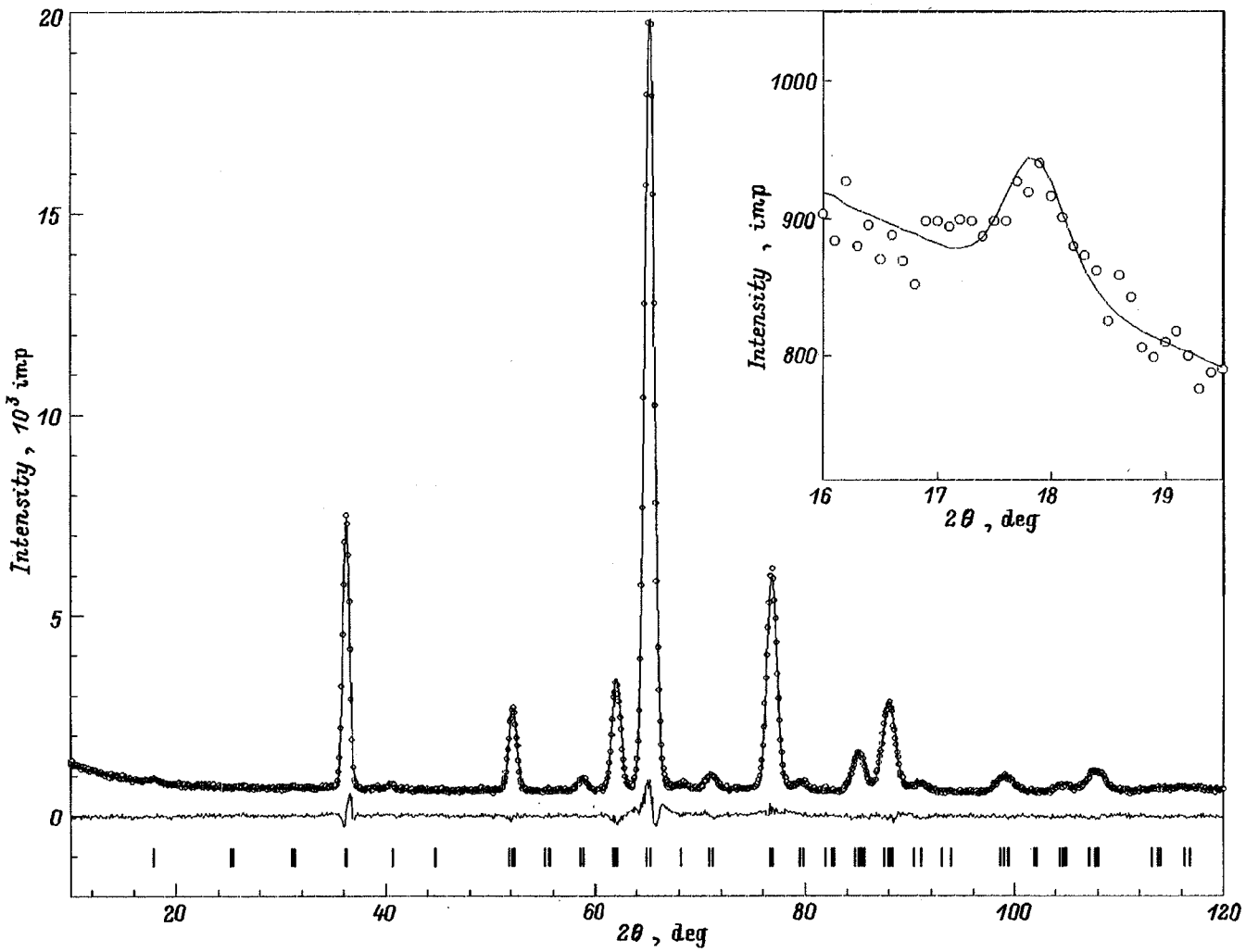

FIG. 2. Neutron diffraction pattern of sample *B* obtained at 4.2 K. Notation same as in Fig. 1. The inset shows a portion of the neutron diffractogram with the (010) reflection.

$=5.527(1)$ Å. A comparison of the experimental pattern with the ones calculated for different versions of mixing of irreducible representations from Table I shows the best fit for the R_{mag} factor (4.3%) to be obtained in the following conditions. The magnetic structure is described by a superposition of repeating representations $\tau_3+\tau_3'$. Representation τ_3' corresponds to antiferromagnetic ordering along the *a* axis, and τ_3, to ferromagnetic ordering along the *b* axis. The antiferromagnetic component of the moment $\mu_{AF}=0.35(5)\,\mu_B$, and the ferromagnetic component, $\mu_F=3.2(1)\,\mu_B$. The magnetic order breaks down at 130 ± 5 K.

Sample *C* has a more complex neutron diffraction pattern (Fig. 3) than samples *A* and *B*. Besides, some of its diffraction lines are not split, which complicates unambiguous establishment of the structure symmetry and of the vector **k**. Therefore we carried out measurements on sample *C* in an instrument having a high resolution (FDWR). The neutron diffraction patterns obtained at 10 and 300 K are displayed in Fig. 4. An analysis of the diffractogram taken at 300 K shows that all of its diffraction lines can be indexed on an orthorhombic unit cell. At 10 K, the sample has an orthorhombic crystallochemical cell and a magnetic one of the same size. The lattice parameters of sample *C* are as follows: $a=5.669(1)$, $b=7.671(1)$, and $c=5.523(1)$ Å. The magnetic structure vector $\mathbf{k}=0$. The minimum value of the R_{mag} of 3.5% can be reached by describing the magnetic ordering both by one representation τ_3' and by a sum $\tau_3+\tau_3'$. The magnetic-moment components are $\mu_{AF}=3.4(1)\,\mu_B$ and $\mu_F=0.2(2)\,\mu_B$. Therefore one can maintain within experimental error that the magnetic structure of the sample under study is a collinear antiferromagnet with moments oriented along the *a* axis and $\mu_{AF}=3.4(1)\,\mu_B$.

Measurements of the peak intensity $I_{(010)}$ of the (010) magnetic reflection were performed to determine the Néel temperature of sample *C*. The temperature dependence of $I_{(010)}$ obtained is presented in the inset to Fig. 1. The reflection is seen to disappear at $T_N=135\pm5$ K.

4. The structural parameters obtained by us for the three $LaMnO_{3+\delta}$ samples (Table II) agree satisfactorily with literature data[3,5,7]. Using the occupation numbers *n* given in Table II, one can estimate the Mn^{4+} concentration and the off-stoichiometry index δ in the samples studied in this work. The La sublattice is not fully occupied in samples *A* and *B*, $n=0.96$. Hence the content of Mn^{4+} ions is $12\pm3\%$, and $\delta=0.06\pm0.01$. Taking into account the difference in magnetic ordering between samples *A* and *B*, one may con-

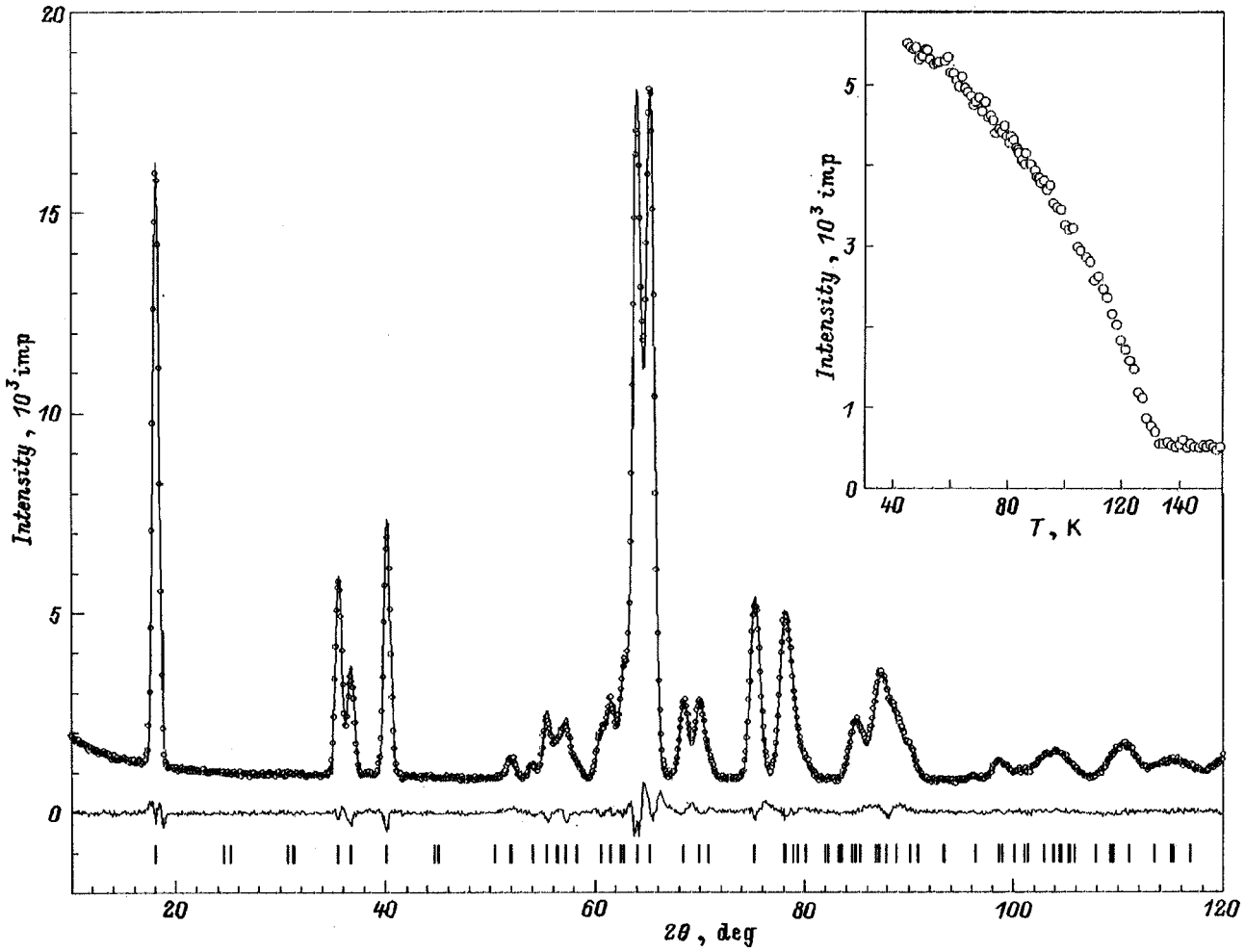

FIG. 3. Neutron diffraction pattern of sample *C* obtained at 4.2 K. Notation same as in Fig. 1. The inset shows the temperature dependence of the peak intensity of the (010) reflection.

clude that the transition from ferromagnetic state to a state with the moment having both ferro- and antiferromagnetic components occurs in $LaMnO_{3+\delta}$ at the Mn^{4+} concentration of $12\pm3\%$. This agrees within experimental error with the magnetic phase diagram of $LaMnO_{3+\delta}$ constructed in Ref. 4, where the Mn^{4+} concentration was determined by chemical analysis.

In sample *C*, the La and O2 sublattices are not fully occupied ($n=0.99$ and 1.99, respectively). It thus follows that the *C* sample contains $1\pm3\%$ Mn^{4+} ions, with $\delta=0.005\pm0.010$. A comparison of these figures with the corresponding values obtained for the *A* sample indicates a decrease in Mn^{4+} concentration and in the off-stoichiometry

TABLE I. Basis functions of the $\mathbf{k}=0$ magnetic representation for the 4*a* site of space group *Pnma*.

	Atoms											
Representation	(0,	0,	0)	(0,	1/2,	0)	(1/2,	1/2,	1/2)	(1/2,	0,	1/2)
τ_1	0	1	0	0	1	0	0	−1	0	0	−1	0
τ_1'	1	0	0	−1	0	0	1	0	0	−1	0	0
τ_1''	0	0	1	0	0	−1	0	0	−1	0	0	1
τ_3	0	1	0	0	1	0	0	1	0	0	1	0
τ_3'	1	0	0	−1	0	0	−1	0	0	1	0	0
τ_3''	0	0	1	0	0	−1	0	0	1	0	0	−1
τ_5	0	1	0	0	−1	0	0	−1	0	0	1	0
τ_5'	1	0	0	1	0	0	1	0	0	1	0	0
τ_5''	0	0	1	0	0	1	0	0	−1	0	0	−1
τ_7	0	1	0	0	−1	0	0	1	0	0	−1	0
τ_7'	1	0	0	1	0	0	−1	0	0	−1	0	0
τ_7''	0	0	1	0	0	1	0	0	1	0	0	1

TABLE II. Structural parameters of $LaMnO_{3+\delta}$ samples at 4.2 K and quality of fit between experimental and calculated nuclear (R_N) and magnetic (R_{mag}) neutron-diffraction patterns.

Atom		Sample A	Sample B	Sample C
La	x	0.021(1)	0.018(1)	0.0455(5)
	z	0.495(1)	0.497(1)	0.4926(5)
	n	0.96(1)	0.96(1)	0.99(2)
O1	x	0.488(1)	0.489(1)	0.4903(6)
	z	0.566(1)	0.565(2)	0.5713(7)
	n	1.0	1.0	1.0
O2	x	0.277(1)	0.275(1)	0.3010(4)
	y	0.0362(7)	0.0358(7)	0.0386(3)
	z	0.230(1)	0.233(1)	0.2248(5)
	n	2.0	2.0	1.99(5)
R_N,%		6.2	6.6	3.4
R_{mag}%		2.8	4.3	3.5

index δ as a result of sample annealing at a reduced oxygen pressure.

The annealing entailed also transformation of the ferromagnetic into antiferromagnetic structure. Several reasons account for this transformation. In $LaMnO_{3+\delta}$, one considers usually three types of exchange interactions. The strongest is the $Mn^{4+}-Mn^{3+}$ interaction. It involves double electron exchange between the Mn^{3+} and Mn^{4+} ions and is responsible for the ferromagnetic ordering of their spins.[4] The $Mn^{3+}-Mn^{4+}$ interaction can be both ferro- and antiferromagnetic. Ferromagnetic interaction involves the p_σ orbitals of oxygen ions and the e_g orbitals of manganese ions, and the antiferromagnetic one, the p_π and t_{2g} orbitals. It is believed[5] that ferromagnetic exchange becomes weaker with a decrease of such parameters as the Mn–O–Mn bond angle φ, the e_g-p_σ covalent-mixing coefficient, and so on. Our data also indicate that the φ angle is larger in ferromagnetic state ($\varphi=158°$) than in the antiferromagnetic one ($\varphi=156°$). The e_g-p_σ mixing coefficient was shown[5] to decrease with decreasing off-stoichiometry index δ. Thus the transformation of the ferromagnetic structure (sample *A*)

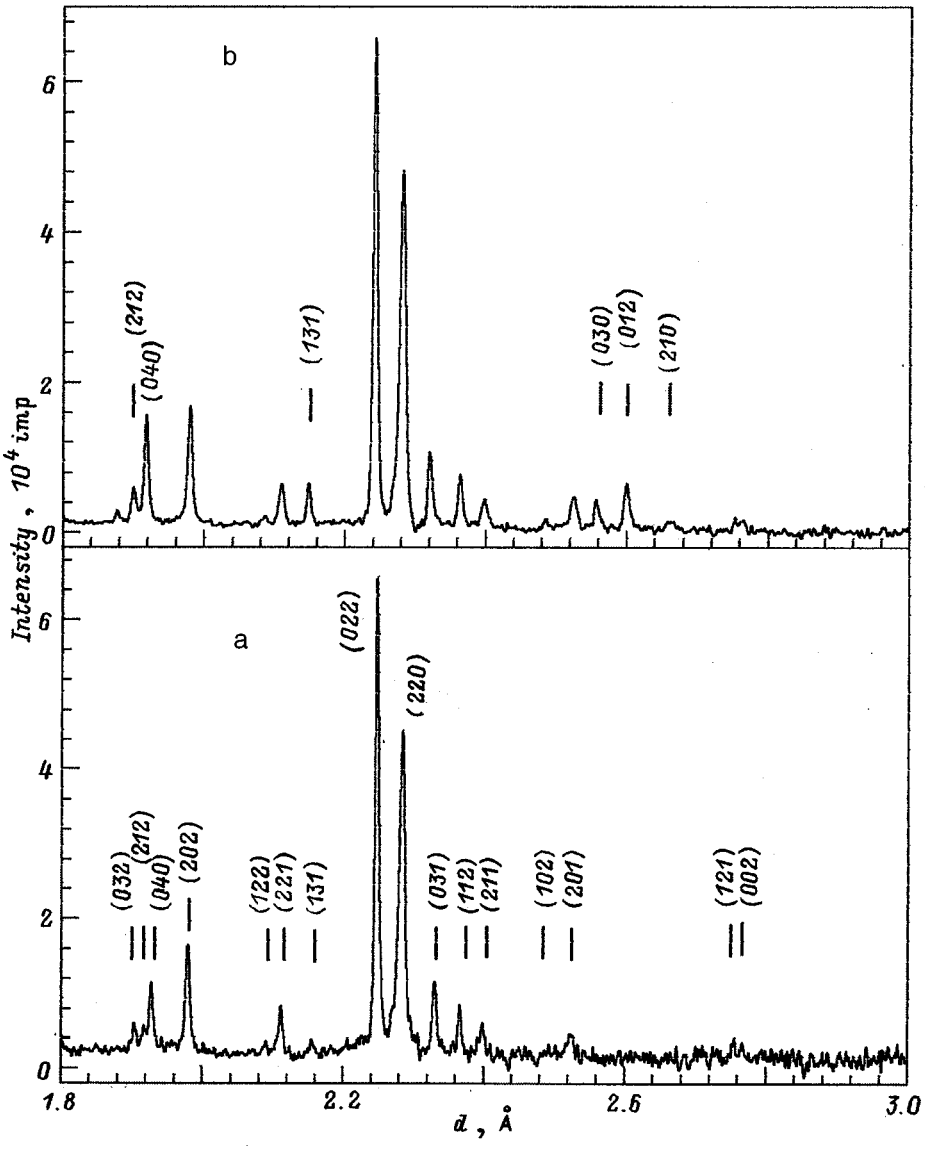

FIG. 4. Neutron diffraction patterns of sample *C* obtained at (a) 300 K and (b) 4.2 K. Given in parentheses are the indices of (a) nuclear and (b) magnetic reflections.

into antiferromagnetic (sample *C*) is due to the fact that the contributions of the ferromagnetic $Mn^{3+}-Mn^{3+}$ and $Mn^{3+}-Mn^{4+}$ interactions decrease making the antiferromagnetic $Mn^{3+}-Mn^{3+}$ exchange dominant.

Our neutron diffraction data on the magnetic structure of the *B* sample allow twofold interpretation. One may consider the magnetic structure as noncollinear with μ_F and μ_{AF} components of the moments, i.e. as a canted antiferromagnet.[8] The other possibility is that this is a two-phase (ferro- and antiferromagnetic) state. We believe that an unambiguous conclusion can be made by taking into account the results of the symmetry analysis of the magnetic structures in sample *B*. The repeating representations τ_3 and τ_3' describing its magnetic state belong to one irreducible representation τ_3 and, hence, they correspond to one exchange multiplet. Thus the ground state of the magnet can be identified with a structure with moments having a τ_3-ferromagnetic and a τ_3'-antiferromagnetic component. One can therefore conclude that the *B* sample has a noncollinear magnetic structure. It accounts for the symmetry relation observed to occur as the ferromagnetic structure transforms to the antiferromagnetic one.

In the $LaMnO_{3+\delta}$ samples studied here, the average magnetic moment of the Mn ion was $\sim 3.4\,\mu_B$. The same average moment was obtained for $LaMnO_{3.13}$.[14] Based on the local moments of the Mn^{4+} and Mn^{3+} ions and their concentration in the samples, one could expect an average moment of 3.9–4.0 μ_B. The value of 3.9 μ_B was obtained experimentally, for example, in Ref. 7. In our case not all Mn ions seem to take part in formation of long-range magnetic order. Following Refs. 4 and 5, one may conjecture that part of Mn ions in ferromagnetic $LaMnO_{3+\delta}$ form magnetic clusters. The cluster formation can be initiated by localization of Mn^{4+} ions at cation vacancies and by $Mn^{4+}-Mn^{3+}$ interaction via the double exchange. Because the concentration of vacancies and, hence, of clusters is not high, the latter do not interact with one another, and double exchange is operative primarily in clusters. Long-range magnetic order in the host lattice is supported predominantly by the $Mn^{3+}-Mn^{3+}$ exchange coupling, which is weaker than the $Mn^{4+}-Mn^{3+}$ interaction. As the temperature increases, the long-range order in the matrix will fail earlier than the short-range one in the clusters. This accounts for the anomaly near T_c in the temperature dependence of magnetization measured in weak fields.[4] We observed such an anomaly in ac susceptibility. As seen from Fig. 5, sample *B* exhibits two magnetic-disordering temperatures. This becomes still more pronounced if the Mn^{4+} concentration is increased by partial substitution of barium for lanthanum.

The size of the clusters can be estimated from the dependence[15] of the cluster magnetic moment on vacancy concentration on the La sublattice. For a concentration of 0.04 (*A* and *B* samples) the cluster size is ~ 20 Å.

The results obtained earlier and in this work can be summarized as follows:

The orthorhombic manganite $LaMnO_{3+\delta}$ can have ferromagnetic, antiferromagnetic, or noncollinear structure with wave vector $\mathbf{k}=0$, depending on composition.

Long-range magnetic order in $LaMnO_{3+\delta}$ is primarily due to $Mn^{3+}-Mn^{3+}$ exchange interaction. Double exchange among the Mn^{4+} and Mn^{3+} ions can initiate nucleation of ferromagnetic clusters ~ 20 Å in size. The presence of clusters accounts for the lowering of the average magnetic moment of Mn ions.

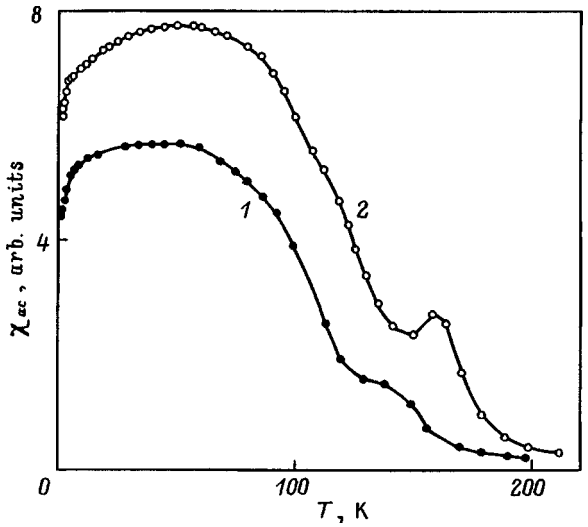

FIG. 5. Temperature dependence of the ac susceptibility of (*1*) sample *B* and (*2*) $La_{0.95}Ba_{0.05}MnO_3$.

The authors owe sincere thanks to Prof. V. E. Naish for fruitful discussions and valuable comments.

Support of the Russian Fund for Fundamental Research (Grants 97-02-17315 and 97-03-33632) and of the State Research & Development Program ''Neutron Studies'' (Grants 96/104 and 96/305) is gratefully acknowledged.

[1] G. H. Jonker and J. H. van Santen, Physica **16**, 337 (1950).
[2] E. O. Wollan and W. C. Köhler, Phys. Rev. **100**, 545 (1955).
[3] J. B. A. A. Elemans, B. van Laar, K. R. van den Veen, and B. O. Loopstra, J. Solid State Chem. **3**, 238 (1971).
[4] V. I. Pavlov, A. K. Bogush, and L. V. Balyko, Cryst. Res. Technol. **19**, 237 (1984).
[5] J. Topfer and J. B. Goodenough, Chem. Mater. **9**, 6 (1997).
[6] R. Mahendiran, S. K. Tiwary, A. K. Raychaudhuri, T. V. Ramakrishnan, R. Mahesh, N. Rangavittal, and C. N. R. Rao, Phys. Rev. B **53**, 3348 (1996).
[7] F. Moussa, M. Hennion, J. Rodríguez-Carvajal, H. Moudden, L. Pinsard, and A. Revcolevschi, Phys. Rev. B **54**, 15149 (1996).
[8] H. Kawano, R. Kajimoto, M. Kubota, and H. Yoshizawa, Phys. Rev. B **53**, 2202 (1996).
[9] J. P. Mitchel, D. N. Argyriou, C. D. Potter, D. G. Hinks, J. D. Jorgensen, and S. D. Bader, Phys. Rev. B **54**, 6172 (1996).
[10] Y. Takeda, S. Nakai, R. Kanno, N. Imanishi, Q. Shen, and O. Yamamoto, Mater. Res. Bull. **26**, 153 (1991).
[11] J. Rodríguez-Carvajal, Physica B **192**, 55 (1993).
[12] P. Czapnik and W. Sikora, Programm Mody 2-74, IFIT J AGH Kracow (1992).
[13] Yu. A. Izyumov, V. E. Naish, and R. P. Ozerov, *Neutron Diffraction in Magnets* [in Russian] (Atomizdat, Moscow, 1981), 311 pp.
[14] I. O. Troyanchuk, H. Szymczak, N. V. Kasper, and A. Nabialek, J. Solid State Chem. **130**, 171 (1997).
[15] J. Z. Sun, L. Krusin-Elbaum, A. Gupta, G. Xiao, and S. S. P. Parkin, Appl. Phys. Lett. **69**, 1002 (1996).

Translated by G. Skrebtsov

Magneto-optical phenomena in $MnAs/CaF_2/Si(111)$ epitaxial films in a transverse magnetic field

A. G. Banshchikov, A. V. Kimel', B. B. Krichevtsov, A. A. Rzhevskiĭ, N. S. Sokolov, and O. A. Yakubtsov

A. F. Ioffe Physicotechnical Institute, Russian Academy of Sciences, 194021 St. Petersburg, Russia
(Submitted June 25, 1998)
Fiz. Tverd. Tela (St. Petersburg) **41**, 110–115 (January 1999)

Field and angular dependences of the rotation of the plane of polarization in a transverse magnetic field $\mathbf{H}\perp\mathbf{k}$ under normal reflection of light ($\lambda=633$ nm) have been studied in MnAs ferromagnetic epitaxial films grown by MBE on $CaF_2/Si(111)$ substrates. The angle of rotation of the plane of polarization α is shown to be determined by contributions even and odd in the magnetization **M**. The odd contribution is associated with the deviation of the easy plane of magnetic anisotropy from the film plane, which originates from misorientation of the Si surface from the (111) plane, or from a presence of small regions of (1011)-oriented MnAs. The even contribution is due to the optical anisotropy of films connected with quadratic-in-**M** terms in the dielectric permittivity tensor ε_{ij} of manganese arsenide. A method based on measuring the angular dependences of α in a rotating magnetic field is proposed to separate these contributions. [S1063-7834(99)02301-1]

Ferromagnet-semiconductor heterostructures recently have become an object of intensive studies.[1–6] The interest in these structures stems primarily from their possible use in hybrid integrated electronic, optic, and magneto-optic devices, which combine the semiconducting and magnetic properties of such systems.[1] MnAs ferromagnetic epitaxial films grown on semiconducting silicon, Si, or gallium arsenide, GaAs, are promising materials for development of ferromagnet-semiconductor–type heterostructures. The coercive fields of MnAs/Si(001) and MnAs/GaAs(001) heterostructures were studied with a vibrating-sample magnetometer, as well as magneto-optically, using the field dependences of the polar Kerr effect.[2–6] It should be pointed out that magneto-optic methods are widely employed in determining the magnetic parameters of crystals and films,[7] and they have certain advantages over magnetic techniques. Among them is high sensitivity, which permits one to investigate the magnetic properties of thin-film structures consisting of several monolayers of a magnetic material, as well as the possibility of locally probing a film. If the absorption coefficient is high enough, magneto-optic methods can provide information on the magnetic properties of near-surface layers.[8,9]

As far as we know, in MnAs films only the polar Kerr effect in a longitudinal magnetic field has been studied so far. At the same time, investigation of magneto-optic phenomena in transverse magnetic fields can permit one to determine the type of magnetic anisotropy and such parameters as the orientation of the easy plane or easy axis of magnetic anisotropy and the corresponding anisotropy fields.[7] Besides, such studies offer a possibility of finding the parameters of magneto-optic effects quadratic in magnetization **M**. This information may prove to be useful both for a deeper understanding of the magnetic properties and structure of epitaxial films and their growth, and for probing the electronic band structure of MnAs.

The object of this work was to investigate the magneto-optic phenomena observed in a transverse magnetic field in reflection of light from MnAs epitaxial films grown on $CaF_2/Si(111)$.

1. EXPERIMENTAL METHOD

The experimental arrangement used in the studies of magneto-optic phenomena in $MnAsCaF_2/Si(111)$ films is shown in Fig. 1. Light from a He–Ne laser ($\lambda=633$ nm, power ~ 3 mW) passed through a polarizer, a polarization modulator based on the Faraday effect, and impinged on the sample placed in the pole gap of an electromagnet. The light reflected from the crystal passed back through the analyzer to be detected by a photodiode. The electrical signal was measured by a lock-in circuit. We measured the rotation of the plane of light polarization produced by application of a transverse magnetic field for different sample and magnetic field orientations and light polarization. Two types of electromagnets were used for this purpose. One of them produced a horizontal magnetic field from -1.5 to 1.5 T in the plane of the sample ($\mathbf{H}\|\mathbf{x}$). The sample was rotated in the magnet gap about the **k** direction within azimuthal angles δ varied from 0 to 360°. This magnet was employed to study the field dependences of the rotation of the plane of polarization. The other magnet generated a dc magnetic field $H\sim 0.2$ T ($\mathbf{H}\perp\mathbf{k}$) and could be rotated about the z axis within the azimuthal angles φ from 0 to 360°. The polarization of incident light θ was determined by the polarizer orientation and was variable from 0 to 360°. As shown later, using a rotating magnetic field offers the possibility of separation of effects odd and even in magnetization in films exhibiting spontaneous optical anisotropy. Figure 1a shows schematically the mutual orien-

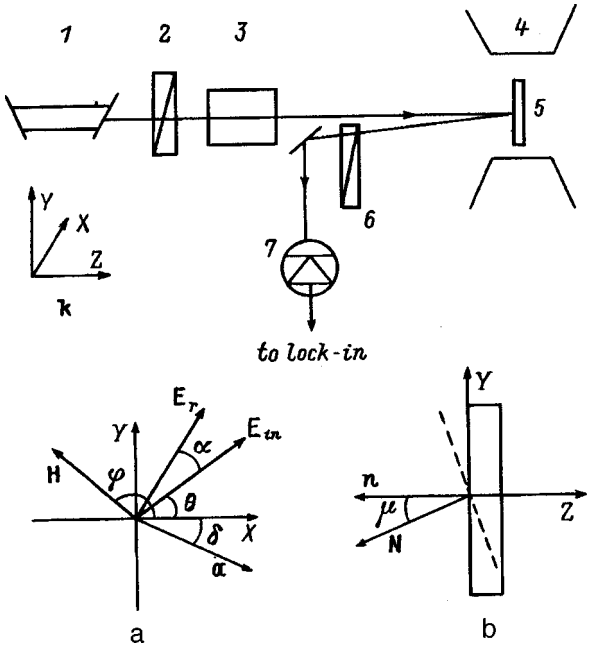

FIG. 1. Schematic diagram of experimental arrangement. *1* — laser, *2* — polarizer, *3* — modulator, *4* — magnet, *5* — sample, *6* — analyzer, *7* — photodiode, *XYZ* -laboratory frame. a — mutual arrangement of magnetic field **H**, incident ($\mathbf{E}_{in}$) and reflected ($\mathbf{E}_r$) polarization, and vector **a** characterizing sample orientation; b — orientation of the easy magnetic-anisotropy plane and film plane. **N** — normal to the magnetic anisotropy plane, **n** — normal to the film plane.

tation of the incident light, magnetic field, and sample azimuth. The sensitivity of measuring the rotation of the plane of polarization was $\sim 1''$.

All MnAs/Si(111) heterostructures were MBE grown. To obtain an atomically clean surface with a 7×7 superstructure, Si(111) substrates were loaded after a standard chemical treatment into the growth chamber, where the SiO_2 surface layer was evaporated by heating for 1–2 min at 1250 °C. To reduce the lattice mismatch between the substrate and the film, a pseudomorphic CaF_2 buffer layer was grown between them by a two-stage technique.[10] The crystal structure of the substrate and the epitaxial growth of the buffer layer and of the ferromagnetic film were monitored *in situ* by RHEED (electron energy 15 keV). The RHEED patterns observed at the [110] and [112] azimuths exhibited streaks characteristic of single-crystal layers with an atomically smooth surface. The MnAs film thickness was measured with a profilometer. In structures 702–743 (Table I), the manganese arsenide was grown at 300 °C. The degree of perfection and the type of crystal structure of the films under study were derived from x-ray diffraction measurements performed within a broad range of angles.[11] To protect the structures thus grown from the adverse effect of ambient air, they were coated with several monolayers of CaF_2. The parameters of the films under study are listed in Table I.

TABLE I. Film parameters.

Film No.	Si(111) substrate misorientation	Film thickness, nm	Presence of MnAs(1011)
702	2′	750	−
703	4°	400	−
740	9′	190	+
741	9′	180	+
742	7′	130	+
743	7′	190	+

2. RESULTS OF EXPERIMENT

In all the samples studied, with the exception of sample 702, application of an in-plane magnetic field results in a rotation of the plane of light polarization which is odd in magnetic field. The angle of rotation α depends on the sample azimuth δ. Figure 2 shows field dependences of the rotation of the plane of polarization for film 703 measured for three values of δ. For $\delta=90$ and 270°, the $\alpha(H)$ rela-

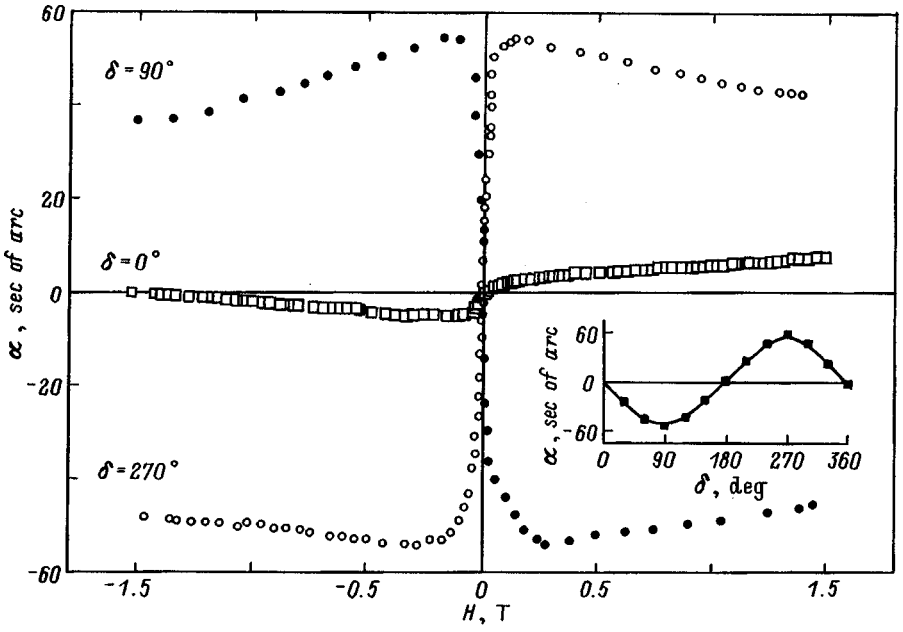

FIG. 2. Field dependence of the turn of the plane of polarization α for different orientations of film 703. The inset shows the angular dependence of the jump $[\alpha(H)-\alpha\times(-H)]/2|_{H\to0}$.

TABLE II. Parameters A and B, easy-plane misorientation angle μ, and spontaneous optical anisotropy of the films under study (error of parameter determination not above 10%).

Film No.	A, arcsec	B, arcsec	μ, deg	Spontaneous optical anisotropy α_m, arcsec
702	0	30	0	<20
703	55	30	4.0	300
740	25	9	1.1	600
741	27	9	1.8	600
742	32	10	1.1	350
743	28	9	1.3	150

tions have opposite signs and are characterized by strong variation within the range $-0.2<H<0.2$ T and a small decrease of α for fields $|H|>0.2$ T. There is practically no $\alpha(H)$ dependence for $\delta=0$. The orientational dependence of the jump $[\alpha(+H)-\alpha(-H)]/2|_{H\to 0}$ derived by extrapolation from the high-field region is well fit by the $\alpha=A\sin\delta$ relation (see inset in Fig. 2). The value of A was different for different films and varied from 0 to 55′ (see Table II).

Figure 3 displays the orientational dependence $\alpha(\varphi)$ obtained by varying the azimuth φ of the magnetic field $H=0.2$ T for sample 703. The pattern exhibits a 360° periodicity and can be described by a combination of harmonics of the first and second order in angle φ:

$$\alpha(\varphi)=A'\sin(\varphi+\psi)+B\sin(2\varphi+\xi), \quad (1)$$

where A' and B are parameters, and ψ and ξ are the phases of the first and second harmonics, respectively. The quantity A' coincides in absolute magnitude with the value of A derived from the field dependences $\alpha(H)$. It should be noted that the $\alpha(\varphi)$ relation depends substantially on sample orientation δ and light polarization θ. Nevertheless, it is fit quite well by Eq. (1) for any δ and θ. As follows from calculations, δ and θ affect the phases ψ and ξ of the first and second harmonics, whereas their amplitudes A' and B practically do not vary.

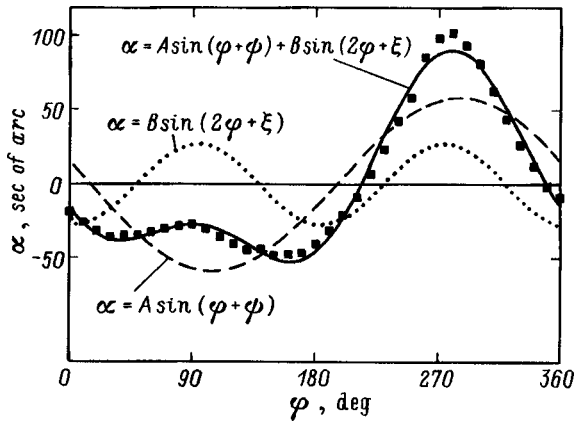

FIG. 3. The turn of the plane of polarization α vs magnetic-field azimuth φ in film 703 for $\delta=170°$ and $\theta=45°$. Solid line — plot of Eq. (1), and the dashed and dotted lines refer to the first and second harmonic contributions, respectively.

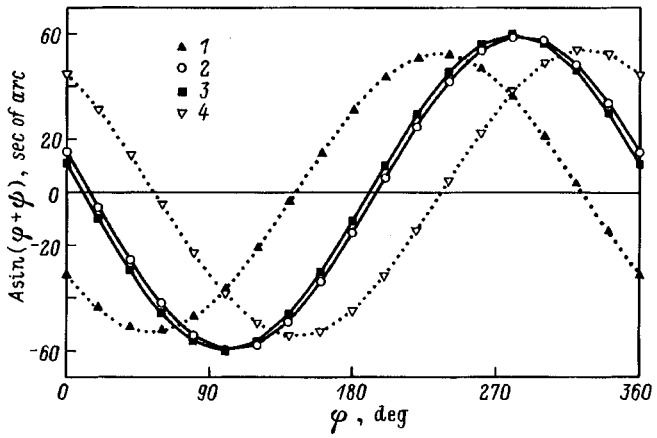

FIG. 4. Angular dependences $A\sin(\varphi+\psi)$ for film 703 [δ (deg), θ (deg)]: *1* — 125, 45; *2* — 170, 45; *3* — 175, 25; *4* — 215, 45.

Figure 4 presents the angular dependences $A'\sin(\varphi+\psi)$ constructed for various δ and θ. One readily sees that the magnitude of ψ is determined by the sample azimuth δ and does not depend on the azimuth of incident polarization θ.

Figure 5 plots $B\sin(2\varphi+\xi)$ relations for different δ and θ. Unlike ψ, the quantity ξ does not depend on δ while varying with θ. The quantity $B\sin(2\varphi+\xi)$ reaches a maximum when the angle between the incident polarization and magnetic field is 45°.

3. DISCUSSION OF RESULTS

The field and orientational dependences $\alpha(H,\varphi,\delta,\theta)$ presented in the preceding Section show that rotation of the plane of polarization in $MnAs/CaF_2/Si(111)$ films observed under normal incidence is determined by effects even and odd in magnetic field. The odd-in-H field dependences $\alpha(H)$ (Fig. 2) suggest that transverse magnetic field $\mathbf{H}\perp\mathbf{Z}$ induces a magnetization projection M_z on the light propagation direction $\mathbf{k}$, which gives rise to a polar Kerr effect. The field-induced projection M_z depends on the magnetic field azimuth φ. This behavior can be explained if one takes into

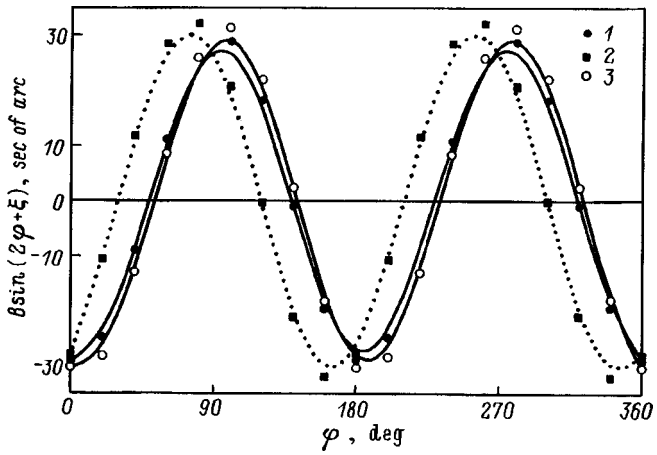

FIG. 5. Angular dependences $B\sin(2\varphi+\xi)$ for film 703 [δ (deg), θ (deg)]: *1* — 0, 45; *2* — 45, 25; *3* — 45, 45.

account the magnetic anisotropy of the films. It is known that at $T=294$ K MnAs single crystals have a hexagonal structure described by space group D_{6h}^4. Below the Curie temperature $T_c=315$ K, the magnetic moment of MnAs lies in the plane perpendicular to the six-fold axis, which corresponds to the easy-plane–type magnetic anisotropy.[12] While MnAs/CaF_2/Si(111) films also have an easy-plane anisotropy, the normal **n** to their surface does not, as a rule, coincide for some reason with the normal to the easy plane of magnetic anisotropy **N**, and makes an angle μ with the latter ($\cos\mu=\mathbf{N}\cdot\mathbf{n}$) (see Fig. 1b). In this case the equilibrium orientation of magnetization **M** in a magnetic field **H** is determined by the minimum of the potential

$$W=K_a(\mathbf{mN})^2-\mathbf{MH}+2\pi(\mathbf{Mn})^2, \tag{2}$$

where K_a is the magnetic anisotropy parameter ($K_a>0$), and **m** is the unit vector in the direction of magnetization. The magnetization **M** will lie exactly in the film plane if $\mathbf{N}\cdot\mathbf{H}=0$. In this case there will be no polar Kerr effect. If $\mathbf{N}\cdot\mathbf{H}\neq 0$, magnetization leaves the plane, and the deviation from the plane is the largest for the maximum value of $\mathbf{N}\cdot\mathbf{H}$. The sign of the angle made by the magnetization with the film plane is determined by that of the field, which means that the sign of the projection M_z varies with varying sign of magnetic field **H**. For fields higher than the saturation field and much weaker than the anisotropy field $H_a\sim 2$ T, the dependence of the polar Kerr effect, which is proportional to M_z, on magnetic-field azimuth φ is described by the function $A'\sin(\varphi+\psi)$. The value of ψ is determined by sample orientation, i.e. by the angle δ, namely, $\psi=-\delta$. For $\varphi=0$, the angular dependence of the polar Kerr effect obtained by rotating the sample has the form $A\sin\delta$, and this is what is observed experimentally (see the inset in Fig. 2). Based on the known magnitude of the polar Kerr effect in MnAs,[5,6] as well as on measurements of this effect made on the films under study for $\mathbf{M}\|\mathbf{n}$, we obtained for μ values ranging from 0 to 4.0° (Table II).

If the rotation of the plane of polarization under normal incidence was determined only by the polar Kerr effect, then the rotational anisotropy measured with the magnetic field swept in the film plane would be proportional to $\sin(\varphi+\psi)$ and would not depend on the incident polarization. The relations shown graphically in Fig. 4 show, however, that this is not so. The rotational anisotropy is approximated by function (1).

We are going to show that the second term in Eq. (1) is connected with quadratic-in-**M** rotation of the plane of polarization. Let the light impinge normally on the film, $\mathbf{k}\|\mathbf{n}$. The axis Z of the laboratory frame coincides with the film normal **n**. Let us assume that for $\mathbf{M}=0$ the cross section of the optical indicatrix is a circle, i.e. that $\tilde{n}_x=\tilde{n}_y$, where $\tilde{n}_x$ and $\tilde{n}_y$ are complex refractive indices for the waves polarized along the X and Y axes, respectively. This assumption is valid for (0001)-type MnAs films, because their optical axis is perpendicular to the film plane. We neglect here the weak optical anisotropy, which is observed in these films in the absence of magnetic field and will be dealt with later. Consider the dielectric permittivity tensor in space group D_{6h}^4 with the magnetization **M** directed along the X axis in the film plane, and with inclusion of terms linear and quadratic in magnetization:

$$\varepsilon_{ij}=\begin{bmatrix}\varepsilon_{xx}+aM_x^2 & 0 & 0\\ 0 & \varepsilon_{xx}-aM_x^2 & i\beta M_x\\ 0 & -i\beta M_x & \varepsilon_{zz}\end{bmatrix}. \tag{3}$$

All ε_{ij} parameters are complex. It can be shown that the cross section of the optical indicatrix by a plane perpendicular to $\mathbf{k}$ ($\mathbf{k}\|\mathbf{z}$) has in this case elliptical shape, with one of the major axes along the magnetization vector **M**, i.e. $\tilde{n}_x\neq\tilde{n}_y$. Then the matrix of light reflection from the film will take on the form[13]

$$R=\begin{bmatrix}1+\rho\cos 2\theta & \rho\sin 2\theta\\ \rho\sin 2\theta & 1+\rho\cos 2\theta\end{bmatrix}, \tag{4}$$

where $\rho=(\tilde{n}_x-\tilde{n}_y)/(\tilde{n}_{xy}-1)$, θ is the azimuth of the incident polarization reckoned from one of the principal directions of the indicatrix, which in this particular case is along **M**, and $\tilde{n}_j=n_j-ik_j$. For $\Delta n\ll n$ and $\Delta k\ll k$, we have $\rho=(\Delta n-i\Delta k)/[(n-ik)^2-1]$. The rotation of the plane of polarization α under normal incidence[14] derived for the case of $|\rho|\ll 1$ and $|\alpha|\ll 1$ can be written

$$\alpha=\mathrm{Re}(\rho)\sin 2\theta. \tag{5}$$

As seen from Eq. (6), taking into account terms linear and quadratic in **M** results in a rotation of the plane of polarization whose anisotropy is described by $\sin 2\theta$, with the phase of the angular dependence of the effect being determined by the angle between the incident polarization $\mathbf{E}_{in}$ and the magnetization vector **M**. The effect reaches a maximum at $\theta=\pm 45°$, in full agreement with the experiment. The quantities Δn and Δk are determined by parameters a and β:

$$\Delta n\approx\frac{2}{n}\,\mathrm{Re}\left(2aM_x^2+\frac{\beta^2M_x^2}{\varepsilon_{zz}}\right), \tag{6}$$

$$\Delta k\approx\frac{2}{n}\,\mathrm{Im}\left(2aM_x^2+\frac{\beta^2M_x^2}{\varepsilon_{zz}}\right). \tag{7}$$

Estimates made using the values of n and k from Ref. 15 and the magnitude of the polar Kerr effect for $\mathbf{M}\|\mathbf{k}$ show that the main contribution to Δn and Δk is due to the term $2aM_x^2$, whereas the $\beta^2M_x^2/\varepsilon_{zz}$ contribution is an order of magnitude smaller. The parameters A and B characterizing the odd and even magnetization contributions to the rotation of the plane of polarization in the films are presented in Table II. The error in determining parameters A and B, as well as the angle μ, is $\sim 10\%$.

Thus the rotation angle of the plane of polarization α induced by magnetization **M** in MnAs/CaF_2/Si(111) epitaxial films in a transverse magnetic field and observed under normal light incidence is associated with the polar Kerr effect because the film plane does not coincide with the easy magnetic-anisotropy plane, and with the manifestation of the quadratic-in-**M** terms in the dielectric permittivity tensor ε_{ij}. The deviation of the easy magnetization plane from the film plane can originate from substrate misorientation or from

imperfections in the crystal structure of the films. X-ray diffraction analysis of films 702 and 703 showed them to contain only MnAs(0001). The misorientation angle between the substrate plane normal **n** and the [111] plane in Si in these films is $\approx 2'$ and 4°, respectively (see Table I). The angles between the normal to the easy magnetic-anisotropy plane **N** in these films and the film normal **n** are the same (Table II). The rotation angle of the plane of polarization quadratic in magnetization is the same for the films. In films 740–743, the deviations of the Si surface from the (111) plane are small enough, $\approx (6-9)'$, but nevertheless they exhibit noticeable, $\approx (1-2)°$, deviations of the easy plane from the film plane. This can be attributed to the presence in the films of small MnAs regions with (1011) orientation, which were detected by x-ray diffraction. Let $\mathbf{M}_1$ denote the magnetization of the MnAs(0001) regions, V_1 the fractional volume of these regions, and $\mathbf{M}_2$ and V_2, the magnetization and volume of the MnAs(1011) regions, with $|\mathbf{M}_1| = |\mathbf{M}_2|$. In a transverse field the ''normal'' phase does not contribute to the Kerr effect, because $\mathbf{M}_1$ lies in the film plane. The (1011) phase can provide a contribution, because the easy plane makes here an angle of 57° with the film plane, and the maximum magnitude of this contribution is proportional to $\beta M_2 V_2 \sin 57°$. When measuring the Kerr effect in a longitudinal magnetic field, where $\mathbf{M}_1, \mathbf{M}_2 \| \mathbf{n}$, the rotation of the plane of polarization is proportional to $\beta (M_1 V_1 + M_2 V_2)$. One can readily show that already 3% MnAs(1011) can account within such a simple model for the observed value of A in films 740–743. Note that the angles of deviation of the easy plane given in Table II for films 740–743 in this case should be considered as ''effective'', i.e., as obtained by averaging the directions of **M** over the film. The quadratic-in-**M** turn of the plane of polarization in films 740–743 is the same and about a factor three smaller than that in films 702 and 703. Such a difference in magnitude of the quadratic effect may be due to different magnetic moments in films 702–703 and 740–743, which is supported by measurements of the magnetic moments of the films and of the polar Kerr effect for $\mathbf{M} \| \mathbf{n}$.

The deviation of the Si surface orientation from the (111) plane and the presence of even small amounts of MnAs(1011) may become manifest also in an optical anisotropy of the films, which is observed in the absence of magnetic field and is not connected with the magnetic moment. The magnitude of this anisotropy was determined by measuring the angular dependences $\alpha(\delta) = \alpha_m \sin 2\delta$ with the sample rotated in zero magnetic field. The amplitude α_m is presented in Table II for different samples. The smallest spontaneous optical anisotropy was observed in film 702, where no additional phase was detected, and where the deviation of the Si surface from the (111) plane is the smallest. Note that the spontaneous optical anisotropy present in films 703–743 does not manifest itself in the field dependences $\alpha(H)$ when the magnetic field direction is fixed, because in such measurements the reckoning for any δ is done from $H = 0$. In experiments with a sweeping magnetic field, it can become seen in the $\alpha(\varphi)$ relations in the form of a φ- independent pedestal, which can be readily eliminated by including a constant term in Eq. (1). Note that taking into account spontaneous optical anisotropy in deriving Eqs. (6) and (7) turns out to be insignificant, because it yields second-order corrections.

It should be pointed out that because of the large light absorption coefficient of MnAs films [$k \approx 2.2$ (Ref. 15)] the magneto-optic phenomena in reflection are not determined by the whole volume of the film but rather by a layer about 20 nm thick.[9]. In principle, the structural properties of the surface layer, such as the fractional volumes of MnAs regions with different orientations, the stresses, and dislocation densities may differ noticeably from those of the bulk, which, in its turn, may entail a difference between the surface and volume magnetic parameters of films. It would be of interest to carry out a comparative analysis of the magnetic parameters obtained by volume magnetic and magneto-optic methods.

The main results of this work is determination of the type of magnetic anisotropy in MnAs/CaF_2/Si(111) heterostructures by the magneto-optical method. We have shown that MnAs epitaxial films have an easy-plane–type anisotropy, which is perpendicular to the [0001] direction in MnAs. The deviation of the easy plane from the film surface plane is associated with the deviation of the Si surface from the (111) plane and with the presence in films of a small amount of MnAs with the (1011) basal plane. Thus this technique can be used for characterization of ferromagnet-semiconductor–type heterostructures. Because the depth probed by the magneto-optic method depends on the light wavelength, spectral studies of the rotation of the plane of polarization in reflection may provide information on the variation of magnetic properties throughout the film thickness.

We have detected a quadratic-in-magnetization turn of the plane of polarization under normal reflection of light from MnAs. Spectral studies of this phenomenon, besides the polar Kerr effect, can be used to probe the electronic structure of MnAs films.

The authors consider it a pleasure to thank R. V. Pisarev for fruitful discussions and N. F. Kartenko for the x-ray diffraction measurements.

Support of the Russian Fund for Fundamental Research and of the ''Fundamental Spectroscopy'' Program is gratefully acknowledged.

[1] G. A. Prinz, Science **250**, 1092 (1990).
[2] M. Tanaka, Mater. Sci. Eng., B **31**, 117 (1995).
[3] K. Akeura, M. Tanaka, M. Ueki, and T. Nishinaga, Appl. Phys. Lett. **67**, 3349 (1995).
[4] K. Akeura, M. Tanaka, T. Nishinaga, and J. De Boeck, J. Appl. Phys. **79**, 4957 (1996).
[5] H. Ikekame, Y. Yanase, M. Akita, Y. Morishita, and K. Sato, J. Magn. Soc. Jpn. **20**, 153 (1996).
[6] Y. Morishita, K. Iida, J. Abe, and K. Sato, *Conference Digest 15th International Coll. Magnetic Films and Surfaces* (Kyoto, 1997), p. 154.
[7] F. V. Lisovskiĭ, E. G. Mansvetova, and V. I. Shapovalov, Opt. Spektrosk. **47**, 1082 (1979) [Opt. Spectrosc. **47** 601 (1979)].
[8] G. S. Krinchik, *Physics of Magnetic Phenomena* [in Russian] (MGU, 1985), p. 321.
[9] V. E. Zubov and A. D. Modestov, Opt. Spektrosk. **82**, 64 (1997).

[10] N. S. Sokolov, J. C. Alvarez, and N. L. Yakovlev, Appl. Surf. Sci. **60/61**, 421 (1992).
[11] A. G. Banshchikov, M. V. Baydakova, B. P. Zakharchenya, K. Saito, N. S. Sokolov, S. M. Saturin, and M. Tanaka, in *Proceedings of the International Symposium on Nanostructures: Physics and Technology* (St. Petersburg, Russia, 1997), p. 288.
[12] G. E. Bacon and R. Street, Nature (London) **175**, 518 (1955).
[13] A. Burau, H.-J. Weber, and V. V. Pavlov, J. Opt. Soc. Am. A **13**, 164 (1996).
[14] R. M. A. Azzam and N. M. Bashara, *Ellipsometry and Polarized Light* [North-Holland, Amsterdam, 1977; Mir, Moscow, 1981].
[15] A. M. Stoffel and J. Schneider, J. Appl. Phys. **41**, 1405 (1970).

Translated by G. Skrebtsov